bbviv5
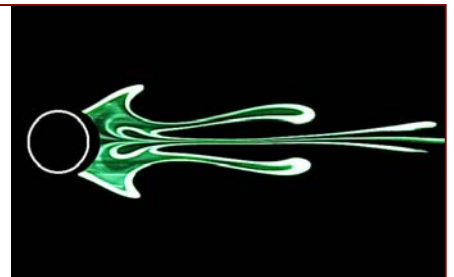
Fifth Conference on Bluff Body Wakes and Vortex-Induced Vibrations

Book of Papers

12-15 December 2007
Costa do Sauípe, Brazil

Proceedings of the

Fifth Conference on
Bluff Body Wakes and Vortex-Induced Vibrations

– BBVIV5 –

Costa do Sauípe, Bahia, Brazil

12 – 15 December 2007

Editors:

T. Leweke, J.R. Meneghini, C.H.K. Williamson

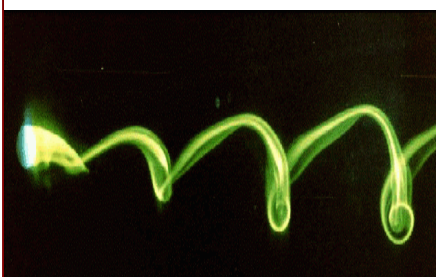# Fifth Conference on Bluff Body Wakes and Vortex-Induced Vibrations

Chairmen:

T. Leweke	(IRPHE/CNRS, France)
J. R. Meneghini	(University of Sao Paulo, Brazil)
C. H. K. Williamson	(Cornell University, USA)

Scientific Committee:

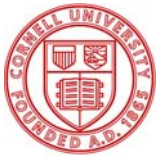|	
P. Anagnostopoulos	(University of Thessaloniki, Greece)
P. W. Bearman	(Imperial College, UK)
E. de Langre	(Ecole Polytechnique, France)
R. N. Govardhan	(Indian Institute of Science, India)
K. Hourigan	(Monash University, Australia)
G. Em Karniadakis	(Brown University, USA)
A. Leonard	(California Institute of Technology, USA)
P. A. Monkewitz	(EPF Lausanne, Switzerland)
C. Norberg	(Lund Institute of Technology, Sweden)
M. P. Païdoussis	(McGill University, Canada)
D. O. Rockwell	(Lehigh University, USA)
M. S. Triantafyllou	(Massachusetts Institute of Technology, USA)

Local Organizers:

E. Casaprima	(Petrobras, Brazil)
C. Morooka	(University of Campinas, Brazil)
A. da Silveira Neto	(Federal University of Uberlândia, Brazil)
K. Nishimoto	(University of São Paulo, Brazil)
A. L.C. Fujarra	(University of São Paulo, Brazil)
C. P. Pesce	(University of São Paulo, Brazil)
F. Saltara	(University of São Paulo, Brazil)
J. H. Silvestrini	(Pontifical Catholic University of Rio Grande do Sul)
S. H. Sphaier	(Federal University of Rio de Janeiro, Brazil)

Fifth Conference on Bluff Body Wakes and Vortex-Induced Vibrations

Supported by:

WELCOME TO YOU ALL IN COSTA DO SAUIPE !

Programme

* presenting author
(P) poster

9:00 – 12:00	**Registration**	
12:00 – 2:00	**Lunch**	
2:00 – 2:40	**Opening Lecture** by *Franz S. Hover *Statistical tools in modeling VIV of distributed structures*	1
2:40 – 3:20	**Invited Lecture** by *J. Michael R. Graham, Nektarios Bampalas *Strip theory prediction of marine riser VIV and hydrodynamics of clashing*	3
3:20 – 3:50	**Break**	
3:50 – 5:10	***Session*: VIV – 1 (Controlled Vibration)**	
	*Willden, McSherry, Graham *Prescribed cross-stream oscillations of a circular cylinder at laminar and early turbulent Reynolds numbers*	7
	*Morse, Williamson *Understanding mode transitions in vortex-induced vibration using controlled vibration*	11
	*Szwalek, Larsen *Reynolds number effects on A/D using forced sinusoidal oscillations*	15
	*Kaiktsis, Triantafyllou *Computational study of hydrodynamic forces on a cylinder vibrating transversely and in-line to a steady stream*	19
5:10 – 5:50	**Invited Lecture** by *Jacques Magnaudet *Spheroidal bubbles as an archetype of light, freely-moving axisymmetric bodies*	25
5:50 – 6:50	***Session*: Wakes – 1 (Spheres)**	
	Miedzik, Gumowski, *Goujon-Durand, Bouchet, Jenffer, Wesfreid *Wake behind a sphere in early transitional regimes*	27
	*Horowitz, Williamson *Dynamics and wake patterns of rising and falling spheres*	31
	*Prahl, Revstedt, Fuchs *The interaction between two spherical particles in an oscillatory flow*	35
7:30	**Reception**	

9:00 – 9:40	**Invited Lecture** by *J. Kim Vandiver *Insights on the Flow-induced Vibration of flexible cylinders*	39

9:40 – 10:55   ***Session*: VIV – 2 (Risers)**

*Lima, Meneghini, Flatschart, Mourelle, Casaprima   43
*Fatigue analysis of a marine SCR (Steel Catenary Riser) due
to Vortex-Induced Vibration*

*Fujarra, Pesce, Nishimoto, Cueva, Faria   47
Non-stationary VIM of two mono-column oil production platforms

*Swithenbank, Marcollo, Vandiver   51
*Time-sharing of frequencies in high-mode number Vortex
 Induced Vibrations*

*Pereira, Maeda, Morooka, Uto   57
(P) Model tests of Self Standing Hybrid Riser in deep-sea basin

*Morooka, Franciss, Matt, Pereira   59
(P) Dynamical analysis of deep water rigid risers: VIV effects

Kato, Uto, Masanobu, *Suzuki, Hiriyama, Mochida   63
*(P) Riser motion estimation of oil production system for ultra
 deep water*

10:55 – 11:25   **Break**

11:25 – 12:05	**Invited Lecture** by *Jean-Marc Chomaz, P. Meliga, D. Sipp *Unsteadiness in the wake of the sphere: receptivity and weakly non-linear global stability analysis*	67

12:05 – 1:30   ***Session*: Wakes – 2 (Stability and Ginzburg-Landau Analyses)**

*Cadot, Thiria, Beaudoin   71
*Sensitivity of global mode instability to local and stationary
 disturbances in a turbulent wake*

*Silveira, Martins, Aranha   75
*A qualitative study of the response of the Ginzburg-Landau
equation when coupled to the structural model of a submerged cable*

Gioria, *Carmo, Meneghini   79
Floquet stability analysis of the flow around an oscillating cylinder

*Chomaz, Donnadieu, Ortiz   85
*Three-dimensionnal instabilities and transient growth of trailing
vortices in homogeneous and stratified flows*

Burr, *Aranha   89
(P) The complex Ginzburg-Landau equation and Norberg's lift crisis

6:35 – 7:15   **Session: Wakes – 4**

Bourguet, Braza, Vos, Perrin, Harran
Anisotropic Organized Eddy Simulation approach for strongly detached unsteady flows

Martinat, Hoarau, Dehaeze, Braza
Numerical simulation of the flow in the wake of Ahmed body using Detached Eddy Simulation and URANS modeling

Friday 14 December 2007

9:10 – 10:45   **Session: Wakes – 5**

10:45 – 11:05   **Break**

11:05 – 1:00   ***Session*: VIV – 4 (Inclined Cylinders and Suppression)**

8:00 – 10:00   **Banquet**

Statistical Tools in Modeling VIV of Distributed Structures

Franz Hover
Department of Mechanical Engineering
Massachusetts Institute of Technology
Cambridge, MA 02139 USA

The rich history of vortex-induced vibrations research is one in which many of the engineered systems suffering from the phenomenon are distributed structures, such as wires and pipes, whereas deep understanding of the underlying fluid mechanics which lead to VIV is well-developed only for certain laboratory systems, in particular the finite-length, rigid circular cylinder in uniform crossflow.

For ocean risers and mooring lines, multiple structural modes are present, comprising both standing wave shapes (real modes, having stationary phase) and traveling waves (complex modes having nonstationary phase); current tools for VIV prediction in such structures generally focus on the participation of each mode, subject to a net zero power flow along the entire length. High-fidelity vibration measurements along the length, which are becoming feasible even in full-scale deployed systems with modern instrumentation, however, often tell a different story. For certain conditions, only one mode is active, but in many other cases, the motion is exceedingly complex, with strong variability in both the in-line and cross-flow amplitudes as well as in their relative phase, and indicative of the combined, sporadic participation of many modes. The figure below indicates the richness of the response from a towed riser experiment. A recent reference which highlights the riser VIV prediction problem is Chaplin *et al*. (2005, *Blind predictions of laboratory measurements of vortex-induced vibrations of a tension riser*, Journal of Fluids and Structures, 21, 25-40).

One of the major design questions in large-scale systems is fatigue or damage rate, and a key observation is that fatigue damage estimates do not require a consistent modal model. Indeed, a time trace of actual motion allows an estimate of damage rate, as does a probabilistic description of that motion (e.g., spectrum). In terms of fatigue prediction in risers, what is really needed is an approach for describing the statistics of response and damage, given a description of the flow environment, a basic model of the fluid mechanics, and a nominal structural model. Reconciliation using measured data is a necessity.

Modern tools for stochastic simulation are appropriate to this problem, with the goal that such simulations should characterize both extreme conditions and spectrum-like quantities useful for damage prediction. Dynamical systems such as risers admit an expansion of probabilistic modes using orthogonal polynomials, the basis of Weiner's polynomial chaos (Ghanem and Spanos, 1991, *Stochastic finite elements*. Mineola, NY: Dover). This approach applies to cases with a number of random parameters less than five or so, and provides actual probability density functions of the system response or

functions of the response. For more complex systems and those with random dimension of order ten, many versions of collocation are available. These methods involve multidimensional quadrature rules for evaluating integrals, and hence statistical moments. Finally, systems having discontinuities in the parameters, or with very large random dimension, demand Monte Carlo techniques. Adaptivity plays a central role in many of these techniques, and can have a dramatic benefit.

Using these tools, we study the range and variability of riser response, as functions of the underlying parameters. The calculations employ a full structural model, with space and time uncertainty in the added mass and lift coefficients. Given the description of motion which results, we also demonstrate how to calculate explicitly fatigue damage on the riser.
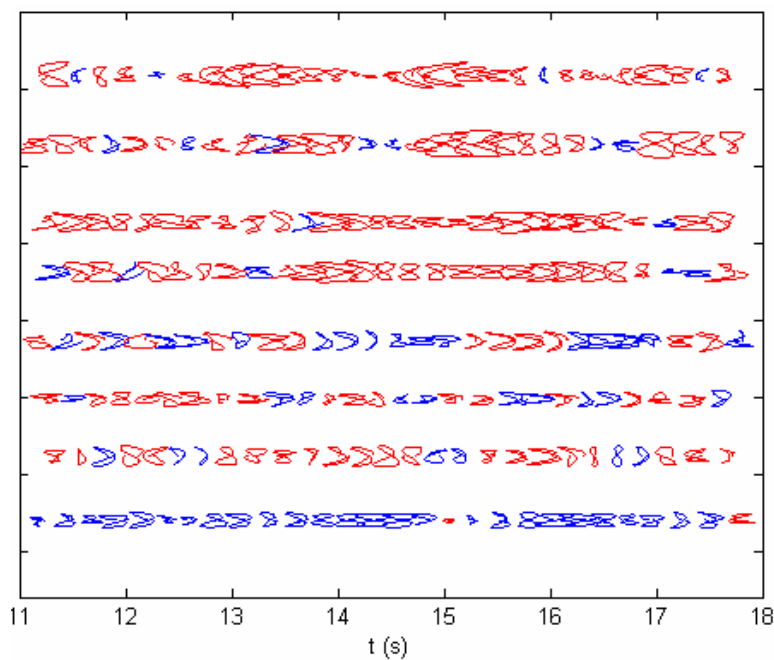
The figure shows riser motion orbits as a function of time; the vertical axis is the spanwise location on the riser, and the horizontal axis is time. Flow is from the left to the right. The motions are characterized by high variability in both time and space, although crescents and figure-eights are prominent. Red and blue colors indicate opposing directions of motion.

Strip Theory Prediction of Marine Riser VIV and Hydrodynamics of Clashing

Michael Graham and Nektarios Bampalas
Department of Aeronautics,
Imperial College,
London SW7 2AZ, UK.

Abstract.

This lecture examines two aspects of riser hydrodynamics. The first concerns the adequacy and related results of strip theory representation of vortex-induced-vibration (VIV) when a long riser pipe of low mass ratio subject to a marine current vibrates in a relatively high structural mode with vortex lock-in over part of its length.

A large number of simulations of VIV have been carried out using the strip theory code VIVIC applied to a long circular, elastic pipe. VIVIC computes locally evolving two-dimensional flow fields from a vorticity-velocity formulation of the Navier-Stokes equations at a large number of sections coupled to a finite (beam) element analysis of the structural dynamics of the pipe. For Reynolds numbers which are sub-critical but above the two-dimensional laminar regime small-scale three-dimensionality present in the wake of the pipe is modelled by a sub-grid eddy viscosity which, with a suitable value of the coefficient, can give quite good agreement for amplitudes and frequencies of response on a straight pipe when lock-in occurs. A comparatively large value of the coefficient is required to achieve this and this will be discussed. On the other hand if the pipe is substantially curved significant differences arise between the application of strip-theory when compared with fully three-dimensional computations. In particular for a pipe curved in-plane with the flow strip theory predicts no difference between a case when the pipe is concave towards the incident flow and a case of the same curvature but convex, whereas three-dimensional computations show a degree of suppression of vortex shedding in the former case not seen in the latter. These differences are reduced when the pipe is subject to transverse vibration causing lock-in of the vortex shedding.
Computations, using strip theory, of long flexible risers which have a low mass ratio and undergo high mode transverse vibration often show multi-modal response at a single vortex shedding frequency. This is possible because lower modes become locked-in to the dominant mode due to a reduction in added mass. Computations of forced vibration cases have been carried out to examine the effects on added mass and transverse excitation/damping when a mode outside the lock-in region vibrates in the presence of a second locked-in mode.

The second part of the lecture examines more closely the hydrodynamic forces that arise when a pair of risers in a current undergo motion excited by VIV and/or wake galloping which causes them to clash. The resulting flows are studied in the ideal situation of two circular cylinders impacting two-dimensionally at a line of contact which is the case causing the largest hydrodynamic forces.

Fifth Conference on Bluff Body Wakes and Vortex-Induced Vibrations (BBVIV 5)
Costa do Sauipe, Bahia, Brazil, 12 - 15 December 2007

3
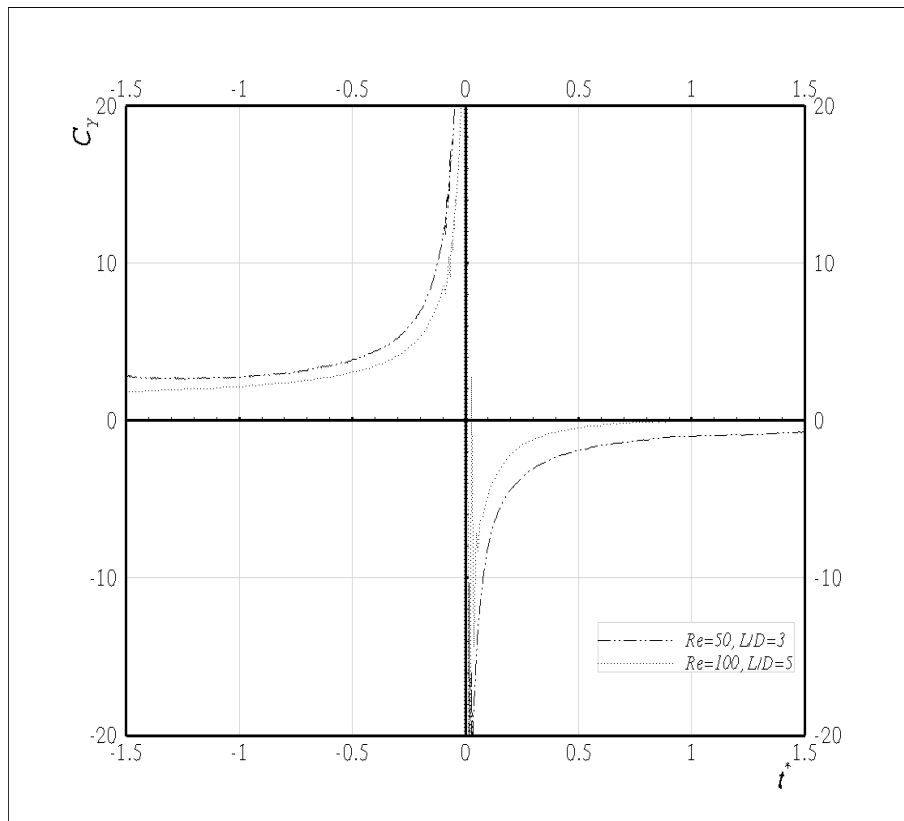
Figure 1. In-line force coefficient on either of a pair of cylinders impacting at constant velocity in a stationary fluid; effect of Reynolds number.

This situation is examined both for inviscid flow in order to investigate the hydrodynamic forces which may occur as contact is approached for very high Reynolds number and for viscous flow using the above code VIVIC with a moving mesh / remeshing system. The force coefficient (of repulsion) in the case of inviscid motion of two cylinders moving towards one another along their line of centres in a stationary fluid is shown to increase as $1/\sqrt{t^*}$ towards impact at $t^* = 0$, where t^* is the non-dimensional time. Viscous flow computations for the same situation show increasing force coefficient with decreasing Reynolds number as shown in Figure 1. In the cases shown the cylinders remain stationary in contact after impact. The more practically relevant situation of two cylinders impacting in the presence of a free stream has also been studied. The phasing and direction of the impact motion in viscous flow with respect to the pre-existing vortex wakes of the cylinders effects the wake development and forces as interaction proceeds and a range of cases have been examined. Figure 2 shows an example of the vortex wakes of a pair of cylinders which are impacting transversely to a uniform stream.
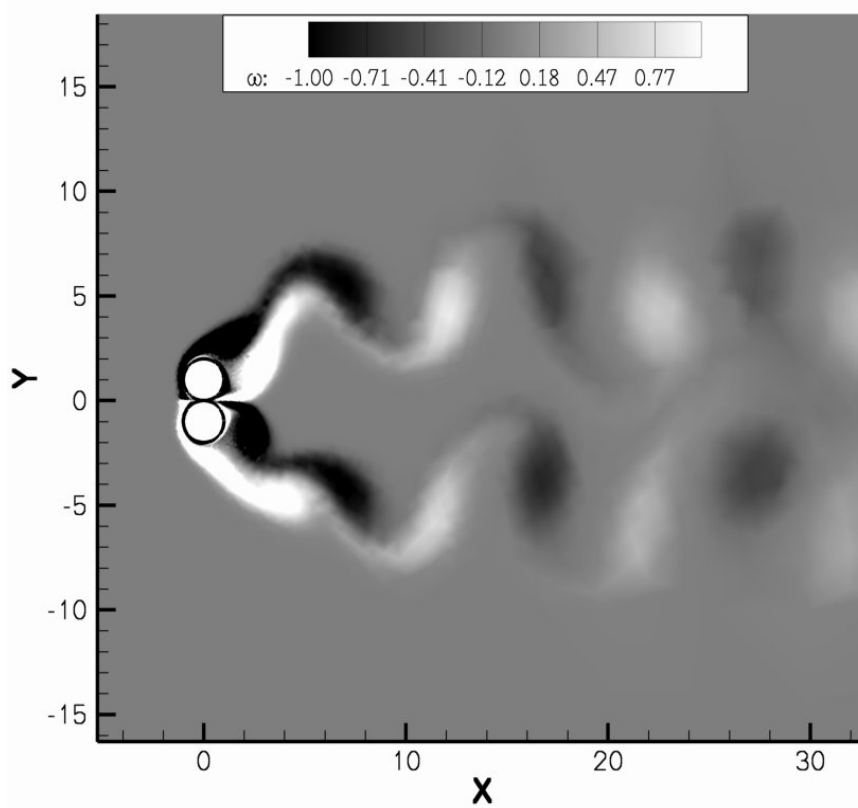
Figure 2. Vortex wakes of a pair of cylinders at the moment of transverse impact in a uniform stream. Velocity ratio = 1.0, Reynolds number = 100.

Prescribed cross-stream oscillations of a circular cylinder at laminar and early turbulent Reynolds numbers

R.H.J. Willden, R.J. McSherry & J.M.R. Graham

Department of Aeronautics,
Imperial College London, SW7 2AZ, U.K.
e-mail: r.willden@imperial.ac.uk

Abstract

Direct Numerical Simulations are conducted in two and three dimensions of the flow past a circular cylinder undergoing prescribed cross-stream oscillations whilst subjected to laminar and early turbulent Reynolds number flows. In the case of laminar flows it is found that the contour, through the amplitude-frequency plane, along which no net fluid excitation occurs matches closely the response envelopes reported from investigations of the free cross-stream vibrations of lightly damped cylinders. Furthermore, the shape of the contour confirms the existence of hystereses at low and high reduced velocities in free vibration. The early turbulent Reynolds number simulations show that the wake aft of a cross-stream oscillating cylinder can be highly three-dimensional in nature, and that the degree of flow-field three-dimensionality increases with oscillation amplitude as the shedding mode switches from the 2S to the P+S and then to the 2P mode.

1 Introduction

The amplitude and character of flow excited cross-stream vibrations are known to be dependent upon the Reynolds number of the incident flow (Govardhan & Williamson 2006). At Reynolds numbers of less than approximately 200, for which the flow is expected to be laminar and two-dimensional, it is known from experiments (Anagnostopoulos & Bearman 1992) and simulations, that the maximum amplitude of cross-stream vibration is approximately $0.6\,D$, where D is the cylinder diameter. Furthermore, as the Reynolds number is increased a free-to-vibrate cylinder can achieve higher amplitudes of cross-stream vibration; circa $1.0\,D$ at $Re = O(10^4)$, where $Re = UD/\nu$ is the Reynolds number, and U and ν are the flow speed and kinematic viscosity of the fluid.

At low Reynolds numbers the mode of vortex shedding in free cross-stream cylinder vibration is reported to be of the 2S type in which two oppositely signed vortices are shed per oscillation cycle (see for example Shiels *et al.* 2001). At higher vibration amplitudes, only achievable through prescribed cylinder oscillation, the mode of shedding switches to the P+S mode in which a pair of oppositely signed vortices and a single vortex are shed per oscillation cycle (Meneghini & Bearman 1995). At laboratory scale Reynolds numbers, $Re = O(10^3)$ to $O(10^4)$, investigators report that the shedding mode switches from the 2S mode on the initial branch of response to the 2P mode, in which two pairs of oppositely signed vortices are shed per oscillation cycle, on the upper and lower response branches (Govardhan & Williamson 2000). Other, more exotic, shedding modes are reported to occur for amplitude-frequency combinations not achievable in free cross-stream vibration (Williamson & Roshko 1988).

It is often argued that when the cylinder oscillation and vortex shedding frequencies are synchronised, i.e. locked-in, the vortex shedding substantially correlates along the cylinder span rendering the resultant fluid flow predominantly two-dimensional. Whilst it is expected that the flow aft of an oscillating cylinder should remain two-dimensional in the laminar shedding regime, $Re < 200$, the same may not be true at higher Reynolds numbers. Indeed, it has been reported that, contrary to the expectations inferred through lock-in, the spanwise correlation of vortex shedding, and ensuing fluid forces, is much reduced on the upper branch (Hover *et al.* 2004).

The objectives of the present investigation are to study the form, and resulting fluid forces, of the wakes aft of cross-stream oscillating circular cylinders. Direct Numerical Simulations (DNS), i.e. simulations in which all pertinent flow scales are resolved, are conducted in two and three dimensions to simulate laminar, $Re = 100$, and early turbulent, $Re = 300$, flows past circular cylinders undergoing prescribed cross-stream oscillations.

2 Numerical Method

The governing incompressible Navier-Stokes equations are solved using a high accuracy Spectral/hp finite element method (Sherwin & Karniadakis 1995). In the case of two-dimensional simulation the flow is computed on a body fitted unstructured mesh comprising triangular elements across which high order interpolation functions are used to approximate the spatial variation of the flow variables. In the case of three-dimensional simulation spanwise Fourier summations are used to extend the flow-field discretisation along the cylinder span.

The flow is simulated in the body fixed frame of reference by subjecting the cylinder to a time-dependent cross-flow velocity that is equal and opposite to the body's velocity. The body motion, $y(t)$, is prescribed according to:

$$y(t) = A \sin\left(2\pi f_o t\right)$$

where A and f_o are the amplitude and frequency of cylinder cross-stream motion.

The computational mesh extended from $15\,D$ upstream to $40\,D$ downstream of, and to $15\,D$ either side of, the cylinder centre. In the case of two-dimensional simulations the mesh consisted of 437 triangular elements across which 9th order interpolation functions were employed. For three-dimensional simulations the in-cylinder-plane mesh consisted of 2361 triangular elements across which 7th order interpolation functions were used, whilst 32 Fourier modes were used to approximate the spanwise variation of flow variables over a periodic domain of extent $4\,D$. A non-dimensional time step, $\Delta t\,U/D$, of between 0.002 and 0.005 was used for all simulations.
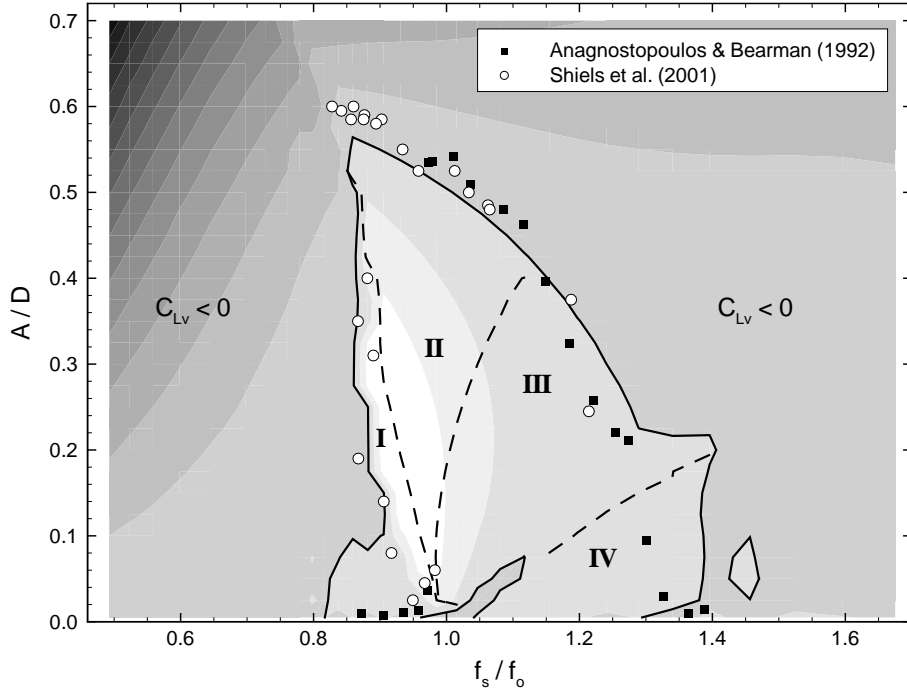
Figure 1: Contours of the lift coefficient in phase with cylinder velocity, C_{Lv}, for a cross-flow oscillating cylinder at $Re = 100$. Light and dark shades are positive and negative, and the solid line depicts $C_{Lv} = 0$. Dashed lines delimit regions of different phase angle, ϕ_o, and vortex phase angle, ϕ_v, within the $C_{Lv}=0$ contour: Region I : $0 < \phi_o < \pi/2$, $0 < \phi_v < \pi/2$, Region II : $0 < \phi_o < \pi/2$, $\pi/2 < \phi_v < \pi$, Region III : $\pi/2 < \phi_o < \pi$, $\pi/2 < \phi_v < \pi$, Region IV : $0 < \phi_o < \pi/2$, $\pi/2 < \phi_v < \pi$. Symbols are from low Reynolds number free vibration experiments and simulations.

3   Prescribed cross-stream oscillations of a circular cylinder at Re = 100

Two-dimensional DNS of the laminar, $Re = 100$, flow past a cross-flow oscillating circular cylinder, have been conducted over a stencil covering a wide range of amplitudes and frequencies of cylinder oscillation; $0.005 \leq A/D \leq 0.7$ and $0.08 \leq f_o D/U \leq 0.34$. The highest stencil density, $\Delta A/D = 0.025$ and $\Delta f_o D/U = 0.005$, was reserved for the vicinity of the primary lock-in region. Particular attention was paid to the variation of the component of the cross-flow lift coefficient in phase with cylinder's velocity, C_{Lv}, which was computed following:

$$C_{Lv} = \hat{C}_{Lo} \sin \phi_o$$

where $\hat{C}_{Lo}$ is the amplitude of $C_{Lo}(t)$, being the component of the lift coefficient at the body oscillation frequency, and ϕ_o is the phase angle by which $C_{Lo}(t)$ leads the body displacement, $y(t)$. The significance of C_{Lv} is that, through its sign, it determines whether the cylinder is subject to fluid excitation, $C_{Lv} > 0$, or damping, $C_{Lv} < 0$, and hence whether, if the cylinder were allowed to vibrate freely, its motion would be excited or damped.

The variation of C_{Lv} with oscillation amplitude and frequency is shown in figure (1), in which the oscillation frequency is presented through the ratio f_s/f_o, where $f_s = St U/D$ is the Strouhal frequency and St is the Strouhal number for the stationary cylinder. The figure depicts a region of positive C_{Lv} located around $f_s/f_o = 1$ for amplitudes of oscillation less than $0.56\,D$. Outside of this region the cylinder experiences fluid damping. The significance of the contour at $C_{Lv} = 0$ is that a cylinder vibrating at a point on this contour experiences neither fluid-dynamic excitation nor damping. Hence, in the absence of structural damping, a freely vibrating cylinder is expected to trace out a response envelope, with increasing reduced velocity, that lies along the $C_{Lv} = 0$ contour.

The free cross-stream vibration experimental data of Anagnostopoulos & Bearman (1992); $90 \leq Re \leq 140$, $m^* = 149$, $0.0012 \leq \zeta \leq 0.0015$, and simulation data of Shiels *et al.* (2001); $Re = 100$, $m^* = 5$, $\zeta = 0$, are overlaid in the figure (ζ is the structural damping ratio, and m^* is the mass ratio, defined as the ratio of vibrating structural mass to displaced fluid mass). It is apparent that except at low amplitudes, $A/D < 0.1$, where multi-frequency responses may occur in free vibration, both sets of low damping free vibration data lie close to the $C_{Lv} = 0$ contour. Interestingly this result is achieved despite the large difference in mass ratio between the two free vibration data sets. It would appear that the $C_{Lv} = 0$ contour presented here offers a universal locus for the response envelopes of lightly damped cylinders undergoing free cross-stream vibrations at $Re \approx 100$.

Also identified in figure (1) are regions, within the $C_{Lv} = 0$ contour, of different ϕ_o and ϕ_v, where ϕ_v is the phase angle by which $C_{Lo\,vort}(t)$ leads $y(t)$, and $C_{Lo\,vort}(t)$ is the component of the vortex force coefficient at the body oscillation frequency. The vortex force is defined as the cross-stream lift force less the inertia force associated with the cylinder's potential flow added mass. Hence, $C_{Lo\,vort}(t) = C_{Lo}(t) + C_A[\pi/2][\ddot{y}(t)D/U^2]$, where $C_A = 1$ is the potential flow added mass coefficient for two-dimensional flow and $\ddot{y}$ is the body acceleration.

With regard to the variation of ϕ_o within the $C_{Lv} = 0$ contour, it is seen that it is only in region III that $\phi_o > \pi/2$, and that elsewhere within the contour $\phi_o < \pi/2$. Hence, a free-to-vibrate cylinder response in regions I or II would correspond to pre-resonant response, i.e. positive added mass, and a response in region III to post-resonant response, i.e. negative added mass. Region IV is found to lie outside of the lock-in region.
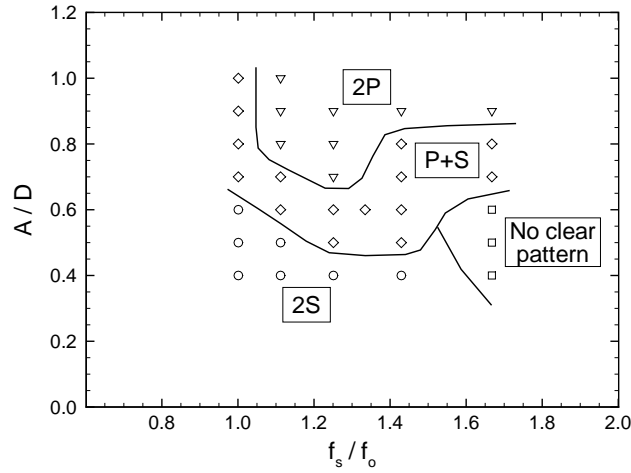
Figure 2: Map of the computed vortex shedding modes for the prescribed cross-stream oscillations of a circular cylinder, at $Re = 300$, as a function of oscillation amplitude, A, and oscillation frequency, f_o.

The vortex phase angle, ϕ_v, undergoes a single transition from $\phi_v < \pi/2$ to $\phi_v > \pi/2$ across the interface between regions I and II. Govardhan & Williamson (2000) identified, at higher Reynolds numbers, that the change in vortex phase angle is associated with the switch from the initial to the upper branch. Following their observations, it is therefore postulated that, for a lightly damped cylinder subject to an incident flow at $Re = 100$ and free to vibrate in cross-flow, the portions of the $C_{Lv} = 0$ contour that bound regions I, II and III, correspond respectively to the initial, upper and lower branches. However, unlike the higher Reynolds number experiments of Govardhan & Williamson, no distinct change in the shedding mode is detected across the interface between regions I and II. The shedding mode remains of the 2S type throughout the computed amplitude-frequency space, save for oscillation frequencies far from the Strouhal frequency for which more exotic shedding modes are observed.

Also of note is the shape of the $C_{Lv} = 0$ contour. At low f_s/f_o the contour has a mildly concave shape, whilst at higher f_s/f_o, between 1.3 and 1.4, the contour has a convex shape, thus enabling hysteretic responses, as reported by some investigators, to occur at low and high reduced velocities in free cross-stream vibration.

4   Prescribed cross-stream oscillations of a circular cylinder at Re = 300

Three-dimensional DNS of early turbulent Reynolds number, $Re = 300$, flow past a cross-flow oscillating circular cylinder, of span $4\,D$, have been conducted over a range of cylinder oscillation amplitudes and frequencies, chosen so as to encompass the cylinder's primary lock-in region and the transition from the 2S to the 2P mode of vortex shedding. Figure (2) presents a map of the computed vortex shedding modes. Three shedding modes; the 2S, the P+S and the 2P mode, were identified over the amplitude-frequency space investigated.

The most notable difference between the computed shedding map and the experimental surface flow visualisations of Williamson & Roshko (1988), who conducted forced oscillation experiments at $300 < Re < 1000$, is the band of P+S shedding that separates the regions of 2S and 2P shedding in the present results. The transition observed by Williamson & Roshko, a large portion of whose experiments were conducted at $Re = 392$, was directly from the 2S to the 2P mode. At a lower, laminar wake, Reynolds number of 200, Meneghini & Bearman (1995) report that the shedding mode switches from the 2S to the P+S mode when the oscillation amplitude exceeds approximately $0.6\,D$. Williamson & Roshko also report, from additional forced oscillation experiments at $Re < 300$, that the 2P mode does not occur at lower Reynolds numbers and instead the P+S mode occurs in its place. Hence, it is speculated that the present results at $Re = 300$ represent an intermediate state between the laminar wake regime, in which the P+S mode occurs at higher amplitudes, and the turbulent wake regime, in which transition occurs directly from the 2S to the 2P mode once a threshold amplitude has been exceeded.

Figure (3 (a)) depicts a vorticity iso-surface image of the 2S wake aft of a cylinder undergoing low amplitude cross-flow oscillations. The wake is dominated by relatively homogeneous spanwise vortices that persist in to the cylinder's far wake. Braid structures, which lie predominantly in planes normal to the cylinder axis, form interconnections between the spanwise vortices. The braid structures dissipate rapidly as they are convected downstream, and past $10\,D$ or so aft of the cylinder there is little evidence of flow-field three-dimensionality.

At a slightly higher amplitude the P+S mode is observed in the cylinder wake, see figure (3 (b)). On the upper side of the wake pairs of oppositely signed spanwise vortices are shed from the cylinder, whilst on the lower side of the wake a row of single positive spanwise vortices is formed. The wake orientation, top to bottom, is a function of simulation initial conditions. Braid structures form interconnections between the spanwise vortices in each pair, and between each pair and the two single vortices located immediately upstream and downstream of the pair on the opposite side of the wake. The braid structures are stronger than those seen in the 2S wake, and persist much further downstream of the cylinder. The spanwise vortices, which are initially reasonably homogeneous in the spanwise direction, interact with the braid structures and become distorted and start to dissipate as they are convected downstream. Within approximately three shedding periods, about $15\,D$ downstream of the cylinder, the weaker vortex in each pair has been largely dissipated and is barely discernible. The P+S wake exhibits a far higher degree of flow-field three-dimensionality than is observed in the 2S wake at lower amplitudes.

(a) 2S mode: $A/D = 0.4$, $f_o / f_s = 0.8$

(b) P+S mode: $A/D = 0.7$, $f_o / f_s = 0.9$

(c) 2P mode: $A/D = 0.9$, $f_o / f_s = 0.7$
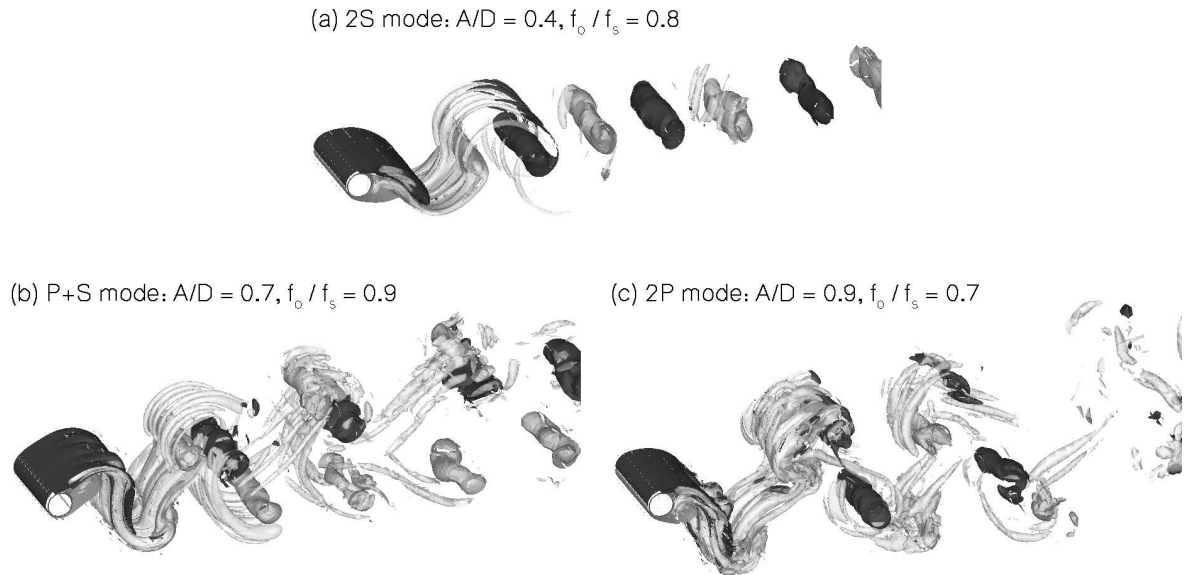
Figure 3: Vorticity iso-surfaces of the flow-field aft of cross-stream oscillating circular cylinders at $Re = 300$. Spanwise vorticity iso-surfaces are shown in black and grey; $\omega_z = \pm 1.0\, U/D$, streamwise and cross-stream vorticity iso-surfaces are shown in semi-translucent light grey; ω_x, $\omega_y = \pm 1.0\, U/D$.

At higher amplitudes still the 2P mode is observed in the cylinder wake, see figure (3 (c)). The vortices in each pair are connected by braid structures, and each pair is itself connected by braids to the pairs immediately upstream and downstream of it on the opposite side of the wake. The interaction of the spanwise vortices with the braid structures leads to the rapid breakup and dissipation of the spanwise vortices, which occurs far more rapidly than in the 2S and P+S wakes. Indeed, only the first full cycle of four shed vortices is readily discernible as two vortex pairs, and within two to three shedding periods aft of the cylinder, $10\,D$ to $15\,D$, there is little evidence of any spanwise vorticity and the flow-field is instead dominated by cross-stream and streamwise vortices.

5 Conclusions

Two and three-dimensional DNS have been conducted of flows past circular cylinders undergoing prescribed cross-stream oscillations whilst subjected to laminar, $Re = 100$, and early turbulent, $Re = 300$, incident flows.

In the case of laminar flows, the zero fluid-dynamic excitation contour was found to match closely the response envelopes reported from experimental and numerical investigations of the free cross-stream vibrations of lightly damped cylinders. Furthermore, the zero contour inferred that the maximum amplitude of free cross-stream vibration is 0.56 cylinder diameters at $Re = 100$, and the shape of the contour confirmed the existence of hystereses at low and high reduced velocities in free vibration.

It has been shown by three-dimensional DNS that, even in early turbulent Reynolds number flows, $Re = 300$, the wake aft of a cross-stream oscillating cylinder can be highly three-dimensional in nature. Furthermore, the degree of flow-field three-dimensionality increases with oscillation amplitude as the shedding mode changes from the 2S mode to the P+S mode and then to the 2P mode.

Acknowledgements

References

Anagnostopoulos, P. & Bearman, P.W. (1992). Response Characteristics of a Vortex-Excited Cylinder at Low Reynolds Numbers. *Journal of Fluids and Structures 6*, 39–50.

Govardhan, R. & Williamson, C.H.K. (2000). Modes of vortex formation and frequency response of a freely vibrating cylinder. *Journal of Fluid Mechanics 420*, 85–130.

Govardhan, R.N. & Williamson, C.H.K. (2006). Defining the "modified Griffin plot" in vortex-induced vibration: revealing the effect of Reynolds number using controlled damping. *Journal of Fluid Mechanics 561*, 147–180.

Hover, F.S., Davis, J.T., & Triantafyllou, M.S. (2004). Three-dimensionality of mode transition in vortex-induced vibrations of a circular cylinder. *European Journal of Mechanics - B/Fluids 23*, 29–40.

Meneghini, J.R. & Bearman, P.W. (1995). Numerical simulation of high amplitude oscillatory flow about a circular cylinder. *Journal of Fluids and Structures 9*, 435–455.

Sherwin, S.J. & Karniadakis, G.E. (1995). A triangular spectral element method; applications to the incompressible Navier-Stokes equations. *Computer Methods in Applied Mechanics and Engineering 123*, 189–229.

Shiels, D., Leonard, A., & Roshko, A. (2001). Flow-Induced Vibration of a Circular Cylinder at Limiting Structural Parameters. *Journal of Fluids and Structures 15*, 3–21.

Williamson, C.H.K. & Roshko, A. (1988). Vortex formation in the wake of an oscillating cylinder. *Journal of Fluids and Structures 2*, 355–381.

Understanding mode transitions in vortex-induced vibration using controlled vibration

T. L. Morse & C.H.K. Williamson

Sibley School of Mechanical & Aerospace Engineering,
Upson Hall, Cornell University, Ithaca, NY 14853, USA
E-Mail: tlm39@cornell.edu

SUMMARY

In this study we have made extensive measurements of the fluid forces on a cylinder that is controlled to oscillate transverse to a free stream at Re = 4000. These measurements were used to create extremely high resolution contour plots of the magnitude of the fluid force, and contour plots of the phase angle between the forces and body motion, in the plane of normalized amplitude and velocity. We find transitions in certain regions of this plane where the character of the fluid forces changes between distinct modes. Interestingly, these transitions correspond well with boundaries separating different vortex shedding modes in the Williamson-Roshko (1988) map of regimes. A further new characteristic, which is only observable with very high-resolution data, is the existence of regimes where two modes overlap. By examining the energy transfer from fluid motion to cylinder motion we are able to predict the response of an elastically mounted cylinder that agrees well with the measured free vibration response of Govardhan & Williamson (2006) at both high and low mass-damping. Furthermore, by looking at the shape of the excitation contours and the transitions between different modes, we are able to exhibit clearly the hysteretic mode transition, and the intermittent switching transition, which occur between different branches of the free vibration response.

In studies of vortex-induced vibration, investigators have employed controlled vibration (where a cylinder is moved with a prescribed motion) to understand the case of a freely vibrating cylinder. For example, Mercier (1973), Sarpkaya (1977), Staubli (1983) and Carberry et al. (2001, 2005) measured the forces on a cylinder that is controlled to oscillate sinusoidally transverse to a flow. Carberry et al. also used digital particle image velocimetry (DPIV) to examine the wake vortex dynamics. Gopalkrishnan (1993) and Hover, Techet & Triantafyllou (1998) made force measurements over a wide range of oscillation amplitudes and frequency, generating contour plots of the fluid forcing.

In the present study, we have conducted controlled vibration experiments over an expansive range of amplitude and frequency with much higher resolution than in any previous data set. The cylinder was suspended vertically in a water channel, and oscillated sinusoidally transverse to a free stream, at a Re of 4000. A total of 5680 runs were conducted, for approximately 500 hours worth of data. Such an expansive data set was only possible because the experiment was conducted in a continuously flowing water channel facility and thus could be automated and run unattended for wide sets of data. Our hope was that with this extremely high resolution data, we could uncover key features that have not previously been observed, and thus we could obtain a more profound understanding of vortex-induced vibration.

Force measurements from controlled vibration experiments can be related to the free vibration case through the equation of motion. For an elastically mounted cylinder, constrained to move transverse to a flow, the motion (y) can be defined by the following equation:

$$m\ddot{y} + c\dot{y} + ky = F(t) \tag{1}$$

When the body motion is synchronized with the vortex shedding, the cylinder motion, $y(t)$ and fluid forcing, $F(t)$ are well approximated as being sinusoidal (in controlled vibration, the motion is prescribed to be sinusoidal):

$$y(t) = A\sin(2\pi ft) \tag{2}$$
$$F(t) = F_0 \sin(2\pi ft + \phi) \tag{3}$$

For such a system, the energy transferred from the fluid to the cylinder is one cycle is given by:

$$E_{IN} = \pi A F_0 \sin\phi \tag{4}$$

Where ϕ is the important phase angle between body motion and fluid force. The energy lost to structural damping (c) is given by:

$$E_{OUT} = 4\pi^3 cAf^2 \tag{5}$$

If the system is oscillating with a constant amplitude and frequency, the energy into the system must exactly balance the energy out of the system, over one cycle. Combining equations (4) and (5) and nondimensionalizing yields:

$$C_Y \sin\phi = \frac{4\pi^3 A^* (m^* + C_A)\zeta}{\left(U^*/f^*\right)^2 f^*} \tag{6}$$

(In this study $A^* = A/D$ = amplitude/diameter, $U^* = U/f_N D$, $f^* = f/f_N$, where U is the free stream velocity, f is the oscillation frequency, and f_N is the natural frequency, and m^* = oscillating mass / mass of fluid displaced.) We can use equation (6) for the energy balance along with contours of the fluid excitation ($C_Y \sin\phi$) from controlled vibration to predict a free vibration response for any particular mass damping. By looking at the energy transfer in more detail, we can understand many of the phenomena that occur in free vibration.

Upon examining our controlled vibration data, we notice that the fluid forcing showed qualitative jumps in certain regions as amplitude or frequency is varied. We plot contours on either side of these jumps separately (as shown in Figure 1), and notice that the boundaries separating these different fluid forcing regimes are remarkably similar to boundaries separating different vortex wake modes in the Williamson & Roshko (1988) map. Thus we expect that the jumps in fluid forcing correspond to changes in the wake vortex dynamics found in the latter work.

There are also some regions where even for a cylinder oscillating at a constant amplitude and frequency, the fluid forcing switches between two distinct modes. These two modes were analyzed separately and are shown as overlapping contours in Figure 1. This is particularly evident for the region of red contours in Figure 1, between $U^*/f^* \approx 4$ - 6. Interestingly, the peak amplitude for a free vibration response exists inside this overlapping region, so that our understanding of this region is essential to an understanding of the dynamics of the cylinder at its maximum vibration.

From this contour plot of the fluid excitation, we used equation (6) to predict the response for a mass-damping of zero and compared it to a measured free vibration response at the same mass-damping from Govardhan & Williamson (2006) as shown in Figure 2. There is a good agreement between the two cases, especially in the lower branch. The Reynolds numbers for the two cases are matched to be around 4000 for the peak amplitude. This is important, as the amplitude in the upper branch depends strongly on Re as explained in Govardhan & Williamson (2006). Similar agreement between the measured and predicted response is also found for higher values of mass-damping.
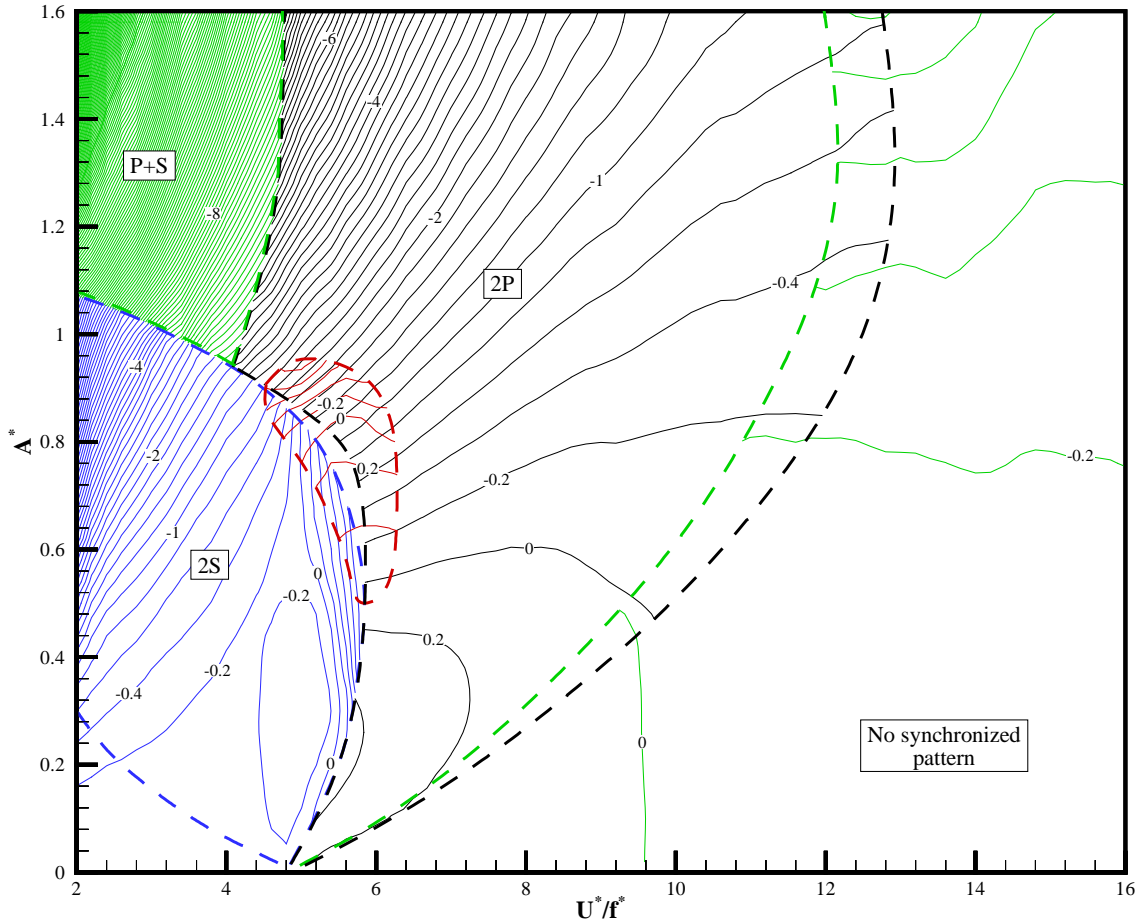
FIGURE 1. Contours of fluid excitation ($C_Y \sin\phi$) in the plane of normalized amplitude and velocity. Different colors indicate different fluid forcing modes, – – – boundaries between modes. In regions where contours overlap, two modes can alternately exist for a given value of normalized amplitude and velocity.
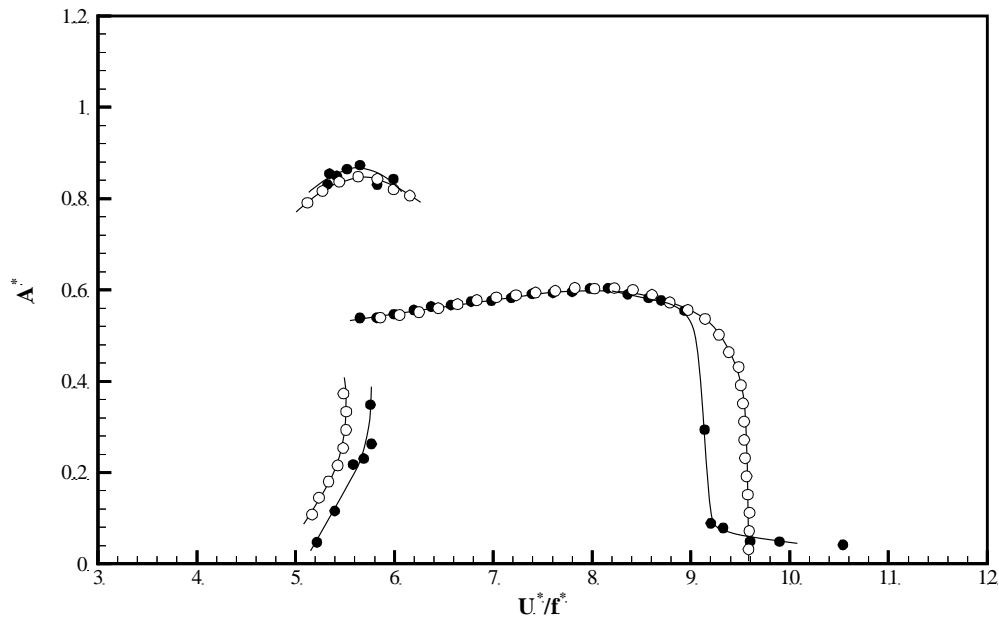
FIGURE 2. Measured and predicted free vibration response for $(m*+C_A)\zeta = 0$, at similar Re. ● measured response from Govardhan & Williamson (2006) ○ predicted response from controlled vibration data (present results). For the predicted response, $Re = 4000$ throughout the plot. For the measured free vibration response, the peak amplitude corresponds to $Re \approx 4000$.

For a free vibration response at low mass damping (such as the one shown in Figure 2) there are three branches: an initial, upper, and lower branch, with a hysteretic mode transition between the initial and upper branch, and an intermittent switching mode transition between the upper and lower branch. We can use the fluid excitation contours to help understand why these transitions occur. For example, for a cut of constant normalized velocity that intersects the initial and upper branch ($U* = 5.4$), the fluid excitation follows an 'S' like shape as amplitude is increased (see Figure 3). The energy lost due to damping follows a straight line with a slope proportional to mass-damping. The free vibration response should lie at the intersections of these two curves where there is a balance of energy. In Figure 3, for a mass damping of 0.05 there are three intersections, *however only two of them are stable*, having a negative rate of change of energy with amplitude ($dE*/dA* < 0$). These stable equilibria correspond to the initial branch and the upper branch of free vibration. The middle intersection is *unstable* ($dE*/dA* > 0$). If the system were perturbed from this equilibrium, say the amplitude was increased slightly, the energy into the system would be greater than the energy out of the system and the amplitude would continue to increase. Steady free vibration would not be found at the unstable equilbria, so they would not appear in a response plot. The movement and disappearance of these stable and unstable equilibria as normalized velocity is varied is what leads to the hysteresis between the initial and upper branches.
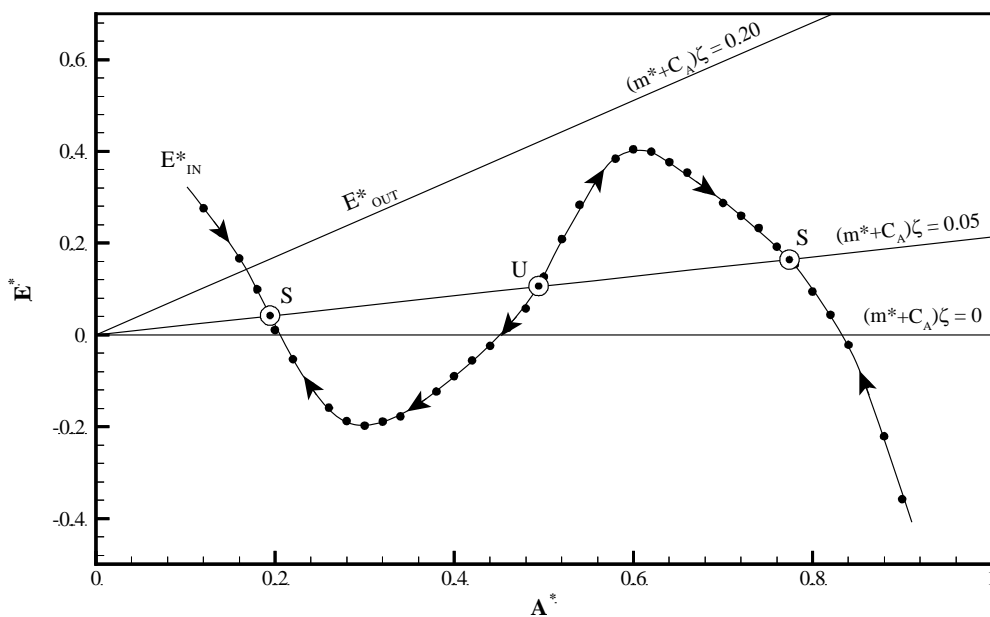
FIGURE 3. "Energy portrait" for $U* = 5.4$ cut. ● fluid excitation from contours in Figure 1, ⊙ equilibrium points, S = stable equilibrium, U = unstable equilibrium. Arrows indicate direction of movement for non-equilibrium states.
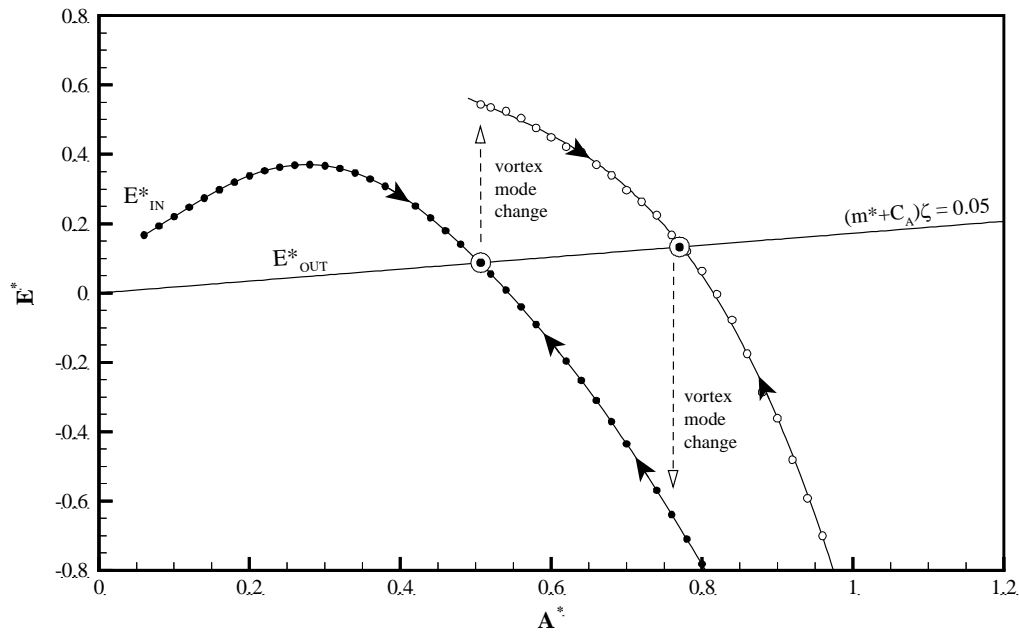
FIGURE 4. "Energy portrait" for $U* = 6.0$ cut. ● fluid excitation from black contours in Figure 1 (lower branch), ○ fluid excitation from red contours in Figure 1 (upper branch). We suggest that an intermittent vortex mode change causes a jump from one fluid excitation curve to the other. ⊙ equilibrium points, arrows indicate direction of movement for non-equilibrium states.

We can also look at the fluid excitation along cuts of constant normalized velocity where the upper and lower branches are intersected ($U* = 6.0$ in Figure 2), passing through a large region where the fluid excitation contours overlap. In Figure 4, we see that there are amplitudes where two possible values exist for the fluid excitation. There are two stable equilibria (corresponding to the lower and upper branches). However, in the overlap region, we suggest that the vortex wake mode can intermittently change. If this occurs, then we would see a jump from one fluid excitation curve to the other, leading to a distinct change in amplitude. In this way, the free vibration response will switch intermittently from one stable equilibrium to the other. This is the type of mode transition found in this region for free vibration experiments.

In conclusion, the contours of fluid excitation shown here have been obtained from precise controlled vibration experiments with a much higher resolution than in any previously existing data sets. Here we have shown just a few examples of the type of analysis that can be performed with these contours. We have looked at the energy balance along constant normalized velocity cuts through the fluid excitation contour plot within the amplitude-velocity plane. This allows us to gain a deeper understanding of the mode transitions that occur in free vibration. The hysteretic mode transition occurs because of the 'S' shape of the fluid excitation contours, leading to a region where $dE*/dA* > 0$. The intermittent switching mode transition occurs because of the existence of overlapping vortex mode regimes.

We intend to present results and phenomena described in this Abstract, as well as to discuss further controlled vibration results, transient behaviors, and to examine the effects of mass ratio, damping, and Reynolds number.

REFERENCES

CARBERRY, J., SHERIDAN, J., & ROCKWELL, D. O. 2001. Forces and wake modes of an oscillating cylinder. *J. Fluids Struct.* 15: 523-32

CARBERRY, J., SHERIDAN, J., & ROCKWELL, D. O. 2005. Controlled oscillations of a cylinder: forces and wake modes. *J. Fluid Mech.* 538: 31-69

GOPALKRISHNAN, R. 1993. *Vortex-induced forces on oscillating bluff cylinders.* Ph.D. Thesis. MIT, Cambridge, MA

GOVARDHAN, R. N. & WILLIAMSON, C. H. K. 2006. Defining the 'modified Griffin plot' in vortex-induced vibration: revealing the effect of Reynolds number using controlled damping. *J. Fluid Mech.* 561: 147-180

HOVER, F. S., TECHET A. H. & TRIANTAFYLLOU, M. S. 1998. Forces on oscillating uniform and tapered cylinders in crossflow. *J. Fluid Mech.* 363: 97-114

MERCIER, J. A. 1973. *Large amplitude oscillations of a circular cylinder in a low speed stream.* Ph.D. Thesis. Stevens Inst. Tech., Hoboken.

SARPKAYA, T. 1977. Transverse oscillations of a circular cylinder in uniform flow. *Rep. No. NPS-69SL77071, Nav. Postgrad. Sch.,* Monterey, CA.

STAUBLI, T. 1983. Calculation of the vibration of an elastically mounted cylinder using experimental data from forced vibration. *ASME J. Fluids Eng.* 105: 225-29

WILLIAMSON, C. H. K. & ROSHKO, A. 1988. Vortex formation in the wake of an oscillating cylinder. *J. Fluids Struct.* 2: 355-381.

Reynolds number effects on A/D using forced sinusoidal oscillations

Jamison L. Szwalek
Centre for Ships and Offshore Structures
Norwegian University of Science and Technology
Trondheim, Norway
Email: jamison.szwalek@ntnu.no

Carl Martin Larsen
Centre for Ships and Offshore Structures
Norwegian University of Science and Technology
Trondheim, Norway
Email: callas@ntnu.no

1   Introduction

It has only recently been noted that Reynolds number has been regarded as a significant parameter in VIV vibration and peak amplitude response [Kalak and Williamson (1996); Ding et al. (2004); Klamo et al. (2005); Govardhan and Williamson (2005)]. In fact, this has lead to a redefined Griffin plot which takes into account the Reynolds number dependence (Govardhan and Williamson 2006). The present study investigates the forced motions of a cylinder with varying Reynolds number to examine the Reynolds number effect on A/D for free VIV. This can be most easily accomplished using forced sinusoidal vibrations and determining the zero lift coefficient conditions. Table 1 shows the relevant parameters to this study. Whereas previous studies have been generally limited to cross-flow motions only and without any flow visualization at these high Reynolds numbers, the present study seeks to address pure in-line, pure cross-flow, and combined in-line and cross-flow oscillations. This also includes qualitative wake imaging using stereo particle image velocimetry (PIV) for cases in which the lift coefficient is found near zero to simulate free vibration. The PIV results can allow for a better understanding of the wake pattern and dynamics associated with increasing Reynolds numbers and peak amplitudes.

2   Experimental Tests

The experiments take place in NTNU's Marine Cybernetics Laboratory in Trondheim, Norway, in June 2007. The tank consists of a 40m long rectangular channel with overhead towing carriage. The tank width and depth are 6.45m and 1.5m, respectively. The test model, a rigid cylindrical cylinder with length 2m and outer diameter 0.1m, is mounted on a streamlined yoke suspended from the tow carriage. The yoke is controlled by a microprocessor servo motor which allows for forced oscillations in five degrees of freedom. The current experiments are used for both vertical (cross-flow) and horizontal (in-line) forced sinusoidal oscillations. The drive carriage system is capable of speeds up to 1m/sec, but is limited from 0.05m/s to 0.8m/s due to PIV equipment restrictions and excessive carriage vibration. All carriage input functions such as carriage speed,

Parameter		Dimension
Cylinder length	L	2.0 m
Cylinder outer diameter	D	0.1 m
Cylinder mass ratio	$M/\rho_w V_{cyl}$	0.61
Aspect ratio	L/D	20
Surface roughness	δ/D	smooth
Blockage ratio	D/D_t	0.067
Constant towing velocity	U_o	0.05-0.8 m/s
Reynolds number range	$U_o D/\nu$	$5 \cdot 10^3$-$8 \cdot 10^4$
Oscillation frequency ratio	$f_{osc}D/U_o$	0.2-0.5
Amplitude to diameter ratio, cross-flow	$A/D|_{CF}$	0.3-1.2
Amplitude to diameter ratio, in-line	$A/D|_{IL}$	0.05-0.2

Table 1: Characteristic properties of the present experimental setup.

forcing amplitude and oscillation frequencies and phase are controlled by the PC computer. The triggering for each run is controlled by a master input file on the carriage's PC.

Lift and drag forces are measured simultaneously via force transducers placed at both ends of the rigid cylinder and instantaneous cylinder displacement is measured via linear variable differential transformer (LVDT). The ends of the cylinder are capped to eliminate potential sloshing effects and end plates are installed to eliminate three-dimensional effects in accordance with the specifications of Stansby (1974). There is a small gap, less than 1mm, between the end plates and the test cylinder so that the end plates do not affect the force measurement. Both free surface and blockage effects are expected to be negligible. The maximum Froude number expected is about 0.33 based on the maximum tow speed and the minimum depth of submergence. Free surface effects should be negligible provided the Froude number is much less than one. Bishop and Hassan (1964) concluded that $Fn = 0.375$ for their experiments was sufficiently low. Blockage effects should also be low for a blockage ratio on the order of 6.7%. Zdravkovich (2002) states that for blockage ratios less than 10%, no empirical blockage corrections are required.

To investigate the trend with Reynolds number, the goal is to examine five Reynolds numbers within the range $5 \cdot 10^3$-$8 \cdot 10^4$. To do this for a given Reynolds number, the forced oscillation frequencies are varied to maintain constant frequency ratios $f_{osc}D/U_o$ and A/D is varied to determine the zero lift condition. The test matrix for the pure in-line and pure cross-flow tests are given in Figure 1 which includes the results of previous studies to determine an appropriate VIV oscillation amplitude study [Johansen (2004); Huse (2004); DNV (2002); Aronsen and Larsen (2007); Vikestad (1998); Gopalkrishnan (1993)]. The study done by Aronsen and Larsen (2007) is at a Reynolds number of $Re = 2.4 \cdot 10^4$ and that of Gopalkrishnan (1993) Vikestad (1998) are approximately $Re = 1.0 \cdot 10^4$; these studies are well within the range of Reynolds numbers to be tested and provide an excellent starting point to map the peak amplitudes.
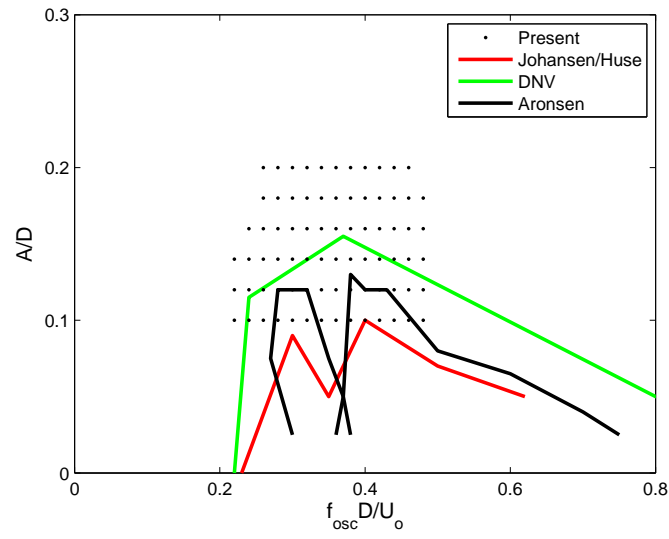
(a) In-line.
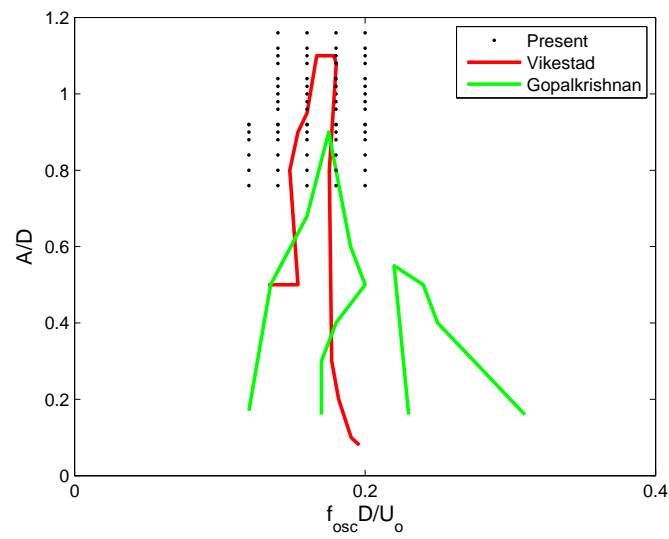
(b) Cross-flow.

Figure 1: Test matrix for present experiment.

References

Aronsen, K. and C. Larsen (2007). Hydrodynamic coefficients for in-line vortex induced vibrations. *Proc. of twenty-sixth international OMAE conference.*

Bishop, R. and A. Hassan (1964). The lift and drag forces on a circular cylinder in a flowing fluid. *Proc. Royal Soc. London 277*, 32–50 and 51–75.

Ding, Z., S. Balasubramanian, R. Lokken, and T.-W. Yung (2004). Lift and damping characteristics of bare and straked cylinders at riser scale reynolds numbers. *Proc. Offshore Tech. OTC 16341.*

DNV (2002). Free spanning pipelines. *DNV-RP-F105.*

Gopalkrishnan, R. (1993). *Vortex induced forces on oscillating bluff cylinders.* Ph. D. thesis, MIT, Cambridge.

Govardhan, R. and C. Williamson (2005). Revealing the effect of reynolds number on vortex-induced vibrations using controlled negative and positive damping. *Proc. fourth conf. BBVIV*, 69–71.

Govardhan, R. and C. Williamson (2006). Defining the 'modified griffin plot' in vortex-induced vibration: revealing the effect of reynolds number using controlled damping. *J. Fluid Mech. 561*, 147–180.

Huse, E. (2004). In-line viv excitation and mass coefficients. *Tech. report MARINTEK.*

Johansen, T. (2004). Hydrodynamiske koeffisienter for virvelinduserte svigninger i strømmens retning. Master's thesis, Norwegian University of Science and Technology, Trondheim.

Kalak, A. and C. Williamson (1996). Dynamics of a hydroelastic cylinder with very low mass and damping. *J. Fluids Struct. 10*, 455–472.

Kamal, R. (2007). *Energy extraction from a steady flow using vortex induced vibration.* Ph. D. thesis, University of Michigan, Ann Arbor.

Klamo, J., A. Leonard, and A. Roshko (2005). On the maximum amplitude of a freely vibrating cylinder in cross-flow. *J. Fluids Struct. 21*, 429–434.

Stansby, P. (1974). The effect of end plates on the base pressure coefficient of a circular cylinder. *Aeronautical J.*, 36–37.

Vikestad, K. (1998). *Multi-frequency response of a cylinder subjected vortex shedding and support motions.* Ph. D. thesis, Norwegian University of Science and Technology, Trondheim.

Zdravkovich, M. (2002). *Flow around circular cylinders Vol. 2.* Oxford Science.

Computational study of hydrodynamic forces on a cylinder vibrating transversely and in-line to a steady stream

Lambros Kaiktsis and George S. Triantafyllou
Department of Naval Architecture and Marine Engineering,
National Technical University of Athens, Athens, Greece

Abstract

We present computational results for the forces on a cylinder oscillating transversely and in-line to a uniform stream at Reynolds number 400. The transverse vibration has a frequency equal to the natural frequency of the Kármán vortex street, whereas the in-line vibration occurs at twice that frequency. The ratio of the transverse amplitude of vibration to the in-line amplitude is kept constant and equal to five. The cylinder thus follows an "eight"-like trajectory, emulating the trajectory of a free vortex-induced vibration. We find that the results of the simulation are greatly influenced by the direction in which the "eight" figure is traversed. We distinguish between a "counterclockwise" mode (if the upper part of the trajectory is traversed counterclockwise), and a "clockwise" mode (if the upper part of the trajectory is traversed clockwise). We find that the counterclockwise mode results in larger fluid forces than the clockwise mode for the same amplitude of oscillation. More important, the power transfer from the fluid to the cylinder remains positive for the counterclockwise mode at higher values of the amplitude-over-diameter-ratio than it does either for the clockwise mode or for a transversely-only vibrating cylinder. For both the counterclockwise and the clockwise modes the wake is characterized by complex vortex patterns.

Problem definition, numerical method and results

The flow past an oscillating cylinder is a reference problem for flow-induced vibrations, e.g. see Sarpkaya (2004), Williamson and Govardhan (2004). We have recently performed a detailed numerical study of forces on a cylinder oscillating transversely to a uniform stream (Kaiktsis et. al., 2007), and related the results to the flow patterns in the wake. It is well known however that vortex-induced vibrations of cylinder are often characterized by an "eight"-like trajectory. In-line oscillations of the cylinder can significantly alter the fluid forces on the cylinder (Sarpkaya (2004), see also Marcollo and Hinwood (2006)). Extending our previous study, we present here results for a cylinder oscillating following an "eight"-like trajectory.

We consider uniform flow past an oscillating cylinder. The fluid has a constant density ρ. Far upstream of the cylinder, the velocity is U_∞. The flow Reynolds number, defined in terms of the free stream velocity, U_∞, and the cylinder diameter, D, is equal to 400, the same value as our initial study for comparison purpose. The coordinates are x, parallel

to the free stream, and y, normal to the stream. The cylinder oscillates around a mean position, with a corresponding instantaneous displacement

$$\eta_y = A_y \sin\left(2\pi f_e t\right) , \qquad \eta_x = \pm A_x \sin\left(4\pi f_e t\right) , \qquad (1)$$

where the plus sign corresponds to a motion which is counter-clockwise in the upper x-y plane, and the minus sign to a clockwise motion in the upper x-y plane. We will refer to the two types of motion, as "counter-clockwise" and "clockwise", respectively.

From dimensional analysis it follows that the flow dynamics and the dimensionless force coefficients depend on the Reynolds number, the reduced y-amplitude, $\xi = A_y/D$, the relative x-amplitude, $\epsilon = A_x/A_y$, and the reduced oscillation frequency, $F = f_e/f_s$ (where f_s is the natural frequency of the Kármán street). It is not so obvious from dimensional analysis, but intuitively reasonable, that the dynamics of the flow depend on the direction that the trajectory is traversed, i.e. on whether the oscillation mode is "counter-clockwise" or "clockwise".

For convenience, we use coordinates fixed on the cylinder. This results in the appearance of a d'Alambert acceleration in the right-hand side of the momentum equation. To transform the forces back to the original frame of reference, we subtract the "dynamic Archimedes" force from the computed force values. The resulting form of the Navier-Stokes equations, subject to proper boundary conditions, is solved with a Legendre spectral element method. Here, we have implemented a discretization consisting of 464 spectral elements, see Fig. 1, with 9×9 elemental resolution. The value of the non-dimensional time step ranged from 0.0075 to 0.0015.

The time-averaged power transferred from the flow to the cylinder (per cylinder unit length), can be normalized by $\rho U_\infty^2 D^2/2$ to yield the non-dimensional "power transfer parameter". In the presence of both in-line and transverse cylinder oscillation, the total power transfer parameter, P, consists of the sum of the corresponding contributions: $P = P_x + P_y$.

The variation of the power transfer parameter with A_y/D is shown in Fig. 2, for $\epsilon = 0.2$ ("counter-clockwise" and "clock-wise" motion), as well as for the transverse-vibrations-only case ($\epsilon = 0$). Here, both the power transfer corresponding to the y-motion, P_y, and the total power transfer, P, are presented. In the case of "counter-clockwise" motion, the range of A_y/D corresponding to positive P is larger, in comparison to either the "clockwise" mode or the trasversely-only oscillating cylinder. For the counter-clockwise mode, the increase of the range of A_y/D corresponding to positive P is due primarily to the work of the fluctuating drag force, that is in phase with the in-line velocity of the cylinder. (A small part of the increase is due to the work of the lift force). For the "clockwise" mode of oscillation, $P < P_y$, i.e. the fluctuating drag force has opposite phase than the in-line velocity of the cylinder. We can conclude therefore that the "counter-clockwise" mode of oscillation is the worst case scenario for a freely vibrating cylinder, because it results to higher values of A/D.

Fig. 3 shows the corresponding variation of drag coefficient with A_y/D. The in-line oscillation almost always increases the value of the mean drag coefficient. Exception to this is observed for a narrow range of high A/D values, for which the "counter-clockwise" mode has lower mean drag coefficient. This can be attributed to the positive power transfer from the fluctuating drag force to the cylinder.
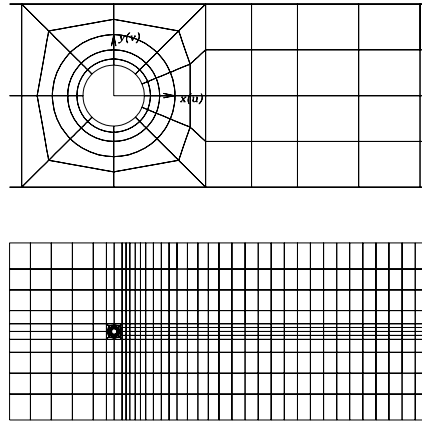
Figure 1. Spectral element skeleton for flow past a circular cylinder, including elements close to the cylinder, and the entire mesh.

Finally, Figs. 4 and 5 show instantaneous vorticity isocontours, plotted at the moment that the cylinder occupies its mean position, for the two types of cylinder motion, respectively. High A_y/D values correspond to a type of wake observed in our previous study of the $\epsilon = 0$ case, and characterized as a "partial S+P" mode: Vortex pairs appear on the one side, and single vortices on the other. This mode originates as a regular "2S" mode, and is then modified through vortex splitting (see Kaiktsis et. al., 2007).

We have also performed simulations for a higher value of the relative in-line oscillation amplitude, in particular $\epsilon = 0.4$. In comparison to the $\epsilon = 0$ case, our results (not presented here because of lack of space) show a reduction in the y-amplitude range of positive power transfer, for both types of the cylinder motion. This reduction was larger for the "clockwise" motion.

It is concluded that in order to reliably predict the vortex-induced vibrations of actual structures one needs to use experimental results for cylinders that undergo simultaneously cross-flow and in-line oscillations.

References

Kaiktsis, L., Triantafyllou, G.S., Özbas M., 2007. Excitation, inertia, and drag forces on a cylinder vibrating transversely to a steady flow. Journal of Fluids and Structures 23(1), 1-21.

Marcollo, H., Hinwood, J.B., 2006. On shear flow single mode lock-in with both cross-flow and in-line lock-in mechanisms. Journal of Fluids and Structures 22(2), 197-211.

Sarpkaya, T., 2004. A critical review of the intrinsic nature of vortex-induced vibrations. Journal of Fluids and Structures 19(4), 389-447.

Williamson, C.H.K., Govardhan, R., 2004. Vortex-induced vibrations. Annual Review of Fluid Mechanics 36, 413-455.
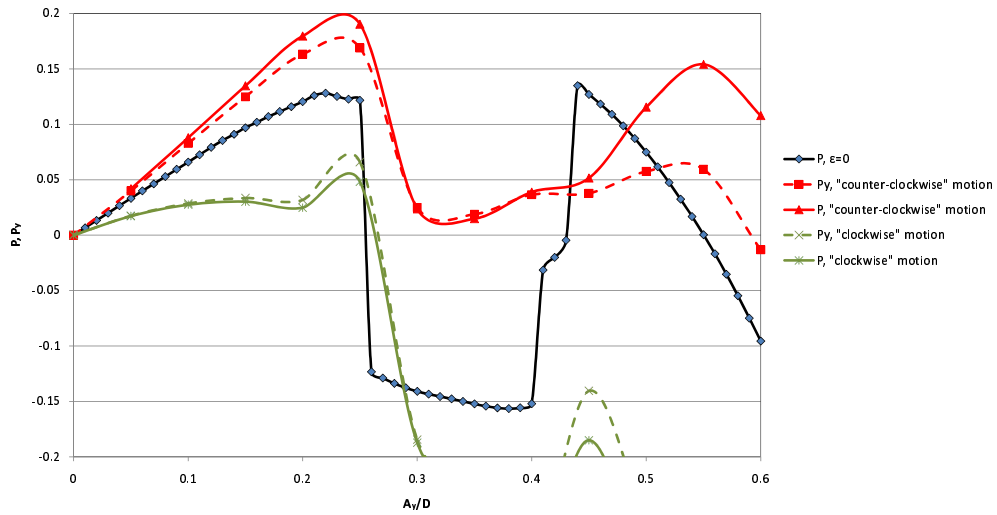
Figure 2. Power transfer parameter values versus non-dimensional y-amplitude, for $\epsilon = 0$, and $\epsilon = 0.2$ ('"counter-clockwise" and '"clockwise" cylinder motions).
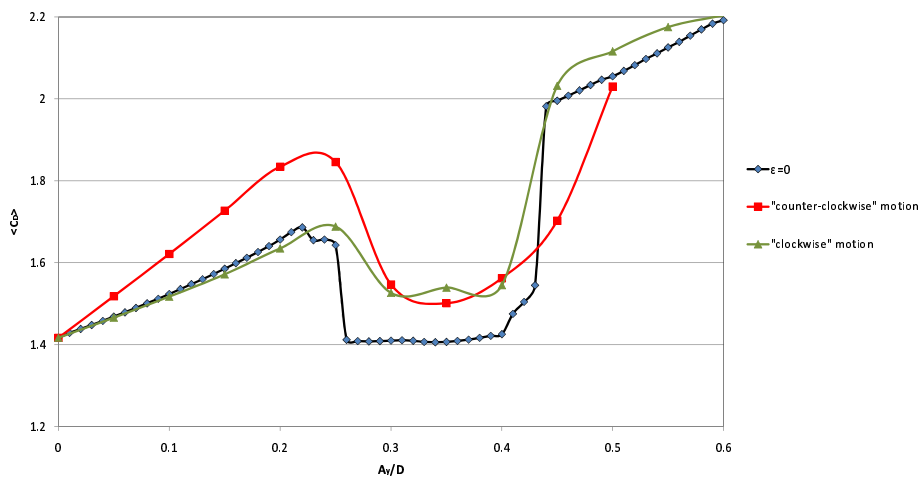
Figure 3. Time-averaged drag coefficient versus non-dimensional y-amplitude, for $\epsilon = 0$, and $\epsilon = 0.2$ ('"counter-clockwise" and '"clockwise" cylinder motions).
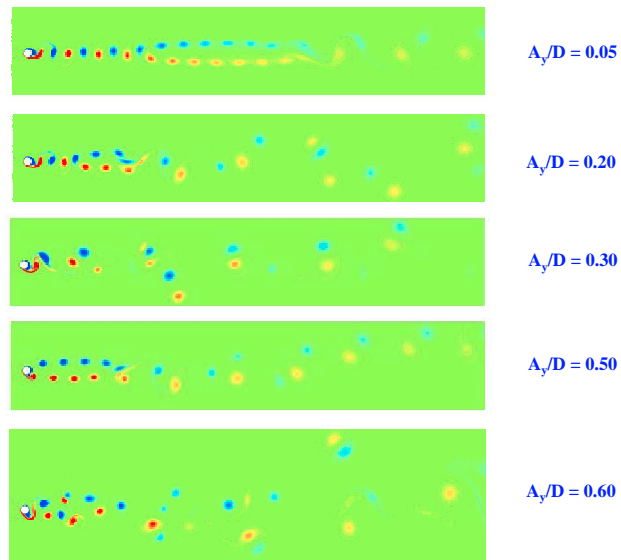
Figure 4. Instantaneous vorticity isocontours, for different values of non-dimensional y-amplitude, for $\epsilon = 0.2$ and "counter-clockwise" cylinder motion.
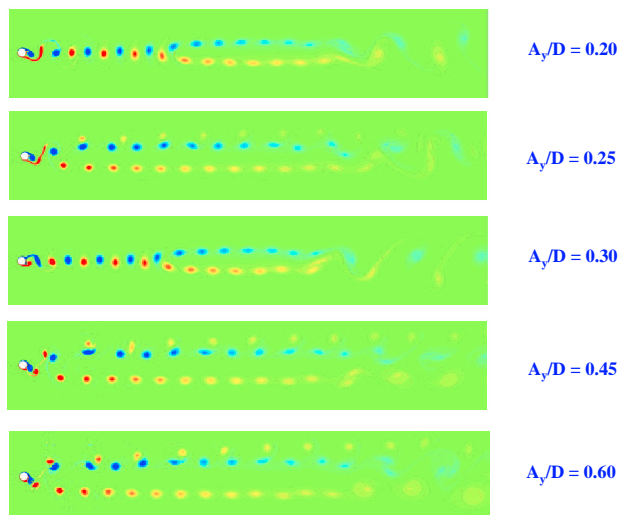
Figure 5. Instantaneous vorticity isocontours, for different values of non-dimensional y-amplitude, for $\epsilon = 0.2$ and "clockwise" cylinder motion.

Spheroidal bubbles as an archetype of light, freely-moving axisymmetric bodies

Jacques Magnaudet

Institut de Mecanique des Fluides de Toulouse, UMR CNRS/IPT/UPS 5502, France.

Modern experimental observations provide evidence that path instability (i.e. the transition from a straight vertical path to a planar zigzag or a helical path) of oblate spheroidal air bubbles rising in a stagnant liquid is related to a wake instability. Direct numerical simulations of a model problem in which bubbles are assumed to keep a prescribed shape reveal many crucial aspect of the phenomena. In particular they show that there is a one-to-one correspondence between the wake topology and the path geometry. They also allow us to determine the nature of the bifurcation from a straight to a non-straight path. By computing *a posteriori* the various forces and torques experienced by a bubble along its trajectory, they shed light on the way wake-induced (i.e. vortical) effects balance added-mass (i.e. irrotational) contributions. Detailed analysis of the flow about a *fixed* oblate spheroidal bubble are also very helpful to determine how, why and when its wake becomes unstable. In particular they indicate that the axisymmetric wake loses its stability when the surface vorticity resulting from the stress-free condition exceeds a certain amount. An empirical criterion capable of predicting whether the wake is stable or not can be built on these findings and is found to apply to solid bodies as well. These simulations may also be used to examine in detail the structure of the very near wake, close to the instability thereshold, and to figure out the generic physical mechanism responsible for the instability of axisymmetric wakes. Last but not least, very recent experimental results obtained in various liquids are found to strongly support the view of a direct connection between the strength of the surface vorticity and the onset of the path instability.

WAKE BEHIND A SPHERE IN EARLY TRANSITIONAL REGIMES

J. MIEDZIK*, K. GUMOWSKI*, S. GOUJON-DURAND,
G. BOUCHET**, P. JENFFER AND J.E. WESFREID
Ecole Supérieure de Physique et de Chimie Industrielles de la Ville de Paris, PMMH,
UMR7636-CNRS ; ESPCI ; P6 ;P7 Paris, France
*Warsaw University of Technology, Institute of Aeronautics and Applied Mechanics, Poland
** Institut de Mécanique des Fluides et des Solides, UMR7507-CNRS ULP, Strasbourg, France
e-mail: sophie@pmmh.espci.fr

Abstract

We present in this communication very controlled experiments concerning first instabilities in the wake of the sphere. We discuss the first transition from homogenous flow to a stationary instability and we present original results about peristaltic instability preceeding the hairpins shedding. In addition we present numerical simulations with a spectral -- spectral-element code [1] covering the early stages of transition.

Introduction

The typical scenario of instability and transition in the flow behind the sphere is following. In the range of Reynolds number [0-212], the flow remains axisymmetric with two different features. For very low Reynolds numbers, the creeping flow exhibits a perfect upstream-downstream symmetry. For higher Reynolds numbers (Re > 20), the flow separates and a vortex forms at the rear stagnation point of the sphere. The primary instability (Re = 212) is due to a regular bifurcation breaking the axisymmetry but keeping the flow steady. The loss of axisymmetry causes the onset of a lift force normal to the symmetry plane, and a torque perpendicular to the flow direction and to the symmetry plane. The onset of unsteadiness appears at Re = 274.

Figure 1 makes it obvious how the axisymmetry breaking influences the drag coefficient. We present the values computed both for the axisymmetric base flow (obtained by forcing axisymmetry beyond the instability threshold) and for the (stable) non-axisymmetric flow. The difference increases with Reynolds number, and it is clear that the instability enhances the drag.

Results

We study the flow behind a sphere in a low velocity water channel built with transparent plexiglas walls of 10x10cm cross section with typical velocity ranging from 0.4 to 4 cm/sec, which corresponds to a Reynolds number from 50 up to 500. The sphere has diameter of d = 1.6 cm. The wake visualizations were performed in the three directions, using Laser Induced Flurosceine (LIF). The dye (flurosceine dye in solution) was injected in the middle of the sphere using a thin vertical or horizontal slit. The measurements of the velocity fields were performed using a standard Particle Image Velocimetry set-up (PIV). The sphere was held from upstream by a rigid bent tube and we test different orientation to study this influence on the instability.

In the Fig. 2 is shown the investigations of the cause of the first bifurcation. The recirculation bubble remain axisymmetric up to Re = 212. With increasing Reynolds number the bubble looses his axial symmetry. The loose of axial symmetry is responsible of two counter rotating vortices apparition. The flow rests steady with planar symmetry.

Starting from Reynolds number Re = 265 it is straightforward to notice small oscillations of two vortices in the sphere wake, from observation of the streak lines. Oscillations are growing with Reynolds number (Fig. 3). The oscillations first we observe in far wake of sphere (for Re 260, about x/d = 15) and with increasing Reynolds number we can observe the oscillations in the whole wake behin a sphere. This flow is not anymore stationary. Still increasing Reynolds number is reached the point of observable hairpins shedding. This situation occurs with Reynolds number about 280 in our experiments. In order to characterize this beginning of the peristaltic instability we defined a peristaltic parameter Δ as the difference between the biggest (b'') and smallest (b') distance between vortices cores $\Delta = (b'' - b')$ observed from the streaklines. The Fig. 4 shows the increase of Δ up to Re = 277 and for higher Reynolds number the value of the Δ reach saturation what corresponds with hairpins shedding apparition. For all distances Δ approches value zero for Re number about Re = 267.

These results were confirmed by PIV measurements with the same experimental conditions. From rear view, PIV images were obtained the frequency of vertical V_y velocity component measured between two vortices. As shown in Fig. 5, for Re = 263 only noise is noticed. Starting from Re around 267 appear oscillations which are growing up to Re = 280 where hairpins developing begins. From numerical simulations is observed in the Fig. 6 that for Re = 275, the sign of the longitudinal vorticity is constant for each thread.

Is observed in the Fig. 7 that frequency of peristaltic instability and of hairpins shedding are lying on the same line which implied the peristaltic undulation frequency is continuation of hairpins shedding frequency. It seams that the hairpin is just the result of enough strong oscillations in the wake. It suggest, this both phenomenon are the same instability, which starts at low Reynolds number here around Re = 267.

Conclusion

From our results, we proposed now a new insight on the generation of hairpins-vortex shedding phenomena. We obtained a new scenario "precursor" of the hairpin vortex shedding as signaled by [2], with a peristaltic instability of oscillations of the two parallel counter-rotating vortices behind a sphere. These results are equally interesting to understand the dynamics of bubbles and drops, which they also shown two counter-rotating vortices induced by the lost of sphericity of the bubbles, as occur here with the loss of sphericity of the recirculation area.

References

1   GHIDERSA, B. AND DUSEK, J.: Breaking of axisymmetry and onset of unsteadiness in the wake of a sphere. J. Fluid Mech., 423, (2000) 33-69.
2   M.C. THOMPSON, T. LEVEKE AND M. PROVENSAL.: Kinematics and dynamics of sphere wake transition. Journal of Fluids and Structures(2001) 15, 575-585.
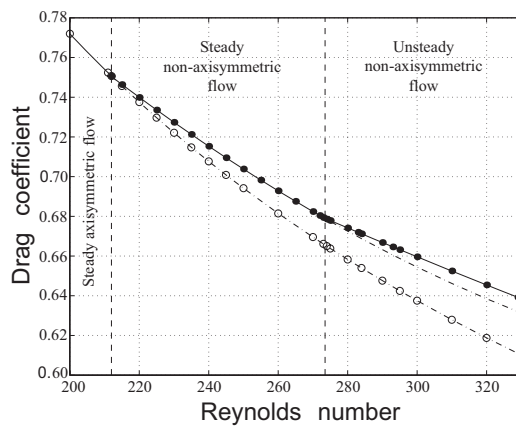
Fig. 1 Drag coefficient obtained from numerical simulation (○ : forced axisymmetric flow ; ● : total flow; the dash-dotted lines represent an extrapolation of the subcritical results ; for Re > 274, the drag coefficient is time averaged).
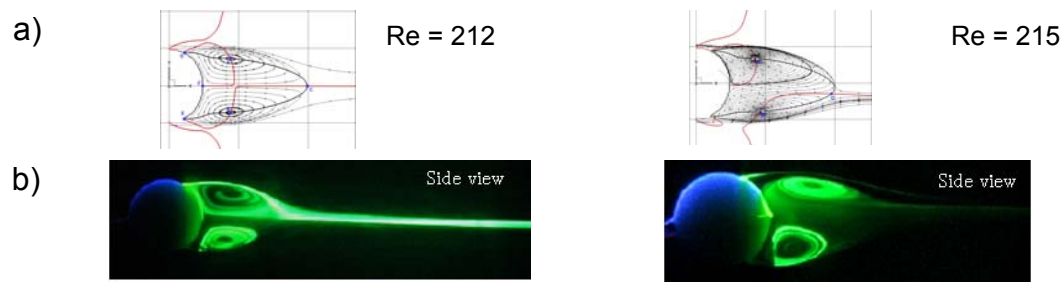
Fig. 2 Recirculation area, numerical simulation (a) and visualization (b) results before and after bifurcation.
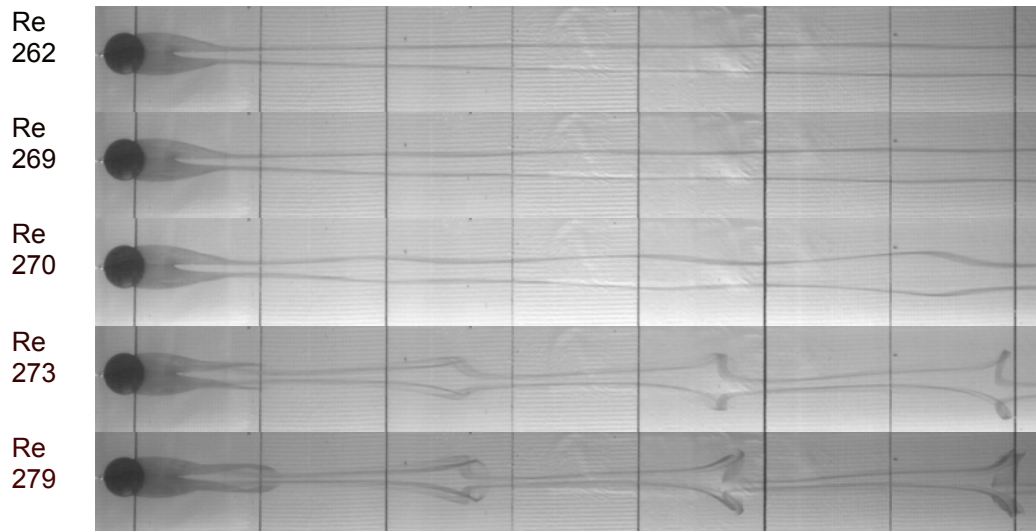
Fig. 3 From peristaltic instability to hairpins shedding.
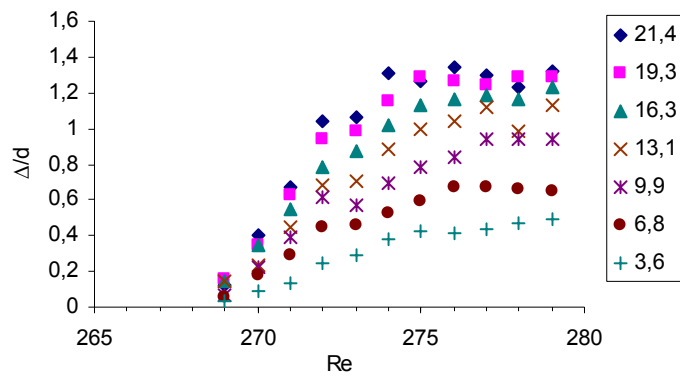
Fig. 4 Peristaltic parameter delta as a function of Reynolds number (experimental results) at different downstream x positions.

Stable (Re 263)

First oscillations (Re = 269)

Re 276

Hairpins shedding (Re = 280)
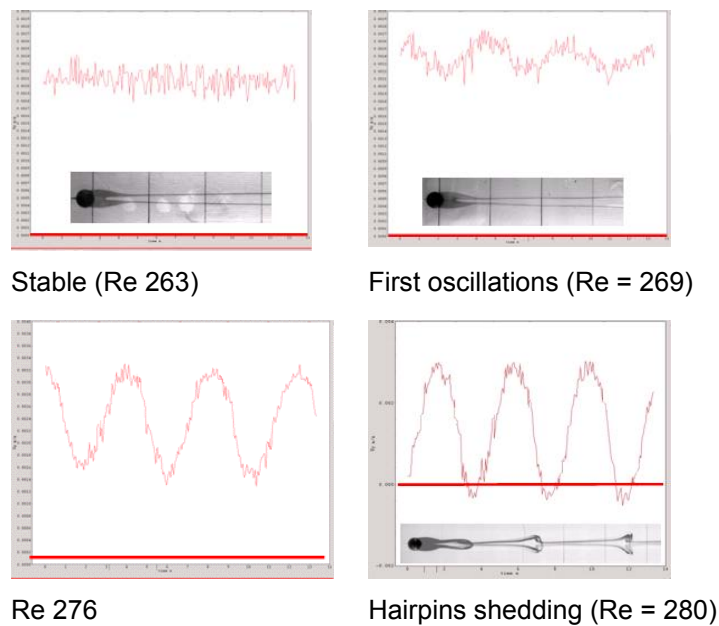
Fig. 5 Spatial mean value of vertical velocity Vy component in function of time obtained at x = 2.5 d in the central plane yz.
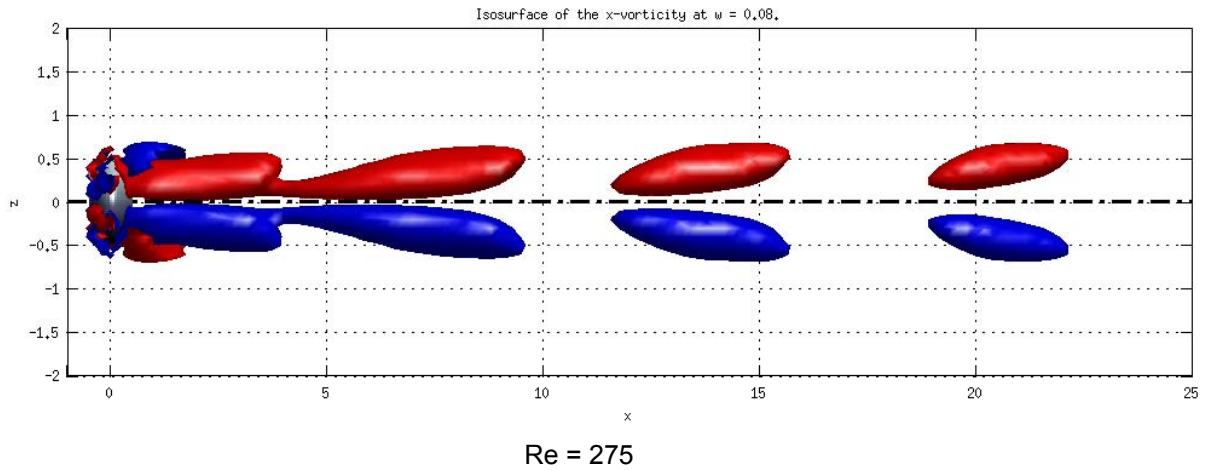
Re = 275

Fig. 6 Logitudinal vorticity in the wake of the sphere obtained from numerical simulations; the color blue corresponds to a positiv vorticity, and the color red corresponds to a negativ vorticity, for Re=275.
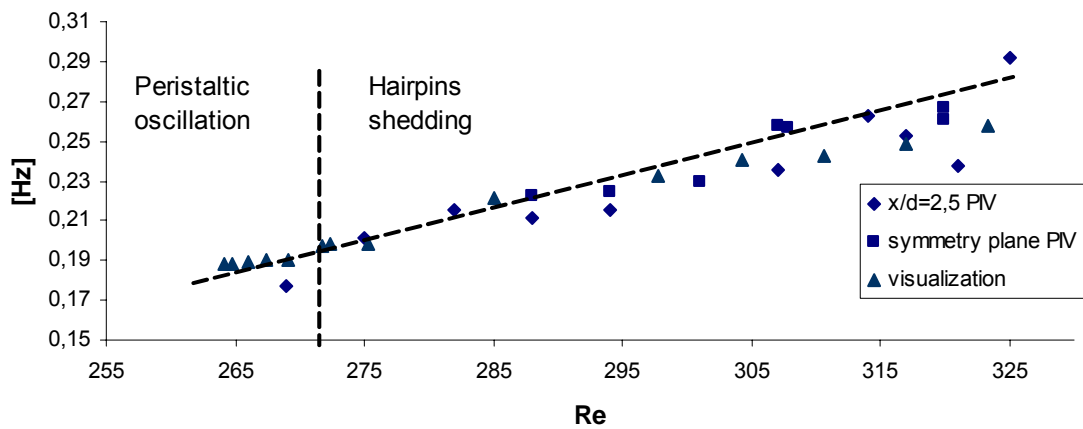
Fig. 7 Frequency of instability

Dynamics and wake patterns of rising and falling spheres

M. Horowitz & C.H.K. Williamson

Sibley School of Mechanical & Aerospace Engineering
Upson Hall, Cornell University, Ithaca, NY 14853, USA
E-Mail: cw26@cornell.edu

SUMMARY

We study the dynamics of spheres rising or falling freely through a fluid at two different Reynolds numbers, Re = 500 and 10,000. Although this problem has been the focus of numerous investigations since it was first considered by Newton (1726), the conditions under which a sphere will vibrate are still unknown. Most studies conclude that the dynamics are determined by the mass ratio (or relative density) m^*, but while some investigators find that all rising spheres ($m^* < 1$) vibrate and all falling spheres ($m^* > 1$) do not, others have observed vibration for both rising and falling cases. For vibrating spheres, it is also unclear what types of trajectories may occur, with both in-plane oscillations and helical motion being suggested. At both values of Re studied, we find that falling spheres descend rectilinearly. In the case of the rising sphere, we find that there exists a critical value of the mass ratio, below which the sphere undergoes large-amplitude oscillations. Despite the difference in the modes of vortex formation at these two Reynolds numbers, associated in part with the instability of the separated shear layer at higher Re, a critical mass exists for both cases. For the higher Reynolds number, we find a critical mass of m^*_{crit} = 0.61, in good agreement with the result for tethered and elastically mounted spheres at similar Re (Govardhan & Williamson, 2005). At Re = 500, performing experiments in glycerin-water mixtures to precisely control the Reynolds number, we find a distinctly lower critical mass, m^*_{crit} = 0.36. For both Reynolds numbers, the motion of the vibrating spheres occurs in a single vertical plane, with no helical trajectories being observed. Visualizing the wake of a vibrating sphere at this Reynolds number reveals another interesting phenomenon; rather than two alternately signed vortex loops being shed in a cycle, as might be expected based on studies of the flow past fixed spheres, four vortex loop structures are shed in each cycle of oscillation.

Whether a sphere vibrates as it rises or falls through a fluid is of interest in a wide range of practical applications from sedimentation to atmospheric measurements using weather balloons, as vibration is known to affect drag as well as heat and mass transfer. The earliest observation of vibration of a freely rising or falling sphere is reported by Newton (1726), who writes in the *Principia* that inflated hog bladders "did not always fall straight down, but sometimes flew about and oscillated to and fro while falling. And the times of falling were prolonged and increased by these motions." More recently, most investigations of freely rising or falling spheres have concluded that the mass ratio of the sphere determines when vibration occurs, with lighter spheres oscillating and heavier ones moving rectilinearly (a notable exception is Karamanev, Chavarie & Mayer 1996, who implausibly claim that the critical parameter is U/ν, the ratio of the terminal velocity and kinematic viscosity, with dimension of inverse length). However, there is a great deal of disagreement over the range of mass ratios where these regimes occur. The experiments of Preukschat at Re = 1000 – 10000, and direct numerical simulation by Jenny, Bouchet & Dusek (2004) at Re = 200 – 500 found that falling spheres ($m^* > 1$) have a rectilinear trajectory, while rising spheres ($m^* < 1$) vibrate, suggesting that there may be some special significance to $m^* = 1$, such that the sphere is able to distinguish between rising and falling. On the other hand, MacCready & Jex (1964), Reid (1964) and Veldhuis, Biesheuvel, van Wijngaarden & Lohse (2004) observed both rising and falling spheres undergoing large lateral motions, while a number of studies considering only falling spheres have found vibration. With such major differences between the results of these studies, a key question remains: when does a rising or falling sphere vibrate?

Our experiments were performed in two vertical tanks, a larger one with dimensions 0.4m x 0.4m x 1.5m, and a smaller one measuring 0.2m x 0.2m x 0.9m. Both solid and hollow spheres were used, with diameters, D, ranging from 0.2cm to 3.8cm, deviating from perfect sphericity by no more than 1.5%. The spheres were held in the tank using a hook inside a hollow launching tube, and were released after the fluid settled. Two ranges of Reynolds number were studied, Re ~ 10,000 in the larger tank, and Re = 500 in the smaller tank, where a constant Reynolds number was achieved using mixtures of glycerin and water to control the viscosity.

We began with experiments using spheres with Re ~ 10,000. A falling sphere with $m^* = 2.84$ descended with only small non-periodic transverse motion, shown from above (the Y-Z plane) and from the side (the Y-X plane) in figure 1(a). A buoyant sphere ($m^* = 0.75$) rose rectilinearly after undergoing an initial transient that quickly damped out. This result, shown in figure 1(b), indicates that contrary to previous observations, some rising spheres do not vibrate. Accordingly, there is nothing inherently special about $m^* = 1$. Spheres with a mass ratio $m^* = 0.27$ were found to undergo large-amplitude oscillations with a transverse amplitude $A_Y^* = A_Y/D = 0.71$. Although it is not evident from figure 1(c), if the mean rising velocity is subtracted, there also exists streamwise vibration with an amplitude $A_X^* = 0.14$. The top view of the trajectory shows that although the sphere is free to move in three-dimensions, the oscillation is confined to a single plane, the orientation of which is determined by the direction of the initial velocity.
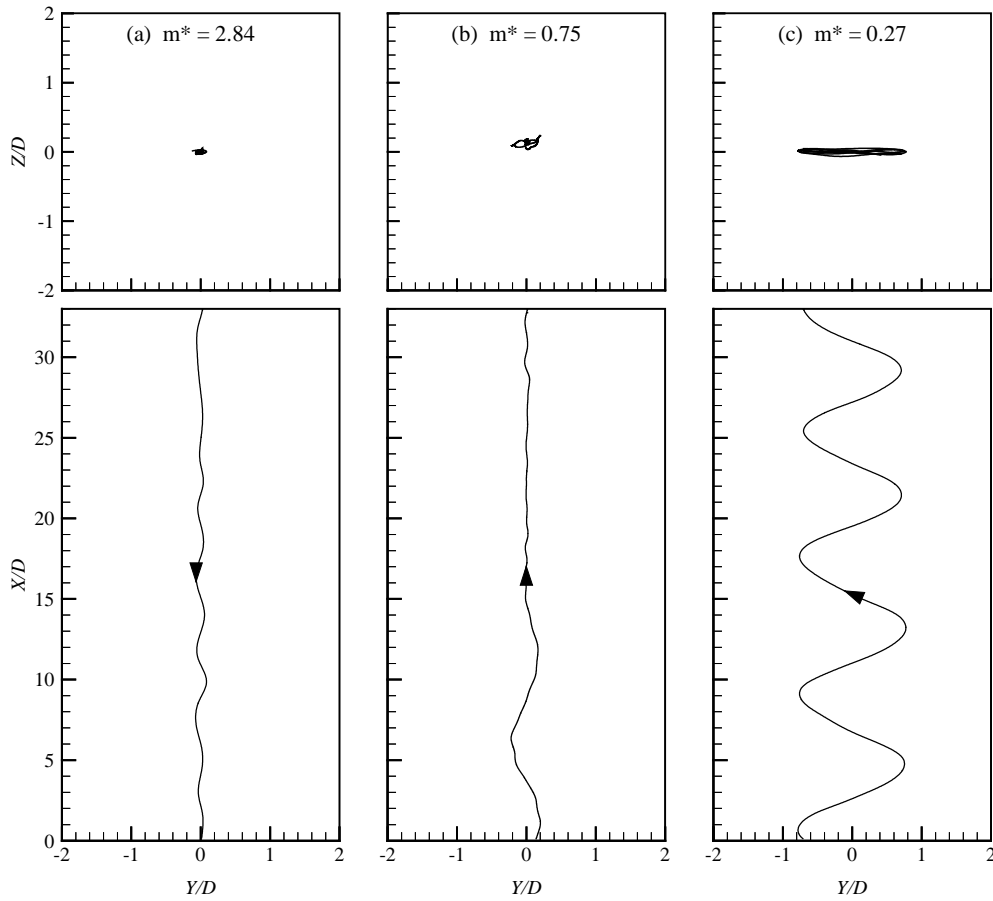
Figure 1. Trajectories of rising spheres viewed from above (upper row) and from the side (lower row). (*a*) $m^* = 2.84$. The sphere falls with very small, nonperiodic transverse motion. (*b*) $m^* = 0.75$. After a brief transient, the sphere rises rectilinearly. (*c*) $m^* = 0.27$. Very light spheres vibrate in a single plane. *Re* ~ 10,000.
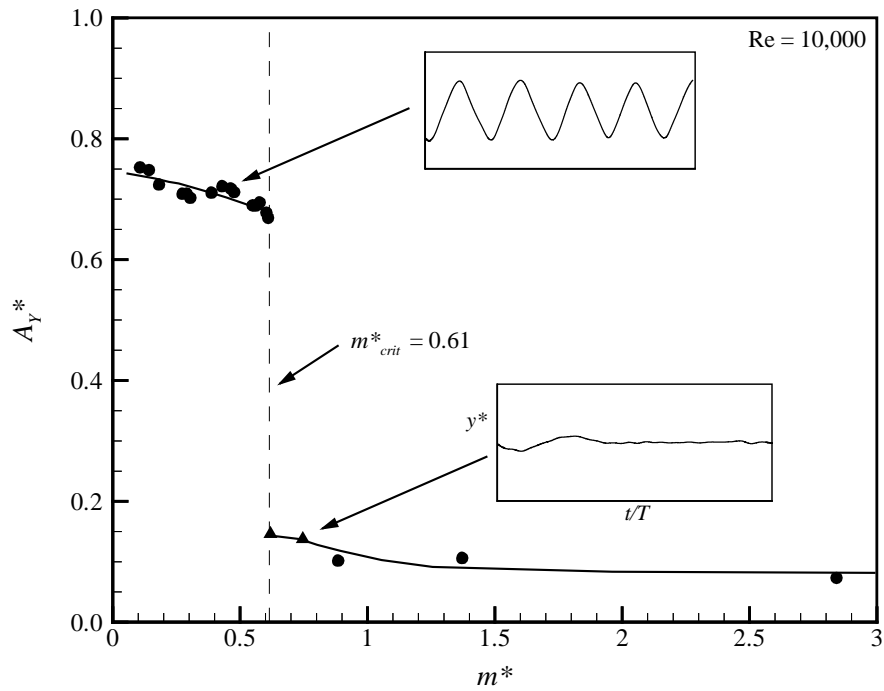
Figure 2. The critical mass for a rising and falling sphere at *Re* ~ 10,000 occurs at $m^*_{crit} = 0.61$, indicating that some rising spheres do not vibrate. Time histories of $y^* = y(t)/D$ are shown for selected m^*. ●, the sphere quickly reaches a steady state; ▲, transient cases, such as the trajectory shown in figure 1(*b*).
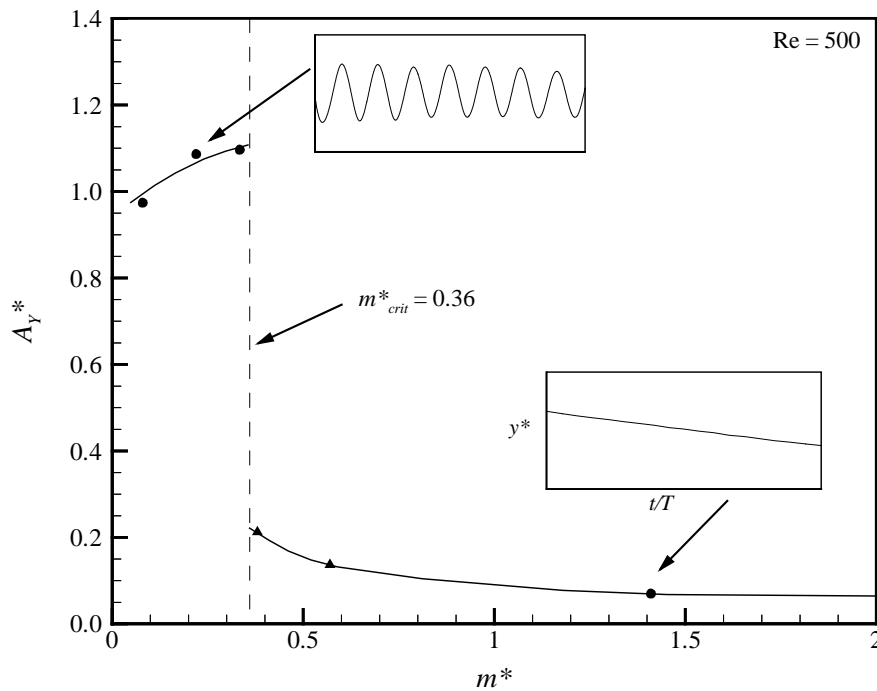
Figure 3. At $Re = 500$, the critical mass for a rising and falling sphere is $m^*_{crit} = 0.36$, distinctly lower than the higher Reynolds number case. ●, steady state; ▲, transient.

Measuring the oscillation amplitude of spheres at many different mass ratios, plotted in figure 2, we find a critical value of the mass ratio below which a sphere will vibrate, $m^*_{crit} = 0.61$. Consequently, there is a broad range of mass ratios over which buoyant spheres will rise without vibration. We attribute this difference with previous studies to the sensitivity of the sphere dynamics to experimental conditions. In particular, spheres heavier than the critical mass were very sensitive to small disturbances in the fluid that could induce large transient motions. To minimize these disturbances and ensure that the fluid was truly quiescent, a settling time of at least two hours between experiments was required, along with a very small stable thermal stratification to eliminate convection currents. It is also noteworthy that the value of the critical mass found for rising spheres agrees well with the estimate of the critical mass made by Govardhan & Williamson (2005) for elastically mounted and tethered spheres, $m^*_{crit} \approx 0.6$.

A similar set of experiments was performed for spheres at $Re = 500$. At this Reynolds number, we find an even wider range of mass ratios where rising spheres do not vibrate, corresponding to a critical mass $m^*_{crit} = 0.36$, shown in figure 3. Like the higher Reynolds number case, vibrating spheres would undergo periodic, large amplitude oscillation in a single plane, and spheres slightly heavier than the critical mass showed transient small-amplitude behavior. The heavier spheres moved rectilinearly, but rather than being vertical, their trajectories were slightly oblique. Although the Reynolds number of the sphere is similar to that of spiraling bubbles, no evidence of spiral trajectories was found. Further experiments are planned to investigate the possibility (or lack thereof) of helical motion.

Many studies have examined the wakes of fixed spheres, however much less is known about the vortex dynamics behind unrestrained spheres, where the wake can interact with the body motion. Using laser-induced fluorescence, we find that in the case of rectilinear trajectories, the sphere sheds a single-sided chain of vortex loops (figure 4a), resembling the wake of a fixed sphere observed by Sakamoto & Haniu (1990) at similar Reynolds numbers. Since the wake is single-sided, there is a mean transverse force that causes the trajectory to deviate from the vertical. From the angle of the trajectory, this force is found to be $C_Y = 0.04$. Such an asymmetric wake pattern would not be expected from the oscillating sphere, whose trajectory is periodic. One might expect to have a double-sided chain instead, as has been found for vibrating tethered spheres by Govardhan & Williamson (2005). However, the actual pattern, shown in figure 4(b) is unlike any wake mode found previously for either fixed or vibrating spheres, with four vortex structures formed per cycle of oscillation. In addition to the two vortices shed near the transverse peaks of oscillation, there are two extra vortices formed closer to the centerline. The origin and precise structure of these additional vortices remain unclear.

We have found values of the critical mass ratio, $m^*_{crit} = 0.38$ for $Re = 500$ and $m^*_{crit} = 0.61$ for $Re = 10,000$, but our understanding of the critical mass phenomenon is not complete. Future work will focus on exploring the reasons behind the existence of a critical mass and variations in the wake phenomena in different Reynolds number regimes. Since the critical mass is closely linked to the forces exerted on the sphere due to the dynamics of vorticity, additional studies of the wake patterns will be performed using particle-image velocimetry and laser-induced fluorescence at high and low Reynolds number, with the goal of improving spatial and temporal resolution to better characterize the vortex structures in the wake and the processes by which they are created.
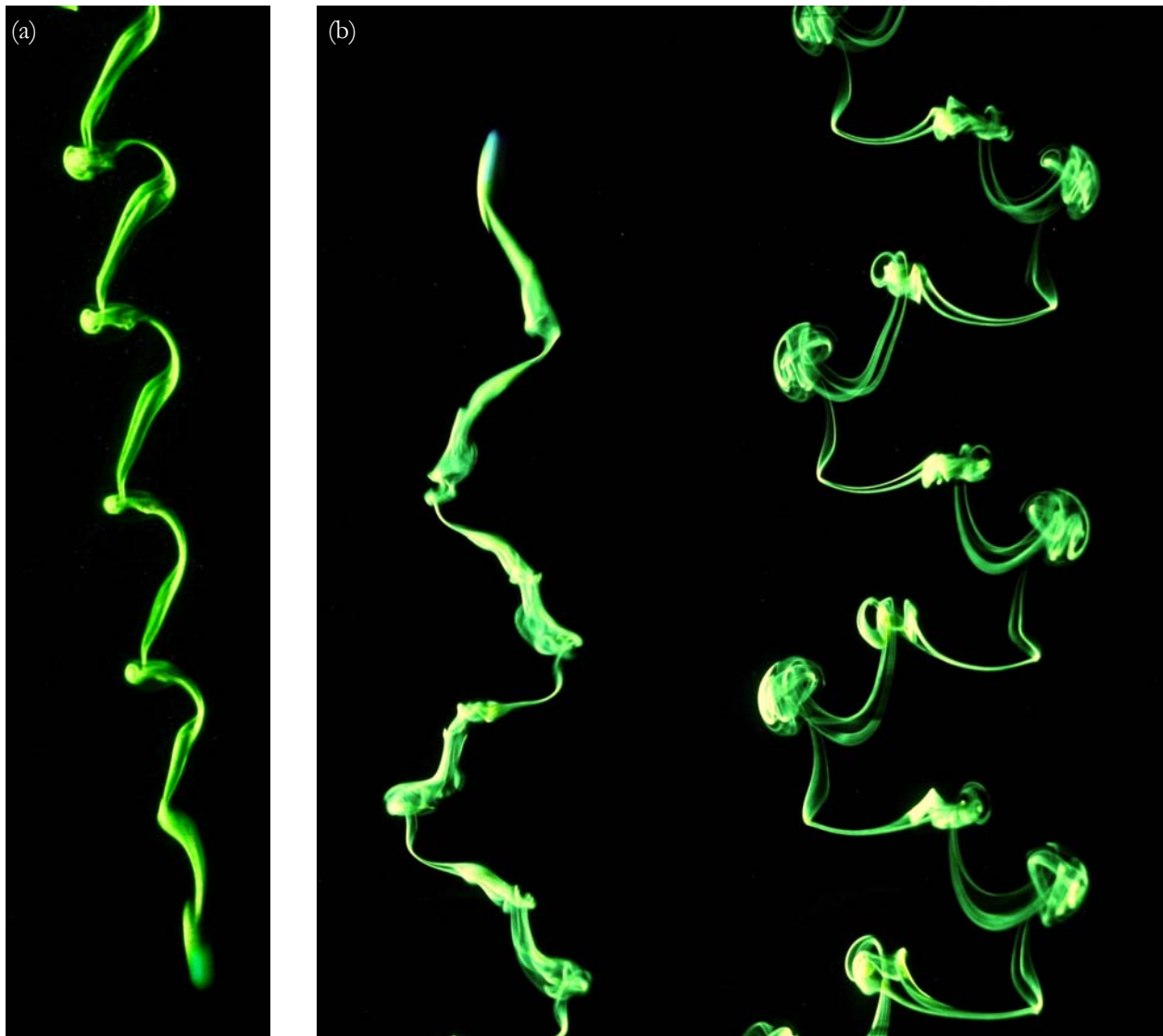
Figure 4. (*a*) A single-sided chain of vortex loops in the wake of a falling sphere in rectilinear motion, *m** = 1.41. (*b*) In the wake of a very light rising sphere, *m** = 0.08, four distinct vortex structures are created in each cycle of oscillation, twice as many as have previously been observed in flows past static or elastically mounted spheres. *Re* = 500.

REFERENCES

GOVARDHAN, R.N. & WILLIAMSON, C.H.K. 2005. Vortex - induced vibrations of a sphere. *J. Fluid Mech.* **531**, 11-47.

JENNY, M., DUSEK, J. & BOUCHET, G. 2004. Instabilities and transition of a sphere falling or ascending freely in a Newtonian fluid. *J. Fluid Mech.* **508**, 201-239.

KARAMANEV, D.G., CHAVARIE, C. & MAYER, R.C. 1996. Dynamics of the free rise of a light solid sphere in liquid. *AIChE J.* **42**, 1789-1792.

MACCREADY, P.B. & JEX, H.R. 1964. Study of sphere motion and balloon wind sensors. NASA Tech. Memo. TM X-53089.

NEWTON, I. 1726. Philosophiae Naturalis Principia Mathematica, 3rd Ed. Trans. I.B. Cohen, A. Whitman. Univ. Calif. Press, Berkeley, CA, USA.

PREUKSCHAT, A.W. 1962. Measurements of drag coefficients for falling and rising spheres in free motion. Aero. Eng. Thesis, Caltech, Pasadena, CA, USA.

REID, D.F. 1964. Instability of spherical wind-sensing balloons. Proc. AFCRL Sci. Balloon Symp.

SAKAMOTO, H. & HANIU, H. 1990. A study on vortex shedding from spheres in uniform flow. ASME J. Fluids Engng. **112**, 386-392.

VELDHUIS, C., BIESHEUVEL, A., VAN WIJNGAARDEN, L. & LOHSE, D. 2005 Motion and wake structure of spherical particles. *Nonlinearity* **18**, C1-C8.

The interaction between two spherical particles in an oscillatory flow

L. Prahl, J. Revstedt and L. Fuchs

Div. Fluid Mechanics, Lund University, SE-221 00 Lund, Sweden

Lisa.Prahl@vok.lth.se

June 2007

Abstract

Simulations of the flow around a pair of spherical particles subjected to either a uniform or a pulsating inflow are performed. The purpose is to study the effects a time dependent velocity profile as well as the inclusion of an additional particle will have on force and flow characteristics. For Reynolds number of 100 applying both a uniform and a pulsating inflow, the distance between the particles is varied from $1.5 - 6.0D$ and the separation angle is $0 - 90°$ using $1.5D$ and $15°$ increments, respectively. Moreover, for pulsating inflow, Reynolds numbers of 300 and 600 are studied to capture the instability characteristics for particles placed in tandem formation, using the same distance range as for $Re = 100$. Furthermore, the Strouhal number of the sinusoidal inlet flow is varied between 0.05 and 0.2 for $Re = 100, 300$ and 600. The Volume of Solid (VOS) method, an approach based on the Volume of Fluid (VOF) method, is used in order to describe the particles. In order to validate VOS, the approach is compared with both experimental and numerical data found in literature regarding the drag force on a single particle for a wide range of Reynolds numbers.

The results show a strong dependency on inflow frequency. For Reynolds number of 100, the drag force is similar for both inflows tested with strong dependency on relative particle position, a feature not as significant for the higher Reynolds numbers.

1 Introduction

Multiphase flow systems are used for a wide range of industrial applications. In order to improve the efficiency of these applications it is important to obtain a better understanding of particle dynamics. The flow around particles as well as the force a particle is subjected to are influenced by the number of surrounding particles, the distance and relative position to other particles in the flow, the Reynolds number and the presence of walls. By examining the effect of these parameters on the flow characteristics, a better understanding of the interaction between particles is achieved.

The flow past a single spherical particle placed in a uniform flow, the wake region is stable and axisymmetric up to Reynolds numbers around 210 ([3], [4], [7]). A regular bifurcation occurs and the flow remains planar symmetric until the wake stability is lost and vortex shedding is initiated as the Reynolds number reaches values around $270 - 285$ ([3], [4], [7]). At Reynolds number of 300, Johnson & Patel [3] and Tomboulides & Orszag [7] found a single dominating frequency, corresponding to a Strouhal number of 0.136, to influence the frequency spectra of the force components. The transition to a almost chaotic wake has been reported to occur for $Re = 300 - 500$. However, Sakamoto & Haniu [6] narrowed this interval down to $Re \approx 420$. The situation for dual particles placed in tandem formation is somewhat different, as a particle is placed in the wake of another, the first transition is delayed and the vortical structure behind the trailing particle remains axisymmetric for all $Re < 250$ [8]. However, for $Re = 250$, the wake structure is highly dependent on the separation distance between the two particles [9]. For small separation distances ($1.5D$), the flow will reach an axisymmetric solution, the reason for this is caused by the elimination of the instability connected to the low pressure region in the wake when a second particle is placed within the recirculation zone of another [9]. A further increase of the separation distance leads to replacement of the axisymmetry of planar symmetry for $D_0 = 2D$ followed by periodic vortex shedding in the wake of the trailing particle for $D_0 > 2.5D$ although the flow remains planar symmetric. Oscilliative motion with a dominant frequency of $f_s = 0.12$ detected in the wakes of both the leading and trailing particle. However, as the separation distance reaches a value of $7.0D$, the flow is again characterized by steady vortical motion in both particle wakes [9].

The purpose with this study is to investigate the interaction among particles subjected to a time dependent flow. The forces exerted on the particles, as well as flow properties, such as wake formation, is studied for a large number of configurations.

2 Numerical method

The Volume of Solid (VOS) method, based on the Volume of Fluid approach, is used to represent the spherical particles. However, in VOS, the "second fluid" is a solid body assumed to have an infinite viscosity. Due to the viscous forces dominating close to the interface, the shear stresses are almost constant at the surface. Together with the assumed infinite viscosity of the solid phase and constant density, a viscosity ratio term can be defined as;

$$\delta\nu = \frac{\nu}{\nu_l} = \frac{1}{\alpha} \tag{1}$$

where ν_l is the kinematic viscosity of the liquid phase and α is the phase variable representing the amount of fluid in each cell, $0 < \alpha < 1$, and μ_l is the dynamic viscosity of the continuous (liquid) phase. Cells containing the solid phase ($\alpha = 0$) will be blocked since there is no flow inside the solid body, and no computations will be carried out for these cells. It should be noted that in most computational cells, the viscosity average will have the value of unity. With the definition of the viscosity term, as stated in (1), the momentum equation can be written as follows;
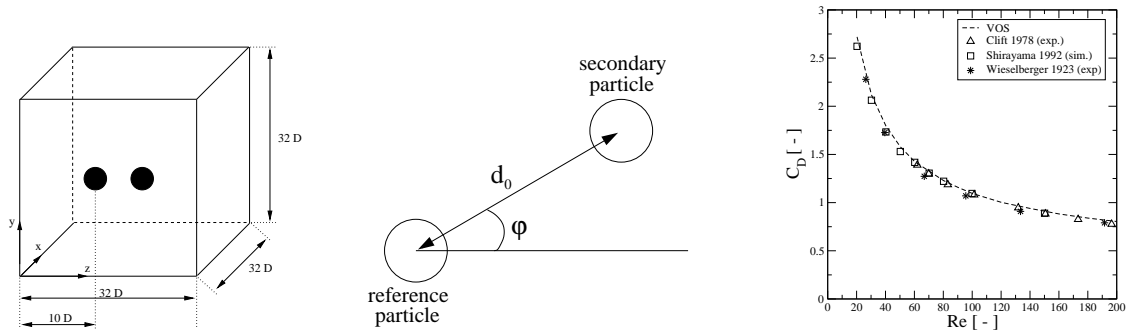
Figure 1: The geometry of the computational domain and the separation distance, D_0 (left) , the angle φ for the dual particle arrangements (middle) and the drag coefficient versus Reynolds number (right).

$$\frac{\partial u_i}{\partial t} + u_j \frac{\partial u_i}{\partial x_j} = -\frac{\partial p}{\partial x_i} + \frac{1}{Re} \frac{\partial}{\partial x_j} \left[\delta \nu \left(\frac{\partial u_i}{\partial x_j} + \frac{\partial u_j}{\partial x_i} \right) \right] \tag{2}$$

with p and Re representing the pressure and the Reynolds number ($Re = \rho U L / \mu$), respectively. The governing equations are discretized on a Cartesian staggered grid, composed of global and locally refined grids, using second order central differences for all spatial derivatives except for the convective terms where a first order upwind scheme is used. The accuracy is increased by using a defect correction method [1] in order to obtain third order accuracy for convective terms and fourth order for the remaining terms. The convergence rate is increased by using a multi–grid method by iteratively solve the system of equations in each time step.

3   Simulations and Results

In this study, two equally sized spherical particles with a diameter D are held fixed at a relative position in a rectangular domain with the dimensions $32 \times 32 \times 32D$ using a grid resolution of $h = D/32$ (Fig. 1 left). The positions are defined by two parameters; the separation distance between the particles, d_0, and the angle, φ, (Fig. 1 middle).

In order to validate the results obtained by using VOS, the drag force of a single particle in a uniform flow with Reynolds numbers in the range of $20 - 200$ is used. As shown in Fig. 1 (right), computations using VOS show good agreement with both experimental and numerical data found in literature. A more detailed validation is found in [5].

3.1   Effect on flow field from pulsating inflow and additional particles

Firstly, regarding the Reynolds number of 100, the introduction of a pulsating inflow does not appear to alter the flow situation significantly. As observed in previous studies for a uniform inflow, [5], the formation of the recirculation zone, especially for particles in tandem formation, is highly dependent on the separation distance between the particles. The shorter the distance, the larger is the effect of the inclusion of an additional particle.

Increasing the Reynolds number, however, leads to clearly visible changes in the flow field between single and tandem formations. Figure 2 shows the vorticies around an isolated particle at $Re = 300$ and $Re = 600$, using the method of Joeng and Hussain [2] for vortex visualization. In this figure, the hair pin vorticies behind the particles for both Reynolds numbers, although the flow field is, as expected, more chaotic for $Re = 600$. Regarding all formations tested, Table 3.1 shows the frequencies of the force components appearing in the flow. Common for all formations is the clear dependency of the inflow frequency. Another observation is regarding particles placed $1.5D$ apart, both $Re = 300$ and 600. Starting with $Re = 300$, Figure 3 shows the vortical structure (left) and a vector plot of the velocity field (right). What is interesting to notice is that the hairpin vorticies have been replaced by a stable and axisymmetric vortex ring behind both particles. The two vorticies in the reference particle wake appears to be isolated from the main flow, as been observed for particles placed in an uniform flow. For $Re = 600$, after being initially unstable, the wake behind the reference particle is stabilized and three distinctive zones can be identified. Two vorticies, that similar to $Re = 300$, appears to be isolated from the main flow, and one zone in-between the two vorticies in which the fluid is moving back and forth but only in stream wise

Table 1: Dominant frequencies found for Re = 300 and 600 for particle placed in tandem formation

	Single	1.5D	3.0D	4.5D	6.0D	T=1.25	T=5
Re 300	0.36, 0.10,	0.10	0.10,	0.10,	0.10, 0.139,	0.20	0.05
	0.13, 0.23		0.148 (sp2)	0.137 (sp2)	0.23		
Re 600	0.10, 0.15	0.10	0.13,	0.10,	0.10, 0.19	0.10	0.05, 0.15
			0.138 (sp2)	0.23 (sp2)			

direction, Fig. 4 (right). As also shown in Fig. 4, hairpin vorticies appears behind the trailing particle and the flow is more similar to the flow of an isolated particle at $Re = 300$ than $Re = 600$.

Increasing the separation distance, vortex shedding is found behind both particles. Figure 5 shows particles at $Re = 600$ and $3D$ where it is depict how the vorticies from the leading particle disturb the trailing particle and thus influencing the development of the re-circulation zone. As presented in Table 3.1, although vorticies are shed from the leading particle as the separation distance is increased to $3D$, the dominant frequency of the force fluctuations still corresponds to that of the inflow. The Strouhal number found for vortex shedding at $Re = 300$, 0.13, is on the other hand found for the trailing particle.

Figure 2: The vortex structure for an isolated particle at Re=300 (left) and Re=600 (right). (Angular view with flow direction from left to right)
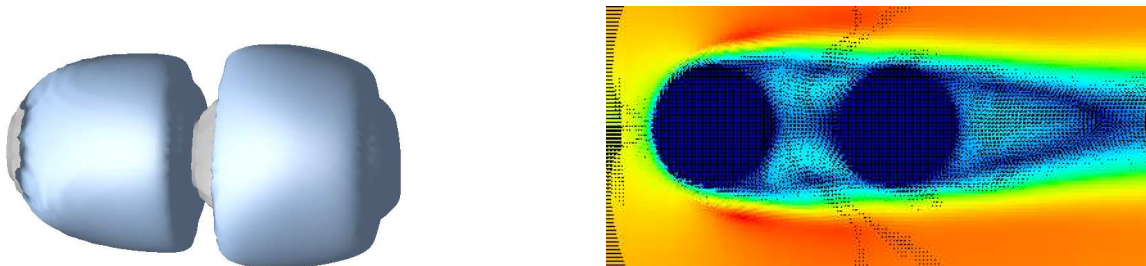
Figure 3: Particles in tandem formation placed 1.5D apart at Re=300. LHS shows the vortical structure and RHS shows the velocity vector plot. (Angular view with flow direction from left to right)
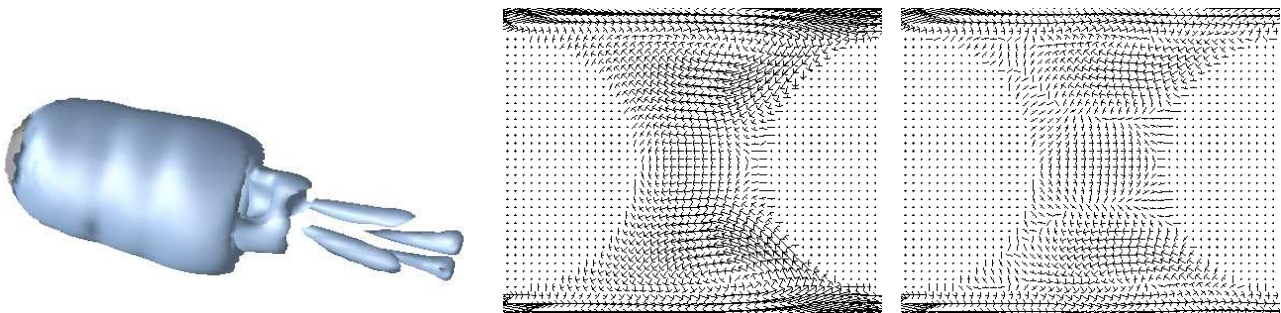
Figure 4: Particles in tandem formation placed 1.5D apart at Re=600. LHS shows the vortical structure. The two plots on the RHS shows the velocity vector plot in-between the two particles. (Angular view with flow direction from left to right)

3.2   Drag and Lift force coefficients

Fig. 6 displays the change in drag (middle) and lift (right) for a dual particle formation as the relative position of the two particles changes for both uniform and pulsating flow at $Re = 100$. Each line represent the drag of the secondary particle as the angle φ is changed from 0 to $180°$ for the four different separation distances. It should be noted that C_D is normalized by the drag of a single particle for a Reynolds number of 100. Furthermore, drag and lift for the sinusoidal inflow are time averaged. The difference in drag between the two inlet conditions is minor whereas there is a substantial difference in lift. For the pulsating inflow, the mean value of the lift force is close to zero for all particle arrangements. However, if placed in a uniform flow, the secondary particle will experience some lift force if placed slightly upstream of the reference particle for $d_0 = 1.5D$. Considering the drag force, the largest drag reduction a secondary particle will be subjected to occurs when placed in the near wake region of the reference particle with the drag as low as 35% of that of a single particle.

Regarding the two higher Reynolds numbers, the drag and lift coefficients for the tandem formations are presented in Table 2. The formations for which the force components were not a clear pulsating curve are marked with "irr". Worth noticing regarding the drag coefficient, is that unlike the case for $Re = 100$, the drag coefficient does not display the same dependency on separation distance.
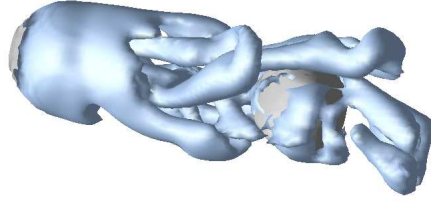
Figure 5: The vortex structure for particles placed $3D$ apart at Re=600. (Angular view with flow direction from left to right)
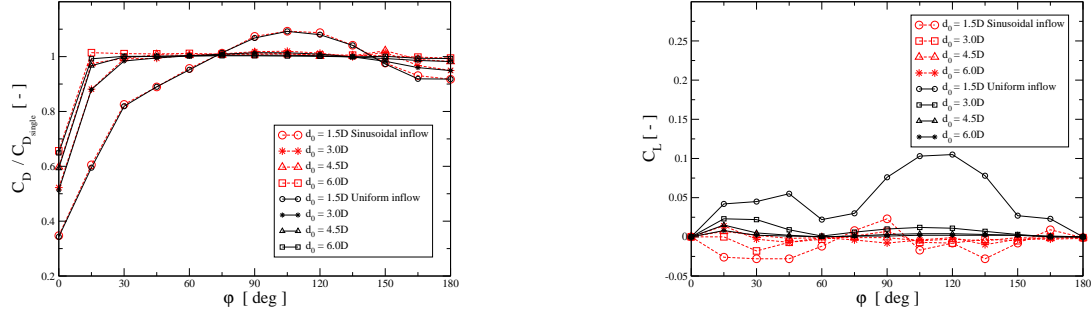
Figure 6: The drag (middle) and lift (right) coefficients for a sinusoidal versus an uniform inlet velocity at a Reynolds number of 100 and different particle distances.

References

[1] Gullbrand, J., Bai, X-S and Fuchs, L. (2001) High-order Cartesian grid method for calculation of incompressible turbulent flow, Int. J. Num. Meth. in Fluids, vol 36, pp. 687-709.

[2] Jeong, J. and Hussain, F. (1995) On the identification of a vortex, J. Fluid Mech., vol 285, pp. 69 –94.

[3] Johnson, T.A. and Patel, V.C. (1999) Flow past a sphere up to a Reynolds number of 300, J. Fluid Mech., vol 378, pp. 19–70.

[4] Natarajan, R. and Acrivos, A. (1993) The instability of the steay flow past spheres and disks, J. Fluid Mech., vol 254, pp. 323–344.

[5] Prahl, L., Hölzer, A., Arlov, D., Revstedt, J., Sommerfeld, M. and Fuchs, L. (2007) On the interaction between two fixed spherical particles, Int. J. Multiphase Flow, vol 33, pp. 707–725.

[6] Sakamoto, H. and Haniu, H. (1990) A study on vortex shedding from spheres in a uniform flow, Trans. ASME J. Fluids Enging., vol 112, pp. 386–392.

[7] Tomboulides, A.G. and Orszag, S.A. (2000) Numerical investigation of transitional and weak turbulent flow past a sphere, J. Fluid Mech., vol 416, pp. 45–73.

[8] Tsuji, T., Narutomi, R., Yokomine, T., Ebara, S. and Shimizu, A. (2003) Unsteady three-dimensional simulation of interactions between flow and two particles, Int. J. Multiphase Flow, vol 29, pp. 1431–1450.

[9] Zou, J.-F., Ren, A.-L. and Deng, J. (2005) Study on flow past two spheres in tandem arrangement using local mesh refinement virtual boundary method, Int. J. Num. Meth. Fluids, vol 49, pp. 465–488.

Table 2: Drag and Lift coefficients for both particles placed in tandem at Re = 300 and 600.

	1.5D	3.0D	4.5D	6.0D	T=1.l25	T=5
Re 300						
C_L (Sp1)	0 ± 0.033	irr	irr	irr	0 ± 0.037	0 ± 0.040
(Sp2)	0 ± 0.026	irr	irr	irr	0 ± 0.034	0 ± 0.021
C_D (Sp1)	0.72 ± 0.17	0.69 ± 0.19	$0.72 \pm \approx 0.2$	$0.73 \pm \approx 0.2$	0.72 ± 0.23	0.71 ± 0.14
(Sp2)	0.076 ± 0.110	$0.36 \pm$ irr	$0.5 \pm$ irr	$0.5 \pm$ irr	0.075 ± 0.15	0.075 ± 0.09
Re 600						
C_L (Sp1)	0 ± 0.023	irr	irr	irr	irr	0 ± 0.025
(Sp2)	-0.01 ± 0.017	irr	irr	irr	irr	irr
C_D (Sp1)	0.67 ± 0.19	0.65 ± 0.23	0.66 ± 0.2	0.69 ± 0.2	0.72 ± 0.23	0.72 ± 0.14
(Sp2)	0.077 ± 0.10	irr	irr	irr	-0.07 ± 0.17	irr

Insights on the Flow-induced Vibration of Flexible Cylinders

Prof. J. Kim Vandiver
kimv@mit.edu
MIT Department of Mechanical Engineering
Cambridge, Massachusetts, USA

Abstract for Keynote Presentation at BBVIV 2007

Introduction

There are several dimensionless parameters which control the observed vortex-induced vibration of flexible cylinders. They include Reynolds number, structural damping ratio, total damping ratio, the current shear, the ratio of power-in region length to wavelength, the ratio of the total cylinder length to wavelength, the length to diameter ratio, the reduced velocity and various combinations from this list. This presentation will describe what the author believes we understand and will outline some questions for which our current understanding falls short. In this abstract some of the key discussion topics are named.

Standing waves or traveling waves

First, why do some cylinders exhibit standing wave behavior, such as is commonly observed with short drilling risers, while traveling waves observed on others? The author's explanations are built on observations from field experiments that span thirty years. In one experiment conducted in 1976, a wire rope 300 meters in length with an L/D of approximately 45 000 exhibited standing wave behavior at about mode fifty. [Vandiver 1993]

In 2006, while towing a 150 meter long pipe in the Gulf Stream with an L/D of 4500, extraordinary traveling wave behavior was observed. Figure 1 shows the fiberglass pipe spooled on a drum on the deck of the research vessel. The pipe was towed from the stern of the ship with a heavy weight on the bottom end. The pipe was instrumented with strain gauges, which measured bending in both planes. The gauge axial spacing was 2.13 m. Figure 2. shows strain measurements made over time at all 70 equally spaced measurement points along the riser. The diagonal colored rows show the crests of waves propagating up the riser at approximately 40 m/s. [Marcollo, Vandiver, Chaurasia, 2007].

In yet another experiment conducted in 1983, a cable 304 m long, with an L/D of approximately 120 000 exhibited zero coherence between the vibration measured at two points separated by only 85 meters. Not only were standing waves not observed over the 85 meter distance, but traveling waves did not persist long enough to result in some correlation between the two points. [Vandiver 1993]

Figure 1. Fiberglass pipe(1.56 cm dia, 153 m long) spooled on the deck of the F.G. Walton Smith. 70 equally spaced, fiber optic, bending strain gauges.
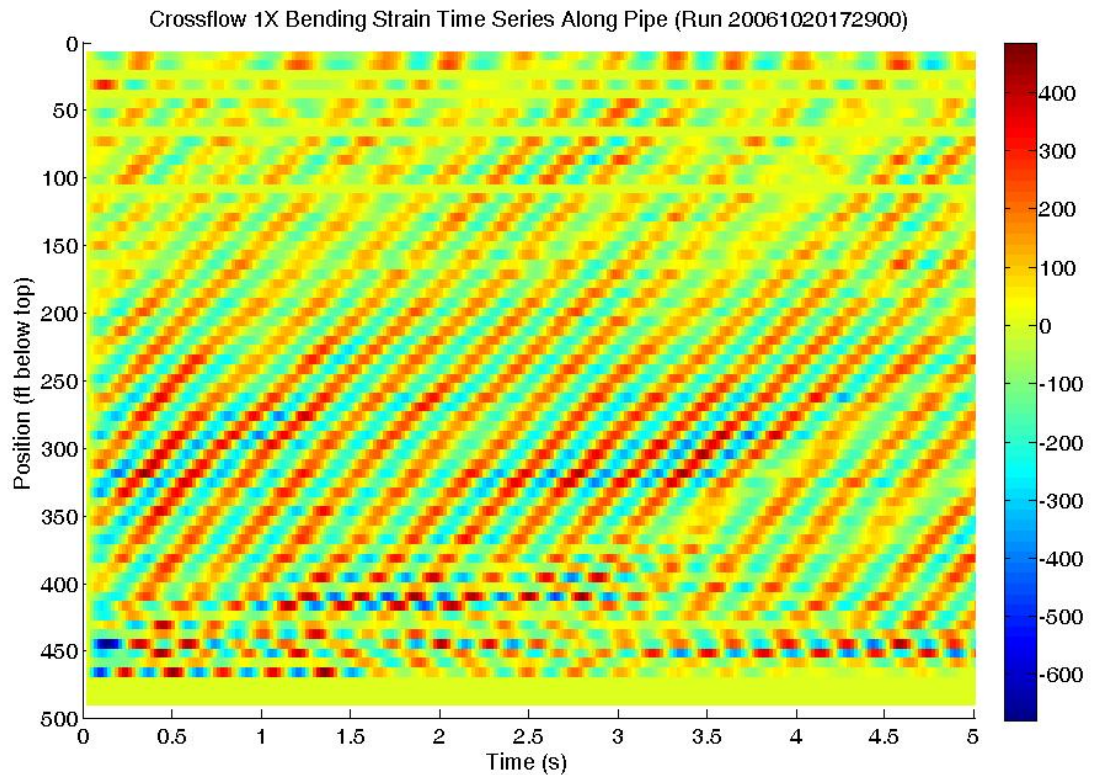
Figure 2. Dynamic bending strain versus time for all axial positions along the riser. Wave propagation at 40 m/s.

Damping, Reynolds number and mass ratio: In the same 1983 experiment a pronounced unproven dependence of A/D on Reynolds number was observed. It has taken twenty-four years to discover a possibly satisfactory explanation. Recent experiments by Govardhan and Williamson[JFM 2006] on spring mounted rigid cylinders in the laboratory have suggested an

explanation, but to fully explain what is going on we must first understand the effects of damping on response. Damping on long flexible cylinders in sheared flow is shown to be a very important parameter. But to understand damping one must understand the importance of mass ratio. Remarkably we find little evidence that mass ratio matters when the cylinder is more than a few wavelengths long. However, nuances remain that are at present beyond our understanding.

Fatigue damage due to higher harmonics: Thirty years ago, our field experiments at Castine, Maine, revealed figure eight motions with large(1.0 diameter) in-line peak to peak displacements.
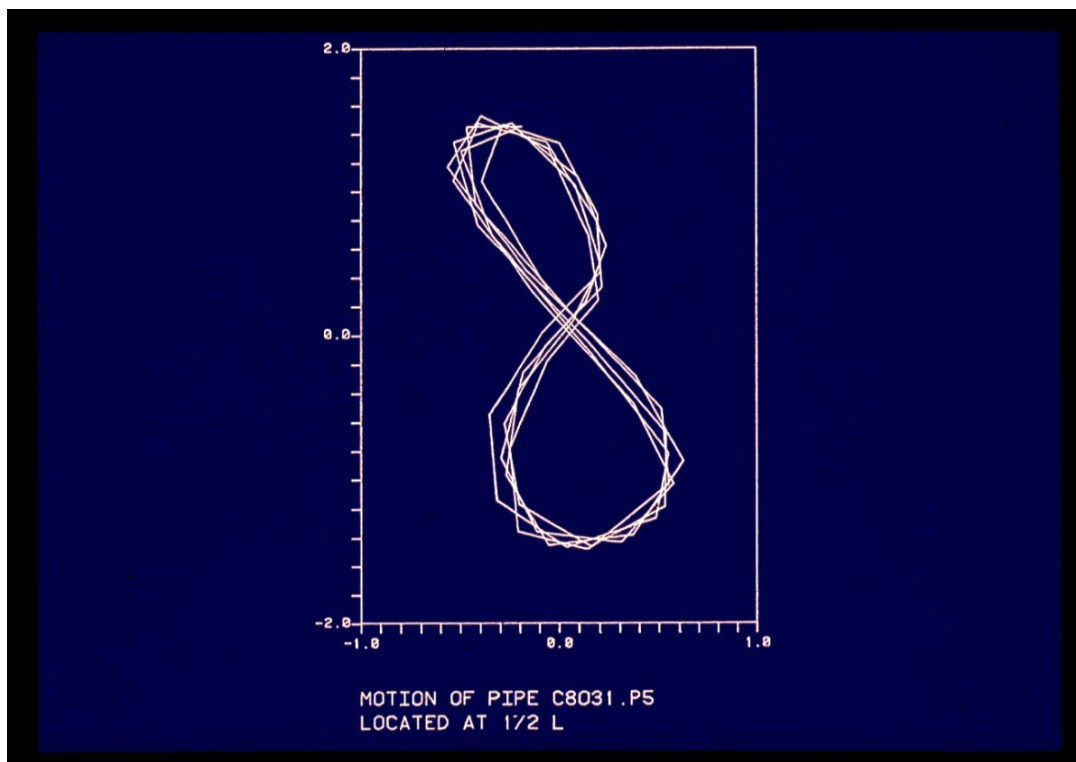
Figure 3. Castine steel pipe, 23 m long, 1981. Figure-8 motion, 3rd mode cross-flow lock-in, and 5th mode in-line resonant response.

We also saw cross-flow response harmonics at three and five times the fundamental cross-flow vibration response frequency. The amplitude of these harmonics was not large enough to create concern with respect to fatigue damage. In the recent 2006 Gulf Stream experiments, the three and five times harmonics were of sufficient amplitude to be a serious potential source of fatigue damage. What was it about the recent experimental conditions that led to dramatic increases in the higher harmonic response? [Jhingran and Vandiver 2007].

Suppression devices: Nearing the end of the talk, we will take a look at the behavior of long cylinders with VIV suppression devices. How much coverage is enough? Do strakes increase damping? What happens if you stagger the positioning of the strakes, leaving bare regions in between? The 2006 Gulf Stream experiments revealed considerable insight about the performance of strakes and fairings. [Vandiver, Swithenbank, Jaiswal, Marcollo, 2006]

Fifth Conference on Bluff Body Wakes and Vortex-Induced Vibrations (BBVIV 5)
Costa do Sauipe, Bahia, Brazil, 12 - 15 December 2007

41
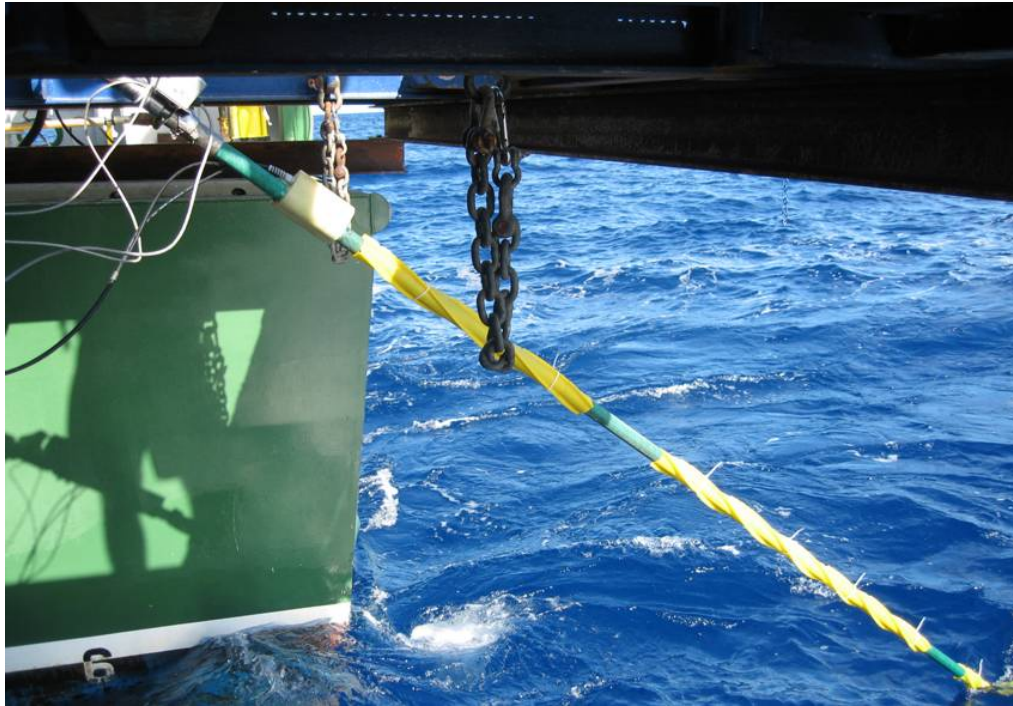
Figure 4. Fiberglass pipe under tow during the 2006 Gulf Stream experiments.

What don't we understand?
1. Will response amplitude continue to grow with Reynolds number as one leaves the subcritical regime?
2. If traveling waves dominate the response, what controls which direction they travel, i.e. up or down the riser?
3. Under what conditions must we worry about fatigue damage from higher harmonic response?

These and other issues will be discussed.

References:

Govardhan, R.N. and Williamson, C.H.K.' "Defining the 'modified Griffin plot' in vortex-induced vibration: revealing the effect Reynolds number using controlled damping", J. Fluid Mech. (2006), vol. 561, pp. 147–180. c 2006 Cambridge University Press.

Jhingran, V. and Vandiver, J.K., 2007, "Incorporating the Higher Harmonics in VIV Fatigue Predictions", Proceedings of OMAE2007, OMAE2007-29352

Marcollo, H., Vandiver, J.K., & Chaurasia, H, "Phenomena Observed in VIV Bare Riser Field Tests", OMAE2007-29562, Proceedings of OMAE 2007: 26th International Conference on Offshore Mechanics and Artic Engineering, June 10-15, 2007, San Diego, USA

Vandiver, J.K., Swithenbank, S., Jaiswal, V. and Marcollo, H. 2006, "The Effectiveness of Helical Strakes in the Suppression of High-Mode-Number VIV", OTC 18276.

Vandiver, J. K.. (1993). Dimensionless Parameters Important to the Prediction of Vortex-Induced Vibration of Long, Flexible Cylinders in Ocean Currents. *Journal of Fluids and Structures*, Vol. 7, No. 5., pp. 423-455.

Fatigue Analysis of a Marine SCR due to Vortex-Induced Vibration

Alessandro A. de Lima[1], Julio R. Meneghini[1], Ricardo B. Flatschart[2], Marcio Mourelle[3], and Enrique Casaprima[4]

[1]NDF, "Escola Politécnica", University of São Paulo, Brazil
[2]Embraer, S.J.dos Campos, Brazil
[3]CENPES, Petrobras, Rio de Janeiro, Brazil
[4]EP, Petrobras, Rio de Janeiro, Brazil

Abstract

In this paper the fatigue analysis of a marine SCR (Steel Catenary Riser) due to vortex shedding is numerically investigated. The riser is divided in two-dimensional sections along the riser length. The discrete vortex method (DVM) is employed for the assessment of the hydrodynamic forces acting on these two-dimensional sections. The hydrodynamic sections are solved independently, and the coupling among the sections is taken into account by the solution of the structure in the time domain by the finite element method implemented in ANFLEX code [4]. Parallel processing is employed to improve the performance of the method. A master-slave approach via MPI (Message Passing Interface) is used to exploit the parallelism of the present code. The riser sections are equally divided among the nodes of the cluster. Each node solves the hydrodynamic sections assigned to it. The forces acting on the sections are then passed to the master processor, which is responsible for the calculation of the displacement of the whole structure. The time histories of stress are employed to evaluate the damage as well as the life expectancy of the structure by the rainflow method to count the cycles in the dynamic response.

Introduction

Vortex-induced vibrations (VIV) has been a substantial challenge in the field of ocean engineering. The onset of cyclic forces due to vortex shedding on marine structures, such as risers employed in the petroleum exploration industry, can cause fatigue damage and collapse of these structures. For a better understanding of the phenomena involved, a good description of the complex flow field developed around the structures is of great importance. Computational fluid dynamics (CFD) is a tool of growing significance in the design phase of these structures. Several CFD methods, such as the finite volume method and the finite element method, have been used for this purpose. These methods are based on the solution of the partial differential equations that describe the flow field, the well-known Navier-Stokes equations. The discretization of the equations is carried out over a mesh. This can be very troublesome in terms of computational efficiency, memory requirements and complexity of the numerical method. These shortcomings lead to the development of Lagrangian methods that do not rely on the use of a mesh. One of these methods of particular interest is the discrete vortex method DVM [5], [7]. This method is based on the surface vorticity boundary integral

approach for potential flow analysis. The computation of the flow field around the structures could be very demanding in terms of computational resources. To overcome this problem, parallel processing is often employed. The main focus of this work is the fatigue analysis of the dynamic response of a SCR due to vortex shedding. A finite element structural model based on a geometrical non-linear beam theory is used, as described in [4]. The dynamic response of the riser is evaluated by solving a general equation of motion in the time domain. The riser is divided in two-dimensional sections along its length. The hydrodynamic forces are evaluated in these two-dimensional strips by the DVM. Viscous effects are modeled through a growing vortex core method [5]. In this way, a quasi three-dimensional analysis is achieved. A similar approach was used by Graham and Willden [3], using a mixed eulerian-lagrangian vortex method, by Yamamoto et al. [7] and Yeung et al. [8] employing a Lagrangian approach. A complete review of vortex methods can be found in Yamamoto et al. [7] and Sarpkaya [6]. In the present method, the hydrodynamic forces are assessed through two dimensional sections by the DVM. In this way, the three-dimensional characteristics of the flow around the riser are neglected. This is a limitation of the method employed in this work. However, according to Graham and Willden [3], assuming that the major component of the wake vorticity is still aligned with the cylinder, and span-wise gradients of all flow variables are assumed to be much less than gradients in the other directions, a two-dimensional simulation for the hydrodynamic part, as a first approach, is expected to provide reasonable results. A SCR marine riser of 2800 meters immersed in a real current is analyzed.

Structural and hydrodynamics models

In this analysis, a static solution of the riser under a current load is firstly obtained. The riser is modeled as an beam element with twelve degrees of freedom. A full description of the structural modeling can be seen in [2]. To solve the dynamic model of the riser through the FEM, it is necessary to evaluate the hydrodynamic forces acting on each section used for the discretization of the structure. To determine these forces, the two-dimensional DVM is employed. Details of this method can be found in [7]. This use of DVM leads to a quasi three-dimensional analysis of the problem. The coupling among the hydrodynamic sections is done solely by the structure. The DVM is a Lagrangian numerical scheme for simulating two-dimensional, incompressible and viscous fluid flow, based on the stream function boundary integral method. In the present method, the body is discretized in a certain number N_w of panels. One discrete vortex with circulation Γ_i is created for each panel, at a certain distance δ of the panel. The vortices created in that way are then convected by the superposition of the effects of the free stream velocity and the induced velocity of the other vortices around the body and in the wake, calculated through the Biot-Savart law. The diffusion of vorticity is incorporated by the method of growing core size (or core spread method) [5].

Analyzed cases and results

First an oil export SCR is modeled. The validation of the numerical method employed in this paper is shown in [1] and [2]. An illustration of the model can be seen in Fig. 1(f) and its mechanical properties are as follow: depth = 1795 m, declivity = -0.87 $degrees$, gravity acceleration = 9.81 m/s^2, steel specific weight = 77 kN/m^3, sea water specific weight = 10.0553 kN/m^3, sea water kinematic viscosity = 9.24×10^{-7} m^2/s, external diameter = 0.32385 m, and elastic modulus = 2.08×10^8 kN/m^2.

The riser is discretized into 1561 elements. Each hydrodynamic section is discretized with 64 panels. Four three

(a) Damage due to current W

(b) Damage due to current E

(c) Damage due to current S

(d) Damage due to current N

(e) Damage due to all current profiles with probability equals to 0.25.

(f) SCR model subjected to a uniform current profile aligned with the catenary plane.
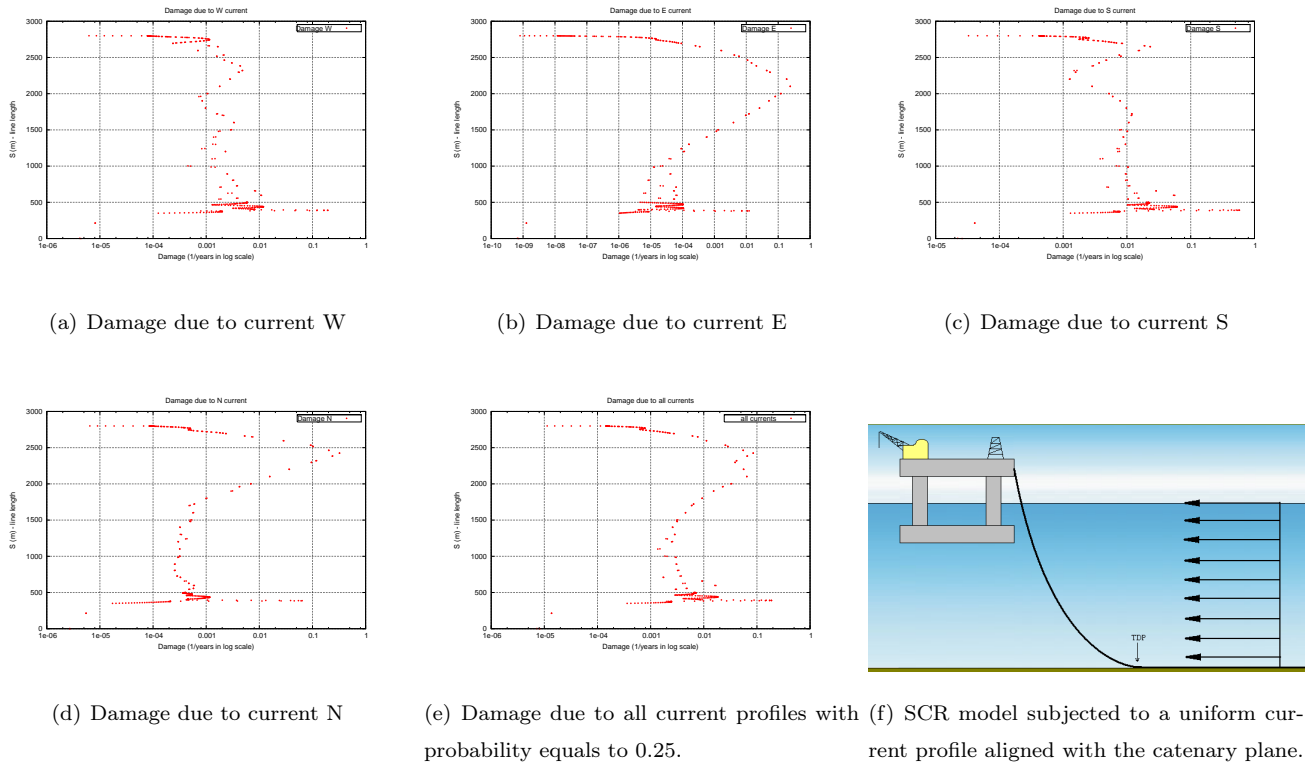
Figure 1: SCR Damage plots due to W, E, S and N currents

dimensional current profiles were employed in the simulated cases and its velocities and directions are shown in the Table 1.

The current profiles are shown in Table 1. As previously carried out, we have simulated the response for 700 *secs*. After the simulation has been completed, the Rainflow method has been employed to evaluate the damage due to VIV in the SCR model. The probability of each current profile to occur has been considered equal to 1.0. The profiles damage can be seen in figure 1. After the single evaluations were done, we proceed the analysis considering the four current profiles actting at the same time with probability equals to 0.25. The results are shown in the figure 1(e).

Table 1: Current profile of the simulated cases.

Depth (m)	(m/s)		(m/s)		(m/s)		(m/s)	
0.0	1.09	W	1.14	E	1.33	S	1.23	N
100.0	0.64	W	0.99	E	1.33	S	1.23	N
350.0	0.56	N	1.02	N	0.84	N	1.16	N
500.0	0.77	N	1.14	N	0.76	N	0.77	N
1000.0	0.73	N	0.65	N	0.71	N	0.69	N
1250.0	0.56	N	0.52	N	0.58	N	0.52	N
1500.0	0.48	N	0.38	N-NE	0.50	N	0.36	N-NE
1795.0	0.00		0.00		0.00		0.00	

Fifth Conference on Bluff Body Wakes and Vortex-Induced Vibrations (BBVIV 5)
Costa do Sauipe, Bahia, Brazil, 12 - 15 December 2007

45

Conclusions

Some results of calculation of risers subject to vortex-induced vibration were verified in this paper. The main feature of the procedure adopted in this paper is the use of an optimized CFD scheme for the calculation of the life expectancy of a SCR. With such an approach, we are able to calculate de damage due to dynamic response of the structure subjected to any three dimensional current. With such computational tool, the study of marine risers installed in very deep water becomes feasible.

Acknowledgments

References

[1] P. W. Bearman, J. R. Chaplin, E. Fontaine, J. M. R. Graham, K. Herfjord, A. A. de Lima, J. R. Meneghini, K. W. Schulz, and R. H. J. Wilden, *Comparisons of cfd predictions of multi-mode vortex-induced vibrations of a tension riser with laboratory measurements*, Proceedings of PVP2006-ICPVT-11, 2006 ASME Pressure Vessels and Piping Division Conference (2006).

[2] A. A. de Lima, J. R. Meneghini, R. B. Flatschart, M. Mourelle, and E. Casaprima, *Numerical investigation of vortex-induced vibration of a marine scr*, Proceedings of OMAE 2007, San Diego, USA **OMAE2007-29269** (2007).

[3] J. M. R. Graham and R. H. J. Willden, *Application of mixed eulerian-lagrangian vortex methods to cross-flow past long flexible circular cylinders*, Proceedings of 2nd International Conference on Vortex Methods, Istanbul, Turkey (2001).

[4] M. M. Mourelle, *Analise dinamica de sistemas estruturais constituidos por linhas maritimas*, Ph.D. thesis, COPPE/UFRJ, Rio de Janeiro, 1993, Ph.D. thesis.

[5] P. R. Spalart, A. Leonard, and D. Baganoff, *Numerical simulation of separated flows*, Ph.D. thesis, Stanford University, California (NASA) (1983).

[6] T.Sarpkaya, *Computational methods with vortices: the 1988 freeman scholar lecture*, Journal of Fluids Engineering **111** (1989), 81–91.

[7] C. T. Yamamoto, J. R. Meneghini, R. A. Fregonesi, F. Saltara, and J. A. Ferrari Jr, *Numerical simulation of vortex-induced vibration of flexible cylinders*, Journal of Fluids and Structures, ISSN 0889-9746 **19** (2004), 467–489.

[8] R. W. Yeung, S. H. Sphaier, and M. Vaidhyanathan, *Unsteady flow about bluff cylinders*, Int. J. Offshore and Polar Eng. **3** (1993), 81–91.

Non-stationary VIM of Two Mono-Column Oil Production Platforms

André L.C. Fujarra[1] **Celso P. Pesce**[1] **Kazuo Nishimoto**[2]

afujarra@usp.br ceppesce@usp.br kazuo@tpn.usp.br

Escola Politécnica, University of São Paulo, Brazil

[(1)] LIFE&MO – Fluid-Structure Interaction and Offshore Mechanics Laboratory

[(2)] TPN – Numerical Offshore Tank

Marcos Cueva **Fernando Faria**

mcueva@oceanicabr.com ffaria@oceanicabr.com

Oceânica Offshore, São Paulo, Brazil

Extended Abstract

Besides high stability, FPSO[1] platforms present high deck load and storage capacities. They can be converted from existing tankers or built as new structures, specific to oil production and storage, what pushes down the construction costs. Despite those advantages, wave motions response can be a problem, increasing the downtime. SS[2] platforms present low response wave motions, though not enough to dry trees application. Low installation costs and high mobility makes a SS also suitable for drilling. However, no storage capacity, besides structural and stability issues still make this well proved concept expensive. Spar platforms combine low wave motions response and stability with high deck load and storage capacities, though at high costs. Spars exhibit VIM (Vortex-Induced Motions) a particular case of VIE (Vortex-Induced Excitation) and are prone to Mathieu like instabilities; [11]. On the other hand, Mono-column platforms (MCP), a relatively new concept, [9], may be designed to combine most of FPSO advantages, as high storage capacity, high stability and simple structures with low response motions and minimum downtime, like the SSs, but at lower costs than Spars.

Many studies have been published, after Miyagawa pioneering work [9], comparing the behavior of MCPs in the sea environment and other floating units, [8], [13], [3]. Meanwhile, some companies, like MPU-SEMO, SEVAN MARINE, AKER KVAERNER and PETROBRAS, developed their own MCP designs. The interest for this type of platform has grown the last four years, with PETROBRAS' investments in R&D and the construction of four units by SEVAN MARINE. The first unit is leased to PETROBRAS to operate at Northeast Brazil. The enormous and approximately rounded cross-section – a bluff-body shape - is the main characteristic of a MCP. Such geometry associated to high speed currents, like those present in Brazil or Gulf of Mexico, can excite VIM, with high amplitude response. This phenomenon was first detected in Spar platforms installed in Gulf of Mexico; [4], [6], [7], [14], [15]. No extensive work, though, has been presented concerning VIM of MCPs. Their small (draft to breath) aspect ratio makes MCPs rather different from Spar platforms. Such difference added to the inherent complexity of VIM phenomena does not allow simple extrapolations of Spar results and demands small-scale models experiments in steady flow. This extended abstract presents some VIM experimental results for two MCs: the MonoBR-GoM and SEVAN-PIRANEMA, including an analysis via the Hilbert-Huang Spectral Analysis technique. More extensive and detailed results will be presented in a full paper, to be submitted. Previous results, on a first unit, may be seen in [2].

Two Mono-Column Offshore Platforms Experiencing VIM

The MonoBR-GoM was designed to operate in 2,500m WD, producing 120,000bbl/day and storing 800.000bbl. Main breath is 100m and draft varies from 28.7m to 47.9m (203,000t to 293,000t displacement). The platform is to be moored with a 13 lines semi-taut spread system and to be equipped with 6 production and 1 export steel catenary risers, besides 3 control umbilicals. Sway natural period lies between 360 and 500s. SEVAN MCP was designed as a versatile hull to operate in several sites around the world. The unit PIRANEMA, leased to PETROBRAS, will operate in 1,100m and 1,300m WD. Main breath is 60m, draft varies from 13m to 17m (39,600t to 51,200t displacement). The mooring system is a 9 lines taut spread arrangement. The platform operates 25 flexible risers. Sway natural period is circa 200s.

A major small-scale study has been carried out at IPT towing tank. Details may be found in [2]. Differently from regular VIV, VIM of MCPs usually presents increasing amplitude responses with respect to reduced velocity, typical of bluff-body shapes. Those tests were planned to cover all major aspects regarding MCPs: small aspect ratio (little spanwise correlation); non-symmetrical hull

---

[1] Floating Production Storage and Offloading
[2] Semi- submersible

(geometry and appendages: chains, anodes, risers, fairleads); long oscillation (moored) periods, so long transient responses, requiring a long testing times; scale effects involving Reynolds number; non-linear and non-symmetrical mooring pattern; simultaneous excitation of in-line and cross-flow motions.

In an effort to address all those aspects, some actions were taken and premises adopted : (i) no results from infinite cylinders, risers or even Spars were used as benchmark; (ii) hull models were built considering small tolerances and all important appendages; (iii) long test times, from 10 to 15min, to allow steady behavior and no kind of mechanism to minimize damping effects (the models were simply supported by means of non-immersed springs); (iv) roughness added to the hull, based on captive tests and results from the literature; [14], [1], [2]; (v) focus only on the behavior around the offset position due to the current effect with in-line and cross-flow restoring stiffness measured according to [1], [4], [15][6] . In the MonoBR-GoM case, a set of four different values of roughness were tested in two different headings (environment conditions), [2]. In the SEVAN PIRANEMA one, two roughness values were tested in four different headings.

The set of tests is quite large, including captive ones to measure drag coefficients. Some of the main results are presented in Fig. 2. Amplitude and period responses are shown for both platforms. Shaded regions highlight current velocities up to 2m/s in full scale (0.14m/s in model scale). Distinct regions in the MonoBr-Gom case are due to differences in mooring stiffness $T_n \approx 360s$ and $500s$. From the large data set, some remarks may be presented. VIM presented high amplitude responses even for Vr>8, with no lock-in behavior, differently form Spars; [14]. Despite a clear resonant behavior, identified by response periods lying between 1.05 and 1.2 times the natural one, the amplitude behavior is quite different from those corresponding to VIV, resembling a typical bluff-body response. Besides, a strong influence on heading was observed, especially in the MonoBR-GoM case. The removal of appendages in SEVAN PIRANEMA case deeply impacted VIM amplitude behavior, showing the importance of such experimental detailing. Care was taken to not include artificial damping in the experiments, though, in full-scale, risers and mooring lines damping will act favorably, reducing amplitudes. For velocities around 2m/s in full scale (0.14m/s in model-scale), that are typical worst conditions offshore Brazil, VIM amplitude was 0.4 and 0.6 diameters, at reduced velocities 7.2 and 9.6, for the MONOBR-GoM (Re~2x10^{8}, full-scale and Re~7.07 x10^{4}, model-scale). At the same velocity, 2m/s, the measured amplitude lied between 0.1 to 0.2 diameters, at reduced velocity 6.7, for the Sevan-Piranema (Re~1.2x10^{8}, full-scale and Re~4.24 x10^{4}, model-scale). As expected, Reynolds dependence seems to play a very important rule in the phenomenon.

The HH Spectral Analysis Technique Applied to MCP VIM

Like VIV and WIV (Wake-Induced Vibration related to wake interference between cylinders), VIM appears as a highly nonlinear dynamic phenomenon. Experimental or numerical time-histories that emerge from VIV, WIV or VIM investigations are nonlinear and non-stationary. Nonetheless, usual Spectral Analysis methods rely on the hypotheses of linear and stationary dynamics. A method envisaged to treat non-stationary signals that emerge from non-linear systems was presented by Huang et al. [5]. It is sometime referred to as Hilbert-Huang or spectral analysis method. This method applies the usual Hilbert transform to a finite set of 'Intrinsic Mode Functions' (IMFs) obtained from the original signal through an 'Empirical Mode Decomposition' (EMD). In the H-H technique, the intrinsic "mode" is temporal, not a structural "mode" (vibration eigenmode) nor a vortex shedding mode. The EMD method, conceived to obtain the set of IMFs, is based on a recursive subtraction of successively calculated mean between the two time-envelope of extrema (maxima and minima) that are contained in the signal. The envelopes are splines-fitting of maxima (and minima). Details can be found in [5], where this method is referred to as a 'sifting' process. In this extended abstract only one example is shown. Discussion is here restricted to few illustrative points. In the paper, to be submitted, other cases are shown and discussed. Applications to VIV and WIV may be found in [10] or in [11].

As mentioned, the oscillations caused by steady current have a non-stationary pattern, as may be seen two examples shown in Fig. 3, referring to two distinct reduced velocities, 6.2 and 10.1. Corresponding amplitude responses are respectively 0.2*D* and 1.3*D*, determined by considering the 1/10th highest peaks. Despite the apparent non-stationarity, the most energetic frequency is quite stable, at both reduced velocities, remaining very close to the moored system natural frequency. Modulations and very-low frequency components are quite evident, though. IMFs are not shown for space saving.

Acknowledgments

References

[1] Allen, D.W., Henning, D.L., 2001, Surface Roughness Effects on Vortex-Induced Vibration of Cylindrical Structures at Critical and Supercritical Reynolds Numbers, OTC13302.

[2] Cueva, M., Fujarra, A.L.C., Nishimoto, K., Quadrante, L., Costa, A.P., 2006, "Vortex-Induced Motion: Model Testing of a Mono-column Floater", Proceedings of OMAE'06, Hamburg, Germany.

[3] Chou, F., Chianis, J., Zhang, X., 2004, Self Installed Single Column Floater, OMAE2004-51466.

[4] Huang, K., Chen, X., Kwan, C-T., 2003, The impact of Vortex-Induced Motions on Mooring System Design for Spar-based Installations, OTC15245.

[5] Huang, N.E. et al, 1998, The Empirical Mode Decomposition and the Hilbert Spectrum for Non-linear and Non-stationary Time Series Analysis, *Proc. R. Soc. Lond. A*, 454, pp. 903-995.

[6] Irani, M., Finn, L., 2004, Model Testing for Vortex Induced Motions of Spar Platforms, OMAE2004-51315.

[7] Magee, A., Sablok, A., Gebara, J., 2003, Mooring Design for Directional SPAR Hull VIV, OTC15243;

[8] Matsuura, M., Isozaki, Y., Ishibashi, Y., 1995, Development of Mono-Column Type Hull Form with Passive Type Motion Damping Devices for Floating Production System, OMAE 1995, Vol. I-A, 403-410.

[9] Miyagawa, M., Isozaki, Y., Yano, S., Matsuura, M., 1989, Development of New Concepts on Floating Production storage and Offload Unit, OMAE 1989, Volume I, pgs 49-55.

[10] Pesce, C.P., Fujarra, A.L.C, Kubota, L., 2006, The Hilbert-Huang Spectral Analysis Method Applied to VIV, Proceedings of OMAE'06, June 4–9, 2006, Hamburg, Germany.

[11] Rho, J.B. et al., 2005, A study on Mathieu-type Instability of Conventional Spar platform in Regular Waves, Int J of Offshore and Polar Engineerring, Vol. 15 (2), 104-108.

[12] Silveira, L.M.Y, Martins, C.A., Cunha, L.D and Pesce, C.P., 2007, An Investigation on the Effect of Tension Variation on VIV of Risers, Proceedings of OMAE 2007, San Diego, USA.

[13] Tanabe, A., Matsuura, M., 1997, FPS Development – A New Concept of MONOCOLUMN, Black SEA-97.

[14] van Dijk, R., Magee, A., Perryman, S. Gebara, J., 2003, Model Test Experience on Vortex Induced Vibrations of Truss Spars, OTC15242.

[15] Yung, T-W., Sandström, R.E. Slocum, S.T., Ding, Z.J., Lokken, R.T., 2004, Advancements of Spar VIV Prediction, OTC16343.
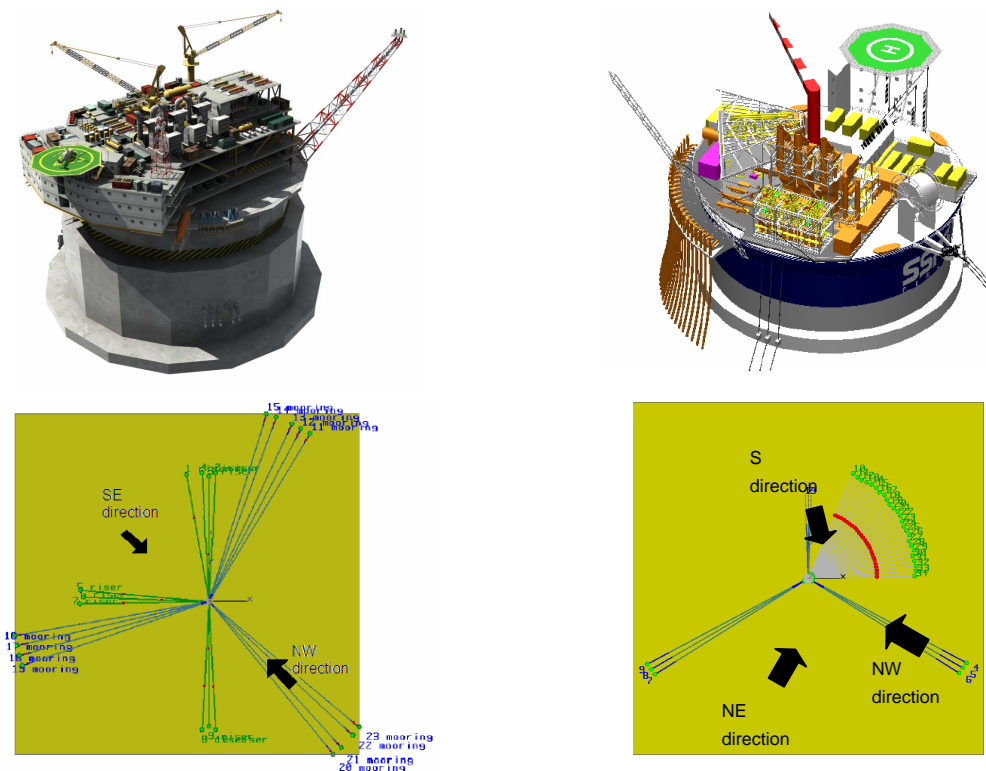
Figure 1. MonoBR-GoM, SEVAN Piranema and mooring systems.
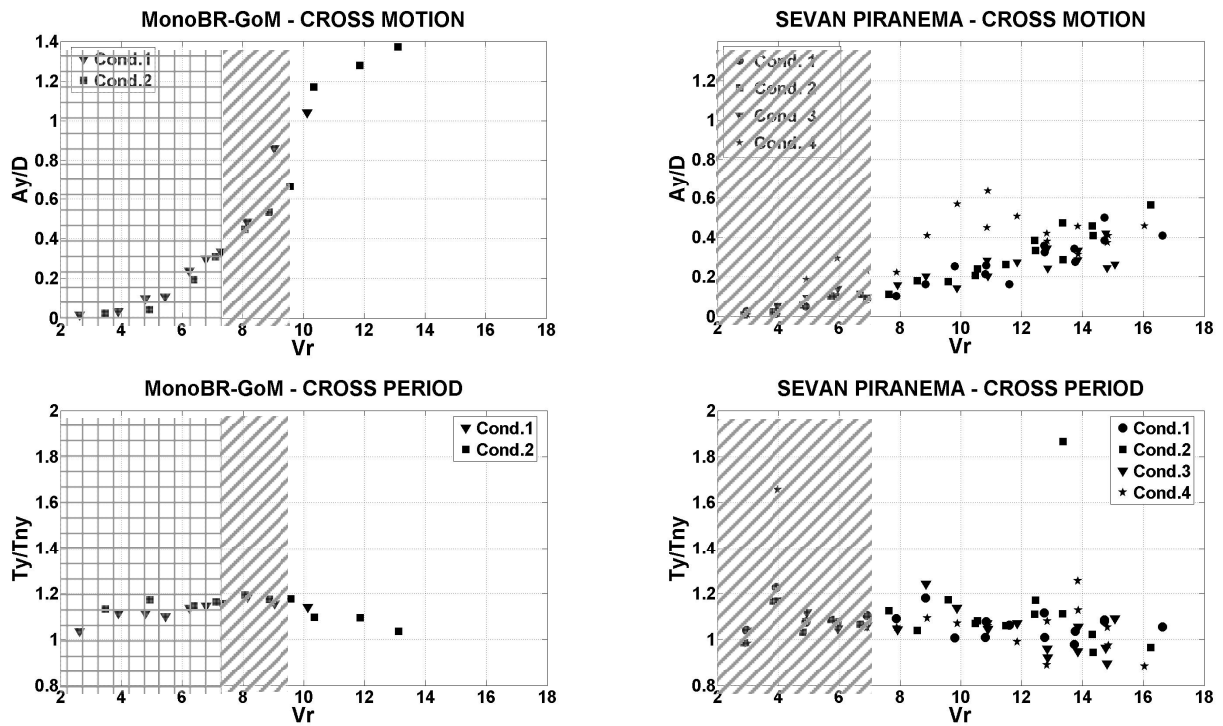
Figure 2. Amplitude-to-Diameter and Dominant Period Responses. MonoBR-GoM: two different headings. SEVAN PIRANEMA: three headings, one without appendages. $V_r = UT_n/D$.
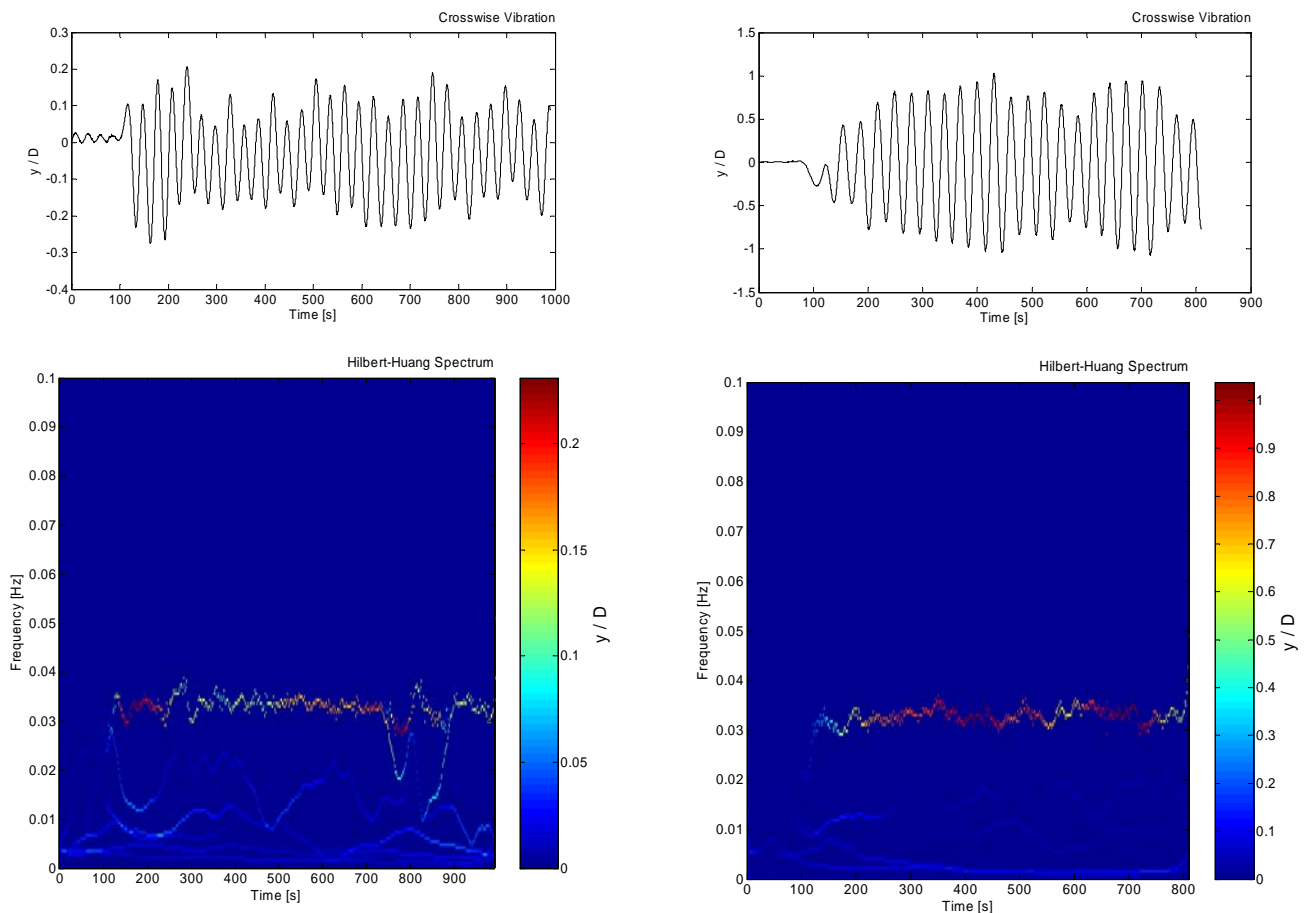
$$V_r = 6.2 \text{ ; } Re \approx 60 \times 10^3$$

$$V_r = 10.1 \text{ ; } Re \approx 100 \times 10^3$$

Figure 3. Crosswise oscillations of a Mono-Column Platform (MonoBr-GoM), and H-H spectra. Natural period in still water $T_n = 26.1s$ **(in small-model scale 1:200)**; $D = 500\text{mm}$; $H/D = 0.395$.

Time-Sharing of Frequencies in High-Mode Number Vortex Induced Vibrations

Susan B. Swithenbank, [1] Hayden Marcollo [2] and J. Kim Vandiver [3]

Abstract

This paper shows that high-mode number large amplitude Vortex-Induced Vibrations (VIV) respond at a single frequency at any one time. The vibrations switch between frequencies in time. This switching of frequency in a short time can appear as a multi-frequency response if the data is not analyzed on a short-time scale. Data from two scaled-model tests completed in 2006 are used to demonstrate this phenomenon called 'time-sharing'. This single frequency time sharing effects the fatigue life of marine risers.

1. Introduction

A question in Vortex-Induced Vibrations (VIV) prediction is when is a response single frequency versus multiple frequency response? Existing industry accepted VIV prediction programs operate on the premise that when more than one frequency is predicted to cause vibrations each frequency is apportioned an section of the riser over which that frequency can input energy. This research shows that each frequency is allowed as much of the riser in space, but will only vibrate at that frequency for a finite amount of time before switching to another frequency. Therefore instead of sharing in space, the frequencies share in time.

The Gulf Stream tests, (Vandiver et al., 2006), provided an opportunity to investigate the difference between single-frequency and multi-frequency behavior at high-mode number. After close examination of the data, it appears that single-frequency response happens for all large amplitude responses, but in sheared flows, where more than one excitation frequency is present the single dominant frequency changes in time. Using

---

[1] Center for Ship and Ocean Structures, NTNU
[2] AMOG Consulting
[3] Department of Mechanical Engineering, MIT
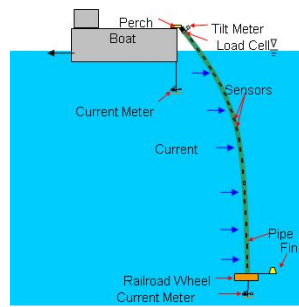
Fig. 1. Experimental Set-Up for the Lake Seneca and Gulf Stream tests

Maximum Entropy Method (MEM) analysis, (Burg , 1968), the data was able to be analyzed on small time scales.

Whether a riser is vibrating with a single-frequency or multiple frequencies has a large influence on the fatigue life of a riser. Single-frequency vibrations cause larger damage than multi-frequency vibrations. With a single frequency response there is no destructive interference between the different frequencies. This causes large amplitude response at the anti-nodes with high damage rates.

2. Experiment Description

The Gulf Stream tests conducted in the fall of focused on a long riser in sheared flow. The goals of the overall test program were to understand the dynamics of a riser undergoing VIV at high mode number. The Gulf Stream tests were conducted on the Research Vessel F. G. Walton Smith from the University of Miami using a composite fiber riser. The riser was 152.5 m with an outer diameter of 0.0363 m and was hanging in the water from the stern of the ship. A railroad wheel weighing 3225 N in the water, was attached to the bottom of the riser to provide tension. The riser was exposed to both uniform and sheared flows. The experiment set-up can be seen in Figure 1.

For instrumentation, fiber optic strain gages were located ever 7 ft along the length of the riser. An Acoustic Doppler Current profiler (ADCP) recorded the current velocity and direction along the length of the riser. On the R/V F. G. Walton Smith, two ADCPs use a different frequency to obtain different currents at different depths. Additional instrumentation included a tilt meter to measure the inclination at the top of the riser, a load cell to measure the tension at the top of the riser, two mechanical current meters to measure current at the top and the bottom of the riser, and in the Gulf Stream 2006 test a pressure gage was used to measure the depth of the railroad wheel.

3. Modal Behavior

Two VIV dynamic responses have largely been studied, the standing wave behavior and the infinite string behavior. Standing wave behavior, is typically found in cylinders with a small length-to-diameter ratio. A large number of tests have been done on cylinders at low mode number both in the laboratory and in the field that show this standing wave behavior. The RMS response shows clear nodes and anti-nodes. At these

low-mode number cases, single-frequency behavior is typically controlled by a single mode.

The infinite string can be shown with a theoretical calculation where there are no boundary conditions; therefore there are no reflections from the boundary. Instead of seeing the standing wave behavior, a finite region where power enters the system is seen with traveling waves leaving this area traveling to outward away from the region with power entering the system. .

The riser's behavior in the Gulf Stream tests is in between the infinite string and the standing wave response cases. Vandiver (1993) suggested a dimensionless parameter of $n\zeta_n$, where n is the mode number and ζ_n is the damping ratio for mode n, be used to differentiate between when standing wave behavior and infinite string behavior will dominate a response. In Vandivers calculations, $n\zeta_n < 0.2$ meant standing wave behavior dominates where $n\zeta_n > 2.0$ indicated an infinite string behavior away from the ends. For both the Gulf Stream tests $n\zeta_n$ is between 0.2 and 2.0 which is indicative of a behavior between these two extremes.

The modal behavior with nodes and anti-nodes is not seen in the Gulf Stream test likely due to the high mode number behavior; instead, fairly uniform RMS response is seen in the power-in region with a damped decay outside the power-in region caused by the traveling waves. RMS strain results from a typical Gulf Stream test are in 3 (right). This figure shows the RMS strain for a Gulf Stream 2006 test on the left, with the normal incident current profile for the test run on the right.

Cylinders with high length-to-diameter ratios with high mode number response are more likely to be closer to the infinite string extreme. It is therefore inappropriate to describe such a behavior as 'singe-mode response' which refers to a stationary wave response; the term 'single-frequency response' is more appropriate Marcollo et al. (2007).

4. Results

Many industry prediction programs divide the riser into sections spatially, and allow each spacial section to have a different input frequency. This research shows that instead of the riser having multiple frequencies vibrating at the same time, the frequencies are divided in time, with one frequency dominating the riser for a finite amount of time, follow by another frequency. This changing of frequencies in time is referred to as 'Time Sharing'.

Figure 2 (left) shows the RMS strain response and the normal incident current proflie for a typical case from the Gulf Stream experiments. When a Power Spectral Density (PSD) is taken using a multi-minute average, more than one dominant frequencies may occur in that time, and would all appear in the PSD. When the data is broken into very small time increments and analyzed, single-frequency response becomes more evident. Figure 2 (right) shows the spectra taken over three minutes in the Gulf Stream tests for one strain gage. The dominant VIV frequency at approximately 2.5 Hz shows multi-frequency participation.

In Figure 3 (left), the same time series is broken into 8.5-second intervals. Each PSD shows a single frequency response, but the three different PSDs show different frequencies. The first two PSDs are from consecutive 8.5 second intervals. The third PSD is from 60 seconds later in the test run.
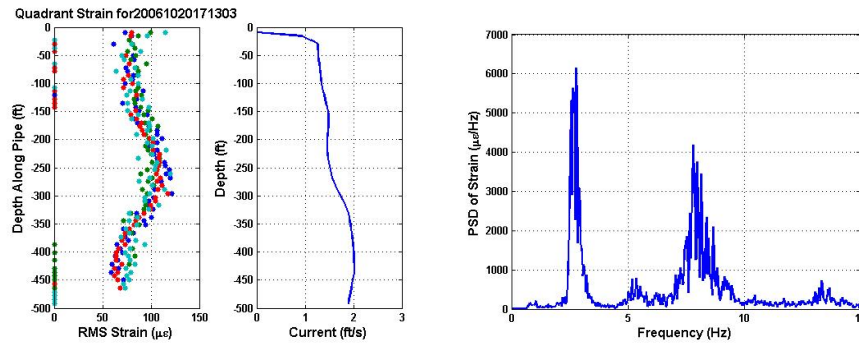
Fig. 2. (left) The RMS of the strain from each sensor. This represents only the dynamic portion of the strain, with the tension component removed and the normal incident current profile.(right) The PSD of a test from the Gulf Steam 2006 (20061020171303) using 3 minutes of data.
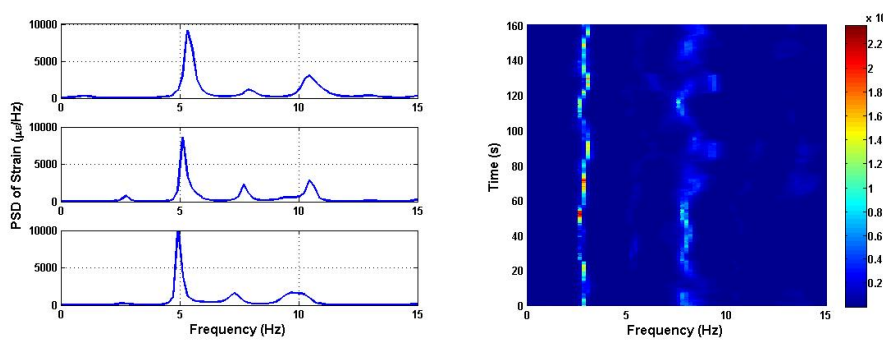
Fig. 3. (left) Three separate PSDs, calculard using MEM analysis, from the Gulf Steam 2006 (20061020171303) each using 8.5 seconds of data. (right)A waterfall plot of 8.5 second MEM spectra from Gulf Steam 2006 (20061020171303). The units of intensity are $\frac{\mu\epsilon}{Hz}$

The existence of time sharing does not prevent all multi-frequency behavior. At times in between dominant frequencies many small-amplitude locally generated vibration frequencies are observed. One frequency will be dominant, then another frequency would begin to gain energy, and the first frequency will lose energy. While the two frequencies transition both frequencies can participate at small amplitudes. When this phenomenon occurred in the Gulf Stream tests the amplitudes of the vibrations are small. When multi-frequency behavior is apparent, the amplitude of the spectral peak is less than 30% of the largest VIV response.

At sufficient distance from the excitation region, the dominant VIV frequency has been damped. At this distance, the dominant VIV frequency does not control the wake and therefore does not surpess all other vibrations. Low amplitude locally generated vibrations are observed in the data. In the sheared currents, these are often at lower frequency than the dominant frequency. These frequencies do not generate significant traveling waves because they are not seen over a large section of the riser.

Figure 3 (right) is a waterfall spectrum of the same case as shown in Figure 2 (left). The dominant VIV frequency is seen to be about 4 Hz. When the amplitude of the vibration is at less than 1e4 $\mu\epsilon$/Hz, some low amplitude vibrations with multiple frequencies

participating is observed, but when the amplitude is large only one dominant fundamental frequency is apparent. Harmonics of the dominant VIV frequency are observed at two and three times the dominant VIV frequency. More discussion on time sharing of frequencies is found in Swithenbank (2007).

5. Prediction Methods using Time Sharing in SHEAR7

Previous prediction methodology dealt with the co-existence of modes via spatial sharing of the riser when calculating the input power for modes. In this other methodology, the different frequencies controlled different sections of the pipe at the same time. Using time sharing, the frequencies can control a larger section of the riser, but for a finite duration of time. In SHEAR7 the frequencies are assigned a probability which accounts for the amount of time that any one frequency will dominant the riser. The program still executes in the frequency domain. The results from analyzing the Gulf Stream test in SHEAR7 using time sharing instead of the previous methodology showed good results.

References

BURG, J. P. 1968 Maximum entropy spectral analysis *Modern Spectrum Analysis IEEE Press* 34–48.

MARCOLLO, H., CHAURASIA, H. & VANDIVER J. K. 2007 Phenomenon Observed in VIV Bare Riser Tests. *Offshore Mechanics and Arctic Engineering Conference San Diego CA 10-15 June 2007* OMAE2007-29562.

SWITHENBANK, S. B. 2007 Dynamics of Long Flexible Cylinders at High-Mode Number in Uniform and Sheared Flows. *PhD Thesis, MIT Department of Mechanical Engineering*

VANDIVER, J. K. 1993 Dimensionless Parameters Important to the Prediction of Vortex-Induced Vibration of Long, Flexible Cylinders in Ocean Currents. *J. Fluid and Structures* **7**, 423–455.

VANDIVER, J. K. & LEE, L. 2003 SHEAR7 Version 4.3 Theory Manual *MIT* 2003

VANDIVER, J. K. & MARCOLLO, H. 2003 High-Mode Number VIV Experiments *IUTAM, 1-6 June 2003*

VANDIVER, J. K., SWITHENBANK, S. B., JAISWEL, V. & JHINGRAN V. 2006 Fatigue Damage from High-Mode Number Vortex-Induced Vibration. *Offshore Mechanics and Arctic Engineering Conference Hamburg Germany 4-9 June 2006* OMAE2006-9240.

Model Tests of Self Standing Hybrid Riser in Deep-Sea Basin

Paulo S.D. Pereira, PETROBRAS/CENPES/PDP/TS (paulod@petrobras.com.br)

Katsuya Maeda, National Maritime Research Institute (kmaeda@nmri.go.jp)

Celso K. Morooka, State University of Campinas (morooka@dep.fem.unicamp.br)

Shotaro Uto, National Maritime Research Institute (uto@nmri.go.jp)

Nowadays, many offshore oil fields in ultra deep water depth have been discovered. However, most of those petroleum reservoirs in water depth over to around 2500 meters are waiting for development of production systems which are technically and economically suitable. Among those, one possible solution should be the Self Standing Hybrid Riser system (SSHR). A SSHR, in general, consists of three parts, which are a long vertical steel pipeline, a floatation buoy and a flexible jumper. The long vertical steel pipeline is connected to a foundation at the seabed and to a floatation buoy at its top end. Throughout a flexible jumper, the outlet of the vertical riser at a floatation buoy is connected to a flexible jumper that ends at its upper part in an oil and gas processing facility, usually a FPSO or other type of floating petroleum production vessel. The authors have been discussing about the initial design of the SSHR through the model tests. Results from the previous model test [1] suggested that the structure design of a floatation buoy should be improved.

Needless to say, the vortex induced vibration (VIV) is an important factor not only for the design but also for the life time of the SSHR. In general, an outer diameter of a floatation buoy is larger than a vertical riser pipeline. Therefore, the important point is how to reduce the VIV effect of a floatation buoy. One possible solution is to install some kind of strake around the flotation buoy. In the present investigation, several flotation buoys with different types of strakes have been prepared. Then, model tests were carried out in uniform current condition in the Deep-Sea Basin of the National Maritime Research Institute (NMRI), and the inline and transverse direction behavior, respectively, of the flotation buoy were measured by the 3 dimensional optical measurement system.

The present paper introduces the results for the effects of strakes against VIV, on the flotation buoy.

Figure 1 schematically shows the layout of strakes with different paths installed around floatation buoys. The number of strakes is three or four. And, the turns of strake are 1.0 (360degree), 1.5
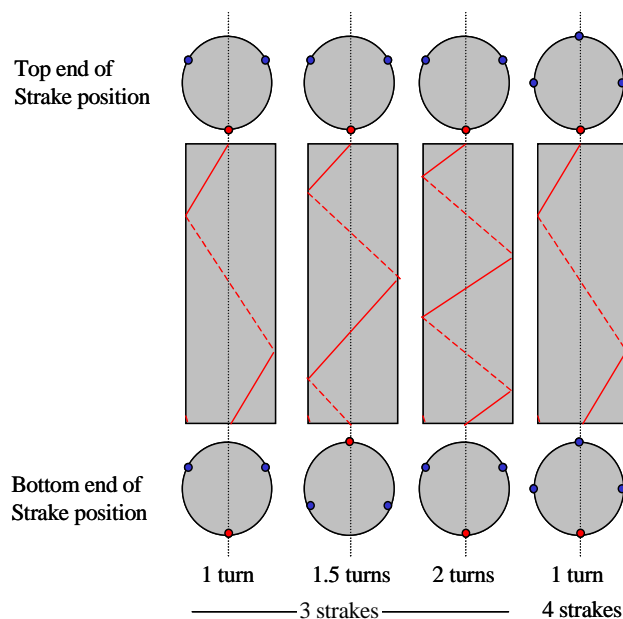
Figure 1. Different type of strakes

(540 degree) and 2.0 (720degree), respectively. The height of the strake is 10% of a diameter of the flotation buoy.

The model here considered is composed by the flotation buoy with the vertical riser. In this case, the length of the vertical riser is 20 meters long. And, the Reynolds number ranges from 0.65×10^{4} to 3.9×10^{4}.

Figure 2 shows measured results for the amplitude of inline and transverse behavior, respectively, of the flotation buoy. Comparisons between without strake and with strakes cases are shown. In the figure, the vertical axis denotes amplitudes for the inline or transverse motions divided by the outer diameter of the flotation buoy. And, the horizontal axis denotes the Reynolds number. Amplitudes for the inline behavior show similar tendencies for all the conditions. However, the transverse amplitudes with strake condition were around a half of the amplitude without strake one.

Figure 3 shows the measured spectra of inline and transverse motion behavior of the floatation buoy. The vertical axis means power of spectrum and the horizontal axis denotes circular frequency. From the results in Figure 3, the inline buoy motion behavior for different type of strakes show similar tendencies. However, the transverse motion behavior of the flotation buoy with strake is shifted to the low frequency, and also the amplitudes are reduced. This tendency is effective for the fatigue problem.
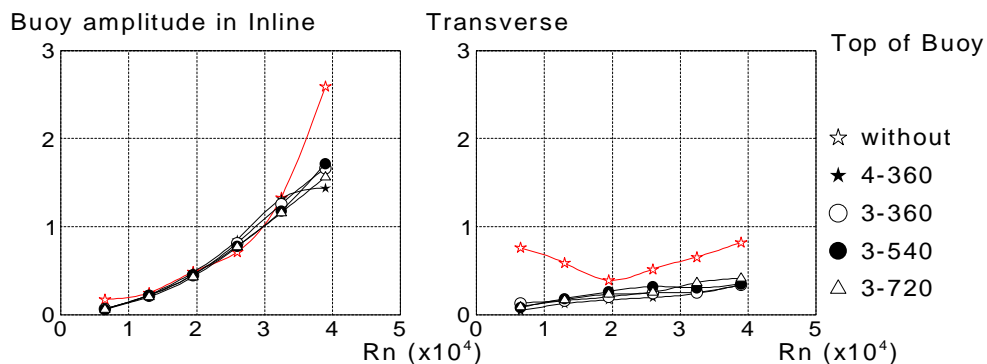
Figure 2. The motion amplitude of the floatation buoy for the inline and transverse behaviors
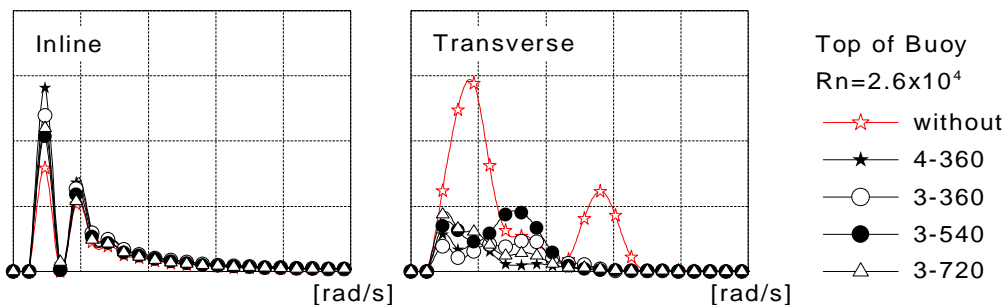
Figure 3. Measured spectra of inline and transverse motion behaviors of the floatation buoy

Reference

[1] Paulo, S, D, Pereira, et al. , Experimental Study on a Self Standing Hybrid Riser System Throughout Tests on a Deep-Sea Model Basin, OMAE2005-67558

Dynamical Analysis of Deep Water Rigid Risers: VIV Effects

Celso K. Morooka [1]

[1] State University of Campinas/Faculty of Mechanical Engineering/Department of Petroleum Engineering
morooka@dep.fem.unicamp.br

R. Franciss; C.G.C. Matt; P.S.D. Pereira [2]

[2] Subsea Techonology-Petrobras/Cenpes
franciss@petrobras.com.br; cyntiagc@petrobras.com.br; paulod@petrobras.com.br

Abstract

The Exploration & Production (E&P) of petroleum in offshore fields in deep and ultra-deep water has been drastically increasing since the late 1970s. One of the most important components of most subsea systems employed in E&P is the riser. The riser is a tube that connects the wellhead or other subsea equipment at the sea floor to the petroleum platform.

Nowadays, there are two different kinds of risers: rigid and flexible, and several configurations in which to apply them. In addition, new configurations of risers have been studied in order to enable E&P, especially, in ultra-deep water. Furthermore, the computational analysis has becoming a crucial and influential tool to help the subsea engineer in the design of these critical constituents of an E&P system.

This paper intends to be an overview of works concerning new proposed riser configurations, experimental and computational analyses including studies on VIV (vibration induced by vortices) effects of which the State University of Campinas, in collaboration with other institutes, has produced.

Introduction

The Exploration & Production (E&P) of offshore petroleum fields has been performed since the late 1800s. However, in the last 30 years the discovery of giant oil fields in deep water (water depths between 300m and 1500m) and ultra-deep water (deeper than 1500m), especially off the Brazilian Coast, the Gulf of Mexico and West Africa, has drastically increased the use of floating platforms in the petroleum industry. These platforms require a way to access the subsea wells and equipment which is a long slender pipeline, called riser by the industry. In terms of constructions, there are basically two kinds of riser; flexible and rigid. The flexible riser is constructed in several layers of polymers and metallic armors. The rigid riser is a tube made usually of steel, however there exists a few examples of rigid risers made of aluminum or titanium alloys They suffer from limitations caused by fatigue, especially resulting from vibrations induced by the floating platform motions due to waves, sea current and winds. Fatigue can also result from the shedding of vortices defined as vortex induced vibrations (VIV).

In the present paper, an overview of research and developments concerning new proposed riser configurations, experimental and computational analyses including studies on VIV (vibration induced by vortices) effects under development at the State University of Campinas, in collaboration with other institutes, will be described depicting main obtained results.

Configurations

There are several configurations of rigid risers that have been studied which are shown in Figure 1. A common configuration is the Top Tensioned Riser (TTR) (Kubota *et al.,* 2004; Coelho *et al.*, 2004; Morooka *et al.,* 2004; Morooka *et al.,* 2006b). The TTR is a vertical riser that is used for both drilling and production operations. The TTR is a put under tension by the use of a buoy or tensioners on the platform.

In addition, there are some hybrid configurations which use both rigid and flexible risers. One example is the Self Standing Hybrid Riser or SSHR (Pereira *et al.*, 2006a; Pereira *et al.*, 2006b; Pereira *et al.,* 2006c). This configuration is composed of a vertically oriented rigid riser with a subsurface buoy affixed to the top end which supports the riser's weight and applies additional tension. On the buoy's top, a goose neck and a jumper line constructed of a flexible riser section connects the buoy to the platform. This isolates the rigid riser from a great majority of forces induced by waves and platform dynamics. PEREIRA *et. al* (2006a) has shown that a typical SSHR will tend to suffer greater lateral displacements in comparison to a comparative TTR configuration which illuminates the need to analyze end connections in a SSHR.

The last example of riser configurations presented in Figure 1 is the Steel Catenary Riser or SCR, which is rigid riser installed in a Catenary shape. The SCR is then ran an additional distance on the seafloor. This distance acts to dampen the movement imposed by the platform and environmental forces. The SCR is an attractive alternative due to the simplicity and reduced cost.

Another subject under investigation is the pipeline with free span lengths which in many ways the analysis is similar to a vertical rigid riser but oriented horizontally. Boundary conditions that represents the contact between pipeline and soil have been modeled as being springs (Morooka, 2006d). Scale model experiments are in the process of being performed to analyze the results for better understand of the dominate forces involved. Further, experimental work needs to be finished in order to determine the effects of the gap between soil and the free span pipeline on hydrodynamic coefficients and VIV.

Fifth Conference on Bluff Body Wakes and Vortex-Induced Vibrations (BBVIV 5)
Costa do Sauipe, Bahia, Brazil, 12 - 15 December 2007

59
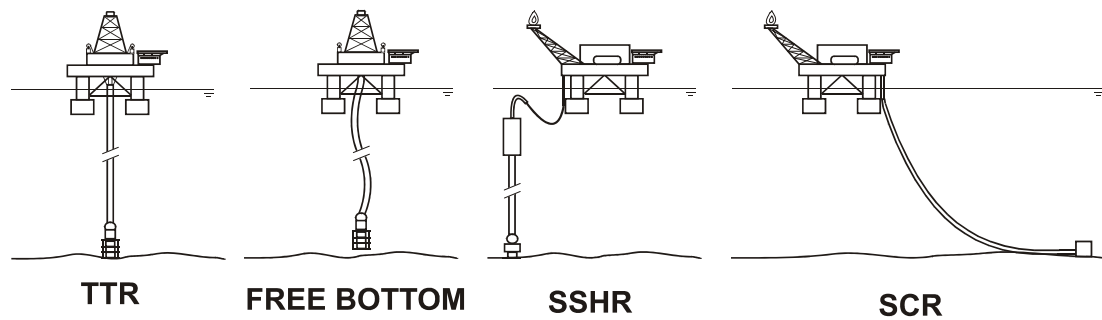
Figure 1. Examples of configurations of rigid risers.

Experimental and Computational Analysis

Since 1999, a set of computer tools has been developed to solve the behavior and condition of a rigid risers in both time and frequency domain (Morooka *et al.*, 2006c). The Finite Element Method (FEM) is used to solve the axial-flexural equation that mathematically models the riser. The numerical approach used to approximate hydrodynamic loads is derived from empirical methods (Ferrari & Bearman, 1999). Figure 2 shows data that indicates this approach as effective and feasible.

The hydrodynamic loads in the fluid flow direction (In-Line) are calculated using the Morison Equation modified to consider the relative motion of the riser body in the fluid. The oscillatory loads in the perpendicular direction of the fluid flow (Transverse) caused by the vortex shedding are calculated using a semi-empirical model (Morooka *et al.*, 2004). Furthermore, the calculations can include the consideration of dynamics of a floating platform connected to the top of the riser (Morooka & Yamamoto, 2006). The numerical computer software resulting from the studies mentioned above and much prior work has been developed to calculate riser dynamics in time domain (Morooka *et. al.*, 2006b). The software also predicts the behavior of risers with the use of buoyancy devices and end conditions and has also been studied (Morooka *et al.*, 2004).

(a)   (b)   (c)
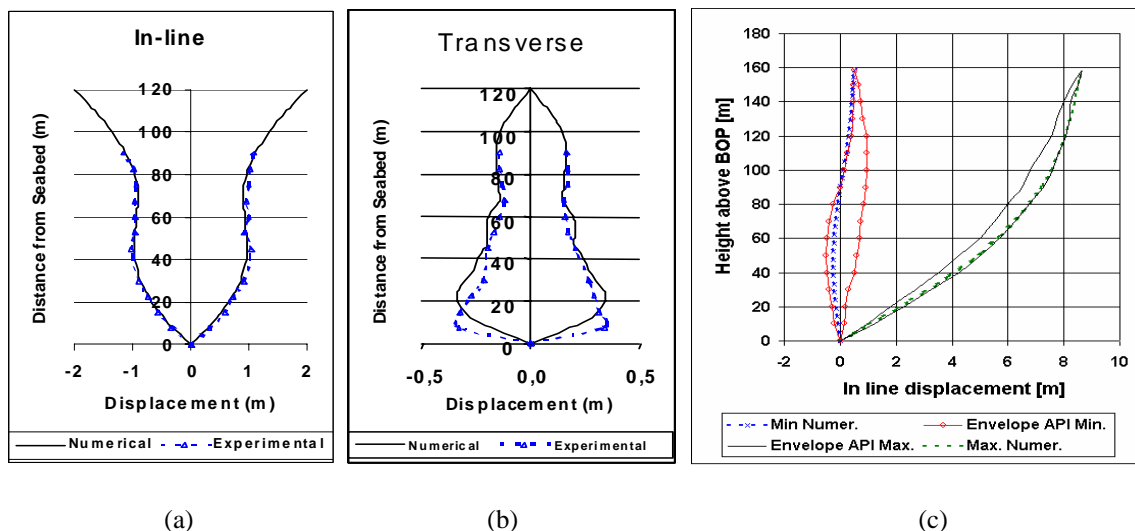
Figure 2. (a) and (b) Comparisons between RiserProd and experiments;
(c) Comparison between RiserProd and other numerical codes (API 16J Bulletin)

Special attention must be paid to VIV because these oscillatory loads can reduce the riser's service life due to fatigue. The method that has been developed can estimate the damage and the service life reduction due to the fatigue caused by VIV and waves (Morooka *et al.*, 2005; Matt *et al.*, 2006). Recent experiments have shown that besides the vortex shedding and the effects of waves there are other factors that induce riser vibrations. The internal multi-phase flow can also induce a vibration on the riser as shown by Bordalo *et al.* (2007) which can contribute to decrease the riser's service life due to fatigue. The paper mentioned previously presents a laboratory experiment of a modeled scale catenary riser suspended in air with a height 12.5 meters and a variable internal flow of a mixture of water and air. The experiment attempts to correlate dynamic phenomena to internal flow patterns.

Work concerning the dynamics of TTRs has been carried out in both time and frequency domain (Morooka *et al.,* 2006c) which illustrated the effects of nonlinearities on riser behavior. Previous studies included the consideration of internal fluid flow and calculations of the local coefficient of drag based on local KC and Re numbers (Morooka *et al.,* 2004). Further studies outlined the need for the most accurate

assessment of semi-empirical hydrodynamic coefficients in the analysis of riser behavior (Kubota *et. al.,* 2004). A comparative analysis of buoyancy device placement and outer riser diameter carried out (Coelho *et. al.*, 2004) gave valuable insight into the relative effects of changes in outside diameter and buoyancy placement. Many studies have been done on the effect of VIV on the service life of a TTR (Matt *et. al.,* 2006; Morooka *et. al.,* 2005) which have resulted in approximations of service life reduction due to VIV and oscillatory forces due to waves that is shown in Figure 3.
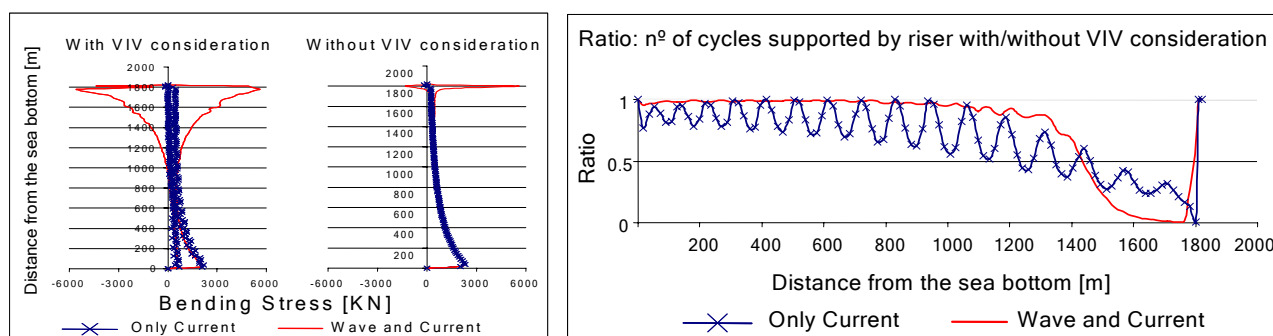
Figure 3. Graphs exemplifying the need to consider VIV effects on TTR (Morooka, 2005)

In the well drilling case the TTR, which is called the drilling riser, is installed with the Blow-Out Preventer (BOP) attached to its lower extremity in a hanging position (Coelho *et al.*, 2006; Yamamoto & Morooka, 2007) which is illustrated in Fig 1 as "Free Bottom". The interaction between riser dynamics and platform motion makes this an extremely time consuming and dangerous operation. A numerical simulation has been undertaken to consider both the dynamics of the riser with attached BOP coupled with platform motions resulting with encouraging results (Morooka *et. al.,* 2007). Previous work concerning riser dynamics was combined with fuzzy logic, control theory and platform behavior. It can be seen that VIV plays a role in the placement of the BOP and should be considered. In addition to considering the dynamics of a BOP hanging from the riser, work has been down comparing the traditional subsurface BOP with a relatively new technology, a surface BOP (Morooka, 2007b). The surface BOP configuration puts the BOP on the platform which eliminates the riser's need to support the massive subsurface BOP.

In order to project a riser system safely and reliably, the numerical simulation is a widely used tool due to the ease of varying system parameters and environment loads compared to varying the parameters in experimental analysis with reduced scale model (Morooka *et al.*, 2006b). It should be stressed that scale model experiments hold a very crucial position in the design process and cannot be replaced entirely by numerical calculations. This set of software also includes a user-friendly graphical tool (Figure 1) was developed to facilitate the modeling and analysis of riser (Morooka *et al.*, 2006a).
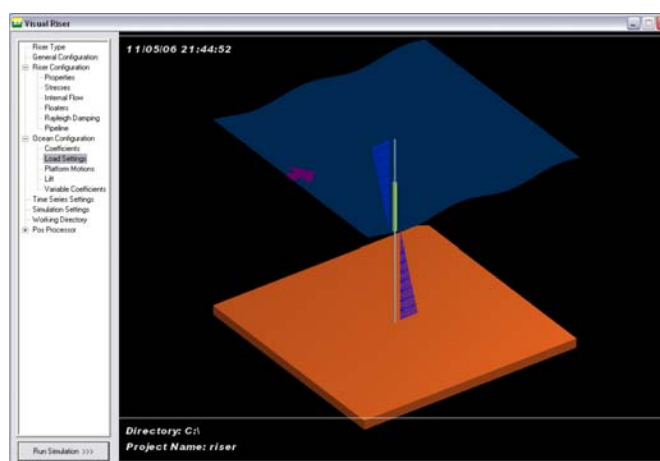
Figure 4. Main window of the user-friendly graphical tool

Conclusion

The use of numerical simulations in order to design a riser system can save time and money. The simulations can cover hundreds of different cases easily and quickly. Special attention must be paid to the damage and service life reduction due to the oscillatory loads especially the VIV under a wide span of environmental situations. The use of a semi-empirical model for the vortex shedding loads have shown to have good correlation with experimental. The current developments in the pursuit of the understanding of riser and pipeline dynamics and especially the effects of VIV continue to generate continual improvements.

References

Bordalo, S.N.; Morooka, C.K.; Cavalcante, C.C.P.; Valdivia, P.G.; Matt, C.G.C.; Franciss, R. (2007): Experimental Verification of the Whipping Phenomenon on Offshore Catenary Risers Caused by the Internal Flow Momentum, 19th International Congress of Mechanical Engineering, COBEM 2007, Brasilia, Brazil. To be published.

Coelho, F.M.; Kubota, H.Y.; Morooka, C.K.; Ferrari Jr., J.A.; Ribeiro, E.J.B. (2004): Estudo Paramétrico dos Deslocamentos em Risers de Produção com Tensionamento de Topo, 20º Congresso Nacional de Transportes Marítimos, Construção Naval e Offshore, SOBENA 2006, Rio de Janeiro, Brazil.

Coelho, F.M.; Morooka, C.K.; Franciss, R.; Matt, C.G.C. (2006): Análise do Comportamento Dinâmico de um Riser Rígido Vertical com a Extremidade Inferior Livre, 21º Congresso Nacional de Transportes Marítimos, Construção Naval e Offshore, SOBENA 2006, Rio de Janeiro, Brazil.

Kubota, H.Y.; Morooka, C.K.; Farfan, D.C.; Ferrari Jr., J.A. (2004): Influência do Coeficiente Hidrodinâmico no Comportamento Dinâmico de Riser de Produção Vertical, 20º Congresso Nacional de Transportes Marítimos, Construção Naval e Offshore, SOBENA 2006, Rio de Janeiro Brazil.

Matt, C.G.C.; Franciss, R.; Morooka, C.K.; Coeho, F.M. (2006): Service Life Reduction of a Top Tensioned Vertical Riser and VIV Effect, 25th International Conference on Offshore Mechanics and Arctic Engineering, OMAE2006-92292, Hamburg, Germany.

Morooka, C.K.; Coelho, F.M.; Kubota, H.Y.; Ferrari Jr., J.A.; Ribeiro, E.J.B. (2004) Investigations on the Behavior of Vertical Production Risers, 23rd International Conference on Offshore Mechanics and Arctic Engineering, OMAE2004-51190, Vancouver, Canada,.

Morooka, C.K.; Coelho, F.M.; Ribeiro, E.J.B.; Ferrari Jr.,J.A.; Franciss, R. (2005): Dynamic Behavior of a Vertical Riser and Service Life Reduction, 24th International Conference on Offshore Mechanics and Arctic Engineering, OMAE2005-67294, Halkidiki, Greece.

Morooka, C.K.; Brandt, D.M.; Fernandes Jr., W.; Coelho, F.M. (2006a): A User-Friendly Graphical Tool to Help Visualize the Analysis of Production Risers, XXVII Iberian Latin American Congress on Computational Methods in Engineering, CILAMCE 2006, Belém, Brazil.

Morooka, C.K.; Coelho, F.M.; Matt, C.G.C.; Franciss, R. (2006b): A Time Domain Simulation Tool for Rigid Risers' Design, Rio Oil&Gás: Expo and Conference, IBP1420-06, Rio de Janeiro, Brazil.

Morooka, C.K.; Coelho, F.M.; Shiguemoto, D.A.; Franciss, R.; Matt, C.G.C. (2006c): Dynamic Behavior of a Top Tensioned Riser in Frequency and Time Domain, 16th International Offshore and Polar Engineering Conference (ISOPE 2006), San Francisco, USA.

Morooka, C.K.; Idehara, A.Y.; Matt, C.G.C. (2006d): Behavior of a Pipeline with Free Span Under Steady Current, XXVII Iberian Latin American Congress on Computational Methods in Engineering, CILAMCE 2006, Belém, Brazil.

Morooka, C.K.; Yamamoto, M. (2006): Dynamic Positioned Semi-Submersible Platform Motion with Riser in Ultra-Deep Water, 9th International Conference on Stability of Ships and Ocean Vehicles, STAB 2006, Rio de Janeiro, Brazil.

Morooka, C.K.; Idehara, A.Y.; Matt, C.G.C. (2007a): In Line and Cross-Flow Behavior of a Free-Spanning Pipeline, 26th International Conference on Offshore Mechanics and Arctic Engineering, OMAE 2007, San Diego, USA. To be published.

Morooka, C.K.; Tsukada, T.I.; Yamamoto, M. (2007b): Comparative Analysis Between Surface and Subsea BOP Offshore Drilling Systems in Waves and Current, 19th International Congress of Mechanical Engineering, COBEM 2007, Brasilia, Brazil. To be published.

Pereira, P.S.D.; Maeda, K.; Morooka, C.K.; Tamura, K.; Itoh, K. (2005): Experimental Study on a Self Standing Hybrid Riser System Throughout Tests on a Deep-Sea Model Basin, 24th International onference on Offshore Mechanics and Arctic Engineering, OMAE2005-67558, Halkidiki, Greece.

Pereira, P.S.D.; Morooka, C.K.; Shiguemoto, D.A.; Coelho, F.M. (2006a): Self Standing Hybrid Riser System in Waves and Current, 25th International Conference on Offshore Mechanics and Arctic Engineering, OMAE2006-92402, Hamburg, Germany.

Pereira, P.S.D.; Morooka, C.K.; Shiguemoto, D.A.; Coelho, F.M. (2006b): Análise da Sistemática de Projeto para um Riser Híbrido de Uso em Águas Profundas, Rio Oil&Gás: Expo and Conference, IBP1839-06, Rio de Janeiro, Brazil.

Pereira, P.S.D.; Morooka, C.K.; Champi, D.F. (2006c): Dynamics of a Vertical Riser with a Subsurface Buoy, 16th International Offshore and Polar Engineering Conference (ISOPE 2006), San Francisco, USA.

Yamamoto, M.; Morooka, C.K., Ueno, S. (2007): Dynamic Behavior of a Semi-Submersible Platform Coupled with Drilling Riser during Re-Entry Operation in Ultra-Deep Water, 26th International Conference on Offshore Mechanics and Arctic Engineering, OMAE2007-29221, San Diego, USA. To be published.

RISER MOTION ESTIMATION OF OIL PRODUCTION SYSTEM FOR ULTRA DEEP WATER

Shunji KATO
National Maritime Research Institute
E-mail: kato@nmri.go.jp

Shotaro UTO
National Maritime Research Institute
E-mail: uto@nmri.go.jp

Sotaro MASANOBU
National Maritime Research Institute
E-mail: masanobu@nmri.go.jp

Hideyuki SUZUKI
The University of Tokyo
E-mail: suzukih@naoe.t.u-tokyo.ac.jp

Hiroaki HIRAYAMA
Japan Oil, Gas and Metals National Corporation
E-mail: hirayama-hiroaki@jogmec.go.jp

Koji MOCHIDA
Japan Oil, Gas and Metals National Corporation
E-mail: mochida-koji@jogmec.go.jp

INTRODUCTION

About thirty percents of the oil come from the sea. Large oil reservoirs have been detected and developed in the Gulf of Mexico, North Sea, offshore Brazil, offshore Western Africa, etc. Recently, offshore, especially the area of ultra deep water more than 2,500m, is a target for oil reservoir detection, since there have been less chances of the detection of large oil reservoir in land area, where oil detection is easier than sea.

In the oil development for deep water, a production system usually consists of floating platform, mooring system and riser system. The scope of riser study shifts to ultra deep water area (water depth 3,000m) as the target water depth of offshore oil development becomes deeper.

Flexible riser systems which can absorb the motion of floating platform have been studied and widely used for offshore oil production. The catenary riser system using steel is available for ultra deep water since a steel riser is relatively flexible. Therefore, various forms of risers such as SCR (Steel Catenary Riser) and CVAR (Compliant Vertical Access Riser) have been proposed.

Prediction of the vortex-induced vibration (VIV) is one of the most important technological issues for the development of riser systems, because VIV leads to fatigue failure of risers. Therefore, in order to establish the design methodology of economic and safe offshore oil production system, it is a key technology to develop the practical VIV simulation method and to estimate appropriately riser fatigue.

Numerous studies on riser VIV problem have been carried out so far. The typical methodologies of analysis are the combination of FEM and (2-D or 3-D) CFD or hydrodynamic force database based on experimental results.

It is important that development and/or verification of estimation method of riser VIV should be based on the experimental results obtained at high Reynolds number which corresponds to the typical value for the full scale riser system, i.e. around 5×10^5. However, most of the estimation methods that have been developed so far are based on the experimental result at the range of low Reynolds number, except for some methods such as SHEAR7 and VIVANA, etc. Furthermore, there have been few efforts to study VIV problems on the inclined riser against current at high Reynolds number.

The purpose of this study is to develop the practical riser VIV estimation method that can be applied to high Reynolds number region and various riser forms such as SCR and CVAR. In this study, the forced oscillation tests of the horizontally-submerged cylinder at high Reynolds number region are performed. The angle of cylinder changes horizontally for simulating not only vertical but also inclined inflow against a cylinder. The estimation method using the FEM and hydrodynamic force database based on the test results is developed.

OUTLINE OF STUDY

The contents of this study are as follows:

1. Force Measurement Test on Large Vertical / Inclined Riser Pipe

Hydrodynamic forces on a riser pipe are measured by towing the submerged cylinder of which axis is horizontal and is forced to oscillate vertically. The attack angle of the current to a riser pipe is changed by rotating the cylinder in a horizontal plane. This test is focused on VIV in the region of high Reynolds number (Re ~ 5x10^5). Test parameters were as follows: "oscillating amplitude", "oscillating period", "attack angle", "current speed (towing speed)". Hydrodynamic force database are constructed by analyzing measured data into (a) drag force coefficient, (b) added mass coefficient in lift direction, (c) damping coefficient in lift direction.

2. Development of Riser Motion Estimation Program Using FEM

The riser motion estimation program which can estimate motions of various full scale risers is developed. This program is based on 3-D FEM and included the above mentioned hydrodynamic force database.

3. Verification of the FEM Program

The FEM program is evaluated through the following verification tests and developed:

(a) Verification test for basic function of program

An inclined cylinder was set in the test basin where current is generated and the VIV was measured. This test was carried out in low Reynolds number region. Test results are used for verifying the basic function of the FEM program. Fig.1 shows the outline of the experimental setup.
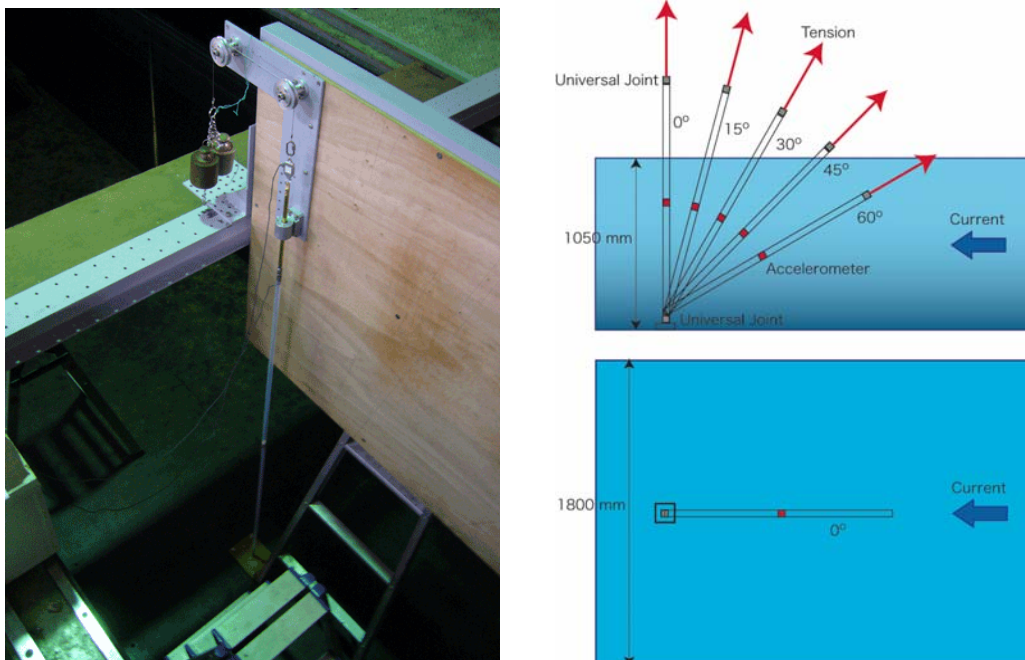
Fig.1 Outline of Experimental Setup for Basic Function Verification Test.

(b) Verification test for program

VIV in high Reynolds number region were measured by towing the horizontally submerged cylinder supported by springs. This test was carried out in MITAKA No.3 Towing Tank of National Maritime Research

Institute. This tank has the dimensions of 150m(L), 7.5m(W), 3.5m(D) and maximum towing speed is 5m/s (Fig.2). Test results are used for verifying the FEM program at high Reynolds number region. Fig. 3 shows experimental model.

Fig.2 Test Facilities for Program Verification Test.

Fig.3 Experimental Model for Program Verification Test.

At-sea measurement test is being planned to verify this program overall.

ACKNOWLEDGEMENTS

Unsteadiness in the wake of the sphere: receptivity and weakly non-linear global stability analysis

Philippe Meliga[1], Denis Sipp[1] and Jean-Marc Chomaz[1,2]

[1]ONERA, Fundamental and Experimental Aerodynamics Department, 92190 Meudon, France
[2]LadHyX, CNRS-Ecole Polytechnique, 91128 Palaiseau, France
philippe.meliga@onera.fr

Introduction   A large body of works has been devoted to the wake of the sphere in the last decades ([1,3,4,7,8]). For Reynolds numbers $\mathrm{Re} \gtrsim 280$, the flow is dominated by an instability of the helical mode, resulting in the low frequency shedding of large-scale coherent structures in the form of two superimposed modes of azimuthal wavenumbers $m = \pm 1$. Low Strouhal numbers of 0.2, characteristic of vortex shedding phenomena, have been reported, based on the body diameter. In this paper, we calculate the global modes leading the successive bifurcations undergone by the axisymmetric steady wake for $\mathrm{Re} < 300$. The corresponding adjoint global modes are computed, whose physical interpretation is discussed in terms of receptivity. These results are used to build an extended dynamical system for which we carry out a weakly non-linear stability analysis. A system of coupled Stuart-Landau amplitude equations is derived, aiming at giving a precise description of the periodic regime which appears after the transition from steady to unsteady wakes.

Base flow computation and global linear stability analysis   We consider a sphere of diameter D in a uniform flow of velocity U_∞. Standard cylindrical coordinates r, θ and z with origin taken at the center of the sphere are used. The fluid motion is governed by the incompressible Navier-Stokes equations made non-dimensional by D and U_∞. $\mathbf{u} = (u, v, w)$ is the fluid velocity where u, v and w are the radial, azimuthal and axial components, and p is the pressure. The computational domain Ω is made of a single azimuthal plane. We impose standard boundary conditions on $\partial\Omega$, namely uniform inlet and no-strain outlet conditions, along with no-slip conditions on the sphere. The condition at the $r = 0$ axis depends on the solution symmetries and will be discussed further. The spatial discretization is achieved by use of Taylor-Hood finite-elements (P2 elements for $\mathbf{u}$ and P1 elements for p).

In the linear global stability theory, the aerodynamic flow field $\mathbf{q} = (\mathbf{u}, p)$ is decomposed into an axisymmetric steady base flow $\mathbf{q_0} = (u_0, 0, w_0, p_0)$ and a three-dimensional perturbation $\mathbf{q_1} = \epsilon^{1/2}(u_1, v_1, w_1, p_1)$ where $\epsilon^{1/2}$ is the small amplitude of the perturbation. The base flow is searched as a steady axisymmetric solution of the governing equations, verifying

$$\nabla.\mathbf{u_0} = 0 \qquad \nabla\mathbf{u_0}.\mathbf{u_0} + \nabla p_0 - \mathrm{Re}^{-1}\nabla^2\mathbf{u_0} = 0\,. \tag{1}$$

$\mathbf{q_0}$ is obtained from time-dependent simulations based on a Lagrange-Galerkin temporal discretization. Figure 1 shows the base flow obtained for a subcritical Reynolds number $\mathrm{Re} = 200$.
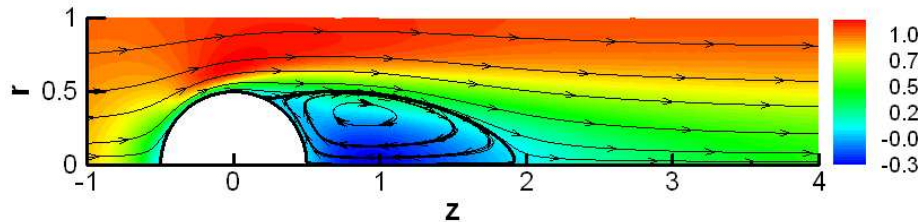
Figure 1: Contours of axial velocity w_0 and streamlines for the base flow $\mathbf{q_0}$ at $\mathrm{Re} = 200$.

At leading order in $\epsilon^{1/2}$, $\mathbf{q_1}$ is a solution of the unsteady equations linearized about $\mathbf{q_0}$

$$\nabla.\mathbf{u_1} = 0 \qquad \partial_t\mathbf{u_1} + C[\mathbf{u_0}, \mathbf{u_1}] + \nabla p_1 - \mathrm{Re}^{-1}\nabla^2\mathbf{u_1} = 0 \tag{2}$$

where $C[\mathbf{u}, \mathbf{v}]$ is the linearized convection operator $\nabla\mathbf{u}.\mathbf{v} + \nabla\mathbf{v}.\mathbf{u}$. Since all quantities are 2π periodic in the azimuthal direction, all perturbations are chosen in the form of global normal modes

$$\mathbf{q_1} = \hat{\mathbf{q}}_1(r, z)e^{\sigma t + im\theta} + \text{c.c.} \tag{3}$$

where $\hat{\mathbf{q}}_1 = (\hat{u}_1, \hat{v}_1, \hat{w}_1, \hat{p}_1)$ is the so-called global mode. m is the integer azimuthal wavenumber and σ is the complex pulsation, σ_r and σ_i being respectively the growth rate and frequency of the global mode ($\sigma_r > 0$ for a global mode whose amplitude grows exponentially in time). Substitution of the development (3) in equations (2) leads to a generalized eigenvalue problem for σ and $\hat{\mathbf{q}}_1$ that reads

$$\mathcal{M}.\hat{\mathbf{q}}_1 = \sigma \mathcal{N}.\hat{\mathbf{q}}_1 \qquad (4)$$

where $\mathcal{M}$ and $\mathcal{N}$ are two real matrices and $\hat{\mathbf{q}}_1$ is the complex eigenvector associated to σ. This eigenvalue problem is solved by use of an Arnoldi method based on a shift-invert strategy. The boundary conditions at the symmetry axis are derived from the asymptotic behavior of $\hat{\mathbf{q}}$ near the axis. We impose $u_0 = \partial_r w_0 = 0$ for the base flow and $\partial_r u_1 = \partial_r v_1 = w_1 = 0$ for $m = 1$ disturbances.

Results of the global stability analysis are consistent with that obtained by use of spectral methods ([6]). The axisymmetric steady base flow undergoes a first bifurcation at the critical Reynolds number $\mathrm{Re}_{c1} = 213$ for an $m = 1$ non-oscillating global mode $\hat{\mathbf{q}}_1^A$ ($\sigma_i = 0$). The spatial structure of the associated eigenmode displays strong large-scale axial velocity disturbances under the form of a pair of counter-rotating streamwise vortices (not shown here). Figures 2(a) and (b) show the bifurcated flow at the supercritical Reynolds number $\mathrm{Re} = 250$, obtained by the superposition of an arbitrary amount of perturbation on the base flow. The vortices induce a loss of symmetry of the base flow and the wake is shifted in a given direction ($\theta = 0$ here, due to the chosen normalization of $\hat{\mathbf{q}}_1^A$), whereas it remains symmetric with respect to $r = 0$ in the orthogonal plane ($\theta = \pi/2$).
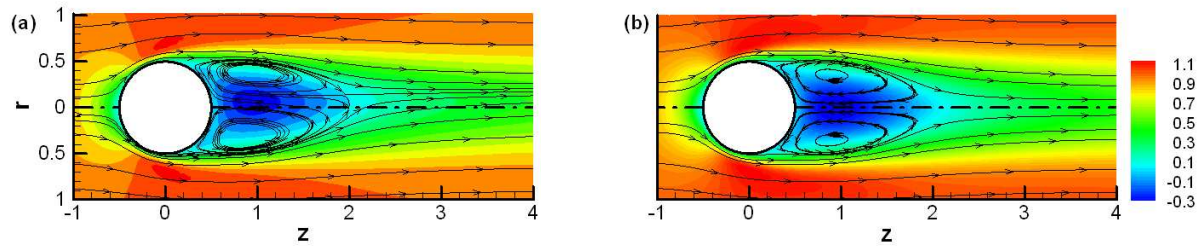
Figure 2: Contours of axial velocity w and streamlines for the total flow $\mathbf{q_0} + \epsilon^{1/2}\mathbf{q}_1^A$ at $\mathrm{Re} = 250$ (arbitrary value of $\epsilon^{1/2}$). The dash-dotted line represents the symmetry axis of the base flow. (a) $\theta = 0, \pi$. (b) $\theta = \pi/2, 3\pi/2$.

A second bifurcation occurs at $\mathrm{Re}_{c2} = 281$ for an $m = 1$ oscillating global mode $\hat{\mathbf{q}}_1^B$ of frequency $\sigma_i = 0.699$. The corresponding Strouhal number $St = fD/U_\infty$ of 0.111 is in excellent agreement with the experimental frequency $St = 0.118$ measured at this transitional Reynolds number ([7]). The associated eigenmode exhibits the spatially periodic downstream structure characteristic of the oscillatory wake instability (figure 3), hence indicating that this mode leads the periodic vortex shedding phenomenon.
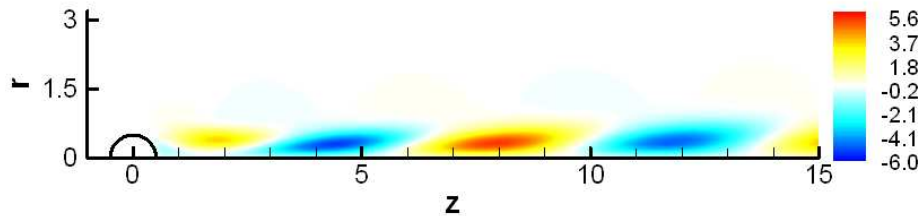
Figure 3: Axial velocity $\hat{w}_1^B$ of the oscillating global mode at $\mathrm{Re} = 281$ (arbitrary normalization).

Adjoint analysis and non-normality The most amplified modes resulting from the global stability analysis, i.e. the leading global modes, govern the large-time dynamics of the flow. In this section, we use an adjoint analysis to investigate how this dynamics is affected by the small imperfections that are encountered in real flows. This point is of particular importance when considering experimental set-ups: for instance even the smallest sphere holding device induces perturbations that can be understood as local modifications of the base flow in the near wake.

Given the linear operator $\mathcal{M}$ defined in (4), the adjoint operator $\mathcal{M}^\dagger$ is defined as the operator such that, for any vectors $\hat{\mathbf{q}}$ and $\hat{\mathbf{q}}^\dagger$ fulfilling respective appropriate boundary conditions,

$$\langle \hat{\mathbf{q}}^\dagger, \mathcal{M}.\hat{\mathbf{q}} \rangle = \langle \mathcal{M}^\dagger.\hat{\mathbf{q}}^\dagger, \hat{\mathbf{q}} \rangle. \tag{5}$$

where $\langle\,,\rangle$ denotes the usual complex scalar product on Ω, *i.e.* $\langle \hat{\mathbf{q}}^1, \hat{\mathbf{q}}^2 \rangle = \int_\Omega \hat{\mathbf{q}}^{1T} \hat{\mathbf{q}}^2 d\Omega$. It can be shown that $\mathbf{q}^\dagger$ is solution of the eigenvalue problem

$$\mathcal{M}^\dagger.\hat{\mathbf{q}}^\dagger = \overline{\sigma} \mathcal{N}.\hat{\mathbf{q}}^\dagger \tag{6}$$

where $\overline{\sigma}$ is the complex conjugate of σ.

Figure 4 shows the adjoint axial velocity and adjoint pressure distributions for the oscillating adjoint global mode $\hat{\mathbf{q}}_1^{B\dagger}$. We find very similar distributions for the non-oscillating adjoint global mode $\hat{\mathbf{q}}_1^{A\dagger}$ (not shown here). Due to the non-normality of the operator $\mathcal{M}$, the adjoint global mode is located slightly upstream of the sphere and mainly within the recirculating area (marked by the thick solid line), whereas the associated global mode is located downstream of the sphere and extends down to large streamwise positions. The adjoint mode can be interpreted in terms of receptivity of the base flow to a volumic forcing, given by the velocity component $\hat{\mathbf{u}}^\dagger$, and to a boundary forcing, given at leading order by the wall pressure component $\hat{p}^\dagger$ ([2]). The adjoint analysis is therefore of particular interest in the elaboration of efficient control strategies (base-bleed, for instance) as we find that the adjoint axial velocity is concentrated within and at the periphery of the recirculating area, whereas the adjoint pressure peaks at the separation point. It can also be shown that it is possible to estimate the receptivity of the base flow to local modifications by considering the cooperation between a global mode and its adjoint global mode ([5], not shown here).
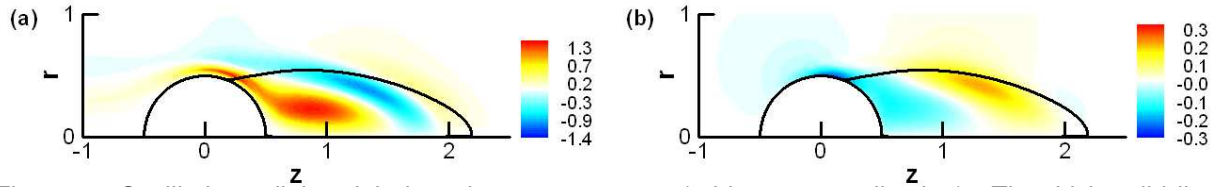
Figure 4: Oscillating adjoint global mode at $\mathrm{Re}_{c2} = 281$ (arbitrary normalization). The thick solid line marks the limit of the recirculating area. (a) Adjoint axial velocity $\hat{w}_1^{B\dagger}$. (b) Adjoint pressure $\hat{p}_1^{B\dagger}$.

Global weakly non-linear analysis   In this section, we model the base flow undergoing two successive bifurcations by an extended dynamical system undergoing a multiple codimension bifurcation at the critical Reynolds number $\mathrm{Re}_{c2} = 281$. This assumption holds at leading order because both critical Reynolds numbers are close one from the other, so that $\xi = \mathrm{Re}_{c1}^{-1} - \mathrm{Re}_{c2}^{-1}$ is a small parameter of the problem. Substitution of the asymptotic expansion

$$\mathbf{q} = \mathbf{q}_0 + \epsilon^{1/2}\mathbf{q}_1 + \epsilon\mathbf{q}_2 + \epsilon^{3/2}\mathbf{q}_3 + ... \tag{7}$$

in the governing equations, where ϵ is the small parameter $\epsilon = \mathrm{Re}_{c2}^{-1} - \mathrm{Re}^{-1}$, leads to a series of equations of successive order $\epsilon^{i/2}$. At order 0, we find the non-linear equation specifying that $\mathbf{q}_0$ is a steady solution of the Navier-Stokes equations at the critical Reynolds number Re_{c2}. At order 1, we obtain the homogeneous linear equation specifying that $\mathbf{q}_1$ may be taken as a superposition of global modes of the steady flow field $\mathbf{q}_0$ at Re_{c2}. We can therefore choose $\mathbf{q}_1$ as the superposition of the marginal eigenmodes existing at the critical Reynolds number, each mode being multiplied by some complex scalar amplitude. Note that three global modes are to be considered, *i.e.* the system undergoes a codimension-three bifurcation: one mode for the first steady bifurcation and two superimposed modes of frequencies $\pm\sigma_i$ for the unsteady bifurcation. $\hat{\mathbf{q}}_1$ can therefore be written in the form

$$\hat{\mathbf{q}}_1 = \left(A\hat{\mathbf{q}}_1^A + B^+\hat{\mathbf{q}}_1^{B+}e^{\sigma t} + B^-\hat{\mathbf{q}}_1^{B-}e^{\overline{\sigma}t}\right)e^{i\theta} + \text{c.c.} \tag{8}$$

where A is the complex amplitude of the non-oscillating mode $\hat{\mathbf{q}}_1^A$, and B^+ (resp. B^-) is that of the oscillating mode $\hat{\mathbf{q}}_1^{B+}$ (resp. $\hat{\mathbf{q}}_1^{B-}$) of frequency σ_i (resp. $-\sigma_i$). At orders 2 and 3, we obtain inhomogeneous linear equations that can be understood as the harmonic linearized Navier-Stokes operator about $\hat{\mathbf{q}}_0$ forced by terms involving quantities of lower orders, which have therefore been determined. The homogeneous

Fifth Conference on Bluff Body Wakes and Vortex-Induced Vibrations (BBVIV 5)
Costa do Sauipe, Bahia, Brazil, 12 - 15 December 2007

69

operator is non-degenerate at order 2 but degenerate at order 3, where the Fredholm alternative is used and compatibility conditions are applied, yielding a system of Stuart-Landau amplitude equations for the complex amplitudes (A, B^+, B^-). Although this system can be calculated from the full equations, it arises naturally by considering that invariance under the transformation $(A, B^+, B^-) \longrightarrow (A, B^+, B^-)e^{i\varphi}$ is required, where φ is an arbitrary phase. The system of coupled amplitude equations finally reads

$$dA/dt = \epsilon\lambda_A A - \epsilon A \left(\mu_A |A|^2 + \nu_A |B^+|^2 + \overline{\nu}_A |B^-|^2 \right) - \epsilon\chi_A B^+ \overline{B^-} A \tag{9a}$$

$$dB^+/dt = \epsilon\lambda_B B^+ - \epsilon B^+ \left(\mu_B |B^+|^2 + \nu_B |B^-|^2 + \eta_B |A|^2 \right) - \epsilon\chi_B B^- A^2 \tag{9b}$$

$$dB^-/dt = \epsilon\lambda_B B^- - \epsilon B^- \left(\mu_B |B^-|^2 + \nu_B |B^+|^2 + \eta_B |A|^2 \right) - \epsilon\chi_B B^+ \overline{A}^2 . \tag{9c}$$

By use of the compatibility conditions, the coefficients of system (9) arise as scalar products between the adjoint global modes computed in the previous section and the forcing terms of order 3 of appropriate complex amplitude. For instance, $\mu_A = \langle \hat{\mathbf{q}}_{1A}^\dagger, \hat{\mathbf{f}}_3^{A|A|^2} \rangle$ where $\hat{\mathbf{f}}_3^{A|A|^2}$ is the forcing term of complex amplitude $A|A|^2$, arising from the non-linear interaction of $\hat{\mathbf{q}}_1^A$ with the order 2 mode of amplitude $|A|^2$ and of $\overline{\hat{\mathbf{q}}_1^A}$ with the order 2 mode of amplitude A^2, *i.e.*

$$\hat{\mathbf{f}}_3^{\,A|A|^2} = -C[\hat{\mathbf{q}}_1^A, \hat{\mathbf{q}}_2^{|A|^2}] - C[\overline{\hat{\mathbf{q}}_1^A}, \hat{\mathbf{q}}_2^{A^2}] . \tag{10}$$

Numerically, we obtain

$$\begin{array}{ll}
\lambda_A = 147 & \lambda_B = 200 - 8.45\,\mathrm{i} \\
\mu_A = 16.2 & \mu_B = 0.355 + 0.0301\,\mathrm{i} \\
\nu_A = 0.415 - 0.0155\,\mathrm{i} & \nu_B = 0.308 + 0.168\,\mathrm{i} \\
 & \eta_B = 20.1 - 1.83\,\mathrm{i} \\
\chi_A = 0.0165 & \chi_B = 8.55 + 1.90\,\mathrm{i} .
\end{array}$$

We will discuss the formation of slowly rotating horseshoe vortices as a particular solution of this complex system, that may even admit chaotic solutions (3 degrees of freedom for amplitudes and 3 others for phases).

Conclusion The first and second bifurcations of the steady axisymmetric wake of the sphere is investigated numerically in the framework of the global linear stability. The adjoint problem is solved as a step towards a weakly non-linear analysis and the adjoint global modes are discussed in terms of receptivity to flow control and base flow modifications. A system of coupled amplitude equations is derived for a dynamical system undergoing a codimension-three bifurcation, whose resolution is expected to provide useful information for the description of the early stage of the periodic regime.

Bibliography
[1] ACHENBACH E. Vortex shedding from spheres. *J. Fluid Mech.* **62**, 209-221 (1974).
[2] GIANNETTI F. & LUCHINI P. Structural sensitivity of the first instability of the cylinder wake. *Accepted for publication in J. Fluid Mech.* (2007).
[3] KIM H.J. & DURBIN P.A. Observations of the frequencies in a sphere wake and of drag increase by acoustic excitation. *Phys. Fluids* **31** (11), 3260-3265. (1988).
[4] LEVI E. Three-dimensional wakes: origin and evolution. *J. Eng. Mech.* **106**, 659-676 (1980).
[5] MARQUET O., LOMBARDI M., SIPP D. & CHOMAZ J.M. Direct and adjoint global modes of a recirculation bubble: lift-up and convective nonnormalities. *Under consideration for publication in J. Fluid Mech.* (2007).
[6] NATARAJAN R. & ACRIVOS J. The instability of the steady flow past spheres and disks. *J. Fluid Mech.* **254**, 323-344 (1993).
[7] ORMIÈRES D. & PROVANSAL M. Transition to turbulence in the wake of a sphere. *Phys. Rev. Lett.* **83** (1), 80–83 (1999).
[8] SAKAMOTO H. & HANIU H. A study on vortex shedding from spheres in a uniform flow. *Trans. Am. Soc. Mech. Eng.* **112**, 386-392 (1990).

Sensitivity of global mode instability to local and stationary disturbances in a turbulent wake

Olivier CADOT, Benjamin THIRIA and Jean-François BEAUDOIN*

Unité de Mécanique de l'Ecole Nationale Supérieure de Techniques Avancées, Chemin de la Hunière
91 761 Palaiseau cedex, France.
cadot@ensta.fr

*Department of Research and Innovation, PSA
Peugeot-Citroen, 2 route de Gisy, 78943 Velizy-Villacoublay, France.

The sensitivity of the global mode instability to stationary local disturbance has been first studied by Sreenivasan & Strykowski [1] near the threshold of the instability of a circular cylinder. The disturbance, a smaller cylinder, referred as the control cylinder delays the instability. Later, Sakamoto et al. [2] have shown the technique to be very efficient to reduce both steady and unsteady fluid forces even for a salient cylinder such as a prism. These experiments recall the pioneering work of Roshko [3] and the effects, in general, of fitted splitter plates on cylindrical bluff bodies [4]. In addition to the drastic effect of drag reduction, this passive manipulation is able to bring more insight to the physics of bluff body wakes regarding frequency selection and drag origin [5].

The wake is produced by a cylinder having a "D" shape (see figure 1). The characteristic length is D=25mm, the velocity of the flow U=20.5m/s and the fluid is air. The Reynolds number for this study is Re=UD/$\nu \approx$ 34 000. The cylinder is placed in an Eiffel-type wind tunnel whose cross-section is 400mmX400mm. As depicted in figure 1, three different measurements are performed: mean velocity field, wake frequency and base pressure. The mean velocity field is measured with a PIV set-up, the measurement plane is situated in the region of the flow at the rear of the "D" cylinder. The wake frequency is measured with a hot wire probe from DANTEC located at the base of the "D" cylinder. The base pressure P_B is measured through a hole having 0.5 mm in diameter and connected to a Scanivalve DSA 3217. The static pressure of the incoming flow is taken upstream using a pitot tube.
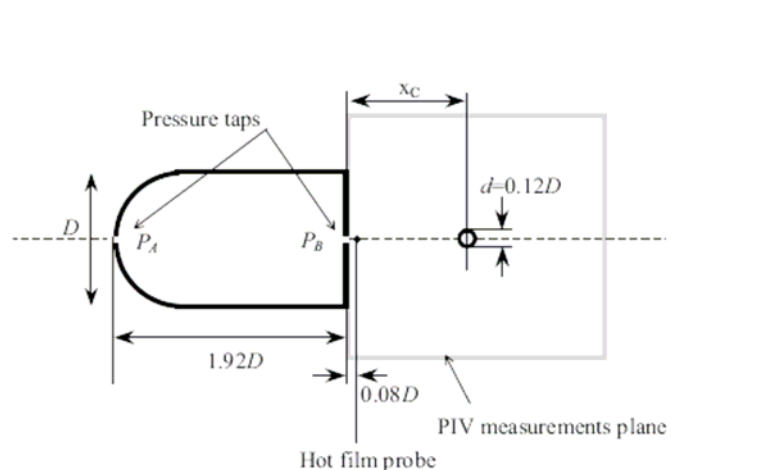
Figure 1 : Flow configuration, dimensions and measurements set-up. The height of the model is D=25mm.

The disturbance of the wake is produced by a smaller circular cylinder parallel and within the symmetry plane of the "D" cylinder (see figure 1). Measurements are performed for different positions of the disturbance cylinder denoted as x_C ranging from 0.08D to 3D.

The figure 2(a) represents the iso-lines of the mean streamwise velocity component of the undisturbed wake. The thicker line corresponds to the zero level. Inside the contour that is defined by this line, the velocity components are negative (reversed flow) and outside this line the velocity components are positive. The important characteristics of the reversed flow are the minimum velocity with its location x_S and the size of the recirculation bubble L. The size L is defined as the intersection of the zero level contour line and y/D=0. We can directly see on these figures the effect of the disturbance cylinder on the reversed flow properties. The reversed flow region is grown by the introduction of the disturbance cylinder. The location x_S of the minimum of velocity is first slightly pushed downstream in (b). Then, as the separating distance x_C between the "D" cylinder base and the disturbance cylinder is increased, x_S moves from the right-hand side (b) to the left-hand side (d) of the disturbance cylinder. Afterwards, the length of the reversed flow region is drastically increased and reaches a maximum corresponding to an increase of 50% (e) of the length measured for the undisturbed case (a).
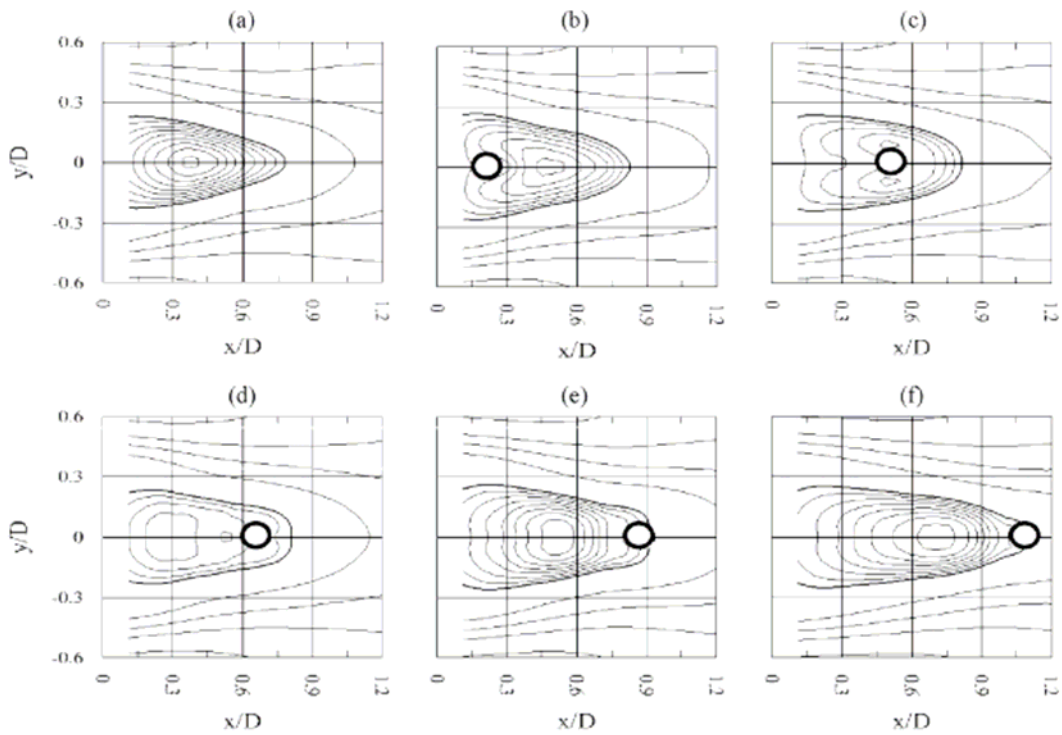
Figure 2: Iso-lines of the u-component (streamwise velocity component) the thick line corresponds to the level 0. Inside the contourline of level 0, the velocity components are negative and the level intervals are 0.5m/s. Outside the contour-line of level 0, the velocity components are positive and the level intervals are 5m/s.The black circle represents the disturbance cylinder localized at x_C, (a) :without, (b) :x_C/D=0.68, (c) : x_C/D=1.16, (d) : x_C/D=1.48.

The figure 3 shows more quantitatively the evolutions of the global properties of the wake versus the separating distance x_C. First of all, we obtain a good correlation between the base pressure coefficient -Cpb and the reversed flow region length L. This correlation follows the rule given by cavity models [6] where the reversed flow is roughly replaced by a cavity of zero velocity, the larger the cavity the larger the base pressure (or the smaller the drag). Looking at the characteristic lengths of the reversed flow, say x_S and L, we find regions where these quantities are locked on the disturbance cylinder position. Firstly, in the region 0.5< x_C <0.68, the minimum velocity position x_S is equal to x_C and then falls abruptly down to x_S=0.34. This lock-on does not affect much the total length of the reversed flow region since only a slight increase is observed.
After this phase, it is the closure of the reversed flow L that is locked on the disturbance cylinder position until x_C=1.2D where L reaches its maximum. Actually, during this phase it seems to be the total reversed flow region that is locked on x_C since x_S also follows, a constant length upstream, the disturbance cylinder position.
The two jumps of x_S that occur after each lock-on phase are correlated to a Strouhal number decrease. This observation emphasizes the dominant role of the position of the maximum of the

reversed flow velocity in the mechanism of the frequency selection. Each jump is associated to a loss in the synchronization. While the jump associated with the bubble closure has already been reported in the literature, the jump associated with the maximum of feedback velocity seems to be new.
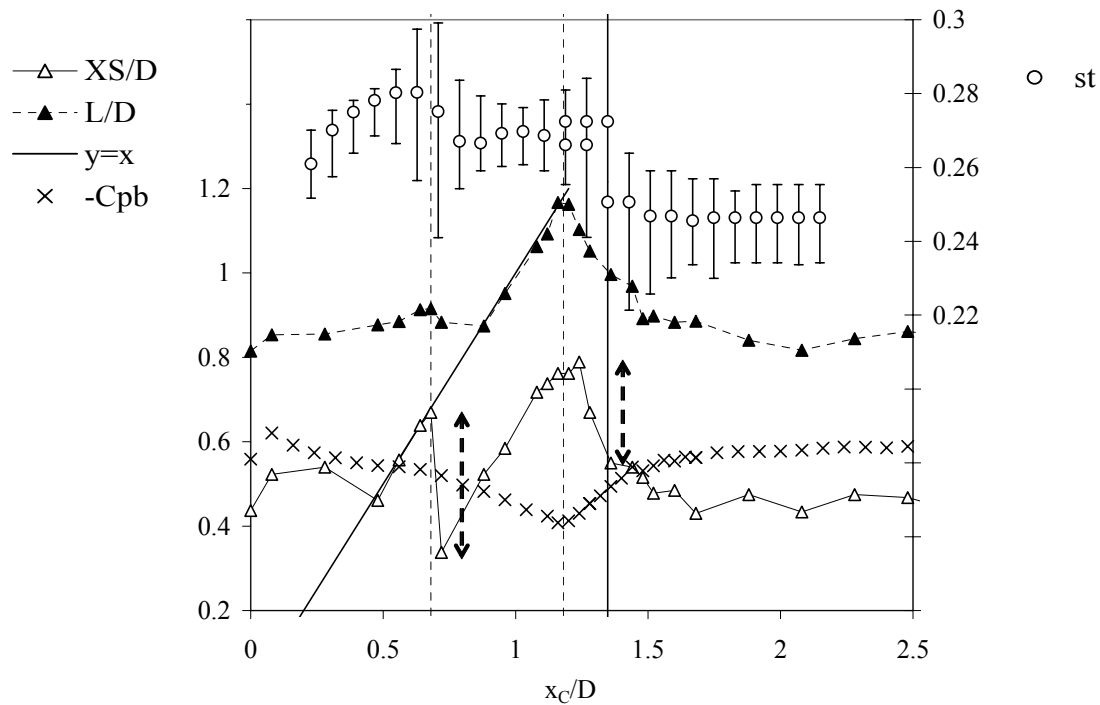
Figure 3: Evolutions of the mean properties of the wake vs. the position of the disturbance circular cylinder.

References

[1] Sreenivasan, K. R. & Strykowski, P.J. 1990 On the formation and suppression of vortex shedding at low Reynolds number. *J. Fluid. Mech.* **218** 71-108.

[2] Sakamoto H., Tan K. & Haniu, H. 1991 An optimum suppression of fluid forces by controlling a shear layer separated from a square prism. *J. Fluid. Eng.* **113**, 183-189.

[3] Roshko, A. 1954 On the drag and shedding frequency of 2D bluff bodies. *NACA Tech. Note 3169.*

[4] Bearman P.W., 1965 Investigation of the flow behind a two-dimensionnal model with a blunt trailing edge and fitted splitter plates *J. Fluid. Mech.* 21, 241.

[5] Roshko, A. 1993 Perspectives on bluff body aerodynamics. *J. Fluid. Wind Eng. and Ind. Aero.* **49**, 79-100.

[6] Wu Y.T. 1978 Cavity and wake Flows. *Ann. Rev. Fluid. Mech.* **4**, 243-284.

A Qualitative Study of the Response of the Ginzburg-Landau Equation when Coupled to the Structural Model of a Submerged Cable

Lauro M. Yamada da Silveira
Prysmian Cables & Systems
lauro.silveira@prysmian.com

Clóvis de Arruda Martins
University of São Paulo
cmartins@usp.br

José Augusto Penteado Aranha
University of São Paulo
japaran@usp.br

1. Introduction

In the past few years, the importance of vortex-induced vibration (VIV) analysis on risers and umbilicals has greatly increased. As the depths of offshore oil fields increases, VIV effects become more and more important, especially on fatigue life estimation and clashing prediction. This analysis, however, is yet an open area of research and some different approaches may be and have been used. Just to illustrate, the commercial package Orcaflex, Orcina (2006), incorporates six different VIV calculation methods.

A possible approach to VIV analysis is the experimental one, which may be carried on controlled water channels, e.g. Chaplin (2004). A huge problem, though, is to overcome the scaling on the experiments in order to extend the results to a practical application. In a real case scenario, risers with typical diameters of 200 millimeters are installed on depths up to 2500 meters. Another possible approach is the Computer Fluid Dynamics (CFD). In this case, VIV analysis can be performed through Discrete Vortex method coupled to the structural model, e.g. Bearman et al (2006). This approach, however, requires a massive (sometimes unfeasible) computational effort. An alternative approach is the use of phenomenological models, e.g. Iwan & Blevins (1974), which couples the structural oscillator to a simple 'wake oscillator'. The problem in this approach is the 'ad-hoc' structure of the model. Also, the 'wake oscillator' – which may be a van der Pol or a Ginzburg-Landau equation, for example – must be 'tuned' for each flow condition, making this model only a fair interpolator.

Recently, however, Aranha (2004) has shown that the Ginzburg-Landau Equation (GLE) results from an asymptotically solution of the Discrete Navier-Stokes problem. In this sense, the formerly phenomenological model becomes supported by a strong theoretical basis. Furthermore, Aranha (2004) has shown that it is possible to numerically calculate all coefficients needed in the coupled fluid-structure oscillator. This approach would require a minor computational effort allied to a solid theoretical basis.

The GLE may be found in other branches of the mathematical-physics, including nonlinear waves, second-order phase transitions, Rayleigh-Bénard convection and superconductivity, Winterbottom (2007). The work of Shraiman et al (1992) presents a study of the qualitative behavior of this (decoupled) equation, which goes from stability to chaos depending on the relation of the imaginary parts of the Ginzburg and Landau coefficients. Our intuition, though, would expect that a chaotic behavior would not be observed when the GLE were coupled to the structural oscillator.

To check this assumption, the present work aims an investigation on the qualitative behavior of the GLE solution decoupled and then coupled to a three-dimensional structural model which simulates a submerged cable. An in-house time-domain software, which calculates VIV response through the GLE, was developed. Some preliminary results show that the structural model organizes the wake oscillator, as expected.

2. The Ginzburg-Landau Equation and the Coupled Fluid-Structure Model

2.1. The Ginzburg-Landau Equation

The classic GLE may be written as

$$\frac{\partial A}{\partial t} - A + \left(1 - ic_3\right)\left|A\right|^2 A - \left(1 + ic_1\right)\frac{\partial^2 A}{\partial z^2} = 0 \tag{1}$$

Shraiman et al (1992) presented a study of the qualitative response of the GLE, which may be condensed in the graph shown in Figure 1. As observed, there is a bifurcation and two types of chaotic behavior may be identified: phase chaos and defect chaos. Below the Benjamin-Feir instability line (LBF), however, the solution is not chaotic.
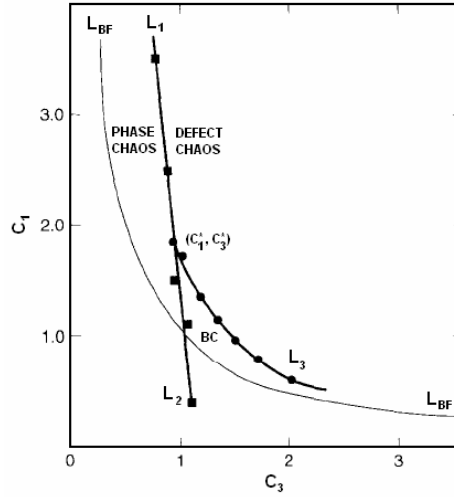
Figure 1 - Qualitative behavior of the GLE; extracted from Shraiman et al (1992).

2.2. The Three-Dimensional Structural Model

The cable is assumed free to twist and bend and is hinged at both ends. Axial and tensioning rigidities are considered.

2.2.1. The Static Problem

Classic equations relating deformation and geometric compatibility, force and moment equilibrium as well as constitutive relations, provide a system of ordinary differential equations that can be numerically integrated using a Runge-Kutta method. The loads taken into account are the immersed weight per unit length of the cable, hydrostatic pressure and hydrodynamic drag due to sea current. The sea current is supposed stationary and the drag force is calculated by the classical Morison's formula. Details may be found in Silveira and Martins (2005).

2.2.2. The Dynamic Problem

The dynamic problem is considered as a small perturbation from the static configuration. Through the application of the Principle of Virtual Work, the dynamic equation in its integral form is obtained and discretized, using a finite element method. Details can be found in Martins (2000). The loads take into account the inertia of the cable, the added inertia and the hydrodynamic lift forces. Such lift forces are calculated at each discretized node through wake-oscillators, of the Ginzburg-Landau type, according to Aranha (2004). The coupled system is then

$$\frac{\partial A}{\partial t} - \sigma A - \gamma\left(1 + ic_1\right)\frac{\partial^2 A}{\partial z^2} + \mu\left(1 - ic_3\right)|A|^2 A = f_V V$$

$$\left(\dot{V} + i\omega_0\right) + \omega_n^2 Y = \frac{1}{m}\int_0^l \left(C_A A + C_V V\right)dz \tag{2}$$

$$\dot{Y} + i\omega Y = V$$

The first equation describes the wake-oscillator; the second and third ones describe the structural oscillator. Notice that the GLE in Equation (1) differs from the GLE in Equation (2) only by some scaling (and, obviously, by the right-term which couples the two oscillators). The GLE was discretized through a finite-difference scheme. The structural oscillator was discretized through a finite element method. The numerical problem was then integrated in time-domain using the implicit Houbolt method.

3. Results and Discussion

Two cases will be investigated here. The first one refers to $\left(c_1; c_3\right) = \left(0.2; 2.0\right)$, corresponding to a non-chaotic region; the second one refers to $\left(c_1; c_3\right) = \left(2.0; 2.0\right)$, corresponding to a defect chaos region (see Figure 1). The system in Equation (2) was firstly numerically integrated with $f_V = C_A = C_V = 0$ (GLE uncoupled) and afterwards with $f_V, C_A, C_V \neq 0$ (GLE coupled), making it possible to distinguish possible differences.

Values of the coefficients $\sigma, \mu, f_V, C_A, C_V$ were obtained from an asymptotically solution of a van der Pol type oscillator based on the Iwan & Blevins (1974) model, which leads to a Landau equation. According to the

work of Aranha (2004), the value $\gamma = 1/\mathrm{Re}$ was used. The structural oscillator corresponds to a 0.10m diameter, 300m length cable of submerged weight 0.1289 kN/m. Flow velocity is 0.2m/s (constant profile).

As a large amount of data is generated, only phase maps will be shown. Phase maps can summarize the qualitative behavior of the solution of the GLE, as will become clear soon. Figure 2 shows the phase maps of the decoupled case in the stable and defect chaos regions. These results are similar to the ones obtained by Shraiman et al (1992).
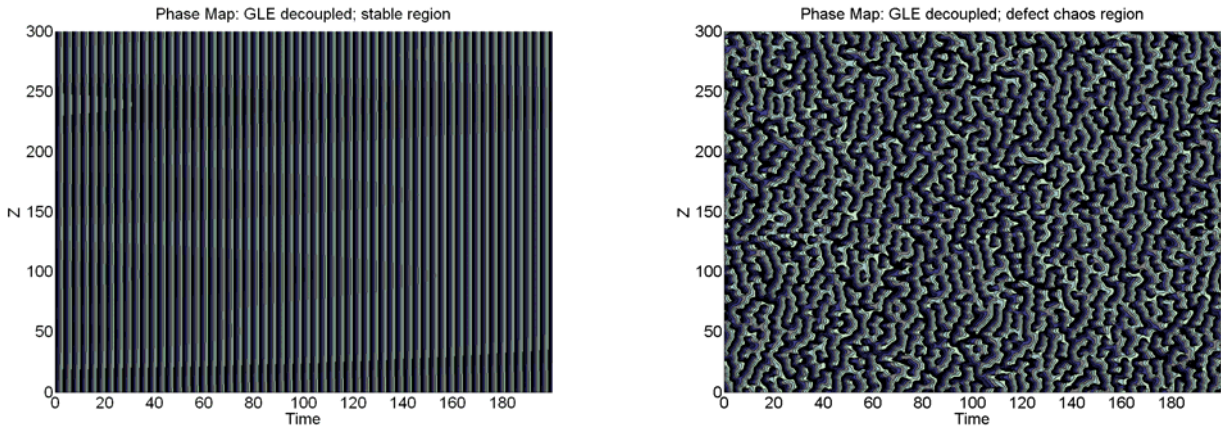
Figure 2 - Phase Maps for the decoupled case.

Figure 3 shows the phase maps of the coupled case in the stable and defect chaos regions. Notice that the two phase maps are almost identical. This fact indicates that the structural oscillator dominates and it becomes even clearer when the displacements Y are shown.
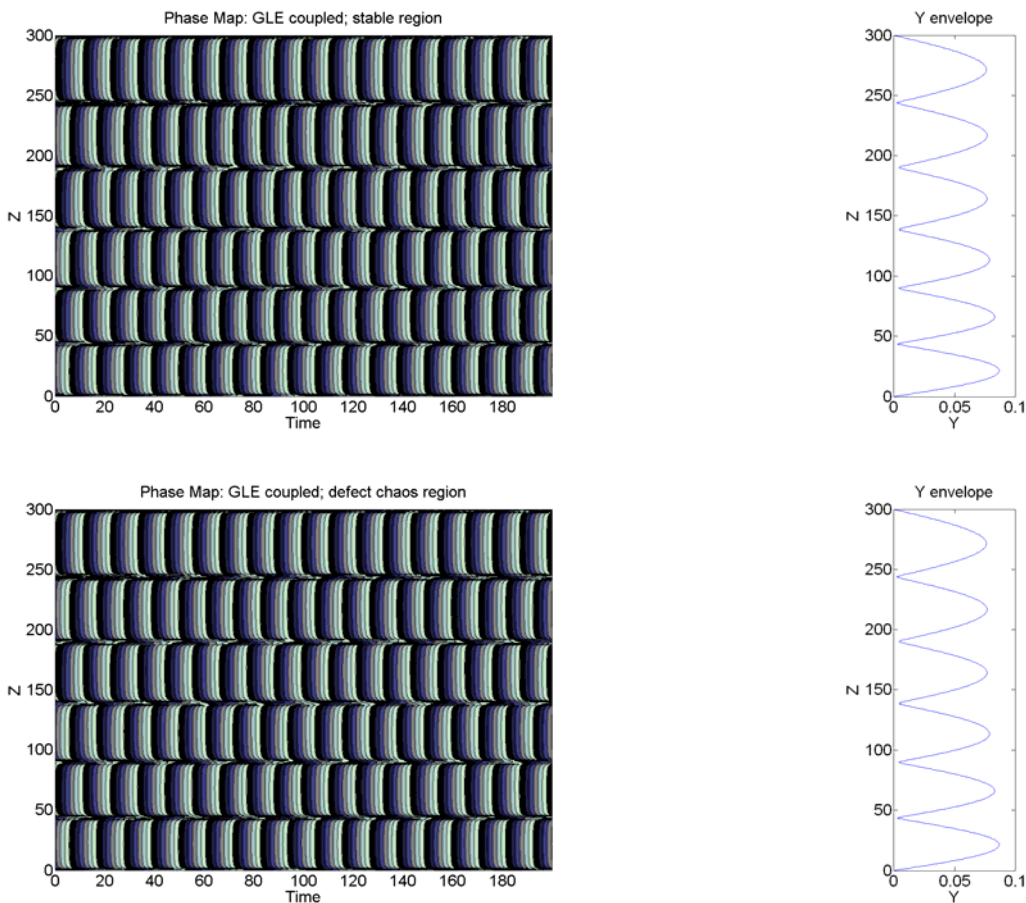
Figure 3 - Phase Maps for the coupled case; envelopes of the displacement Y (cable diameter = 0.10).

A conclusion that can be drawn from this study is that the structural oscillator dominates and organizes the 'wake-oscillator' based on the GLE.

4. References

Aranha, J. A. P. "Weak Three Dimensionality of a Flow Around a Slender Cylinder: The Ginzburg-Landau Equation", Journal of the Brazilian Society of Mechanical Sciences and Engineering, Vol. XXVI, No. 4, 2004, pp 355 – 367.

Bearman, P. W., Chaplin, J. R., Fontaine, E., Graham, J. M. R., Herfjord, K., Lima, A. A., Meneghini, J. R., Schulz, K. W., Wilden, R. H. J., 2006, "Comparisons of CFD Predictions of Multi-Mode Vortex-Induced Vibrations of a Tension Riser with Laboratory Measurements", Proceedings of PVP2006 – ICPVT – 11, 2006 ASME Pressure Vessels and Piping Division Conference, Vancouver, Canada.

Chaplin, J.R. et al, 2004, "Laboratory measurements of Vortex-Induced Vibrations of a vertical tension riser in a stepped current", 8th International Conference on Flow-Induced Vibration, FIV2004, Paris, France, 6-9 July, 2004, 2, pp. 279-284.

Iwan, W. D., Blevins, R. D., 1974, "A Model for Vortex Induced Oscillation of Structures", Journal of Applied Mechanics, September 1974, p. 581-586.

Martins, C.A., 2000, "An Expedited Tool for the Study of Rigid Catenary Risers", Livre-Docencia Thesis (in Portuguese), University of São Paulo.

Orcina Ltd., 2006, Orcaflex User's Manual, version 9.0a.

Shraiman, B., Pumir, A., van Saarlos, W., Hohenberg, P., Chaté, H. & Holen, M., 1992, "Spatiotemporal chaos in the one-dimensional complex Ginzburg-Landau Equation". Physica 57, 241 – 248.

Silveira, L. M. Y., Martins, C. A., 2005, "A Numerical Method to Solve the Three-dimensional Static Problem of a Riser with Bending Stiffness", Proceedings of the 24th International Conference on Offshore Mechanics and Artic Engineering, Halkidiki, Greece.

Winterbottom, D. M., "The Complex Ginzburg-Landau Equation", 2007, available at the site <http://www.maths.nottingham.ac.uk/personal/pmxdmw/tutorial/>, Access on June, 1st, 2007.

Floquet stability analysis of the flow around an oscillating cylinder

Rafael S. Gioria (rafael.gioria@poli.usp.br)[1], Bruno S. Carmo[2], and Julio R. Meneghini[1]

[1]NDF, "Escola Politécnica", University of São Paulo, Brazil

[2]Imperial College London, Dept. of Aeronautics, United Kingdom

Abstract

This investigative work is about the flow around a circular cylinder submitted to forced transverse oscillations. The goal is to investigate how the transition to turbulence is initiated in the wake for cases with different Reynolds numbers (Re) and displacement amplitudes (A). For each Re the motion frequency is kept constant, close to the Strouhal number of the flow around a fixed cylinder at the same Re. Stability analysis of two-dimensional periodic flows around a forced-oscillating cylinder is carried out in respect to three-dimensional infinitesimal perturbations. The procedure consists in performing a Floquet type analysis (Iooss & Joseph, 1990; Barkley & Henderson, 1996) of time periodic base flows, computed using the Spectral/hp element method. With the results of the Floquet calculations, considerations about the stability of the system are made, and also about the form of the instability at its onset.

1 Introduction

Vortex shedding can be dramatically changed when a bluff body is oscillating in a fluid stream. The body motion can take control of the instability mechanism that leads to vortex shedding in certain ranges of amplitude and frequency of oscillation. When the body is forced to oscillate in a sinusoidal way, the frequency of vortex shedding can be controlled over a limited range of body oscillation frequency and amplitude. This phenomenon is usually known as lock-in. When the synchronization between vortex shedding and body oscillation frequencies happens, it is usually thought that the flow becomes essentially two-dimensional. As it is going to be seen in this paper, three-dimensionalities can develop in the wake even if the conditions for lock-in are matched. One of the objectives of the work described here is to examine closely how these three-dimensionalities build up. Hydrodynamic stability concepts, based on Floquet analysis, are employed in order to verify the existence of a threshold value of amplitude above that the flow becomes unstable in respect to any perturbation and three-dimensionalities emerge.

2 Results

For base flows simulations, after a convergence analysis of flow results like Strouhal number, mean drag coefficient and lift coefficient RMS, a mesh of 485 spectral elements has been chosen. Its dimensions are: $40D$ wide, $16D$ from inflow to cylinder centre and $35D$ to outflow. Polynomial of 9th order was used in most cases (exceptions were 12th order for $Re = 260$ with $A/D = 0.4$ and for $Re = 300$ with $A/D = 1.0$ due to lack of periodicity of the resulting wake if a lower mode was employed). 2nd order time integration was used for most cases except on those cited above which 1st order and smaller time step were used. After obtaining the snapshots of the periodic base flows, we proceeded with the Floquet stability analysis. The calculations were carried out for $0.0 \leqslant \beta \leqslant 15.0$ with intervals of 0.5. Next the results regarding the base flow and Floquet analysis calculations are presented.

2.1 Base flow

The vortex emission modes observed on the wakes resulting from two-dimensional DNS of forced-oscillating circular cylinder are listed in table 1. These vortex emission modes are associated to the three-dimensionalities that emerge in three-dimensional simulations and captured in Floquet stability analysis.

Table 1: Vortex shedding regime of two-dimensional base flow around a forced-oscillating circular cylinder.

Reynolds	Amplitude						
	$0.4D$	$0.5D$	$0.6D$	$0.7D$	$0.8D$	$0.9D$	$1.0D$
200	2S	2S	2S	2S	P+S	P+S	P+S
240	2S	2S	P+S	P+S	P+S	P+S	P+S
260	2S	2S	2S	P+S	P+S	P+S	P+S
300	2S	2S	P+S	P+S	P+S	2P	2P

2.2 Floquet analysis - $Re = 200$

In all results presented in this paper, the cylinder is forced to oscillate at a ratio $f_{osc}/f_s = 0.95$, in which f_{osc} is the oscillation frequency and f_s is the vortex shedding frequency of a fixed cylinder. Figure 1a shows the results for the four smaller amplitudes, from 0.4 to 0.7 diameters. All those curves have similar shapes and, as far as the linear Floquet stability analysis is concerned, the two-dimensional periodic flow is stable to three-dimensional infinitesimal perturbations for all the cases in the figure, at this Re. It is important to notice that, for this Re, the two-dimensional periodic flow around a fixed cylinder is already unstable to three-dimensional perturbations – the calculations result in a mode A instability for $\beta \approx 1.5$, following the taxonomy proposed by Williamson (1996). Figure 1e brings the results for $0.8 \leqslant A \leqslant 1.0$. For $A = 0.8$, the flow is stable and a point of maximum

(a) $Re = 200, 0.4 \leqslant A/D \leqslant 0.7$

(b) $Re = 240, \ 0.4 \leqslant A/D \leqslant 0.7$

(c) $Re = 260, \ 0.4 \leqslant A/D \leqslant 0.7$

(d) $Re = 300, \ 0.4 \leqslant A/D \leqslant 0.6$

(e) $Re = 200, \ 0.8 \leqslant A/D \leqslant 1.0$

(f) $Re = 240, \ 0.8 \leqslant A/D \leqslant 0.9$

(g) $Re = 260, \ 0.8 \leqslant A/D \leqslant 1.0$

(h) $Re = 300, 0.7 \leqslant A/D \leqslant 0.9$
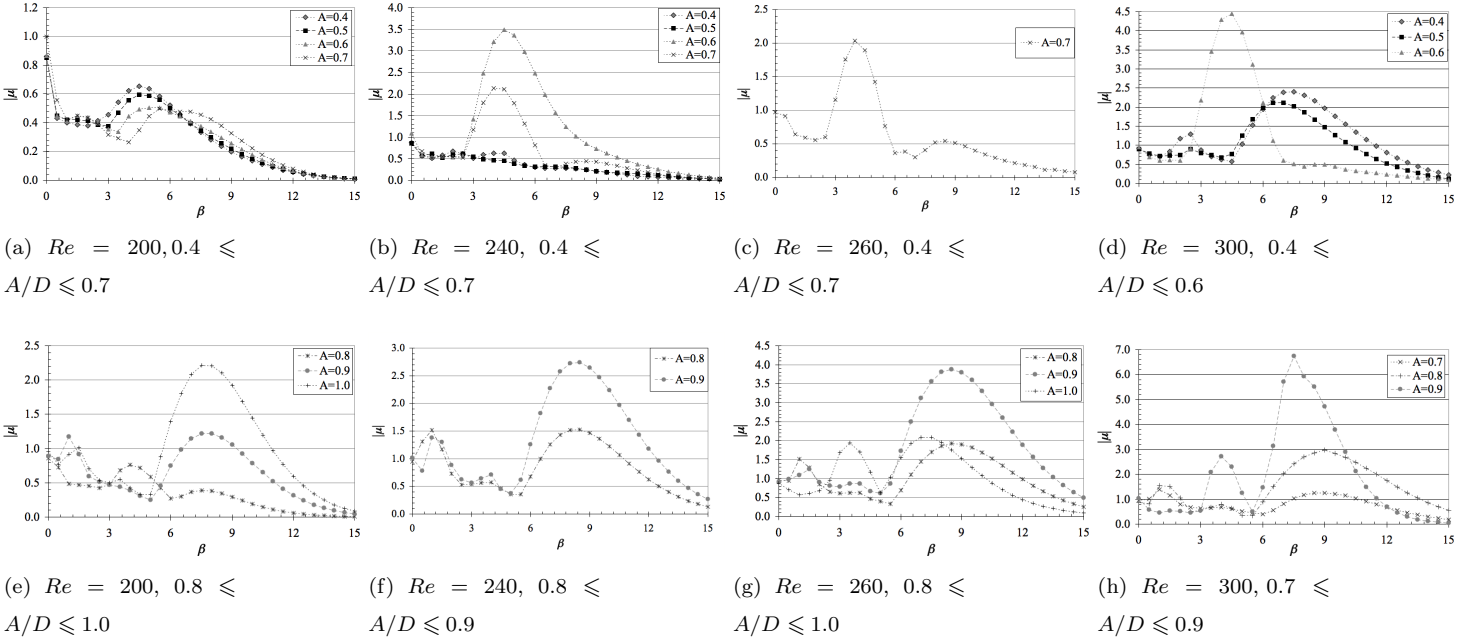
Figure 1: Floquet multiplier μ as a function of the spanwise wavenumber β. (a)-(d) are lower amplitudes and (e)-(h) are higher ones.

at $\beta \approx 4.0$, similarly to the cases of smaller amplitudes. However, a second, non-dominant peak can be observed, for $\beta \approx 7.5$. Increasing the amplitude to 0.9, the peak at $\beta \approx 4.0$ disappears, the peak at $\beta \approx 7.5$ becomes more pronounced, exceeding the stability limit $|\mu| = 1$, and a new peak, also unstable, appears at $\beta \approx 1.0$. The curve for $A = 1.0$ has the same features as that for $A = 0.9$, but with a clear dominance of the mode with higher β.

Figure 2a contains instantaneous x-vorticity contours of the mode of smaller β. We see that this mode have some similarities with mode A, such as the wave number and the fact of getting stronger in regions of vortex interaction. The x-vorticity of the shear layers change sign according to the side of the wake centreline they are, and this happens in mode A as well. However, the translational symmetry of this mode is different. As can be seen in figure 2b, the mode has T-periodicity, but there is no mirror symmetry in half periods translations. In contrast, the patterns are fairly parallel. This might be related with the vortex shedding pattern P+S. In this pattern, the wake is wider, and opposite vortices do not alternate in half periods, but they pair in a parallel fashion, instead. Since the eigenvectors are always connected with the shedding of the base flow, this could explain the differences between the results obtained here and mode A. So, due to the striking similarities between the results and mode A, we understand that the mode observed here is indeed of type A. Changing the focus now to the higher

(a) $Re = 200$, $A = 0.9$ and $\beta = 1.0$.

(b) $Re = 200$, $A = 0.9$ and $\beta = 1.0$.

(c) $Re = 200$, $A = 0.9$ and $\beta = 7.5$.

(d) $Re = 200$, $A = 0.9$ and $\beta = 7.5$.
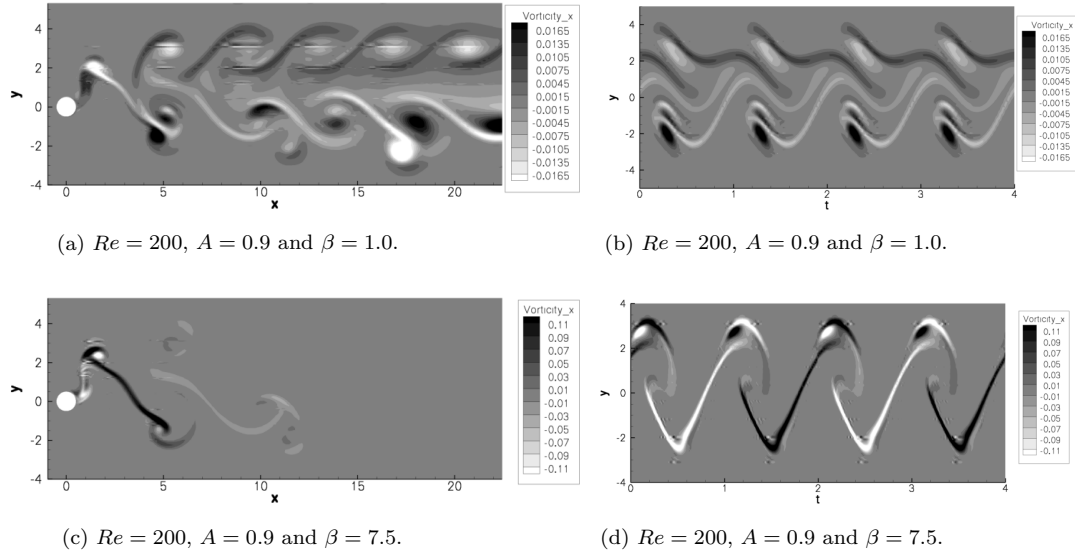
Figure 2: x-vorticity contours of the Floquet normalised eigenvector.(a) and (c) are instantaneous countours, (b) is contours on the line $x = 7.0$ and (d) on $x = 2.0$, and t is given in shedding periods.

wave number mode, we observe in figure 2c that this mode is stronger in the shear layers, reaches its peak in the near wake to the cylinder and rapidly dies out downstream. Examining figure 2d we notice that a period doubling occurs, since the mode has periodicity $2T$, and this can also be evidenced by the negative sign of the Floquet multiplier. In addition, the x-vorticity contours in figure 2d are not symmetric in respect to the wake centreline. All these characteristics are found in a mode C instability. However, the wave number we observe here is approximately the same found for a mode B instability.

2.3 Floquet analysis - $Re = 240$

Figure 1b shows the results for low amplitudes. As for $Re = 200$, the cases with $A/D = 0.4$ and $A/D = 0.5$ are stable for the entire β range. However, the cases with $A/D = 0.6$ and $A/D = 0.7$ are unstable to perturbations of intermediate wave numbers. The maximum growth rate for these cases occur for $\beta \approx 4.5$, which is the same as for mode C (Carmo *et al.*, 2007; Sheard *et al.*, 2003). The Floquet multiplier for this instability is real and negative, indicating a period-doubling character. Curiously, the results for $A/D = 0.6$ gave more unstable values than for $A/D = 0.7$. In both cases, the shedding mode is P+S. For larger amplitudes, $A/D = 0.8$ and $A/D = 0.9$ (the base flow was not periodic for $A/D = 1.0$, probably because the shedding is in a transitional range between regimes P+S and 2S), the shape of the graphs change again, as can be seen in figure 1f. The general behaviour is similar to that observed for larger amplitudes at $Re = 200$: there is a peak for lower β, which corresponds to mode A, and another peak for higher β, relating to a period-doubling mode.

In order to analyse the differences between the period-doubling modes that are detected for intermediate and high β, figure 3 shows the eingenmodes x-vorticity contours and base flow spanwise vorticity contours. In figure 3a, it can be seen that the mode of intermediate β, which appears for $A/D = 0.6$ and $A/D = 0.7$, is stronger in the braid shear layers that link the

downstream vortex of the pair (P) to the single vortex (S). Those vortices have opposite vorticity sign. On the other hand the period-doubling mode for higher β, which is unstable for $0.8 \leqslant A/D \leqslant 0.9$ and is illustrated in figure 3b, is stronger in the braid shear layers that link he single vortex (S) to the upstream vortex of the pair. These vortices have the same vorticity sign, and actually they originate from the same vortex in the near wake. This difference between the regions of higher strength associated to the different wavenumbers these modes have suggest that those are actually different modes, despite the fact that both are period-doubling modes.
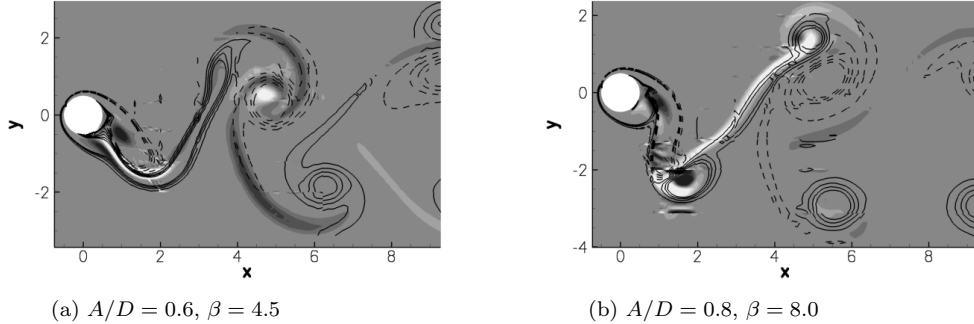

(a) $A/D = 0.6$, $\beta = 4.5$ (b) $A/D = 0.8$, $\beta = 8.0$

Figure 3: Eingenmode x-vorticity contours (flood) superposed to base flow spanwise vorticity contours (lines), $Re = 240$. Light colours and dashed lines represent negative values of vorticity, and dark colours and continuous lines represent positive values of vorticity.

2.4   Floquet analysis - $Re = 260$

Increasing Re to 260 did not alter significantly the behaviour of the graphs for $0.7 \leqslant A/D \leqslant 0.9$.[1] All these three amplitudes exhibited a P+S vortex shedding regime for this Re. Figure 1c shows the results for $A/D = 0.7$, in which a single peak at $\beta \approx 4.0$ is observed. The corresponding mode is period-doubling and has the same topology as that for the same amplitude and wavenumber at $Re = 240$. The results for $A/D = 0.8$ and $A/D = 0.9$, displayed in figure 1g, exhibit two-peaks, like the results for $Re = 240$; one corresponds to mode A at low β and the other corresponds to a period-doubling mode at high β. The case $A/D = 1.0$ produced novel results. For $Re = 260$, the vortex shedding regime observed for this case was 2S, and it seems that this changing of shedding regime lead to a dramatic change in the stability of the system. In figure 1g, it can be seen that two distinct peaks appear in the results for $A/D = 1.0$. In the peak corresponding to $\beta \approx 3.5$ the Floquet multipliers are real and positive. Looking at the streamwise vorticity contours of this mode on figure 4a, similarities with mode B can be noticed: the symmetry is the same and the mode is stronger in the braid shear layers. The wavenumber for this mode, however, is approximately half of mode B wavenumber. In the peak corresponding to $\beta \approx 7.0$ μ is complex, which indicates that this is a quasi-periodic mode. The streamwise vorticity contours of this mode can be seen in figure 4b. The fixed cylinder case also presents an unstable quasi-periodic mode for higher Re, which is named QP (Blackburn & Lopez, 2003),but the wavenumber for this mode is around 4.0, so the wavenumber found in the present results is roughly twice that for a fixed cylinder. Interestingly, it seems that there was a "swap" between mode QP and mode B for this case of oscillating cylinder.

2.5   Floquet analysis - $Re = 300$

Figure 1d and 1h show the results for $Re = 300$. For this Re, the shedding for $A/D = 1.0$ was not periodic, therefore no Floquet analysis was carried out for this case. For $A/D = 0.4$ and $A/D = 0.5$ (figure 1d), whose base flows presented 2S vortex shedding regimes, two distinct peaks can be observed, one for small wave number and one for big wave number. The Floquet multiplier at those maxima are real and positive, and they correspond to modes A and B. They are both unstable for $A = 0.4$, and only mode B (bigger wave number) is unstable for $A = 0.5$. At this same Re, the plot $\mu(\beta)$ for a fixed cylinder presents modes A an B as well, being both unstable, and the value of μ is higher. Still in figure 1d, it can be seen that the graph for

---

[1]There are no comments about the cases $0.4 \leqslant A/D \leqslant 0.6$ because the base flows for these cases were not analysed yet.

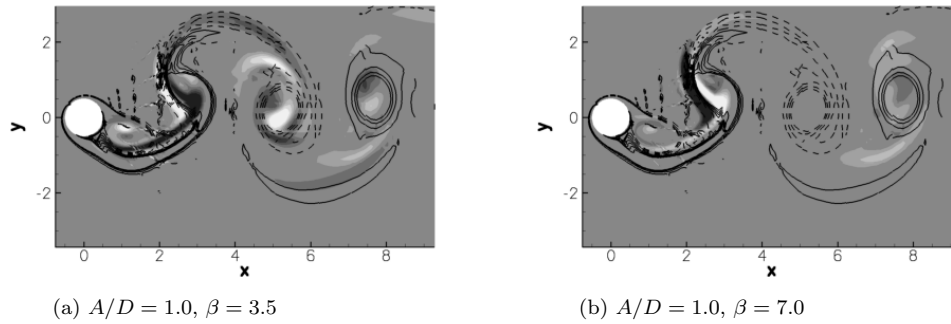(a) $A/D = 1.0$, $\beta = 3.5$ (b) $A/D = 1.0$, $\beta = 7.0$

Figure 4: Eingenmode x-vorticity contours (flood) superposed to base flow spanwise vorticity contours (lines), $Re = 260$. Light colours and dashed lines represent negative values of vorticity, and dark colours and continuous lines represent positive values of vorticity.

$A/D = 0.6$ is similar to those for $Re = 240$ and $Re = 260^2$, with a peak for intermediate β corresponding to a period-doubling mode (μ is real and negative). The shedding mode for this case is P+S. Differently from $A/D = 0.6$, the case $A/D = 0.7$ presented a different behaviour when compared to the results for $Re = 240$ and $Re = 260$, as can be seen in figure 1h. The peak for intermediate wavenumbers disappeared, and two other peaks, one for low β and another for high β come into sight. The graph has the same shape as those observed for $A/D = 0.8$ and $A/D = 0.9$ at $Re = 200$, $Re = 240$ and $Re = 260$, and the Floquet multipliers at those peaks also behave accordingly, being real and positive at the peak at low β and real and negative for the peak at high β. The case $A/D = 0.8$, whose results are also plotted in figure 1h, did not show any significant change regarding its stability in respect to three-dimensional perturbations when compared to the results at all the other lower Re. However, the case $A/D = 0.9$ had its vortex shedding regime changed to 2S at this Re, and presented the same behaviour observed for $A/D = 1.0$ at $Re = 260$.

3   Discussion

The results presented here show that the wake transition in the flow around an oscillating cylinder is remarkably different from that in the flow around a steady cylinder. The stability of the flow in respect to three-dimensional perturbations and the topology of the unstable modes observed are highly dependent of the amplitude of vibration and vortex shedding mode.

For small amplitudes, $A/D = 0.4$ and $A/D = 0.5$, the vibration of the body makes the flow more stable. For example, for $200 \leqslant Re \leqslant 240$ the flow was stable for these amplitudes, despite the fact that the instantaneous Re can reach values 30% higher than the global Re. Besides this, when the flow became unstable for these cases at $Re = 300$, the values of μ were smaller than those observed in the steady cylinder case.

If the amplitude was increased, the vortex shedding regime changed from 2S to P+S, and the stability of the flows were dramatically altered. In general, for this shedding regime two different scenarios were observed. For smaller amplitudes, the graphs of $\mu(\beta)$ exhibited just one peak for intermediate wavenumbers. This was a period-doubling mode (μ real and negative) and it was stronger in the braid shear layers that linked vortices of different vorticity signs and located at opposite sides of the wake. In the vorticity contours shown in figure 3a it can be seen that this mode seems to originate in the region where the shear layer interacts with the opposite vortex being formed. The same was observed in previous works in which mode C was observed (Carmo *et al.*, 2007; Sheard *et al.*, 2003). Given that the wavenumber for this modes is also similar to those reported in the same works, we suggest that this instability is of mode C type.

The second scenario for P+S shedding mode happened for higher amplitudes. In this case, two different peaks were observed. One for small β, which has a mode A character, as discussed in section 2.2, and another for large β. The latter has many similarities with mode B, such as the wavenumber and the regions where it is strong. However, differently from mode B, it is a period-doubling mode. This difference may be caused by the asymmetry in the wake, which prevents a strong interaction between the shear layers of two consecutive shedding cycles. We wonder if the lack of such feedback could lead to

---

[2] Although the results for $Re = 260$ are not ready yet, it is expected the results for $Re = 260$ to be similar

an alternation of sign from cycle to cycle. In this report this mode will be named B_{pd}, in order to distinguish from the other period-doubling mode, which is mode C.

A further increase in the amplitude makes the vortex-shedding regime to be 2S again. However, the wake transition was completely different from what was observed for small amplitudes. As discussed in section 2.4, there is a mode similar in shape and symmetry to mode B for intermediate β (B_{iwn}) and a quasi-periodic mode for high β (QP_{hwn}). As far as we are aware, there is no work that reported the existence of these modes at such wavenumbers. Since the shedding mode is 2S, i.e. the same for a steady cylinder case, we suspect that the phase angle could have some influence in the stability of the flow and wavenumbers of the modes.

References

BARKLEY, D. & HENDERSON, R. D. 1996 Three-dimensional Floquet stability analysis of the wake of a circular cylinder. *Journal of Fluid Mechanics* **322**, 215–241.

BLACKBURN, H. M. & LOPEZ, J. M. 2003 On three-dimensional quasiperiodic floquet instabilities of two-dimensional bluff body wakes. *Physics of Fluids* **15** (8), 57–60.

CARMO, BRUNO SOUZA, SHERWIN, S. J., BEARMAN, P. & WILLDEN, R. 2007 Wake transition in the flow around two circular cylinders in staggered arrangements. Under consideration for publication in the Journal of Fluid Mechanics.

IOOSS, GÉRARD & JOSEPH, DANIEL D. 1990 *Elementary Stability and Bifurcation Theory*, 2nd edn. Springer-Verlag.

SHEARD, G. J., THOMPSON, M. C. & HOURIGAN, K. 2003 From spheres to circular cylinders: the stability and flow structures of bluff ring wakes. *Journal of Fluid Mechanics* **492**, 147–180.

WILLIAMSON, C. H. K. 1996 Three-dimensional wake transition. *Journal of Fluid Mechanics* **328**, 345–407.

Three-dimensionnal instabilities and transient growth of trailing vortices in homogeneous and stratified flows

Jean-Marc Chomaz[1], Claire Donnadieu [1] and Sabine Ortiz[1,2]

[1] *LadHyX, CNRS–Ecole Polytechnique F-91128 Palaiseau Cedex, France*
[2] *UME/DFA, ENSTA, chemin de la Hunière, 91761 Palaiseau Cedex, France*
November 16, 2007

Abstract

An aircraft wake is made of counter-rotating vortices and is known to be affected by a long (Crow) and a short (elliptic) wavelength instabilities. Numerical investigations on the three-dimensionnal instabilities and transient growth of such dipole are performed. By means of a three-dimensionnal linear stability analysis, we retrieve the instability bands corresponding to the Crow and elliptic modes but we also observe less unstable oscillatory modes with very broad peaks. The transient growth of perturbations on this dipole, investigated by computing the optimal linear perturbations with a direct-adjoint technique, demonstrates the crucial role of the region of maximal strain at short time and of the hyperbolic point at intermediate time . Investigations on the three-dimensionnal dynamics of trailing vortices in stratified fluids are performed. The elliptic instability is almost unaffected by weak and moderate stratifications.

1 Introduction

Trailing vortices behind aircrafts consist of a horizontal pair of counter-rotating vortices propagating downwards. Depending on atmospheric conditions, such dipole can persist over a long time or be rapidly destroyed. If the vortex pair remains coherent, it can be hazardous to following aircrafts, especially during take-off and landing thus limiting the frequency between airplanes at airports. Studies of the dynamics of a pair of counter-rotating vortices in unstratified flows have shown that this vortex pair is unstable with respect to three-dimensionnal perturbations. [Crow (1970)] has discovered a long-wavelength instability, symmetric with respect to the plane separating the two vortices. The existence of a short-wavelength elliptic instability has been revealed by [Tsai & Widnall (1976)], [Moore & Saffman (1975)] and numerous articles ever since for both symmetric and antisymmetric modes. This instability, due to the elliptic deformation of the core of the vortices, is a resonant interaction between the strain and Kelvin waves of azimuthal wavenumbers $m = 1$ and $m = -1$ when both waves have the same frequency ω and are particularly intense for $\omega = 0$.

However in many atmospheric situations, as such dipoles propagate downwards, they evolve under the influence of the stable stratification of the atmosphere and the three-dimensionnal dynamics of this vortex pair in stratified flow has yet received much less attention. Direct numerical simulations of [Nomura *et al.* (2006)] on the short-wavalength instability of a counter-rotating vortex pair in presence of stable stratification have suggested that the instability mechanism corresponds, despite the stratification, to the elliptic instability as in homogeneous media. The instability appears earlier than in the unstratified case, owing to the decrease due to the stratification of the separation distance between the vortices as they propagate downwards, decrease that induces larger ellipticity of the vortices and then enhances the instability.

In this paper, we perform a three-dimensionnal linear stability analysis of a Lamb-Oseen vortex pair in unstratified fluid in section 2. The transient growth of perturbations on this vortex pair, investigated by computing the optimal perturbations with the direct-adjoint technique introduced by [Corbett & Bottaro (2000)], is presented in section 3. In the stratified case, the two-dimensional flow is unsteady and the optimal perturbations are computed at several times, with a direct-adjoint technique similar to the one used in the steady case and which takes into account the evolution of the flow. The results of this study are presented in section 4.

2 Linear three-dimensional instabilities in unstratified fluid

We investigate the three-dimensionnal instabilities of the pair of counter-rotating vortices represented on Figure 1, obtained by computing the two-dimensional evolution of initially two circular Lamb-Oseen vortices (i.e a gaussian distribution of vorticity), of circulation Γ, radius a and with a separation distance b, as in [Sipp *et al.* (1999)]. Since this base flow is symmetric with respect to
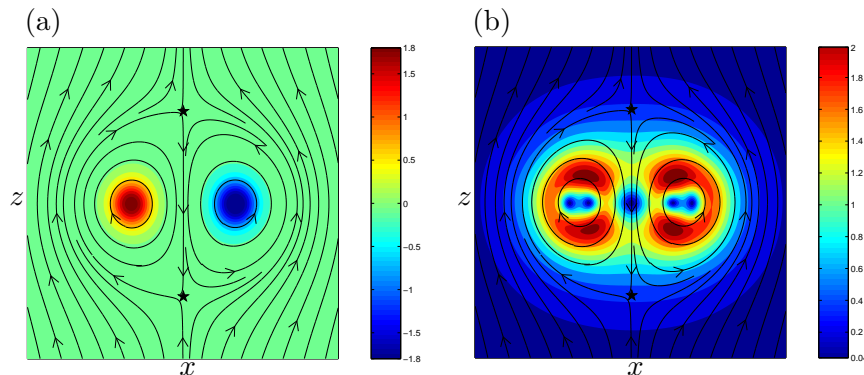
Figure 1: *Isovalues of (a) axial vorticity $\omega_{By}2\pi a^2/\Gamma$ and (b) the absolute value of the local strain rate $|\epsilon|$ of the base flow in the (x,z) plane for $a/b = 0.206$. The stars represent the two hyperbolic points of the base flow and the arrowed lines correspond to the streamlines of the base flow.*

the plane separating the two vortices, the linear stability modes may be decomposed in symmetric and antisymmetric parts. Figure 2 shows the real part of the growthrates σ of the modes scaled by $2\pi b^2/\Gamma$ as function of the axial wavenumber k_y scaled by the core radius a for a dipole of aspect ratio $a/b = 0.206$ and for two Reynolds numbers based on the circulation of the vortices $Re_\Gamma = 10^5$ and $Re_\Gamma = 2000$. The first band of Figures 2(a) and 2(b) with a maximum at $k_ya = 0.19$ is the
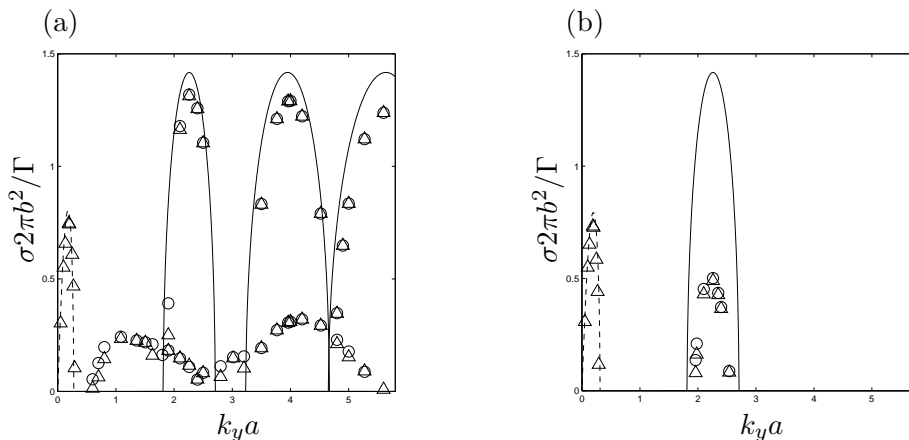
Figure 2: *Scaled growthrates $\sigma 2\pi b^2/\Gamma$ of symmetric ($\triangle$) and antisymetric ($\circ$) modes as function of the scaled axial wavenumber k_ya for (a) $Re_\Gamma = 10^5$ and (b) $Re_\Gamma = 2000$. Dashed line corresponds to the theory of [Crow (1970)] for the low wavenumber symmetric instability of a pair of vortex filaments. Continuous lines correspond to the inviscid theoretical prediction of [Le Dizès & Laporte (2002)] for a pair of Lamb-Oseen vortices in the limit $a/b = 0$.*

long-wavelength symmetric Crow instability. The three other peaks of Figure 2(a) with maxima at $k_ya = 2.26$, $k_ya = 3.96$ and $k_ya = 5.64$ and the single peak of Figure 2(b) with a maximum at $k_ya = 2.26$ corresponds to the elliptic instability. The growthrates of symmetric and antisymmetric modes are almost identical. The two broad lower peaks of Figure 2(a) with maxima at $k_ya = 1.09$ and $k_ya = 4.2$ correspond to a novel oscillatory instability, which was not found by

[Sipp & Jacquin (2003)]. This instability exists for both symmetries and appears for sufficiently high Reynolds numbers. This oscillatory instability may be interpreted as an elliptic instability mode resulting from a resonance between the strain and Kelvin waves of azimuthal wavenumbers $m = 0$ and $|m| = 2$.

3 Optimal perturbations in unstratified fluid

We investigate the transient growth of perturbations on the vortex pair for the wavenumber corresponding to the maximum of the elliptic instability $k_y a = 2.26$ for $Re_\Gamma = 2000$ and for both symmetries. We use the technique introduced by [Corbett & Bottaro (2000)] to determine the optimal initial condition and the optimal response at finite time consisting of alternatively integrating forward in time the direct linearized Navier-Stokes (NS) operator and backward in time the adjoint NS operator. The Figure 3 displays the enstrophy of the optimal perturbation and the optimal response at short time $t = 0.1$ (Figure 3(a)) and intermediate time $t = 6$ (Figure 3(b)) for the antisymmetric and the symmetric cases. At short time $t = 0.1$, the optimal perturbation is very
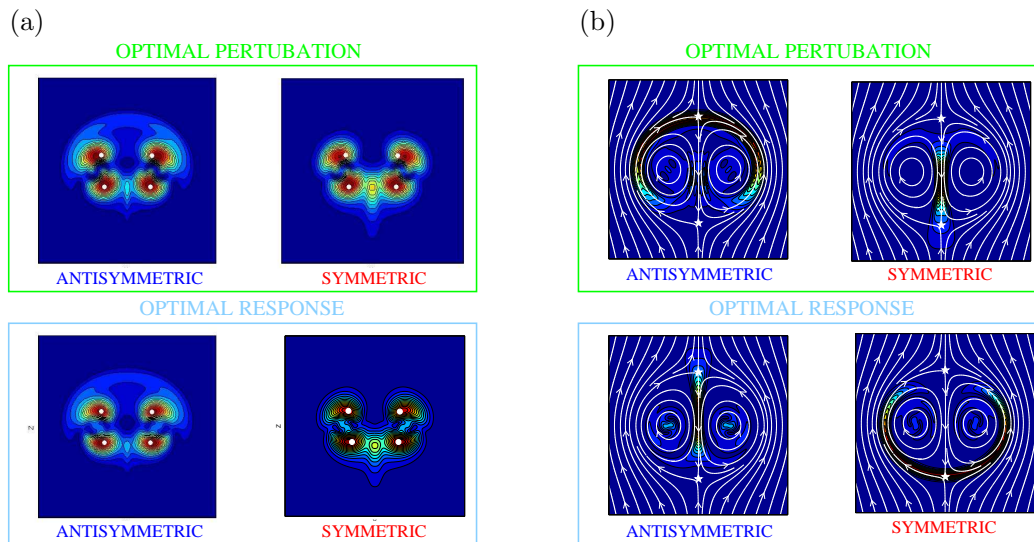
Figure 3: *Enstrophy of the optimal perturbation and optimal response in the (x, z) plane for the antisymmetric and the symmetric case at $k_y a = 2.26$ and at times (a) $t = 0.1$ and (b) $t = 6$. White dots of figure (a) correspond to the points of maximum strain of the base flow. White arrowed lines of figure (b) correspond to the streamlines of the base flow and white stars represent the stagnation points of the base flow.*

similar the one the optimal response and, for both symmetries, the enstrophy is localized in the regions where the strain is maximum (dark red areas of Figure 1(b)). At intermediate time $t = 6$, the spatial distributions of the optimal perturbation and the optimal response are different and concentrated respectively on the contracting and stretching manifold of one of the stagnation points of the base flow. The symmetric mode involves mainly the leading stagnation point (bottom star of Figures 3(b)) and the symmetric mode the trailing stagnation point (top star of Figures 3(b)).

4 Optimal perturbations in stratified fluid

In the case of strong stratification, i.e. for small Froude numbers, the unsteadiness of the flow makes the standard stability theory ineffective. In order to study the dynamics of this unsteady flow, the optimal perturbations are determined at each time. The direct-adjoint technique developped for the unstratified case is still valid in the case of unsteady base flow and it has been adapted by

taking into account this evolution and adding the density in the equations.

The instability mechanism is the elliptic instability, even for small Froude numbers for which the characteristic timescale is comparable to that of the instability. The elliptic theory predicts well the wavelength of the instability and, at the same instant, the growthrates of the instability are higher for stronger stratification since the elliptic deformation of the core of the vortices is enhanced due to the decrease of the separation distance between the vortices, as observed by [Nomura et al. (2006)].

References

[Billant et al. (1999)] Billant, P., Brancher, P., Chomaz, J.M. 1999 Three-dimensional stability of a vortex pair *Phys. Fluids* **11** 2069-2077

[Corbett & Bottaro (2000)] Corbett, P., Bottaro, A. 2000 Optimal perturbations for boundary layers subject to stream-wise pressure gradient *Phys. Fluids* **12** 120-130

[Crow (1970)] Crow, S.C. 1970 Stability theory for a pair of trailing vortices *AIAA J.* **8**(12) 2172-2179

[Le Dizès & Laporte (2002)] Le Dizès, S., Laporte, F. 2002 Theoretical predictions for the elliptical instability in a two-vortex flow *J. Fluid Mech.* **471** 120-130

[Moore & Saffman (1975)] Moore, D.W., Saffman, P.G. 1975 The instability of a straight filament in a strain field *Proc. R. Soc. Lond. A.* **346** 413-425

[Nomura et al. (2006)] Nomura, K.K, Tsutsui, H., Mahoney, D., Rottman, J.W. 2006 Short-wavelength instability and decay of a vortex pair in a stratified fluid *Phys. Fluids* **11** 2069-2077

[Sipp et al. (1999)] Sipp, D., Jacquin, L., Cossu, C. 1999 Self-adaptation and viscous selection in concentrated 2D vortex dipole, *Phys. Fluids* **12**, 245 - 248.

[Sipp & Jacquin (2003)] Sipp, D., Jacquin, L. 2000 Widnall instabilities in vortex pairs *Phys. Fluids* **15** 1861-1874

[Tsai & Widnall (1976)] Tsai, C.-Y., Widnall, S.E. 1976 The stability of short waves on a straight vortex filament in a weak externally imposed strain field *J. Fluid Mech.* **73** 721-733

The Complex Ginzburg-Landau Equation and Norberg's Lift Crisis.

Burr, K. P. & Aranha, J. A. P.

NDF, Department of Mechanical Engineering, University of São Paulo, Brazil

Corresponding Author: kpburr@gmail.com

1   Introduction

Important features of the flow behavior in the wake of two-dimensional bluff bodies, especially circular cylinders, placed in a uniform stream can be accurately described by a phenomenological Ginzburg-Landau model using the one-dimensional complex amplitude equation, which has the form

$$\frac{\partial A}{\partial t} - A(z,t) - (1 + ic_1)\frac{\partial^2 A}{\partial z^2} + (1 - ic_3)|A(z,t)|^2 A(z,t) = 0, \tag{1}$$

in terms of the non-dimensional variables t, z and A and in terms of the parameters c_1 and c_3. Previous work in these line follows:

Albarède & Monkewtiz (1992) demonstrated that many features of flow visualization involving oblique vortex shedding from two-dimensional bluff bodies, cylinders in particular, are qualitatively well described by the complex Ginzburg-Landau (CGL) equation, in which its parameters were determined experimentally.

Leweke et all (1993) investigated experimentally the vortex street in the wake behind a ring of circular cross section and large aspect ratio. Different modes of annular and helical vortex shedding were identified by phase and frequency measurements. They verified that the stability domain of these modes overlap in a large Reynolds number interval, where the mode selection depends on the initial conditions only. They also observed an instability of the vortex shedding process involving characteristic mode transitions, and they used the CGL equation to explain this instability by a mechanism resembling formally the Eckhaus instability of spatially periodic patterns.

Leweke & Provansal (1994) investigated the transition from a periodic vortex street to a less ordered state of vortex shedding in the wake of a ring. They showed experimental results characterizing this transition. From the experimental results they determined the coefficients of the CGL equation and compared its prediction with experimental findings. The good agreement allowed them to interpret the instability of the periodic vortex shedding in terms of the Benjamin-Feir instability of the CGL equation.

Monkewitz et all (1996) studied experimentally and modeled the response of the vortex shedding pattern to time-dependent boundary conditions imposed to a cylinder ends. The cylinder was placed at right angles to a uniform flow for Reynolds numbers in the range between 80 and 140. By appropriate impulsive change of the end conditions, spanwise wave number "shocks" were produced. These shocks experiments, together with data from steady oblique shedding patterns, were used to determine the coefficients of the CGL equation. They verified that the CGL equation described well the "expansion waves" of the spanwise wavenumber demonstrated experimentally.

In all previous works mentioned above, the CGL equation had its parameters determined from experiments and it was used only as an interpolator and hardly to extrapolate results to situations much beyond the empirical data on which the CGL equation parameters were based. Furthermore, the direct link of the Ginzburg-Landau models used in these previous works with the Navier-Stokes equation is lacking.

In Aranha (2004), the CGL equation was derived from a consistent asymptotic approximation of the 3D (discrete) Navier-Stokes equation. The coefficients of this equation (the Landau coefficient of the non-linear term and the Ginzburg's coefficient of the diffusive term) were not inferred from experiments, but it is shown that they can be directly computed by well established numerical procedures based on the Finite Element Method applied to the 2D cross-flow problem. The CGL equation resulted as the evolution equation of the amplitude of the mode which becomes unstable at the onset of the Bernard-von Karman instability.

We would like to show that the CGL equation has the potential to explain flow phenomena, in particular the "lift crisis" reported in Norberg (2001) and in Norberg (2003), related to the wake of elongated bluff bodies placed in a uniform stream. We do not try to fit the CGL equation parameters to any experimental data. We just study the behavior of the CGL equation in the form given by equation (1) with respect to its parameters c_1 and c_3 and use results from Aranha (2004) to explain the considered flow phenomenon.

In the context of the asymptotic theory presented in Aranha (2004), the pressure around a circular cylinder is given by the pressure field related to the 2D stationary cross-flow plus a perturbation pressure field proportional to $A(z,t)$ and higher order terms. Since the 2D stationary cross-flow is symmetric with respect to a plane passing through the cylinder center and aligned with the free stream, its contribution to the pressure integral around the cylinder section is only in the free stream direction. Only the pressure field term proportional to $A(z,t)$ gives a non-zero resultant for the pressure integral around the cylinder cross section orthogonal to the free stream direction. Therefore, the sectional lift coefficient and all quantities related to it are proportional to $A(z,t)$ and their behavior is dictated by the behavior of $A(z,t)$.

2 Numerical experiment

For appropriate values of the coefficients c_1 and $c-3$, the CGL equation presents behavior which could represent the phenomenon denoted as "lift crisis" in Norberg (2003). To illustrate this behavior of the CGL equation we did numerical experiments. We considered a line in the first quadrant of the space parameter (c_1, c_3). This line pass through the points $(c_1, c_3) = (2, 1.25)$, $(c_1, c_3) = (10, 6.25)$ and $(c_1, c_3) = (100, 62.5)$.

According to figure 3 of Shraiman et. all (1992), the line defined above lies in the region of the parameter space (c_1, c_3) where the CGL equation presents the spatiotemporal chaotic behavior denoted as defect chaos. Defects occur at points of the (t, z) plane when $A(z,t)$ goes through zero locally, and at these points the phase is not defined, resulting in a phase dislocation event.

As we travel along the line defined above towards larger values of c_1 and c_3, we observe through our numerical experiment that the r.m.s. of $|A(z,t)|$ for fixed values of z decreases. This r.m.s. decrease is not related to a decrease in the correlation length for $A(z,t)$ along the z domain, but it is due to a decrease in the amplitude of the power spectrum density peaks of the variable $A(z,t)$ with respect to the wavenumber for large values of the non-dimensional time and due to a broadening of the power spectrum density of $A(z,t)$ with respect to the wavenumber.

In our numerical experiments, the square root of the integral of the power spectrum density (psd) with respect to the wavenumber ($I = \sqrt{\int_0^\infty S(k)dk}$, where $S(k)$ is the psd value at wavenumber k) is very close to the r.m.s. value of the $A(z,t)$ for a fixed value of z, as expected and illustrated in figure 1.

We performed numerical simulations of the CGL equation with periodic boundary conditions for the three values of the coefficients c_1 and c_3 given above. The non-dimensional time interval $[0, 2 \times 10^4]$ used in the numerical simulations is much longer than the non-dimensional time necessary for the transient regime to vanish. We consider the interval $[0, 1000]$ as the domain for the non-dimensional z variable. We use a Fourier base pseudo-spectral method for the space discretization. The one-dimensional spatial grid has 1024 points. To advance in time we used the the stiffly scheme (see Karniadakis et all (1991) and Averbuch et all (1995)) of fifth order. For the linear (non-linear) part of the CGL equation the time-integration rule is implicit (explicit). The time step depends on the value of the parameter c_1. For $c_1 = 2, 10$ and 100, we used, respectively, $\Delta t = 0.01, 0.0025$ and 0.00025.

We obtained from our numerical simulations the r.m.s. of $|A(z,t)|$ for a fixed value of z for large values of the non-dimensional time for the three different values of the parameters c_1 and c_3 along the line mentioned above. Figure 1 presents the r.m.s. of $|A(z = L/2, t)|$ (with $L = 1000$) for these three different values of the parameters c_1 and c_3 for the non-dimensional time in the interval $[1.95 \times 10^4, 2 \times 10^4]$. This figure shows a considerable decrease in the r.m.s of $|A(z = L/2, t)|$ from the case $(c_1, c_3) = (2, 1.25)$ to the case $(c_1, c_3) = (10, 6.25)$, but not from the case $(c_1, c_3) = (10, 6.25)$ to the case $(c_1, c_3) = (100, 62.5)$.

From results of our numerical simulation, we estimated the psd with respect to the wavenumber for the three points in the parameter space (c_1, c_3) mentioned above for large values of the non-dimensional time, where the transients in the numerical solution had already vanished. To estimate the psd we considered $A(z,t)$ in the non-dimensional time interval $[1.95 \times 10^4, 2 \times 10^4]$. We consider $A(z,t)$ at 20 different values of the non-dimensional
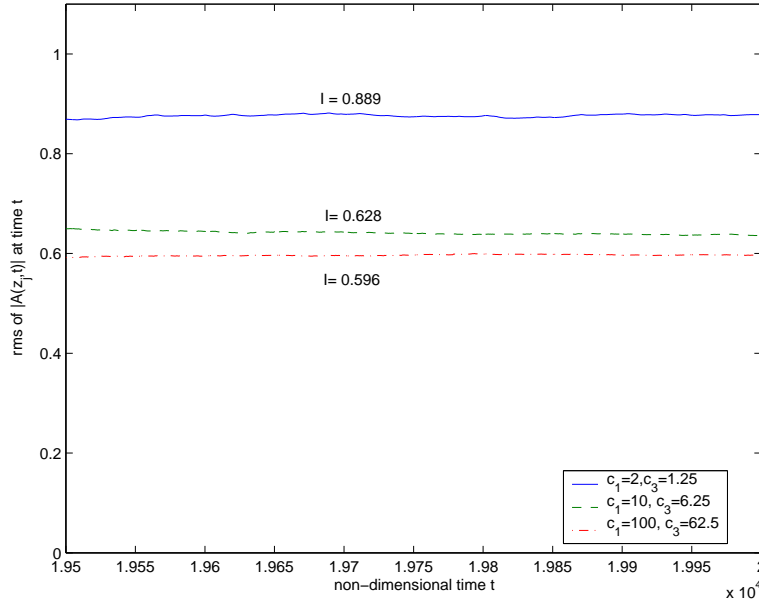
Figure 1: R.m.s. of $|A(z = L/2, t)|$ for $1.95 \times 10^4 < t < 2 \times 10^4$. Solid line: $(c_1, c_3) = (2, 1.25)$, Dashed line: $(c_1, c_3) = (10, 6.25)$ and dash-dotted line: $(c_1, c_3) = (100, 62.5)$. Values of the psd integral $I = \sqrt{\int_0^\infty S(k)dk}$ for each set (c_1, c_3) given close to the respective r.m.s. curve.

time in the interval mentioned above. The difference between two consecutive non-dimensional times is around 50, large enough such that the correlation between $A(z, t_j)$ and $A(z, t_{j+1})$ is less than 0.01, so they can be considered linearly independent of each other. We evaluated the psd of each $A(z, t_j)$, for $j = 1, \ldots, 20$ and took their average value as the estimate of the psd. To smooth this estimate, we consider a smaller number of subdivisions of the wavenumber interval $[0, \pi]$, and integrate the psd in each new subinterval. The result of the integral of the psd in each subinterval divided by the wavenumber subinterval length represents the psd value for the mean wavenumber of each subinterval. The resulting estimate of the psd for the three points along the line mentioned above in the parameter space (c_1, c_3) is given in figure 2.

In figure 2, the psd is shown only for wavenumbers in the interval $[0, 1.2]$, since the psd for wavenumbers larger than 1 is very small. As we progress along the line mentioned above towards larger values of the parameters c_1 and c_3, energy spreads to higher wavenumbers, but the psd decreases for all wavenumbers. This means that the dynamics of the complex Ginzburg-Landau equation becomes more and more chaotic.

3 Discussion and Conclusions.

As we illustrated above, the CGL equation has potential to explain the phenomenon denoted as "lift crisis" in Norberg (2001) and Norberg (2003) if its parameters c_1 and c_3 move inside the defect chaos regime region of the parameters space (c_1, c_3), like the line considered above, as the Reynolds numbers increases in the range $[270 - 4000]$ (see figure 2 of Norberg (2001)). As the parameters the c_1 and c_3 vary along the line considered above, the r.m.s of $A(z, t)$ for a given z (a point at the cylinder span) decreases as illustrated in figure 1, which implies that the r.m.s. of the sectional lift coefficient should decrease in a fashion illustrated by this same figure, and so we recover the behavior illustrated in figure 2 of Norberg (2001) for Reynolds number in the range $[270 - 4000]$. The CGL equation also furnish an explanation for this behavior. The decrease in the r.m.s for the sectional lift coefficient is not due to a decrease in spanwise correlation length for the perturbation velocity, but due to a decrease in the amplitude of the perturbation velocity since the flow becomes more and more chaotic as indicated in figure 2. Actually, according to figure 3 of Norberg (2001), the correlation length for the perturbation velocity increases with the Reynolds number in the interval $[1600, 5000]$.
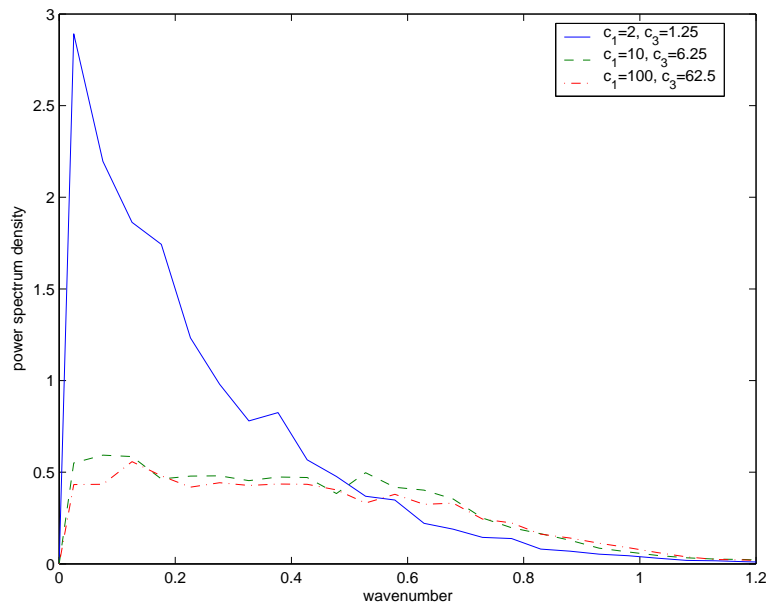
Figure 2: Psd estimate for $A(z,t)$ from results of our numerical simulation in the non-dimensional time interval $1.95 \times 10^4 < t < 2 \times 10^4$. Solid line: $(c_1, c_3) = (2, 1.25)$, Dashed line: $(c_1, c_3) = (10, 6.25)$ and dash-dotted line: $(c_1, c_3) = (100, 62.5)$.

4   References

Albarede, P.; Monkewitz, P. A. (1992) A model for the formation of oblique shedding and "chevron" patterns in cylinder wakes. Phys. Fluids A vol. 4, issue 4, pp. 744-756.

Aranha, J. A. P. (2004) Weak Three Dimensionality of a Flow Around a Slender Cylinder: the Ginzburg-Landau Equation. Journal of the Brazilian Society of Mechanics Science & Engineering, vol 26, no. 4, pp. 355-367.

Averbuch, A.; Israeli, M. & Vozovoi, L. (1995) Parallel Implementation of Non-linear Evolution Problem using Parabolic Domain Decomposition. Parallel Computing, vol. 21, no. 7, pp. 1151-1183.

Karniadakis, G. E.; Israeli, M. & Orzag, S. A. (1991) High-order Splitting Methods for the Incompressible Navier-Stokes Equations. Journal of computational Physics, vol. 97, pp. 414-443.

Leweke, T.; Provansal, M. (1994) Model for the Transition in Bluff Body Wakes. Physical Review Letters, vol. 72, number 20, pp. 3174-3176.

Leweke, T.; Provansal, M. & Boyer, L. (1993) Stability of Vortex Shedding Modes in the Wake of a Ring at Low Reynolds Numbers. Physical Review Letters, vol. 71, number 21, pp. 3469-3472.

Monkewitz, P. A.; Williamson, C. H. K. & Miller, G. D. (1996) Phase dynamics of Karman vortices in cylinder wakes. Phys. Fluids, vol. 8, pp. 91-96.

Norberg, C. (2001) Flow Around a circular Cylinder: Aspects of Fluctuating Lift. Journal of Fluids and Structures, vol. 17, pp. 459-469.

Norberg, C. (2003) Fluctuating lift on a circular cylinder: review and new measurements. Journal of Fluids and Structures, vol. 17, pp. 57-96.

Shraiman, B. I.; Pumir, A.; van Saarloos, W.; Hohenberg, P. C.; Chaté, H. & Holen, M. (1992) Spatiotemporal Chaos in the One-dimensional Complex Ginzburg-Landau Equation. Physica D, vol. 57, pp. 241-248.

Cylinder Wakes and Transitions: Bend, Stretch, Rock & Roll

Kerry Hourigan[1,2], Mark C. Thompson[1,2], Thomas Leweke[3],
Gregory J. Sheard[1], Kris Ryan[1], Justin S. Leontini[1,3], Bronwyn E. Stewart[1,3]

[1]*Fluids Laboratory for Aeronautical and Industrial Research (FLAIR), Monash University, Melbourne, Australia*
[2]*Division of Biological Engineering, Monash University, Melbourne, Australia*
[3]*Institut de Recherche sur les Phénomènes Hors Equilibre (IRPHE), Université d'Aix-Marseille, Marseille, France*

Abstract

The richness of the wake structures and transitions of bluff bodies is enhanced when geometries and relative flow motions different to the generic fixed circular cylinder are involved. In this paper, an overview of the results of bluff body studies at moderate Reynolds numbers in recent years obtained by the FLAIR and IRPHE groups is presented. These include the effect on wake structure and transition due to bluff body geometry changes and of rocking and rolling of circular cylinders. In particular, the two dimensional wake structures and the order of wake transitions to three-dimensionality are found to vary enormously.

Introduction

The generic nature of the circular cylinder for the two-dimensional view of bluff body wakes emerged through the Universal Strouhal Number (USN), whereby the two-dimensional wake structures of different short bluff body shapes could be collapsed with respect to the vortex shedding frequency [12]. The USN is based on the velocity, which is related to the base pressure, just outside the shear layer at separation rather than the free stream velocity. The USN was also related to the distance between the free shear layers as they roll up to form vortices. A large range of bluff body shapes was studied in experiments which confirmed the USN [5].

Since then, many studies have looked at the appearance in the wake of circular cylinders of three-dimensional instabilities. These include both experimental investigations (1, 3-4, 27-30) and computational predictions [e.g. 2, 6-7, 11, 24-25], which have been undertaken of the transition to first mode A (at approximately Re = 190) and then a further bifurcation to mode B (at Re = 230-240). Some differences in the transition Reynolds number occur, particularly for mode B, depending on whether the analysis is a linear analysis, or direct numerical simulations/experiments in which the base flow is modified due to the saturation of mode A. A quasi-periodic mode (QP) is predicted by linear stability analysis to occur at Re = 377; however, it is usually not observed due to significant modification of the base flow by the saturation of mode B at this stage.

The FLAIR and IRPHE groups have undertaken a significant number of studies of the effect of body shape and motion on wake transition [8-10, 13-23]. In this paper, we consider the effect on the two dimensional structures and the three dimensional wakes and transitions of stretching the cylinder (with an aerodynamic nose and a square trailing edge), of curvature through the bending of an infinite two dimensional cylinder into tori, of rocking or transversely oscillating the cylinder, and of rolling the cylinder along a wall (see Figure 1).

Results and Discussion

Two-Dimensional Wakes of Bluff Bodies

Figure 2 shows the standard Bénard-von Kármán wake for a fixed circular cylinder and sample wakes for other geometries and motions. The wake behind the elongated plate displays a structure similar to the fixed circular cylinder. The wake behind the torus and the rolling cylinder show pairing and a lateral motion of the vortex pairs. The wake behind the oscillating cylinder displays a double row wake in the P+S mode. Furthermore, different transitions occur when bluff bodies undergo oscillations of varying amplitudes A* (scaled on the cylinder diameter) at the Strouhal number 0.2 (see Figure 2).

Three-Dimensional Transitions

Predictions of the three-dimensional modes in the wakes of the different bluff bodies have been undertaken via Floquet analysis on the base two-dimensional flows and via full three-dimensional simulations.
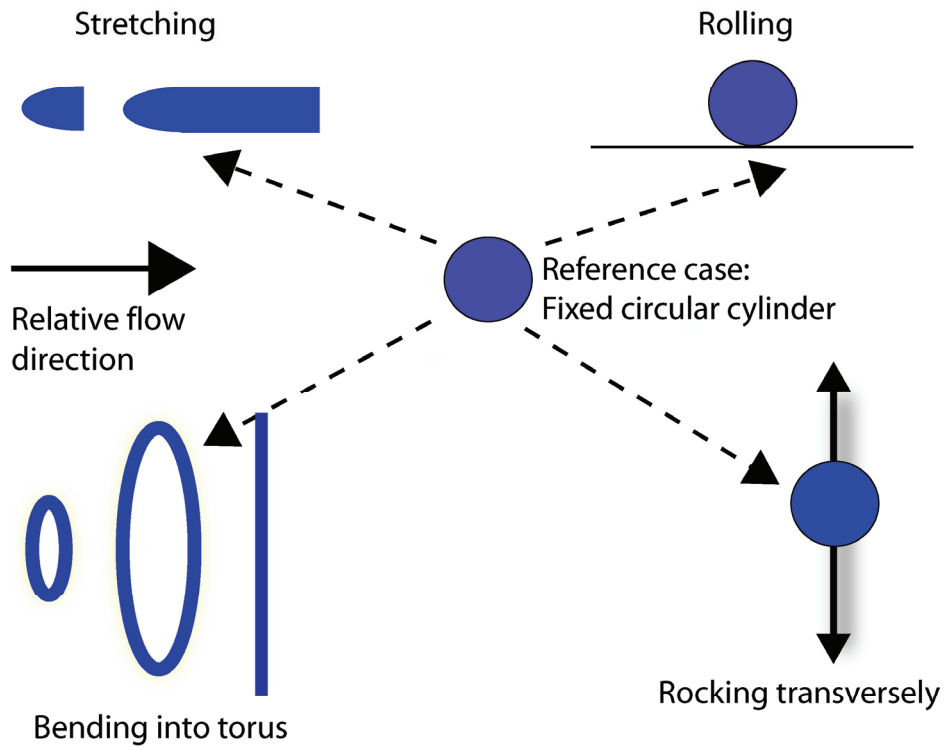
Figure 1. The different cases of geometry and motion change made to the reference case of a fixed circular cylinder in a uniform flow.

(a)

(b)

(c)

(d)

(e)
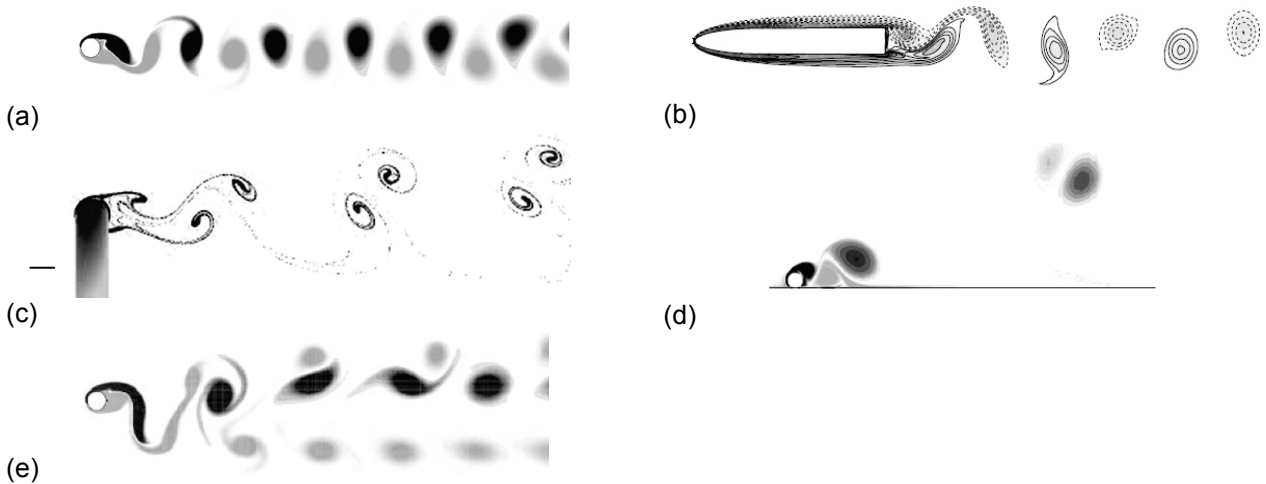
Figure 2. two dimensional wake cross-sections for (a) a fixed circular cylinder at Re = 200, (b) a elongated plate of aspect ratio AR = 7.5 and Re = 400, (c) torus of aspect ratio AR = 4.9 and Re =100, (d) a circular cylinder rolling along a wall at Re = 200, and (e) a circular cylinder oscillating transverse to the flow, St/St_{fixed} =0.95, Re = 200 and normalized amplitude A* = 0.7 (P+S mode).

In Figure 3, the different wake modes and Reynolds number at which they first appear are shown for the fixed circular cylinder, elongated plates (with aerodynamic leading and square trailing edges) for different aspect ratios (length to thickness), and tori for different aspect ratios (major to minor radii). Clearly seen is that in each case, there is a reversal of the appearance of the modes A, B and the quasiperiodic mode QP or mode C as the aspect ratio increases for the elongated plates and decreases for the tori.

Figure 3 also shows the case when the circular cylinder is oscillated transverse to the flow. There is a reversal of the modes A and B when the normalized amplitude A* has increased to 0.4. At A* = 0.7 and 0.8, two new subharmonic modes appear: a long wavelength mode SL and a short wavelength mode SS.

Figure 3. Sample of different types of modes and transitions for different types of bluff bodies and motions. Modes A, B, C are the same as for the circular cylinder, B' is similar to mode B but has much longer wavelength, mode QP is the Quasi Periodic mode, SL and SS are the long and short subharmonic S modes, respectively.
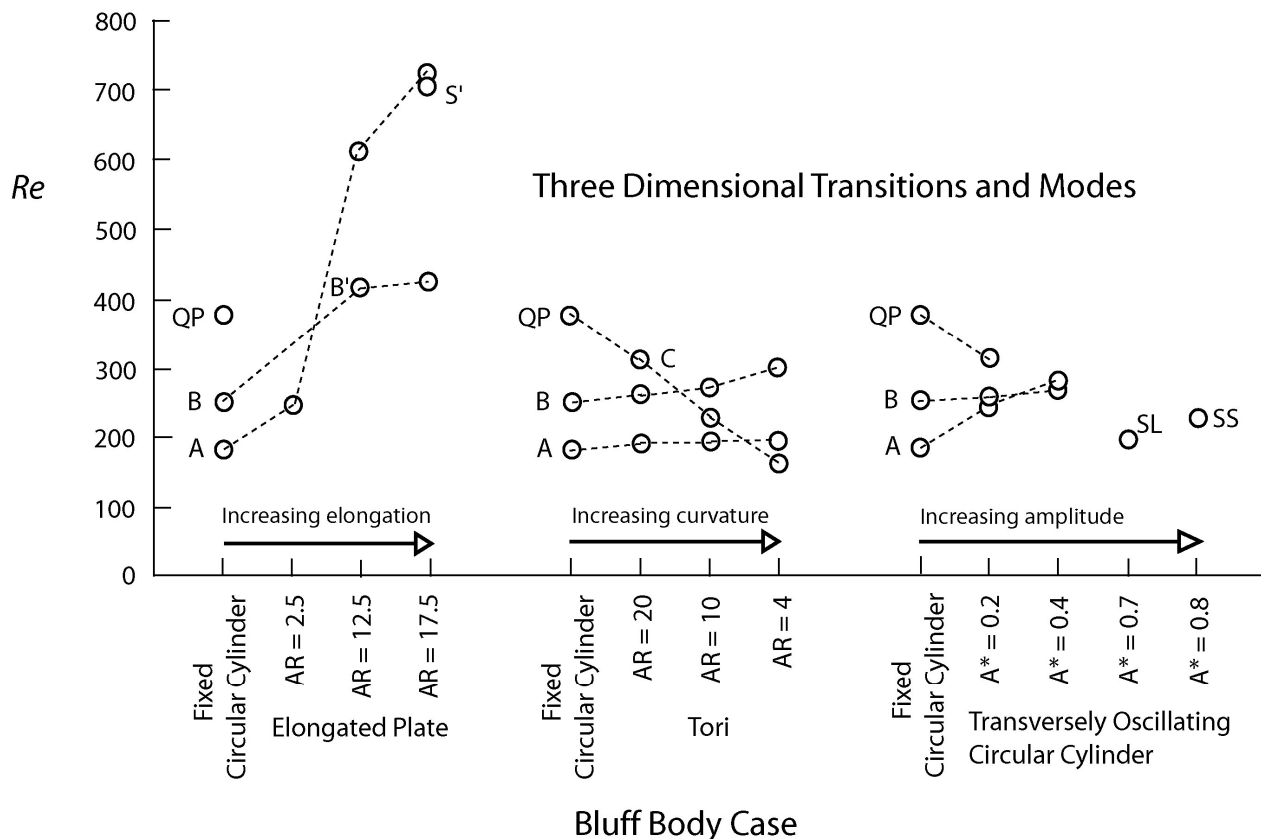
Other types of transitions and wake structures have been found as geometry and motion is varied. For example in the case of tethered cylinders, there are different branches of oscillation depending on the mass ratio of the cylinder [15]. Also, a range of sphere studies has been undertaken, such as sphere impact [26] and spinning spheres in swirling flows. In addition, stability analysis of wakes to determine the global frequency selection is being undertaken. An overview of the transitions and wake structures of these various bluff body studies will be presented at the conference.

Conclusions

The generic bluff body of a circular cylinder provides a useful reference point but is not necessarily representative of a wider variety of flows around circular cylinders that undergo topological change or different motions. A rich variety of wake structures and transitions to three-dimensions arises which may have implications for routes to turbulence.

References

1. Bays-Muchmore, B. & Ahmed, A., On streamwise vortices in turbulent wakes of a cylinder, Phys. Fluids A, 5(2), 387, 1993.
2. Barkley, D. & Henderson, R. D., Three-dimensional Floquet stability analysis of the wake of a circular cylinder, J. Fluid Mech., 322, 215–41, 1996.
3. Brede, M., Eckelmann, H. & Rockwell, D., On secondary vortices in a cylinder wake, Phys. Fluids, 8, 2117–24, 1996.
4. Gerrard, J. H., The wakes of cylindrical bluff bodies at low Reynolds numbers, Philos. Trans. R. Soc. London Ser. A, 288, 351–82, 1978.
5. Griffin, O. M., Universal similarity in the wakes of stationary and vibrating bluff structures, ASME J. of Fluids Eng., 103, No. 1, 52–8, 1981.
6. Henderson, R. D., Nonlinear dynamics and pattern formation in turbulent wake transition, J. Fluid Mech., 352, 65–112, 1997.
7. Karniadakis, G. E. & Triantafyllou, G. S., Three-dimensional dynamics and transition to turbulence in the wake of bluff objects, J. Fluid Mech., 238, 1–30, 1992.

8. Leontini, J, Thompson, M. & Hourigan, K., Three-dimensional transition in the wake of a transversely oscillating cylinder, Journal of Fluid Mechanics, 577, 2007, 79 - 104.
9. Leontini, J., Stewart, B., Thompson, M. & Hourigan, K., Wake-state and energy transitions of an oscillating cylinder at low Reynolds number, Physics of Fluids, 18, 067101, 2006.
10. Leontini, J.S., Thompson, M.C. & Hourigan, K., The beginning of branching behaviour during vortex-induced vibration at 2-D Reynolds numbers, Journal of Fluids and Structures, 22, 857-864, 2006.
11. Mittal, R. & Balachandar, S., Generation of streamwise structures in bluff body wakes, Phys. Rev. Lett., 75, 1300, 1995.
12. Roshko, A., On the wake and drag of bluff bodies, J. Aero. Sci., 22, 124–32, 1955.
13. Ryan, K, Thompson, M.C. & Hourigan, K., Three-dimensional transition in the wake of elongated bluff bodies, Journal of Fluid Mechanics, 538, 1-29, 2005.
14. Ryan, K., Pregnalato, C.J., Thompson, M.C. & Hourigan, K., Flow-induced vibrations of a tethered circular cylinder, Journal of Fluids and Structures, 19, 1085-1102, 2004.
15. Ryan, K., Thompson, M. & Hourigan, K., The effect of mass ratio and tether length on the flow around a tethered cylinder, Journal of Fluid Mechanics (accepted).
16. Ryan, K, Thompson, M.C. & Hourigan, K., Variation in the critical mass ratio of a freely oscillating cylinder as a function of Reynolds number, Physics of Fluids (Letters), 17(3), 038106-9, 2005.
17. Sheard, G.J., Hourigan, K. & Thompson, M.C., Computations of the drag coefficients for low-Reynolds-number flow past rings, Journal of Fluid Mechanics, 526, 257-275, 2005.
18. Sheard, G.J., Thompson, M.C. & Hourigan, K., From spheres to circular cylinders: the stability and flow structures of bluff ring wakes, Journal of Fluid Mechanics, 492, 147 – 180, 2003.
19. Sheard, G.J., Thompson, M.C. & Hourigan, K., A coupled Landau model describing the Strouhal-Reynolds number profile of a three-dimensional cylinder wake, Physics of Fluids, 15(9), L68-71, 2003.
20. Sheard, G.J., Thompson, M.C. & Hourigan, K. From spheres to circular cylinders: Non-axisymmetric transitions in the flow past rings, Journal of Fluid Mechanics, 506, 45-78, 2004.
21. Sheard, G.J., Thompson, M.C. & Hourigan, K., The evolution of a subharmonic mode in a vortex street, Journal of Fluid Mechanics, 534, 23-38, 2005.
22. Sheard, G.J., Thompson, M.C. & Hourigan, K., The subharmonic mechanism of the Mode C instability, Physics of Fluids, 17(11), 111702, 2005.
23. Stewart, B.E., Leweke, T., Thompson, M.C. & Hourigan, K., Flow dynamics and forces associated with a cylinder rolling along a wall, Physics of Fluids 18(11), 111701, 2006.
24. Thompson, M. C., Hourigan, K. & Sheridan, J., Three-dimensional instabilities in the cylinder wake, Proc. Int. Colloq. Jets, Wakes, Shear Layers, eds K Hourigan and I Shepherd (CSIRO), Melbourne, Australia, April 18-20, 1994.
25. Thompson, M. C., Hourigan, K. & Sheridan, J., Three-dimensional instabilities in the wake of a circular cylinder, Exp. Therm. Fluid Sc., 12, 190–96, 1996.
26. Thompson, M.C., Leweke, T. & Hourigan, K., Sphere-wall collision: vortex dynamics and stability, Journal of Fluid Mechanics, 575, 121-148, 2007.
27. Williamson, C. H. K., The existence of two stages in the transition to three dimensionality of a cylinder wake, Phys. Fluids, 31, 3165–8, 1988.
28. Williamson, C. H. K., Three-dimensional wake transition, J. Fluid Mech., 328, 345–407, 1996.
29. Williamson, C. H. K., Vortex dynamics in the cylinder wake, Ann. Rev. Fluid Mech., 28, 477–539, 1996.
30. Wu, J., Sheridan, J., Welsh, M. C. & Hourigan, K., Three-dimensional vortex structures in a cylinder wake J. Fluid Mech., 312, 201–22, 1996.

MOTION OF A MÖBIUS BAND IN FREE FALL

Thomas Leweke[*], Kerry Hourigan[**], Mark C. Thompson[**]

[*]IRPHE-CNRS, B.P. 146, F-13884 Marseille Cedex 13, France
[**]Monash University, Dept. of Mechanical Engineering, Melbourne, VIC 3800, Australia

This presentation deals with the free fall of a three-dimensional object having the topology of a Möbius strip. Experimental results are shown concerning the free-fall trajectory, body motion and wake structure.

There have been scientific studies on a range of free-fall or free-rise problems, such as the free fall of plates (Dupleich 1941; Willmarth, Hawk & Harvey 1964; Smith 1971; Field *et al.* 1997; Belmonte, Eisenberg & Moses 1998; Mahadevan, Ryu & Samuel 1999; Andersen *et al.* 2005; Pesavento & Wang 2006), seed dispersal by wind (McCutchen 1977; Augspurger 1986), air bubbles or buoyant disks rising freely in a liquid (Magnaudet & Eames 2000; Wu & Gharib 2002; Fernandes *et al.* 2005). Some of the studies have looked at the vorticity dynamics and fluid forces that lead to a range of observed motions, such as zigzagging, spiralling, gyrating, tumbling and fluttering.

The present study focuses on the free-fall of a well-known body, the Möbius band. Mathematically, this shape is famous because it has only one side and one edge. The band also possesses intriguing aerodynamic properties. When placed in a uniform flow perpendicular to the plane of the centreline, the band will locally act like a thin flat plate. Due to its particular geometry, the different elements around the band will cover all possible angles of attack, positive and negative, from perpendicular to the flow to aligned with it. One therefore encounters a range of different flow situations, from flow around streamlined bodies, over high-angle of attack flows, up to bluff body wakes, all for the single object of a Möbius band. Different parts of the strip are naturally expected to experience significantly different drag forces.

If the band is not held perpendicularly to the flow, but allowed to fall freely under its own weight, it is not obvious in advance which mean orientation it will choose, since the fact that all angles of attack are present remains true, no matter from which direction the flow comes. In addition, the twisted nature of the band is likely to lead to torque forces and a resulting spinning motion, as the band moves down.

A simple physical model of a Möbius band, which is a two-dimensional non-orientable surface, can be obtained by taking a sufficiently long rectangular strip of material, twisting one end by 180°, and then gluing the two short ends together. The resulting three-dimensional object will assume a complicated shape in space, depending on the aspect ratio of the initial rectangle and the elastic properties of the material (Mahadevan & Keller 1993). There exists, however, a simple geometrical model, consisting of a circular centreline and surface elements which are locally perpendicular to this line and continuously twist around it, completing one half turn going once around the circle. A sketch of this geometry, which is defined by the diameter D of the ring and the width d of the band, is shown in figure 1.

In the present study we investigate experimentally the free fall of such an object at low Reynolds numbers.

Fifth Conference on Bluff Body Wakes and Vortex-Induced Vibrations (BBVIV 5)
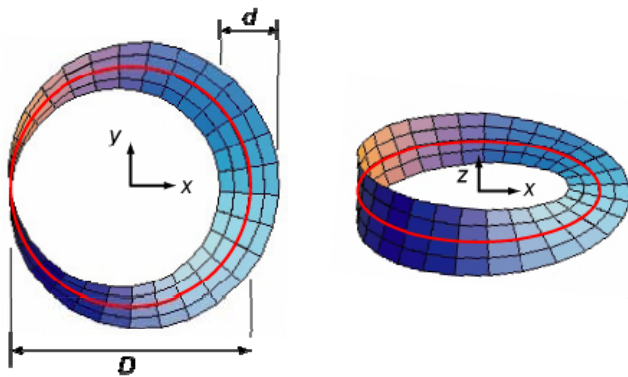Costa do Sauipe, Bahia, Brazil, 12 - 15 December 2007

97

Fig. 1. Schematic of a Möbius band with a well-defined simple shape in three-dimensional space.

Fig. 2. Polyester Möbius ring (D = 45 mm) used in the experiments.

The Möbius bands were made out of sheets of polyester and polycarbonate. Since the surface depicted in figure 1 is not developable (Schwarz 1990), an approximate shape of the projection was determined empirically. The results presented here were obtained with two bands of aspect ratio $A = \pi D/d = 14$, differing by their size (D = 18 mm and 45 mm) and weight, which leads to different average sink speeds U. The larger band is shown in figure 2. The Reynolds number $Re = Ud/\nu$ is based on the sink speed, the width of the band, and the kinematic viscosity ν. For the smaller and larger ring they were Re = 130 and Re = 560, respectively.

The free-fall experiments were carried out in a water tank with glass walls of dimensions 50 cm x 50 cm x 120 cm, in which the bands were released just below the water surface. The interior of the tank was illuminated with either white light from a neon lamp placed underneath its glass base (for recordings of the ring dynamics and trajectories), or by the light from an Argon ion laser (for visualisations using fluorescent dye painted on the bands prior to release). The motion of the falling band was recorded using a digital camera, which could be displaced vertically at about the same rate as the speed of the band. The average speed of the strip was calculated from the time it took to fall from the free surface to the bottom of the tank. The frequencies characterising the time-dependent motion of the bands during their descent were obtained from analysis of the video recordings.
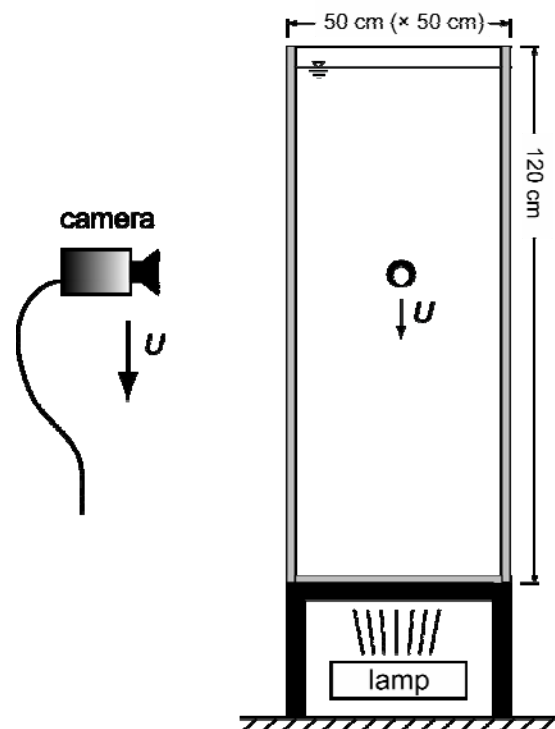

Fig. 3. Experimental setup.

The following observations were made concerning the free fall of Möbius bands at low Reynolds numbers:

- The rings orient themselves in a way that their centreline plane is almost vertical, and the blunt edge faces upstream (= downwards).

- The overall shape of the trajectory is a downward spiral with an amplitude of order D and a wavelength of around $10D$, caused by the lift force on the angled surfaces at the sides of the body. While moving along this spiral path, the band spins around the vertical axis.

- The blunt leading edge induced vortex shedding which causes a vortex-induced pitching oscillation, which is superposed to the spiralling fall, at a frequency.

- Even at low Reynolds numbers, the wake structure of the falling Möbius band is extremely complicated, consisting of a system of interconnecting vortex loops and rings.

Figures 4-7 illustrate some of these observations. More details, also concerning quantitative measurements of the dynamics of the Möbius band motion, will be presented at the conference.
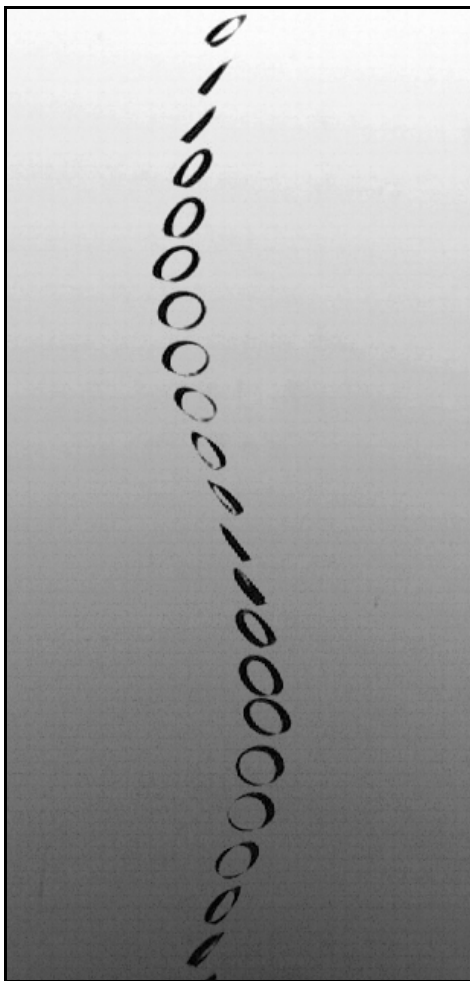

Fig. 4. Stroboscopic visualisation of Möbius band trajectory for Re = 130.

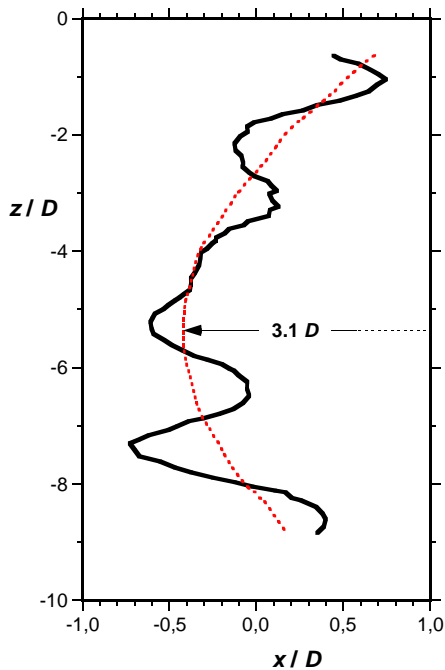Fig. 5. Dye visualisation of the wake for Re = 130.

Fifth Conference on Bluff Body Wakes and Vortex-Induced Vibrations (BBVIV 5)
Costa do Sauipe, Bahia, Brazil, 12 - 15 December 2007

99

Fig. 6. Side view of the trajectory of the centre of the band for *Re* = 560. The horizontal scale (*x*) is stretched by a factor 3 w.r.t. the vertical (*z*). The red line corresponds to the overall. spiral The shedding-induced lateral oscillations are clearly seen.
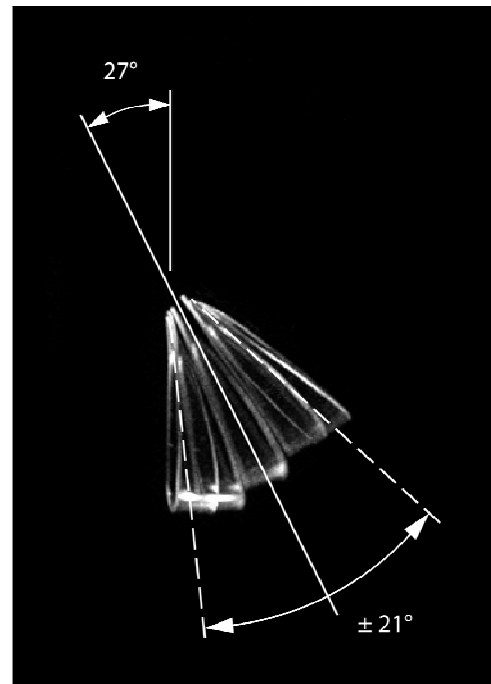

Fig. 7. Instantaneous and mean inclination of the band for *Re* = 560. Images from an "ascending" half cycle of the VIV motion were superposed after compensation for the vertical motion of the trailing edge

References

Andersen, A., Pesavento, U. & Wang, Z. Jane 2005 Unsteady aerodynamics of fluttering and tumbling plates. *J. Fluid Mech.* **541**, 65.

Augspurger, C. K. 1986 Morphology and dispersal potential of wind-dispersed diaspores of neotropical trees. *Am. J. Bot.* **73**, 353

Belmonte, A., Eisenberg, H. & Moses, E. 1998 From flutter to tumble: Inertial drag and Froude similarity in falling paper. *Phys. Rev. Lett.* **81**, 345.

Dupleich, P. 1941 Rotation in free fall of rectangular wings of elongated shape. NACA Technical Memorandum 1201.

Fernandes, P. C., Ern, P., Risso, F. & Magnaudet J. 2005 On the zigzag dynamics of freely moving axisymmetric bodies. *Phys. Fluids* **17**, 098107.

Field, S., Klaus, M., Moore, M. & Nori, F. 1997 Instabilities and chaos in falling objects. *Nature* (London) **387**, 252.

Magnaudet, J. & Eames, I. 2000 The motion of high-Reynolds-number bubbles in inhomogeneous flows. *Annu. Rev. Fluid Mech.* **32**, 659.

Mahadevan, L. & Keller, J. B. 1993 The shape of a Moebius band. *Proc. R. Soc. Lond.* A **440**, 149.

Mahadevan, L., Ryu, W. S. & Samuel, A. D. T. 1999 Tumbling cards. *Phys. Fluids* **11**, 1.

McCutchen, C. W. 1977 The spinning rotation of ash and tulip tree samaras. *Science* **197**, 691.

Pesavento, U. & Wang, Z. J. 2006 Falling Paper: Navier-Stokes solutions, model of fluid forces, and center of mass elevation. *Phys. Rev. Lett.* **93**, 144501.

Schwarz, G. E. 1990 The dark side of the Moebius strip. *Am. Math. Monthly* **97**, 276.

Smith, E. H. 1971 Autorotating wings: an experimental investigation. *J. Fluid Mech.* **50**, 513.

Willmarth, W. W., Hawk, N. E. & Harvey, R. L. 1964 Steady and unsteady motions and wakes of freely falling disks. *Phys. Fluids* **7**, 197.

Wu, M. & Gharib, M. 2002 Experimental studies on the shape and path of small air bubbles rising in clean water. *Phys. Fluids* **14**, L49.

Fifth Conference on Bluff Body Wakes and Vortex-Induced Vibrations (BBVIV 5)
Costa do Sauipe, Bahia, Brazil, 12 - 15 December 2007

100

Non-Linearities Exhibited in Control of Separated Flows

Hassan Nagib [a,*], Paul Reinhard [a], John Kiedaisch [a],

[a]*Illinois Institute of Technology (IIT), Chicago, IL 60616, USA*

Abstract

Recently, there have been a number of successful demonstrations of effectiveness of Active Flow Control (AFC) for controlling flows exhibiting large separated regions in fixed-wing and rotorcraft applications. These demonstrations utilized open-loop periodic AFC methods. Based on observations made during these studies, a series of wind tunnel tests was carried out using a hump model to generate a flow with a large separation region starting from a meandering location to compare different types of steady, oscillatory, and pulsed AFC containing blowing and/or suction components. The results of these tests provided valuable insight into physical mechanisms by which various AFC methods affect the flow, and suggest that suction (or the suction component of oscillatory AFC) has the greatest effect on the flow. The role of various non-linearities, such as asymmetries between suction and blowing and hysteresis, have been documented and examined to understand the requirements for closed-loop control implementations of AFC.

1. Introduction

ꞓamlined or bluff bodies, and in many internal flows, can hold the key for improved performance and reduced steady or unsteady loads. Active Flow Control (AFC) technology is being investigated as a means for meeting these challenges. Some examples of potential AFC applications include lift enhancement on high-lift airfoil and flap sections for extreme short take-off and landing (XSTOL) transport aircraft (1; 2), dynamic stall control and drag/download reduction on various forms of rotorcraft (3; 4), increasing L/D performance of airfoils for improved fuel economy and increased loiter times, and the reduction in size or complete elimination of control surfaces on aircraft and aircraft components, such as aerial refueling booms. Based on the successful results of recent AFC demonstrations, we now recognize that not all separated flows are amenable to the same strategies for their effective control; e.g., small versus large separated regions, and localized as contrasted to meandering initiation of the separation zone. In carefully examining the full spectrum of recent AFC activities, one realizes that for flows where separation is sufficiently deterministic and not dependent on time, open-loop control may often be the more effective approach, at least on the basis of simplicity. However, for dynamically maneuvering or unsteady applications, effective separation control may only be achievable with closed-loop adaptive systems.

Pioneering efforts by Wygnanski and his colleagues in AFC (5; 6), exploited periodic excitation and demonstrated great promise in open-loop experiments by completely altering the mean flow much more quickly than is possible with conventional ailerons or rudders. Periodic excitation should be distinguished from periodic forcing of the flow, because it relies on the natural amplification of the input disturbances by the pre-existent external flow. In order to obtain the desired response of the flow to a prescribed input, one has to know the initial and final states of the flow as well as the dependence of any transitions from state to state on the change in the input

---

* Corresponding author.
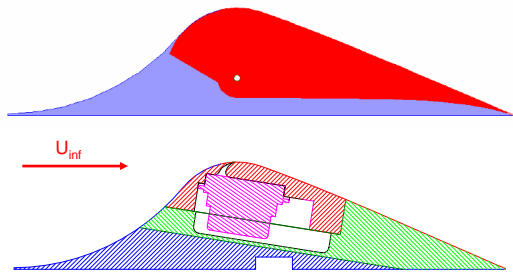*E-mail address:* nagib@iit.edu (H. Nagib).
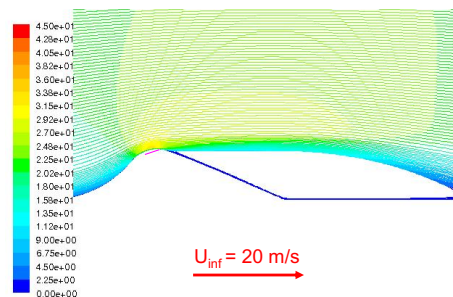
Fig. 1. The pseudoflap model.

Fig. 2. Computed streamlines displaying baseline separation.

parameters. Each end state generates known integral forces and moments on the body, but the transition between them may not be homogenous, and the rate at which the transition occurs might depend on the initial and final input parameters. Therefore, by using periodic excitation correctly, one may increase the maximum lift generated by an airfoil and reduce its drag. For example, AFC studies of flow past a generic flap (5; 6) have revealed a rich nonlinear dynamical behavior in the processes of separation and reattachment, providing a glimpse of the global phase portrait. However, the transients occurring during controlled transitions between separated and attached flow states have received limited effort so far. The recent XV-15 flight tests documented similar hysteresis behavior under the conditions of a complex application (4). In this case the power required for hover was measured while the weight of the aircraft was precisely known. After the pilot turned "ON" the AFC, less power was required for the aircraft to retain its hovering position. However, when the AFC was turned "OFF", there was a significant period of time before the power required for hover increased again to its original value measured in the absence of AFC.

2. Experimental Configuration

The experiments described in this article were conducted in the National Diagnostic Facility (NDF) wind tunnel. The AFC model used in these tests, known as the "pseudoflap" model, is shown in Fig. 1. This model is a simple hump on a flat plate with a well-documented separated flow. It is called the pseudoflap model because it was designed to exhibit separation characteristics similar to those seen over a wing with a highly deflected flap. The separation region is large and extends downstream by nearly two chord-lengths. Unlike some hump models used by other researchers, this model does not have a fixed separation location. Different cover sections were fabricated with AFC slots at different chordwise locations. For most of the work presented here, the slot location selected was at 44.7% chord (or $x/c = 0.447$), which was slightly upstream of the separation location.

3. Results

During the experimental program, we utilized the commercial code FLUENT with standard turbulence models to compute the flow over the test model, and thereby, aid us in the design and execution of the tests and the interpretation of the results. Figures 2, 3 and 4 are samples of our computational results. They demonstrate the behavior of the separated region as a function of the amount of suction or blowing from the AFC slot. Such computations predicted that lower slot velocities are more effective in controlling separation with suction, compared to blowing, which was subsequently confirmed by the experiments. These results revealed the first asymmetry in the control of large separation, especially when using Zero Mass Flux (ZMF) actuators.

Sample static pressure distributions are presented in Figs.5 and 6 using increasing slot velocities for suction only and combined suction and blowing from two slots, respectively. Here we show data with suction slots normal to the surface and blowing slots at 30° tangent to the surface pointing downstream. The behavior of the peak in these C_p distributions reveals a great deal about the non-linearities of such AFC, as shown in Fig. 7. It is clear from this figure that the path of the performance measure depends on the initial condition, and that hysteresis is essential to the system. The nominally equivalent net mass flow conditions marked with A_1 and A_2 on Fig. 7 lead to markedly different control outcomes, and are utilized to examine the effects of unsteady AFC in Fig. 8. Again different outcomes are reached and the effects of the frequency are demonstrated to be monotonic. Using our special ATEAM actuators(4; 7) we varied the wave form to achieve similar duty cycle variations under ZMF conditions from a single slot and examined the dynamics of the control as demonstrated in Fig. 9.
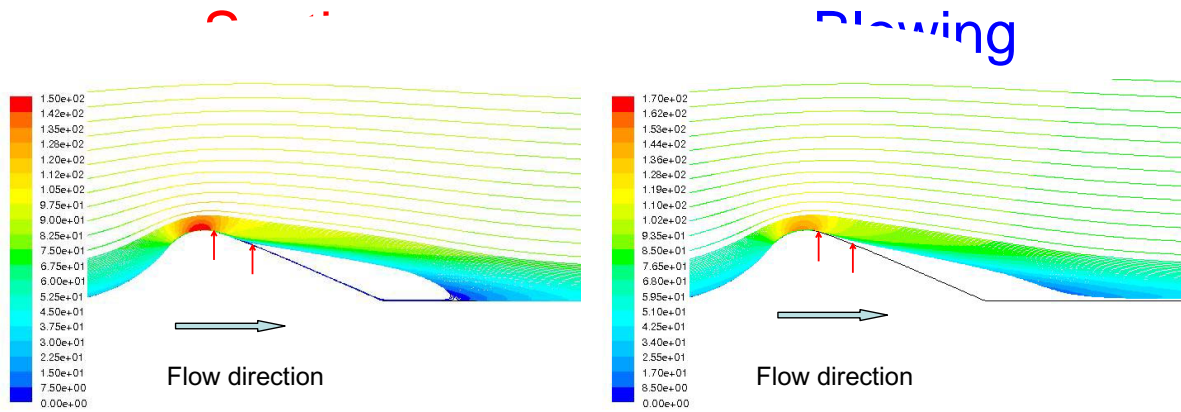
Fig. 3. Effect of 64 m/s normal suction or 144 m/s downstream blowing at $x/c = 0.47$ on separation for 20 m/s freestream.
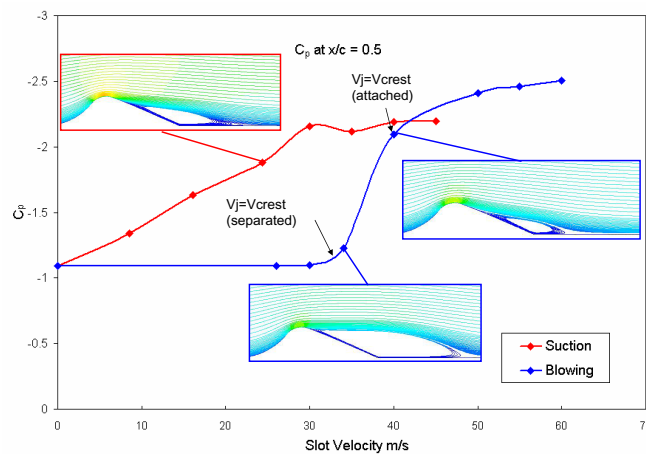

Fig. 4. Effect of level of suction or blowing at $x/c = 0.45$ on static pressure level at $x/c = 0.5$ for 20 m/s freestream.

4. Conclusion

We find that in order to control large separation using AFC employing a closed loop system, the control algorithms must account for non-linearities, such as non-symmetrical behavior and hysteresis. The non-linearities exhibited in our experiments as a function of the direction and magnitude of the forcing function render the system not amenable to linearized closed-loop control.

References

[1] Kiedaisch, J., Nagib, H., and Demanett, B.: "Active Flow Control Applied to High-Lift Airfoils Utilizing Simple Flaps". AIAA Paper No. 2006-2856, 3rd AIAA Flow Control Conference, San Francisco, CA, USA, June 2006.
[2] Nagib, H., Kiedaisch, J., Reynolds, T., Reinhard, P., and Demanett, B.: "Control Technniques for Flows with Large Separated Regions: A New Look at Scaling Parameters". AIAA Paper No. 2006-2857, 3rd AIAA Flow Control Conference, San Francisco, CA, USA, June 2006.
[3] Nagib, H., Kiedaisch, J., Greenblatt, D., Wygnanski, I., and Hassan, A.: "Effective Flow Control for Rotorcraft Applications at Flight Mach Numbers". AIAA 2001-2974, 31st AIAA Fluid Dynamics Conference, Anaheim, CA, USA, June 2001.
[4] Nagib, H., Kiedaisch, J., Wygnanski, I., Stalker, A., Wood, T., and McVeigh, M.: "First-In-Flight Full-Scale Application of Active Flow Control: The XV-15 Tiltrotor Download Alleviation". NATO RTO-MP-AVT-111-P-29, NATO AVT-111/RSM, Prague, Czech Republic, October 2004.
[5] Nishri, B. and Wygnanski, I.: "Effects of Periodic Excitation on Turbulent Flow Separation from a Flap". *AIAA J.* **36**, 1998, pp. 547-556.
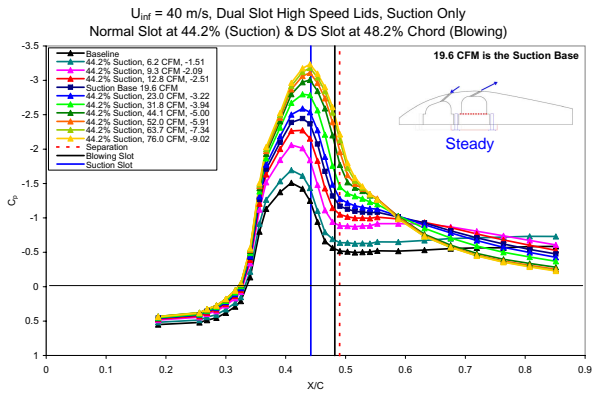
Fig. 5. Effect of suction level on pressure distribution.
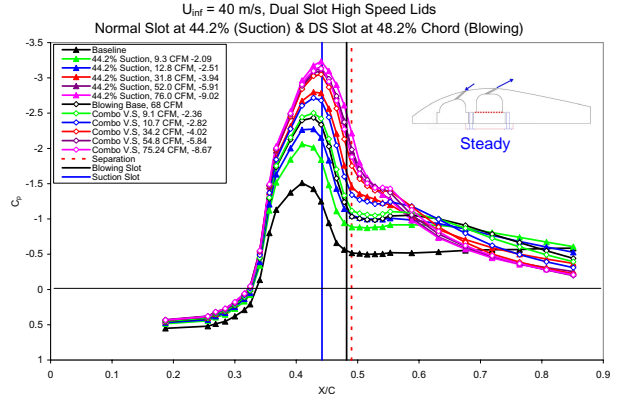
Fig. 6. Effect of combined suction and blowing levels on C_p.
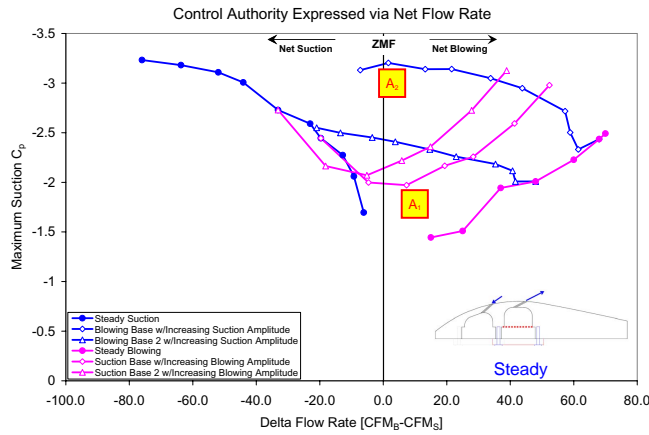
Fig. 7. Dependence of maximum C_p on combined levels of suction and blowing and path to final state.
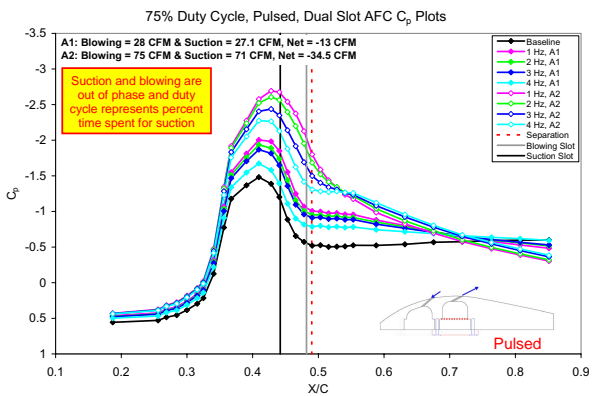
Fig. 8. Effects of pulsed suction and blowing on C_p.
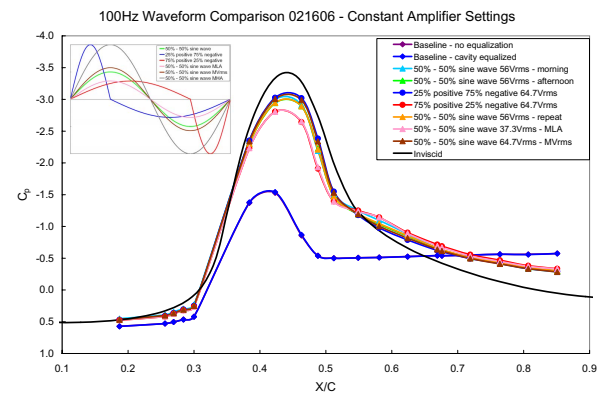
Fig. 9. Effects of ZMF pulsation waveform on C_p.

[6] Darabi, A. and Wygnanski, I.: "Active Management of Naturally Separated Flow over a Solid Surface". *J. Fluid Mech.* **510**, 2004, pp. 105-144.

[7] Nagib, H., Kiedaisch, J., Reynolds, T., Reinhard, P., and Demanett, B., "Active Control of Large Separation Using Zero Mass Flux and Steady, Oscillatory, and Pulsed Suction," Notes on Numerical Fluid Mechanics and Multidisciplinary Design: Conference on Active Flow Control 2006, Springer-Verlag, New York, 2006.

Flow over a bluff body with a flexible splitter plate

S.Shukla, R.N. Govardhan & J.H.Arakeri.
Department of Mechanical Engineering
Indian Institute of Science, Bangalore - 560012, INDIA
raghu@mecheng.iisc.ernet.in

SUMMARY

Previous work on rigid splitter plates in the wake of a bluff body has shown that the primary vortex shedding can be suppressed for sufficiently long splitter plates. In the present work, we study the problem of a *flexible* splitter plate in the wake of a circular cylinder. In this case, the splitter plate can deform due to the fluid forces acting on it, and hence the communication between the two sides of the wake is not totally disrupted like in the rigid splitter plate. Results from experimental studies are presented for the measured dynamics of a flexibly-mounted (hinged) splitter plate, for the case when there is almost no structural restoring force or damping. These measurements indicate that large amplitude oscillations of the splitter plate with peak-to-peak amplitudes of the order of 1 diameter are possible. Both the normalized amplitude and frequency of oscillations appear to reach a nearly constant value at higher Reynolds numbers, Re > 5000. The constant value of amplitude reached is nearly the same for splitter plate length to diameter ratio (L/D) of 1 and 3, while the constant frequency level reached is significantly lower for the longer splitter plate.

The problem of a rigid splitter plate in the wake of a bluff body has been studied by Roshko (1954), Apelt, West & Szewczyk (1973) and others. Their studies show that the vortex formation in the wake can be suppressed or inhibited by the presence of a sufficiently long splitter plate. In the present work, we investigate the problem of a *flexible* splitter plate in the wake of a circular cylinder. In this configuration, the splitter plate is allowed to deform due to the fluid forces acting on it, and hence the communication between the two sides of the wake is not completely inhibited as in the case of a rigid splitter plate. Apart from being an interesting extension to the rigid splitter plate problem and the more recent study of a permeable splitter plate (Cardell, 1993), this problem could also have practical applications in energy extraction (Allen & Smiths, 2001) and in suppression of vortex-induced vibrations (VIV). This problem is also related to the flag flutter problem that has been studied extensively [e.g. Argentina & Mahadevan, 2005; Connell & Yue, 2007], for the case when the flag pole diameter is not negligible compared to the flag/membrane thickness.

In the present study, we use two kinds of flexible splitter plates. In the first case, the splitter plate is rigid but is flexibly mounted (hinged) to the cylinder, as shown in figure 1(a). In the second case, the entire splitter plate is flexible, as shown in figure 1(b). In both cases, we restrict ourselves to two dimensional motions of the splitter plate. In this paper, we shall present results only for the first case where a rigid splitter plate is flexibly-mounted (hinged) to the cylinder. In our experiments, this is done by using a 30 micron thick plastic sheet with very low flexural rigidity as the hinge. This thin plastic sheet is embedded into the rigid splitter plate on one side and into the cylinder on the other side.

(a) Flexibly mounted (hinged) rigid splitter plate   (b) Fully flexible splitter plate
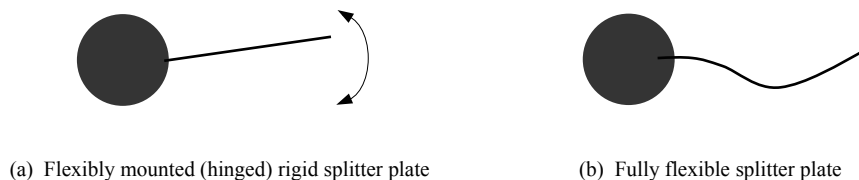
Figure 1. Schematic of two types of flexible splitter plates. In case (a), a rigid plate is flexibly-mounted (hinged), while in case (b), the entire splitter plate is flexible. Results presented in this paper correspond to case (a).

The main non-dimensional parameters in the present problem are the splitter plate length-to-diameter ratio (L/D), the Reynolds number (Re) and the mass ratio, $\rho^* = (\rho_s/\rho_f)(t/D)$, where ρ_s is the density of the splitter plate, ρ_f is density of fluid, t is the thickness of splitter plate and D is the cylinder diameter. The definition of the mass ratio here is taken along the lines of the definitions used in the flag flutter problem, as used for example in Connell and Yue (2007). In addition, there can be non-dimensional parameters that are related to the bending stiffness and internal structural damping. In the particular case of the experiments here with a very thin flexible hinge, as explained above,

the stiffness and structural damping are very small and are unlikely to influence the dynamics. Hence, for the flexibly-mounted rigid splitter plate, we have effectively three non-dimensional parameters.

The experiments reported here were conducted in a 1m x 1m cross-section water tunnel in the Mechanical Engineering department, which has a maximum speed of 1 m/s. The cylinder diameter used was 1.78 cm and the flow velocity was varied from about 0.01 m/s to 0.60 m/s, resulting in a Reynolds number range, Re ≈ 200 − 10,000. The aspect ratio of the cylinder used was 13. In all the experiments reported here, end-plates of streamwise length 6 diameters were used to encourage two-dimensional vortex shedding. The flexible splitter plate motions were visualized at rates up to 40 Hz using a CCD camera in conjunction with a halogen lamp or a PIV Nd-Yag laser. Time traces of the displacement of the trailing edge of the splitter plate were obtained from image processing of the acquired images.

(a) L/D = 1.0   **(b) L/D = 3.0**
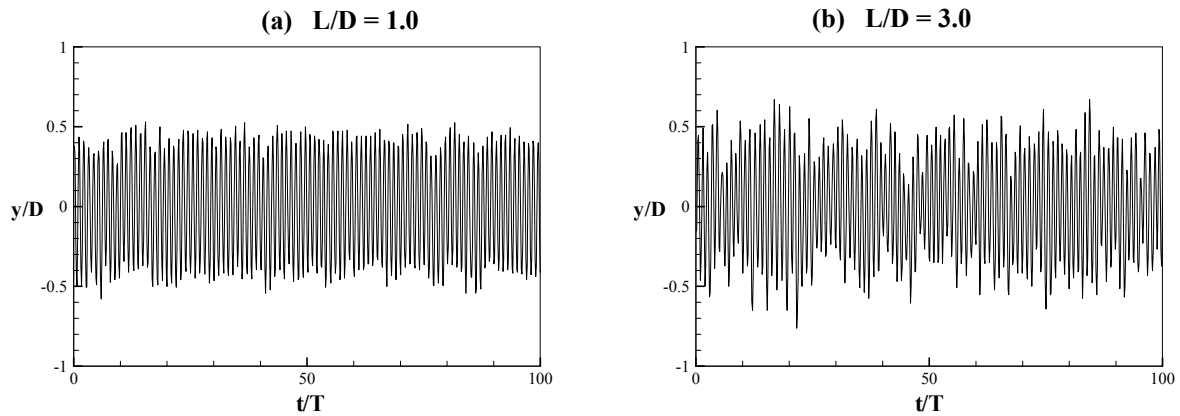
Figure 2. Sample displacement time traces for the trailing edge of the splitter plate for two splitter plate length (L) to diameter ratios. In case (a), (L/D) = 1.0 and in case (b), (L/D) = 3.0. Both cases correspond to a flexibly-mounted (hinged) rigid splitter plate with mass ratio of 0.032 at Re=6400.

Example displacement time traces of the trailing edge of the splitter plate obtained from experiments are shown in figure 2, for two different L/D values. For L/D=1.0 case, the oscillations are very periodic with nearly constant amplitude, as may be seen from figure 1(a). In the case of a longer splitter plate with L/D=3.0, the oscillations remained at nearly the same amplitude, although more variations were observed from cycle to cycle as may be observed in figure 1(b). Time traces of the type shown above were obtained for a range of Reynolds numbers up to Re ~ 10,000 for both the L/D =1.0 and 3.0 cases. From each of these time traces, the normalized amplitude of oscillation, defined as (A/D) =√2 (y_{rms}/D), and the normalized frequency of oscillation (fD/U) were obtained. The normalized frequency was found from the spectrum of the time trace, which showed a distinct peak in all cases reported here.
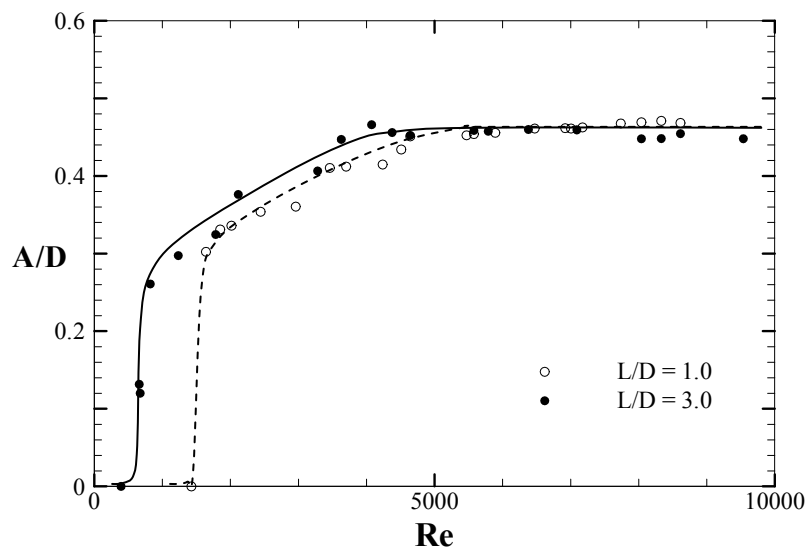
Figure 3. Variation of the amplitude of splitter plate trailing edge motions versus the Reynolds number for two splitter plate lengths, (L/D) = 1.0 and 3.0. In both cases, the amplitude increases and appears to saturate at higher Re to nearly the same amplitude. The mass ratio is 0.032 for both the cases.

Figure 4. Variation of the normalized frequency (fD/U) of splitter plate trailing edge motions versus the Reynolds number for two splitter plate lengths, (L/D) = 1.0 and 3.0. In both cases, the frequency decreases and appears to reach a nearly constant level at higher Re. For the L/D=1.0 case, the constant level reached is reasonably close to the Strouhal number for a bare cylinder in the present Re range, while for the L/D=3.0 case, the constant level reached is significantly smaller.

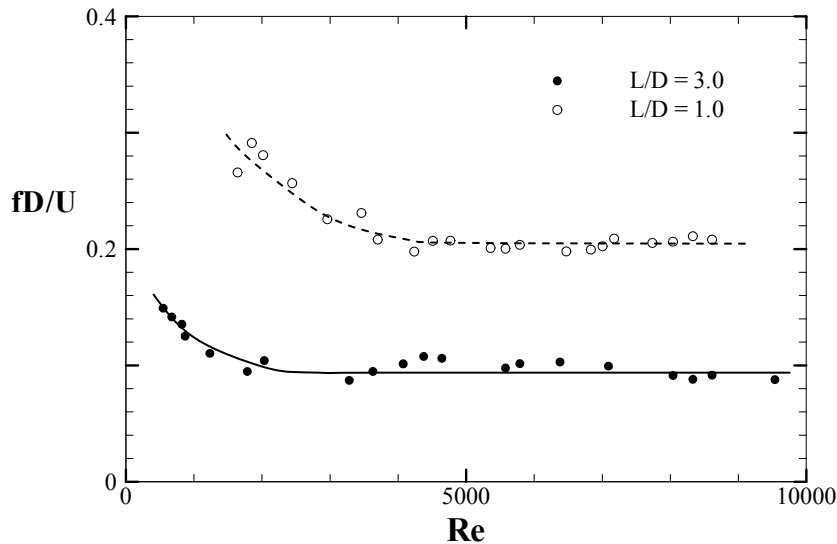The amplitude response plot for L/D =3.0 splitter plate indicates that the response starts at Re ~ 500, increases rapidly at first and then more gradually, reaching a nearly constant amplitude level for Re > 5000, as may be seen from figure 3. The shorter splitter plate with L/D = 1.0, shows essentially the same form of response reaching almost the same constant level of amplitude at higher Re. However, there is a reasonable difference on the lower Re side between the two cases, in particular, the Re at which the oscillations begin is substantially different. The frequency response plots in figure 4 again show that a nearly constant level of normalized frequency (fD/U) is reached at higher Re. For the L/D=1.0 case, the constant level reached is close to the Strouhal number for a bare cylinder (S=0.2), while for the larger splitter plate case, the constant level reached is smaller, (fD/U) ~ 0.1. It should be noted that all the results presented here are for the case when there is almost no mechanical restoring force in the system. The present amplitude and frequency results (at higher Re) are therefore reminiscent of the corresponding results for the zero restoring force transverse vibration study of a cylinder by Govardhan & Williamson (2002), where the normalized amplitude and frequency are nearly independent of Re over a large Re range.

Further experiments are in progress to determine the effects of splitter plate length, mass ratio and complete flexibility of the plate on the dynamics of the splitter plate. Flow visualization and PIV measurements are also planned to understand the wake vortex dynamics. Results from these measurements will be presented at the conference.

REFERENCES:

ALLEN, J.J. & SMITS, A.J. (2001) Energy harvesting eel. *J. Fluids Struct,.* **15**, 629–640.

ARGENTINA, M. & MAHADEVAN, L. (2005) Fluid-flow-induced flutter of a flag. *Proceedings of the National Academy of Sciences*, **102**, 1829–1834.

APELT, C.J., WEST, G.S. & SZEWCZYK, A.A. (1973) The effects of wake splitter plates on the flow past a circular cylinder in the range $10^4 < R < 5 \times 10^4$. *J. Fluid Mech.* **61**, 187–198.

CARDELL, G.S. (1993) Flow past a circular cylinder with a permeable wake splitter plate. PhD thesis, Caltech..

CONNELL, B.S.H. & YUE, D.K.P. (2007) Flapping dynamics of a flag in a uniform stream. *J. Fluid Mech.* **581**, 33–67.

GOVARDHAN, R. & WILLIAMSON, C. H. K. (2002) Resonance forever: existence of a critical mass and an infinite regime of resonance in vortex-induced vibration. *J. Fluid Mech.* **473**, 147–166.

ROSHKO, A. (1954) On the drag and shedding frequency of two-dimensional bluff bodies. NACA TN 3169.

Some Physical Aspects of the Wake Behind a Two-dimensional Body with a Blunt Trailing Edge and Fitted with Splitter Plates

Marcos A. Ortega
ITA - Technological Institute of Aeronautics
email: ortega@ita.br

Roberto M. Girardi
ITA - Technological Institute of Aeronautics
email: girardi@ita.br

Jorge H. Silvestrini
PUC/RS - Pontifical Catholic University
email:jorgehs@pucrs.br

Contact e-mail: ortega@ita.br

Abstract

This work focusses on some physical aspects of the wake behind a two-dimensional blunt-trailing-edged body. The method of analysis is numerical, and flow data are obtained by means of a DNS code. The present authors are dedicated to a general study of this special geometry. In this paper some attention is given to the damping action of the splitter plates and to some interesting aspects of the wake flow, especially to a kind of surge of fluctuations just downstream of the body base. The plates have the "ability" to damp the Kármán vortices shedding and, consequently, the oscillations that appear in the wake "commutes" to a mixing-layer type. The raising of the fluctuation level, just downstream of the base region, for larger values of the Reynolds number, is attributed to an entrainment effect.

1   Introduction

The quest for the understanding of flow phenomena at the wake of a bluff body is an old one. For historical perspectives the reader is referred to the literature (among others, a very good retrospective is that of Williamson, 1996a). Our aim here is to study the influence of splitter plates on the régimes of the wake behind a bluff body, especially the main origin of the fluctuations. The two-dimensional body, extensively investigated by Bearman (1964, 1965, 1967) has an elliptic front nose, followed by a straight section that ends in a blunt trailing edge. The height of the base, "d", is equal to one-sixth of the body chord.

This elliptical-front-nose body, with a blunt base, is a very important geometrical form that has not received the due attention in the literature (from now on we shall call it the "body of Bearman"). Among other characteristics, one calls for the researcher's attention: the boundary layers separation points are fixed, and the shear layers, initially, are parallel to the body center line. Therefore, it is very interesting to investigate the general conditions of the flow about this geometry, especially those related to stability, and compare it with the cylinder with the hope of better understanding these difficult wake flows. It is common knowledge the importance of the boundary layer characteristics at the separation point upon the shear layer overall conditions. In terms of near wake stability there is an important difference between the body of Bearman and the cylinder. In this latter case, the three points at the onset-of-shedding Reynolds number, the separation and reattachment points at the recirculation bubble, are of the Hopf bifurcation type (Unal and Rockwell, 1988), while, in the former case, one has two Kelvin-Helmholtz instabilities (at separation) and a Hopf bifurcation (at reattachment). Much probably, it is because of this difference that the Reynolds number at the onset of shedding is larger for the body of Bearman, $Re \approx 90$ (Ortega et al., 2007), than for the cylinder, $Re \approx 45$ (Sumer and Fredsœ, 1997, reports $Re = 40$, while Williamson, 1996a, gives $Re = 49$). (One must bear in mind that the Reynolds number here, for the body of Bearman, is defined in relation to the body base height.) In other words, one could ascertain (at this point in time, without proof) that the the near-wake "system" for the cylinder at onset of shedding is more unstable than the near-wake system for the body of Bearman.

As yet, we have investigated systematically the two-dimensional body of Bearman for three values of the Reynolds number: 200, 500, and 1000. The flow is numerically simulated by a DNS code, called Incompact3D, which, by the way, has already been extensively validated and verified (Ortega et al., 2007). The ultimate objective of this research project is the calculation and analysis of the many characteristics of the flow, and the many influences upon it, primarily relative to the variation of the Reynolds number. Numerical anemometers are strategically scattered on the field of flow in order to capture the history of the flow, and a varied assortment of data are obtained. In this paper we shall present some aspects concerning the actuation of the splitter plates, and also some discussion about the phisics of the near wake.
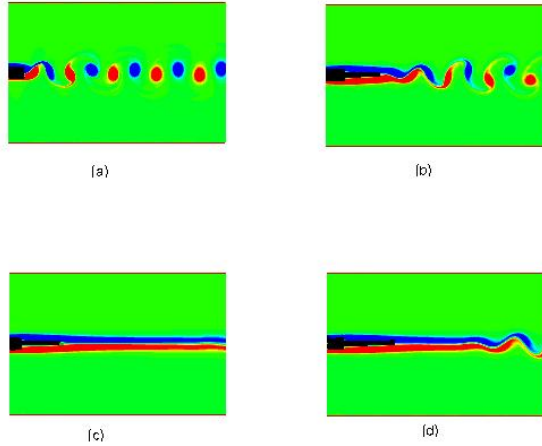
Figure 1: The wake at the rear of the bluff body for $Re = 500$, and for some lengths of the splitter plate. (a) Plain body; (b) Splitter plate length, $l/d = 3.5$; (c) Splitter plate length $l/d = 4.5$, initial stages of the establishment of the wake; (d) Splitter plate length $l/d = 4.5$, steady periodic oscillation.

2 Results and Discussion

Fig. 1 shows some very illustrative examples of the wake behaviour in terms of the splitter plate length. The Reynolds number is equal to 500. The case of the body of Bearman without the dividing plate is shown in part (a) of the figure. One can observe the classical case of the von Kármán street. In part (b) the wake is shown for $l = 3.5d$, where l is the plate length and d is the body base height. The effect upon the Kármán vortexes formation is considerable but, as yet, not sufficient to stop completely the genesis of these structures. What happens is that the base formation region stretches donwnstream, until after the end of the plate. But, in fact, the very nature of the oscillations in the wake is still determined by the alternating Kármán vortices sequence. In Fig. 1(c), on the other hand, for which $l = 4.5\,d$, the Kármán vortices are already completely inhibited. Albeit this, one can see that the wake is still oscilating, but, now, the oscillations are of the mixing-layer type. These oscillations are born somewhere downstream due to a Kelvin-Helmholtz instability and grow and move up as the time passes. In case (d) of Fig. 1, the final steady oscillatory state of the wake is shown, where the reader can also apreciate that the intensity of the oscillation has grown with the time (relative to case (c)). Another evidence to confirm the type of wake behaviour can be seen in Fig. 2. Here, the anemometer "indication" for the initial stages of the calculation is shown, and the signal grows in a "modulating" fashion, a result of the amplitude variation as the instability moves upstream.

Another very interesting feature of the body of Bearman wake is illustrated in Fig. 3, where longitudinal distributions of root-mean-square, horizontal-velocity fluctuations, are plotted for some values of the splitter plate length. These data were collected at a distance of a quarter of the base height from the base centerline. The symbol x/d in the figure indicates the longitudinal distance measured relative to the base of the body, in terms of the base height. The figure contains data relative to the plain body and the body fitted with a splitter plate, in such a way that the influence of the plate is also taken into account. For $Re = 500$, and for $l/d = 0$, one observes that there are two maxima, one for $x \approx 1d$, which practically determines the length of the formation region, and the other for $x \approx 6d$. In the case of the other plate lengths this effect is somewhat damped, but still observable. On the other hand, for $Re = 200$, the velocity fluctuation distributions after the first maximum diminish almost monotonically as function of x/d.

Hence, one can see that there is a kind of velocity fluctuation surge in a region around $x \approx 6d$. We believe that the explanation is given by figures 4 and 5. These figures correspond to instantaneous data distributions, and the dimensionless time is $t = 27.55$. In this case and for this instant of time, the periodic steady flow at the wake is already established. These plottings correspond to the vision of an observer that is following the wake with a speed equal to the free-stream flow. For $Re = 500$ (and probably for other high values of the Reynolds number) the effect of wake entrainment is such that a rather large amount of "potential" flow is drawn to the interior of the vortical region, especially in a position whose distance to the base body is equal to $6d$. From Fig. 4 it is apparent that the two first great structures are blocking completely the entrainment from the upper half of the flow. Inclusively, there is a saddle point just above the first structure (which is, by the way, in the process of formation). But, just after the second large eddy, entrainment is very effective. The "fresh" potential
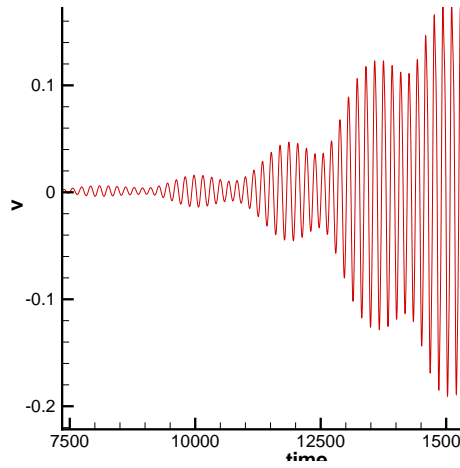
Figure 2: The initial time history of the y-component of velocity at $Re = 500$, $l/d = 4.5$.
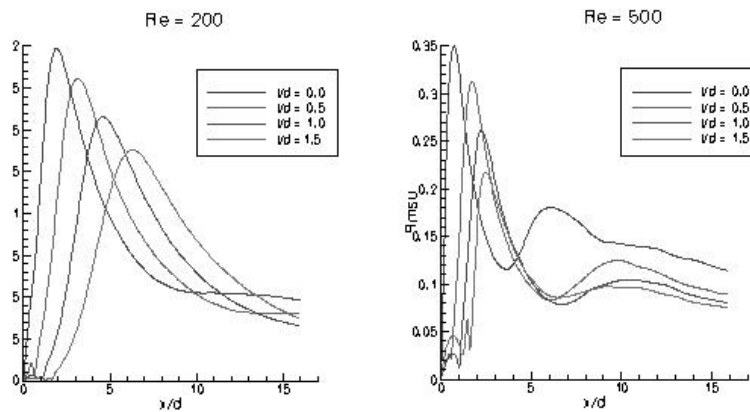
Figure 3: Longitudinal distributions of the mean horizontal velocity fluctuation for some values of the splitter plate length, and for different Reynolds numbers.

flow will, much probably, feed momentum, especially to the third and fourth structures (this is clear from Fig. 5). We have observed peaks of velocities around these vortices which are in excess relative to other peaks in the wake. Therefore, activity in the braid regions between those structures will raise, with a consequent raising of the Reynolds stresses and the velocity fluctuations.

3 Conclusion

This paper reports on an extension of a former research work by the present authors. Here, a discussion of the flow in the near wake region was done, having in mind a better insight into the flow mechanisms. The kind of overall instabilities that govern the wake régimes was stressed, and an explanation for the surge of velocity oscillations in the near wake was attempted. The reader should have in mind that the results that were presented above are preliminary. We are starting to run the $Re = 1000$ case. Only after that, and with all the data banks in hand, we will be able to present a complete analysis of the body of Bearman.

Acknowledgments
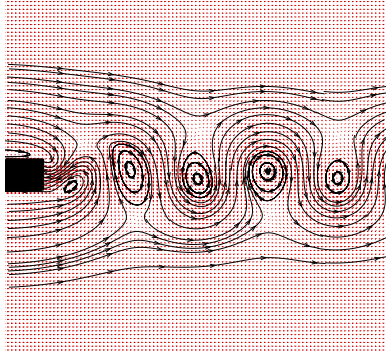
Figure 4: Instantaneous velocity field at the near wake of the body of Bearman. The dimensionless time is equal to 27.55, the splitter plate length is equal to zero, and $Re = 500$.
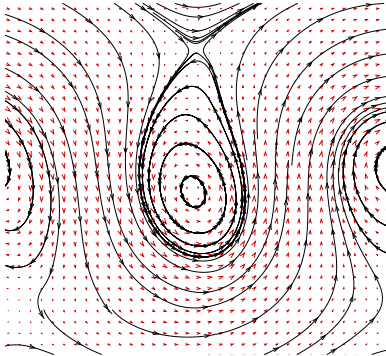
Figure 5: Detail of figure 4 showing the relative velocity field around the third structure.

4 References

Bearman, P. W., "Investigation of the Flow Behind a Two-Dimensional Model with a Blunt-Trailing Edge and Fitted with Splitter Plates," *Journal of Fluid Mechanics* Vol. 21, Part 2, 1965, pp. 241-255.

Bearman, P. W., "The Effect of Base Bleed on the Flow Behind a Two-Dimensional Model with a Blunt-Trailing Edge," *Aerospace Quarterly*, Vol. 18, 207, 1967.

Bearman, P. W., "On Vortex Street Wakes," *Journal of Fluid Mechanics* Vol. 28, part. 4, 1967, pp. 625-641.

Ortega, M. A., Girardi, R. M., and Silvestrini, J. H., "The Formation Region Behind a Blunt Body Fitted with Splitter Plates," AIAA Paper 2007-1306, Jan. 2007.

Sumer, B. M., and Fredsœ, *"Hydrodynamics Around Cylindrical Structures,"* World Scientific Publishing, London, UK, 1997.

Unal, M. F., and Rockwell, D., "On Vortex Formation from a Cylinder: Part 1. The Initial Instability," *Journal of Fluid Mechanics* Vol. 190, 1988, pp. 491-512.

Williamson, C. H. K., "Vortex Dynamics in the Cylinder Wake," *Annual Review of Fluid Mechanics* Vol. 28, 1996a, pp. 477-539.

Temporal Development of an Inviscid Asymmetric Wake

Elmer Mateus Gennaro

Escola de Engenharia de São Carlos/USP

Department of Aeronautical Engineering

E-mail: elmer@sc.usp.br

Marcello A. Faraco de Medeiros

Escola de Engenharia de São Carlos/USP

Department of Aeronautical Engineering

E-mail: marcello@sc.usp.br

RESUME

1. Introduction

Bluff body wake flows have been a subject of interest to engineers and scientists for many years as they have direct engineering application. The alternate shedding of vortices may cause among other things structural vibrations and acoustic noise. One aspect of interest is to establish a relationship between the vortex shedding from bluff bodies and stability theory Monkewitz (1988).

The study of bluff body wake flows presents difficulties. Bluff body wakes are complex, as they involve the interaction of various shear layers in the same problem, namely, a boundary layer, a separating free shear layer and a wake , Williamson (1996). Several authors investigated the stability of a two-dimensional wake behind a cylinder. The cylinder geometry has less complexity in relation to other bluff body and is representative of the phenomenon. Besides this aspect, cylindrical structures are found in several engineering aplications such as risers, transmission cabled, landing geard etc., which also justifies the study the of a cylinder.

Williamson (1996) revised works of several authors that describe the vortex dynamics in the cylinder wake. He discusses the various instabilities and flow regimes. The definition of flow regimes is based on mensurents of velocity fluctuation (Roshko, 1954). He found a laminar vortex shedding regime, a transition regime and an "irregular" regime.

The study of the instability of symmetric wake profile is well justified, since the hypothesis of parallel flow can be decribed for Orr-Sommerfeld equation, also considered the normal mode assumption Betchov and Criminale (1966), Hultgren and Aggarwal (1987) and Monkewitz (1988). There are methods of resolution to the Orr-Sommerfeld equation thereby is determined by the location in the complex angular frequency plane of a certain branch-point singularity in the complex dispersion relation. However, the asymmetric wake is found in practical applications of engineering. For example, in an aircraft wing, high-lift idevices operating in high angle of attack provide asymmetric wake that due to hydrodynamics instability can exert an influence in the aerodynamic performance besides and noise generation for example.

This work, in development, numerical investigation of an inviscid asymmetric wake.

The current work presents the tests performed to investigate the flow instability if is possible of reproduce the parallel hypotheses by canceling the viscous difusion at the base flow in the y-direction of a compressible two-dimensional wake at low Mach number and infinite Reynolds number. In the present work, we will use the code originally developed by Germanos and Medeiros (2005) to investigate flow instability of a compressible mixin layer. It uses a high order compact finite difference scheme for computing the spatial derivatives and a 4th order Runge-Kutta scheme for the time integration. Germanos and Medeiros (2005) verified the code against the Linear Stability Theory (LST). Colaciti and Medeiros (2006) implemented a 6th order compact finite difference scheme, proposed by Lele (1992) and a formulation proposed by Sesterhenn (2001) to solver the Navier-Stokes equations in the non-conservative form for compressible flow.

2. Methodology

The methodology used to investigate the effect of the shear in the vortex shedding of an asymmetric wake was the direct numerical simulation (DNS) without the cylinder, only considering the base flow gives by mean velocity flow profile (1). This methodology differs from the others. The mechanism of hydrodynamics instability depends mainly on the base flow. The body in itself exerts a second any influence by promoting new instabilities at high on Reynolds number and modifying the first instability. Numerical simulations that considered the presence of the cylinder has some inconveniences. Need a long compatational domain and the presence of the body is a huge problem. In spite of techniques improved with virtual boundary and same a bigger capacity of the computers are not enough to diminish the simulation time. A large time of simulation used in getting the base flow during this time errors can grow and trigger the flow inatability. On the other hand, considering only the velocity profile is possible of reproduce the parallel hypotheses by canceling the viscous difusion at the base flow in the y-direction it possible study the hydrodynamics instability of cheaper computational. As our objective is to understand the essence of the phenomenon this approach is interesting.

3. Numerical Aspects

The asymmetry of the wake can be produced by adding a mixing layer to a symmetric wake profile. The symmetric wake profile $U(y)$ is defined as $U_w(y) = 1 - \Lambda + 2\Lambda \left[1 + \sinh^{2N}(y \sinh^{-1}(1))\right]^{-1}$, where $\Lambda = (U_{w_c}^* - U_{w_{max}}^*)/(U_{w_c}^* + U_{w_{max}}^*)$, $U_{w_{max}}^*$ is the maximum velocity of the profile, $U_{w_c}^* = U_w^*(y = 0)$ is the centerline velocity and the $*$ superscript denotes a dimensional quantity. U_w represents a parallel mean flow in the streamwise direction, namely x, and y is the cross-stream coordinate where $y = 0$ is the origin that is the wake centerline. Distances are nondimensionaled by local half-width b^* of the wake defined as $U_w^*(b^*) = \bar{U}_w^*$, where $\bar{U}_w^* = (U_{w_c}^* + U_{w_{max}}^*)/2$ is the average mean velocity by which the velocities are made nondimensional. The parameters are the velocity ratio Λ and N is the "shape parameter".

The tan-hiperbolic profile of the shear layer is given by $U_s(y) = U_{s_{max}} \tanh \left(\frac{2y}{\delta_w}\right)$ where δ_w is the mixing layer vorticity thickness.

Thus, we can construct to an asymmetric profile as follows:

$$U(x,y) = (1 - \beta)U_w(y) + \beta U_s \tag{1}$$

where β is parameter that control the amount of asymmetry.

The problem set-up is: $\delta_w = b^* = 1$, $c_{ref} = 340.21$, $Ma = 0.1$, $0 < \beta < 1$, $Re = \frac{\rho_{max} U_{max} \delta_w}{\mu} \to \infty$, where c_{ref} is the reference speed of sound, Ma is the Mach number and Re is the Reynolds number.

They adopt a domain $0 < x < 2\pi\alpha$ and $-16 < y < 16$, where α is the wave number, with a grid of 64 x 128 points along the x and y direction, respectively. They used a mesh with stretching in the y-direction and compact filter in the x and y directions.

They therefore focus solely on the dominant sinuous mode, which justifies the choice of initial disturbance used.

For the nondimensionalization, considering the reference scale b^*, the temperature is non-dimensionalized by $T_{ref} = \frac{c_{ref}^2}{\gamma R}$, the dynamic pressure by $\rho_{ref} U_{max}^2$ and $\gamma = \frac{c_p}{c_v}$.

4. Results

The figure 1 shows the temporal amplification rates at infinite Reynolds nunber and Mach number 0.1 forvarious wave numbers. For the symmetric cases, the theoretical curve were taken from (4). In the case, J. Delfs et all (1997) solved the Orr-sommerfeld equation for large Reynolds nunber.

The simulations presented with addition of asymmetry to the wake profile, namely, $\beta = 0.05, 0.1, 0.15$ and 0.2, indicate that the effect diminishes the temporal amplification rates. The figure 1 shows that neutral mode is between $\alpha = 1, 7$ and $\alpha = 1.8$ for $\beta = 0.05, 0.1, 0.15$ and 0.2 larger that $\alpha = 1.8$ the flow remains stable, namely, $\omega_i < 0$.

The time development of the vorticity field obtained from this simulation considering a symmetric wake profile is showed in the frame sequence of figure 2. The symmetric case represents the sinous mode known as mode of von Kàrman. For this wave number ($\alpha_r = 0.4$), the amplification rate is $\omega_i = 0.1291$ for $\beta = 0.05$ and ($\alpha_r = 0.4$) the amplification rate is $\omega_i = 0.009111$. The figures 2 and 3 shows the time development of the vorticity field obtained from this simulation considering a symmetric wake profile and $\beta = 0.1$, respectively, it shows since the linear region to the nonlinear region. The frames it relates for nondimensional time 180, 211.5, 225, 236.5, 245.25, 252, 262.35 and 268.8.
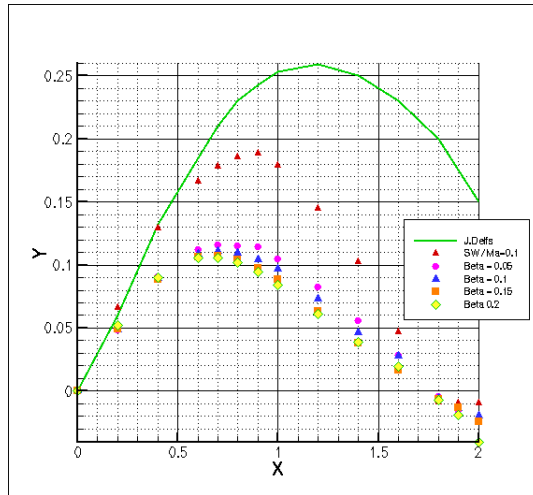
Figure 1: Temporal amplification rates for base flow (1) to $Re = \infty$ and $Ma = 0.1$

Figure 2: Time development of the vorticity field of the symmetric wake to $Re = \infty$, $\alpha_r = 0.4$ and $Ma = 0.1$
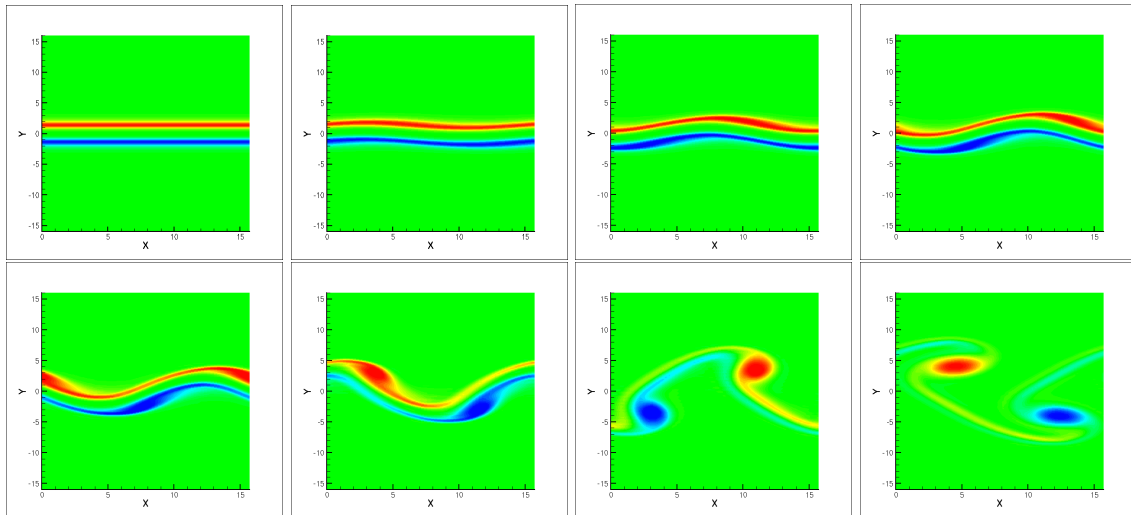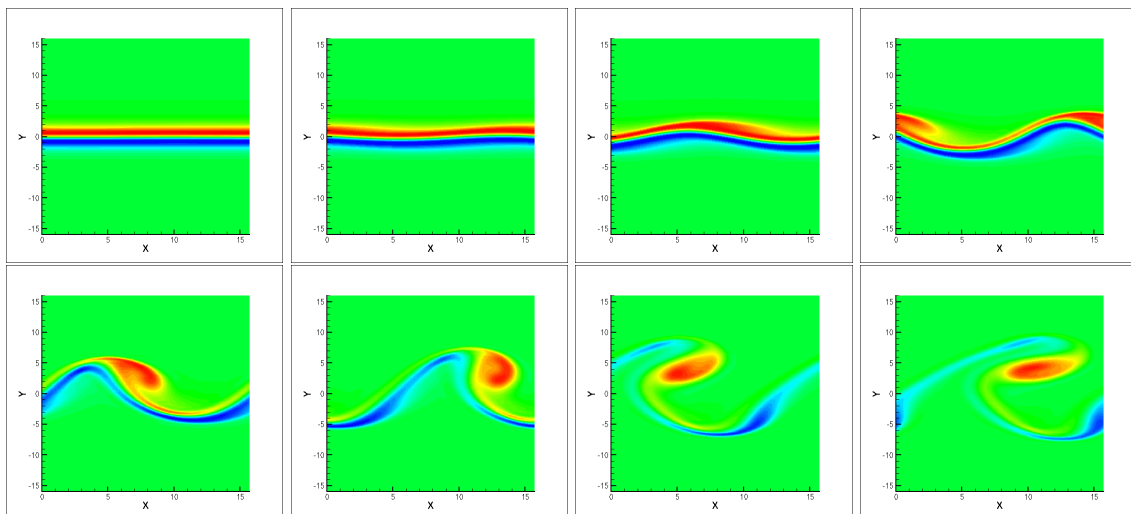

Figure 3: Time development of the vorticity field of the asymmetric wake to $Re = \infty$, $\alpha_r = 0.4$, $Ma = 0.1$ for $\beta = 0.1$

Fifth Conference on Bluff Body Wakes and Vortex-Induced Vibrations (BBVIV 5)
Costa do Sauipe, Bahia, Brazil, 12 - 15 December 2007

115

The results presented in this section that if it relates to the linear region do not depend on the chosen mesh. The test for this result was made for wave number $\alpha = 0.7$ and $\beta = 0.2$ for meshes: 16x32, 32x64, 64x128 and 128x256 and 256x512.

5. Summary

The simulations presented with addition of asymmetry to the wake profile indicate that the effect diminishes the temporal amplification rates. The figure 1 shows that neutral mode is between $\alpha = 1,7$ and $\alpha = 1.8$ for $\beta = 0.05, 0.1, 0.15$ and 0.2 larger that $\alpha = 1.8$ the flow remains stable, namely, $\omega_i < 0$. Our interest wass to study the asymetry effect for $Ma = 0.1$, however, in future works, the effect of mach can be investigated together to the effect of the asymmetry. The methodology adopted presented good qualitative results and the code was efficient in computing the physics of the problem described. The results showed that the asymmetry promote stability.

The expectation is to get a comparison of the results of the direct numerical simulation with the linear theory until the event.

6. Acknowledgements

7. References

Betchov, R. and Criminale Jr., W. O., 1966, "Spatial Instability of the Inviscid Jet and Wake", Phys. Fluids 9 (2), pp. 359-362.

Briggs, R.J., 1964, "Electron Stream Interaction with Plasmas" (MIT Press, Cambrigde).

Colaciti, A. K. et all, 2006, "On the Vortex Pairing Aeroacoustics of a 2D Mixing Layer under Temporal Development", Proceedings of the 11 th Brazilian Congress of Thermal Sciences and Engineering, Brazil.

Delfs, J. et all, 1197, "Lagrange indetification os absolutely unstable regimes in wakes", Acta Mechanica 122, pp. 89-97.

Hultgren, Lennart S. and Aggarwal, Arunk K., 1987, "Absolute Instability of the Gaussian wake profile", Phys. Fluids 30 (11), pp. 3383-3387.

Mattingly, G. E. and Criminale, W. O., 1972, "The stability of an incompressible two-dimensional wake", J. Fluid Mech., vol 51, part 2, pp. 233-272.

Monkewitz, Peter A., 1988, "The absolute an convective nature of instability in two-dimensional wakes at low Reynolds numbers", Phys. Fluids 31 (5), pp. 999-1006.

Sato, H and kuriki, K., 1961, "The mechanism of transition in the wake of a thin flat plate placed parallel to a uniform flow", J. Fluid Mech., vol 11, pp. 321-352.

Vitola, M. A., 2006, "Influência de um contorno plano sobre o desprendimento de vórtices ao redor de um cilindro circular", Tese de doutorado, UFRGS.

Williamson, C. H. K., 1996, "Vortex dynamics in the cylinder wake", Ann. Rev. Mech, vol 28, pp. 477-539.

NUMERICAL SIMULATION OF VORTEX WAKE FROM A CYLINDER IN AN ELLIPTICAL TRAJECTORY

Leandro Conceição Pinto[1], Diogo Costa Buarque[1], Edith Beatriz Camaño Schettini[1,3] & Jorge Hugo Silvestrini[2]

[1]Instituto de Pesquisas Hidráulicas,
Universidade Federal do Rio Grande do Sul - IPH/UFRGS
Av. Bento Gonçalves 9600, CEP 90650-001, Porto Alegre - RS, Brasil

[2]Faculdade de Engenharia,
Pontifícia Universidade Católica do Rio Grande do Sul - PUCRS
Av. Ipiranga 6681, CEP 90619-900, Porto Alegre - RS, Brasil

Abstract

In this paper the Direct Numerical Simulation in two-dimensional configuration is used to identify the vortex street wake patterns from a cylinder in an elliptical trajectory in a constant flow. The computational code uses sixth-order compact finites differences schemes for the spatial derivatives and a third-order low-storage Runge-Kutta method for the temporal derivative of the Navier-Stokes equations. The incompressible condition is verified by the solution of a Poisson equation for the pressure. The elliptical trajectory of the cylinder is represented by the Virtual Boundary Method using the methodology originally proposed by Goldstein *et al.* (1993)[1]. As a qualitative validation for our computation code, it is considered the canonical case of the flow around a cylinder in forced vertical oscillation. Results show the vortex wake pattern P+S in agreement with the classification given by Williamson & Roshko (1988)[8]. Vortex fields obtained in the simulation are compared with experimental (Williamson & Govardhan, 2004[6]) and numerical (Udaykumar *et al.* (2001)[5]) results. They were considered four cases for the cylinder in different elliptical trajectories, each of them corresponding to a vertical amplitude. The results show that increasing the vertical amplitude (A) of the elliptical trajectory, the mean lift coefficient $< C_L >$ moves away from zero and its root mean square (C_{Lrms}) increases. The analysis of four instantaneous vorticity fields and of the C_D and C_L coefficients time history for a simulation with $A/D = B/D = 1.5$, where B is the transversal amplitude of the elliptical trajectory, indicates that each extremes values of C_D and C_L signals correspond to one vortex shedding.

Key − words : numerical simulation, virtual boundary methods, cylinder, elliptical trajectory, vortex wake.

Introduction

Vibrations in heat exchanger tubes, risers movement due the marine stream during the transport of the oil from ocean deep and vegetations as macrophytes in lakes and wetlands are some of the practical examples of the interest in the study of the flow around bluff body in movement. Experiments carried out by Williamson & Roshko (1988)[8] show that the vortex patterns in the wake can be modified in function of the characteristic parameters as the non-dimensional wavelength (λ/D) and non-dimensional oscillations amplitude (A/D) of the cylinder. Williamson and Rohsko constructed a map of vortex synchronization regions (*WR* map) illustrated in Figure 1. The *WR* map shows a domain with the vortex patterns using a symbolic code of letters and numbers that describes the combination of pairs and singles vortices shedded during each cycle of movement of the cylinder.

Direct Numerical Simulation (*DNS*) is an useful tool to describe the physical behavior of the flow for different imposed conditions being used as complement of experimental and analytical researches (Moin & Mahesh, 1998[3]). DNS can accurately resolve all spatial and temporal scales present in the flow, providing details of flows structure.

The cylinder is represented through of the Virtual Boundary Method (*VBM*), where an external force field is added in the momentum equation. An advantage of this method is that the re-mesh to accommodate changes in geometry (or on the position of the body) is not necessary, since the force term is independent of the mesh grid.

The purpose of this work is to study the vortex street wakes behind a cylinder in an elliptical trajectory using *DNS*. The complete methodology used by the computational code is described in the following section.

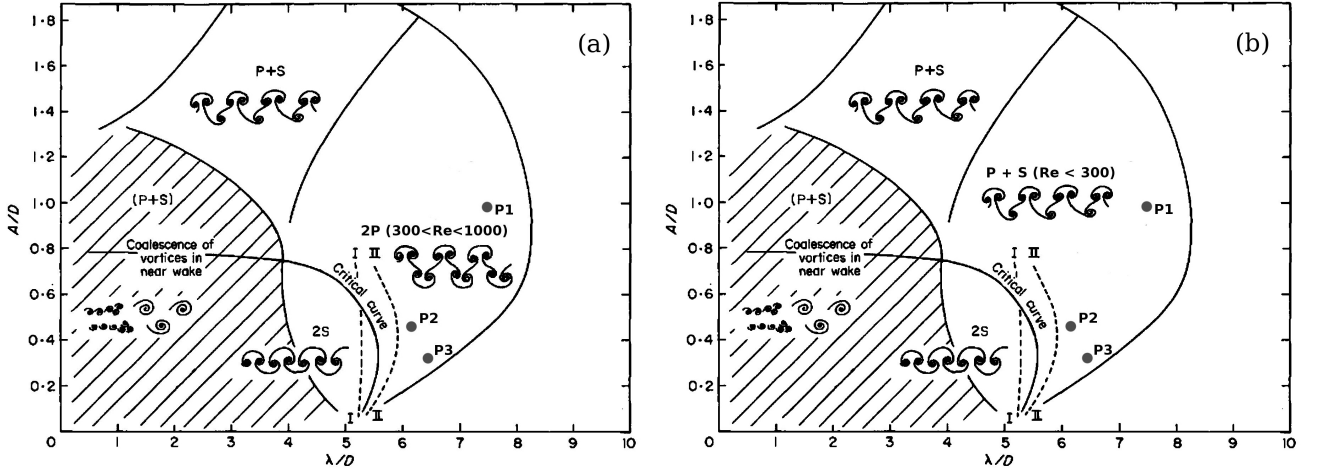[3]corresponding author: *bcamano@iph.ufrgs.br*

Figure 1: *WR* map of vortex synchronization regions proposed by Williamson & Roshko (1988)[8] (adapted from Williamson & Roshko (1988)[8]). Point *P1* indicates the regions of the parameters used in the present numerical simulations and the points *P2* and *P3*, the parameters used by Williamson (1987, unpublished, *apud* Williamson & Govardhan, 2004[6]) and Udaykumar *et al.* (2001)[5] respectively. (*a*) $300 < Re < 1000$; (*b*) $Re < 300$

Numerical Methodology

In order to model the flow of interest, we use the non-dimensional time-dependent incompressible Navier-Stokes equations

$$\frac{\partial \vec{u}}{\partial t} + \vec{\omega} \times \vec{u} = -\vec{\nabla}\Pi + \frac{1}{Re}\nabla^2 \vec{u} + \vec{f}, \tag{1}$$

and the continuity equation

$$\vec{\nabla} \cdot \vec{u} = 0, \tag{2}$$

where t is the time, $\vec{u}(\vec{x}, t)$ is the velocity field, $\vec{\omega}(\vec{x}, t)$ is the vorticity field ($\vec{\omega} = \vec{\nabla} \times \vec{u}$), ρ is the density, ν is the kinematic viscosity, $\Pi(\vec{x}, t)$ is the modified pressure field ($\frac{P}{\rho} + \frac{u^2}{2}$), and $\vec{f}(\vec{x_s}(t), t)$ is an external feedback force field applied in the boundary locations $\vec{x_s}(t)$ to model the presence of the obstacle.

In this study, the time integration of the governing equations is performed with three sub-time step applying the low-storage third-order Runge-Kutta method proposed by Williamson (1980)[7]. In order to provide an improved representation of the range scale present in the flow, all the spatial derivatives of the governing equations are discretized using a sixth-order compact finite-differences scheme proposed by Lele (1992)[2] and applied on a regular Cartesian grid. The incompressible condition is verified by solution of a Poisson equation for the pressure.

To represent the presence of the immersed boundary in the Cartesian grid, we used the explicit feedback forcing Immersed Boundary Method proposed by Goldstein *et al.* (1993)[1], where the no-slip condition is imposed with the aid of an external force field ($\vec{f}$) added in the momentum equation. Introducing the cylinder speed vector ($\vec{V_c}$), this force field can be defined by:

$$\vec{f}(\vec{x_s}(t), t) = \alpha \int_0^t \left[\vec{u}(\vec{x_s}(t'), t') - \vec{V_c} \right] dt' + \beta \left[\vec{u}(\vec{x_s}(t), t) - \vec{V_c} \right], \tag{3}$$

where α and β are negative constants. The cylinder speed is defined by the cylinder center displacement derivatives. This can be express for $y_c = y_0 + A sin(2\pi f t)$ and $x_c = x_0 + B cos(2\pi f t)$, where x_0 and y_0 are the cylinder center coordinates, A and B the vertical and horizontal amplitude of the cylinder trajectory, respectively, and f is the displacement frequency.

Validation of the Simulations in Computational Code

Validation tests of the computational code have been carried out using a domain size of $L_x = 24D$ and $L_y = 16D$, where x and y are the streamwise and vertical coordinates, respectively. The mesh resolution was $\Delta x/D = \Delta y/D = 0.03125$. The Reynolds number adopted in the simulations was $Re = 140$.

According to Williamson & Roshko (1988)[8], the vortex synchronization regions in the *WR* map (Fig. 1) remain invariant for $300 < Re < 1000$. On the other hand, for $Re < 300$, the 2*P* mode disappears with the $P + S$ mode taking its place (Fig. 1*b*). Our simulation, for the Point *P1* ($\lambda/D = 7.5, A/D = 1$) produced clearly the $P + S$ arrangement. Figure 2 shows a comparison of the vorticity field produced by an unpublished experimental laser-fluorescence photograph for an oscillating cylinder for $Re = 140$, $\lambda/D = 6.07$ and $A/D = 0.5$

retired of Williamson & Govardhan (2004)[6] (Fig. 2a), for point $P2$ in the WR map; the numerical work of Ponta (2006)[4] for $Re = 140$, $\lambda/D = 7.5$ and $A/D = 1$ (Fig. 2b), for point $P1$; numerical work of Udaykumar *et al.* (2001)[5] for $Re = 200$, $\lambda/D = 6.30$ and $A/D = 0.33$ (Fig. 2c), for point $P3$; and our numerical simulation for point $P1$ (Fig. 2d).
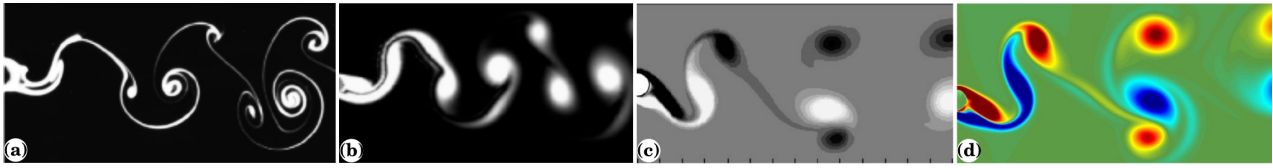

Figure 2: Comparison of vorticity fields for point $P1$ produced by: (a) Williamson (1987, unpublished, *apud* Williamson & Govardhan, 2004[6]); (b) numerical work of the Ponta (2006)[4]; (c) numerical work of Udaykumar *et al* (2001)[5]; (d) present numerical simulation.

The vorticity field of the simulation $P1$ (Fig. 2d) showed the vortex mode $P + S$. Additional numerical simulations have being carried out using parameters relative to the others regions of the WR map, aiming to represent the others existing vortex patterns.

Preliminary Results and Discussion

Numerical simulations for $Re = 300$ and frequency $f = 0.1$ have been done with the cylinder motion in an elliptical trajectory. Four simulations have been carried out varying the vertical amplitude A/D in 0, 0.5, 1.0 and 1.5. The horizontal amplitude B/D was kept constant and equal to 1.5, and the computational domain was not modified. The lift coefficients (C_L) time history are shown in Figure 3. The C_L time history of the simulation 4 (Fig. 3d) reveals to be more regular than the other signals.
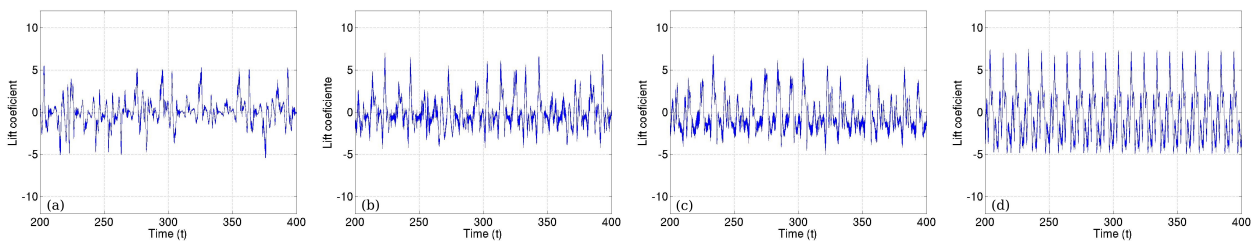
Figure 3: Lift coefficient (C_L) time history for $Re = 300$ and $f = 0.1$. (a) Simulation 1, $A/D = 0$; (b) Simulation 2, $A/D = 0.5$; (c) Simulation 3, $A/D = 1.0$; (d) Simulation 4, $A/D = 1.5$.

Table 1 shows the results of the average C_L ($< C_L >$) and its root mean square (C_{Lrms}) calculated over a time period of $T = 200$. When the vertical amplitude A/D increases, the value of the C_{Lrms} increase too and $< C_L >$ tends to move away from zero. At this moment, it is not clear for us, if the non-zero value of the mean C_L for $A/D = 0$ is due to the sampling time used for the calculation of the mean values or to some assymetrical vortex pattern like the $P + S$ configuration. The examination of vorticity fields for this simulation corresponding to two extreme positions of the cylinder (Figure 4) reveals a highly complex pattern, a priori, not related with those of the WR map.
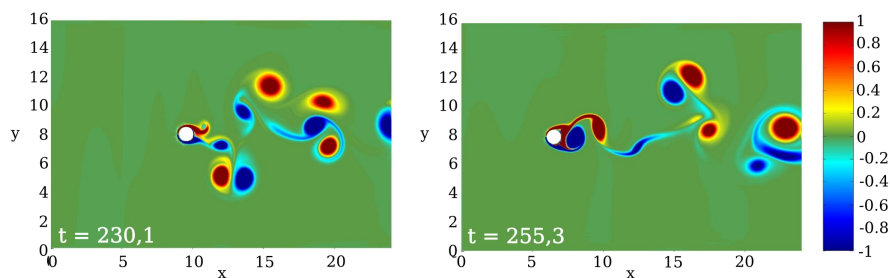
Figure 4: Instantaneous vorticity fields for two extreme positions of the cylinder.

Figure 5a shows the time history of the drag (C_D) and lift (C_L) coefficients for a cycle of the simulation 4 and four instantaneous vorticity fields at the times $t_1 = 201.2$, $t_2 = 202.8$, $t_3 = 203.6$ and $t_4 = 205.4$, where t_1, t_2 and t_4 correspond to extremes values of C_D and C_L (Fig. 5b). The analysis of these vorticity fields indicates that the vortex shedding in the simulation 4 can be associated with the extremes values of the C_D and C_L, that is, each extreme value corresponding to one vortex shedded.

The maximum values of C_D occur between the positions 1 and 3 ($200 < t < 204$) of the cylinder trajectory shown in Fig. 5a, where the relative velocity between the cylinder and the flow is higher than the mean inflow

Table 1: Parameters and results of the simulations 1, 2, 3 and 4, for $Re = 300$.

Simulation	A/D	$< C_L >$	C_{Lrms}
1	0.0	0.065	1.55
2	0.5	-0.069	1.70
3	1.0	-0.361	1.95
4	1.5	-0.427	2.81

(a) (b)
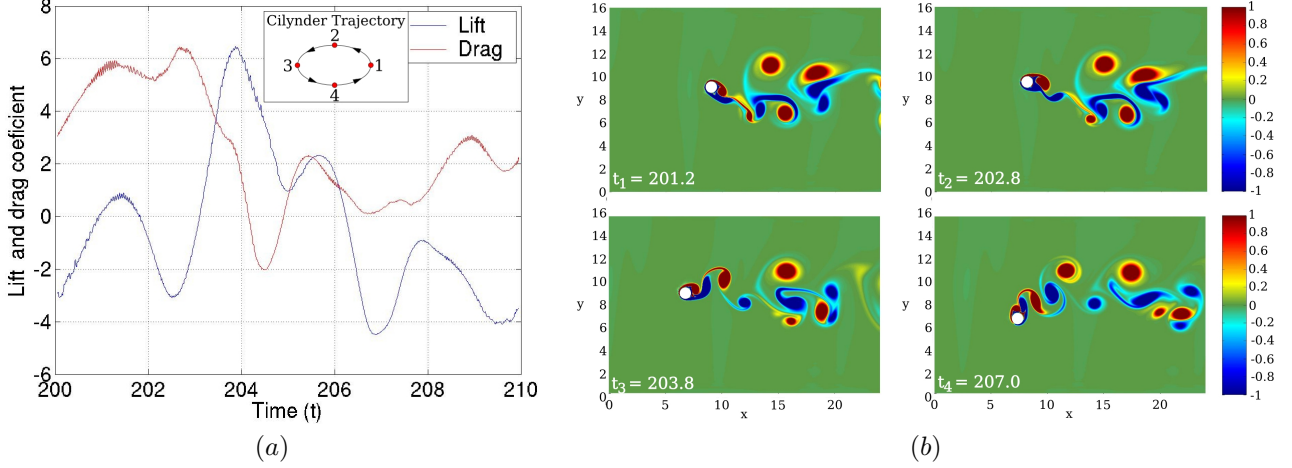
Figure 5: Influence of the vortex shedding on C_D and C_L time history. (a) C_D and C_L time history evidencing the main peaks. (b) Instantaneous vorticity fields at times $t_1 = 201.2$, $t_2 = 202.8$, $t_3 = 203.6$ and $t_4 = 205.4$.

velocity. For a time around $t \approx 207$, the C_D is approximately zero, because the relative velocity is practically zero near the position 4. Between the positions 4 and 1, the shedding vortices keep in touch with the cylinder, as can be seen in Figure 6.
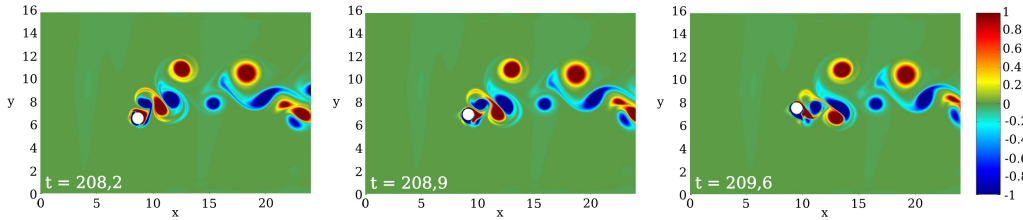
Figure 6: Vorticity fields near the position 4 of the cylinder trajectory shown in Fig. 5a.

Others numerical simulations with different frequencies on the same trajectories for this flow configuration are being considered, as well as, longer time sampling to elucidate the question about the non-zero value of the mean C_L coefficient for $A/D = 0$. All these results will be presented at the conference.

References

[1] D. GOLDSTEIN, R. HANDLER, and L. SIROVICH. Modeling a no-slip flow boundary with an external force field. *J. Comp. Phys.*, **105**:354–366, 1993.

[2] S. LELE. Compact finite difference schemes with spectral-like resolution. *J. Comp. Phys.*, **103**:16–42, 1992.

[3] P. MOIN and K. MAHESH. Direct numerical simulation: a tool in turbulence research. *Annu. Rev. Fluid Mech.*, **30**:539–578, 1998.

[4] F. L. PONTA and H. AREF. Numerical experiments on vortex shedding from an oscillating cylinder. *J. of Fluids Structures.*, **22**:327–344, 2006.

[5] H. S. UDAYKUMAR, R. MITTAL, P. RAMPUNGGOON, and A. KHANNA. A sharp interface cartesian grid method for simulating flows with complex moving boundaries. *J. Comp. Phys.*, **174**:345–380, 2001.

[6] C. H. K. WILLIAMSON and R. GOVARDHAN. Vortex-induced vibrations. *Annu. Rev. Fluid Mech.*, **36**:413–455, 2004.

[7] J. H. WILLIAMSON. Low-storage runge-kutta schemes. *J. Comp. Phys.*, **35**:48–56, 1980.

[8] J. H. K. WILLIAMSON and A. ROSHKO. Vortex formation in the wake of an oscillating cylinder. *J. of Fluids Structures.*, **2**:355–381, 1988.

Numerical investigation into the asymptotic solution of the viscous flow around a circular cylinder for $Re \leq 600$

Iago C. Barbeiro, José A. P. Aranha and Julio R. Meneghini

iago.barbeiro@poli.usp.br

NDF, *Escola Politécnica*, University of São Paulo, Brazil

Abstract

The viscous flow around a circular cylinder seems to be already well accepted as a stability problem characterized by a *Hopf bifurcation* that takes place in the vicinity of a critical Reynolds number ($Re_{cr} \approx 46$). In this sense, as the presence of just one unstable mode has been evidenced in many previous works, an asymptotic solution of this flow can be derived based on this mode. This work investigates this asymptotic solution, reproducing its spectral structure from two-dimensional numerical simulations of this flow by means of Fourier series decomposition. Some care has been taken to capture and quantify all symmetrical and anti-symmetrical patterns present in the Fourier series and related to the asymptotic solution.

1 Introduction

The subject of this work is the oscillatory behavior of the flow around a circular cylinder that is observed when the Reynolds number is greater than a critical value. Just before this critical value the flow is still steady and its wake consists of a pair of recirculating bubbles with opposite vorticity signal. Crossing this critical value, that has been found by many experimental and numerical works to be around 46, the flow is no more steady and rapidly achieves an harmonic oscillatory state, or a limit-cycle defined by a frequency and an amplitude. This kind of switch, in the dynamic systems theory, is identified as a *Hopf bifurcation*, where just one pair of complex conjugate eigenvalues with nonzero imaginary parts passes through the imaginary axis to the unstable region. Experimental and numerical verifications of this assumption can be found in the works of Provansal (1987) and Noack and Eckelmann (1994) respectively.

The *Hopf bifurcation* theory allows an asymptotic solution for the equation that must be valid in the vicinity of the bifurcation, and empirical evidences suggest that this asymptotic solution should hold far beyond the bifurcation ($Re \gg Re_{cr}$). Presenting $\mathbf{u}_s(\mathbf{x})$ as the steady-state *symmetrical* solution that becomes unstable for $Re > Re_{cr}$ and $\lambda = \sigma + \omega$ as the eigenvalue of the unstable *anti-symmetrical* mode $\mathbf{e}(\mathbf{x})$, the solution proposed by Aranha (2003) can be written as follows:

$$
\begin{aligned}
\mathbf{u}(\mathbf{x}, t) = \mathbf{u}_s(\mathbf{x}) + \boldsymbol{\varphi}_{20}(\mathbf{x}) + \tfrac{1}{2}[a(t)\mathbf{e}(\mathbf{x})e^{iwt} + \boldsymbol{\varphi}_{31}(\mathbf{x})e^{iwt} + (*)] + \\
+ \tfrac{1}{2}[\boldsymbol{\varphi}_{22}(\mathbf{x})e^{2iwt} + (*)] + \tfrac{1}{2}[\boldsymbol{\varphi}_{33}(\mathbf{x})e^{3iwt} + (*)] + \mathcal{O}((\sigma^{1/2})^4)
\end{aligned}
\tag{1}
$$

where $\mathbf{x} = x\mathbf{i} + y\mathbf{j}$, $\mathbf{u}(\mathbf{x}, t) = u(\mathbf{x}, t)\mathbf{i} + v(\mathbf{x}, t)\mathbf{j}$, (*) stands for the complex conjugate of the term on the left and the amplitude $a(t)$ of the unstable mode is small and changes slowly in time : $a(t) \cong \mathcal{O}(\sigma^{1/2})$; $\frac{\partial a}{\partial t} \cong \mathcal{O}(\sigma a)$.

In this sense, the Fourier harmonics of the simulated flow come to provide a good preview of the terms of the asymptotic solution in the equation 4. The first harmonic, for example, approximates the unstable mode $\mathbf{e}(\mathbf{x})$ to an order of $\mathcal{O}(\sigma^2)$ and using a convenient normalization of the harmonics one can also estimate the amplitude of the unstable mode.

2   Numerical Simulations

The evolution of this flow is well known to be defined by the incompressible Navier-Stokes equation and here the Penalty Method is employed to take care of the pressure-velocity coupling. This method is characterized by a *pseudo-bulk viscosity* ε that allows, by means of the *Virtual Power Principle*, a relation between pressure and very small specific volume changes:

$$\nabla.\mathbf{u} = -\varepsilon p. \tag{2}$$

It is then possible to extract the variable pressure of the traditional equation, giving:

$$\frac{\partial \mathbf{u}}{\partial t} = -(\mathbf{u}.\nabla)\mathbf{u} + \frac{1}{\varepsilon}\boldsymbol{\nabla}(\nabla.\mathbf{u}) + \frac{1}{Re}\nabla^2\mathbf{u} \tag{3}$$

The discrete set of equations is obtained by the *Finite Element Method* using linear shape functions. A second order time integrator was implemented based on the Implicit Euler Method. Just one half of the mesh was generated by Delaunay triangulation and the second half was reflected to guarantee symmetry. The relation of the mirrored nodes is kept to permit the easy decomposition of any field in *symmetrical* and *anti-symmetrical* parts in the post-processing phase.

Figure 1 shows the computational domain, whose external shape and approximate main dimensions were similar to those employed by Henderson (1997). Mesh refinement and the Penalty's parameter ε were calibrated and the final results of vortex shedding frequency and drag coefficient RMS are in a very closed agreement with those presented by Henderson (1997).

20 D   *60 D*
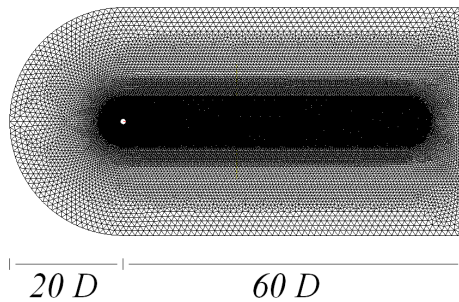
Figure 1: Computational mesh with dimensions with 52.152 nodes

3   Fourier Analysis

Taking $w_s = 2\pi f_s$, where f_s is the vortex shedding frequency for a given Reynolds number, one can perform a Fourier series decomposition of the velocity field based on w_s and its multiples. The Fourier coefficients can be calculated by simple integration through a few number of vortex shedding cycles, and the series can be written in terms of complex amplitude as:

$$\mathbf{u}(\mathbf{x},t) = \mathbf{u_0}(\mathbf{x}) + \tfrac{1}{2}[\mathbf{u_1}(\mathbf{x})e^{iw_s t} + (*)] + \tfrac{1}{2}[\mathbf{u_2}(\mathbf{x})e^{2iw_s t} + (*)] +$$
$$+ \tfrac{1}{2}[\mathbf{u_3}(\mathbf{x})e^{3iw_s t} + (*)] + \tfrac{1}{2}[\mathbf{u_4}(\mathbf{x})e^{4iw_s t} + (*)] + ... \tag{4}$$

The pattern of the complex harmonic fields is mostly the same for the simulated range of Reynolds ($60 \leq Re \leq 600$) and is shown for $Re = 200$ in the figure 2. Every harmonic was decomposed in *symetrical* and *anti-symmetrical* parts and a kinetic energy norm was used to determine the ratio of *symmetry* of each one, which is presented in the figure 3(a).

(a) $u_{0,r,x}$[-0.18;1.36]   (b) $u_{0,r,y}$[-0.71;0.71]

(c) $u_{1,r,x}$[-0.47;0.47]   (d) $u_{1,r,y}$[-0.57;0.67]   (e) $u_{1,i,x}$[-0.34;0.34]   (f) $u_{1,i,y}$[-0.58;0.61]

(g) $u_{2,r,x}$[-0.10;0.14]   (h) $u_{2,r,y}$[-0.12;0.12]   (i) $u_{2,i,x}$[-0.12;0.11]   (j) $u_{2,i,y}$[-0.12;0.12]

(k) $u_{3,r,x}$[-0.06;0.06]   (l) $u_{3,r,y}$[-0.13;0.14]   (m) $u_{3,i,x}$[-0.06;0.06]   (n) $u_{3,i,y}$[-0.14;0.14]

Figure 2: Fourier complex harmonics for $Re = 200$: where r/i means real/imaginary, x/y are the cartesian components of the velocity and the numbers inside the brackets are the range of the grayscale (from black to white).

(a) *Symmetry* ratio versus *Re*

(b) Harmonics amplitude normalized by the harmonic zero

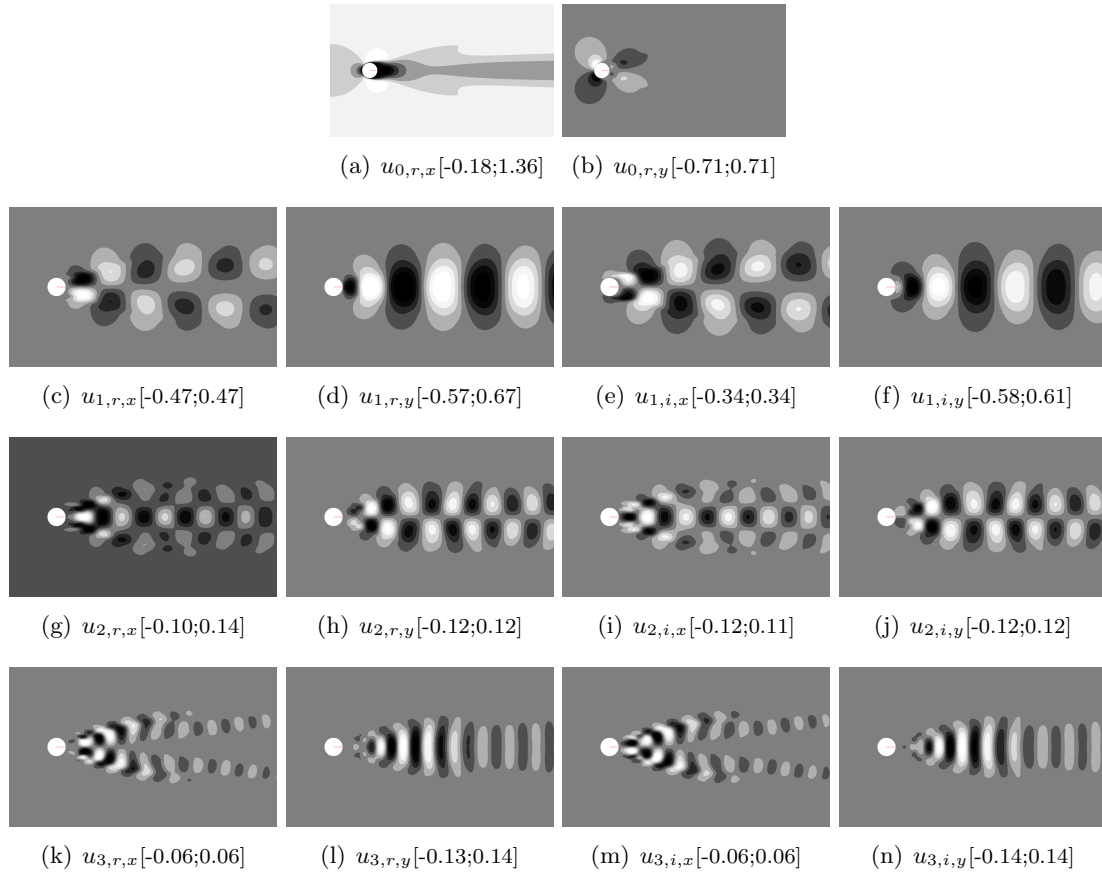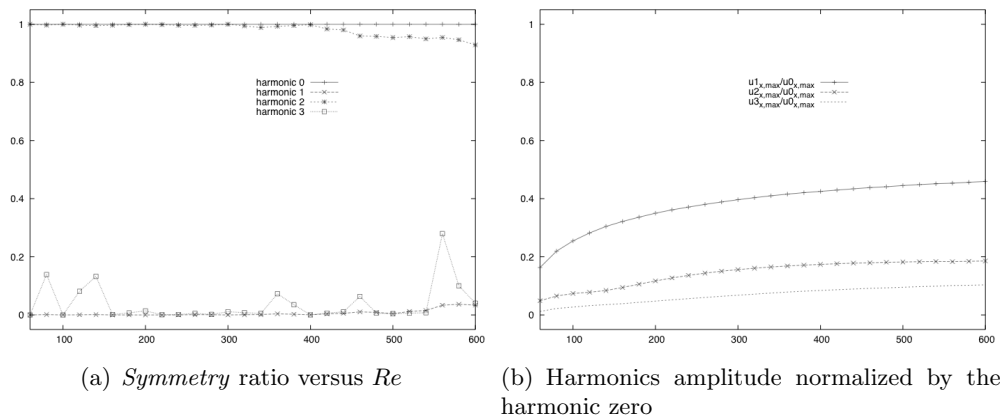Figure 3: Fourier hamonics evolution through Reynolds

4   Final Remarks

The amplitude results shown in the figure 3(a) come to reinforce the idea that the asymptotic solution should hold far beyond the critical Reynolds. It might be true since all amplitudes seems to go for constant values and the first, which tells about the unstable mode amplitude, keeps well behaved and small. The alternate *symmetrical/anti-symmetrical* pattern of the harmonics provides a decomposition facility that can be usefull in some cases.

Next efforts will be concentrated on the investigation of how the first approximation of the unstable mode given by the first harmonic can be used as a start to the stability study of this flow.

Acknowledgements

References

Aranha, J. A. P. (2003). Weak three dimensionality of a flow aroud a slender cylinder: The guinzburg-landau equation. *Journal of the Brazilian Society of Mechanical Sciences and Egineering*, XXVI:No. 4, 355–367.

Henderson, R. D. (1997). Nonlinear dynamics and pattern formation in turbulent wake transition. *Journal of Fluid Mechanics*, 352:1–22.

Noack, B. R. and Eckelmann, H. (1994). A global stability analisys of the steady and periodic cylinder wake. *Journal of Fluid Mechanics*, 270:297–330.

Provansal, M. (1987). Bernard-von karman instability: transient forced regimes. *Journal of Fluid Mechanics*, 182:65–112.

2D STEADY SYMMETRIC FLOW AROUND A CIRCULAR CYLINDER FOR Re<600: SENSIBILITY TO STANDARD FAR-FIELD BOUNDARY CONDITIONS AND "WAKE IMPEDANCE" ALTERNATIVE FORMULATION

P.N. Lavinas, I.C. Barbeiro, J.A.P. Aranha

NDF, Department of Mechanical Engineering, University of São Paulo, Brazil

Corresponding author: pnlavinas@yahoo.com.br

Abstract

This paper aims at the numerical study of the symmetric steady flow past a circular cylinder up to Reynolds number 600. This is the first step to obtain the Ginzburg-Landau Equation as an asymptotic solution of the Navier-Stokes Equations. This steady flow has proved to be very sensitive to small perturbations in the far flow field, and very large computational domains are needed to obtain an accurate solution, when the simple outflow boundary condition is imposed on the outlet boundary. The purpose of this paper is to show that a mixed boundary condition, called here the "wake impedance", can be used to shorten the computational domain.

1. Introduction

The onset of vortex shedding in the flow around a fixed circular cylinder is characterized as a Hopf bifurcation as the Reynolds numbers Re grows above a critical value $\mathrm{Re}_{cr} \approx 45$. The steady solution which takes place for $\mathrm{Re} < \mathrm{Re}_{cr}$ becomes unstable and a periodic solution appears, with a well defined vortex shedding frequency f_s given non-dimensionally by the Strouhal number $St = f_s D / U$, in which U is the free-stream velocity and D is the cylinder diameter.

The ongoing research aims to study the dynamics of this periodic flow through the stability properties of the 2-D steady symmetric flow field. The essential assumption underlying the theory is that the linearized problem has, for $\mathrm{Re}_{cr} < \mathrm{Re} < 10^5$ interval, only one unstable mode, which is anti-symmetric. This assumption is strictly valid only for Re just above Re_{cr}, but experimental evidences suggest that it should hold for higher Reynolds numbers. The discontinuities in this curve are due to (weak) three-dimensionalities present in the flow (Henderson, 1997; Noack and Eckelmann, 1994), whose influence is to be introduced in a further step of investigation. This unstable mode and its corresponding eigenvalue are directly related to the numerical determination of the coefficients of the Ginzburg-Landau Equation (GLE), see Aranha (2004), filling the gap between the "model approach" analysed in Mathis, Provansal and Boyer, 1984; Albarède, Provansal and Boyer, 1990; Albarède and Monkewitz, 1992; Leweke and Provansal, 1994; Monkewitz, 1996, Monkewitz, Williamson and Miller, 1996; and the more fundamental Navier-Stokes Equations (NSE). The basic point in the stability analysis is to determine the steady solution. Roughly speaking, this flow field consists of a recirculating bubble whose length and width grow with Re, see Fornberg(1985). However, this steady state – the bubble geometry, for example – is extremely sensitive to the size of the discretized domain if the standard outflow condition on the outlet is used, even for Reynolds number as small as 300. In order to overcome this difficulty, the "wake impedance", obtained from the approximated linear equation in the far field, is imposed at the outlet, as it is usually done in linear wave problems; this approach is similar to the one proposed by Bao(2000).

As a side remark, it is interesting to point out that the error behavior of the 2D steady flow field follows closely, as it will be shown, the landmarks observed experimentally at $\mathrm{Re} \approx 45$ (2D instability), $\mathrm{Re} \approx 180$ (3D instability) and $\mathrm{Re} \approx 350$ (end of hysteretic region).

2. Discrete Steady Flow

The steady flow is governed by the Navier-Stokes-Equations (NSE), which for incompressible flows in its non-dimensional form read:

$$\left(\mathbf{u} \cdot \nabla\right)\mathbf{u} - \frac{1}{\mathrm{Re}} \nabla^2 \mathbf{u} + \nabla \mathrm{p} = 0 \,, \tag{1}$$
$$\nabla \cdot \mathbf{u} = 0$$

in which the symbols have usual meanings. The boundary conditions for this problem are: $\mathbf{u}\big|_{|\mathbf{x}|=D/2} = \mathbf{0}$; $\lim\limits_{|\mathbf{x}|\to\infty} \mathbf{u} = \mathbf{i}$ and $\lim\limits_{|\mathbf{x}|\to\infty} \mathrm{p} = 0$. The NSE are discretized by a standard Galerkin Finite Element Method (FEM) using piecewise linear shape functions in triangular elements, in a finite region around the cylinder, as shown in fig. 1. A semicircular shape has been chosen because the perturbation in velocity and pressure on the uniform flow

caused by the cylinder tend to spread radially. The calculations using the "wake impedance" formulation (see section 4), are carried out in the mesh shown in fig. 2, which is the same as in fig. 1 for r = 600D, but cut vertically at a downstream distance of 100D.
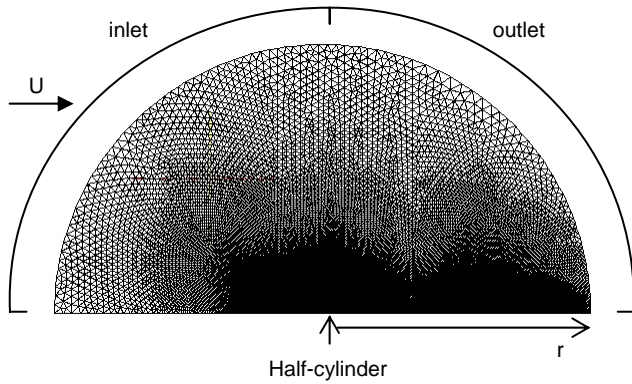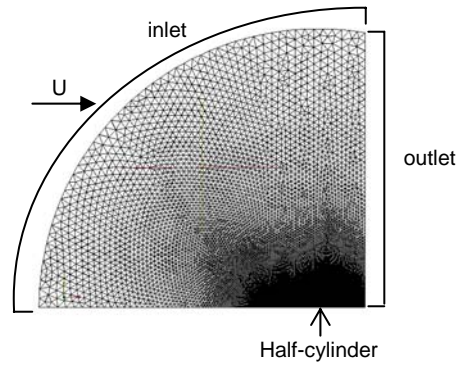

Figure 1 - Semicircular mesh with radius r

Figure 2 - Mesh for calculations with"wake impedance"

The discrete NSE equations read:

$$\left\{\frac{1}{Re}\mathbf{D}+\mathbf{N(U)}\right\}\cdot\mathbf{U}-\mathbf{R}\cdot\mathbf{P}=\mathbf{0} \; ; \; \mathbf{R}^t\cdot\mathbf{U}=\mathbf{0} , \tag{2}$$

where, being *n* the number of nodes of the (unstructured) mesh, $\mathbf{U}_{2n\times1}=\{U_1,...,U_n;V_1,...,V_n;\}$ and $\mathbf{P}_{n\times1}=\{P_1,...,P_n\}$ are the nodal velocity and pressure vectors; $\mathbf{D}_{2n\times2n}$ is the diffusion matrix and $\mathbf{N}_{2n\times2n}(\mathbf{U})$ the convective matrix; $\mathbf{R}_{2n\times n}$ is the gradient and its transpose is the divergence matrix. The velocity-pressure coupling is resolved by the penalty method (Gunzburger, 1985), in which the incompressibility constraint is satisfied asymptotically: $\mathbf{R}^t\cdot\mathbf{U}=-\varepsilon\mathbf{P}$, being $\varepsilon>0$ a small parameter. $\varepsilon=10^{-6}$ proved to be sufficiently small: decreasing ε caused no changes in the flow field. Some algebraic manipulation in (2) leads to the non-linear problem whose solution is the steady-state velocity field:

$$\left\{\frac{1}{Re}\mathbf{D}+\frac{1}{\varepsilon}\mathbf{R}\cdot\mathbf{R}^t+\mathbf{N(U)}\right\}\cdot\mathbf{U}=\mathbf{0} , \tag{3}$$

3. Sensibility to Domain Size

This test consisted of extensive calculations using semicircular meshes having radii from 40D up to 1000D. As comparison parameters the drag coefficient C_d, the bubble length L and width W were chosen. Figures 3, 4, and 5 show how these values vary with *Re* for various domain sizes. Since there is – obviously - no experimental data about this flow, the results are compared only against Fornberg(1985).
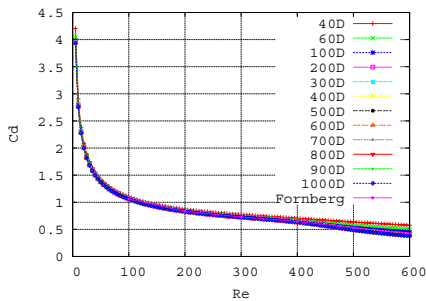
Figure 3 – Cd(Re) for varying domain radii
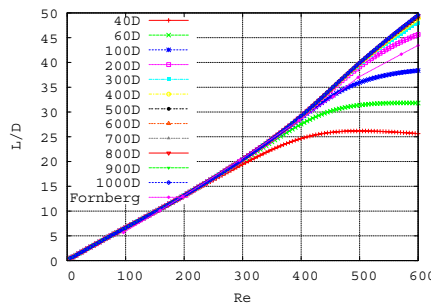
Figure 4 – L(Re) for various domain radii
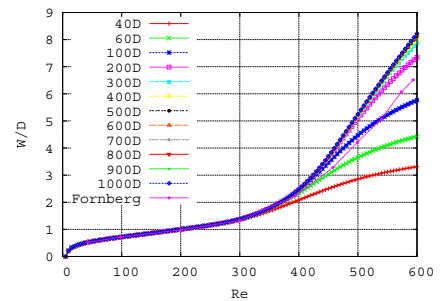
Figure 5 – W(Re) for various domain radii

One can see that up to *Re=300*, no significant differences can be seen among all meshes. When *Re* is increased, the smaller meshes begin to give results which deviate from the obtained with the larger ones. For *Re=600*, the difference observed between the meshes with 40D and 1000D are as large as 34,01% for C_d; 48,30% for L and 59,75% for W. One sees that bringing the infinity boundary conditions to a finite distance

causes a large influence on the steady-state flow, even for large distances as 200D where the perturbation on the uniform flow is small. It is to notice also that the curves coalesce into the 1000D curve, being all virtually the same for *r>600D*, so that, for 5<*Re*<600, r = 600D has proved to be large enough for setting "outflow (zero-force)" boundary conditions.

Fornberg's curves look very much like the ones obtained by the authors with smaller domains, and in his work they were in fact much smaller than here, although he does test the convergence of his results with regard to domain size. The comparison is not straightforward because his formulation is quite different, especially regarding the boundary conditions on the far field, and he does not give details about testing the convergence of this boundary condition model.

An intriguing and suggestive result comes from the Newton method used for resolving the non-linearity in the algebraic system. The calculations are started for an initial *Re* from a uniform $\mathbf{u}(x, y) = \mathbf{i}$ field and the converged solution (at the j-th iteration, $error = \dfrac{1}{2\mathbf{n}} \sum_{i=1}^{2n} \left| \mathbf{u}_i^j - \mathbf{u}_i^{j-1} \right| < 10^{-7}$) for this *Re* is used as the initial field for the next *Re* step. Fig. 6 shows the error in the converged solution in the analysed *Re* range:
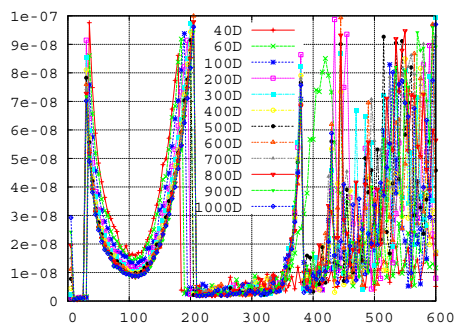
Figure 6 - Error of the converged solution for all Re and meshes

The authors expected a 'cloud' of points randomly distributed below 10^{-7} for all *Re* and meshes, but, for each *Re*, all meshes showed similar behaviors, changing radically at $\mathrm{Re} \approx 45$, $\mathrm{Re} \approx 180$ and $\mathrm{Re} \approx 350$, values in which abrupt changes in the flow behavior also occur: for $\mathrm{Re} \approx 45$, the wake begins to oscillate; for $\mathrm{Re} \approx 180$, the vortex emission pattern is altered by three-dimensionalities of the flow; and $\mathrm{Re} \approx 350$ is associated with the end of the hysteretic regime. This correspondence suggests that the 2D steady field actually carries with its stability properties some kind of "digital impression" of the 3D unsteady flow.

4. Wake Impedance

The perturbation caused by the cylinder on the velocity field far away from it can be assumed small, say, of order $\mathrm{O}(\varepsilon)$. This allows the expansion of this field as an asymptotic series in integer powers of ε. The convective (non-linear) term is $\mathrm{O}(\varepsilon^2)$ and the first-order problem is thus linear, i. e., solvable by standard Fourier series. One supposes that the flow field at the wake boundary $\mathbf{U}_w$ is known and writes the solution of the linear problem as a function of this profile. This solution can then be integrated in order to obtain the nodal forces applied by the fluid outside on the fluid inside the discretized domain. These forces are written as matrix operators which are summed together with the FEM matrices in order to determine the flow solution, including $\mathbf{U}_w$, which is actually not known *a priori*. The flow calculation with impedance is carried out on the mesh shown in fig. 2. Fig. 7, 8, and 9 compare C_d, L and W in the range $400 < \mathrm{Re} < 600$ using this mesh with "wake impedance" and with "outflow" boundary conditions at the outlet against the "benchmarking" results from the full 600D mesh:

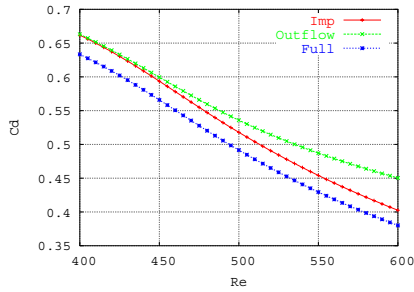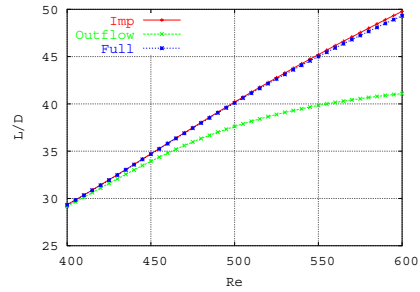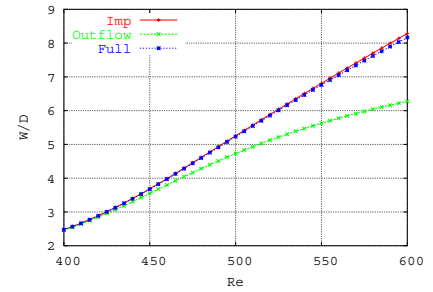| Figure 7 – Cd(Re) comparison | Figure 8 – L(Re) comparison | Figure 9 – W(Re) comparison |

As *Re* increases above 400, the 100D distance downstream becomes too short for the use of the outflow boundary condition and the control parameters begin to deviate from the benchmarking ones in a similar manner as seen for the smaller meshes in fig. 3, 4 and 5. Fig. 7, 8 and 9 show that the use of the "wake impedance" boundary condition recovers the influence of the region which was cut out from the full mesh, as expected. The errors in the control parameters for *Re = 600* (the most problematic case) are shown in table 1:

Table 1 - Cd, L and W for Re=600

	Full 600D	Cut Mesh - Outflow	Error(%)	Cut Mesh- Impedance	Error(%)
Cd	0.3801	0.4504	18.47	0.4025	5.88
L/D	49.32	41.08	16.7	49.78	0.94
W/D	8.166	6.2760	23.2	8.282	1.40

The errors still observed seem to be due to higher-order impedance terms (especially for the pressure force) which are not taken into account in the linear impedance formulation used here.

5. Conclusions

The present work has recognized the extreme sensitivity of the steady symmetric flow field around a circular cylinder to small perturbations on the far flow field, namely to the only approximate setting of boundary conditions on the wake outer edge of the calculation domain. The determination of this field is an important step onto the study of the transient wake dynamics through stability properties of the steady flow. An impedance formulation has been implemented and the results are good, what can make possible to study much larger *Re* ranges. The authors would like to acknowledge FAPESP and PETROBRAS for supporting this work.

6. References

1. Albarède, P, Monkewitz, P. (1992): *A model for the formation of oblique shedding and "chevron" patterns in cylinder wakes.* Phys. Fluids A **4 (4)**, 744-756.
2. Albarède, P., Provansal, M. and Boyer, L. (1990): *Modèlisation par l'équation de Ginzburg-Landau du sillage tridimensionnel d'un obstacle allongé.* C.R.Acad.Sci. Paris, Sér. **II**, 459-464.
3. Aranha, J.A.P. (2004): *Weak three-dimensionality of the flow around a slender cylinder: the Ginzburg-Landau Equation.* J. of the Braz. So. Of Mech. Sci. & Eng., vol. **XXVI**, 355-367.
4. Bao, W. (2000): *Artificial boundary conditions for incompressible Navier-Stokes Equations: A well-posed result.* Comput. Methods Appl. Mech. Engrg., **188**, 595-611.
5. Fornberg, B. (1985): *Steady viscous flow past a circular cylinder up to Reynolds number 600.* Journal of Computational Physics **61**, 297-320.
6. Gunzburger,M.D. (1985): *Finite Element Methods for Viscous Incompressible Flows.* Academic Press Inc.
7. Henderson, R.D. (1997): *Nonlinear dynamics and pattern formation in turbulent wake transition.* Journal of Fluid Mechanics **352**, 65-112.
8. Leweke,T. & Provansal,M. (1994): *Model for transition in bluff body wakes.* Physical Review Letters **72**, **N.20**, 3174-3177.
9. Mathis, C., Provansal, M. and Boyer, L. (1984): *The Benard-Von Karman instability: an experimental study near the threshold.* J. Physique Lett. **45**, L-483 – L-491.
10. Monkewitz, P.A. (1996): *Modeling of self-excited wake oscillations by amplitude equations.* Experimental Thermal and Fluid Science **12**, 175-183.
11. Monkewitz, P.A., Williamson, C.H.K. and Miller, G.D. (1996): *Phase Dynamics of Kármán vortices in cylinder wakes.* Phys. Fluids **8** (1), 91-96.
12. Noack, B.R. and Eckelmann, H. (1994): *A global stability analysis of the steady and periodic cylinder wake.* J. Fluid Mech. **270**, 297-330.
13. Roshko, A. (1954): *On the development of turbulent wakes from vortex streets.* NACA Report **1191**.

An iterative algorithm for the numerical computation of bluff-body wake instability modes and its application to a freely vibrating cylinder

P. Luchini, F. Giannetti, J. Pralits
DIMEC, Università di Salerno, Italy
luchini@unisa.it

1 Introduction

The linear stability of recirculating flows is, from an abstract mathematical viewpoint, an eigenvalue problem like any other. However, its numerical resolution by full-matrix QR algorithms like those found in LAPACK [1] requires the handling of exceptionally large matrices; while examples of this approach do exist in the literature, researchers have generally turned to iterative methods, the best known example of which is the Arnoldi algorithm as implemented by Sorensen in ARPACK [2]. This too has drawbacks, however, since for performance reasons a shift-and-invert preconditioner is practically always necessary which itself contains a costly matrix inversion. For this reason many computations can still be found in the literature that determine a critical Reynolds number by looking for a bifurcation in a time-resolved numerical simulation but are unable to provide eigenvalue and eigenvector information about this critical point.

In addition all these techniques, eigenvalue-based or otherwise, must confront themselves with the choice of a suitable discretization, particularly insofar as body-surface and infinity boundary conditions are concerned, and with the problem of calculating the reaction force on the body when a coupled fluid-structure interaction is concerned.

Within the above framework, one and a half year ago we started a project (funded by the Italian Ministry of University and Research) to develop an iterative algorithm suitable for two-dimensional and three-dimensional stability analysis of the wake of a, possibly moving, bluff body. Our requirements were that the algorithm should not contain any matrix inversion, not even as a preconditioner, and should provide the first few eigenvalues and eigenvectors of the stability problem with an easily parallelizable code structure that resembled as much as possible that of a time iteration. The resulting modular structure is composed of a multigrid pseudo-time-iteration module, an immersed-boundary module for the handling of the body and a completely separate subspace-iteration module for the computation of eigenvalues.

2 Multigrid computation of eigenvalues

Multigrid computation of eigenvalues (or for that matter, the computation of eigenvalues by any other iterative technique that is already available for the solution of steady flow problems) is not dissimilar in concept from the iterative techniques that use a matrix inversion as an intermediate step, except that it uses an approximate inverse (as introduced for a symmetric matrix in [3]). Generally speaking, all iterative eigenvalue algorithms have their roots in the so called "direct iteration":

$$\mathbf{x}_{k+1} = \mathbf{A}\,\mathbf{x}_k \quad ; \quad \sigma_{k+1} = \mathbf{x}_k^* \cdot \mathbf{x}_{k+1} / \left|\mathbf{x}_k\right|^2$$

which is known to converge to the largest-in-module eigenvalue σ and corresponding eigenvector $\mathbf{x}$ if there are no other eigenvalues of the same module. Direct iteration generalizes to subspace

iteration if $\mathbf{x}$ is interpreted as the orthogonal representation of a subspace of dimension n (usually much smaller that the dimension of the original problem), and σ as an $n \times n$-matrix containing the n eigenvalues of largest module. The reason why preconditioning becomes necessary is that the typical spectrum of the matrix $\mathbf{A}$ derived from the discretization of a differential problem has its physically relevant eigenvalues near zero, whereas the eigenvalues representative of discretization error are of much larger module and would be found first by a direct iteration.

The simplest preconditioning is provided by a first-order explicit discretization in time: if matrix $\mathbf{A}$ is replaced by $\mathbf{B} = 1 + \mathbf{A}\,\Delta t$, the physically relevant eigenvalues acquire a module near 1, whereas the discretization eigenvalues (which are of large negative real part unless the discretization itself is unstable) acquire a module less than 1 provided Δt stays within its numerical stability limit. On the positive side, it should be noted that unstable physical eigenvalues are no harder to determine than stable ones, and that the eigenvalues of $\mathbf{A}$ can be recovered exactly from those of $\mathbf{B}$, so that no time-discretization error is involved and higher-order schemes need not be considered. On the negative side, a small Δt slows down the convergence of the direct iteration because it reduces the distance between the subset of n computed eigenvalues and all the others, and the allowed Δt, determined by the largest eigenvalue of the discretization error, rapidly decreases with the fineness of the spatial grid.

A much faster convergence of the eigenvalue is offered by an implicit time discretization: if matrix $\mathbf{A}$ is replaced by $\mathbf{C} = (1 - \mathbf{A}\,\Delta t)^{-1}$, once again the interesting eigenvalues are pushed near 1 and the others near 0 but with a much larger separation between them. This is the shift-and-invert preconditioner that other authors have used in connection with the Arnoldi algorithm; the drawback is that the exact inversion of a very large matrix is required.

A mid ground can be struck by using an approximate inverse. Let us assume that an approximate inverse $\mathbf{C}'$ is available (this need not be stored in matrix form but can be the result of an algorithm, *e.g.* multigrid), with the property that the iteration

$$\mathbf{x}_{k+1} = \mathbf{x}_k + \mathbf{C}' \left[\mathbf{y} - (1 - \mathbf{A}\Delta t)\mathbf{x}_k\right]$$

converges to the solution $\mathbf{x}$ of the linear system $(1 - \mathbf{A}\Delta t)\mathbf{x} = \mathbf{y}$. We can then solve the eigenvalue problem for $\mathbf{C} = (1 - \mathbf{A}\,\Delta t)^{-1}$ by iteratively setting

$$\mathbf{y}_{k+1} = \mathbf{x}_k + \mathbf{C}' \left[\mathbf{y}_k - (1 - \mathbf{A}\Delta t)\mathbf{x}_k\right] \quad ; \quad \sigma_{k+1} = \mathbf{y}_k^* \cdot \mathbf{y}_{k+1} / |\mathbf{y}_k|^2 \quad ; \quad \mathbf{x}_{k+1} = \sigma_{k+1}\mathbf{y}_{k+1} \,.$$

This is the key formula used in our algorithm. It is clear that, if the iteration converges, σ_k will tend to an eigenvalue of $(1 - \mathbf{A}\,\Delta t)^{-1}$ and both $\mathbf{y}$ and $\mathbf{x}$ will become proportional to the corresponding eigenvector, no matter what $\mathbf{C}'$ is; at the same time, if $\mathbf{C}'$ were the exact inverse $\mathbf{C}$, $\mathbf{x}_k$ would cancel out and the algorithm would become identical to a direct iteration of $\mathbf{C}$.

The description has been formulated above, for the sake of simplicity, in terms of a single eigenvalue. Actually, a subspace-iteration version of this algorithm is needed in order to determine more than one eigenvalue (and necessarily when the dominant eigenvalue is a member of a complex-conjugate pair). In subspace-iteration form, σ becomes an $n \times n$-matrix and both $\mathbf{x}$ and $\mathbf{y}$ become subspace representations (arrays of n orthogonal vectors). After each step these two sets of vectors must be orthonormalized and are at the same time rotated so as to lead σ to a canonical (Schur) form.

3 Brief description of the algorithm

It should be mentioned that different techniques have been developed for the multigrid computation of eigenvalues, mostly in the context of applications to the wave equation, *e.g.* [4]. In these, generally, an eigenvalue problem is formulated at each grid level and made to converge by a local smoother, with a suitable right-hand-side correction added so as to make the solution identical across levels. By contrast here the eigenvalue and multigrid code modules are completely separate, and the action of matrix $\mathbf{C}'$ could as well be provided by any other iteration suitable for the solution of a steady flow problem. This also implies that the two code modules can be tested

independently, multigrid on the steady flow and eigenvalue iteration with a simple smoother, and that the base flow of the stability analysis can be generated by the same code simultaneously with the eigenvectors. Our present discretization is a standard Harlow-&-Welch formulation on a staggered grid, with a V-cycle and a red-black smoother applied in round-robin fashion on each velocity component and the pressure-correction equation.

Boundary conditions at the body surface are enforced by a third completely independent immersed-boundary module, which interfaces with the multigrid module only through an array of right-hand-side forcings. These r.h.s. forcings are obtained by first applying a suitable interpolation to the velocity points nearest to the boundary, and then simply equating the r.h.s to the residuals in such a way that these interpolated values will satisfy the equations exactly when all other points will, much as each multigrid level interfaces with the next coarser level.

The calculation of reaction forces and torques exerted by the fluid upon the solid body must in principle be obtained from the integration of pressure and stress over the surface, which may require rather intricate coding and tricky interpolations when the surface does not pass through grid points or contains corners. However, a much easier alternative is available when the discretization scheme conserves momentum exactly (as Harlow & Welch's does): In such a scheme the discretized surface-stress integral remains exactly constant (under steady flow) when the integration path is moved to any arbitrary boundary that completely surrounds the body, including surfaces that pass through gridpoints. In addition, this integral exactly equals the sum of residuals of the discrete equations at all grid points enclosed by this boundary, including gridpoints that fall within the body; but these are precisely the residuals that are computed by the immersed-boundary module in order to be passed to the multigrid module, so that the calculation of forces comes basically for free.

The equations of motion of the rigid body are written in an explicit time discretization and iterated upon in such a way that the time discretization error cancels out exactly at convergence.

4   Application to a freely vibrating cylinder

Whereas the stability modes of the wake of a fixed cylinder have been by now studied by a number of techniques, very little linear stability analysis seems to have been done with regard to the wake of a cylinder that is free to move. The only paper we have been able to find that confronted this specific problem (as opposed to direct numerical simulations or experiments) is the one by Cossu & Morino [5], where the cylinder was only free to move in the direction normal to the stream and was attached to a spring. Here, on the other hand, the cylinder has three degrees of freedom of in-plane motion (two of translation and one of rotation) and is free of any constraints.

To be precise, it should be noted that the cylinder is never literally free, since the base flow exerts a drag on it and an external force must be assumed to exist and balance this drag. The way this force is applied has an influence on the stability problem. In a first attempt we had just subtracted a fixed force (i.e., used the same base flow as for a fixed cylinder and introduced no force in the linearized equations); later, however, we realized that the force most likely to balance drag in reality is gravity, and that is applied in the barycenter of the moving cylinder. The motion of the barycenter implies an additional term in the angular momentum balance equation without which a fictitious instability appears.

A sample of our results is given in figure 1.

(a)

(b)
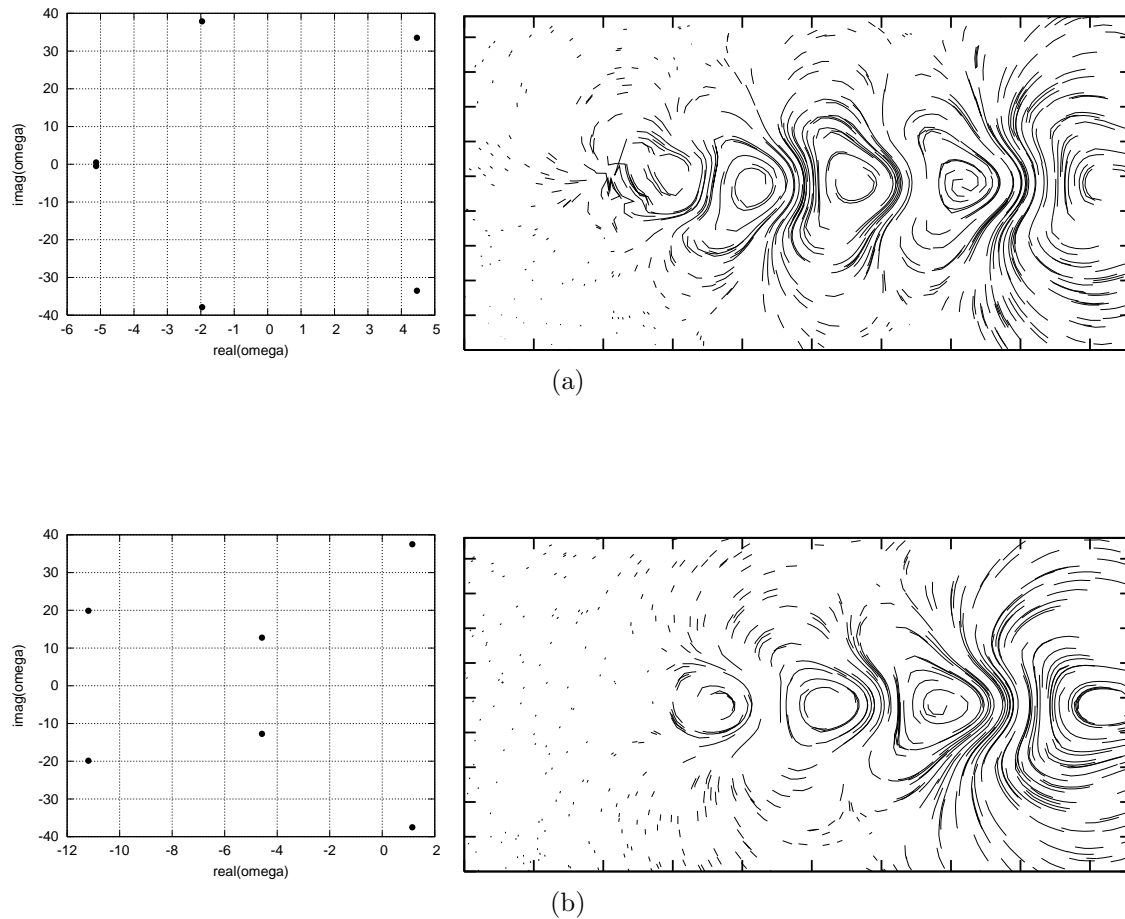
Figure 1: Spectrum and streamlines of the leading mode for a free cylinder (a) at Reynolds number 50 and density of the cylinder material equal to density of the surrounding fluid, compared to similar data for a fixed cylinder (b).

References

[1] http://www.netlib.org/lapack

[2] http://www.caam.rice.edu/software/ARPACK

[3] J. Bramble, A. Knyazev, and J. Pasciak. A subspace preconditioning algorithm for eigenvector/eigenvalue computation. Advances Comp. Math., 6:159 (1996)

[4] S. Costiner, S. Ta'asan. The algebraic multigrid projection for eigenvalue problems; backrotations and multigrid fixed points. NASA Contractor Report 194990 ICASE Report No. 94-82 Y3 f S – ntrs.nasa.gov (1994)

[5] C. Cossu, L. Morino. On the instability of a spring-mounted circular cylinder in a viscous flow at low Reynolds numbers. J. Fluids Struct. 14, 183 (2000)

The influence of constant shear over the structures developed in the wake of a circular cylinder

Marcelo de Araujo Vitola
Universidade Federal do Rio de Janeiro - LabOceano,
Parque Tecnolgico, Quadra 7, 21945-970, Rio de Janiero, RJ
`vitola@peno.coppe.ufrj.br`
Edith Beatriz Camano Schettini
, Universidade Federal do Rio Grande do Sul - PPGRHSA - IPH,
Av. Bento Gonalves, 9500 - 91501-970 - Porto Alegre, RS, Brasil
`bcamano@iph.ufrgs.br`
Jorge Hugo Silvestrini
Departamento de Engenharia Mecâ nica e Mecatrônica - PUCRS,
Av. Ipiranga, 681 - Porto Alegre, RS, Brasil
`jorgehs@pucrs.br`

Abstract: In this paper we are interested in the effect of a shear on the development of three-dimensional structures in the wake of a circular cylinder in the context of Direct Numerical Simulation (DNS). The flow was studied for Reynolds number 300 and shear parameter 0.0, 0.15 and 0.25. The incompressible Navier-Stokes equations are solved using a sixth-order compact difference schemes to evaluate the spatial derivatives, a low-storage third-order Runge-Kutta scheme for time integration and a direct partially spectral method for the pressure equation. The no-slip boundary condition at the cylinder is imposed using the immersed boundary method. The temporal evolution of spanwise enstrophy was used to evaluate the influence of shear parameter in the development of three-dimensional structures. The temporal evolution of the spanwise kinetic energy spectrum for each shear parameter was also investigated.

1 Introduction

The transition to turbulence and the wake formation behind a circular cylinder in a uniform flow has been widely investigated both experimentally and numerically due to the theoretical and practical applications. Although in some particular cases, the structures are subject to non-uniform flow. This affects the distribution of the pressure acting upon it and modifies the aerodynamic forces as the mechanism of vortex shedding. The simplest case is the free constant shear flow where the cylinder axis is parallel to the vorticity of the oncoming flow (Fig. 1).

This kind of problem has attracted research more recently, due principally the difficult of generating a constant shear flow in laboratory. Most of previous investigations that handle with this kind of flow have been developed using two-dimensional numerical simulation [10]. Only recently some experimental [9] and three-dimensional numerical simulations [11] have been developed.

In this paper we are interested in the effect of a shear on the development of three-dimensional structures in the wake of a circular cylinder in the context of Direct Numerical Simulation (DNS). The flow was studied for Reynolds number 300 and shear parameter $\beta = K/DU_c = 0.0$, 0.15 and 0.25, where $K = dU(y)/dy$ is the shear parameter, D is the diameter of the cylinder and U_c is the velocity corresponding to the location of the cylinder centre.

2 Numerical Methodology

The incompressible Navier-Stokes equations,

$$\overrightarrow{\nabla} \cdot \overrightarrow{u} = 0 \tag{1}$$

$$\frac{\partial \overrightarrow{u}}{\partial t} + \overrightarrow{\omega} \times \overrightarrow{u} = -\overrightarrow{\nabla}p + \nu\nabla^2\overrightarrow{u} + \overrightarrow{f} \tag{2}$$

were directly solved in a non-staggered uniform mesh. In this equation, $p(\overrightarrow{x}, t)$ is the modified pressure field while $\overrightarrow{u}(\overrightarrow{x}, t)$ and $\overrightarrow{\omega}(\overrightarrow{x}, t)$ are the velocity and vorticity field, respectively and $\overrightarrow{f}(\overrightarrow{x}, t)$ is an additional force included in the momentum equations to model the circular cylinder. The spatial derivatives have been evaluated using a sixth-order compact finite difference scheme, except near the inflow and outflow boundaries where single side schemes were employed for x-derivative calculation [5]. A third-order low-storage Runge-Kutta has been used for the time integration [12].

The immersed boundary method have been used to model the circular cylinder. This method consists in adding an external force to the momentum equation (Eq. 2). This approach allows the imposition of the no-slip condition at the surface of the cylinder. Various formulations have been proposed in the literature [6]. In the present, the feedback force methodology proposed by Goldstein *et al.* [2], has been adopted. This force term is given by

$$\overrightarrow{f} = \alpha \int_0^t \overrightarrow{u}(x_s, t)dt + \beta \overrightarrow{u}(x_s, t) \tag{3}$$

where α and β are negative constants. More details about the numerical code can be found in [4], and [8], and about the immersed boundary methods, can be found in [3].

The computational flow configuration is schematically showed in Fig. 1, where the cylinder axis is normal to the xy plane.
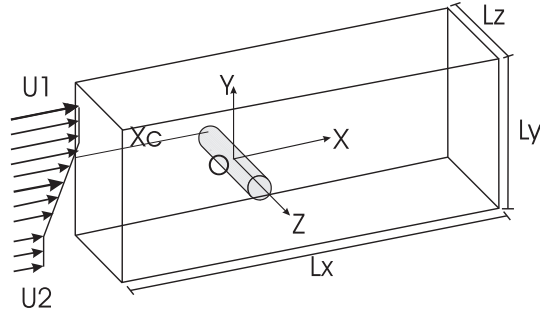

Figure 1: Schematic view of the flow configuration.

At the inflow section, a velocity profile with a constant shear, given by Eq. 4 was set

$$u(y) = \frac{U_1 + U_2}{2} + \frac{U_2 - U_1}{12} \frac{D}{L'_y} ln \left\{ \frac{cosh[\frac{6}{D}(y + \frac{L'_y}{2})]}{cosh[\frac{6}{D}(y - \frac{L'_y}{2})]} \right\} \tag{4}$$

where U_1 and U_2 is the higher and lower stream velocity, respectively, and L'_y is the width of the shear flow. At the outflow a simple advection equation is prescribed. A free-slip boundary condition is set in the transversal y-direction and a periodic condition was used for the spanwise z-direction. For all simulation the domain was of $(L_x \text{ x } L_y \text{ x } L_z) = (19D\text{x}12D\text{x}4D)$ with $(nx \text{ x } ny \text{ x } nz = 343 \text{ x } 217 \text{ x } 64)$ and the cylinder was located $8D$ from the inlet. A weak white noise ($\approx 10^{-3}$) was superposed to the three components of the inflow velocity to accelerate the transition process.

3 Results

Before study the influence of the shear on the structures developed in the wake of a free constant shear flow, intensive tests have been carried out in the uniform flow case to validate the numerical code. The profiles of mean longitudinal velocities and turbulent intensities presented in Fig. 2 are found to be in excellent agreement with the spectral DNS data of Mittal and Balachandar [7].
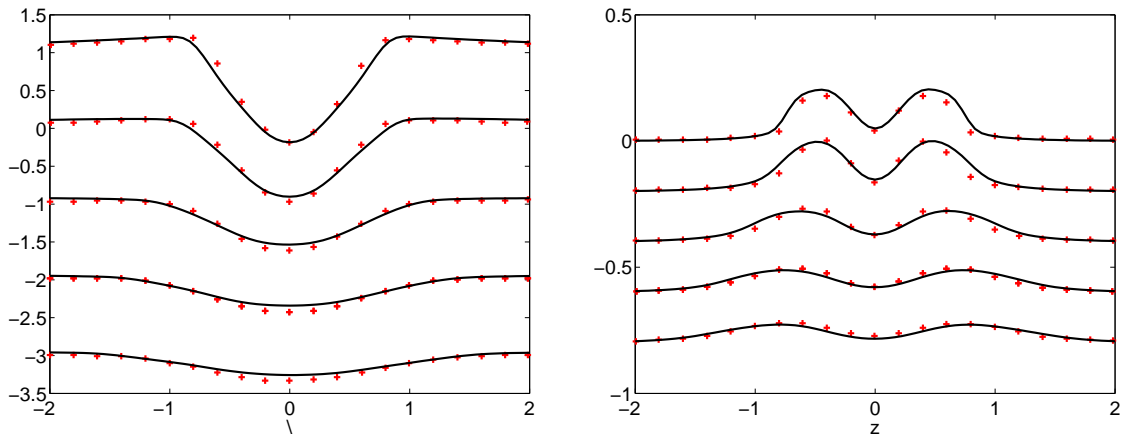
Figure 2: Mean velocity profiles at different streamwise locations $(x - x_c/D) = 1.2, 1.5, 2.0, 2.5, 3.0$ from top to bottom respectively: $-$ present results; $+$ spectral DNS.

The temporal evolution of spanwise enstrophy, defined as $Z(t) = \frac{1}{2}(||\omega_x||_2^2 + ||\omega_y||_2^2)$, was used to evaluate the influence of the shear parameter in the development of three-dimensional structures. The results obtained for the three shear parameters are presented in Fig. 3. In this figure is possible to identify a region (at $T < 20$) where the enstrophy is null, this corresponding to the two-dimensional flow. After this period the enstrophy has an exponential development (at $T \approx 20 - 50$), where the flow becomes three-dimensional structured. The results presented in the Fig. 3 indicated that the shear parameter seems to delay the exponential development of the enstrophy.

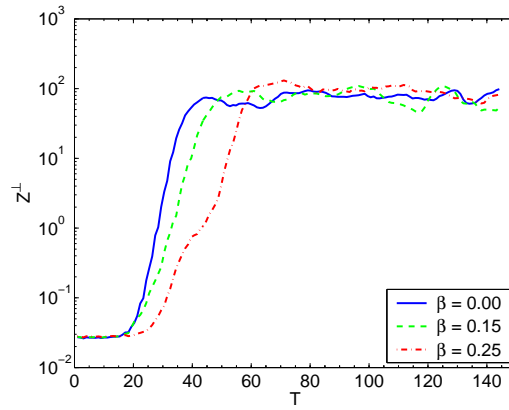Figure 3: Temporal evolution of the axial enstrophy for different shear parameter.

The temporal evolution of the spanwise kinetic energy spectrum for each shear parameter is shown in Fig. 3. The uniform case, $\beta = 0$, shows at $T = 30$ a peak for $k_z = 5$ corresponding to a spanwise wavelength $\lambda_z = 0.8$. This wavelength is very near to the value found for B-mode instability ($\lambda_z = 0.82$) using Floquet stability theory by Barkley and Henderson [1]. The results for the other shear values have shown different wavelengths selection. For the $\beta = 0.15$ case the peak value at $T = 30$ was $k_z = 3$ that is a spanwise wavelength $\lambda_z = 1.33$ while for the high shear case, $\beta = 0.25$, the spectrum indicates a concentration of kinetic energy near $k_z = 2$ corresponding to a wavelength of $\lambda_z = 2$. This results seems to induce the idea that an increasing spanwise wavelength selection is obtained when the shear parameter is augmented. Fig. 3 also shows the delay in the development of a "full" spectrum when the shear parameter is increased.
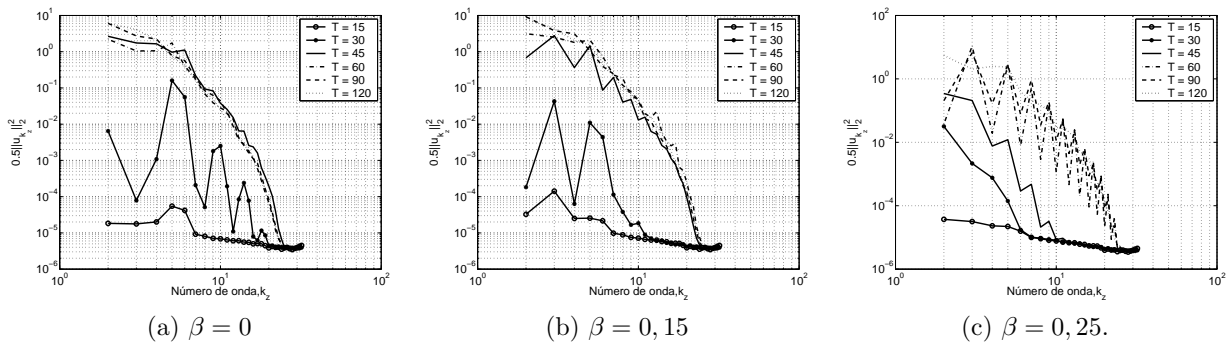

Figure 4: Axial energy spectrum for different shear parameter ($Re_D = 300$).

The distribution of the kinetic energy for a given spanwise wavelength of the spanwise energy spectrum was used to capture the structures. The results obtained for the three shear parameters are shown in Fig. 5. The upper row shows the distribution for wave number $k_z = 2$ for $\beta = 0.0$, 0.15 and $\beta = 0.25$ while the lower row indicate the concentration of energy for $k_z = 5$ for the three shear parameters. At the middle, it is shown iso-surface of Q-criterion coloured by the streamwise vorticity. For the upper row pictures, the energy is more concentrate near the vortex core. On the other hand, a intense concentration of energy in the region of the braids has been observed for $k_z = 5$. This concentration was associated with the development of the streamwise vortices.

4 Conclusions

The results seems to indicate a delay in the development of three-dimensional structures in the wake of a circular cylinder in a free constant shear flow and the increase of spanwise wavelength selection with the shear parameter augment. The energy of small spanwise wavenumber is concentrated near the vortex core while for larger wavenumber it is concentrated in the region of the breads.
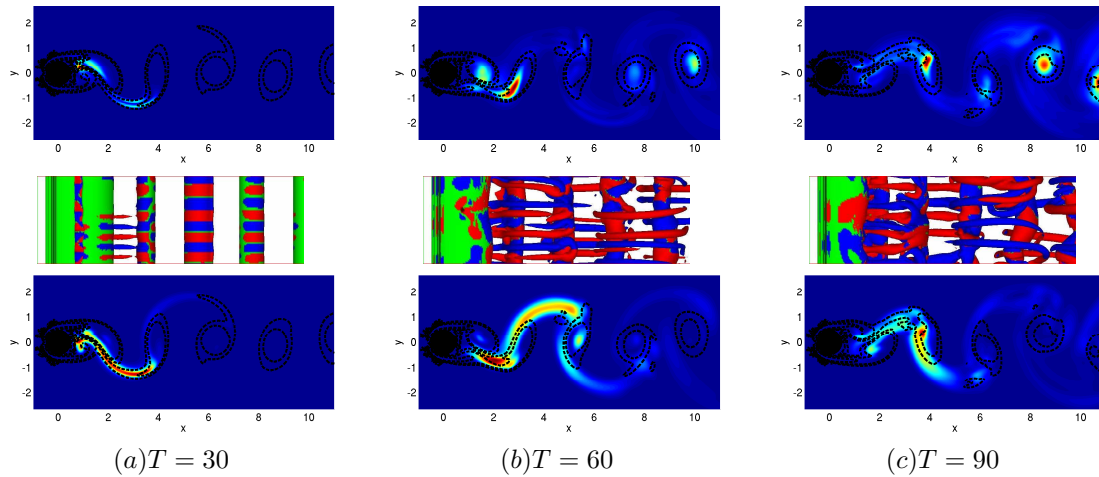
5 Acknowledgements

Figure 5: Spatial distribution of the energy for a given wavelength and three-dimensional structures ($Re_D = 300$ and $\beta = 0$ - $k_z = 2$ top; isosurface of Q middle; $k_z = 5$ bottom).

References

[1] BARKLEY, D., AND HENDERSON, R. Three dimensional floquet stability analysis of the wake of a circular cylinder. *J. Fluid Mech. 322* (1996), 215–241.

[2] GOLDSTEIN, D., HANDLER, R., AND SIROVICH, L. Modeling a no-slip boundary condition with an external force field. *J. Comp. Phys. 105* (1993), 354–366.

[3] LAMBALLAIS, E., AND SILVESTRINI, J. H. Direct numerical simulation of interactions between a mixing layer and a wake around a cylinder. *J. Turbulence 3*, 28 (2002).

[4] LARDEAU, S., LAMBALLAIS, E., AND BONNET, J. P. Direct numerical simulation of a jet controled by fluid injection. *J. Turbulence 3*, 2 (2002).

[5] LELE, S. K. Compact finite difference schemes with spectral-like resolution. *J. Comp. Phys. 103* (1992), 16–42.

[6] LINNICK, M. N., AND FASEL, H. F. A high-order immersed boundary method for unsteady incompressible flow calculations. In *41st AIAA Aerospace Science Meeting and Exhibit* (Reno, NV, Jan 6-9 2003), pp. AIAA–2003–1124.

[7] MITTAL, R., AND BALACHANDAR, S. On the inclusion of three-dimensional effects in simulation of two-dimensional bluff-body wake flows. In *Proceedings of the 1997 ASME Fluids Engineering Division Summer Meeting* (Vancouver,B.C. - Canada, June 1997), ASME, pp. 1–10.

[8] SILVESTRINI, J. H., AND LAMBALLAIS, E. Direct numerical simulation of wakes with virtual cylinders. *Int. J. Comp. Fluid Dynamics 16*, 4 (2002), 305–314.

[9] SUMNER, D., AND AKOSILE, O. O. On uniform planar shear flow around a circular cylinder at sbucritical Reynolds number. *J. Fluids Struct. 18* (2003), 441–454.

[10] VITOLA, M. A., SCHETTINI, E. B. C., AND SILVESTRINI, J. H. Uniform shear flow around a circular cylinder at sub-critical Reynolds number. In *10th The Brazilian Congress of Thermal Engineering and Sciences - ENCIT* (Rio de Janeiro, Brasil, 2004).

[11] VITOLA, M. A., SCHETTINI, E. B. C., AND SILVESTRINI, J. H. Three dimensional wake structure of free planar shear flow around a horizontal cylinder. In *6th DLES* (Poitier, France, 2006).

[12] WILLIAMSON, J. H. Low-storage Runge-Kutta schemes. *J. Comp. Phys. 35* (1980), 48–56.

Shear-layer-reattachment-induced vibration on a circular cylinder placed behind another

Md. Mahbub Alam and Y. Zhou

Department of Mechanical Engineering, The Hong Kong Polytechnic University
Hung Hom, Kowloon, Hong Kong
Email: mmalam@polyu.edu.hk, Fax: 852-23644703

Abstract: An unusual violent vibration of a circular cylinder was observed when this cylinder was placed behind another of smaller diameter. The upstream cylinder diameter d was varied from 0.24-1.00 times the diameter D of the downstream cylinder, which was cantilever-supported. Experimental observation was made at a ratio, L/d, of $1 \sim 2$, where L is the centre of the upstream cylinder to the forward stagnation point of the downstream. At this range of L/d, the shear layers separating from the upstream cylinder reattached on the downstream cylinder. The violent vibration only occurred at $d/D = 0.24 \sim 0.8$ for L/d =1 or $d/D = 0.24 \sim 0.6$ for $L/d = 2$, but not at $d/D = 1$. It is proposed that the high-speed slice of the shear layer separating from the upstream cylinder reattaches on the downstream cylinder and could flow alternately along the upper and lower body of this cylinder, thus exciting the downstream cylinder. The violent vibration occurs at a reduced velocity U_r (= U_∞/Df_n, where U_∞ is the free-stream velocity and f_n is the natural frequency of the downstream-cylinder-fluid system) $\approx 13 \sim 22.5$, depending on d/D and L/d, and increases rapidly, along with the fluctuating lift, for a higher U_r. To our knowledge, this phenomenon has not been reported previously and may have important implication in engineering applications. It is further noted that the flow behind the downstream cylinder is characterized by two predominant frequencies, corresponding to the cylinder vibration frequency and the natural frequency of vortex shedding from the downstream cylinder, respectively. While the former persists downstream, the latter vanishes rapidly.

1. Introduction

Non-linear interaction between flow around and elastic behavior of a structure may generate a high magnitude of fluctuating forces and vibration. Fluid-flow interaction on the multiple structures is very complex. Flow-induced forces, elastic response, Strouhal frequencies and flow structure generated are major parameters considered for the aerodynamic design of the structures. Thus the study of these parameters of two closely separated cylinders is of both fundamental and practical significance.

Bokaian & Geoola (1984) investigated the case of two identical cylinders where the upstream cylinder is fixed and the downstream one is both-end-spring-mounted, allowing both ends to vibrate at the same amplitude (i.e., two-dimensional model) and in the cross-flow direction only. Depending on d/D, the cylinder exhibited only galloping ($L/d = 0.59$), or only vortex resonance ($L/d > 2.5$) or a combined vortex-resonance and galloping ($L/d = 1.0$), or a separated vortex excitation (VE) and galloping ($1.5 \le L/d \le 2.5$); see Fig. 1 for the definitions of d, D and L. For both VE and galloping, vortex shedding frequency f_v was found to lock-on to vibration frequency. Note that the vibration always occurs at the natural frequency f_n of the cylinder. The VE corresponds to vibration occurring near the reduced velocity U_r (=$U_\infty/(f_nD)$, U_∞ is the free-stream velocity) where the natural vortex shedding frequency is close to f_n, and the galloping vibrations persist for higher U_r corresponding to a higher natural vortex shedding frequency than f_n. The investigated ranges of L/d and mass-damping parameter $m^*\zeta$ were 0.59~4.5 and 0.018~0.2, respectively, where m^* is the mass ratio and ζ is the damping ratio. Brika and Laneville (1997, 1999) investigated response of the downstream cylinder with the upstream cylinder stationary or vibrating, for L/d =6.5 ~ 24.5, $U_r = 4 \sim 21$ (Re =5.1×10³ ~ 2.75×10⁴). The system had a very low $m^*\zeta$ of 0.00007. When the upstream cylinder is stationary, the response of the downstream cylinder was no more hysteretic and it was strongly dependent on L/d; VE regime became wider and shifted to lower U_r with increasing L/d. For $L/d = 6.5 \sim 8$, the cylinder exhibited a combination of VE and galloping. Hover & Triantafyllou (2001) examined response of the spring-mounted downstream cylinder for $L/d = 4.25$. They observed both VE and galloping to occur when U_r was varied from 2 to 17, with changing f_n at constant U_∞ corresponding to $Re = 3.05×10^4$. Time-averaged coefficient (C_D), and fluctuating drag coefficient (C_{Drms}) were remarked to increase by about two times in the vortex-resonance and galloping regimes, but fluctuating lift (C_{Lrms}) increased in VE regime and decreased with U_r in galloping regime. A detail survey of research relating to flow-induced response of tandem cylinders suggest that previous investigations mostly were performed for (i) two cylinders of an identical diameter, (ii) two-dimensional model (spring mounted at both ends), (iii) single degree of freedom (either cross-flow or streamwise), and (iv) at a low $m^*\zeta$ value. The literatures mainly clarified L/d range where vortex-resonance or galloping persists. There does not seem to have a systematic study on flow-induced response when upstream cylinder size (diameter) is changed.

Fig. 1. (a) Experimental set-up, (b) definition of symbols

The above mentioned points raise a number of questions. Firstly, what is the effect of upstream cylinder diameter on flow-induced response of the downstream cylinder? Secondly, what would be the response of the cylinder if it is cantilevered mounted where the vibration amplitude is dependent on spawise location of the cylinder, three-dimensional model? Thirdly, is galloping or VE generated for a high value of $m^*\zeta$? Fourthly, how much forces on the structure base are induced when a structure experiences VE or galloping? Finally, what is the physics behind the generation of galloping for tandem cylinders, though galloping in general is not generated on an isolated circular cylinder (axis-symmetric body)?
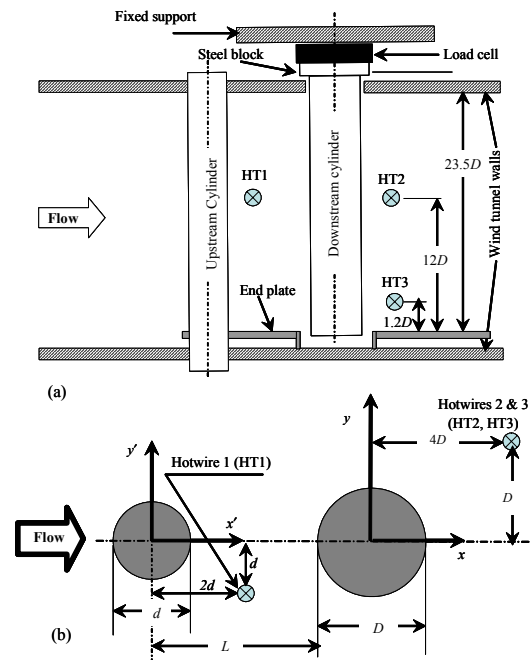
This work aims to study experimentally flow-induced response of a cantilever circular cylinder at a high $m^*\zeta$ (=3.95) value in the presence of an upstream cylinder of different diameters. The free end of the cantilever cylinder is free to move in two degrees of freedom. The upstream cylinder diameter (d) is varied, with the downstream cylinder diameter (D) unchanged, so that the ratio d/D varies from 1.0 to 0.24. Two L/d = 1.0 and 2.0 are considered, and they are within the reattachment regime. The flow-induced responses A_x and A_y in the x- and y-direction (where A stands for amplitude of vibration at the free-end of the cylinder), forces on the cylinder base C_D, C_{Drms}, C_{Lrms} and cylinder vibration frequency are systematically measured for U_r = 0.8 ~ 32. Furthermore, f_v behind the downstream cylinder and in the gap between the cylinders are examined.

2. Experimental details

Measurements were conducted in a low-speed, close-circuit wind tunnel with a 2.4-m-long test section of 0.60 m × 0.60 m. Two cylinders were mounted in tandem in the horizontal mid plane of the working section. Figure 1 shows schematically experimental setup and the definitions of coordinates (x', y') and (x, y), with the origins defined at the upstream and downstream cylinder centers, respectively. All cylinders were made of brass. The upstream cylinder of diameter d was solid and fixed-mounted at both ends, inserting through the same diameter hole of 30 mm length at the wind tunnel walls. There was no detectable flow-induced vibration on it. On the other hand, the downstream cylinder of outer diameter D = 25 mm was hollow, inner diameter 21 mm, 700 mm in length, and cantilever-mounted on an external rigid support detached from the wind-tunnel wall. To avoid further interference/complexities by cylinder free-edge vortex, an end plate was used. The free end of cylinder was just into the hole of end plates (Fig. 1a). The size of the hole on the end plate was 2D, ensuring enough clearance to allow the cylinder to undergo vibrations. The active span of the cylinder, exposed in the wind tunnel is 23.5D (587 mm). d was 25, 20, 15, 10 and 6 mm, respectively, and the corresponding d/D was 1.0 ~ 0.24, resulting in a maximum blockage of about 2.4%, and a minimum aspect ratio of 23.5. U_∞ was varied from 0.5 to 20 m/s, corresponding to variation of U_r from 0.8 to 32, Reynolds numbers (Re) of 825 to 3.3×10^4 based on the downstream cylinder.

Three tungsten wires of 5 μm in diameter and approximately 2 mm in length, one (HW1) placed at x'/d = 2, y'/d = - 1, and the other two (HT2 and HT2) placed at x/D = 4, y/D = 1. Spanwise location of HT1 and HT2 is 12D and that of HT3 is 1.2D from the free-end of the cylinder (Fig. 1a). They were used to measure the frequencies of vortex shedding from the cylinders.

A three-component strain-gauge load cell (KYOWA Model LSM-B-500NSA1), characterized by high response, resolution and stiffness, was installed at one end of the downstream cylinder to measure the fluid forces. Free end vibration displacement of the cylinder was measured by using a standard laser vibrometer.

3. Results and discussion

3.1. Rigidity, mode of vibration and f_n of the downstream cylinder

The values of $m^*\zeta$ and f_n provide information on rigidity of a structure. The cylinder corresponds to the values of $m^*\zeta$ of 3.95 and first, second and third modes natural frequency f_{n1} = 24.9, f_{n2} = 159.8 and f_{n3} = 364 Hz, respectively. Goverdhan & Williamson (2000) surveyed the literatures available to get the information on the value of $m^*\zeta$ examined. It was found that the researches were conducted mostly in the range of $m^*\zeta$ = 0.006~0.05 and few in the range 0.2~0.8. The value in the present case is substantially higher than that examined previously.

3.2. Vibration response of the cylinder

Normalized vibration amplitude A_y/D and A_x/D at L/d = 1 and 2 are shown in Figs. 2 and 3. Presently, vibration of the cylinder occurred dominantly at the first mode (f_{n1} =24.9 Hz). Hence the horizontal axis U_r is based on f_{n1}. The figures also include the data for a single isolated cylinder (d/D = 0). First at L/d = 1, violent vibration is unveiled at d/D = 0.24, 0.4, 0.6 and 0.8 for U_r > 13, 13, 19.5 and 22.5, respectively, in addition to a visible VE at around U_r = 4.75 for d/D = 0.24 and 0.4. For other d/D, a very tiny hump generated at the same U_r (see the insert of Fig. 2a) is the sign of VE, A_y/D at the hump is less than 0.003 corresponding to 0.075 mm vibration amplitude; hence, it can be said that VE is practically suppressed. Note that VE speed U_{r0} calculated from Strouhal number of the cylinder fixed at both ends was 5, 5.3, 5.12, 5.1, 4.74 and 4.58 for d/D = 0, 0.24, 0.4, 0.6, 0.8 and 1.0, respectively. It is well known that an isolated circular cylinder experiences a VE at around U_r = 5, but presently a noticeable VE is absent. This is due to fact that presently $m^*\zeta$ is remarkably high. Bokaian & Geoola (1984), at d/D = 1 and L/d = 1, observed both VE and galloping excitation for a two dimensional model restrained to oscillate in cross-flow direction only. Their experimental
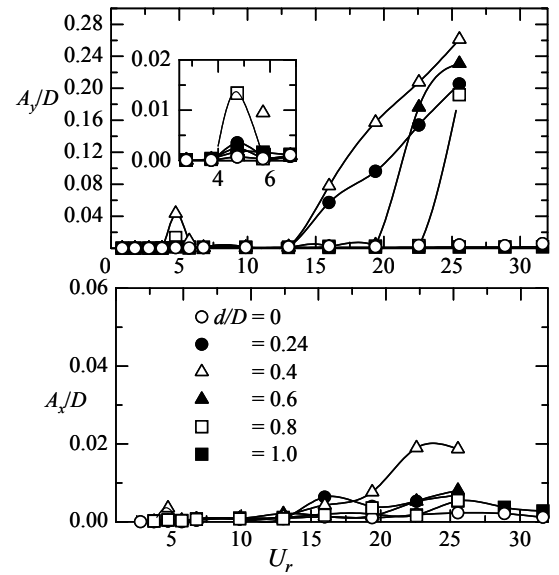

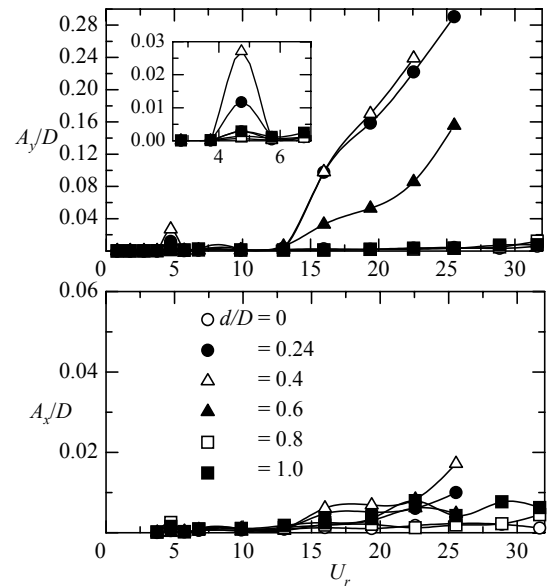Fig. 2. Normalized vibration amplitude A_y/D and A_x/D in y- and x-direction at L/d = 1.

Fig. 3. Amplitude of vibration in y- and x-direction A_y/D and A_x/D at L/d = 2.

conditions were $m^*\zeta = 0.022$, $U_{r0} = 6.1$ and $Re = 800 \sim 5800$. Vibration due to VE started at $U_r = 4.4$ and reached to a maximum at $U_r = 7.54$. On the other hand, the galloping occurred for $U_r > 11.3$. But presently the absence of the vibration (galloping) for $d/D = 1$ could be attributed to either the higher value of $m^*\zeta$ or three-dimensional model or two-degree of freedom, or combination of these. For the vibration generated cases $d/D = 0.24 \sim 0.8$, the starting U_r of vibration generation is lower for lower d/D, implying that a decreasing d/D anyhow causes a higher instability of flow and/or an increase of negative damping on the cylinder. Fig. 2(b) reveals that A_x/D is very small compared to A_y/D, except for $d/D = 0.4$, $U_r > 20$. At $L/d = 2$ (Fig. 3), vibration in cross-flow direction is generated at $d/D = 0.24 \sim 0.6$ for $U_r > 13$, this d/D range is smaller than that at $L/d = 1$. Furthermore, VE is observed for $d/D = 0.24$ and 0.4 and almost suppressed for other d/D. Hence it can be conferred that a cantilevered cylinder submerged in the wake of another may experience catastrophic vibration in the cross-flow direction. In addition, a decreasing d/D is prone to generate violent vibration, which is reverse in the sense that a small cylinder placed upstream of a large cylinder may weaken forces on and vortex shedding from the large cylinder (Lesage and Gartshore 1987; Strykowski and Sreenivasan 1990).

3.3. Forces generated in the base of the cylinder

Figure 4 show variation of C_D, C_{Drms} and C_{Lrms} with U_r at $L/d = 1$. It is observed that C_D is slightly dependent on U_r for $d/D = 0.24 \sim 1.0$, but not for a single isolated cylinder $d/D = 0$. C_D for $d/D = 0$ is about 1.22 which is close to the well-known value 1.2. Increase in d/D from 0 to 0.8 causes a reduction in C_D, by $10 \sim 13\%$, $14 \sim 24\%$, $70 \sim 75\%$ and $90 \sim 98\%$ for $d/D = 0.24$, 0.4, 0.6 and 0.8, respectively, the counterpart is that for $d/D = 0$. However, for $d/D = 1$, C_D is negative, about -0.5. At the same L/d and d/D, Biermann & Herrnstein (1933), Zdravkovich & Pridden (1977) and Alam et al. (2003) observed C_D of -0.45 ($Re = 6.5 \times 10^4$), -0.53 ($Re = 3.1 \times 10^4$) and -0.42 ($Re = 6.5 \times 10^4$), respectively, consistent with our result. On other hand, C_{Drms} and C_{Lrms} are highly sensitive to U_r for $d/D = 0.24 \sim 0.8$, but less for $d/D = 0$ and 1.0. For $d/D = 0$, they are more or less constant at about 0.11 and 0.23, respectively for $U_r < 25$. It could be noted that these values are the same as those measured for both ends fixed. They however increase slightly for $U_r > 25$. This is due to synchronization of f_v with f_{n2}. Note that the value of U_r corresponding to

Fig. 4. Time-averaged drag (C_D), rms lift (C_{Lrms}) and rms drag (C_{Drms}) forces at $L/d = 1$.

f_v synchronization at f_{n2} is 32, estimated from Strouhal number. The most important feature in the figure is that C_{Lrms} for $d/D = 0.24$, 0.4, 0.6 and 0.8 launches to intensify itself at $U_r = 13$, 13, 19.5 and 22.5, respectively, where vibration starts to occur. At $U_r = 25.5$, where A_y/D is about 0.23, 0.26, 0.205 and 0.192 for $d/D = 0.24$, 0.4, 0.6 and 0.8, respectively, C_{Lrms} intensified by 48, 78, 57 and 45 times, respectively, compared with that for $d/D = 0$ or for a fixed cylinder. C_{Drms} is quite low even in the high-amplitude vibration regime, confirming vibration generated dominantly in the cross-flow direction. Similar observation is made at $L/d = 2$ (not shown).

3.4. Wake of the cylinder

Figure 5 shows f_v/f_{n1} at $L/d = 1$ where f_v was obtained from power spectral analysis of HW2 signal. As we see, f_v/f_{n1} closes to 1 at about $U_r = 4.75$, consistent with the existent of a small peak at the same U_r in A_y/D-U_r and C_{Lrms}-U_r plots (Figs. 2 and 4). At $d/D = 0$, f_v/f_{n1} increases linearly and reaches $f_v/f_{n2} = 1$ at $U_r = 32$, confirming an increased C_{Lrms} at $U_r = 32$ due to frequency resonance at f_{n2}, as discussed in the earlier section. f_v/f_{n1} for other d/D also climbs monotonically except for $d/D = 1$ which

displayed a sudden drop between $U_r = 22.6$ and 25.5, marked by a dashed line. Note that f_v/f_{n1} for this d/D corresponds to Strouhal number of about 0.2 for $U_r \leq 22.6$ ($Re = 2.34 \times 10^4$) and 0.14 for $U_r \geq 25.5$ ($Re = 2.65 \times 10^4$). A deep observation made on the power spectrum results (not shown) at these two U_r explored that (i) at $U_r = 22.6$ power spectrum of HW1 signal did not display any peak, however that of HW2 signal displayed small peak at vortex shedding frequency, and (ii) at $U_r = 25.5$ each power spectrum of HW1 and HW2 signals displayed quite strong peak at vortex shedding frequency. These points direct that the two shear layers emanating from the upstream cylinder reattach steadily on the downstream cylinder for $U_r \leq 22.6$, and those reattach alternately for $U_r \geq 25.5$. At $d/D = 0.24$, 0.4, 0.6 and 0.8 for $U_r \geq 16$, 16, 19.5 and 22.5, respectively where vibration is generated, another frequency at $f_v/f_{n1} = 1$ was observed as presented in the figure. The existence of this frequency in the power spectra (not shown) may result from either large scale vortex shedding at f_{n1} or perturbation by the cylinder vibration. An interesting point may be here that which frequency persists as the vortices go downstream. In order to reveal it we traversed HW2 and HW3 up to $x/D = 50$, results suggest that as x/D increases the peak at the $f_v/f_{n1} = 1$ persists and the other decays quickly.
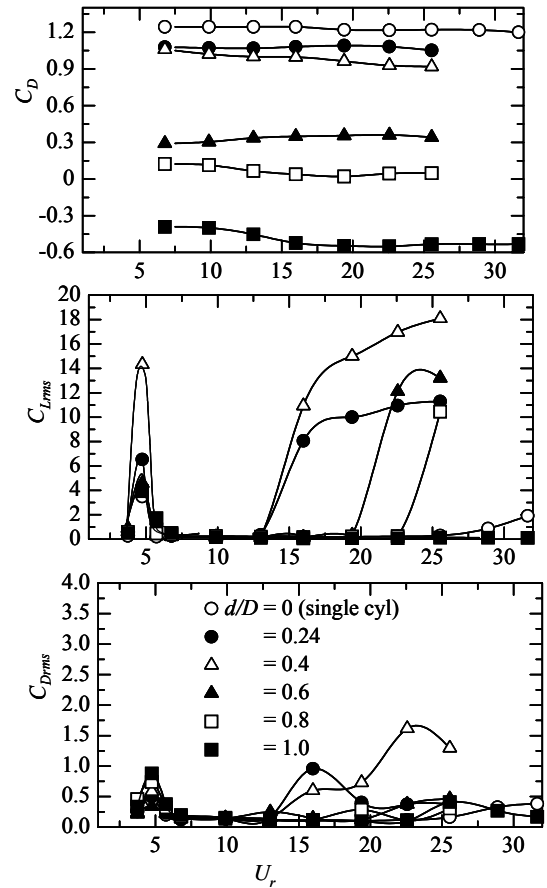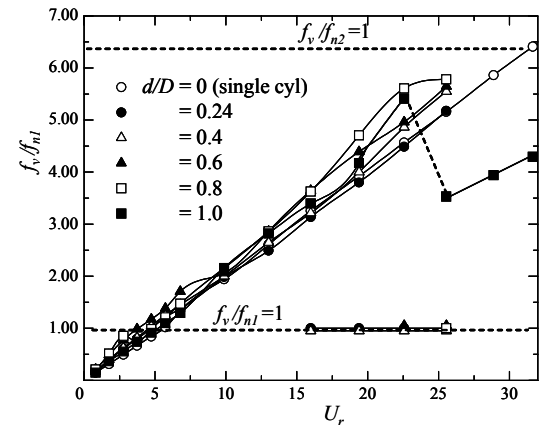

Fig. 5. Variation of f_v/f_{n1} at $L/d = 1$.

3.5. Mechanism of vibration generation

For fixed cylinders (Fig. 6a), the two shear layers emanating from the upstream cylinder reattach steadily on the downstream cylinder. The thickness of a shear layer can be divided into three slices: highly turbulent slice, high velocity middle slice and outer slice close to the free-stream. As we are going to propose, the vibration for two tandem cylinders mainly results from the switching instability of the shear layers originated from the upstream cylinder, sketched in Fig. 6. The switching instability is generated from whether the high velocity slice of a shear layer passes on the same side or opposite side of the downstream cylinder. The high velocity slice generates highly negative pressure on the surface over which it goes. Now let us discuss the flow phenomena on the vibrating downstream cylinder. When the cylinder is moving upward from its centerline (Fig. 6b), the high velocity slice of the upper shear layer goes on the upper side and causes an upward lift force to pull the cylinder upward. On the other hand, when the cylinder is moving down (Fig. 6c), toward the centerline, the high velocity slice of the same shear layer sweeps the lower side; hence a downward lift force is generated to pull the cylinder toward the centerline. Similarly, the next half cycle is associated with the lower shear layer. The vibration may be termed as shear-layer-reattachment-induced vibration. Previous sections proved that a smaller d/D is more prone to generate vibration. Why? As d/D tends to be small, the upstream cylinder wake narrows, and the shear-layer reattachment position on the downstream cylinder moves to the front stagnation point. Hence the shear layer is more prone to switch and results in the vibration. If the upstream cylinder is larger than the downstream one, i.e., $d/D > 1$, the upstream wake becomes wider, the shear layers get stability to pass over the respective side of the downstream cylinder, hence no vibration generation. Lam and To (2003) performed experimental investigation for $d/D = 2$ and observed no vibration.

Fig. 6. Flow structure generating galloping. (a) No vibration. For a given displacement, (b) the cylinder moving upward, (c) the cylinder moving downward.

4. Conclusions

A detailed investigation on flow-induced forces, vibration characteristics and vortex shedding frequency of a cantilevered circular cylinder in the presence of an upstream cylinder of different diameters is performed. The flow is in the reattachment regime ($L/d = 1$ and 2); the diameter ratio d/D is varied from 1 to 0.24. The cylinder system had a high value of $m^*\zeta = 3.95$. The preliminary investigation leads to following conclusions.

(i)   A lateral violent vibration on the downstream cylinder occurs at $d/D = 0.24\sim0.8$ for $L/d = 1$ and at $d/D = 0.24\sim0.6$ for $L/d = 2$, with the vibration amplitude reaching about $0.2D$. Decreasing d/D is prone to generate vibration. Meanwhile, C_{Lrms} is greatly amplified, increasing by a factor of more than 40 at $U_r = 25.5$. Compared with that for $d/D = 0$ or for a fixed cylinder, C_{Lrms} increases

(ii) Two predominant frequencies of vortices were identified, associated with natural vortex shedding and the vibration of the downstream cylinder, respectively. While the vortices associated with the natural vortex shedding frequency decay rapidly and those associated with the vibration frequency persist.

(iii) A possible mechanism is proposed. The shear layer separating from the upstream cylinder reattaches on the downstream cylinder. At a small d/D, the upstream cylinder wake narrows, and the shear-layer reattachment position on the downstream cylinder approaches the front stagnation point, and hence the high-speed slice of the shear layer could flow alternately along the two different sides of this cylinder, thus exciting the downstream cylinder.

References

Alam, M.M, Moriya, M., Takai, K., Sakamoto, H., 2003. Fluctuating fluid forces acting on two circular cylinders in a tandem arrangement at a subcritical Reynolds number. *J. Wind Eng. Ind. Aerodyn.* 91, 139-154.

Biermann, D., Herrnstein, Jr., 1933. The interference between struts in various combinations. *National Advisory Committee for Aeronautics*, Tech. Rep. 468.

Blevins, R.D., 1990. Flow-Induced Vibrations, second ed. Van Nostrand Reinhold, New York.

Bokaian, A., Geoola, F., 1984. Wake-induced galloping of two interfering circular cylinder. *J. Fluid Mech.* 146, 383-415.

Brika, D., Laneville, A., 1997. Vortex-induced oscillations of two flexible circular cylinders coupled mechanically, J. Wind Ind. Aerodyn. 69-71, 293-302.

Brika, D., Laneville, A., 1999. The flow interaction between a stationery cylinder and a downstream flexible cylinder. *J. Fluids Struc.* 13, 579-606.

Den Hartog, J.P. 1956 Mechanical Vibrations, forth ed. McGraw-Hill, New York.

Govardan, R., Williamson, C. H. K., 2000. Modes of vortex formation and frequency response of a freely vibrating cylinder. *J. Fluid Mech.* 420, 85-130.

Lam, K.M., To, A.P., 2003. Interference effect of an upstream larger cylinder on the lock-in vibration of a flexibly mounted circular cylinder. *J. Fluids Struc.* 17, 1059-1078.

Lesage, F., Gartshore, I.S., 1987. A method of reducing drag and fluctuating side force on bluff bodies. J. Wind Eng. Ind. Aerodyn. 25, 229-245.

Zdravkovich, M. M., Pridden, D.L., 1977. Interference between two circular cylinders; series of unexpected discontinuities. *J. of Ind. Aerodyn.* 2, 255-270.
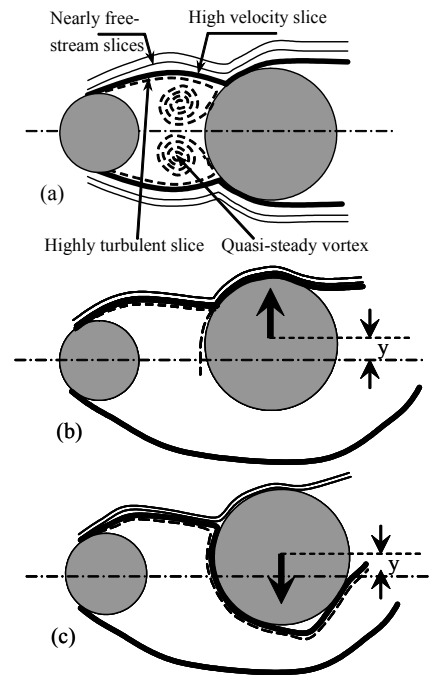
NUMERICAL SIMULATION OF THE FLOW-INDUCED VIBRATION IN THE FLOW AROUND TWO CIRCULAR CYLINDERS IN TANDEM ARRANGEMENTS

Bruno S. Carmo*, Spencer J. Sherwin, Peter W. Bearman and Richard H. J. Willden

Department of Aeronautics, Imperial College London, UK

* contact e-mail address: b.carmo@imperial.ac.uk

Abstract – Numerical simulations of the flow around two circular cylinders in tandem arrangements are performed. The upstream cylinder is fixed and the downstream cylinder is free to oscillate in the transverse direction, in response to the fluid loads. The in-line centre-to-centre distance is varied from 3.0 to 8.0 diameters, and the results are compared to that of a single isolated flexible cylinder with the same structural characteristics, $m^* = 2.0$ and $\zeta = 0.007$. Preliminary calculations show that significant changes occur in the dynamic behaviour of the cylinders, when comparing a tandem arrangement to the isolated cylinder case.

INTRODUCTION

The flow-induced vibration of cylindrical structures is a key issue in engineering, due to the numerous situations where this type of geometry is used in structures immersed in fluid streams. In many engineering environments it is also common to have multiple cylinders arrangements; transmission lines and riser pipes are typical examples. When two or more bodies are placed in close proximity, the flow field, fluid forces and, consequently, structural response can change completely, and such phenomena are called flow interference. Structures are usually designed to operate under specific limits of vibration, thus knowledge of their flow-induced vibration under flow interference conditions is crucial.

When two fixed identical circular cylinders in tandem arrangement are considered, it is found that the downstream body experiences cross-stream lift forces dramatically higher than those of an isolated cylinder (Mahbub Alam *et al.*, 2003; Carmo, 2005). This is due of the vortex street impinging on the body. To understand how the wake interacts with the body if it is elastically supported, it is reasonable to choose a configuration where this interaction is kept as isolated as possible. An appropriate choice is the flow around a circular cylinder mounted on an elastic basis, allowed to move only in the transverse direction, immersed in the wake of an upstream fixed circular cylinder of the same diameter.

Few papers have been published on the flow-induced vibration of this configuration. Bokaian & Geoola (1984) carried out a series of water channel experiments and reported that, depending on the cylinders' separation and structural damping, the downstream cylinder exhibited vortex-resonance and/or galloping. Brika & Laneville (1999) performed wind tunnel experiments also on a cylinder free to vibrate in the wake of an upstream fixed cylinder. When comparing to the single cylinder case, their main findings were that the dynamic response of the downstream cylinder is not hysteretic, the onset of synchronisation occurs at higher reduced velocities and the synchronisation range is wider. Hover & Triantafyllou (2001) conducted experiments in a water channel, for a tandem configuration with centre-to-centre spacing, L_x/D, of 4.75. They reported that frequency lock-in occurred at a low reduced velocity and persists until a reduced velocity of 17 and that the phase change, which typically occurs for an isolated cylinder at a reduced velocity of around 6, occurred at higher flow speeds. More recently, Assi *et al.* (2006) have presented experimental results for low mass-ratio cases and reported that in some cases the amplitude of transverse vibration of the downstream cylinder could be up to 50% higher than that of an isolated cylinder with the same structural parameters and subjected to the same flow conditions. Numerical investigations have previously addressed the problem of the fluid-structure interaction of tandem arrangements (Jester & Kallinderis, 2004; Mittal & Kumar, 2001), but these studies have not addressed the case of a freely vibrating downstream cylinder in the wake of an upstream fixed cylinder.

Computational simulations allow for detailed investigation of the flow field, being extremely useful to understanding the physics of fluid mechanics phenomena. Nevertheless, to our knowledge, no paper using this tool to analyse the flow interaction between a stationary cylinder and a downstream flexible cylinder has been published to date. In the present work, two and three-dimensional numerical simulations are being carried out to investigate this particular case of fluid-structure interaction. We focus on the results of oscillation amplitude and frequency, vortex shedding frequency and phase angle and propose a physical mechanism to explain the observed phenomena.

METHODOLOGY

The incompressible fluid flow was simulated by evolving the incompressible Navier-Stokes equations, which were discretized using the high accuracy Spectral/hp element method (Karniadakis & Sherwin, 2005). Specifically for the three-dimensional simulations, a Fourier expansion will be used in the spanwise direction (Karniadakis, 1990). A stiffly stable time splitting scheme (Karniadakis *et al.*, 1991) was used to advance the solution
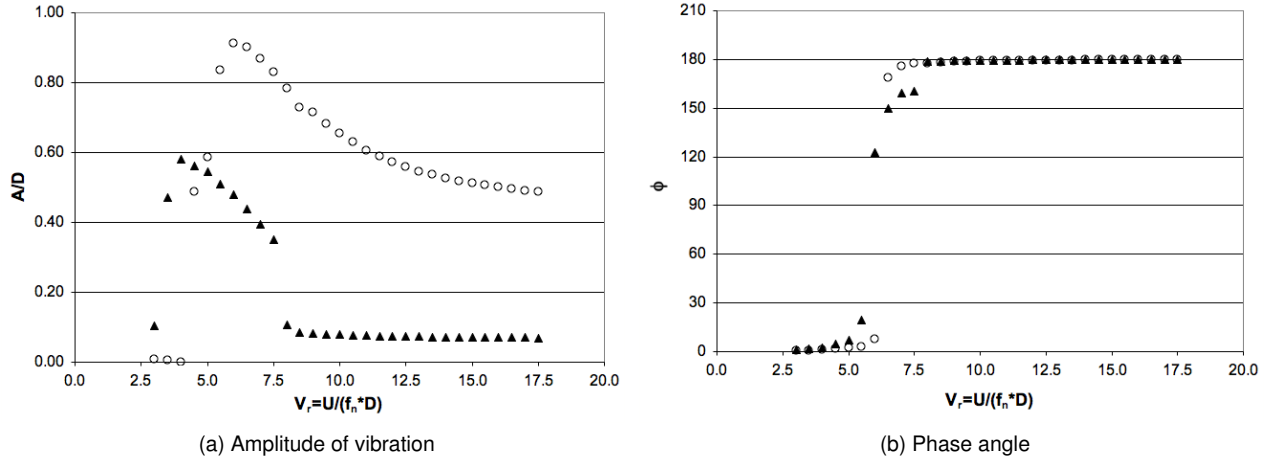
(a) Amplitude of vibration

(b) Phase angle

Figure 1: (a) Amplitude of vibration and (b) phase angle as functions of V_r; ▲ - isolated cylinder, ○ - tandem arrangement, $L_x = 3.0D$. Two-dimensional simulations, $Re = 150$.

in time. Because the two cylinders have non-zero relative displacement in time, the method had to comply with domain deformation. Therefore, an Arbitrary Lagrangean-Eulerean (ALE) scheme was incorporated into the code. Following Batina (1990), the mesh was adapted to the boundary displacement in every time step by modelling each mesh element edge by a spring with stiffness inversely proportional to its length. The mesh movement was coupled to the time splitting scheme in a similar fashion as detailed in Beskok & Warburton (2001).

The dynamics of the downstream cylinder were modelled as a uni-dimensional linear mass-spring-damper system. The cylinder was able to move in the transverse direction only. The structural equation was integrated using Newmark's scheme (Newmark, 1959) and was loosely coupled to the time stepping scheme of the flow solver (Jester & Kallinderis, 2004).

NUMERICAL SIMULATIONS

Two and three-dimensional numerical simulations will be performed for a single flexible circular cylinder and for two circular cylinders with diameter D in tandem configurations with $L_x/D = 3.0, 5.0$ and 8.0, where L_x is the in-line centre-to-centre distance between the cylinders. For the tandem arrangements, the upstream cylinder is stationary and the downstream cylinder is mounted on an elastic basis and allowed to move in the cross-stream direction y. The structural parameters used for the downstream cylinder are $m^* = 2.0$ and $\zeta = 0.007$, matching the parameters of some of the experiments performed by Assi *et al.* (2006). The reduced velocity, V_r, where $V_r \equiv U_\infty/(D f_n)$, U_∞ is the free stream speed and f_n is the natural frequency of the structure in vacuum, will be varied from 3.0 to 30.0, and the Reynolds numbers (Re) tested will be fixed at 150 for the two-dimensional simulations and 300 for the three-dimensional simulations.

PRELIMINARY RESULTS AND DISCUSSION

Figures 1 and 2 show preliminary results obtained from two-dimensional simulations ($Re = 150$), for an isolated cylinder and for cylinders in tandem with $L_x = 3.0D$ and V_r varying from 3.0 to 17.5. For each flow velocity, we start the flow simulation with the cylinders fixed, and then, once a periodic wake has been established, release the downstream cylinder to respond freely in the transverse direction.

The difference in the dynamical behaviour of the two cases can clearly be seen in figure 1a. While the isolated cylinder responded with high amplitudes for a limited range of reduced velocities ($3.5 \le V_r \le 7.5$), the tandem arrangement exhibited significant amplitudes of vibration from $V_r = 4.5$ to the end of the range of V_r investigated. The peak amplitudes were also very different; the maximum value for the tandem arrangement is approximately 50% higher than the maximum value for the isolated cylinder. The reduced velocity for which the peak amplitude was observed was also different in each of the cases. The increase in reduced velocity for the tandem case may be caused by the deceleration the flow experiences in the region between the upstream and the downstream cylinders.

Figure 1b displays the variation of the phase angle ϕ, being the phase angle by which the the lift force leads the displacement. Comparing figures 1a and 1b, it can be seen that for the single cylinder case the range of V_r for which there is high amplitude response corresponds to the range where the phase angle changes from approximately $0°$ to approximately $180°$. For the tandem cylinder case, once the phase change has occurred and ϕ stabilises in a value close to $180°$, the amplitude of vibration does not exhibit an abrupt decrease, as

(a) Single cylinder

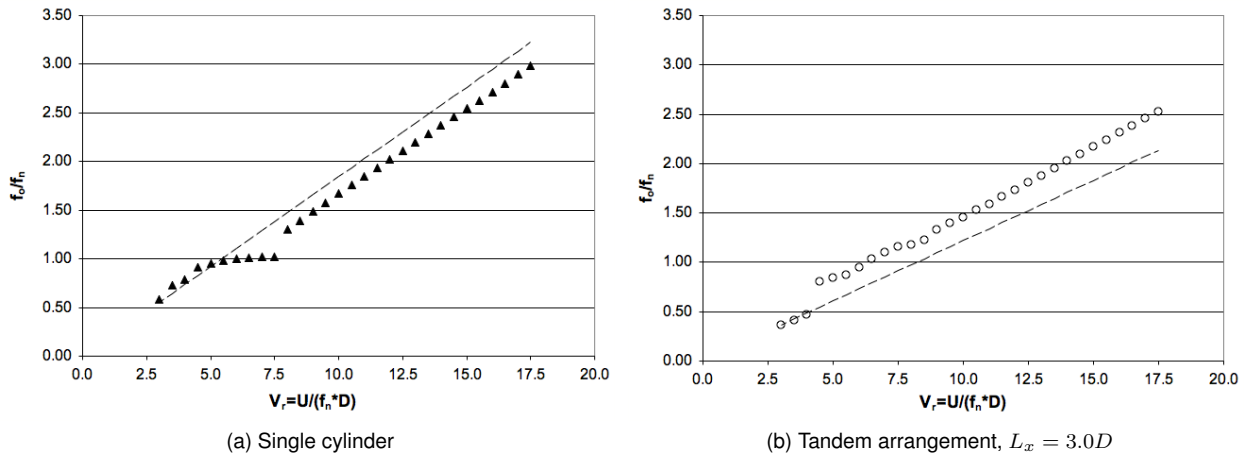

(b) Tandem arrangement, $L_x = 3.0D$

Figure 2: Ratio between the oscillation frequency (f_o) and the natural frequency (f_n) plotted against V_r. The dashed lines denote the ratios between the Strouhal frequency for fixed configurations and the structural natural frequency in vacuum of the elastic base.
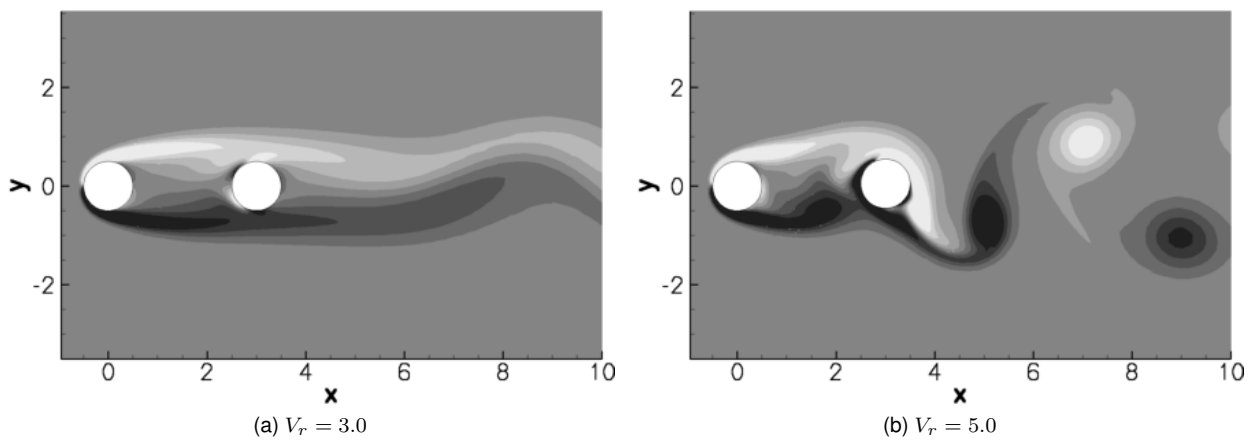

(a) $V_r = 3.0$

(b) $V_r = 5.0$

Figure 3: Instantaneous vorticity contours for tandem arrangements, $L_x = 3.0D$. Dark contours represent positive vorticity and light contours represent negative vorticity.

observed in the single cylinder case, but shows a steady smooth decrease with increasing V_r instead.

Plots of the response frequency are shown in figure 2. For the single cylinder case, figure 2a, the significant amplitude lock-in region can be clearly identified, as the frequency of oscillation locks to a value close to f_n for $3.5 \leq V_r \leq 7.5$. Of note is the fact that the amplitude of vibration is high for this range. For $V_r \geq 8.0$ the oscillation frequency graph is a straight line with roughly the same slope of the Strouhal line. However, the maplitude of vibration is very low, $A/D \leq 0.1$. On the other hand, the tandem arrangement does not exhibit the lock-in plateau, as can be seen in figure 2b. The oscillation frequency follows the Strouhal curve for $V_r \leq 4.0$, and there is a jump of frequency for $4.0 \leq V_r \leq 4.5$. After this jump, the frequency is always higher than the Strouhal frequency and the graph of f_o/f_n has a different slope than the Strouhal curve.

The reason for the jump in the phase observed in figure 2b can be discerned from the visualisation in figure 3. For $V_r \leq 4.0$, the shear layers that separate from the surface of the upstream cylinder do not roll up to form vortices before reaching the downstream cylinder, and the wake resulting from this vortex shedding regime is formed only far downstream, as can be seen in figure 3a. For these low values of V_r, the mean drag coefficient of the downstream cylinder is negative. As V_r is further increased, the initial impulse given to the cylinder by instantaneously releasing it is able to sufficiently displace the cylinder so as to make the vortex shedding regime change, and the shear layers originating from the upstream cylinder roll up in the region between the cylinders, as can be seen in figure 3b. This change of regime completely alters the values of the integral quantities of the flow (Carmo, 2005). For example, the mean drag coefficient becomes positive, and the Strouhal number becomes higher, as seen in the change of slope of the data points in figure 2b.

The high amplitudes observed for the tandem arrangement at high V_r are not due to a resonant phenomenon, as can be inferred from the frequency variation displayed in figure 2b. In fact, there were some striking similarities between the single cylinder configuration and the tandem arrangement at high V_r. First of all, the phase angle was very close to $180°$, second, the body vibrated at the same frequency as the vortices

were shed. However, there are two key changes. The first was the value of the amplitude of the lift coefficient C_L. For the tandem arrangement, the RMS value of the force imposed on the downstream body was roughly 5 times higher than the force imposed on the isolated cylinder for the same V_r, for $V_r \geq 8.0$. This difference is not an exclusive feature of configurations with flexible cylinders; a systematic difference between the RMS of the lift coefficients on the downstream cylinder of tandem arrangements and an isolated cylinder was also observed for fixed configurations at various Re in Carmo (2005). This difference was attributed to the vortices impinging upon the downstream cylinder and also to the high fluctuation of the position of the stagnation point on the same cylinder, due to the presence of oscillatory flow in the interstitial region. As the amplitude of vibration is directly proportional to the force applied, it seems reasonable that this difference in C_L accounts for a significant part of the difference between the amplitudes shown in figure 1a. The second change is a small difference in the phase angle when comparing the tandem arrangement with the isolated cylinder. Considering the model of a mass-spring-damped system subjected to a harmonic force, it can be shown that the amplitude of vibration is directly proportional to the sine of the phase angle Sarpkaya (2004). Since the value of ϕ is very close to $180°$, a small variation in ϕ results in a considerable change in the amplitude. Typically, for $V_r \geq 8.0$, ϕ for the tandem arrangement was $0.1°$ less than that for the isolated cylinder, and the effect of this difference is to increase the excitation force, being the component of C_L in phase with the body velocity.

The results presented here do not indicate the presence of the wake-galloping mechanism (Bokaian & Geoola, 1984). When this mechanism is present, experiments show that A/D increases with V_r (Assi *et al.*, 2006; Bokaian & Geoola, 1984) and the frequency of oscillation is typically not synchronised with the shedding frequency. Experimental results showed that the wake-galloping can be observed for a tandem arrangement with $L_x = 3.0D$ with equivalent structural parameters (Assi *et al.*, 2006). The most likely causes for the discrepancies between the results presented here and those experiments are the difference in Re and the presence of three-dimensional effects. These points are being presently addressed and will be contemplated in the presentation, together with the analysis of tandem arrangements with $L_x = 5.0D$ and $L_x = 8.0D$.

References

ASSI, G. R. S., MENEGHINI, J. R., ARANHA, J. A. P., BEARMAN, P. W. & CASAPRIMA, E. 2006 Experimental investigation of flow-induced vibration interference between two circular cylinders. *Journal of Fluids and Structures* **22**, 819–827.

BATINA, J. T. 1990 Unsteady euler airfoil solutions using unstructured dynamic meshes. *AIAA Journal* **28** (8), 1381–1388.

BESKOK, A. & WARBURTON, T. C. 2001 An unstructured hp finite-element scheme for fluid flow and heat transfer in moving domains. *Journal of Computational Physics* **174**, 492–509.

BOKAIAN, A. & GEOOLA, F. 1984 Wake-induced galloping of two interfering circular cylinders. *Journal of Fluid Mechanics* **146**, 383–415.

BRIKA, D. & LANEVILLE, A. 1999 The flow interaction between a stationary cylinder and a downstream flexible cylinder. *Journal of Fluids and Structures* **13**, 579–606.

CARMO, B. S. 2005 Numerical investigation of the flow around two cylinders in tandem arrangements. Msc dissertation, Escola Politécnica - University of São Paulo, Brazil.

HOVER, F. S. & TRIANTAFYLLOU, M. S. 2001 Galloping response of a cylinder with upstream wake interference. *Journal of Fluids and Structures* **15**, 503–512.

JESTER, W. & KALLINDERIS, Y. 2004 Numerical study of incompressible flow about transversely oscillating cylinder pairs. *Journal of Offshore Mechanics and Arctic Engineering - Transactions of the ASME* **126**, 310–317.

KARNIADAKIS, G. E. 1990 Spectral element-fourier methods for incompressible turbulent flows. *Computer Methods in Applied Mechanics and Engineering* **80**, 367–380.

KARNIADAKIS, G. E., ISRAELI, M. & ORSZAG, S. A. 1991 High-order splitting methods for the incompressible navier-stokes equations. *Journal of Computational Physics* **97**, 414–443.

KARNIADAKIS, G. E. & SHERWIN, S. J. 2005 *Spectral/hp Element Methods for Computational Fluid Dynamics*, 2nd edn. Oxford University Press.

MAHBUB ALAM, MD., MORIYA, M., TAKAI, K. & SAKAMOTO, H. 2003 Fluctuating fluid forces acting on two circular cylinders in a tandem arrangement at a subcritical reynolds number. *Journal of Wind Engineering and Industrial Aerodynamics* **91**, 139–154.

MITTAL, S. & KUMAR, V. 2001 Flow-induced oscillations of two cylinders in tandem and staggered arrangements. *Journal of Fluids and Structures* **15**, 717–736.

NEWMARK, N. M. 1959 A method of computation for structural dynamics. *Journal of the Engineering Mechanics Division of ASCE* **85**, 67–94.

SARPKAYA, T. 2004 A critical review of the intrinsic nature of vortex-induced vibrations. *Journal of Fluids and Structures* **19**, 389–447.

VIV of two circular cylinders in tandem arrangement at low Re

T.K. Prasanth, S. Mittal

Department of Aerospace Engineering
Indian Institute of Technology Kanpur, UP 208 016, India
Email: smittal@iitk.ac.in, Phone: +91 512 597906, Fax: +91 512 597561

Abstract

Results are presented for the vortex-induced vibrations (VIV) of a pair of equal-sized circular cylinders of low non-dimensional mass ($m^* = 10$) in tandem arrangement. The computations are carried out for various values of structural frequencies of the oscillator ($2 < U^* < 15$) at $Re = 100$ using a stabilized space-time finite element formulation. In this study, the downstream cylinder lies in the wake of the upstream cylinder and, therefore, experiences an unsteady in-flow. The transverse response of the upstream cylinder is found to be qualitatively similar to that of a single cylinder. The downstream cylinder undergoes large amplitude oscillations when compared to the upstream one. Lock-in behavior is observed for both the cylinders. The response of, both, upstream and downstream cylinders are hysteretic for certain U^* values. In general, the vortex shedding pattern observed is *2S* and *C(2S)*. In the far wake the vortex street degenerates to a lower frequency mode. The location of the transition to this mode moves upstream with increase in U^*.

Keywords: vortex shedding, cylinders in tandem, hysteresis, lock-in

1 Introduction

Vortex-induced vibration of more than one cylinders is highly complex when compared to a single cylinder. It is encountered in various practical situations. A comprehensive review of the problem involving single cylinder can be found in the review article by Williamson and Govardhan (2004). The case of stationary cylinders in various arrangements has been studied extensively in the past mainly via experimental studies (Zdravkovich (1977), Sumner *et al.* (2000)). When the cylinders are free to oscillate, the vortex shedding pattern of the two cylinders can undergo substantial modification (Zdravkovich (1985), Bokaian and Geeola (1989a,b), King and Johns (1976)). It is possible to have wake galloping effects where the downstream cylinder can undergo large amplitude oscillations (Mittal *et al.* (1997), Laneville and Brika (1999), Jester and Kallinderis (2004), Assi *et al.* (2006)).

In this paper, the vortex-induced vibration of a pair of circular cylinders in tandem arrangement placed in a uniform flow at $Re = 100$ is studied. The cylinders are of low non-dimensional mass ($m^* = 10$) and free to vibrate in, both, streamwise and transverse directions. There are very few studies that address the oscillation of two cylinders. The cylinders are kept sufficiently apart, with a centre to centre spacing of $5.5D$, so that the upstream cylinder undergoes complete vortex shedding cycle. The downstream cylinder lies in the wake of the upstream cylinder. The flow is modeled with incompressible flow equations in primitive variables form and the motion of the cylinder is governed by a simple one degree of freedom spring-mass system in each of the directions along the cartesian axes. A stabilized space-time finite element formulation is utilized to solve the flow equations. To overcome the numerical instabilities arising out of dominant advection terms and equal-order-interpolation for velocity and pressure, the Streamline-Upwind/Petrov-Galerkin (SUPG) and Pressure-Stabilizing/Petrov-Galerkin (PSPG) terms are added to the basic Galerkin formulation. Equal-in-order bilinear basis functions (four noded quadrilateral elements) for velocity and pressure are used. The non-linear equation systems resulting from the finite element discretization of the flow equations are solved using the Generalized Minimal RESidual (GMRES) technique in conjunction with diagonal preconditioners. Details about the mesh moving schemes and finite element formulations can be found in Mittal and Kumar (2001).
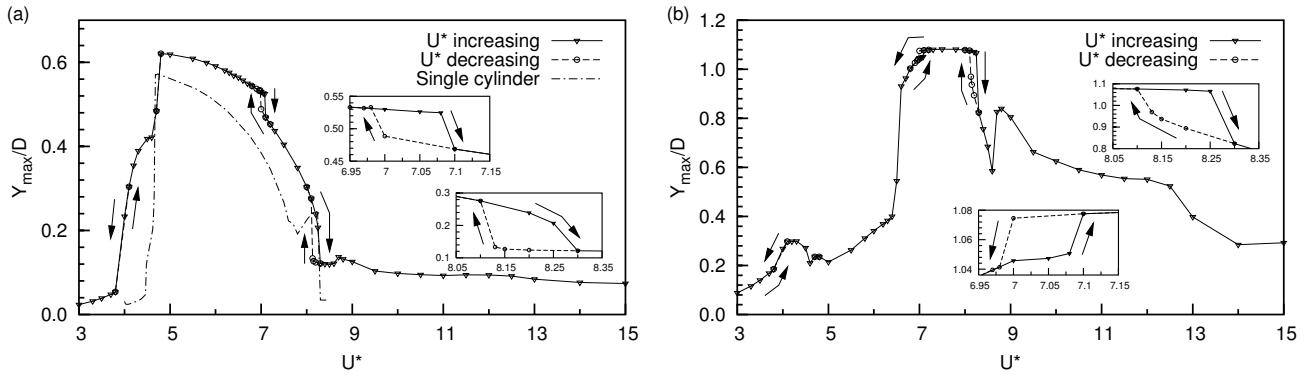
Figure 1: Variation of maximum amplitudes of transverse oscillations of (a)upstream and (b)downstream cylinders with U^*. The variation for a single cylinder is also shown.
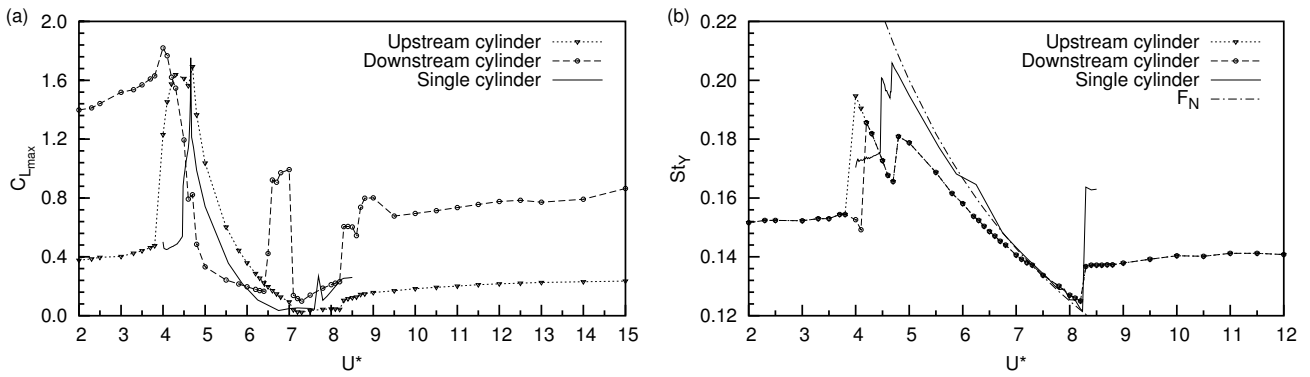

Figure 2: Variation of (a) maximum lift coefficient and (b) transverse oscillation frequency of both cylinders with U^*. The corresponding variations for a single cylinder is also shown.

2   Results

The cylinders mounted on elastic supports are allowed to oscillate, both, in streamwise and transverse directions. To encourage high amplitude of oscillations, the structural damping coefficient is set to zero. The springs in both streamwise and transverse directions are assumed to be linear and with same stiffness. Computations are carried out at a Reynolds number, Re=100. The blockage of the computational domain is very low (2%). The two cylinders are separated by a centre to centre spacing of $5.5D$, where D is the diameter of the cylinder.

Figure 1 shows the variation of non-dimensionalized maximum amplitude of transverse oscillation of both upstream and downstream cylinders. The presence of the downstream cylinder has some effect on the behavior of the upstream cylinder. The upstream cylinder undergoes large amplitude of oscillation at a much lower reduced velocity, U^* when compared to a single cylinder. The behavior of the downstream cylinder is very different from that of the upstream one. The maximum amplitude of transverse oscillation is very high ($\sim 1.1D$), almost twice that observed for the upstream cylinder and is very similar to the response of the single cylinder observed by Khalak and Williamson (1999) with an upper branch. The peak amplitude of oscillation for the downstream cylinder is observed at a much higher reduced velocity, U^* when compared to that of the upstream cylinder. The downstream cylinder response is found to have two more local peaks. The response of both cylinders are found to be hysteretic at two locations. The first hysteresis is observed at a point where the downstream cylinder reaches the maximum amplitude of oscillation ($U^* \sim 7$). The second hysteresis is observed at the higher U^* end of lock-in for both cylinders ($U^* \sim 8.3$).

Figure 2(a) shows the variation of maximum lift coefficient on both upstream and downstream cylinders with reduced velocity, U^*. The variation of maximum lift coefficient of a single cylinder with reduced velocity, U^* is also shown in the figure. The variation of maximum lift coefficient of the upstream cylinder is qualitatively similar to that of a single cylinder. The downstream cylinder is found to have a higher value of lift coefficient compared to that of upstream cylinder during the initial reduced velocities ($U^* \sim 2$ to 4). For both upstream
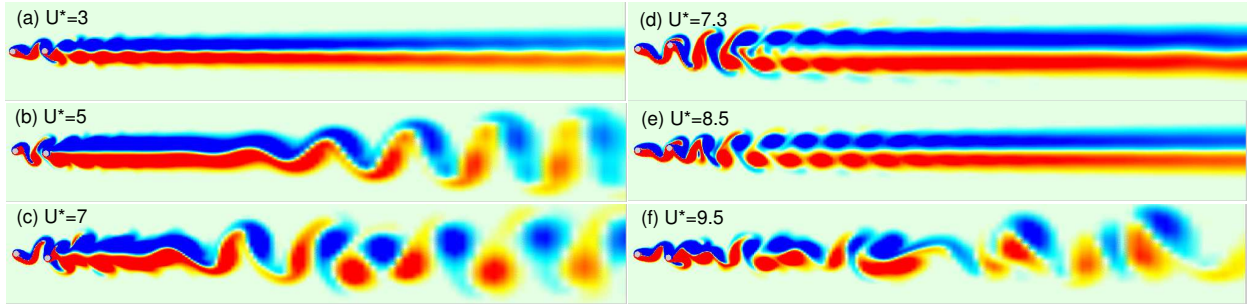
Figure 3: Instantaneous vorticity field at selected reduced velocities.

and downstream cylinders, the maximum value of lift coefficient occurs at a much earlier reduced velocity, U^* than the reduced velocity at which maximum transverse oscillation occurs. The maximum lift coefficient for downstream cylinder occurs at a U^* much earlier than that for the upstream cylinder. But the downstream cylinder undergoes a maximum amplitude of oscillation at a much larger U^* than that for the upstream cylinder. Even though the maximum amplitude of oscillation observed for the downstream cylinder is very large compared to the upstream cylinder, the maximum value of lift coefficient is comparable in both cases. For a range of reduced velocity $4.3 < U^* < 6.3$, the maximum value of lift coefficient experienced by the downstream cylinder is not only lesser than that of upstream cylinder but lesser than that of a single cylinder.

Figure 2(b) shows the variation of frequency with U^* of transverse oscillation of the two cylinders. The variation of reduced natural frequency of the system, F_N and non-dimensional transverse oscillation frequency for a single cylinder are also shown. The lock-in behavior of both upstream and downstream cylinders is clearly seen from the figure. The upstream cylinder undergoes a soft lock-in before the primary lock-in. This is similar to the observation made by Mittal and Kumar (1999), Singh and Mittal (2004) and Prasanth and Mittal (2006) for a single cylinder. The range of U^* for which the upstream cylinder undergoes soft lock-in is much larger than that for the single cylinder. This is evident in the response of the upstream cylinder where it reaches a fairly large amplitude of transverse oscillation at a lower reduced velocity, U^*, while the response amplitude of the single and isolated cylinder is very small at the corresponding U^* (for example, at $U^* = 4.0$, figure 1(a)).

The downstream cylinder undergoes a soft lock-in at a slightly higher U^* compared to that of upstream cylinder. Apart from a small range of U^* near the starting of soft lock-in of the upstream cylinder, the transverse oscillating frequency of upstream cylinder and downstream cylinder are found to remain same through out the entire reduced velocity. This is inline with the observation of Mittal and Kumar (2001) where the non-dimensional frequency of lift coefficient and cross-flow oscillations of both cylinders were found equal. It is interesting to note that outside the lock-in range, the non-dimensional transverse oscillation frequency for both cylinders in tandem are less than that for a single cylinder. This indicates that the presence of an oscillating downstream cylinder has a considerable influence on the vortex shedding of the upstream cylinder, even though both cylinders are separated by a distance of $5.5D$.

Depending upon the amplitude of transverse oscillations of the two cylinders, their phase difference and the vortex shedding frequency of the upstream cylinder, it is possible to have complex vortex shedding patterns in the wake of downstream cylinder. In the initial range of U^*, vortices are found to coalesce just behind the downstream cylinder forming a row of vortices (figure 3(a)). At a higher reduced velocity, a secondary shedding is observed in the far wake. It is observed that a further increase in reduced velocity results in the secondary shedding moving closer to the downstream cylinder (figure 3(b),(c)). The maximum amplitude of oscillation of downstream cylinder corresponds to a $C(2S)$ mode of vortex shedding (figure 3(d),(e)). In the no-lock-in region at higher U^*, $2P$ mode is observed in the far wake (figure 3(f)).

3   Conclusions

Results have been presented for the free vibrations of a pair of equal-sized circular cylinders of low non-dimensional mass $(m^* = 10)$ in tandem arrangement. The computations are carried out for various values of structural frequencies of the oscillator $(2 < U^* < 15)$ at $Re = 100$ using a stabilized finite element method in two dimensions. It is found that even though the response of the cylinder in the transverse direction is qualitatively similar to that of a single cylinder, there are significant effects of the presence of the downstream cylinder on the upstream one. The vortex shedding frequency and the amplitude of transverse oscillation of upstream

cylinder is different from that of a single cylinder. The downstream cylinder undergoes large amplitude of oscillations with an upper branch. The vortex shedding frequency of both upstream and downstream cylinders are found to be same except for a small range of U^*. Lock-in is observed for both cylinders. The response of both cylinders are found to be hysteretic for certain values of U^*. Different modes of vortex shedding are observed in the wake of the downstream cylinder depending on the amplitude of oscillation. In the far wake the vortex street degenerates to a lower frequency mode. The location of transition to this mode moves upstream with increase in U^*.

References

[1] G.R.S. Assi, J.R. Meneghini, J.A.P. Aranha, P.W. Bearman, E. Casaprima. Experimental investigation of flow-induced vibration interference between two circular cylinders. *Journal of Fluids and Structures*, 22:819–827, 2006.

[2] A. Bokaian, F. Geoola. Wake-induced galloping of two interfering circular cylinders. *Journal of Fluid Mechanics*, 146:383–415, 1984.

[3] A. Bokaian, F. Geoola. Proximity-induced galloping of two interfering circular cylinders. *Journal of Fluid Mechanics*, 146:417–449, 1984.

[4] W. Jester, Y. Kallinderis. Numerical study of incompressible flow about transversely oscillating cylinder pairs. *Journal of Offshore Mechanics and Arctic Engineering, Transactions of the ASME*, 126:310–317, 2004.

[5] A. Khalak, C.H.K. Williamson. Dynamics of a hydroelastic cylinder with very low mass and damping. *Journal of Fluids and Structures*, 10:455–472, 1996.

[6] R. King, D.J. Johns. Wake interaction experiments with two flexible circular cylinders in flowing water. *Journal of Sound and Vibration*, 45:259–283, 1976.

[7] A. Laneville, D. Brika. The fluid and mechanical coupling between two circular cylinders in tandem arrangement. *Journal of Fluids and Structures*, 13:967–986, 1999.

[8] S. Mittal, V. Kumar, A. Raghuvanshi. Unsteady incompressible flow past two cylinders in tandem and staggered arrangements. *International Journal of Numerical Methods in Fluids*, 25:1315–1344, 1997.

[9] S. Mittal, V. Kumar. Flow induced oscillations of two cylinders in tandem and staggered arrangement. *Journal of Fluids and Structures*, 15:717–736, 2001.

[10] T.K. Prasanth, S. Behara, S.P. Singh, R. Kumar, S. Mittal . Effect of blockage on vortex-induced vibrations at low Reynolds numbers. *Journal of Fluids and Structures*, 22:865–876, 2006.

[11] S.P. Singh, S. Mittal. Vortex-induced oscillations at low Reynolds numbers: hysteresis and vortex shedding modes. *Journal of Fluids and Structures*, 20:1085–1104, 2005.

[12] D. Sumner, S.J. Price, M.P. Paidoussis. Flow pattern identification for two staggered circular cylinders in cross flow. *Journal of Fluid Mechanics*, 411:263–303, 2000.

[13] C.H.K. Williamson, R. Govardhan. Vortex Induced Vibration. *Annual Review of Fluid Mechanics*, 36:413–455, 2004.

[14] M.M. Zdravkovich. Review of flow interference between two circular cylinders in various arrangements. *Journal of Fluids Engineering, Transactions of ASME*, 99:618–633, 1977.

[15] M.M. Zdravkovich. Flow induced oscillations of two interfering circular cylinders. *Journal of Sound and Vibration*, 101:511–521, 1985.

DYNAMIC RESPONSE OF A CIRCULAR CYLINDER IN THE WAKE OF AN UPSTREAM FIXED CYLINDER

G.R.S. ASSI - P.W. BEARMAN - J.R. MENEGHINI*

Department of Aeronautics, Imperial College, SW7 2AZ, London, UK
*Dep. Mechanical Eng. - NDF, University of São Paulo, 05508-970, São Paulo, Brazil

ABSTRACT. This paper presents force measurements during flow-induced vibration of a pair of circular cylinders with low mass and damping aligned in a tandem arrangement. A particular case with a separation of 3 diameters from centre to centre is used to examine flow-interference mechanisms occurring on a downstream cylinder, free to oscillate only in the transverse direction. Oscillations are observed for reduced velocities, based on cylinder natural frequency measured in air, as high as 35. The amplitude of oscillation is reaching a level of saturation of about 1.5 diameters, while the frequency of vibration is increasing at an approximate constant rate. As reduced velocity is increased two regimes of flow-induced vibration are observed: first vortex-induced vibration and then a wake-induced vibration regime. In addition, the presence of the second cylinder affects the dynamics of the upstream wake, but it is found not to synchronize the vortex shedding frequency of the upstream cylinder for the second regime of oscillations.

INTRODUCTION

Risers are very long pipes used to carry oil from the sea bed to floating platforms on the surface. Under the effect of the sea currents, these flexible structures are especially susceptible to flow-induced vibrations, particularly since they have a relatively low mass compared to the mass of the displaced fluid. Generally, an offshore floating platform accommodates more than 40 riser pipes together with many other cylindrical structures. The interaction of these flexible structures can produce an even more complex problem, resulting in vibrations with even higher amplitudes. As a result, the possibility of collision between the structures and the damage risk caused by structural fatigue are increased. Consequently, it is fundamental to study not only the dynamic behaviour of a single riser, but also the responses of different grouped arrangements.

The case where two risers are aligned to the current is the starting point for the present investigation. Even this simple arrangement shows complex interference phenomena. However, complex conditions found underwater cannot be perfectly reproduced at laboratorial scales. Simplifying riser systems into circular cylinder models helps to understand the characteristics of the flow and its effect on the bodies. The present work presents measurements of the flow-induced vibration of a pair of circular cylinders aligned in tandem arrangement. The downstream body, free to oscillate only in the transverse direction, is immersed in the wake of a fixed upstream cylinder with the same diameter.

EXPERIMENTAL SET-UP

A pair of rigid circular cylinders was placed in a recirculating water channel with a free surface test section. Both cylinders were aligned in the vertical direction passing through the free water surface down to almost the full depth of the section. The upstream cylinder was rigidly attached to the structure of the channel preventing displacements in any direction, while the downstream one was clamped at its upper end to an elastic mounting free to move only in the transverse direction (*y-axis* in Fig. 1(a)). A load cell connects the moving parts of the base to the top end of the model and is adjusted to measure the lift force (fluid force acting in the transverse direction). The restoration force of the system is provided by a pair of springs connecting the moving base to the fixed supports. A positioning sensor was installed on the elastic base to measure the y-displacement of the cylinder

The whole system had a structural damping factor of $\zeta = 0.7\%$, calculated as a percentage of critical damping obtained from free decay oscillations performed in air. The natural frequency of oscillation in air (f_0) was also determined during the same tests. Repeating the procedure for the immersed body, it is possible to obtain the natural frequency of oscillation in still water (f_w), which takes into account the added fluid mass of the cylinder. All the moving parts of the elastic base contribute to the effective mass, resulting in a mass ratio of $m^* = 2.0$ (defined as the ratio of the total oscillating mass to the mass of displaced fluid).

Contact: g.assi@imperial.ac.uk.

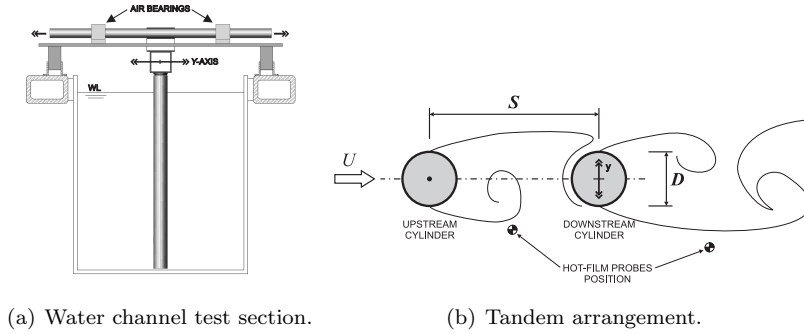(a) Water channel test section.   (b) Tandem arrangement.

FIGURE 1. Experimental set-up.

As shown in Figure 1(b), where the upstream cylinder is not oscillating, the upstream and downstream cylinders are aligned in the direction of the flow (known as tandem arrangement). The separation between the two is $S/D = 3.0$, measured from the centre of one model to the centre of the other. A hot-film anemometer was employed to measure velocity fluctuations in two important regions of the flow, either in the gap between the cylinders or in the developed wake downstream of the second cylinder. A PIV system was also applied to map the velocity field around the cylinders.

RESULTS AND DISCUSSION

The dynamic response of the downstream cylinder was analysed over a wide velocity range. The same pair of springs was used during the whole experiment and the velocity of the flow in the test section was varied in order to cover a large range of reduced velocity. Consequently, the Reynolds number (based on the cylinder diameter and the free stream velocity) varied within the range 1500 <Re< 20000. The reduced velocity (U/f_0D) presented on the abscissas of all graphs is a non-dimensional value based on the free stream velocity of the flow (U), the natural frequency of oscillation in air (f_0) and the cylinder diameter (D). The amplitude of oscillation (A) is non-dimensionalised by the cylinder diameter (D) and the actual frequency of oscillation (f), by the natural frequency of oscillation in air (f_0). The amplitude of oscillation is defined as the harmonic amplitude, obtained from the *rms* of the signal and expressed as $A = \sqrt{2}\langle \hat{y} \rangle_{rms}$.

Following the force decomposition presented by Williamson & Govardhan (2004), the lift force acting on the cylinder can be split into two components (Eq. 1): a potential-force component ($C_{y_{POTENTIAL}}$), given by the ideal flow inertia force and a vortex-force component ($C_{y_{VORTEX}}$), related to the dynamics of the vorticity field. In Eq. 1 ϕ is the phase angle between the lift force and the displacement of the body. By definition, the potential-force component is always opposing the body's acceleration and its magnitude is proportional to the product of the displaced fluid mass and the acceleration magnitude. On the other hand, the vortex-force component has a phase shift in relation to the displacement of the body defined by the phase angle ϕ_{VORTEX}.

(1) $$C_y \sin(2\pi f\ t + \phi) = C_{y_{POTENTIAL}} \sin(2\pi f\ t) + C_{y_{VORTEX}} \sin(2\pi f\ t + \phi_{VORTEX})$$

Bokaian & Geoola (1984) state that "depending on the cylinders' separation, and structural damping, the [downstream] cylinder exhibited a vortex-resonance, or a galloping, or a combined vortex-resonance and galloping, or a separated vortex-resonance and galloping" response. The authors found high amplitude responses which they called *wake-induced galloping* and also stated that "whilst some characteristics of wake-excited galloping were found to be similar to those of galloping of sharp-edge bodies, others were observed to be fundamentally different". In the present work the reduced velocity range is larger than that found in other many experiments, achieving $U/f_0D = 35$ for the uppermost case. This paper presents new results on the lift force acting on the downstream cylinder and its decomposition as discussed previously.

The first notable feature observed in the A/D graph of Figure 2(a) is the high-amplitude of oscillation that persists through the whole range of reduced velocities. A local peak of amplitude is found approximately around the region where a peak is found for an isolated cylinder. In fact it occurs at a slightly increased reduced velocity when compared to the single cylinder case. Subsequently, the amplitude curve falls over a short reduced velocity range, but then enters a second regime of increasing amplitude. The first regime is identified as a *vortex-induced* response followed by a *wake-induced* excitation, which has also been called *wake-induced galloping*. The frequency graph also shows these two distinct regimes. After a reduced velocity of 13 the frequency presents a different behaviour, increasing at an almost constant rate exceeding that for a single cylinder case as high as twice the natural frequency. Analysing the bottom graph of Figure 2(a),
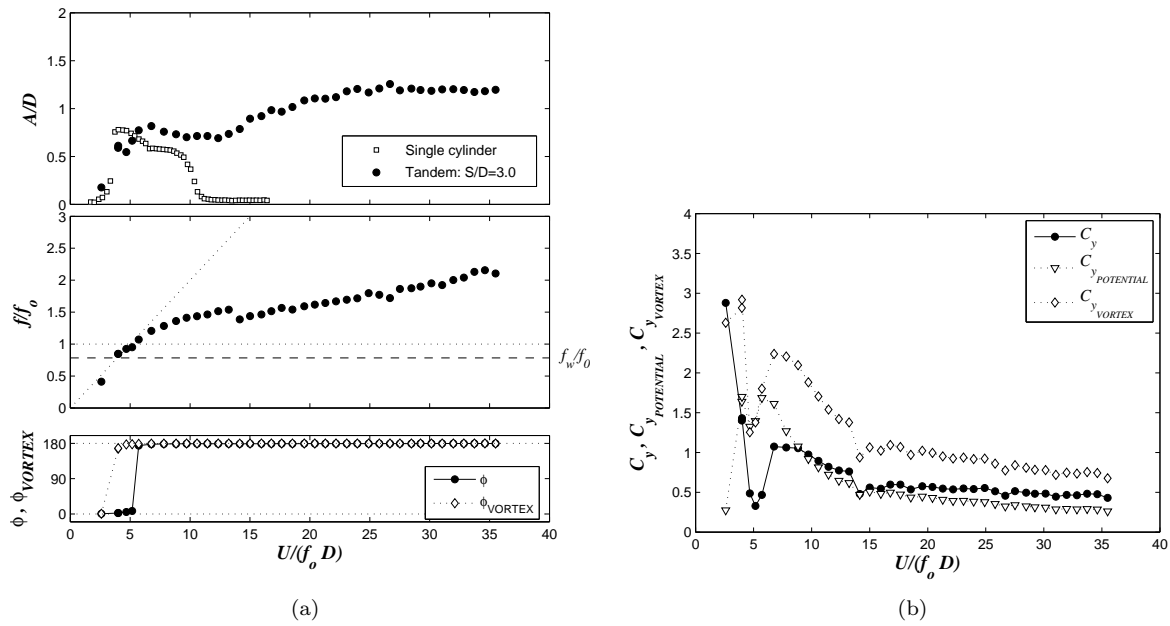
FIGURE 2. (a) Dynamic response and (b) lift coefficients for the second oscillating cylinder of a tandem pair under wake-induced vibrations.

(a) Gap flow between the two cylinders.

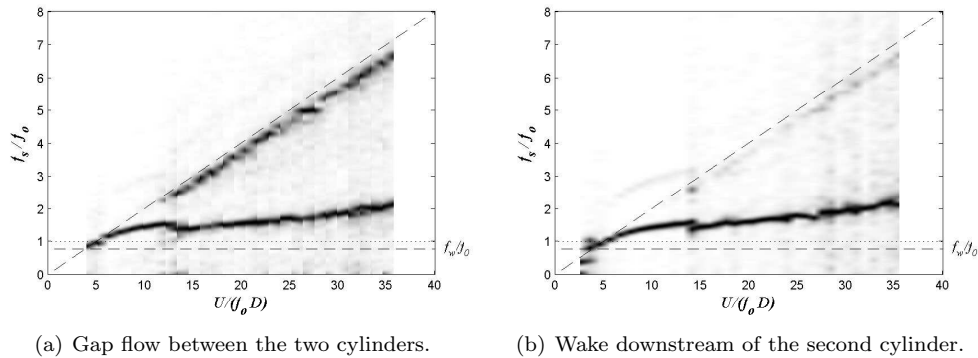(b) Wake downstream of the second cylinder.

FIGURE 3. Spectra of velocity fluctuation measure with a hot-film in the wake. Power spectral density is represented by the intensity of colour. A darker grey spot stands for a higher magnitude power peak in the frequency domain.

the total force phase angle ϕ shows a 180 degrees jump coinciding with the peak in amplitude in the vortex-vibration range. However, the phase angle related to the vortex-force ϕ_{VORTEX} has an almost constant value close to 180 degrees across the range of reduced velocity studied. An important feature to note is that within the vortex-induced vibration regime, for a particular value of reduced velocity, the amplitude of oscillation remains nearly constant. This contrasts with the wake galloping regime where the amplitude is much more variable. It also contrasts with the classic galloping of sharp-edged bluff bodies where the amplitude levels tend to be stable.

Figure 3(a) shows the frequency spectra of velocity fluctuations measured in the gap flow between the two cylinders, i.e., downstream of the fixed cylinder and upstream of the oscillating one. Comparatively, Figure 3(b) presents similar spectrum measurements in the wake downstream of the second cylinder. The approximate positions of the hot-film probes are shown in Figure 1(b). Two regimes of vortex shedding are observed for the upstream cylinder in Figure 3(a). During the first regime, up to reduced velocity 13, the vortex shedding of the upstream cylinder is locked with the frequency of oscillation of the second cylinder. This regime is associated with an excitation due to vortex synchronization between the bodies. On the other hand, for reduced velocities greater than 13, the upstream cylinder sheds vortices according to the Strouhal law expected for a single fixed cylinder. It means that the oscillations of the second cylinder do not control the shedding of the first body, although some perturbation from the downstream cylinder can be sensed in

the velocity field in the gap. The lower frequency shown in Figure 3(a) is associated with the wake-galloping oscillations of the downstream cylinder. This frequency appears as the dominant one in Figure 3(b) where the hot-film probe is now downstream of the second cylinder.

Figure 2(b) shows how the lift coefficient varies with reduced velocity for the downstream cylinder. Once more, two different regimes are observed with a clear transition happening around a reduced velocity of 13. The first regime follows the same behaviour observed for a single cylinder. In contrast, the second regime is associated with the wake-galloping excitation and shows a roughly constant level around $C_y = 0.5$. Since the potential component represents the ideal flow inertial force of the system, the lift force that is driving the high amplitude oscillations comes from the vortex component. During the wake-galloping regime $C_{y_{VORTEX}}$ is slowly decreasing but over a considerable range of reduced velocity it is between about 1.0 and 0.7. It is the product of this large force and the sine of its phase angle that provides the excitation to maintain the amplitude setting at a level around $A/D = 1.5$.

The oscillations of the downstream cylinder seem to synchronise the vortex dynamics of the first cylinder within the range where the frequency of oscillation is roughly close to the expected frequency of vortex shedding for a single fixed cylinder. However, for reduced velocities greater than 13, the first cylinder sheds its vortices following the Strouhal law expected for a fixed cylinder. Assi (2005) shows that even if the upstream cylinder is free to oscillate in the transverse direction it will behave like a single isolated cylinder, developing its own vortex-induced oscillations and not being affected by the movements of the downstream body.

The wake-galloping oscillations are caused by the interference effect coming from the upstream wake. In attempting to apply ideas from galloping theory, we note that when the downstream cylinder is stationary and aligned with the upstream one there can be no excitation. However, once it moves away from a straight in-line position we know from previous work that a destabilising lift force is observed. Hence it seems that buffeting forces disturb the cylinder sufficiently to move it to a region where it experiences an excitation. We observe that at sufficiently low mass and damping there is sufficient excitation to sustain oscillations. Classically, galloping is associated with a constant amplitude of oscillation at a particular reduced velocity. During a cycle of oscillation in the wake-galloping regime observed here, the cylinder may move between regions of excitation and regions of damping. However, the net energy transfer to the cylinder is sufficient to cause oscillations but not sufficient to sustain a stable amplitude.

Conclusion

We conclude that a cylinder with sufficiently low mass and damping immersed in the wake of another can develop flow-induced oscillations persisting for a large range of reduced velocity. Wake-induced oscillations are observed for velocities as high as $U/f_0 D = 35$. Apparently, the amplitude of oscillation is reaching a saturated level of about $A/D = 1.5$, while the frequency of vibration is increasing at an approximate constant rate.

The oscillations of the downstream cylinder are synchronised with the vortex shedding of the upstream cylinder up to a reduced velocity of 13.0. This first regime is identified as a vortex-induced excitation very similar to what happens for a single cylinder. After this point, a second regime is observed, defined as wake-induced galloping, when the upstream cylinder is shedding vortices on a regular increasing frequency but the downstream cylinder oscillates with high amplitudes at much lower frequencies. We assume these high amplitude oscillations, which are excited by the vortex component of the lift force, will persist to high values of reduced velocity. But the precise mechanism that is generating this galloping response is still uncertain.

A detailed investigation of the nature of these forces and the dynamics of the wake is in progress. Future work will also take into account the effects of cylinder separation and structural stability on wake-induced oscillations.

Acknowledgements

References

ASSI, G. 2005 Experimental study of the flow interference effect around aligned cylinders. Master's thesis, University of São Paulo, São Paulo, Brazil, in portuguese.

BOKAIAN, A. & GEOOLA, F. 1984 Wake-induced galloping of two interfering circular cylinders. *Journal of Fluid Mechanics* **146**, 383–415.

WILLIAMSON, C. & GOVARDHAN, R. 2004 Vortex-induced vibrations. *Annu. Rev. Fluid Mech.* **36**, 413–55.

Interference and clashing experiments with two flexible cylinders on a cavitation tunnel

Adriano Axel Pliopas Pereira
Escola Politécnica of the University of São Paulo (EPUSP) - Undergraduate
adriano.pliopas@poli.usp.br

André Luis Condino Fujarra
Escola Politécnica of the University of São Paulo (EPUSP)
afujarra@usp.br

Elton J.B. Ribeiro
Petrobrás
elton@petrobras.com.br

The importance that VIV plays in real engineering problems is largely known. To better understand the phenomena, an uncountable number of experimental and theoretical works has been done during the last decades. While many of these works focus on the fundamental case of a single cylinder, real cases of VIV manifestation often involve two or more cylinders closely arranged. In the field of offshore engineering another important difference arise: risers and umbilicals are more appropriately modeled as flexible entities and nonetheless most experimental work on VIV deals with rigid cylinders. For an overview of the implications of VIV on other fields besides the offshore industry, refer to .

The experimental study described in this paper addressed the simplest real case where the influence problem is present, using only a pair of flexible cylinders. The first analysis on the available data employed classical analysis technique. The cylinders were tested in side-by-side and tandem arrangements, with 4.8 and 2.4 diameters gap for each arrangement.

The facility used for the tests was the Cavitation Tunnel of the Technological Research Institute of São Paulo (IPT). The test section is square with rounded corners and 500 mm wide. It is possible to reach speeds up to 7 m/s but in the present case the limit of 2.9 m/s was enough for the intended range of reduced velocities. The Reynolds number reached about 3.5×10^4 during the runs, and it was about 1.9×10^4 during the higher amplitudes in the lock-in regime. The turbulence level in the test section is not expected to be high, but recent measurements are not available.

The cylinders employed were 12 mm in the outside diameter and 500 mm in span, therefore with an aspect ratio above 40. They were built with a brass core surrounded by a silicon layer employed to raise its linear density and outside diameter without contributing to raise its bending stiffness. The boundary condition was pinned-pinned. For this arrangement, the natural frequency, in water, was about 16.5Hz. The mass-damping parameter m*ζ was found to be around 0.067, after some decay tests. To measure and record the displacements, two strain-gages were installed symmetrically around the half plane of the test section for each degree of freedom, thus making it easier to eventually filter second-mode deformation by just summing up the signals. The calibration procedure registered the displacement due to an applied load, through an LVDT transducer, and the displayed voltage for each strain gage. Corrections were later applied between static and dynamic strain.

As these experiments involved untypical high natural frequency and a different kind of facility from traditional studies, the first measurements concentrated on the case of a single cylinder in order to validate the procedures adopted. Results of six independent runs with the single cylinder are depicted on , and show good agreement between the runs. Some dispersion of the results appears at reduced velocities greater than 7, specially for the region of peak amplitude (around 1.2 diameters for the higher case). This could be attributed to the presence of the second mode, but much of its distortion on the strain gauges measurements are filtered by just adding up the signal of each correspondent gage and considering the average. Some of the distortion, however, may have persisted. The peak amplitude occurred at Vr=8, a value a little bit higher than traditionally reported in most single cylinder studies (where the peak usually happens at 5 < Vr < 6). This is

not a surprise because most studies focus on rigid cylinder while this one deals with flexible ones. The transition between the branches occurred around Vr=9.5, involving a sudden jump as expected.
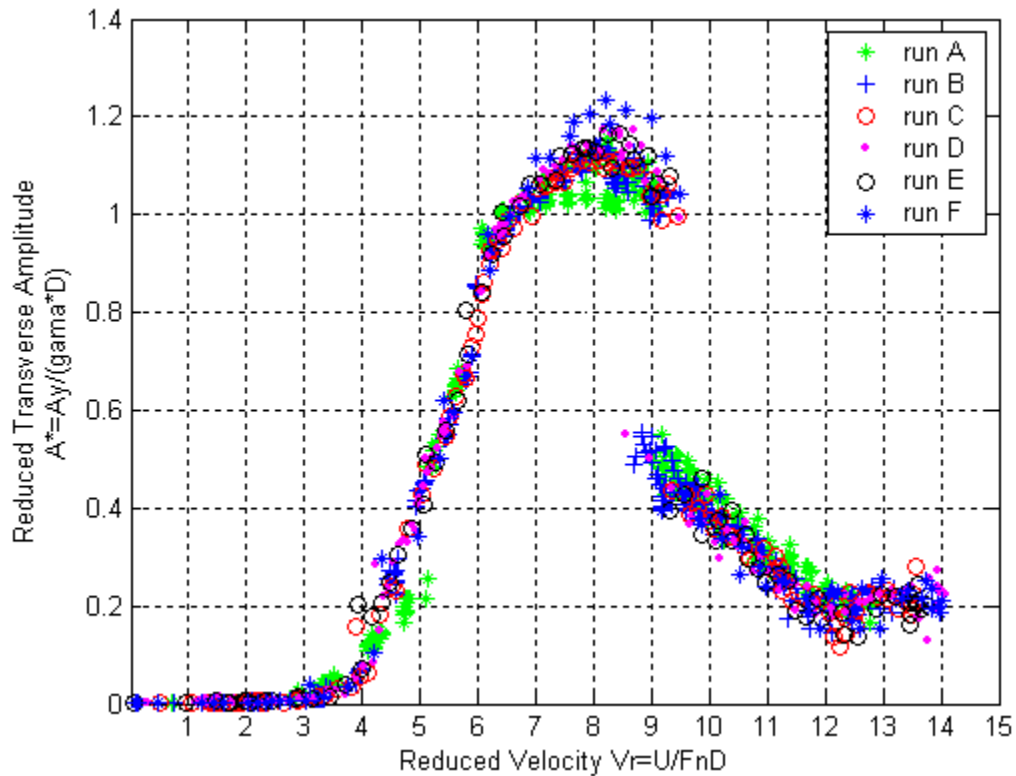

Fig. 1. Amplitude response on the transverse direction for the single cylinder experiments. Results of six different runs are depicted, showing good agreement.

After the classical single cylinder case the tandem arrangement with two cylinders was tested. The first gap tried was of 4.8 diameters. The response amplitude for this case is exhibited in . The behavior exhibited by the front cylinder was quite similar to that of the single cylinder case, but it seems that the transition to the lower branch came about somewhat earlier (more detailed investigation is needed to verify this small difference).

The rear cylinder, however, showed a very different amplitude response. The transverse amplitude in this case increased monotonically up to 0.7 diameters, and showed no tendency to decrease in the range of reduced velocities investigated. During an extensive investigation on interference phenomena between rigid cylinders mounted on elastic bases, Ássi found a similar pattern when the two cylinders were allowed to oscillate. The complete work is in reference .

There is some greater dispersion of the results for the rear cylinder for reduced velocities around 8. This is the velocity in which the transition from the upper branch to the lower branch takes place for the front cylinder. It is reasonable to conclude, therefore, that the greater dispersion of the rear cylinder amplitude is caused by the amplitude jumps of the front cylinder.

The illustration in allows a better understanding of the phenomena by showing the trajectories of the cylinders as a function of the reduced velocity and in association with the amplitude response graph. Not only the difference in peak amplitude becomes again evident but the eight-shape trajectory seems not to happen for most of the rear cylinder behavior, being verifiable only during reduced velocities up to 5.5. After this point the trajectory of the rear cylinder becomes mostly irregular.
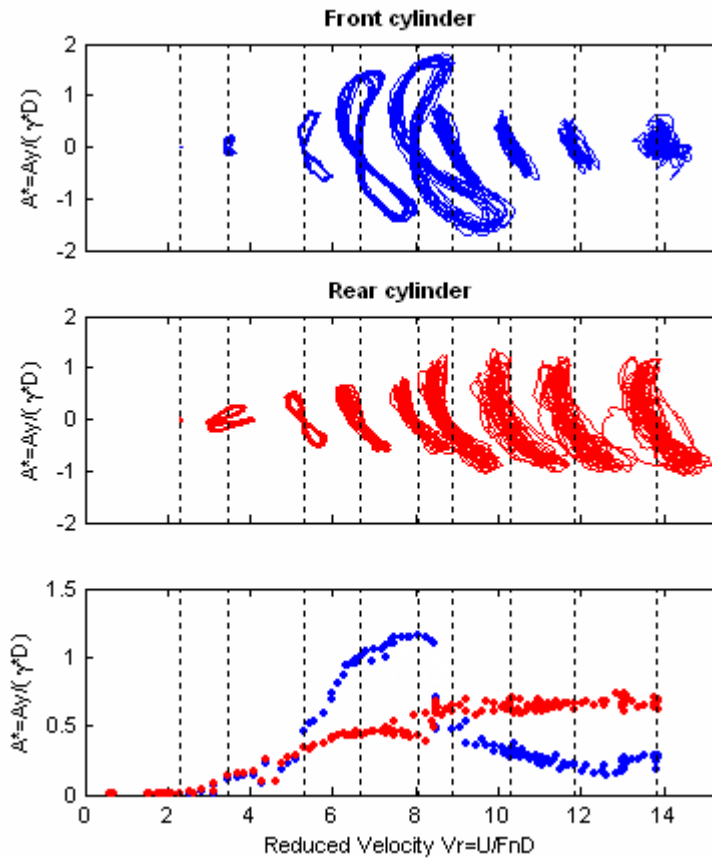
Fig. 2. Amplitude response and trajectories for two cylinders in tandem arrangement and a gap of 4.8 diameters.

After the trials with the 4.8 gap, a closer arrangement was installed in which the models were 2.8 diameters apart (distance between centers). Clashing phenomena was observed in this case, and a detailed analysis of the available data is being carried on. There is the possibility of executing more runs on this particular setup to validate the results.

References:

[1]   Païdoussis, M. P., "Real-life experiences with flow-induced-vibrarion", *Journal of Fluid and Structures*, 22 (2006) 741-755

[2]   Ássi, Gustavo Roque da Silva, "Estudo experimental do efeito de interferência no escoamento ao redor de cilindros alinhados", (in portuguese). Doctoral Thesis, Escola Politécnica, University of S. Paulo, xxx p.

[3]   Franciss, R. and Fujarra, A.L.C., "Interference between Risers", *26th International Conference on Offshore Mechanics and Arctic Engineering*, June 10–15, 2007, San Diego, USA.

Simulation of vortex induced vibration of pairs of cylinders in *tandem* arrangement using deforming meshes

A. D`Agostini Neto, F. Saltara

NDF, Department of Mechanical Engineering, University of São Paulo, Brazil

Corresponding Author: alexandre.dagostini@poli.usp.br

ABSTRACT

The 2D unsteady flow around pairs of cylinders in tandem arrangement is simulated using a deforming mesh technique. Both cylinders have the same diameter D. The distances between the centers of the cylinders are in the range 2D-4.5D, and the Reynolds number is Re=200 (laminar flow) for all simulations. The commercial code Fluent® is used, and a User-Defined Function (UDF) is developed in order to calculate drag and lift forces on both cylinders and solve the mass-spring-damper system of each body. The triangular mesh is deformed and remeshed in order to allow the relative motion between the cylinders. The main goal of the research is to study how the bodies interact when they are free to vibrate. The mass-damping parameter of the simulations is low (m*ζ=0.013) and similar to the value characteristic of oil risers.

INTRODUCTION

The simulation of a freely vibrating cylinder has been subject of many studies, and still is being studied for many groups around the World. Most recently, some groups started to study the interferences between two circular cylinders in *tandem* arrangement when both of them are free to vibrate in a transversal direction of the flow.

As pointed out by Meneghini et al (2001), the flow interference is responsible for several changes in the characteristics of fluid loads when more than one body is placed in a fluid stream. As a consequence, mutual interferences between two cylinders at close proximity caused significant change in dynamic loads applied on both of them. Velocity and pressure fluctuations and vortex wake mean speed are important parameters for the dynamic response of cylinders under interference. The gap (S), distance between cylinders, is also a very important and determining factor, of the flow at issue.

The commercial finite-volume code FLUENT® modified through a User Defined Function (UDF) in order to solve the motion of an elastically mounted cylinder is used on this study. Dynamic meshes are employed on the simulations due to the change of domain shape with time.

Dynamic meshes can be employed, basically, in three different ways. Two of them were employed here: rigid-body moving mesh and deforming mesh. The employment of deforming mesh methods just made practical the simulations of a freely vibrating pair of cylinders, due to the fact that the rigid mesh does not allow relative motion between them.

For deformable meshes, the edges (faces, in 2D cases) are idealizes as interconnected springs. The original configuration of the mesh is idealized as the equilibrium state of the mesh. For ensuring the mesh quality, when displacements are large when compared to original cell sizes, new elements are created (remeshing). The integral form of the conservation equation for a general scalar ϕ is corrected with the grid velocity of the moving mesh (u_g).

$$\frac{d}{dt}\int_V \rho\phi dV + \int_{\partial V} \rho\phi\left(\vec{u} - \vec{u}_g\right)\cdot d\vec{A} = \int_{\partial V} \Gamma\nabla\phi \cdot d\vec{A} + \int_V S_\phi dV \tag{1}$$

On the present work, simulations of a single fixed cylinder at 100<Re<200 were firstly performed in order to calibrate the model. Then, the dynamic mesh method was employed on a single freely oscillating cylinder, firstly with a rigid domain moving coupled to it, and, then, with deformable mesh. Fixed *tandem* cylinders were simulated too, with different gaps, and, finally, free oscillating *tandem* cylinders results were obtained.

FLOW-INDUCED VIBRATION

A standard mass-spring-damper system was used to evaluate the vortex induced vibrations on the cylinder. For a cylinder with just one degree of freedom (transverse to the flow stream direction), as show in Fig. 1, the movement of it can be described by the equation:

$$m\,\ddot{y} + c\,\dot{y} + k\,y = F_y \tag{2}$$

With addition of lift coefficient (C_l), fluid displaced mass (m_d), mass parameter ($m^*=m/m_d$, m = structural mass) and damping (ζ), the final model equation is given by:

$$\ddot{Y} + 4\pi\xi\sqrt{1+\frac{1}{m^*}}\,\dot{Y} + 4\pi^2\left(1+\frac{1}{m^*}\right)Y = C_l\,\frac{2}{\pi D}\,U_0^{\,2}\,\frac{1}{m^*} \tag{3}$$

On the equation showed above, C_l is calculated through the integration of pressure and viscous stresses on the cylinder surface.

According to Blevins (1977) and Khalak and Williamson (1996), the amplitude of vibration A/D is a function of the mass parameter m^*, the damping ζ and the natural frequency ω_n of the cylinder. The mass parameter is the relation m/m_d, where m_d is the displaced fluid mass $\rho\pi D^2/4$. In general, experiments for given values of ζ are carried out, and curves of Ay/D as a function of the reduced velocity V_r are plotted. The reduced velocity is given by $V_r = U_\infty\,T_n\,/D$, in which U_∞ is the free stream velocity, and T_n is the natural period associated with ω_n.
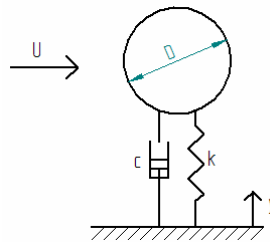

Fig. 1) Cylinder free to vibrate in the transverse direction.

Meneghini et al (1997) carried out some simulations for m* ζ = 0.013 and Re=200, and their results present peak amplitudes A/D close to 0.6. Those results are going to be compared with our numerical calculations.

NUMERICAL METHOD

First simulations that should be mentioned are those performed for a single freely vibrating cylinder with dynamic mesh coupled to it as a rigid body. Those were carried out for Re=200 with a non-structured mesh with 8730 triangular cells. For all single-cylinder cases, the grid extended 10D upstream, above and under the body and 20D downstream. For all *tandem*-cylinders simulations, the grid extended 15D upstream, above and under the body and 25D downstream, with 28510 triangular cells. The non-dimensional time step ($U_\infty\Delta t/D$) used was 0.05. Inlet boundary conditions were used in the front, upper and lower boundaries, and outflow boundary condition in the back boundary. For all cases, the cylinder surface is divided in 120 equal faces.

For simulations of a single freely vibrating cylinder with deforming mesh, in order not to damage the boundary layer elements, a rigid-body zone was created enclosing it, that means, the cylinder plus a region near the boundary layer haves a rigid body motion, without any kind of distortion. In an exterior region, the elastic model described previously was employed with remeshing. The same procedure was employed for the *tandem*-cylinders, but each cylinder with its own rigid "boundary layer zone".

Simulations without any kind of dynamic meshes were performed with second-order time scheme of FLUENT® for time discretization. Simulations with dynamic meshes were performed with a first-order time scheme.

Cell fluxes were calculated through the standard central-differences scheme, due to low-Reynolds number.
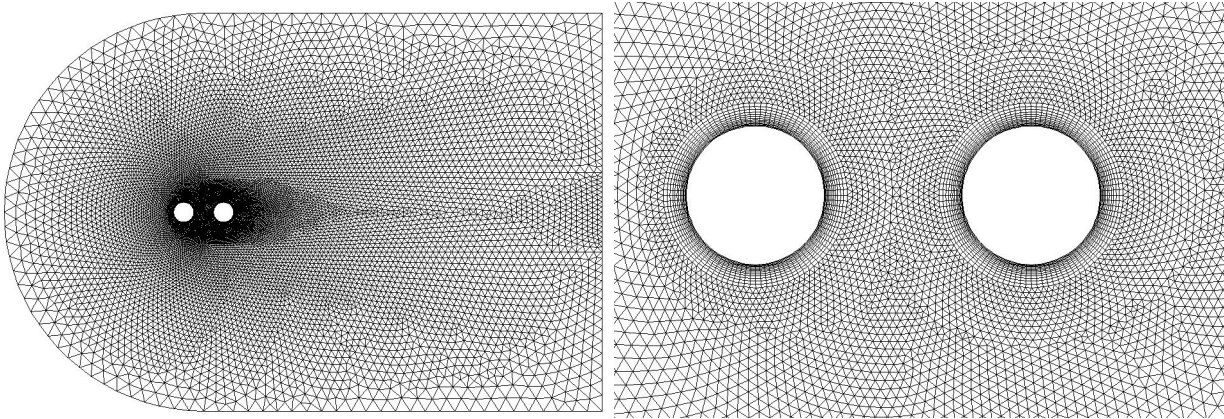
Fig. 2) Mesh view for the *Tandem* case with 2D spacing between cyliners.

The forces calculated by the User Defined Function are applied on equation 3 in order to determine the new position of the cylinder in the new time step. The subsequent equations are used:

$$m\ddot{Y} + c\dot{Y} + kY = F$$

$$m\frac{d\dot{Y}}{dt} + c\dot{Y} + kY = F$$

(4) and (5)

Substituting eq. (5) in eq. (2), the body acceleration can be calculated for a given time *t*. The body displacement is calculated through:

$$y(t + \Delta t) = y(t) + \dot{y}(t)\,\Delta t + 0.5\,\ddot{y}(t)\,\Delta t^2$$

(6)

The velocity of the body for the next time step is calculated using the following equation:

$$\dot{Y}(t + \Delta t).\left(\frac{m}{\Delta t} + \frac{c}{2} + \frac{k.\Delta t}{4}\right) = \dot{Y}(t)\left(\frac{m}{\Delta t} - \frac{c}{2} - \frac{k\Delta t}{4}\right) - kY(t) + \frac{F(t + \Delta t) + F(t)}{2}$$

(7)

With:

$$m = (m*)\frac{\rho\pi D^2}{4}.L \,;\; c = 2m\varpi_n\xi \,;\; k = m\varpi_n^2$$

RESULTS

The simulations for a single oscillating cylinder with rigid moving mesh and deforming mesh can be seen on Fig. 3. The graphic shows the dimensionless amplitude (*A/D*) for V_r ranging from 2.0 to 12.0. Both peak amplitudes agree with the reference mentioned previously. The results for deforming mesh showed to have lower amplitude in *lock in* region of the curve, but, in general, both of them agree with reference results, shown also on Fig. 3.

Once it was shown that the results for deforming mesh are acceptable, Fig 4 shows the results for *tandem* cylinders with, in all cases, *Vr=6.0*. Upstream and downstream cylinders vibration amplitude results are shown for different spacing between them. The center horizontal line corresponds to a reference value, that is, a single oscillating cylinder with same V_r, using deformable mesh.
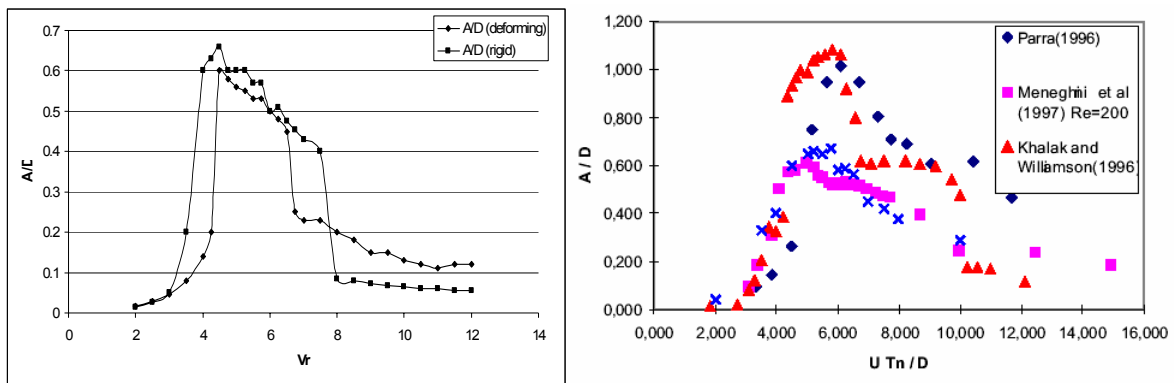
Fig. 3) Amplitude of vibration *A/D* as a function of reduced velocity V_r (results on left, references on right)
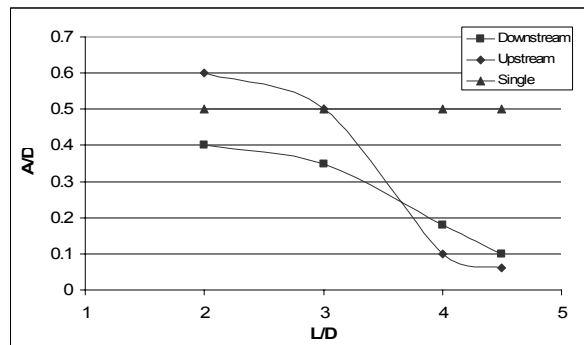

Fig. 4) Amplitude of vibration *A/D* as a function of cylinders spacing

CONCLUSIONS

The simulations using dynamic mesh with first-order time scheme for Re=200 has shown to reasonably predict the dynamic behavior of a single oscillating cylinder. Thus, it is supposed that results obtained for *tandem* cylinders should be reasonable too. A more detailed analysis of the results will be performed in order to evaluate the phase angle between forces and displacements for each cylinder and amplitude values for more cases. Although the simulations covered a single value of reduced velocity (*Vr=6*), and more results should be obtained in order to take more conclusions.

REFERENCES

Blevins, RD. "Flow Induced Vibratio", Van Nostrand Reinhold Ltd, 1977

D`Agostini Neto, A. "Estudo da vibração induzida pelo escoamento em pares de cilindros em arranjo *tandem* usando malha elástica", Relatório Científico FAPESP, 2006

Khalak, A, and Williamson, CHK,. " Dynamics of a Hydroelastic Cylinder with very Low Mass and Damping ", Journal of Fluids and Structures 10, 455-472,1996.

Meneghini, J. R., Saltara, F., Siqueira, C. L. R., Ferrari, J. A., "Numerical Simulation of flow interference between two circular cylinders in tanden and side-by-side arrangements", Journal of Fluids and Structures, 15, 327 – 350, 2001

Meneghini J. R. Saltara, F. and P.W. Bearman, "The simulation of vortex shedding from an oscillating circular cylinder with turbulence modeling", in Bearman and Williamson, 1997

Saltara, F. "Simulação numérica do escoamento ao redor de cilindros", University of São Paulo, Department of Mechanical Engineering, 1999

Versteeg, H.K., Malalasekera, W. "An Introduction to Computational Fluid Dynamics: The Finite Volume Method", Research Studies Pr, 1995

Two- and Three-Dimensional Force Coefficients of the flow around Two Circular Cylinders in Tandem

By PAULO J. S. JABARRDO[1]
and BRUNO S. CARMO[1]† and JULIO R. MENEGHINI[1]

[1]NDF, "Escola Politécnica", Department of Mechanical Engineering, University of São Paulo, CEP 05508-900, São Paulo, SP, BRAZIL

The incompressible flow around two circular cylinders in tandem is investigated in this paper. The emphasis is on the force coefficients and how these forces behave for different Re and spacings, and the influence of three-dimensional flow. The spectral element method is employed to carry out two- and three-dimensional simulations of the flow. The centre-to-centre distance (l_{cc}) of the investigated configurations varies from 1.5 to 8 diameters (D), and they are compared to the isolated cylinder case. The Reynolds number range goes from 160 to 320, covering the transition in the wake. Data of Strouhal number, mean drag coefficient, fluctuation of the lift coefficient, and axial correlation coefficient are presented.

1. Introduction

The flow around pairs of circular cylinders has been the subject of many investigations. The flow interference that occurs in such configurations is responsible for changes in the fluid loads and in important features of the flow field. In addition, investigations of the flow around pairs of cylinders can provide a better understanding of the vortex dynamics, pressure distribution and fluid forces in cases involving more complex arrangements.

Among the many possible arrangements in which two circular cylinders can be positioned relatively to a cross-flow, one that has been extensively studied is the tandem arrangement, as sketched in 1(a). In this configuration, the type of interference present is wake interference, where the wake of the upstream cylinder touches the downstream one Zdravkovich (1987). The effect of this interference is seen, for example, in the variation of the Strouhal number (St) and force coefficients with the Reynolds number (Re) and with the centre-to-centre distance (l_{CC}). The Strouhal number is the nondimensional frequency of vortex shedding and is defined as follows: $St \equiv fD/U_{\infty}$, where f is the dimensional frequency in Hz.

Many of the previous works regarding the flow around two circular cylinders identified diverse interference regimes and were based primarily on flow visualization in experiments. Investigations such as Igarashi (1981), Zdravkovich (1987) and Summer *et al.* (2000) proposed classifications of these regimes. The classification of Igarashi (1981) deals essentially with tandem arrangements, and therefore is the one we adopt here. According to this classification, six different interference regimes can be identified (Fig. 1(b)): (A) the free shear layers that originate from the separation on the surface of the upstream cylinder do not re-attach to the surface of the downstream cylinder; (B) the shear layers that come from the upstream cylinder are captured by the downstream one, but there is no vortex formation in the gap between the bodies; (C) symmetric vortices are formed between the cylinders; (D) the symmetric vortices become unstable and start to grow in proximity to the downstream cylinder; (E) the shear layers originating from the upstream cylinder roll up very near the downstream cylinder; and (F) the near wake region (formation region) ends before the downstream body and vortices are shed in the gap region in a regular way.

From regime A to regime D, the drag coefficient in the downstream cylinder is considerably lower than in the upstream cylinder. This can be understood when we note that, from A to D, the downstream cylinder is inside the near wake behind the upstream cylinder and therefore is in a low pressure region. In these cases, the drag in the second cylinder is usually negative. When the flow is in regime F, the drag in the downstream cylinder is positive. The spacing at which the downstream cylinder drag changes sign is called drag inversion spacing or critical spacing, and it depends on the Re.
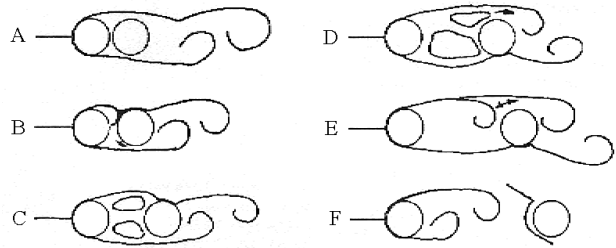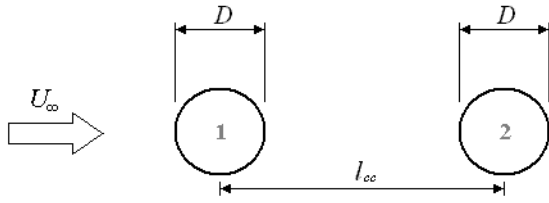
This investigation is a continuation of Carmo & Meneghini (2006). Here we focus on the effects of three-dimensionality of the flow on the force coefficients ($\overline{C_D}$ and $\sqrt{\overline{C_L^2}}$).

2. Methodology

The flow is assumed to be incompressible and isothermal and the Navier-Stokes equations are used. From dimensional analysis, only two independent non-dimensional paramters are possible. The Reynolds number

$$Re = \frac{U_{\infty}D}{\nu}$$

---

† Present address: Imperial College, Department of Aeronautics, London SW7 2BY, UK.

Fifth Conference on Bluff Body Wakes and Vortex-Induced Vibrations (BBVIV 5)
Costa do Sauipe, Bahia, Brazil, 12 - 15 December 2007

161

(a) Schematic drawing of the flow around two cylinders in a tandem arrangement.

(b) Interference regimes in the flow around pairs of circular cylinders in tandem arrangements. Extracted and adapted from Igarashi (1981).
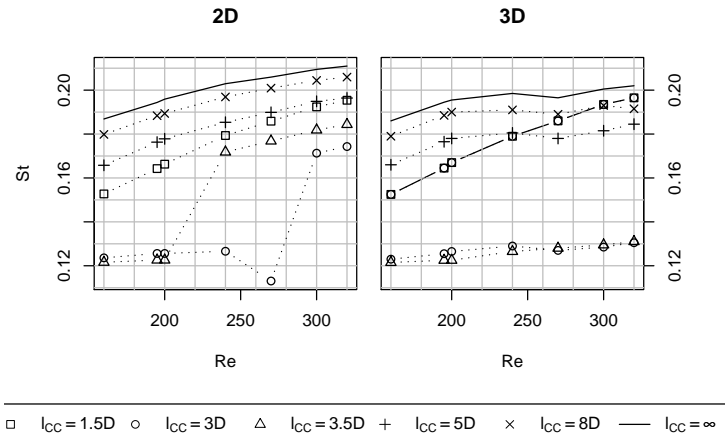

FIGURE 1. Strouhal number of cylinders in 2D and 3D simulations.

and the ratio of cylinders separation to the diameter: l_{CC}/D.

The equations are solved using the spectral/hp element method Karniadakis & Sherwin (2005). For the solution of the three-dimensional equations, the solution is expanded in Fourier series along the spanwise direction (z) and each mode is solved independently. At the end of each iteration the nonlinear coupled terms are calculated in physical space and using the FFT the modes are recalculated, Karniadakis (1990).

The code Nektar developed by Karniadakis & Sherwin (2005) and others is used to accurately simulate both two and three-dimensional flows.

The results presented here are calculated using the same discretization presented on Carmo & Meneghini (2006). New simulations using longer cylinders, finer grids in the near wake and new spacings are currently under way to improve the results presented here.

3. Results

Figure 1 presents the Strouhal numbers obtained. The behaviour of 2D and 3D flows show some differences. The most obvious is a jump of St for spacings close to $3D$ due to drag inversion (in figure 1(b), from E to F). The 3D flow is less sensitive to Re number. For $3D$ and $3.5D$ spacings, the Re number could not change the flow regime. The only exception occurs when both cylinders are very close ($1.5D$) and the St keeps increasing and both 2D and 3D simulations show very close behaviour.

Figure 3 presents the mean force coefficients and RMS of the lift coefficient for the up and downstream cylinder. Compared to St number, the differences in force coefficients are much larger between 2D and 3D simulations. Again, the drag inversion for the 2D case is the most striking difference. The upstream force coefficient clearly shows that there is a change of the behaviour around $Re = 200$ and $Re = 270$, changes already observed for the single cylinder, and can be related to ther triggering of modes A and B in Williamson (1996).

4. Discussion

Even though the qualitative behaviour of 2 and 3D flows is the very close, three-dimensional effects are important when Re is large. Some effects observed for single cylinders are also present when two circular cylinders are positioned in tandem. Carmo & Meneghini (2006) has shown that these changes are related to the triggering of modes A and B present in single cylinders.
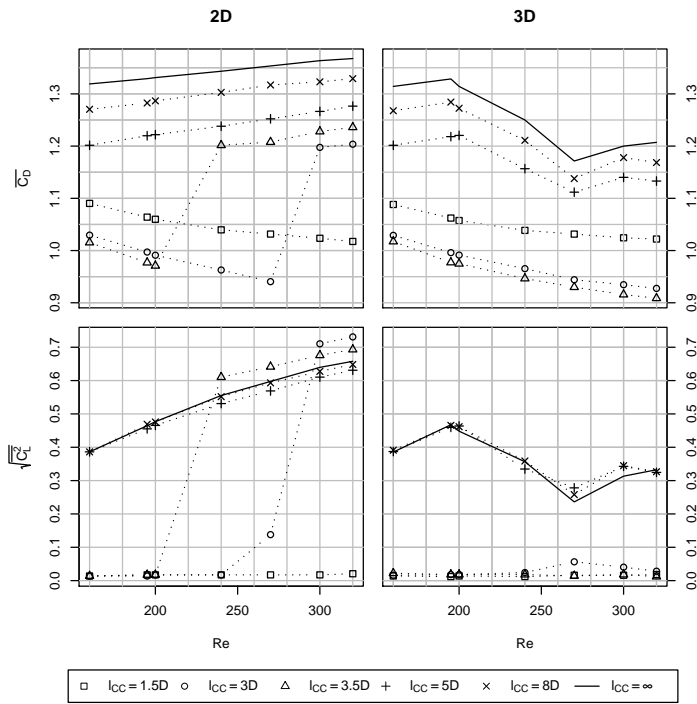
(a)Upstream cylinder.
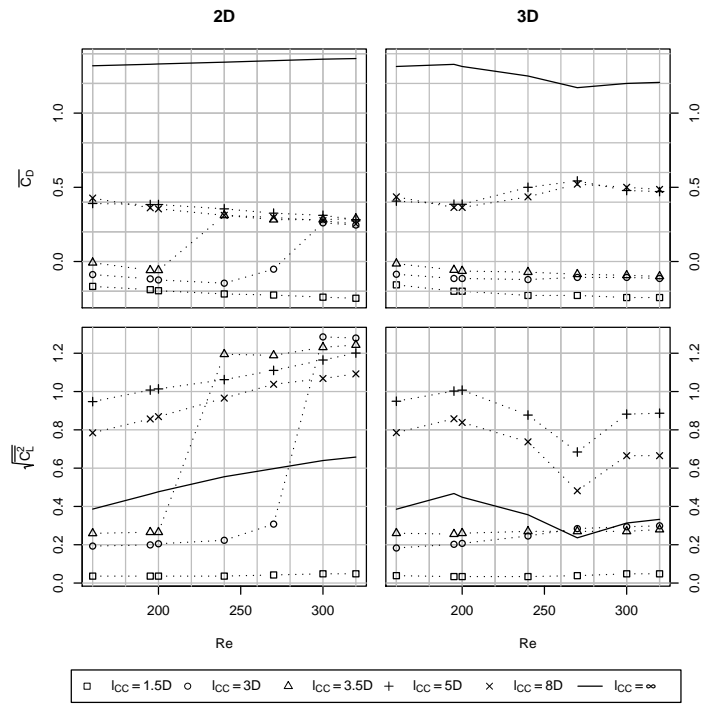
(b)Downstream cylinder.

When the flow is 2D, the lift coefficient (actually the RMS of the lift coefficient) increases with Re in every case studied. This show the decreasing importance of viscous forces near the walls in relation to the pressure forces. Once three-dimensional effects exist, the flow changes and smaller $\sqrt{\overline{C_L^2}}$ are observed. Large $\sqrt{\overline{C_L^2}}$ are related to strong vortices close to the cylinder and therefore is a good parameter to observe qualitative changes in the flow.

For two-dimensional flows, the $\sqrt{\overline{C_L^2}}$ provides a nice interoretation of the flow. As Re increases pressure becomes more important and higher lift coefficients are expected. This, in turn, affects the drag coefficient. There is one exception though: the drag inversion observed in spacings close to $3 - 3.5D$. But now there is big change in flow regime and the flow must be more sensitive to vortex formation and the change in drag inversion with Reynolds and spacing is reasonable.

When the flow is three-dimensional, on the other hand, other possibilities arise. Three dimensional structures couple the flow along the cylinder axis. The exact processes involved are more complex. Carmo & Meneghini (2006) observed similarities with the modes presented in Williamson (1996) and this is sensitive to Re number.

Since three dimensional effects do not change the qualitative features of the flow, another way to study three-dimensional effects is to determine how different levels along the cylinder's axis are correlated. The correlation coefficient is defined as:

$$\rho(z) = \frac{\overline{(\phi(0) - \Phi)(\phi(z) - \Phi)}}{\overline{(\phi(0) - \Phi)^2}} \tag{4.1}$$

The correlation is expected slowly decrease as the distance between levels increases (since the flow is assumed periodic it will later increase again). The correlation can integrated along the axis to calculate the correlation length. Figure 2 show the correlation coefficient obtained from the lift coefficient. Szepessy (1991) has presented some results on correlation and correlation length for a single cylinder and Jabardo *et al.* (2001) extended this results for flows around groups of cylinders, including tandem arragements. It is true that these results involve much higher Re numbers (larger than $\approx 10,000$).

Simulations are under way to calculate the correlation *field*, that is, how different properties (mainly pressure) are correlated along the axis direction throughout the flow domain. From this correlation, a map of correlation length is obtained that shows how three-dimensional effects are distributed. This might provide some insight as to how three-dimensionality develops.
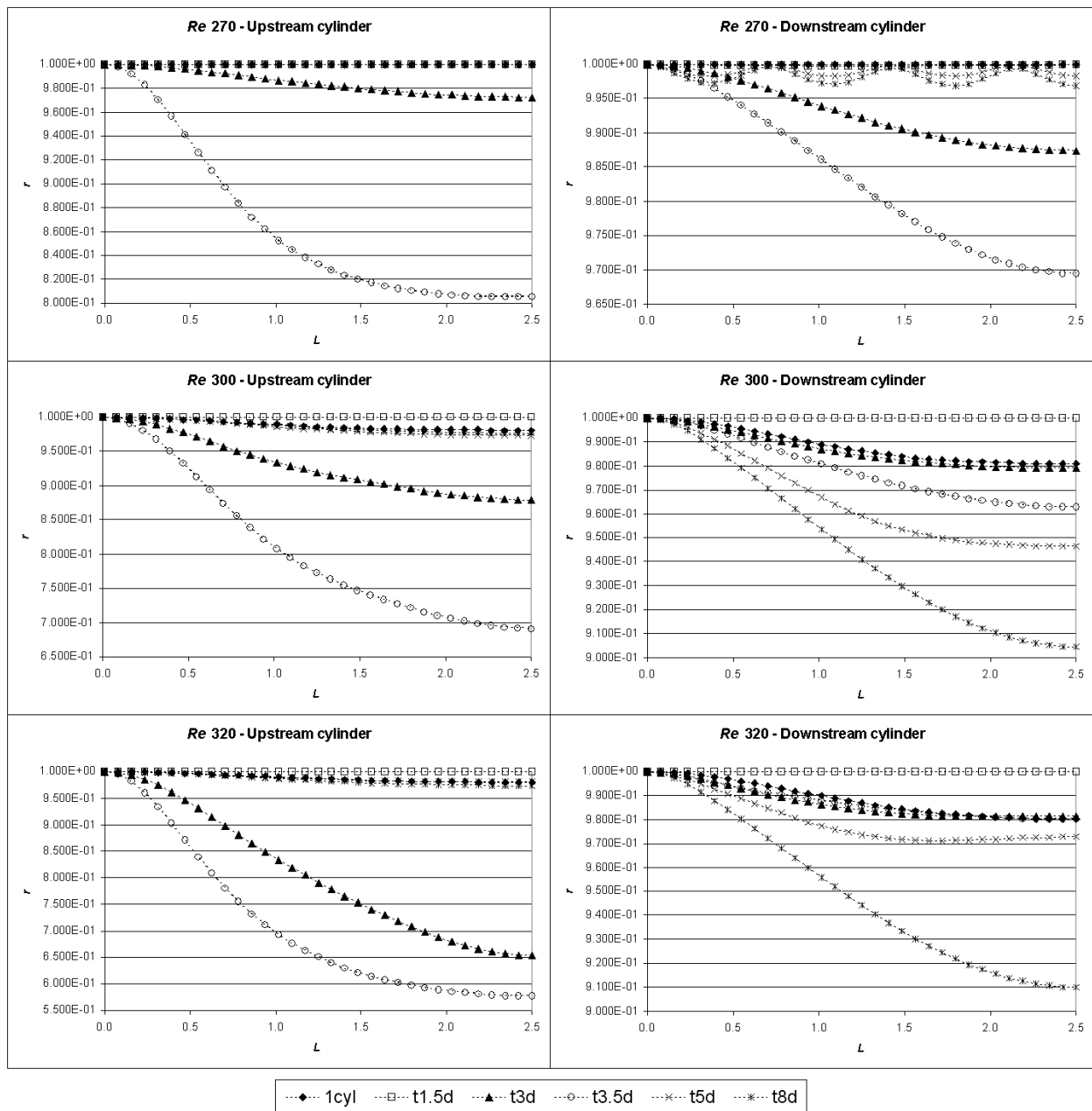
FIGURE 2. Axial correlation coefficient. Reynolds numbers: 270, 300 and 320.

REFERENCES

CARMO, B. S. & MENEGHINI, J. R. 2006 Numerical investigation of the flow around two cylinders in tandem. *Journal of Fluid and Structures* **22**, 979–988.

IGARASHI, T. 1981 Characteristics of the flow around two circular cylinders arranged in tandem. *Bulletin of JSME* **24** (188), 323–331.

JABARDO, P. J. S., CALY, J. P. & PEREIRA, M. T. 2001 Estudo do escoamento ao redor de cilindros. Relatório técnico no. 54804. Instituto de Pesquisas Tecnológicas do Estado de São Paulo, São Paulo, Brasil.

KARNIADAKIS, G. E. 1990 Spectral element-fourier methods for incompressible turbulent flows. *Comp. Meth. Appl. Mech. Eng.* **80**.

KARNIADAKIS, G. E. & SHERWIN, S. J. 2005 *Spectral/hp element methods for CFD*, 2nd edn. New York: Oxford University Press.

SUMMER, D., PRICE, S. J. & PÄIDOUSSIS, M. P. 2000 Flow-pattern identification for two staggered circular cylinders in cross-flow. *Journal of Fluid Mechanics* **411**, 263–303.

SZEPESSY, S. 1991 On the three-dimensionality of vortex shedding from a circular cylinder. Phd thesis, Chalmers University of Technology, Göteborg.

WILLIAMSON, C. H. K. 1996 Three-dimensional wake transition. *Journal of Fluid Mechanics* **328**, 345–407.

ZDRAVKOVICH, M. M. 1987 The effects of interference between circular cylinders in cross flow. *Journal of Fluids and Structures* **1**, 239–261.

The Interaction of Gravity Currents with Submarine Installations: High-Resolution Simulations of the Impact Stage

E. D. Gonzalez-Juez and E. Meiburg
Department of Mechanical Engineering
University of California at Santa Barbara
Email: meiburg@engineering.ucsb.edu

S. G. Constantinescu
Department of Civil and Environmental Engineering
University of Iowa

June 1, 2007

Gravity currents form in many natural environments, as well as in engineering applications, when a heavier fluid propagates into a lighter one in a predominantly horizontal direction (Simpson (1997)). They can be driven by density differences of the liquids or gases involved, or by differential particle loading. In many situations (a freshwater river flowing into a saltwater ocean, atmospheric flows involving warm and cold air, and many others), the density differences are no more than a few percent, so that the Boussinesq approximation can be employed. An example of a numerically simulated lock exchange gravity current is shown in figure 1 (from Hartel *et al.* (2000)). However, there are many circumstances when the density differences can be much more substantial (industrial gas leaks, tunnel fires, powder snow avalanches, pyroclastic flows), and the full variable density equations have to be solved (Birman *et al.* (2005)).

Of particular interest is the situation when a gravity current forms as a result of an underwater landslide. The subsequent flow of sediment-laden fluid is referred to as turbidity current. If such a current spreads over an erodible bed, the geometry of the base may allow the current to resuspend sufficient particles so that its mass and velocity increase as it progresses downslope (Blanchette *et al.* (2005)). Turbidity currents are the most significant agents of sediment transport into the deep sea, creating accumulations that include the Earth's largest sediment bodies. Such currents can be extremely large, transporting many cubic kilometers of sediment, and propagating over more than 1,000 km along the bottom of the ocean.

Natural turbidity currents occur infrequently and unpredictably in remote and hostile environments, and they tend to be destructive of submarine equipment. Their interaction with submarine engineering structures, such as oil and gas pipelines, wellheads and submarine cables, hence constitutes an important challenge to design engineers. Laboratory and numerical experiments constitute essential means of investigating these important large scale natural phenomena. The prediction of the dynamic force loads exerted by such currents onto the submarine structures is particularly important for the design of submarine structures, in order to avoid failures that can potentially lead to severe environmental disasters.

In this context, high-resolution numerical simulations can be of great value, as they offer access to quantitative information that is hard to measure experimentally. Spatially and temporally resolved particle distribution and erosion fields represent examples in this regard. Furthermore, simulations have the capability to elucidate time-dependent vortical flow structures during the impact stage, along with the associated forces exerted on the solid object. Understanding the effect of these flow structures on the unsteady forces is crucial for the development of design guidelines for submarine

installations.

Figure 2 shows the temporal evolution of the concentration field as the gravity current interacts with a square cylinder mounted on the bottom wall. The light fluid is shown in grey. Zoom-in views close to the obstacle of the time frames in figure 2a are shown in figure 2b, with superimposed instantaneous streamlines. In the first frame ($t = 7.0$), the gravity current front is approaching from the left with a constant velocity. The next frame ($t = 7.6$) shows the current encountering the obstacle. At about this time the maximum drag and lift (directed upward) are seen. By exploring a wide range of parameter combinations, we found that the most drastic time variation of the forces usually occurs during this initial impact stage. The third and fourth frames ($t = 8.6$ and $t = 9.6$) of figure 2 show the formation of recirculation regions upstream and downstream of the obstacle. Although the upstream recirculation is seen not to have a noticeable effect on the forces for the particular set of parameters shown here, it does have a strong effect at other sets of parameters. By the time of the fifth frame ($t = 10.2$), the minimum lift (directed downward) is found. The last frame of figure 2 shows a time during a quasi-steady state stage of the interaction, in which the flowfield and the forces do not vary much with time. The drag at this stage is usually about half the value of the maximum drag found in the impact stage.

In conclusion, detailed information about the vortical flow structures and associated forces from the impact of gravity currents on submarine structures can be gained from high-resolution simulations.

References

BIRMAN, V. K., MARTIN, J. E. & MEIBURG, E. 2005 The non-Boussinesq lock-exchange problem. Part 2. High-resolution simulations. *Journal of Fluid Mechanics* **537**, 125–144.

BLANCHETTE, F., STRAUSS, M., MEIBURG, E., KNELLER, B. & GLINSKY, M. E. 2005 High-resolution numerical simulations of resuspending gravity currents: Conditions for self-sustainment. *Journal of Geophysical Research-Oceans* **110** (C12), –.

HÄRTEL, C., MEIBURG, E. & NECKER, F. 2000 Analysis and direct numerical simulation of the flow at a gravity-current head. Part 1. Flow topology and front speed for slip and no-slip boundaries. *Journal of Fluid Mechanics* **418**, 189–212.

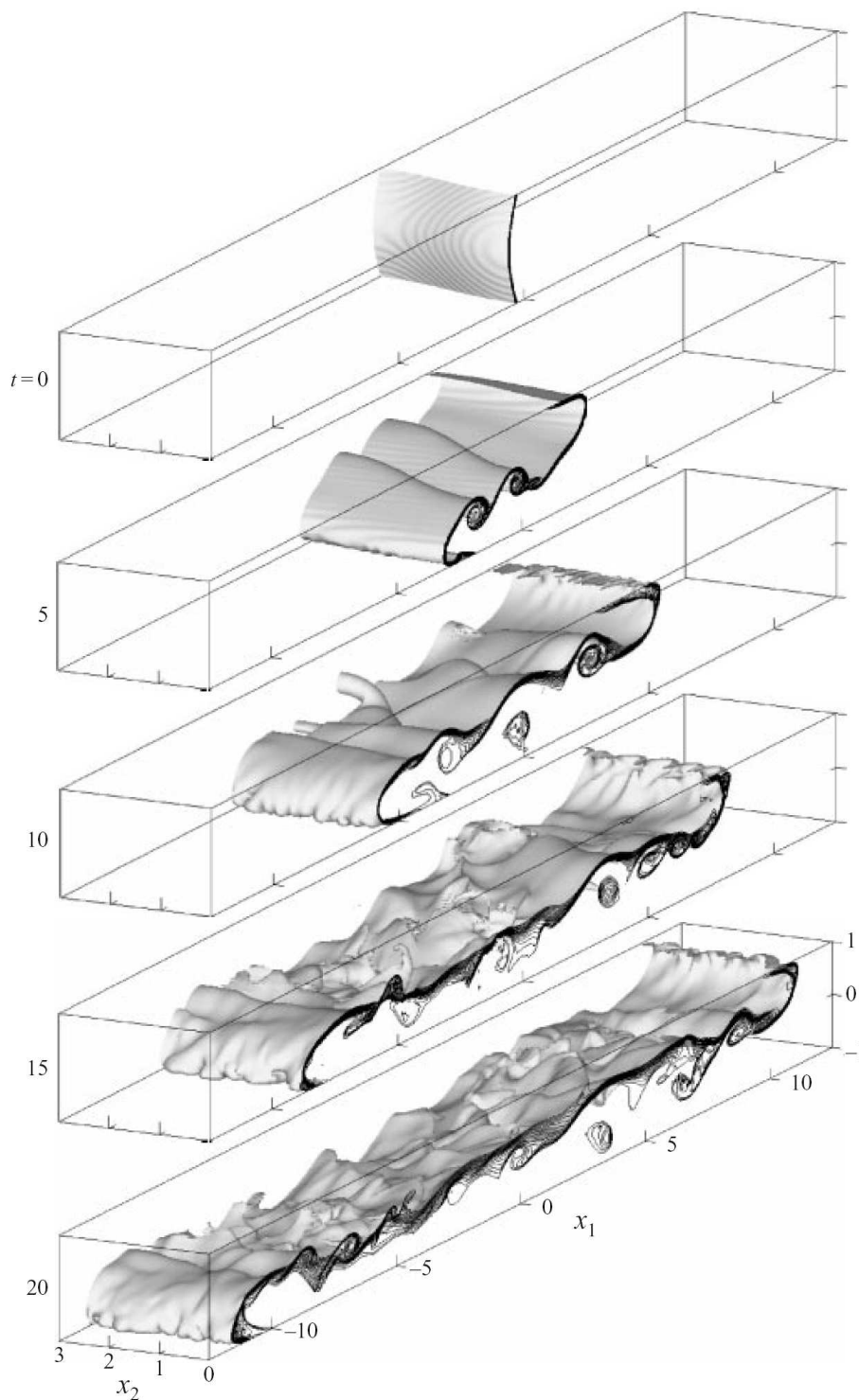SIMPSON, J. E. 1997 *Gravity Currents in the Environment and the Laboratory*. Cambridge University Press.

Figure 1: Lock exchange gravity current at Re=1,225 (from Hartel *et al.* (2000)).
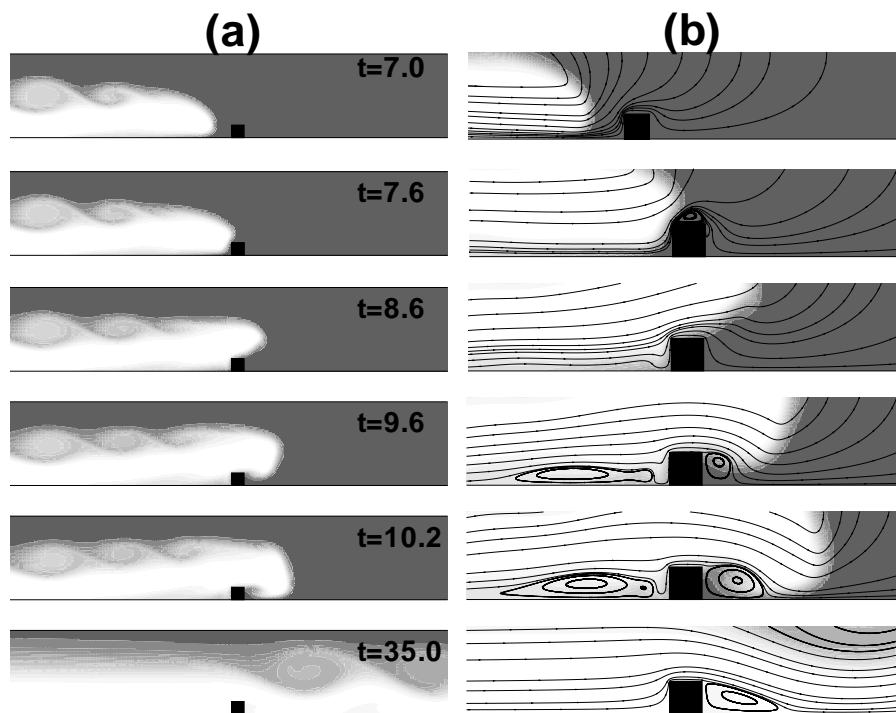
Figure 2: Temporal evolution of the concentration field as the gravity current interacts with a square cylinder mounted on the bottom wall. The gravity current moves from left to right. The light fluid is shown in grey. Zoom-in views close to the obstacle with superimposed instantaneous streamlines are shown on the right.

A Study of the Interaction of a Gravity Current with a Circular Cylinder

E. D. Gonzalez-Juez and E. Meiburg
Department of Mechanical Engineering
University of California at Santa Barbara
Email: meiburg@engineering.ucsb.edu

S. G. Constantinescu
Department of Civil and Environmental Engineering
University of Iowa

June 1, 2007

Abstract

We study numerically the interaction of a gravity current with a circular cylinder mounted above a bottom wall, at moderate Reynolds numbers. The size of the gap between the circular cylinder and the bottom wall is seen to have a small effect on the maximum drag, while noticeably altering the maximum lift. Morison's equation is seen to underpredict the maximum drag by about 25%.

While forces from currents and waves are usually taken into account in the design of submarine structures, very little is known about the forces involved in the potential impact of a gravity current. With this in mind, we conducted a series of two-dimensional numerical simulations to study the interaction of a Boussinesq compositional lock-exchange gravity current with a submerged circular cylinder. Emphasis was placed on understanding the forces acting on the circular cylinder. The present work complements recent numerical work on square cylinders (Gonzalez-Juez *et al.* (2007)), and experimental work on circular and rectangular cylinders (Ermanyuk & Gavrilov (2005*a,b*)). A schematic of the flow configuration is shown in figure 1. Initially, two quiescent miscible fluids of different densities are separated by a vertical gate. The gate is then removed and, after an initial transient, a gravity current flow is established. A circular cylinder of diameter D is positioned downstream from the gate at a gap distance G from the bottom boundary. The Reynolds number based on the diameter D and the gravity current front speed V was $Re_D = 120$. The ratio of the cylinder diameter and the channel height h was $D/h = 0.15$.

Figure 2 shows the evolution in dimensionless time of the vorticity field as the gravity current interacts with a circular cylinder positioned at a gap distance of $G/D = 1$. We render time t^* and vorticity ω^* dimensionless using the height of the channel h and the buoyancy velocity u_b, which is defined as $u_b \equiv \sqrt{gh\Delta\rho/\rho}$, where g is the gravitational acceleration, $\Delta\rho$ the difference in the fluids densities, and ρ the fluid density. The temporal evolution of the (total) drag and lift coefficients for different values of G/D is shown in figure 3. The drag and lift coefficients are defined respectively as $C_D \equiv F_D/0.5\rho D V^2$ and $C_L \equiv F_L/0.5\rho D V^2$, where F_D is the force in the streamwise direction, and F_L is the force in the vertical direction. Figure 3 shows that the maximum drag and lift amplitudes occur during the initial impact stage. G/D is seen to have a small effect on the maximum drag, but a noticeable one on the maximum lift amplitude.

Figure 4 compares the temporal evolution of the drag coefficient for $G/D = 1$ with that predicted using Morison's equation (Morison *et al.* (1950) and Sarpkaya & Isaacson (1981) p.9). In spite of its limitations, Morison's equation is usually used to predict the drag force on cylinders immersed in time-dependent flows. This equation can be written as:

$$C_D = \frac{\pi}{2}C_m \left(\frac{dU(t)/dt}{V^2/D}\right) + C_d \left(\frac{U(t)}{V}\right)^2 . \tag{1}$$

Here, the total drag force is expressed as a sum of a potential-flow component and a vortex-flow component (Lighthill (1986)). We employ $C_m = 2$ for the inertia coefficient, and we set the damping coefficient C_d equal to the drag coefficient of a circular cylinder immersed in a steady flow at $Re_D = 120$ ($C_d = 1.24$). We justify the use of these coefficients by assuming that the circular cylinder is far enough from the bottom wall for $G/D = 1$ to approach free stream conditions. Using the results from a simulation of the gravity current flow without the obstacle, the velocity $U(t)$ in Morison's equation was obtained by integrating the horizontal velocities at the location where the obstacle would have been situated. Figure 4 also shows this velocity $U(t)$. We have made the assumptions here of a predominantly horizontal velocity field that would not be distorted "much" by the presence of the obstacle. It can be seen in figure 4 that the present modeling attempt captures qualitatively the drag variation with time, although the maximum drag coefficient is under-predicted by about 25%. In contrast, the quasisteady drag, i.e. the drag during the later stages, is rather well captured. Future work should address the applicability of Morison's equation for a large set of different parameters, and potential modifications to this equation to improve the accuracy of its predictions.

References

ERMANYUK, E. V & GAVRILOV, N. V. 2005*a* Interaction of an internal gravity current with a submerged circular cylinder. *Journal of Applied Mechanics and Technical Physics* **46** (2), 216–223.

ERMANYUK, E. V & GAVRILOV, N. V. 2005*b* Interaction of an internal gravity current with an obstacle on the channel bottom. *Journal of Applied Mechanics and Technical Physics* **46** (4), 489–495.

GONZALEZ-JUEZ, E. D., CONSTANTINESCU, S. G. & MEIBURG, E. 2007 A study of the interaction of a gravity current with a square cylinder using two-dimensional numerical simulations. *26th International Conference on Offshore Mechanics and Arctic Engineering* .

LIGHTHILL, J. 1986 Fundamentals concerning wave loading on offshore structures. *Journal of Fluid Mechanics* **173**, 667–681.

MORISON, J.R., O'BRIEN, M.P., JOHNSON, J.W. & SCHAAF, S.A. 1950 The forces exerted by surface waves on piles. *Petroleum Transactions of the AIME* **189**, 149–157.

SARPKAYA, T. & ISAACSON, M. 1981 *Mechanics of Wave Forces on Offshore Structures*. New York: Van Nostrand Reinhold Company.
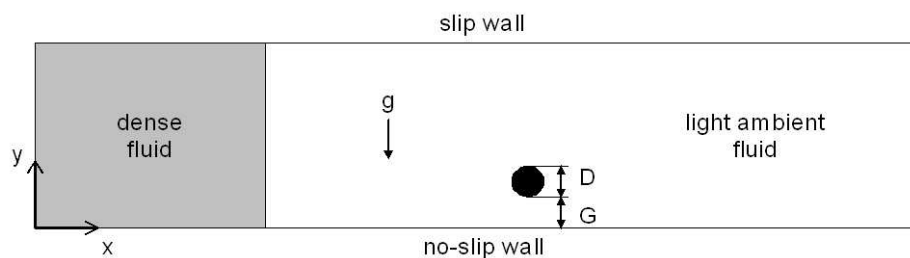
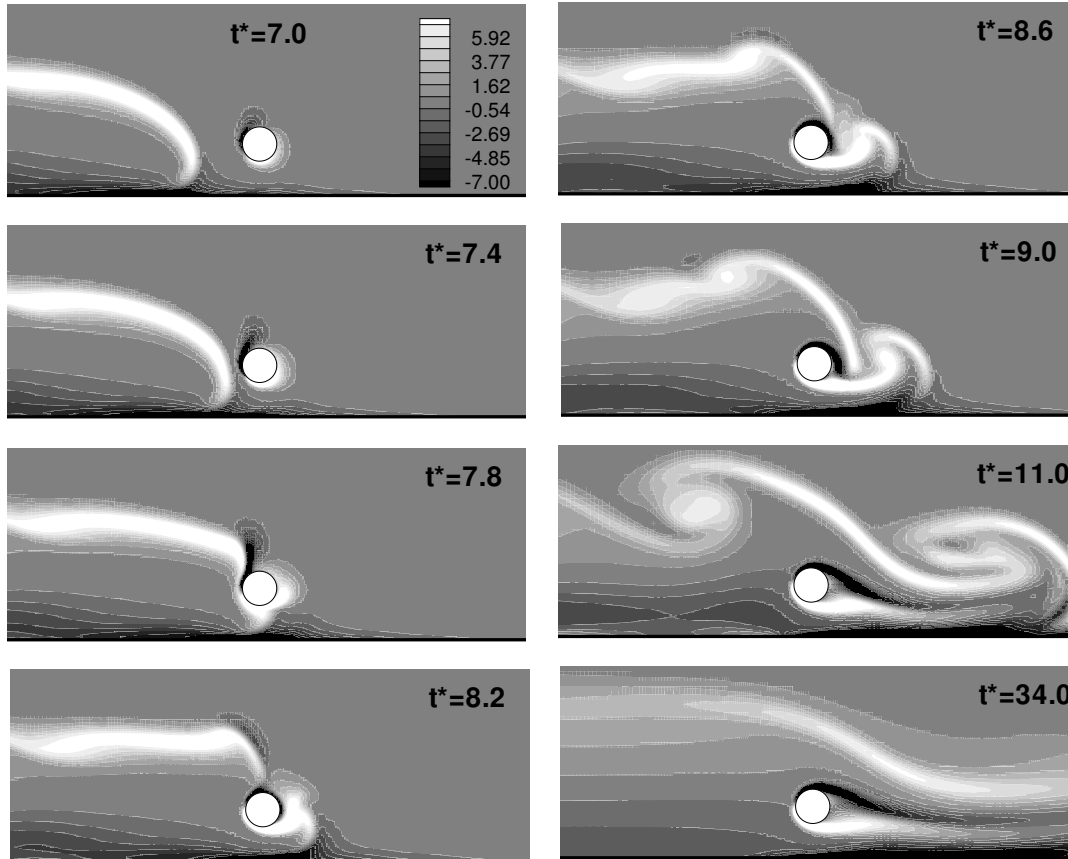Figure 1: Schematic of the flow configuration.

Figure 2: Temporal evolution of the vorticity field as the gravity current interacts with the circular cylinder for $G/D = 1$. The gravity current front moves from left to right. The shear layer between the two fluids can be clearly seen in this figure. The maximum lift occurs at $t^* = 7.4$ and the maximum drag at $t^* = 8.4$.
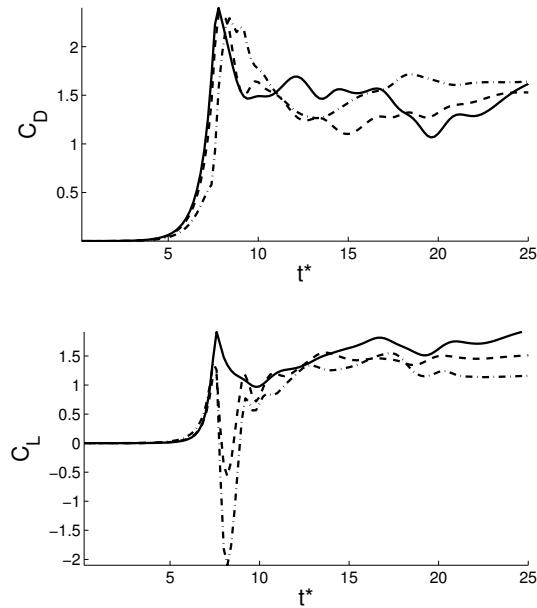
Figure 3: Temporal evolution of the total drag (C_D, top frame) and lift (C_L, bottom frame) coefficients for different values of the gap distance between the bottom wall and the circular cylinder: $G/D = 0.066$ (solid line), 0.3 (dashed line), 1.0 (dashed-dotted line). The gap size is seen to have a small effect on the drag, but a much larger effect on the lift.
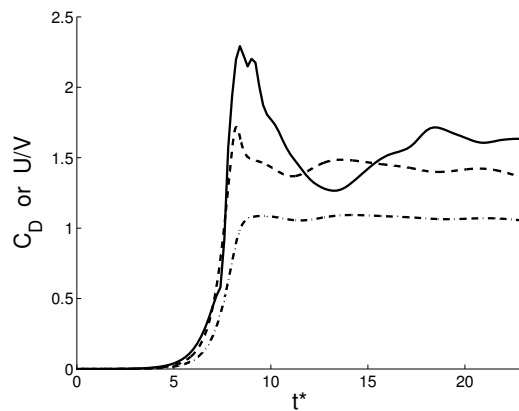

Figure 4: Comparison of the drag coefficient variation with time for the gravity current flow past a circular cylinder for $G/D = 1$ (solid line) with that predicted using Morison's equation (dashed line). Also shown is the velocity $U(t)$ used in Morison's equation (dashed-dotted line). Morison's equation is seen to underpredict the maximum drag by about 25%.

Three-Dimensional Simulation of Flow Around A Rectangular Flat Plate

Kunihiko Taira & Tim Colonius

Mechanical Engineering, Division of Engineering and Applied Science,

California Institute of Technology, Pasadena, California, 91125, USA

kunihiko@caltech.edu, colonius@caltech.edu

Abstract

Three-dimensional incompressible flow simulations are performed to investigate the flow field around a low-aspect-ratio rectangular flat plate. At high angles of attack, the separated flow exhibits strong interaction between the leading edge and tip vortices. Steady actuation is also considered to increase lift exerted on the plate by modifying the topology of the vortical wake structure.

Introduction

Separated flows behind low-aspect-ratio wings have been of interest for the development and control of small unmanned aerial vehicles[1] as well as for understanding the flight mechanism of insect wings.[2] While translating flight studies have been experimentally performed in the past,[3–5] there is scarcity of three-dimensional numerical studies of flow around low-aspect-ratio wings at low Re in general.

Here, we focus on the general behavior of the three-dimensional flow around purely translating rectangular wings at the range of $Re \approx \mathcal{O}(10^2)$ where many insects maneuver their wings and future bio-inspired micro air vehicles could operate. In addition, applications of steady actuation are considered to alter the vortical wake structure to enhance lift exerted on the rectangular wing. This translating wing study is a part of a larger research effort to assist future design, control, and reduced order modeling of bio-inspired micro-air-vehicles.[6–8]

Flow Simulation

The immersed boundary projection method[9] is used to perform three-dimensional incompressible flow simulations around an impulsively started low-aspect-ratio rectangular flat plate. This method allows us to simulate flows around arbitrary geometries on a Cartesian grid by introducing a regularized delta function along the immersed surface to satisfy the no-slip condition. In this study, impulsively started flows are considered by instantaneously materializing the plate at $t = 0^+$ in a uniform flow. We study both the initial transient and long time behavior of the wake and the force exerted on the plate.

For validation, DPIV measurements from an oil tow tank experiment is considered. Flow field around an impulsively translated rectangular plate of $AR = 2$ at $\alpha = 30°$ and $Re = 100$ is compared with the current simulation results. Numerical and DPIV snapshots of the spanwise vorticity profile at the midspan are in agreement in Figure 1. Lift and drag coefficients are also found to be in accord between the simulation and force measurements.

We consider various aspect ratios (AR) and angles of attack (α) to study the interaction of the leading edge and tip vortices. The wake behind the plate is strongly influenced by the aspect ratio as exhibited in Figure 2. Here the vortical structures are shown behind plates of $AR = 1$ and 2 well into separation at $\alpha = 30°$ for $Re = 300$. In the case of a square plate, the flow structures stay stably attached to the plate and are able to achieve a steady profile. On the other hand, for a rectangular plate of $AR = 2$, the wake shows unsteady shedding of leading edge vortices interacting strongly with the tip vortices. For both plates, a trailing edge vortex is formed only immediately after the impulsive start (see snapshots from $t = 1.5$). Later in time, the vortex sheet generated at the trailing edge is rolled into the tip vortices.
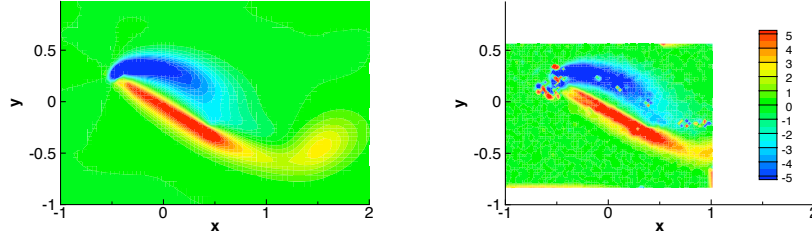
Figure 1. Spanwise vorticity profiles along the midspan for a rectangular flat plate of $AR = 2$ and $\alpha = 30°$ from the simulation (left) and the DPIV measurement (right) for $t = 1.5$ and $Re = 100$.

It should be noticed that the tip vortices are distinct from the leading edge vortex throughout the simulation. In the wake of the plate of $AR = 2$, the tip vortices can interact with the detaching leading edge hairpin vortices. However, these vortical structures never merge. Early in time, the leading edge vortex is able to grow in size and circulation, enhancing lift experienced by the plate. At $t \approx 10$, two hairpin vortices start to detach from the plate and interact with the tip vortices. The tip vortices consequently lose their columnar structure reducing the downward induced velocity on the plate, resulting in a reduction of lift. Consecutive leading edge vortices are formed while strongly interacting with the tip vortices as depicted by the snapshots in the right most column of Figure 2.
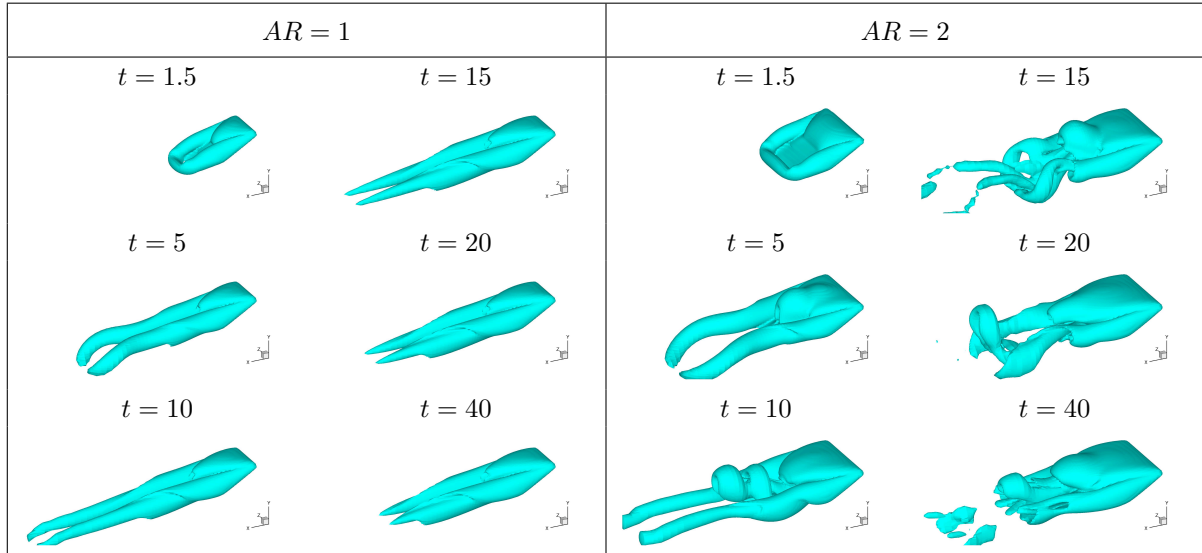

Figure 2. Snapshots of the wake represented by isosurface of $\|\boldsymbol{\omega}\|_2 = 2$ behind rectangular flat plates of $AR = 1$ and 2 at $\alpha = 30°$ and $Re = 300$. Viewing downward from the starboard side of the plate.

Steady Flow Control

We investigate alternative wake structures that could possibly enhance lift by introducing steady actuation at different locations. Actuation is modeled with an external body force located $3\Delta x$ above the top surface along the leading edge, midchord, and trailing edge. The body force is given by the form of $\mathbf{f}d(x - x_0)d(y - y_0)H(b/2 - z)H(b/2 + z)$, where d, H, and b are the discrete delta function, Heaviside step function, and span of the plate, respectively. Coordinates (x, y, z) correspond to the streamwise, vertical, and spanwise directions. The actuator position is specified by x_0 and y_0 and actuation directions of upstream, sideways (outward spanwise), and downstream parallel to the plate are set by choosing an appropriate $\mathbf{f}$.

Here we apply steady control to the previously considered unsteady flow around a rectangular plate of $AR = 2$ at $Re = 300$ and $\alpha = 30°$. In present simulations, the momentum coefficient is set to $c_\mu = 0.01$. This value is larger than what is used in experimental studies at high Reynolds number since the slot width of the modeled actuator, limited by the grid size, is larger than that of the experimental

setup. However, we use this momentum coefficient to investigate the possibility of modifying the wake pattern with different actuator inputs. Companion oil tunnel experiments are underway to validate the current control study.

Figure 3 illustrates the lift history over time for different cases of actuation. Compared to the baseline case without control, actuation in the downstream direction is found to be most effective for the considered actuator directions yielding an increase in lift of about 40 to 100% at large times. While drag also increased, the lift to drag ratio, L/D, remained at about 20 to 30% in increase for cases of downstream actuation, as shown by the bottom right plot of Figure 3. Another interesting observation is that for some cases, the shedding behavior of the wake became periodic unlike the aperiodic unactuated flow.

With actuation, the topology of the wake structure has been modified as shown in Figure 4. At large time, the tip vortices are still in distinct columnar structures similar to those found in the wake of the $AR = 1$ plate or at early time behind the $AR = 2$ plate in Figure 2. By having stably formed tip vortices by downstream actuation, the leading edge vortex is located closer to the top surface of the plate. In the case of downstream actuation at midchord, the leading edge vortical structure is found to achieve a steady state profile. For the other two cases, hairpin vortices do detach but with less interaction between the tip and hairpin vortices, allowing the downward induced velocity from the tip vortex pairs to remain effective at all times.
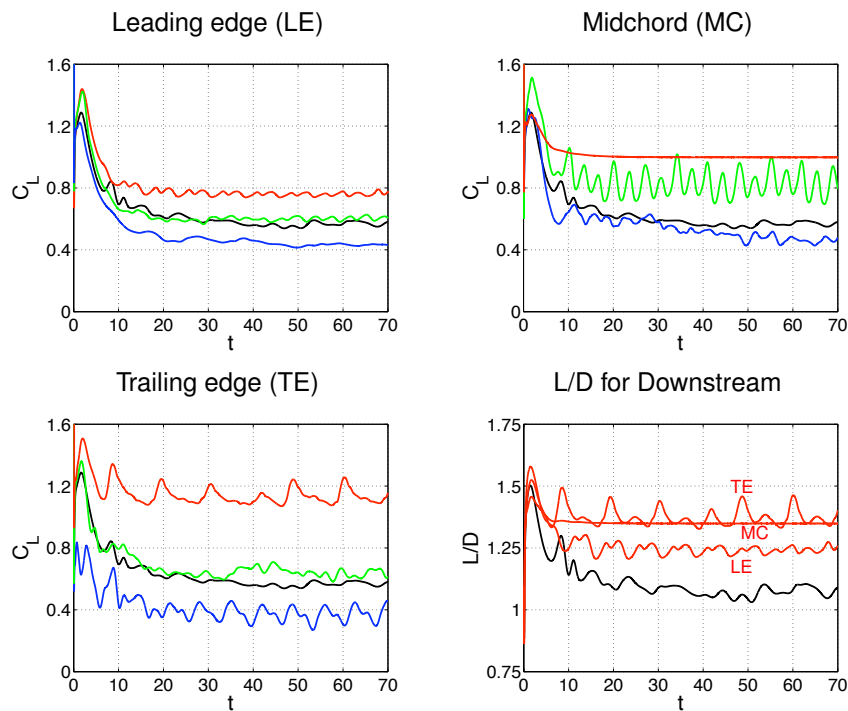

Figure 3. Lift coefficients over time with different locations and directions of steady actuation for a rectangular plate of $AR = 2$ **at** $Re = 300$ **and** $\alpha = 30°$ **(Downstream ———; Sideways ———; Upstream ———; and No actuation ———). Also shown at the bottom right is the lift to drag ratio for cases of downstream actuation.**
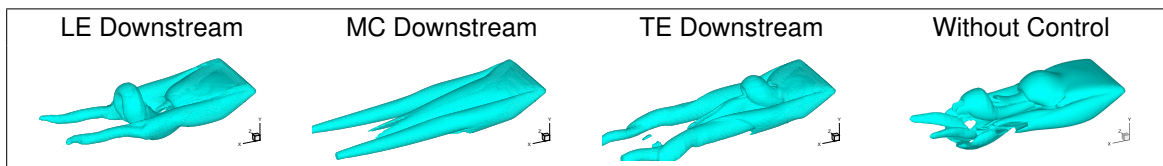

Figure 4. Snapshots of the wake represented by isosurface of $\|\boldsymbol{\omega}\|_2 = 2$ **behind rectangular flat plate of** $AR = 2$ **at** $\alpha = 30°$ **and** $Re = 300$**. Wake structures are presented at** $t = 70$ **with and without steady actuation at different locations. Viewing downward from the starboard side of the plate.**

Summary

Three-dimensional flow simulations were performed to study the wake structure behind low-aspect-ratio rectangular flat plates in low Reynolds number. The vortical structures in the wake of the plate exhibit strong interaction between the tip and leading edge vortices. For a Reynolds number of 300, the vortical structure was found to reach a steady state for $AR = 1$ while the wake was found to be aperiodic in time exhibiting complex wake structures for $AR = 2$. For $AR \gtrsim 1$, the leading edge vortex is observed to detach as a hairpin vortex and interact with the tip vortices. The tip vortices consequently lost their columnar structures, decreasing the downward induced velocity and reducing lift after the initial transient.

Steady actuation was also considered to alter the wake structure to increase lift. Downward actuations along the midchord and the trailing edge were found to be effective in increasing lift by about 70 and 100%, respectively. While the drag also increased, the lift to drag ratio remained at an increase of about 20 to 30%. This was achieved by reducing the amount of interaction between the tip and leading edge vortices to take advantage of the downward induced velocity by the tip vortices. In some cases of actuated flows, vortex shedding was suppressed allowing the wake to reach a steady state. Findings from the present control study are to be compared to future measurements from oil tunnel experiments at the California Institute of Technology.

Acknowledgment

References

[1] T. J. Mueller and J. D. DeLaurier, "Aerodynamics of Small Vehicles," *Annual Review of Fluid Mechanics*, Vol. 35, pp. 89-111, 2003.

[2] J. M. Birch, W. B. Dickson, and M. H. Dickinson, "Force Production and Flow Structure of the Leading Edge Vortex on Flapping Wings at High and Low Reynolds Numbers," *Journal of Experimental Biology*, Vol. 207, pp. 1063-1072, 2004.

[3] A. E. Winkelmann and J. B. Barlow, "Flowfield Model for a Rectangular Planform Wing beyond Stall," *AIAA Journal*, Vol. 18, No. 8, pp. 1006-1008, 1980.

[4] G. E. Torres and T. J. Mueller, "Low-Aspect-Ratio Wing Aerodynamics at Low Reynolds Numbers," *AIAA Journal*, Vol. 42, No. 5, pp. 865-873, 2004.

[5] G. R. Spedding, J. McArthur, and M. Rosén, "Deducing Aerodynamic Mechanisms from Near- and Far-Wake Measurements of Fixed and Flapping Wings at Moderate Reynolds Number," *44th Aerospace Sciences Meeting and Exhibit*, AIAA, Reno, NV, Jan. 9-12, 2006.

[6] T. Colonius, C. W. Rowley, G. Tadmor, D. R. Williams, K. Taira, W. B. Dickson, M. Gharib, and M. Dickinson, "Closed-Loop Control of Leading-Edge and Tip Vortices for Small UAV," *Conference on Active Flow Control*, DFG, Berlin, Sep. 27-29, 2006.

[7] K. Taira, W. B. Dickson, T. Colonius, M. H. Dickinson, and C. W. Rowley, "Unsteadiness in Flow over a Flat Plate at Angle-of-Attack at Low Reynolds Numbers," *45th Aerospace Sciences Meeting and Exhibit*, AIAA, Reno, NV, Jan. 8-11, 2007.

[8] K. Taira and T. Colonius, "Three-Dimensional Flow Simulations and Control around Low-Aspect-Ratio Flat Plates," *Journal of Fluid Mechanics*, in preparation, 2007.

[9] K. Taira and T. Colonius, "The Immersed Boundary Method: A Projection Approach," *Journal of Computational Physics*, accepted, 2007.

Vortex dynamics of a separated boundary layer on a rounded edge by Direct Numerical Simulation

Jorge Silvestrini[1] and Eric Lamballais[2]

[1]Faculdade de Engenharia,
Pontifícia Universidade Católica do Rio Grande do Sul
Av. Ipiranga 6681, 90619-900 Porto Alegre - RS, Brasil, `jorgehs@pucrs.br`

[2]Laboratoire d'Etudes Aérodynamiques UMR 6609,
Université de Poitiers, CNRS
Téléport 2 - Bd. Marie et Pierre Curie B.P. 30179
86962 Futuroscope Chasseneuil Cedex, France

Separated boundary layers on a rounded edged, as arrives in vehicle aerodynamics, are very common and plays an important role in engineering. The formation of separation bubbles causes the presence of eddying wakes in near-body region of the flow. The unsteady nature of the resulting vortex dynamics is of practical importance in many applications where noise emissions or structure vibrations have to be reduced through a passive or active control. Separation bubbles can be triggered by adverse pressure gradients or by curvature effects of the wall geometry. In this work, we are interested by the latter type of influence that remains significantly less studied than the former. Moreover, because most of separation bubbles are 3D in practical flow geometries [7], it is worth considering the influence of the aspect ratio of the body in cross directions.

Measurements and visualisations have been conducted by [3, 2, 4] for a constant flow (of velocity U_∞) over a generic bluff body with different front edge radii and cross frontal sections. The model geometry and its parameters R, H_s (deduced from H), L and l are presented in figure 1. Using a low-speed water tunnel, [3, 2, 4] have considered flow regimes at moderate Reynolds numbers ($O(10^3) < Re = u_\infty H_s/\nu < O(10^4)$) so that a comparative study using direct numerical simulation (DNS) can be performed. Our goal is to carry out this study using a numerical code based on high-order compact schemes combined with an Immersed Boundary Method (IBM) for the modelling of the body. To be as close as possible from the experimental arrangement, only the part of the flow above the horizontal plane (x, z) including the stagnation point is considered in the simulation while the cross section of the computational domain fits exactly the experimental one. Using the location of the stagnation point reported by [3, 2, 4], the height of the half-body considered in present DNS is $H_s = 0,82H$ (see figure 1) while its length is $l = 12H_s$. The computational domain $L_x \times L_y \times L_z = 20H_s \times 5H_s \times 12H_s$ is discretized on a Cartesian grid (stretched in y) of $n_x \times n_y \times n_z = 601 \times 151 \times 401$ points. The pressure grid is staggered from the velocity grid to avoid spurious pressure oscillations. Boundary conditions are inflow/outflow in x and free-slip in y and z. The constant inflow velocity U_∞ is perturbed by fluctuations corresponding to a time and spatial correlated noise (of large band-width spectrum) with a maximal amplitude $|u'|_{max} \approx 1\%U_m$ consistent with the residual perturbations inside the working section of the wind tunnel of [3, 2, 4]. At this time, only the case $Re = 1250$ is addressed numerically. Our aim is to investigate the influence of the aspect ratio $\Lambda = L/H$ and the non-dimensional radius of the rounded edge $\eta = R/H$ by considering the cases $\Lambda = 2.2, 4.4, 8.8$ and $\eta = 0.8, 0.4$, these specific flow configurations being well referenced in the database of [3, 2, 4]. To better identify the specific three-dimensional effects associated with the moderate values of the aspect ratios, the case $\Lambda \to \infty$ is also considered using $L = L_z$ and $n_z = 400$ while the free-slip boundary condition is replaced by a periodic one in z-direction, this limit case corresponding the body configuration considered by [8] using Large Eddy Simulation. DNS are being conducted considering the combinations of η and Λ reported in table 1. Some preliminary statistical results are shown in Figs. 2,3,4, while instantaneous pictures of Q-criterion can be observed in figure 5.

The longitudinal expansion of the separation bubble can be considered through the reattachment length l_r that corresponds to the maximum of the x-location where the time-averaged mean flow reattaches. Examples of separation bubble viewed in the section $z = 0$ are presented in figure 2. The values of l_r obtained in each case are given in table 1. A good agreement is found with [3, 2, 4] for the four flow configurations reported by these authors. The effects of η on l_r seems to be rather limited, with a more marked influence on the shape of the separation bubble through its height h_r that is higher at $\eta = 0.4$ than at $\eta = 0.8$ for all the cases considered here (see table 1). An example of this effect can be seen in figure 2 where the increase of the height bubble seems to be related to the increase of the separation angle.

The 3D structure of the separation bubble can be characterised by the analysis of the skin-friction lines on the surface. In figure 3 the velocity vectors in the neighbourhood of the top of the body with $\eta = 0.8$

and $\Lambda = 2.2$ are presented. For this case, the flow pattern immediately adjacent to the surface reveals the presence of six singular points. At the centre $z = 0$ of the separation line, one saddle point can be identified. Slightly further downstream, to close the separation line near each edge of the body, two foci of separation are clearly observed. Finally, one nodal attachment point located between two saddle points ends the bubble. This surface flow pattern, corresponding to a stable configuration as described by [6], corresponds very well to the measurements of [3, 2, 4] who identified the same type of surface flow topology. A quantitative comparison between present DNS and previous experimental results will be presented at the conference.

Fig. 4 shows velocity vector at $x/l_r = 0.5, 0.75, 1$ and 1.5 for the case $\eta = 0.8$ and $\Lambda = 2.2$. The analysis of this figure shows that above and behind the separation bubble, in agreement with the usual description of 3D separated/reattached flows, the mean flow remains highly 3D with the presence of a counter-rotating pair of longitudinal vortices that tend to pump fluid from the sides toward the plane $z = 0$ where the fluid is ejected toward the top of the domain.

In the cases considered here, the flow separation remains steady but lead to the formation of an unstable shear layer where Kelvin-Helmholtz vortices form and roll-up though three-dimensional processes. Fig. 5 shows instantaneous pictures of the the resulting motion leading to a highly three-dimensional dynamics composed of periodic lateral flow and ejections outside the separation bubble.

At the moment, all the data collected from the simulations are being processed. For the conference, extended comparisons between experimental and present DNS results will be presented. Finally, a fundamental question, very delicate to address experimentally, will be addressed with the present DNS methodology. This point is related to the possible globally unstable nature [5, 1] of the three-dimensional flow, especially for small curvature $\eta = 0.4$ and aspect ratio $\Lambda = 2.2$. By comparing the behaviour of the flow with and without inflow perturbation, the eventual self-excited nature of the dynamics in the bubble region will be tested and discussed.

References

[1] J.-M. Chomaz. Global instabilities in spatially developing flows: non-normality and nonlinearity. *Ann. Rev. Fluid Mech.*, **37**:357–392, 2005.

[2] S. Courtine. *Etude expérimentale des décollements provoqués par une paroi courbe : Topologie et évolution spatio-temporelle. Experimental study of flow separation on rounded front edges: Topology and spatiotemporal evolution.* PhD thesis, Université de Poitiers, 2006.

[3] S. Courtine and A. Spohn. Dynamics of separation bubbles formed on rounded edges. In *12th International Symposium on Applications of Laser Techniques to Fluid Mechanics*, Lisbon, Portugal, 2004.

[4] S. Courtine, A. Spohn, and J.-P. Bonnet. Vortex dynamics in the reattaching flow of separation bubbles with variable aspect ratio. In *Proc. of the 11th European Turbulence Conference, EUROMECH*, Porto, Portugal, 2007.

[5] P. Huerre and P. A. Monkewitz. Local and global instabilities in spatially developing flows. *Ann. Rev. Fluid Mech.*, **22**:473–537, 1990.

[6] A. E. Perry and M. S. Chong. A series-expansion study of the Navier-Stokes equations with applications to thee-dimensional separation patterns. *J. Fluid Mech.*, **173**:207–223, 1986.

[7] M. Tobak and D. J. Peak. Topology of three-dimensional separated flows. *Ann. Rev. Fluid Mech.*, **14**:61–85, 1982.

[8] Z. Yang and P. Voke. Large-eddy simulation of boundary-layer separation and transition at a change of surface curvature. *J. Fluid Mech.*, **439**:305–333, 2001.
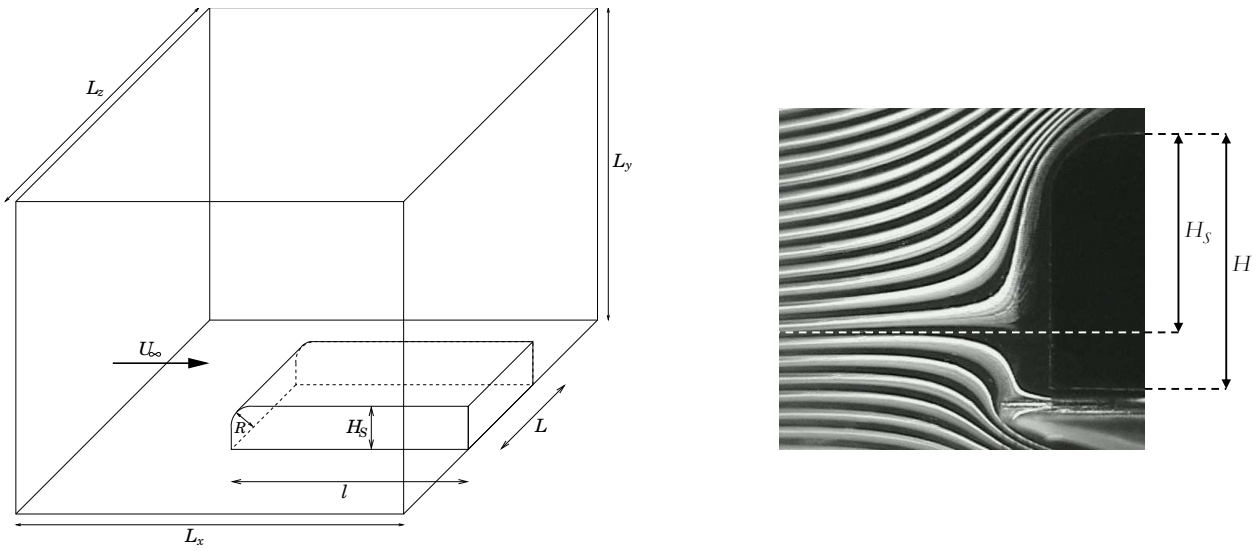
Figure 1: Left: schematic view of the flow configuration. Right: relation between the height of the half-body H considered by [3, 2] and its corrected value H_s used in present DNS (stagnation point located in the lower horizontal boundary of the computational domain $y = 0$).

Λ	2.2		4.4		8.8		∞	
η	0.4	0.8	0.4	0.8	0.4	0.8	0.4	0.8
h_r	0.31	0.25(0.30)	0.36	0.26	0.35	0.21	0.25	0.18
l_r	2.7	2.7(3.4)	3.3	3.2	3.6	3.4	3.1	3.2
Exp.	2.9	2.8	–	3.4	–	3.9	–	–

Table 1: Separation bubble height h_r and reattachment length l_r for each case. The values between brackets correspond to the DNS performed without inflow perturbations. Experimental measurements are from [3, 2, 4]
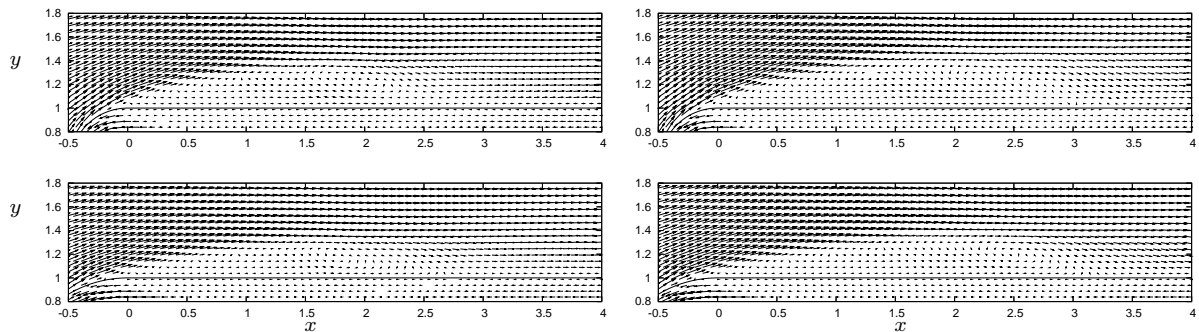

Figure 2: Velocity vectors (u, v) in $z = 0$ section for $\eta = 0.4$ (top) and $\eta = 0.8$ (bottom) for $\Lambda = 2.2$ (left) and $\Lambda = 4.4$ (right).
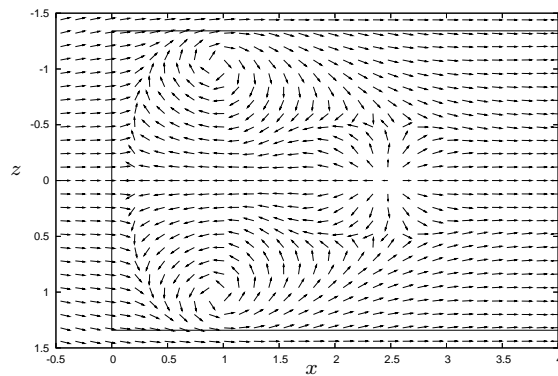

Figure 3: Velocity vectors (u, w) in the plane $y = 1.06 H_s$ for $\Lambda = 2.2$ and $\eta = 0.8$.

Fifth Conference on Bluff Body Wakes and Vortex-Induced Vibrations (BBVIV 5)
Costa do Sauipe, Bahia, Brazil, 12 - 15 December 2007
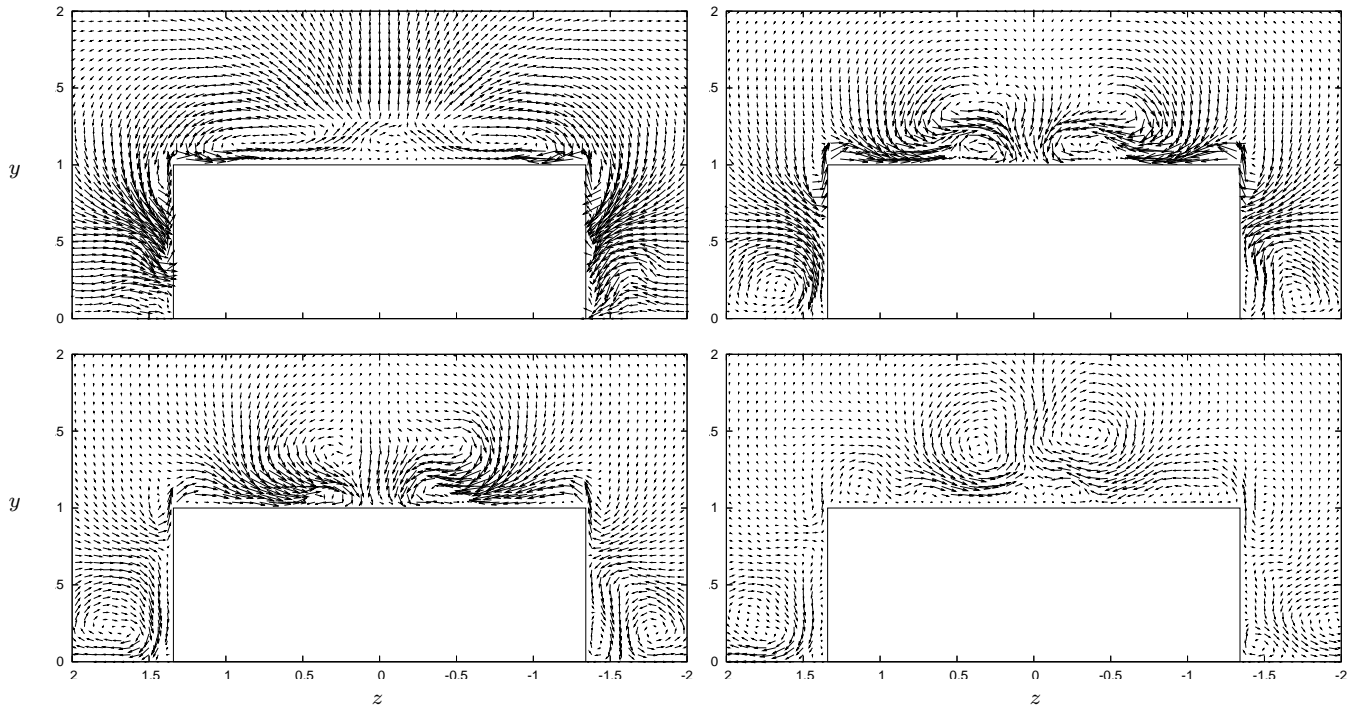
179

Figure 4: Velocity vectors (w, v) in $x/l_r = 0.5, 0.75, 1.$ and 1.5 for $\eta = 0.8$ and $\Lambda = 2.2$ (from top to bottom and left to right).
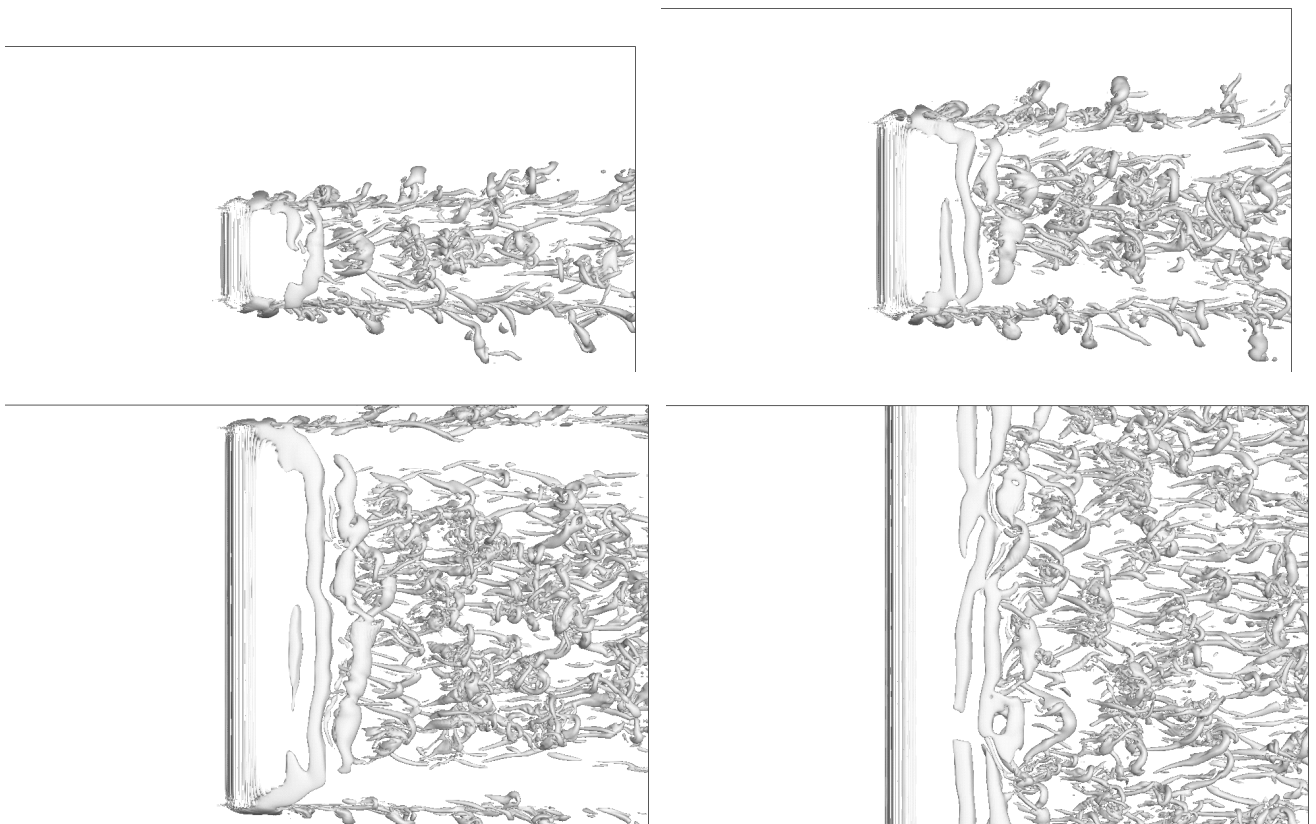

Figure 5: Top views of the isosurface $Q = 0.25$ for $\eta = 0.8$ with $\Lambda = 2.2, 4.4, 8.8, \infty$ (from top to bottom and left to right).

VORTEX MODELS FOR FEEDBACK STABILIZATION OF BLUFF BODY WAKE FLOWS

B. PROTAS

Department of Mathematics & Statistics, McMaster University, Hamilton, Ontario, Canada
bprotas@mcmaster.ca

1 Introduction

The goal of this presentation is to review recent progress concerning the design of feedback control strategies for bluff body wake flows based on point vortices. This investigation grows out of a long–term research effort which seeks to integrate rigorous methods of modern control theory and computational fluid dynamics. We will use a combination of mathematical analysis and numerical computation to study properties of a family of flow control algorithms and will focus on circular cylinder wake flows which are canonical examples of massively separated flows. In principle, application of the linear control theory to systems described by partial differential equations (PDEs) is relatively well understood, however, in practice even the design of "simple" linear control strategies, such as the Linear Quadratic Regulator (LQR), may result in computationally intractable problems when applied to discretizations of the full Navier–Stokes system [1]. Therefore, in order to facilitate synthesis and application of such control strategies, it is necessary to introduce reduced–order models of the Navier–Stokes system and in this investigation we study one such family of reduced–order models.

2 The Föppl System as Reduced–Order Model

In this research we are interested in stabilizing the steady symmetric flow past a circular cylinder which is known to become unstable for $Re \gtrsim 46$. In order to simplify the mathematical description, we will assume that the system satisfies the steady–state Euler equations which can be written in the form

$$\begin{cases} \Delta \psi = f(\psi) & \text{in } \Omega, \\ \psi = 0 & \text{on } \partial\Omega, \\ \psi \to U_\infty y & \text{for } |(x,y)| \to \infty, \end{cases} \tag{1}$$

where Ψ is the streamfunction and the right–hand side function f is a priori undetermined. Taking this function in the form $f(\Psi) = -\omega H(\Psi - \Psi_0)$, where $H(\cdot)$ is the Heaviside function, we obtain a family of Prandtl–Batchelor flows [3], characterized by constant–vorticity vortex patches embedded in irrotational flow, as solutions of problem (1). Assuming that the circulation of every vortex region is fixed results in a one–parameter family of solutions of (1) depending on the area of the vortex region [3] (see Fig. 1a). Taking the limit of the vanishing vortex area reduces the Prandtl–Bachelor flow family to an equilibrium point vortex system discovered by Föppl [2] in 1913 (Fig. 1b). Analysis of the linear stability of the Föppl equilibrium shows that it is unstable and, in addition to a linearly growing mode associated with a real positive eigenvalue, is also characterized by a decaying mode associated with a real negative eigenvalue and a neutrally stable oscillatory mode associated with a conjugate pair of purely imaginary eigenvalues. These stability properties make the Föppl system a feasible candidate for a reduced–order model of the onset of the vortex shedding instability in bluff body wakes.
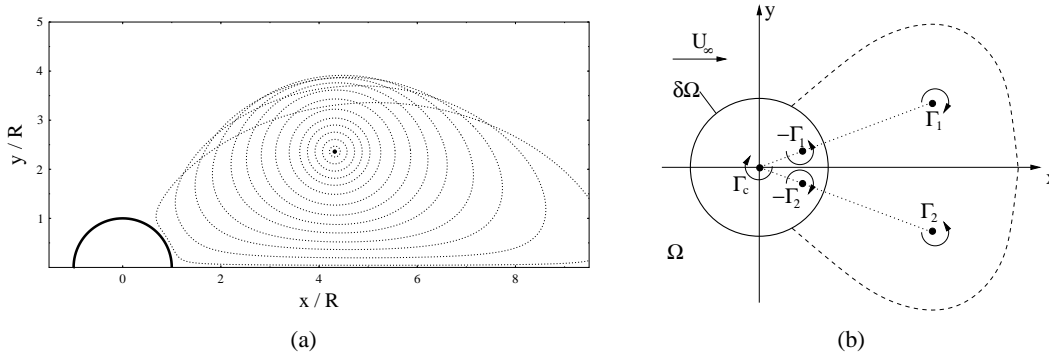
Figure 1: (a) Boundaries of the vortex patches with different areas and constant circulation obtained as solutions of (1) and the limiting point vortex Föppl system (represented by a solid circle), (b) schematic showing the location of the singularities in the Föppl system with control representing the cylinder rotation.

3 Control Design

Our goal is to stabilize the steady symmetric wake flow represented, for the control design purposes, by the unstable equilibrium of the Föppl system as a reduced–order model. The flow actuation (system input) has the form of the cylinder rotation and is represented in the Föppl system as a vortex with the circulation $\Gamma_C = \Gamma_C(t)$ located inside the obstacle, whereas the system output has the form of velocity measurements $\mathbf{y}$ at the flow centerline. Using $\mathbf{x} \in \mathbb{R}^4$ to denote the perturbation variables (i.e., perturbations of the vortex positions around the equilibrium), the linearization of the Föppl system around this equilibrium can be expressed in the canonical state–space representation as [4]

$$\frac{d}{dt}\mathbf{x} = \mathbf{A}\mathbf{x} + \mathbf{B}\Gamma_C, \tag{2a}$$

$$\mathbf{y} = \mathbf{C}\mathbf{x} + \mathbf{D}\Gamma_C, \tag{2b}$$

where $\mathbf{A}$, $\mathbf{B}$, $\mathbf{C}$ and $\mathbf{D}$ are suitable matrices. We seek to determine the control in the *feedback* form $\Gamma_C(t) = -\mathbf{K}\mathbf{x}(t)$, so that it will stabilize model equation (2a) and at the same time will minimize the cost functional $\mathcal{J}(\Gamma_C) = \frac{1}{2}\int_0^\infty (\mathbf{y}^T\mathbf{Q}\mathbf{y} + \Gamma_C R \Gamma_C)\,dt$, where $R > 0$ and $\mathbf{Q}$ is a suitably chosen positive–definite weighing matrix. Before we can devise a control algorithm, we need to verify that model system (2) has an appropriate internal structure. It was shown in [4] that problem (2) is fully *observable*, however, it is not *controllable*. Performing the Kalman decomposition in order to transform system (2) to the minimal representation, i.e., one which is both observable and controllable, shows that the neutrally stable oscillatory modes are in fact not controllable, so the whole system remains *stabilizable*. The stabilization problem is solved by constructing a linear–quadratic–Gaussian (LQG) compensator [4] and in Fig. 2a we show the results concerning LQG stabilization of the Föppl equilibrium. We note that the vortex trajectory is indeed stabilized, however, instead of returning to the equilibrium, the trajectory lands on a circular orbit circumscribing the equilibrium. The same LQG approach was then applied to stabilization of the circular cylinder wake at $Re = 75$ (Fig. 2b). We observe that, while the far wake is remarkably symmetrized, the level of oscillations in the near wake region is in fact increased. Properties of the Föppl system responsible for the behavior observed in these two cases are investigated next.
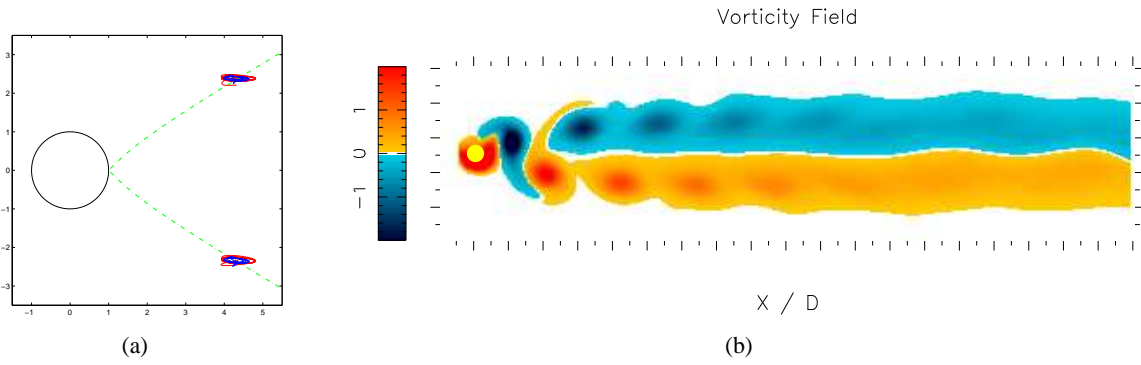
Figure 2: (a) Trajectories of the Föppl vortices with the LQG control, (b) instantaneous vorticity field in a cylinder wake at $Re = 75$ with the LQG control.

4   Center Manifold Analysis

It is well–known that, if a linearization of a nonlinear system possesses pairs of purely imaginary eigenvalues, then such linearization may not provide conclusive information about stability of the original nonlinear system and higher–order information must be analyzed. To this end we consider the minimal representation of system (2) with the feedback control $\Gamma_C = -\mathbf{K}\mathbf{x}$

$$\frac{d}{dt}\begin{bmatrix}\boldsymbol{\xi}\\\boldsymbol{\eta}\end{bmatrix} = \begin{bmatrix}\mathbf{A}_{11} & 0\\0 & \mathbf{A}_{22}-\mathbf{B}\mathbf{K}\end{bmatrix}\begin{bmatrix}\boldsymbol{\xi}\\\boldsymbol{\eta}\end{bmatrix} + \begin{bmatrix}\mathbf{g}_1(\boldsymbol{\xi},\boldsymbol{\eta})\\\mathbf{g}_2(\boldsymbol{\xi},\boldsymbol{\eta})\end{bmatrix}, \tag{3}$$

where $\boldsymbol{\xi}$ and $\boldsymbol{\eta}$ represent, respectively, the controllable and uncontrollable parts of the state of the Föppl system with the feedback control and the matrix $\mathbf{A}_{11}$ has purely imaginary eigenvalues only. In [5] we proved the following two theorems in regard to system (3):

Theorem 1. *System* (3) *possesses an invariant (center) manifold given by the function* $\boldsymbol{\eta} = \boldsymbol{\phi}(\boldsymbol{\xi}) = \mathbf{0}$.

Theorem 2. *For sufficiently small initial data the reduced system*

$$\frac{d}{dt}\boldsymbol{\xi} = \mathbf{A}_{11}\boldsymbol{\xi} + \mathbf{g}_1(\boldsymbol{\xi},\mathbf{0}), \tag{4}$$

obtained via an invariant reduction of system (3)*, possesses stable periodic orbits.*

The significance of these results concerning the observed behavior of the Föppl system under feedback control is as follows. Theorem 1 implies that the controllable and uncontrollable parts of the state are essentially uncoupled. Therefore, as soon as the control stabilizes the unstable mode, the system trajectory converges to the center manifold $\boldsymbol{\xi} = \mathbf{0}$. Since this manifold is in fact spanned by the uncontrollable modes, the dynamics on this manifold is unaffected by the flow actuation and, as asserted by Theorem 2, stable periodic oscillations are observed. We conclude that the presence of this center manifold is clearly an undesirable effect from the control point of view. Next we attempt to modify the internal structure of the Föppl system so as to disrupt the center manifold.

5   Beyond the Classical Föppl System

In Section 2 we argued that the classical Föppl system represents an extreme member of the Prandtl–Batchelor family of vortex flows. In [6] we showed that it is in fact possible to construct point vortex systems corresponding to the Prandtl–Batchelor flows with finite area vortex
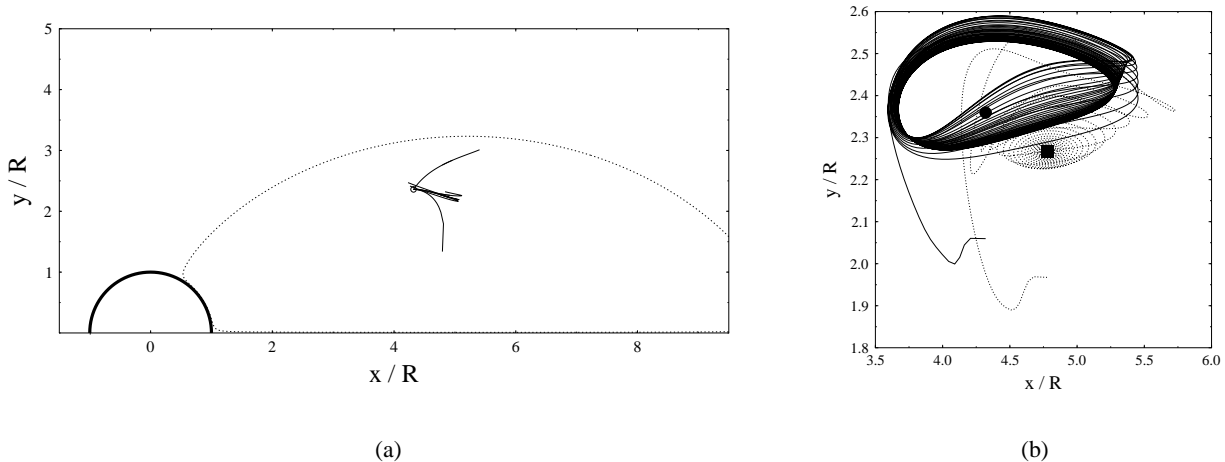
Figure 3: (a) Loci of the higher–order equilibria parametrized by the area of the vortex region in the Prandtl–Batchelor solution for different truncation orders (the dotted line represents the boundary of a vortex region, whereas the thick solid line represents the obstacle), (b) trajectories of the state of (solid line) the classical and (dotted line) higher–order Föppl system stabilized with an LQG compensator in the neighborhood of the corresponding equilibrium solutions.

patches. This can be accomplished by adding higher–order terms representing corrections due to the finite size of the vortex patch to the classical Föppl system. As shown in [6], the equilibria of such higher–order Föppl systems form loci parametrized by the area of the vortex patch and the truncation order (Fig. 3a). In addition to a range of properties interesting from the mathematical point of view, such higher–order Föppl systems have an important characteristic relevant for our control applications, namely, the uncontrollable modes are now exponentially, rather than just neutrally, stable, This means that a center manifold is no longer present in this new reduced–order model and, as shown in Fig. 3b, the LQG compensator is now able to completely stabilize the equilibrium. Control–theoretic advantages of the higher–order Föppl systems as reduced–order models are being now investigated. It is anticipated that controllers designed based on such higher–order systems will be characterized by more robust performance, especially when applied to actual systems.

Acknowledgments

References

1 J. Kim & T. Bewley, "A linear systems approach to flow control", *Annual Review of Fluid Mechanics* **39**, 383–417, (2007).

2 L. Föppl, "Wirbelbewegung hinter einem Kreiscylinder", *Sitzb. d. k. Bayr. Akad. d. Wiss.* **1**, 17, (1913).

3 A. Elcrat, B. Fornberg, M. Horn and K. Miller, "Some steady vortex flows past a circular cylinder", J. Fluid Mech. **409**, 13-27, (2000).

4 B. Protas, "Linear Feedback Stabilization of Laminar Vortex Shedding Based on a Point Vortex Model", *Phys. Fluids* **16**, 4473-4488, (2004).

5 B. Protas, "Center Manifold in the Controlled Föppl System", *Physica D* (in press) (2007).

6 B. Protas, "Higher–order Föppl models of steady wake flows", *Phys. Fluids* **18**, 117109, (2006).

Database Variation and Structure Identification via POD of the flow around a Wall-Mounted Finite Cylinder

O. Frederich, J. Scouten, M. Luchtenburg and F. Thiele

Berlin University of Technology, Institute of Fluid Mechanics and
Engineering Acoustics, Mueller-Breslau-Str. 8, 10623 Berlin, Germany
octavian.frederich@tu-berlin.de

Abstract

The unsteady separated vortical flow around a finite cylinder with ground plate has been predicted using large-eddy simulation. The decomposition of the flow using POD has been used here to analyse the unsteady flow. The objectives here are twofold. Primarily, variation in the sampling rate and domain size were investigated, and it is found that the first harmonic can be captured in a small region situated just behind the cylinder, whereas a larger domain is necessary to capture the second and subharmonics. Secondarily, two procedures are investigated to measure the certainty that the first and second harmonics have been resolved. Shannon's information entropy yields a quantitative measure for the information in the power spectrum densities of the POD time coefficients, and a conditional sampling technique is shown to filter out coherent structures associated with specific modes.

1 Configuration, Procedure and Contribution

The configuration investigated is a finite cylinder mounted on a ground plate with an aspect ratio of 2 and a Reynolds number of $\mathrm{Re}_D = 200\,000$. The numerical investigations of the flow field are carried out using a large-eddy simulation (LES) with the Smagorinsky subgrid-scale (SGS) model. To analyse and understand the predicted unsteady and complex flow field the usual evaluation of statistical moments has been supplemented by the application of POD [4].

In addition to the analysis of the currently available database, the number of snapshots and the weighted region for POD has been varied intermediately (fig. 1). The results of this parameter variation allows to identify the requirements for an enhanced database.

The time-averaged velocity field as ensemble of $40\,000$ time steps and the double correlations reveal a very good agreement between the experiments [5] and the performed LES [1]. Moreover, the results of the POD decomposition are valid for the joint experimental and numerical study, this work is based on.
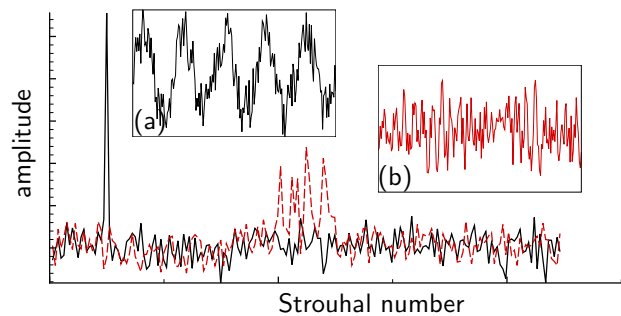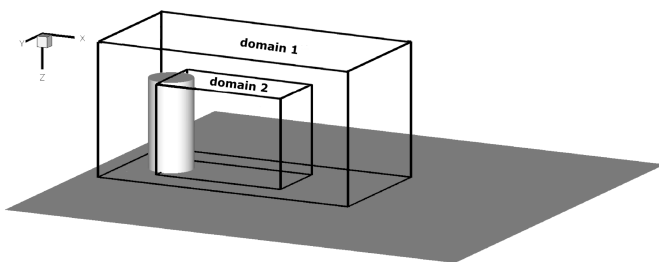

Figure 1: Different domains sizes decomposed with POD.

Figure 2: Two time signals and their spectra with low (a) and high (b) information entropy.

A procedure investigated here uses the information entropy, which exploits the time-coefficients in the POD decomposition. This is Shannon's information entropy, for measuring the amount of uncertainty in a system, as described by Jaynes [3]. It is defined as $S_I = -\Sigma p_i \log p_i$ for some (sub)system described by the probability densities $\{p_i\}$, which are taken here as the normalised power spectrum densities of the time coefficient for a single POD mode. For a signal with

one single frequency, $S_I = 0$, as all of the information in the signal is known, i.e. there is no uncertainty. In case of a broadband signal, the measure takes the value $S_I > 0$, as the more frequency content in a signal, the more uncertainty there is in the power spectrum (cf. fig. 2).

2 Selected Results

Data set variation. The database available as ensemble for the POD consisted of 2300 snapshots (every 5th timestep) distributed equidistantly over 60 convective units D/U_∞. The spectrum of the POD time coefficients, obtained using all available snapshots, reveal that the dominant frequency corresponds to a Strouhal number of 0.158 (fig. 3, left), which is consistent with the DFT results of local pressure and velocity signals. This result and at least the first 10 eigenvalues does not change significantly with varying sampling rate of the snapshots, from every 5th to every 100th timestep (fig. 3, right).
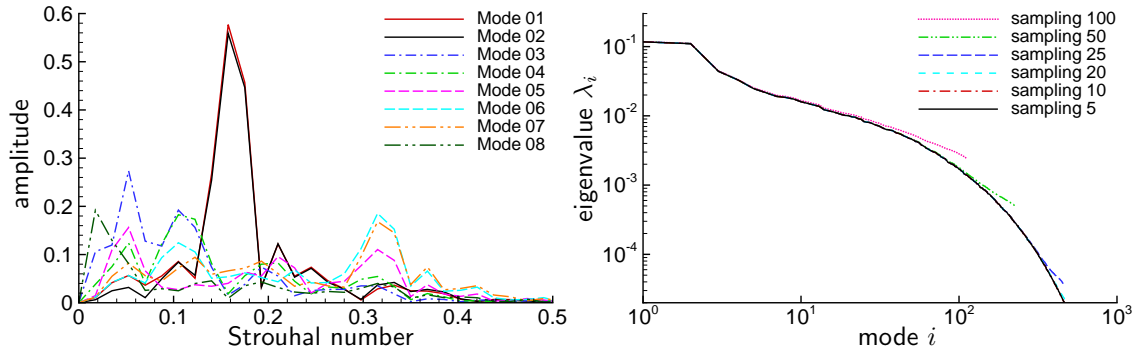

Figure 3: Spectrum of time coefficients in domain 1 for a sampling rate of 5 (left) and normalised POD eigenvalues with varying sampling rate (right).

As seen in the eigenvalues 23% of the kinetic energy is captured by the first harmonic modes (1,2) and 35% by the first seven modes. Although a strict decomposition of different frequencies is only found for the first two modes (1,2), the frequencies of the high-energetic modes corresponding to the Strouhal number $\text{St} = fD/U_\infty$ in figure 3 (left) are sampled at least with a frequency f_{samp} corresponding to $\text{St} = f_{samp} D/U_\infty = (1/100\Delta t) D/U_\infty = 2.0$. This minimum sampling frequency is sufficient for the present configuration where the kinetic energy is concentrated in a few modes.

The reduction of the weighted region for POD to a subdomain of interest can be used to separate superimposed phenomena. Originally, the region containing all interesting flow phenomena [1] was chosen to be 6 diameters streamwise and 3 diameters in lateral and vertical direction ($6D \times 3D \times 3D$, domain 1). This region was reduced to $3D \times 1.5D \times 2D$ (domain 2) such that the POD weighting is focused to the recirculation region downstream of the finite cylinder, in order to get a detailed picture of the interacting phenomena there (see fig. 1).
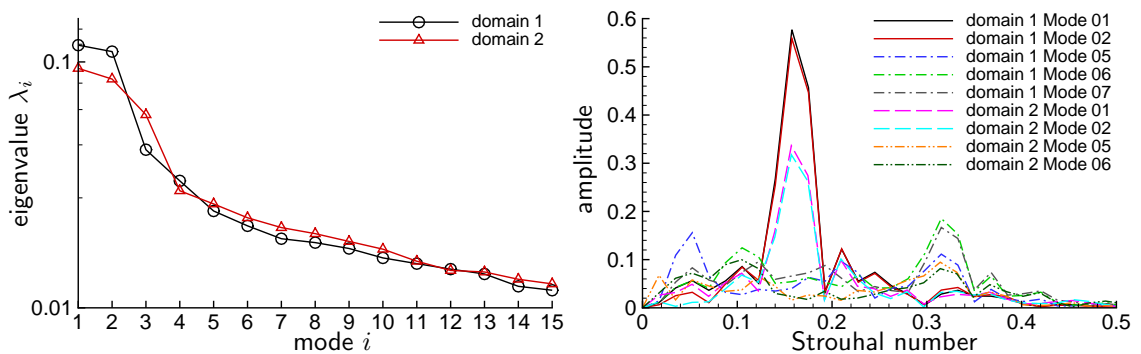

Figure 4: Normalised POD eigenvalues (left) and spectrum of Fourier coefficients with varying domain size (right), for sampling 20.

The first and second harmonics are similar to those of an infinite cylinder behind the recirculation region downstream of the cylinder [2]. The first harmonic is captured in both domains by the mode pair (1,2). As shown in figure 4 the eigenvalues of the first mode pair decrease with smaller domain size, due to the reduced fraction of the fluctuation energy

in these modes. Nevertheless, the frequencies captured with different domains are comparable, but the dominance of the first two modes reduces clearly. An important difference is that leakage into the next higher Strouhal number is significantly reduced in the larger domain (independent of the POD sampling rate).

The second harmonic, however, varies qualitatively between the domains, in that it is resolved by different mode sets. In domain 1 it is represented by the modes 6 and 7 with a contribution from mode 5, whereas in domain 2 it is found in modes 5 and 6 with contributions from several modes. Furthermore, in the larger domain the spectra of modes 6 and 7 (as well as modes 1 and 2) are more congruent than in the smaller domain, implying that the second harmonic could possibly be resolved in a single mode pair given a large enough domain.

Information entropy. In order to compare the capability of POD to capture similar frequency content in the different-sized domains, Shannon's information entropy has been applied to the power spectrum densities of the POD time coefficients of the first 30 modes for both domains. As can be seen in figure 5(left) the information entropy is only slightly lower for the Fourier coefficients of domain 1. As expected for both domains, the entropy increases moving to the higher modes, as the frequency content captured by POD tends to mix more at smaller wavelengths.
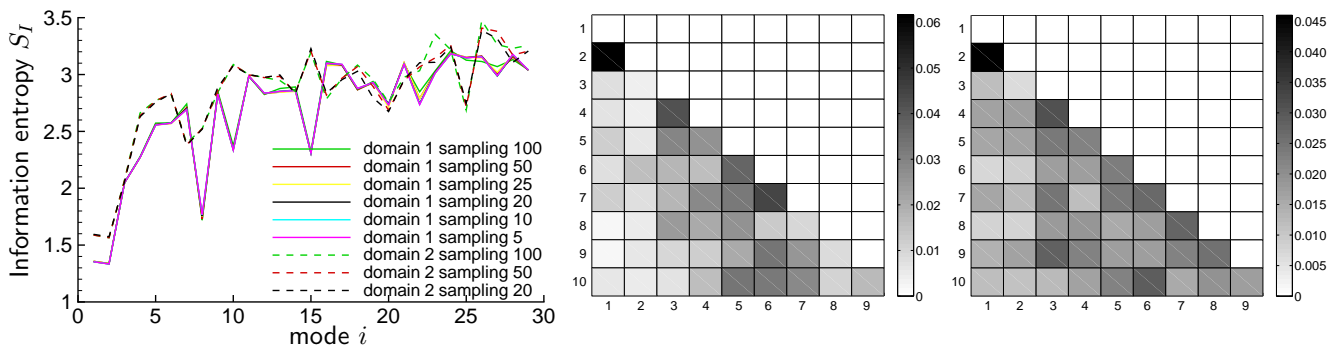

Figure 5: Information entropy in the spectrum of the POD time coefficients for domain 1 and 2 (left) and correlations between the first 10 modes sampling rate of 20 for both domain 1 (middle) and domain 2 (right).

To reveal the relative degree to which time coefficients interact to produce relevant harmonics, all correlations were computed between the first ten modes for both domains at a sampling rate of 20 (see fig. 5). Mode pair (1,2) stands out in both domains. Moreover, mode sets resolving the second harmonic are strongly correlated only in the large domain, mode pairs (5,6) and (6,7), and this difference also holds when modes are weighted with energy from the eigenvalue spectrum. There is, however, good correlation between mode pair (3,4) in both domains, which resolves a subharmonic (cf. fig. 4), describing the interaction of the harmonics with plate's boundary layer.
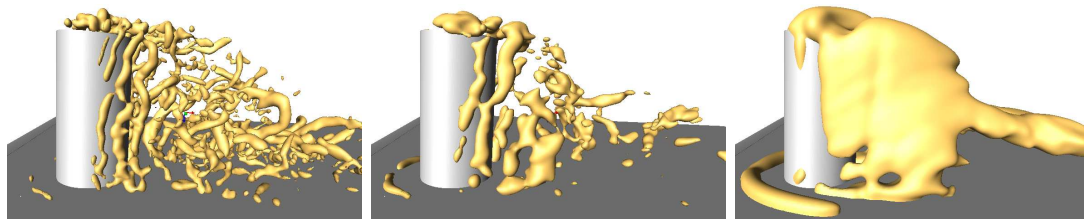

Figure 6: Vortex structures displayed with λ_2. Instantaneous (left), conditionally sampled based on the time coefficient of mode 1 (middle) and time-averaged (right).

Conditional sampling. Research in the turbulent boundary layer has applied conditional sampling to study *inter alia* bursts [6]. In the present work the condition for sampling (averaging) is taken from the time coefficient of single POD modes, specifically an average is taken over all snapshots corresponding to a maximum (or minimum) in the amplitude of the time coefficient. This filtering allows the extraction of information inaccessible from instantaneous or time-averaged reprensentations of the flow.

Fig. 6 (middle) depicts vortex structures resulting from the application of this technique using the maxima of the time coefficient from mode 1 for sampling. The visualisation reveals that the shed vortices remain intact typically one half diameters downstream of the cylinder, and merge for up to one full diameter but only at half of the height.

Conditional sampling to compare first and second harmonics was carried out using time coefficients from POD of domain 1 at a sampling rate of 5. As one aspect resulting from this comparison, the filtered structures displayed in fig. 7 show that fluctuations corresponding to the first harmonic extend vertically downwards to the plate, whereas in case of the second harmonic they remain distant to the plate. One possible explanation is the damping of fluctuations of higher frequencies due to the presence of the wall.
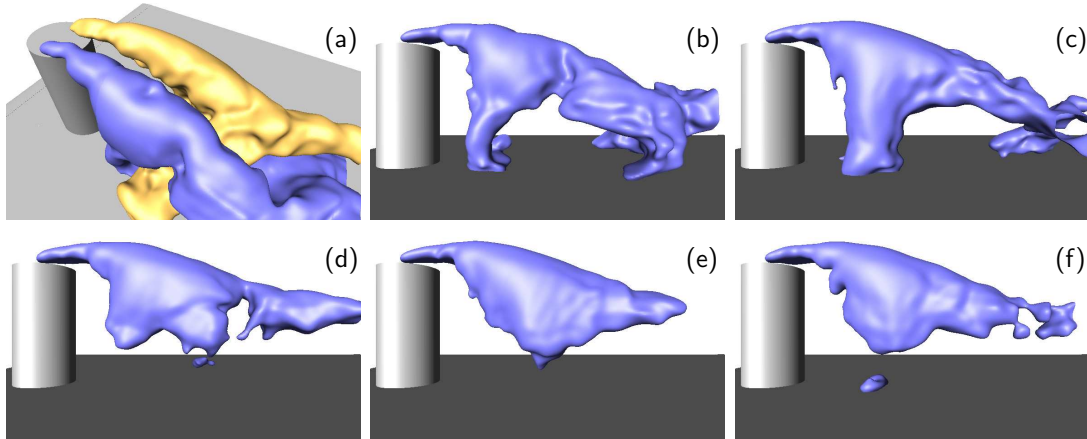
Figure 7: Conditional sampling based on time coefficient maximums. First (modes 1 and 2) and second harmonics (modes 5, 6 and 7) from domain 1 are displayed using isosurfaces of the lateral velocity at ± 0.13 (yellow positive, blue negative). (a) overview of lateral velocity, (b) mode 1, (c) mode 2; (d) mode 5, (e) mode 6 and (f) mode 7.

3 Conclusion and Outlook

The application of POD to various data sets reveals that a sampling rate of 50 is minimal to gain a fair resolution of both first and second harmonics, and the spatial domain should be chosen as large as possible. Physical understanding of the modes obtained by POD can be augmented by the additional techniques used. For example, the spatial extension of sideways vortex shedding is extracted using conditional sampling and the interaction between different harmonics is clarified by correlating the time coefficients.

The ongoing work will continue to expand the understanding of this complex turbulent flow. POD of the full simulation domain including a longer time series is currently underway, and will hopefully allow for convergence in the relevant harmonics and their physical interpretation.

Acknowledgements

References

[1] Frederich, O., Wassen, E., Thiele, F., Jensch, M., Brede, M., Hüttmann, F., Leder, A. (2007a) *Numerical simulation of the flow around a finite cylinder with ground plate in comparison to experimental measurements*. In: C. Tropea, S. Jakirlic, H.-J. Heinemann, R. Henke, H. Hönlinger (eds.) *Notes on Numerical Fluid Mechanics and Multidisciplinary Design*, vol. 96, Springer, Berlin Heidelberg New York, (to be published).

[2] Frederich, O., Luchtenburg, M., Wassen, E., Thiele, F. (2007b) *Analysis of the unsteady flow around a wall-mounted finite cylinder at Re=200 000* Proc. of the 11th EUROMECH European Turbulence Conference, (to be published).

[3] Jaynes, E.T. (1957) *Information theory and statistical mechanics*, Physical Review, 106(4):620-30, Am. Phys. Soc.

[4] Lumley, J.L. (1970) *Stochastic Tools in Turbulence*, Academic Press, New York.

[5] Richter, F. (2005) *Experimentelle Untersuchungen zur Charakterisierung der Strömungs- und Wirbelstrukturen im Nachlauf eines Kreiszylinderstumpfes ... .* PhD thesis, University Rostock.

[6] Robinson, S.K. (1991) *Coherent Motions in the Turbulent Boundary Layer*, Ann Rev. of Fluid Mech, 23:601-39.

Simulation of the flow past three-dimensional bluff bodies using Immersed Boundary Method and the Virtual Physical Model

João Marcelo Vedovoto[a*], Rubens Campregher[b], Aristeu Silveira-Neto[a]

[a]*School of Mechanical Engineering, Federal University of Uberlândia, Uberlândia-MG, Brazil 38400-902*

[b]*Department of Mechanical Engineering, Dalhousie University, A1B 3X5 - Halifax, NS - Canada*

[a]* *Telephone: (5534)32394149, Fax: (5534)32394282, jmvedovoto@mecanica.ufu.br*

Abstract

The state-of-art of flow simulation around complex geometries requires mathematical modeling and large computer resources. Thus computational fluid dynamics (CFD) has, inherently, high costs and the search for accurate and viable solutions constitutes a great challenge. The purpose of this paper is to present the Virtual Physical Model, an Immersed Boundary Method approach, as a viable alternative for modeling and simulating flow over complex three-dimensional geometries. In this work the flow around a bluff bodies are simulated and discussed.

Key words: Immersed Boundary Method, Virtual Physical Model, Flow around Complex Geometries.

1 Introduction

The flow around complex geometries is present in most applications of fluid mechanics in engineering. However, the numerical simulation of such type of flows requires sophisticated numerical methods, and, in most situations, high computational costs are involved. In the present work the Immersed Boundary method is used a an viable alternative to represent a complex geometry placed into the flow field. Immersed Boundary (IB) methods reproduce the presence of solid or fluid-fluid interfaces inside a flow by adding an extra component into the source term of the Navier-Stokes equations. Another important feature found in IB methodologies is that the immersed body can be represented by

a Lagrangian mesh while the flow domain can be discretized by an Eulerian grid such as Cartesian or cylindrical.

The development of the Immersed Boundary method is credited to Charles Peskin (Peskin, 1977) and his collaborators, with the purpose of simulating the blood flow through cardiac valves. More recently, Lima e Silva *et al.* (2003) have proposed a model that evaluates the force field from the momentum equation discretized using a three point stencil, similar to what can be viewed in Mohd-Yusof (1997), however, with a simplified interpolation scheme requiring less computational resources. The aforementioned method was named Virtual Physical Model (VPM). This paper outlines a continuation of the work done by Campregher (Campregher, 2005) in which the VPM was adapted and extended to three-dimensional domains. The main purpose of the present work is to demonstrate the capabilities of the Immersed Boundary Method in simulate the flow past complexes geometries.

2   Mathematical and Numerical Modeling

2.1   The Eulerian Domain

An incompressible flow of a Newtonian fluid with constant physical properties is considered. The problem presented in the present work is governed by continuity and Navier-Stokes equations (Eq. 1 and Eq. 2, respectively, given in vectorial notation). A finite-volume method is employed to discretize the differential equations on a non-uniform mesh in co-location arrangement of variables. The pressure-velocity coupling is done by the SIMPLEC method. The linear system originated from the velocity components discretization is solved by the SOR method. The SIP algorithm is used to solve the linear system generated by the discretization of the pressure correction equation. The time derivative is approximated by a second-order three-time level (Ferziger and Peric, 2002), and the spatial derivatives by the Central-Difference Scheme. The code has also parallel processing capabilities, with communications among processors via MPICH libraries.

$$\nabla \cdot \mathrm{u} = 0 \tag{1}$$

$$\rho \left(\partial \mathrm{u}/\partial \mathrm{t} + \mathrm{u} \cdot \nabla \mathrm{u} \right) = -\nabla p + \nabla \cdot \left[\mu \left(\nabla \mathrm{u} + \nabla \mathrm{u}^{\mathrm{T}} \right) \right] + f \tag{2}$$

where ρ and μ are respectively, the density and kinematic viscosity. The characteristics of the flow are given by the pressure, p, the components of the velocity vector u, and the force field f that acts in the flow.

2.2 The Virtual Physical Model

The fluid/solid interface is a surface discretized by a triangular elements mesh. The Virtual Physical Model evaluates the force field by applying the momentum balance equation over the Lagrangean points at the boundary. Then, let k be a Lagrangean point, placed at x_{ki} having velocity components u_{ki}. The index i refers to each direction of the Eulerian coordinate system. Applying the momentum balance equations over this Lagrangean point, one has:

$$F_{ki} = \rho \frac{u_{ki} - u_{fki}}{\Delta t} + \rho \frac{\partial}{\partial x_{kj}} (u_{ki}u_{kj}) - \frac{\partial}{\partial x_{kj}} \left(\mu \left(\frac{\partial u_{ki}}{\partial x_{kj}} + \frac{\partial u_{kj}}{\partial x_{kj}} \right) \right) + \frac{\partial P_{ki}}{\partial x_{ki}} \quad (3)$$

where F_{ki} is the Lagrangean force, along the direction i, necessary to change the fluid particles velocity adjacent to the Lagrangean point k to attain the wall velocity, i.e., imposing the no-slipping condition at the geometry wall. The spatial discretization of the Eq. 3 is done by constructing a referential three-dimensional axis with origin at k. Then, a Lagrangian polynomial is used to obtain the space derivatives along each direction using auxiliary points, Lima e Silva *et al.* (2003).

3 Results

Several simulations corresponding to the unstable flows past a bluff bodies were carried out. One of them is the flow past a surface mounted cube. Figure 1 (left) shows streamlines for the simulation of such configuration of geometry. One can clearly note the presence of horseshoes-type vortices. Still in figure 1 (right), one can also note the presence of recirculations and coherent structures as hairpin vortices, common in flow past bluff bodies. In this figure isosurfaces of $Q = 75$, colored by u velocity component are shown.
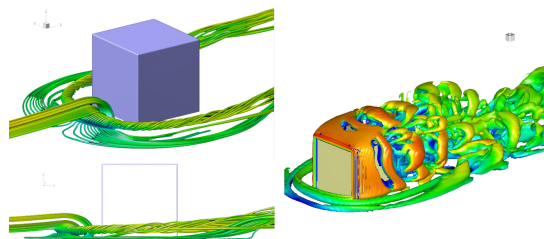

Fig. 1. Left: Streamlines indicating coherent structures in the flow past a surface–mounted cube. Right: Isosurfaces of $Q = 75$ colored by u velocity (Both simulations $Re = 1.000$

Another complex geometry simulated was a car prototype. In figure 2 one

can see the streamlines(left) and the iso-surfaces of $Q = 6$ (right). In this figure one can note the presence of recirculations and coherent structures as hairpin vortices.
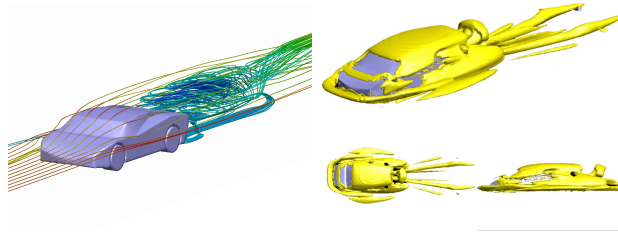

Fig. 2. Left: Streamlines indicating coherent structures in the flow past a car prototype. Right: Isosurfaces of $Q = 10$, $Re = 500$, $t = 0, 6$s

4   Conclusion

Three-dimensional unsteady numerical simulations of the flow past complex geometries were successfully performed employing the Virtual Physical Model. The methodology has shown great capability in dealing with complex geometries, mainly because both Eulerian and Lagrangean mesh present no further difficulties to be generated and manipulated. This feature is a huge advantage specially when compared with other methodologies where the flow and structure domains are part of the same mesh. The problem is aggravated in Fluid-Structure Interaction problems when every change in shape and/or position undergone by the structure must be followed by a remeshing procedure. The simulations presented results physically consistent results with good agreement with literature.

References

[1] R. Campregher, Modelagem Matemática tridimensional para problemas de interação fluido-estrutura, PhD thesis, Uberlândia, 2005.
[2] J. Ferziger and M. Peric, Computational methods for fluid dynamics 3th ed., Springer-Verlag, New-York, USA, 2002.
[3] A.L.F. Lima e Silva , A. Silveira-Neto, and J.J.R Damasceno, Numerical simulation of two dimensional flows over a circular cylinder using the immersed boundary method. J. Comp. Phys. 189, 351, 2003
[4] J. Mohd-Yusof, Combined immersed boudaries/B-splines methods for simulations in complex geometries. CTR Annual Research Briefs, NASA Ames/Stanford University, 1997
[5] C.S. Peskin, Numerical analysis of the blood flow in the heart. J. Comp. Phys. 25, 220, 1977

Topology of the flow around a vehicle A-pillar: an experimental characterization.

B. Levy[*+], P. Brancher[*] A. Giovannini[*]

[*]*Institut de Mecanique des Fluides de Toulouse, France (IMFT)*
[+]*MECAPLAST GROUP*
Benjamin.Levy@imft.fr

Abstract

The A-pillar vortex is a three-dimensional coherent structure that appears on automobiles in motion. The structure has a conical shape and evolves along the vehicle A-pillar. A dihedron with a 30° angle has been chosen as a good configuration to reproduce the generic features of this phenomenon. A large-scale model has been built and set in a wind tunnel. The topology of the flow around this geometry has been experimentally investigated and preliminary measurements, including Particle Image Velocimetry and the quantification of mean and fluctuating wall pressure, have been performed.

Keywords: Vehicle aerodynamics, A-pillar vortex, PIV, Mean and fluctuating wall pressure

1. Introduction

While in motion, a road vehicle generates turbulence, coherent vortical structures and noise. The A-pillar, the corner edge between the windshield and the front side window, is among the most problematic aerodynamic components of an automobile. The flow passing round the A-pillar generates an intense three-dimensional coherent structure (the A-pillar vortex), which is not only a localized distribution of vorticity but also a source of aerodynamical noise and aeroelastic phenomenons. Above 100 km/h, the major noise disturbance inside a vehicle is due to the airflow around the A-pillar. Therefore, it has become the focus of a large amount of research in order to improve the driving quality of passengers.

In average, the windshield of a road vehicle makes a 29°-31° angle with the horizonal axis. We designed a simplified vehicle model with a 30° angle, like former studies by Alam *et al.* [1], Lehugeur *et al.* [2] and Hoarau [3]. The model is made out of two parts: a dihedron (500 mm length, 390 mm wide and 290 mm high) and a body (840 mm length, 390 mm wide and 290 mm high). The characteristic length scale L_0 is defined as the square root of the cross section *(Figure 1)*.
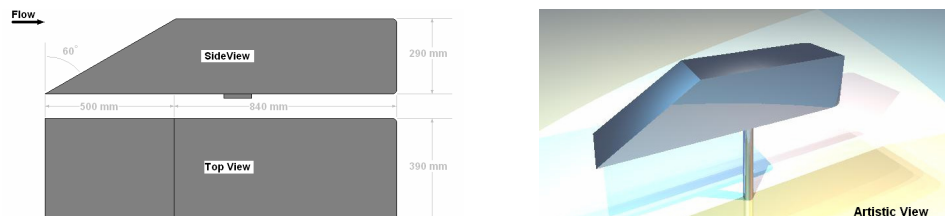

Figure 1: Dimensions and artistic view of the model

2. Experimental setup

The wind tunnel used for the experiments is the S1 wind tunnel (Eiffel type) at the "Institut de Mécanique des Fluides de Toulouse" (IMFT). It is an open tunnel with an open section. The diameter of the cross section is 2400 mm. The model was set on a pillar at the centre of the wind tunnel in order to avoid any disturbance from the boundary layer *(Figure 1)*. The speed of the wind tunnel was set at V_0 = 8 m/s. The comparison of the pressure coefficient C_p at the wall of the model at different wind velocities shows that the A-pillar vortex is clearly established at such a speed. The typical Reynolds number for our experiments is $Re = V_0 L_0 / \nu$ = 170,000.

Two different set-ups were used for the Particle Image Velocimetry (PIV). The first set of acquisitions consisted of different cross sections of the vortex and the second set were frames parallel to the sidewall *(Figure 2)*. With the help of smoke visualisations, we were able to identify the axis of the A-pillar vortex. It came out that it was not strictly parallel to the A-pillar edge: the axis of the vortex was rather at a 25°

angle with the horizontal axis. Therefore, for the first set-up, we placed the camera behind the model with a 25° angle with the horizontal axis. That way we were able to obtain cross-sections of the vortex normal to its axis. The second set-up was more traditional, the camera being simply located on the side of the model, parallel to the wall. On the whole, twenty-five different sets of acquisitions were performed *(Figure 2)*: eight perpendicular to the axis of the vortex and eighteen parallel to the wall (at 25 mm, 12 mm, 2 mm from the wall).

The material used for the PIV was a Quantel Laser CFR 200 with 2x200 mJ cavities at a frequency of 4Hz and a Sensicam camera with a resolution of 1280 x 1024 pixels mounted with a Nikon lens (55 mm to 160 mm).

For the wall pressure measurements, we perforated one side of the model with 105 holes, each with an outside diameter of 0.7mm *(Figure 2)*. In each cavity, we could either put a microphone for wall pressure fluctuations measurements or put an electronic Pitot tube for mean pressure measurements. In total, 141 sets of acquisitions were performed (105 and 36 respectively).

The material used was a Bruel & Kjaer 1/4" pressure-field microphone with a frequency range of 4 Hz to 70 kHz, a dynamic range of 42 dB to 172 dB and a sensitivity of 1.6 mV/Pa.
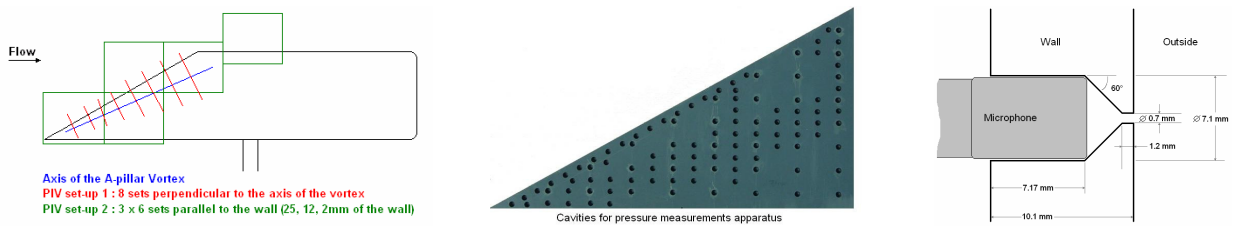

Figure 2: Set-up for the PIV and wall pressure acquisitions.

3. Experimental results
a. PIV

From each set of data, we were able to obtain information on the flow velocity, vorticity, fluctuations of kinetic energy and Reynolds stress. Streamlines of the flow normal to the A-pillar vortex axis are presented in Figure 3. The center of the A-pillar vortex is clearly identified as well as its elliptic shape due to the proximity of the wall. A recirculation zone at the wall located between the vortex tube and the airflow going around the A-pillar is also observed.
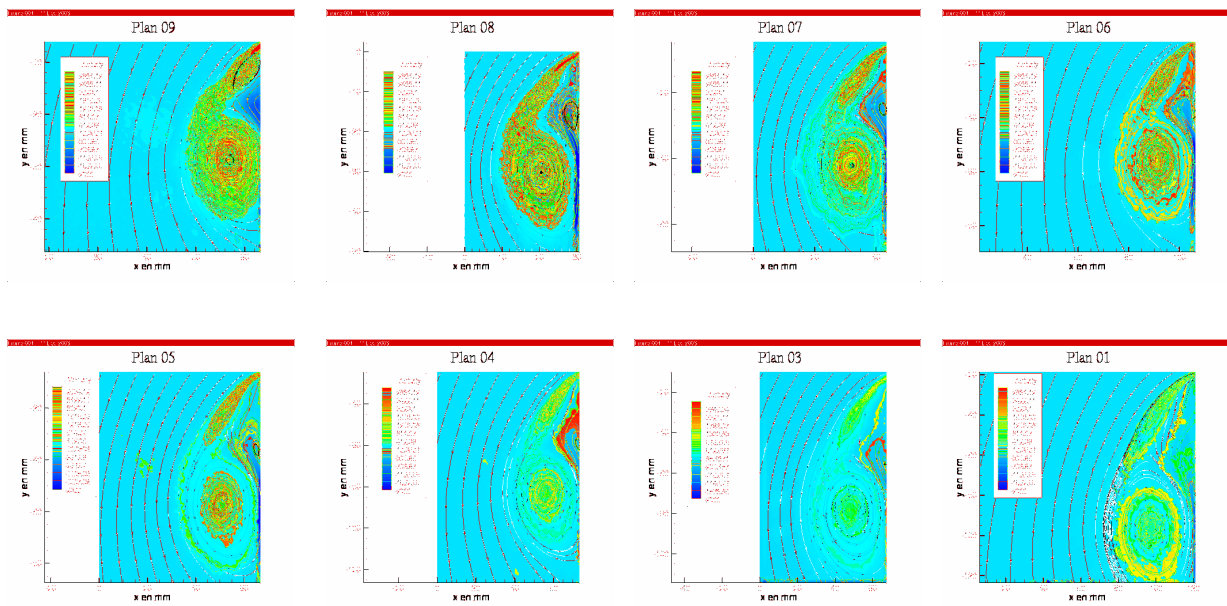

Figure 3: Evolution of the streamlines and vorticity along the axis of the A-pillar vortex from the bottom tip of the model (Plan 09) to the top (Plan 01).

There are three regions of high levels of vorticity. The first one is located at the corner of the model. The flow comes from the front wall (windscreen) of the model on the right side and is qualitatively similar to a downward step with an associated strong shear layer. The second region is the center of the vortex tube. The third one corresponds to the boundary layer due to the flow induced by the vortex close to the wall. The recirculation zone is related to the separation of this boundary layer due to the adverse pressure gradient generated by the vortex.

Moving up along the A-pillar, the phenomenon becomes larger while vorticity diffuses. Between Plan 09 (tip of the model) and Plan 01 (top of the dihedron), there is a reduction of 84% of the vorticity at the center of the vortex tube.

The evolution of the fluctuations kinetic energy leads to similar conclusions *(Figure 4)*. The phenomenon is much more energetic at its origin than at the top of the A-pillar. The dissipation at the centre of the vortex tube is about 59% and at some areas up to 67%. We can also identify that the most unsteady region is where the vortex and the recirculation area meet the flow coming from the corner of the A-pillar.
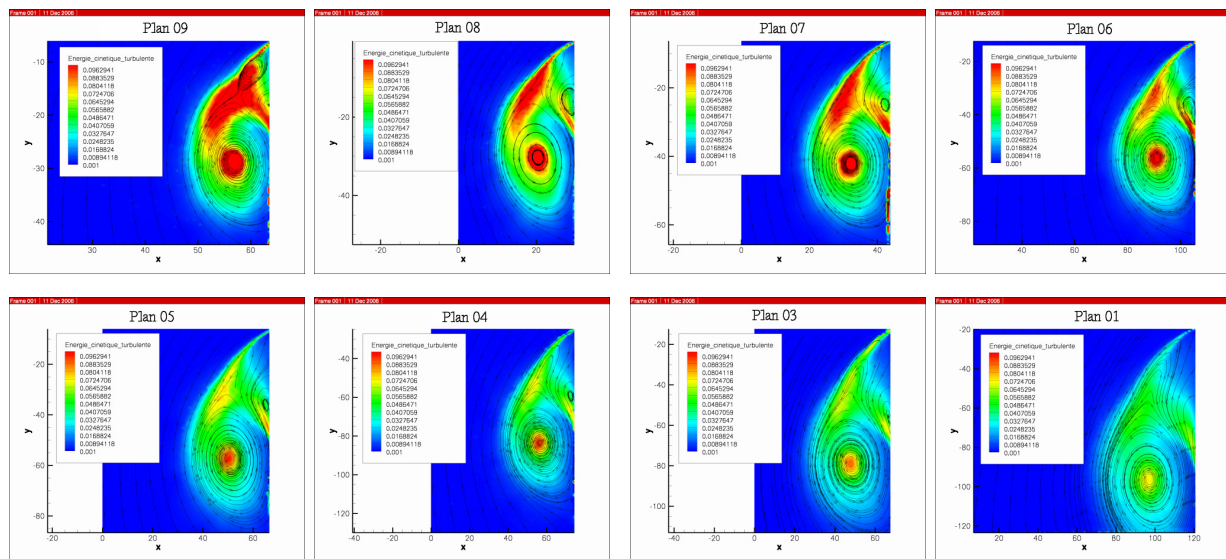

Figure 4: Evolution of the fluctuations kinetic energy along the axis of the A-pillar vortex.
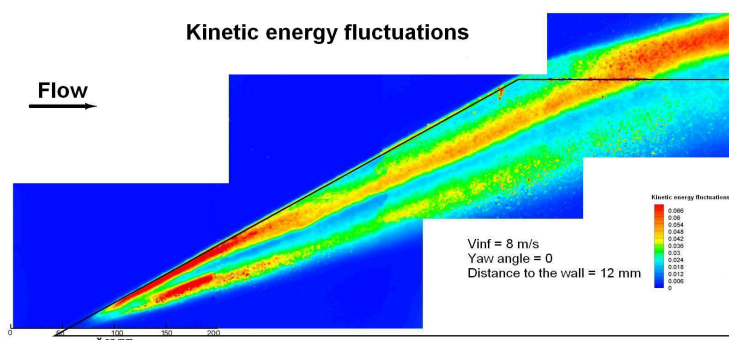

Figure 5: Fluctuations kinetic energy (distance to the wall: 12 mm).

With the second PIV set-up, a complete visualization of the phenomenon is obtained *(Figure* 5). Not only can we exactly define the axis of the A-pillar vortex, but we can also see how kinetic energy and vorticity (data not shown) are distributed. It can be observed that the kinetic energy increases as the vortex reaches the top of the model. There, the vortex can move freely on top of the model, possibly participating to the induced drag of the vehicle (Ahmed *et al.* [4]).

b. Pressure measurements

The noise disturbance inside a road vehicle is partly due to the vibrations of the side window. Therefore, pressure measurements are a necessity for the understanding of the mechanism of the phenomenon. The mean wall pressure measurements give a general idea on the pressure distribution *(Figure 6)*: a high-pressure coefficient C_p close to the vortex tube and very little interaction below that one. As we get closer to the tip of the model, the Cp gets bigger. This is in agreement with the fact that this area is the most energetic one, with the greatest velocities. Similar results were obtained by Ono *et al.* [5].
However, this is an unsteady phenomenon and the pressure fluctuations measurements show a broadband spectrum with no emerging frequency (most of them below 300 Hz).
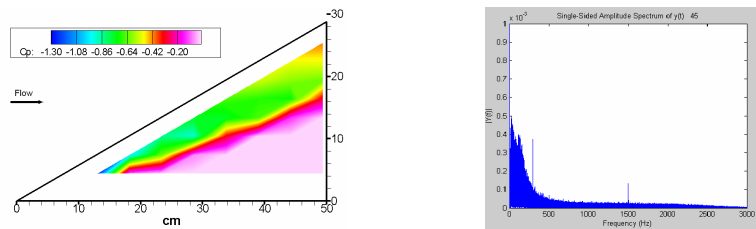

Figure 6: Wall distribution of pressure coefficient (left) and spectrum of the wall pressure fluctuations at x=357 mm, y=102 mm (right).

4. Conclusions

Preliminary PIV and wall pressure measurements allowed the topology of the airflow around the A-pillar of a road vehicle to be characterized. More specifically we measured the axis, shape and intensity of the A-pillar vortex, and investigated its interaction with the wall of the vehicle. PIV results at 2 mm distance from the wall and measurements of the wall pressure fluctuations can then be used as inputs to a numerical or analytical model of the phenomenon including the deformations and vibrations of the window and the generation of noise inside the vehicle, which will be the focus of future work.

5. References

[1] F. Alam, S. Watkins & G. Zimmer (2003) *Mean and time-varying flow measurements on the surface of a family of idealised road vehicles*. Experimental Thermal and Fluid Science **27**, 639-654.
[2] B. Lehugeur & P. Gilliéron (2006) *Drag Reduction by Active Control of A-Pillar Vortex Breakdown on a Simplified Car Geometry*. European Drag Reduction and Flow Control Meeting, April 2006
[3] C. Hoarau (2006) *Mesures multipoints, pression-vitesse pour l'analyse de l'aérodynamique d'écoulements décollés instationnaires – Application aux véhicules terrestres*. Ph.D. Thesis, University of Poitier, France.
[4] S.R. Ahmed & G. Ramm (1984) *Some Salient Features of the Time-Averaged Ground Vehicle Wake*. SAE-Paper 840300.
[5] K. Ono, R. Himeno & T. Fukushima (1999) *Prediction of wind noise radiated from passenger cars and it's evaluation based on auralization*, Journal of Wind Engineering and Industrial Aerodynamics **81**, 403-419

Low Drag Solutions for Suppressing VIV of Circular Cylinders

G.Assi and P.W. Bearman

Department of Aeronautics

Imperial College

London,

SW7 2BY

p.bearman@imperial.ac.uk

Abstract

Measurements are presented for a circular cylinder with low mass and damping which is free to respond in the cross-flow direction. It is shown how vortex-induced vibration can be practically eliminated by using free to rotate, two-dimensional control plates. Unlike helical strakes, the devices achieve VIV suppression with drag reduction. The device producing the largest drag reduction was found to have a drag coefficient equal to about 70% of that for a plain cylinder at the same Reynolds number.

Introduction

Vortex-induced vibrations are a continuing problem in offshore operations. A widely used method for suppressing VIV, developed originally in the wind engineering field, is the attachment of helical strakes. However, strakes suffer from two major problems: the first being that they increase drag and the second that their effectiveness reduces with decreases in the response parameter $m^*\zeta$, where m^* is the ratio of structural mass to the mass of displaced fluid and ζ is the fraction of critical damping. Whereas a strake height of 10% of cylinder diameter is sufficient to suppress VIV in air at least double this amount is required in water, and this increase in height is accompanied by a corresponding further increase in drag. It is known that if vortex shedding from a rigid cylinder is eliminated, say by the use of a long splitter plate, then drag is reduced hence conceptually an effective VIV suppression device should be able to reduce drag rather than increase it. This simple idea was the motivation for the work described here.

A simple analysis for a linear oscillator-based model of flow-induced vibration, assuming harmonic forcing and harmonic response, shows that response is inversely proportional to the product of m^* and ζ. Hence the most rigorous way to test the effectiveness of a VIV suppression device is to work at low mass and damping. In the experiments to be described in this paper the parameter $m^* \zeta$ was equal to 0.014. Owen et al (2001) describe a method for low drag VIV suppression that had shown itself to be effective down to values of $m^*\zeta$ of about 0.5. This was the attachment of large scale bumps to induce three-dimensional separation and eliminate vortex shedding. However, later experiments at lower values of $m^*\zeta$ have shown a return of VIV with amplitudes similar to those of a plain cylinder. This behaviour has been repeated with even grosser forms of continuous surface, three dimensionality where regular vortex shedding has been eliminated from the body when it is fixed but it returns under conditions of low mass and damping. From this experience it is concluded that sharp-edged separation from strakes, with its accompanying high drag, is required to maintain three-dimensional separation and that three-dimensional solutions will not provide the required combination of VIV suppression and low drag.

There are a number of two-dimensional control devices that have been used to weaken vortex shedding and reduce the drag of fixed circular cylinders, with the most well known being the splitter plate. In this paper we describe the results of experiments to suppress VIV and reduce drag using various configurations of two-dimensional, control plates.

Experimental Arrangement

Experiments have been carried out on devices fitted to a rigid length of cylinder free to respond in only the transverse direction. A recirculating water channel with a test section 0.6m wide, 0.7m deep and 8.4m long is used. The flow speed is continuously variable and good quality flow can be obtained up to at least 0.6 m/s. The cylinder model is constructed from 50mm diameter Perspex tube, giving a

maximum Reynolds number of approximately 30,000. Models are mounted on a very low damping, air bearing support system allowing vibration in one direction. A load cell is mounted between the cylinder and the support system in order to deduce the instantaneous and time-averaged hydrodynamic forces on a responding cylinder. In order to obtain the hydrodynamic transverse force acting, the inertia force (cylinder structural mass x acceleration) is subtracted from the force recorded by the load cell. Drag is measured by repeating experiments with the load cell orientated in the flow direction. With the load cell in place, the mass ratio, where mass ratio is defined as vibrating mass divided by the displaced mass of water, was 2. The structural damping is around 0.007, as a fraction of critical damping, giving a value of the product of mass ratio and damping of only 0.014. Measurements were made using one set of springs and the reduced velocity range covered was from 1.5 to 23, where reduced velocity (U/Df_0) is defined using the cylinder natural frequency measured in air.

In addition to response and force measurements, flow visualisation has been carried out using laser-illuminated fluorescent dye. Flow field measurements to obtain instantaneous spatial distributions of velocity and vorticity were obtained using a Dantec PIV system.

Experimental Results and Discussion

Initially experiments were conducted on a circular cylinder with a fixed splitter plate equal in length to one cylinder diameter. The result was a very vigorous transverse galloping oscillation that, with increasing reduced velocity, would apparently increase without limit. Since a device to be used in the ocean must have omni-directional effectiveness the next stage was to pivot the splitter plate about the centre of the cylinder. Following the disappointing experience with a fixed plate, it was thought that a plate free to rotate might provide damping to help suppress the galloping; but when the experiment was resumed a totally unexpected result was obtained. There were found to be two stable positions for the splitter plate at roughly ±20º to the free stream direction and the plate rapidly adopted one or other of these positions when it was released. VIV was suppressed, throughout the range of reduced velocity investigated, and drag reduced below that of a plain cylinder. Visualisation showed that on the side to which the plate deflected the separating shear layer from the cylinder appeared to attach to the tip of the plate and this had the effect of stabilising the near wake flow. Vortex shedding was visible downstream but this did not feed back to cause vibrations. An unwanted effect was that a steady transverse lift force developed on the cylinder. The splitter plate was free to rotate so the force, caused by differing flow on the two sides of the cylinder, must be acting primarily on the cylinder rather than the plate. The direction of the force was opposite to that which occurs on an aerofoil with a deflected flap, and caused the cylinder to adopt a steady offset position to the side to which the splitter plate deflected. It was this force which was responsible for the strong galloping response with the fixed splitter plate.

In order to try to eliminate the steady transverse force a pair of plates, one cylinder diameter long, were set at ±20º to the free stream direction. The angle between the plates was fixed but the pair of plates was free to pivot about the centre of the cylinder. This configuration suppressed VIV, reduced drag below that of a plain cylinder and removed the steady side force. In this arrangement the shear layers from the cylinder stabilised and reattached to the tips of the plates. Downstream of the plates vortex shedding was observed but this did not generate an excitation sufficient to cause any serious VIV. Maximum amplitudes recorded were around 5% of the cylinder diameter. Plates between 0.5 and 1.5 cylinder diameters long were all effective in suppressing VIV and reducing drag but, perhaps as might be expected, the shorter the plate the larger the angle required to stabilise the shear layers. When longer, free to rotate plates were attached to the cylinder a transverse flow-induced vibration returned.

Variations on the concept of double plates, some inspired by the early work of Grimminger (1945) related to suppressing VIV of submarine periscopes, were also studied. These included plates parallel to the flow and trailing back from the ±90° points on the cylinder. In one case there was a very small gap between the plates and the cylinder and in a second case the gap was set at 10% of the cylinder diameter. In Grimminger's experiments the plates were fixed since the flow direction was known but in our work the plates were free to rotate. Some of the configurations examined in this investigation are illustrated in figure 1. As shown in the plots in figures 2 and 3 of amplitude and drag coefficient against reduced velocity, every configuration with plates provided excellent VIV suppression and a reduction in drag below the plain cylinder value. The maximum drag reduction achieved was almost 30% and this was for the parallel plates with no gap. In figures 2 and 3 results for a fixed and a freely

responding cylinder are also presented to provide reference data. It should be noted that amplitude levels in figure 2 are measured root mean square values multiplied by √2.

Conclusions

Suppression of cross-flow, vortex-induced vibration of a circular cylinder, with resulting drag coefficients less than that for a fixed plain cylinder, has been achieved with the use of two-dimensional control plates. Suppression has been accomplished at a value of the combined mass and damping parameter of 0.014. The maximum drag reduction was about 30%.

References

Grimminger, G. The effect of rigid guide vanes on the vibration and drag of a towed circular cylinder. David Taylor Model Basin Report 504, 1945.
J.C.Owen, P.W.Bearman and A.A.Szewczyk. Passive control of VIV with drag reduction. J.Fluids and Struct., 15**,** 597-605, 2001.
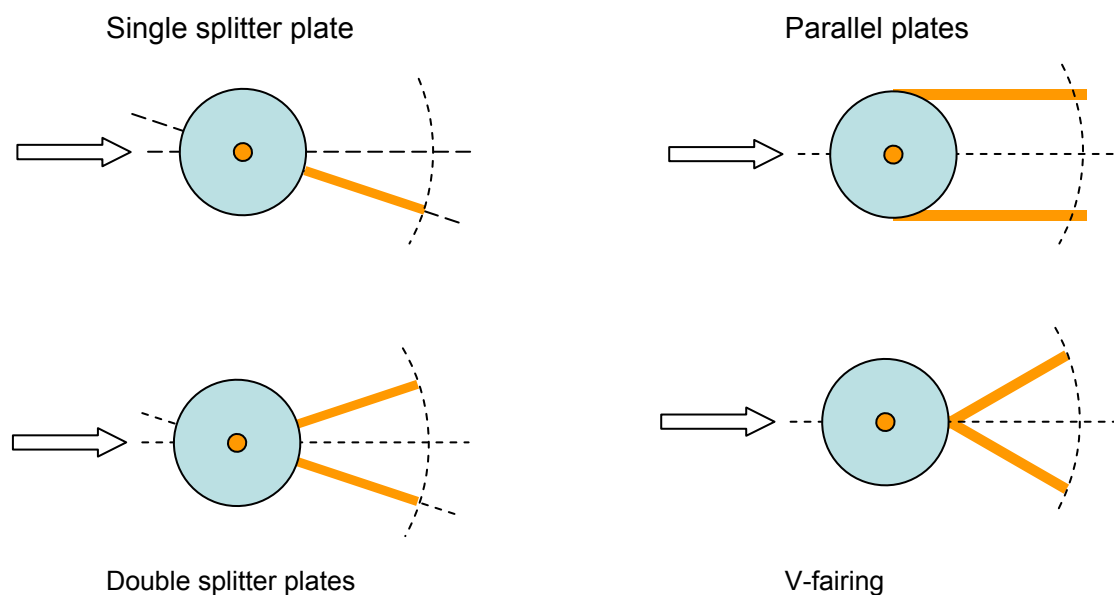
Acknowledgements
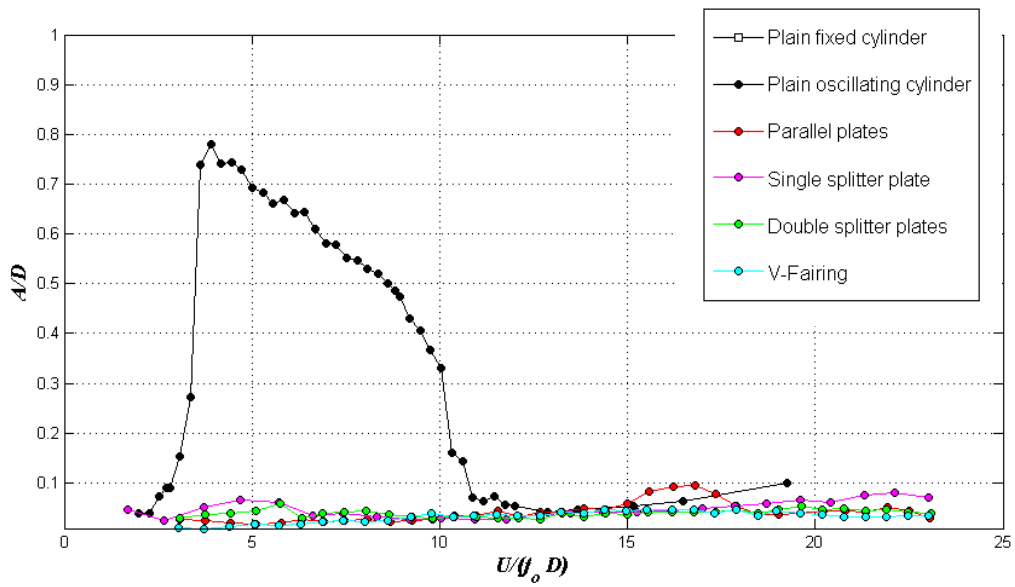
Figure 1 Plate configurations

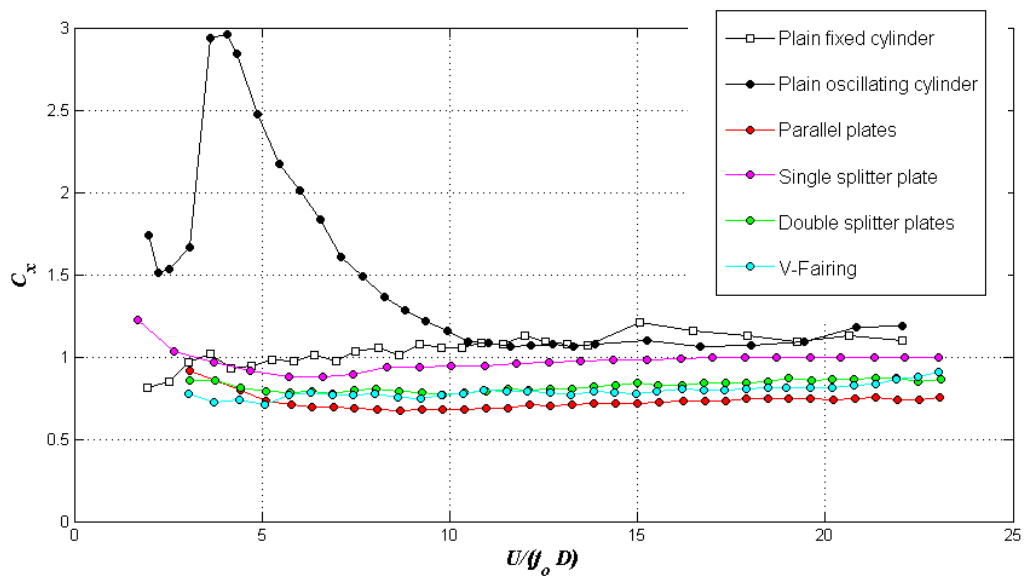Figure 2 Amplitude of Vibration versus Reduced Velocity

Figure 3 Drag Coefficient versus Reduced Velocity

Suppressing the Fluctuating Lift and Vortex Induced Vibration of a Circular Cylinder

By S. DONG[1]† and G. E. KARNIADAKIS[2]

[1]Center for Computational & Applied Math, Department of Mathematics, Purdue University, USA
[2]Division of Applied Mathematics, Brown University, USA

Prevention of undesirable vortex induced vibrations resulting from the fluctuating lift force on cylindrical structures is important to many engineering applications. In this paper we investigate the effects of three flow control schemes – pure suction, pure blowing, and combined windward suction/leeward blowing – on the fluctuating lift of a stationary circular cylinder and on the free oscillation of a cylinder subject to vortex induced vibrations. Results of three-dimensional direct numerical simulations at the Reynolds number $Re = 500$ show that overall the combined suction/blowing control is the most effective amongst the three. With this control, for suction/blowing velocities below a certain value the *r.m.s.* lift coefficient decreases linearly with increasing blowing/suction velocity, and beyond that point the lift coefficient becomes essentially negligible. Simulation of a freely vibrating cylinder with the flow control shows that the cross-flow cylinder oscillation decreases with increasing blowing/suction velocity and is completely suppressed at high blowing/suction velocities. Stability analysis relates the effectiveness of the flow control to the manipulation of the absolute instability in the cylinder wake.

---

1. Introduction

Vortex-induced vibration (VIV) of cylindrical structures is crucial to many engineering applications. A high level of fatigue damage to the structures can be produced by VIV in a relatively short period of time. In recent years a great deal of efforts have been devoted to the understanding and prediction of VIV with the ultimate goal of its prevention; see the reviews by Williamson & Govardhan (2004) and Sarpkaya (2004) and the references therein. The unsteady cross-stream force, the fluctuating lift, acting on the structure is the primary source of the flow-induced oscillations. Suppressing the fluctuating lift on a cylinder is therefore of tremendous importance and can potentially lead to practical methods for the ultimate prevention of undesirable VIVs.

Among the variety of techniques for manipulating the near-wake structure and vortex shedding of a circular cylinder are the use of a splitter plate, base bleed, small control cylinder, forced rotary motion or oscillation, cylinder heating, and synthetic jets; see for example Roshko (1961), Wood (1964), Strykowski & Sreenivasan (1990), Bearman & Owen (1998) for several representative techniques, and Zdravkovich (1981) for a review of the passive control methods. Blowing or suction as a means for drag reduction or vortex manipulation is the subject of several previous studies (Williams *et al.* 1992; Park *et al.* 1994; Lin *et al.* 1995; Min & Choi 1999; Delaunay & Kaiksis 2001; Mathelin *et al.* 2001). Williams *et al.* (1992) experimentally studied the effects of unsteady ejection or sucktion of fluid through two rows of small holes, parallel to the cylinder axis, on the cylinder surface at an angle $\pm45^0$ from the front stagnation line. They observed that the produced localized disturbances modified the vortex shedding patterns and frequencies as well as the chatacteristics of the mean flow profiles. Employing two-dimensional numerical simulations, Delaunay & Kaiksis (2001) investigated the effect of steady suction or blowing applied at the cylinder base around the Reynolds number $Re = 47$, at which the steady flow transitions to an unsteady state with vortex shedding. They showed that in the supercritical regime ($Re > 47$) slight blowing or high enough suction stabilized the wake while in the subcritical regime suction destabilized the wake and blowing had no detectable effect on the flow stability. More recently, Kim & Choi (2005) numerically investigated a forcing scheme for cylinder drag reduction by blowing or suction of fluid, whose intensity was sinunoidally modulated along the cylinder axis, through two slits placed on the top and bottom cylinder surfaces (at an angle around $\pm90^0$ from the front stagnation line) respectively. It was observed

† Corresponding author, sdong@math.purdue.edu

Cases	Re	N_z	P	C_D	C_L	St
DNS-STAT-A	500	128	4	1.122	0.207	0.212
DNS-STAT-B	500	128	5	1.132	0.227	0.200
DNS-STAT-C	500	128	6	1.134	0.227	0.203
DNS-STAT-D	500	192	4	1.131	0.223	0.203
Wieselsberger (1921)	500	–	–	1.10	–	–
Norberg (2003)	500	–	–	–	0.239	0.204

TABLE 1. Global physical parameters of flow past a stationary cylinder, without control, at $Re = 500$. Symbols: Nz, number of Fourier planes in spanwise direction; P, element order; C_D, drag coefficient; C_L, $r.m.s.$ lift coefficient; St, Strouhal number. Cases starting with "DNS-" denote current simulations.

that the in-phase forcing at the two slits reduced the drag substantially and could also attenuate or annihilate the Karman vortex shedding.

Studies of the above flow control techniques, including blowing or suction and the other techniques, have so far been confined to the context of flows past stationary cylinders. While several techniques seem capable of suppressing the vortex shedding in the wake of a stationary cylinder, the effect is not clear for cylinders subject to vortex induced vibrations. Indeed, it has been shown for wavy cylinders and cylinders with bumps that even though the vortex shedding can be suppressed when the cylinder is stationary, significant amplitudes of oscillation still develop if the cylinder is allowed to freely vibrate (Owen & Bearman 2001; Bearman & Brankovic 2004).

In this paper we investigate the effects of three flow control schemes – suction, blowing, and a new scheme combining suction and blowing – on the fluctuating lift of a stationary circular cylinder, and on the free oscillation of a cylinder subject to vortex induced vibrations. With the combined suction/blowing control, suction is applied on the windward half of the cylinder surface while blowing is applied on the leeward half of the surface. This scheme will be referred to as the WSLB scheme hereafter in this paper. Employing three-dimensional direct numerical simulations (DNS) at a Reynolds number $Re = 500$, we demonstrate that overall the WSLB scheme is the most effective among the three in terms of reducing the fluctuating lift. The underlying reasons for the lift/VIV reduction/suppression will be explored.

2. Simulation Parameters

We consider the flow past a long rigid circular cylinder under two situations: (1) The cylinder is stationary (stationary case); (2) The cylinder is allowed to freely vibrate, but only in the cross-flow direction (VIV case). We solve the three-dimensional incompressible Navier-Stokes equations by employing a Fourier spectral expansion of the flow variables in the homogeneous spanwise direction and a spectral element discretization in the two-dimensional streamwise-crossflow planes. For the VIV case, a coordinate system attached to the axis of the cylinder is used and the cylinder becomes stationary in this system. Details of the numerical methods for the stationary case and VIV simulations are documented in Dong *et al.* (2006) and Newman & Karniadakis (1997).

For the WSLB control, steady suction and blowing are applied on the windward half and the leeward half of the cylinder surface, respectively. For pure blowing (or pure suction) control, steady blowing (or suction) is applied on the entire cylinder surface. These controls are characterized by a blowing/suction velocity normal to the cylinder surface with a uniform magnitude (referred to as control velocity magnitude, $V_{control}$, hereafter). Dirichlet boundary condition is applied on the cylinder surface in accordance with the flow control. For cases without control, the no-slip condition is imposed on the cylinder surface.

Three-dimensional direct numerical simulations (DNS) are conducted at the Reynolds number $Re = 500$, based on the free-stream velocity U_0 and the cylinder diameter D. The computational domain extends from $-20D$ at the inlet to $40D$ at the outlet, and from $-20D$ to $20D$ in the crossflow direction. The spanwise dimension of the flow domain is $L_z = 3\pi D$. Extensive grid refinement tests have been conducted. We employ a spectral element mesh with 1860 quadrilateral elements in the streamwise-crossflow planes, and the element order varies from 4 to 6. In the spanwise direction we employ 64 to 96 Fourier modes (or 128 to 192 grid points), all with 3/2-dealiasing. Table 1 summarizes the global physical parameters of the flow past a stationary cylinder, without control, computed with various resolutions together with the experimentally measured values from the literature. The computed values agree with the experimental data reasonably well.
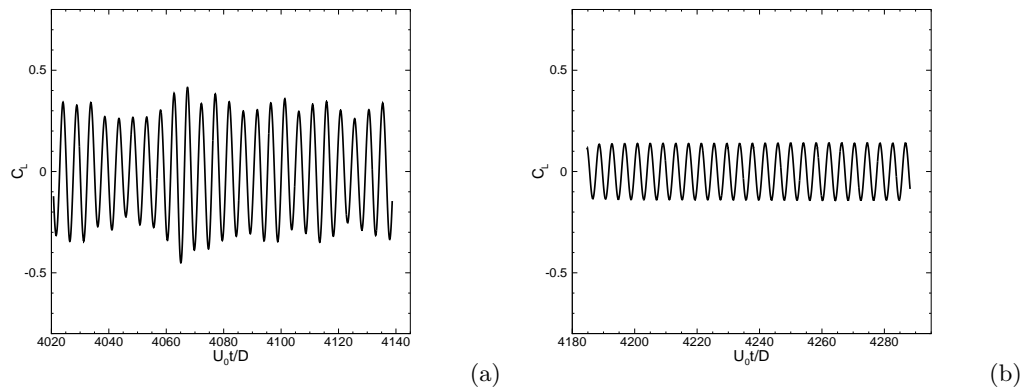
FIGURE 1. Time histories of instantaneous lift coefficient (stationary case): (a) without control; (b) with WSLB control (control velocity $V_{control}/U_0 = 0.1$).

3. Results

Pure suction, blowing, and the WSLB control significantly affect the fluctuating lift force on the cylinder. In Figure 1 we compare histories of the instantaneous lift coefficient for cases without control (Figure 1a) and with the WSLB control at a control velocity $V_{control}/U_0 = 0.1$ (Figure 1b) for the flow past a stationary cylinder at $Re = 500$. Applying the control has reduced the amplitude of the fluctuating lift force substantially.

We systematically vary the magnitude of the control velocity and investigate the effect on the fluctuating lift of the cylinder (stationary case). Figure 2(a) compares the root-mean-square ($r.m.s.$) lift coefficient as a function of the normalized control velocity ($V_{control}/U_0$) with the three controls. The overall observation is that the fluctuating lift is significantly reduced with the flow controls, and even completely suppressed at high control velocities. However, the three schemes exhibit quite different characteristics. Pure suction is only effective for lift reduction at high suction velocities ($V_{control}/U_0 = 0.1$ or above). Low suction velocity, on the other hand, appears to have the opposite effect; With a suction velocity $V_{control}/U_0 = 0.05$, the $r.m.s.$ lift coefficient is increased somewhat. For the WSLB control, the $r.m.s.$ lift coefficient decreases linearly with increasing blowing/suction velocity below a certain control velocity value ($V_{control}/U_0 = 0.15$). Beyond this point the r.m.s. lift coefficient becomes essentially negligible. Both the WSLB control and the pure suction can completely suppress the fluctuating lift at the highest control velocity considered here ($V_{control}/U_0 = 0.2$). At the same control velocity values, the WSLB scheme appears to be more effective than pure suction in terms of lift reduction. With pure blowing, the lift coefficient decreases with increasing control velocity. At the lowest control velocity ($V_{control}/U_0 = 0.05$), pure blowing appears the most effective among the three schemes. However, as the control velocity increases it becomes less effective compared to the other two. At the highest control velocity considered here ($V_{control}/U_0 = 0.2$) the fluctuating lift still remains quite significant with the pure blowing control. Overall, the WSLB control appears the most effective in terms of lift reduction among the three schemes. At low control velocities it avoids the lift increase as observed with pure suction, and at high control velocities it produces a high rate of reduction unlike the pure blowing control.

Since the ultimate goal is to reduce the VIV, we have simulated the flow past a freely vibrating cylinder (in cross-flow direction only) at $Re = 500$ to verify the effectiveness of the flow control in reducing VIV. Two cases have been simulated: without control and with the WSLB control. Since the WSLB scheme is overall the most efficient among the three, we have considered only this control for the VIV case. Figure 2(b) shows the $r.m.s.$ displacement of the cylinder in the cross-flow direction as a function of the control velocity for two damping coefficients (0.0046 and 0.046). This is for a cylinder mass ratio (with respect to the fluid) of 5.09. The inherent frequency of the cylinder oscillation is set to be equal to the Strouhal frequency of the flow past a stationary cylinder at the same Reynolds number. It can be observed that the cylinder oscillation amplitude decreases consistently with increasing control velocity. At high control velocities the cylinder oscillation is completely suppressed.

To explore the underlying reasons for the lift reduction/suppression with the flow controls, we have performed the stability analysis for the flow past a stationary cylinder using the method in Triantafyllou *et al.* (1986). By solving the Orr-Sommerfield equation on the mean streamwise velocity profiles at different
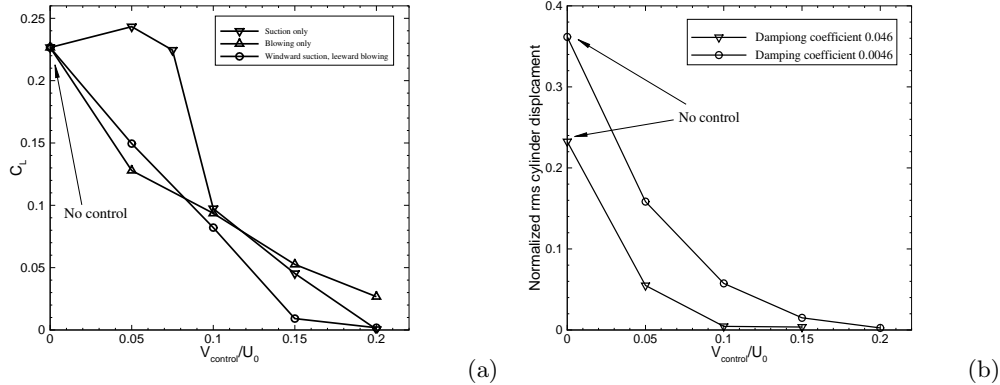
FIGURE 2. Lift/VIV reduction: (a) *r.m.s.* lift coefficient C_L as a function of the normalized control velocity $V_{control}/U_0$ for the stationary case. (b) *r.m.s.* cylinder displacement in cross-flow direction as a function of control velocity with the WSLB control for a freely vibrating cylinder subject to VIV.
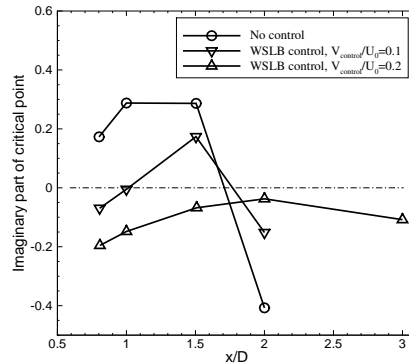

FIGURE 3. Stability analysis: Imaginary part of the critical point as a function of the streamwise location in the cylinder wake (positive values denoting absolute instability, negative values denoting convective instability).

downstream locations, the coordinates of the "critical point" (Triantafyllou *et al.* 1986) in the ω-plane (ω is the complex frequency) can be determined. We computed the coordinates of the critical points based on the mean streamwise velocity profiles at different downstream locations for cases without control and with the WSLB control. Figure 3 shows the imaginary part of the critical point as a function of the streamwise location for several cases. Without control, we observe a region of absolute instability (positive ω_I) near the cylinder, and a region of convective instability further downstream (negative ω_I), consistent with Triantafyllou *et al.* (1986). With the WSLB control, the region of absolute instability is displaced downstream and shrinks in size. The nature of the instability in the near-wake region changes from an absolute instability (no-control) to a convective instability (see the case $V_{control}/U_0 = 0.1$). With increasing blowing/suction velocity, the highest ω_I value in the region of absolute instability also decreases, suggesting a decrease in the rate of growth of perturbations. At $V_{control}/U_0 = 0.2$, all the ω_I values have become negative, indicating a convective instability in the entire wake. As a result, the vortex shedding and the fluctuating lift are completely suppressed.

4. Summary

We have studied the effects of three flow control schemes – pure suction, pure blowing, and windward suction/leeward blowing – on the fluctuating lift of a circular cylinder at $Re = 500$. Pure suction is only effective for lift reduction at high control velocities; At low control velocities it induces an increase in the lift coefficient. Pure blowing appears effective at low control velocities; It becomes less effective as the control velocity increases compared to the other two schemes. Overall, the WSLB control appears the most effective among the three schemes. With this control, the lift coefficient decreases linearly

with increasing control velocity below a certain control velocity value, and beyond that point the lift coefficient becomes essentially negligible. Simulation of a freely vibrating cylinder with the WSLB control demonstrates its effectiveness in reducing the VIV. At high control velocities the cylinder oscillation is completely suppressed.

REFERENCES

BEARMAN, P.W. & BRANKOVIC, M. 2004 Experimental studies of passive control of vortex-induced vibration. *Eur. J. Mech. B* **23**, 9–15.

BEARMAN, P.W. & OWEN, J.C. 1998 Reduction of bluff-body drag and suppression of vortex shedding by the introduction of wavy separation lines. *J. Fluids Struct.* **12**, 123–130.

DELAUNAY, Y. & KAIKSIS, L. 2001 Control of circular cylinder wakes using base mass traspiration. *Phys. Fluids* **13**, 3285–3302.

DONG, S., KARNIADAKIS, G.E., EKMEKCI, A. & ROCKWELL, D. 2006 A combined DNS-PIV study of the turbulent near wake. *J. Fluid Mech.* **569**, 185–207.

KIM, J. & CHOI, H. 2005 Distributed forcing of flow over a circular cylinder. *Phys. Fluids* **17**, 033103.

LIN, J.-C., TOWFIGHI, J. & ROCKWELL, D. 1995 Near-wake of a circular cylinder: control study by steady and unsteady surface injection. *J. Fluids Struct.* **9**, 659–669.

MATHELIN, L., BATAILLE, F. & LALLEMAND, A. 2001 Near wake of a circular cylinder submitted to blowing - I, boundary layer evolution. *Int. J. Heat Mass Trans.* **44**, 3701–3708.

MIN, C. & CHOI, H. 1999 Suboptimal feedback control of vortex shedding at low reynolds numbers. *J. Fluid Mech.* **401**, 123–156.

NEWMAN, D. & KARNIADAKIS, G.E. 1997 A direct numerical simulation study of flow past a freely vibrating cable. *J. Fluid Mech.* **344**, 95–136.

NORBERG, C. 2003 Fluctuating lift on a circular cylinder: review and new measurements. *J. Fluids Struct.* **17**, 57–96.

OWEN, J.C. & BEARMAN, P.W. 2001 Passive control of VIV with drag reduction. *J. Fluids Struct.* **15**, 597–605.

PARK, D.S., LADD, D.M. & HENDRICKS, E.W. 1994 Feedback control of von karman vortex shedding behind a circular cylinder at low reynolds numbers. *Phys. Fluids* **6**, 2390–2405.

ROSHKO, A. 1961 Experiments on the flow past a circular cylinder at very high reynolds number. *J. Fluid Mech.* **10**, 345–356.

SARPKAYA, T. 2004 A critical review of the intrinsic nature of vortex-induced vibrations. *J. Fluids Struct.* **19**, 389–447.

STRYKOWSKI, P.J. & SREENIVASAN, K.R. 1990 On the formation and suppression of vortex shedding at low reynolds numbers. *J. Fluid Mech.* **218**, 71–107.

TRIANTAFYLLOU, G.S., TRIANTAFYLLOU, M.S. & CHRYSSOTOMIDIS, C. 1986 On the formation of vortex streets behind stationary cylinders. *J. Fluid Mech.* **170**, 461–477.

WIESELSBERGER, C. 1921 Neuere feststellungen uber die gesetze des flussigkeits-und luftwiderstandes. *Physikalische Zeitschrift* **22**, 321–328.

WILLIAMS, C.R., MANSY, H. & AMATO, C. 1992 The response of asymmetry properties of a cylinder wake subjectted to localized surface excitation. *J. Fluid Mech.* **234**, 71–96.

WILLIAMSON, C.H.K. & GOVARDHAN, R. 2004 Vortex-induced vibrations. *Annu. Rev. Fluid Mech.* **36**, 413–455.

WOOD, C.J. 1964 The effect of base bleed on a periodic wake. *J. R. Aeronaut. Soc.* **68**, 477.

ZDRAVKOVICH, M.M. 1981 Review and classification of various aerodynamic and hydrodynamic means for suppressing vortex shedding. *J. Wind Eng. Ind. Aerodyn.* **7**, 145–189.

WAKE DYNAMICS OF AN EXTERNAL FLOW PAST OSCILLATING CURVED CYLINDERS

A. de Vecchi, S.J. Sherwin and J.M.R. Graham,
Department of Aeronautics, Imperial College London, UK
Email address: a.devecchi@imperial.ac.uk

INTRODUCTION

The aim of the present study is to investigate the intricate dynamics of vortex shedding past curved riser pipes with the free-stream aligned with the plane of curvature. This problem is particularly significant for many engineering applications, especially in the offshore industry: the increasing need to exploit deep-water reservoirs has highlighted the lack of a complete insight into the Vortex-Induced Vibrations (VIV) dynamics on long structures such as the marine riser pipes used to convey fluids from the seabed to the sea surface. Steel catenary riser pipes and flexibles are being increasingly used offshore but, in spite of their practical importance, curved configurations like the ones studied in this work have received in the past much less attention than straight cylinders: recent studies of the flow dynamics behind curved riser pipes and wavy cylinders can be found in [1, 2, 3].

PROBLEM DESCRIPTION

The fundamental mechanism of vortex shedding past a curved cylinder has been investigated at a Reynolds number of 100 using three-dimensional spectral/hp computations (see [4, 5]).

Two different configurations are presented herein: in both cases the main component of the geometry is a circular cross-sectioned cylinder whose centreline is a quarter of a ring with a radius of curvature close to the limit value for real flexible pipes. The inflow direction is parallel to the plane of curvature; depending on whether the in-flow is directed towards the outside or the inside of the bend, these two configurations will be referred to as "convex" and "concave".

Forced vibration simulations have been performed at constant amplitudes and different input frequencies, ranging from $0.8f_s$ to $1.2f_s$, where f_s is the Strouhal frequency value for a fixed straight cylinder at $Re = 100$ ([6]). Two different types of motion were investigated: in the first set of simulations (type 1) a sinusoidal translation in the transverse direction is prescribed to the body, while in the second set (type 2) an oscillatory roll motion is imposed on the structure, which is forced to rotate transversely back and forth about the axis of its bottom section.
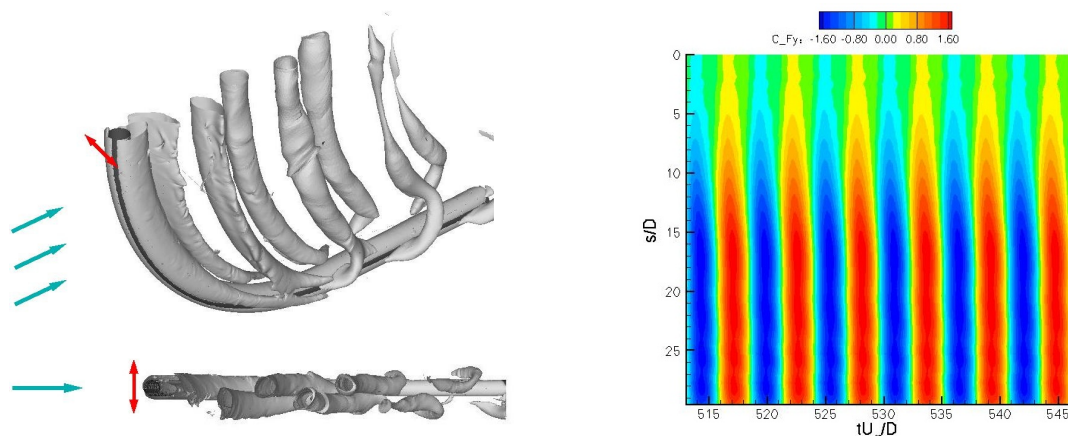

Figure 1. *Left*: Wake topology for the flow past the convex configuration at $f_i = 1.1f_s$ visualised through isosurfaces at $\lambda_2 = -0.1$. *Right*: Time evolution of the sectional lift coefficient along the cylinder's span. s/D is the non-dimensional arc length: $s/D = 0$ denotes the top section of the cylinder, while the end of the ring part is located at $s/D = 19.6$.
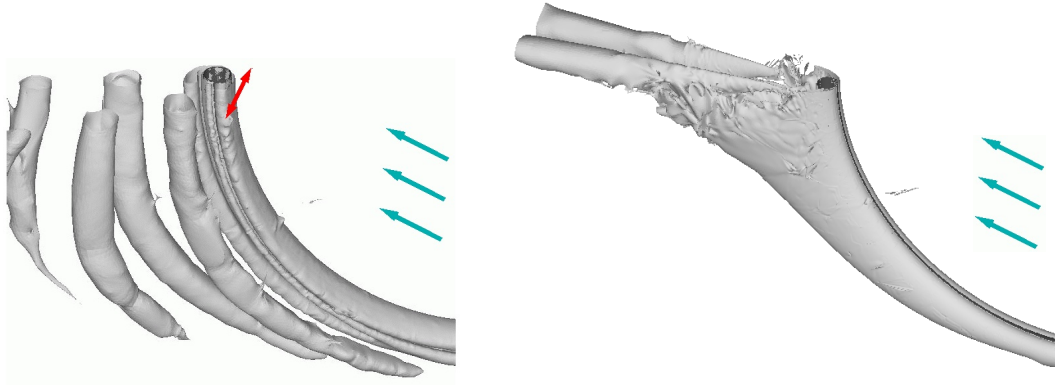
Figure 2. Comparison of the wake topology for the flow past the concave configuration. *Left*: forced (type 1) oscillation at $f_i = 1.1 f_s$ and $A/D = 0.5$ (isosurfaces at $\lambda_2 = -0.1$). *Right*: steady wake in the stationary case visualised at $\lambda_2 = -0.01$ (from [1, 2]).
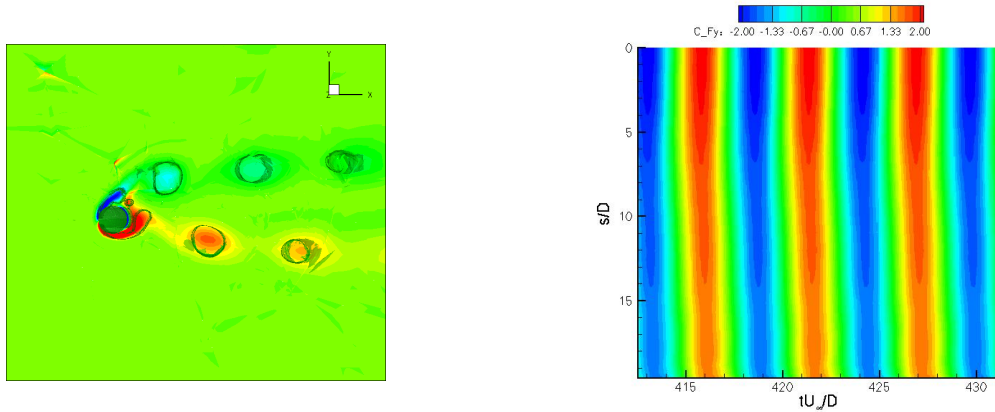

Figure 3. *Left*: Spanwise vorticity isocontours overlaid on $\lambda_2 = -0.1$ isosurfaces in the case of the concave configuration in forced translation. *Right*: Time evolution of the sectional lift coefficient along the cylinder's span, with the non-dimensional arc-length $s/D = 0$ denoting the top section of the cylinder.

INFLUENCE OF CURVATURE ON WAKE TOPOLOGY IN FORCED MOTION

When the cylinder is forced to oscillate transversely (type 1 motion) at fixed amplitudes, equal to $0.5D$ and $0.25D$, both configurations exhibit a 2S type of vortex shedding (as described in [7]), with the cores bent according to the body's curvature. However, the wake topology is markedly different: in the convex case depicted in figure 1, the wake at $A/D = 0.5$ and $f_i = 1.1 f_s$ is narrow and the formation length is found to decrease as the frequency is increased, whereas the concave configuration with the same input parameters is characterised by a much wider wake with a secondary vortex between the two shear layers and a formation region which appears remarkably contracted at all input frequencies (figure 2 and 3 *left*). This configuration was found to suppress vortex shedding in the absence of oscillatory transverse motion, giving rise to a steady wake without interaction between the shear layers, as shown in figure 2 *right*. Moreover, a variation of the wake width along the span was observed in the steady case: the top section exhibited the widest wake, while the bottom one the narrowest. This phenomenon was related to the strong component of axial flow stemming from the stagnation face curvature and to the associated production of vorticity in the x- and y-direction in the developing shear layers ([1, 2]). The cylinder's transverse motion results in a disruption of the stabilising mechanism arising from this vorticity generation: the axial flow direction is not constant along the span and the formation of vorticity in the part of the cylinder most susceptible to periodic
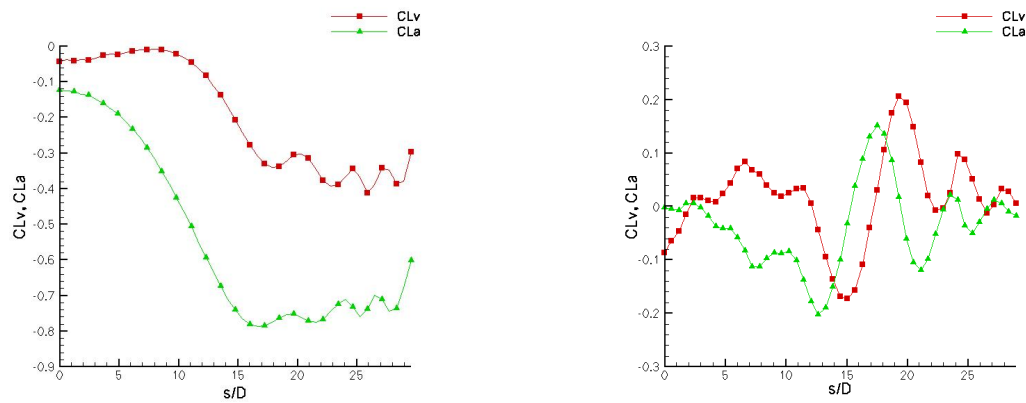
Figure 4. Distribution of the time-averaged lift coefficient components in phase with the velocity, CL_v, and with the acceleration, CL_a, along the span of the convex configuration. *Left*: translational case (type 1 motion). *Right*: rotational case (type 2 motion).

vortex shedding is thus weakened.

As expected from theoretical considerations ([8]), if the body oscillates the correlation length of the vortices increases and the coupling of the flow in the spanwise direction becomes stronger, resulting in a more correlated form of shedding. Considering figures 1 and 3, which show the time evolution of the lift coefficient isocontours in every section of the cylinder, the vortex shedding appears to be in phase along the span without variation in sign of C_{F_y} as the non-dimensional arc-length s/D increases for a fixed time instant.

ENERGY TRANSFER MECHANISM

The fact that the sectional forces in figure 1 (*right*) do not decrease with increasing s/D may appear in contrast to the weakening of the shedding in the lower part of the cylinder shown in figure 1 (*left*): however, in the horizontal extension ($s/D > 19.6$) the body undergoes only a drag type force in the y-direction due to the cross flow, since the inflow is parallel to the cylinder's axis and does not generate vortex shedding. Therefore the horizontal part behaves like a slender body and provides a strong hydrodynamic damping to the whole structure. In figure 4 (*left*) the time-averaged components of the lift coefficient in phase with the velocity, CL_v, and with the acceleration, CL_a, are plotted against the non-dimensional arc-length. Positive CL_v is the same as negative damping and excites free vibration. Here CL_v is most negative (i.e. positive damping) for $s/D > 20$ and increases towards the top sections, where vortex shedding induced excitation of free vibration might be expected to occur: therefore the overall net energy transfer per cycle is negative, whereas flow-induced vibrations require positive energy transfer from the fluid to the cylinder. If the prescribed amplitude of oscillation is halved, i.e. $A/D = 0.25$, the curved part generates excitation by the fluid ($CL_v > 0$) but the damping effect from the horizontal extension dominates, leading once again to an overall negative energy transfer.

To see if the structure can be excited to undergo VIV, a second set of simulations has been performed imposing the type 2 oscillatory roll motion on the body. For the convex case presented herein the horizontal extension at the lower end of the cylinder is fixed axially and the whole body is forced to rotate rigidly about this axis: the maximum amplitude, equal to $0.5D$, is thus reached at the top section and linearly decreases with decreasing distance to the roll axis. This kind of motion might be considered to simulate the flow configuration near a touch-down point.

This case exhibits a totally different wake topology and sectional forces distribution, as illustrated in figure 5: the λ_2 isosurfaces show that the shed cores twist around their axes and exhibit spanwise waviness. Furthermore they are only slightly bent according to the cylinder's curvature and detach from the main vortex at different spanwise locations for every time instant: the imposed motion leads to out-of-phase shedding and thus to the non uniform spanwise distribution of the sectional lift coefficient illustrated in figure 5 (*right*). In contrast to the translational (type 1) motion previously considered, the main vortex is weaker and does not envelope the horizontal extension, which now appears fixed to the flow. Therefore the damping effect generated in (type 1) motion on the part of the body parallel
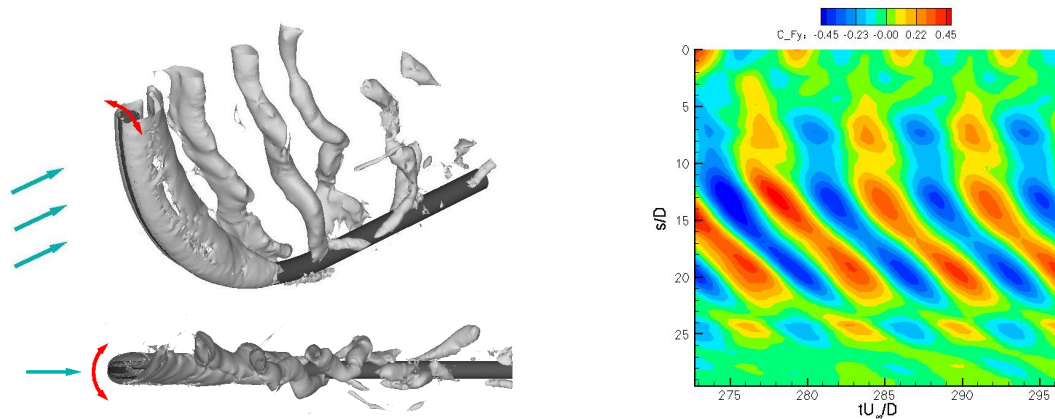
Figure 5. *Left*: Wake topology for the flow past the convex configuration at $f_i = 0.9 f_s$ visualised through isosurfaces at $\lambda_2 = -0.1$. *Right*: Time evolution of the sectional lift coefficient along the cylinder's span, with the non-dimensional arc-length $s/D = 0$ denoting the top section.

to the flow is no longer produced by the (type 2) rotation, resulting in a total positive energy transfer from the fluid to the structure.

On the basis of these results obtained with forced motion of the cylinder, free response simulations are currently being performed for the cases that showed a positive energy transfer under forced oscillation.

CONCLUDING REMARKS

Three-dimensional simulations based on spectral/*hp* element methods have been used to investigate the flow characteristics of vortex shedding from curved cylinders in a uniform stream under stationary body conditions and under imposed oscillatory body motions: the latter condition is meant to capture the fluid dynamic features of a freely vibrating pipe under the simplified assumptions provided by forced oscillations, giving an indication of flow regimes that may produce VIV.

The effect of curvature and body oscillation was found to play a key role on the vortex shedding dynamics, showing substantial differences from the shedding past straight cylinders studied in the past. For all the frequencies tested the mode of shedding was found to be 2S, even when the input frequencies and amplitudes lay in the 2P region of the parameter space compiled by Williamson and Roshko [7]. This highlights the lack of a full correspondence between the flow states observed in forced oscillations for curved and straight cylinders, suggesting that a redefinition of the lock-in boundaries for more complex geometries should be undertaken in order to understand the combined influence of motion and curvature on the vortex shedding.

References

[1] Miliou A. and Sherwin S.J. and Graham J.M.R.: Fluid dynamic loading on curved riser pipes. *J. Offshore Mech. Arctic Eng.* **125-3**:176-182, 2003.

[2] Miliou A. and de Vecchi A. and Sherwin S.J. and Graham J.M.R.: Wake dynamics of external flow past a curved circular cylinder with the free-stream aligned with the plane of curvature. Under consideration for publication in *J. Fluid Mech.*.

[3] Darekar R.M. and Sherwin S.J.: Flow past a square-section cylinder with a wavy stagnation face. *J. Fluid Mech.* **426**:263-295, 2001.

[4] Karniadakis G.E. and Sherwin S.J.: Spectral/hp element methods for computational fluid dynamics. *Oxford University Press*, 2005.

[5] Sherwin S.J and Karniadakis G.E.: A triangular spectral element method: applications to the incompressible Navier-Stokes equations. *Comp. Meth. Appl. Mech. Eng.*, **123**:189-229, 1995.

[6] Williamson C.H.K.: Vortex shedding in the wake of a circular cylinder at low Reynolds numbers. *J. Fluid Mech.* **206**:597-627, 1989.

[7] Williamson C.H.K. and Roshko A.: Vortex formation in the near wake of an oscillating cylinder. *J. Fluids Struct.* **2**:355-381, 1988.

[8] Bearman P.W.: Vortex shedding from oscillating bluff bodies. *Annu. Rev. Fluid Mech.* **16**:195-222, 1984.

Experimental Investigation of Vortex-Induced Vibrations on Rigid, Smooth and Inclined Cylinders

Guilherme R. Franzini
guilherme.franzini@poli.usp.br

André L.C. Fujarra
afujarra@usp.br

Julio R. Meneghini
jmeneg@usp.br

NDF, *Escola Politécnica*, University of São Paulo, SP, Brazil
Ricardo Franciss
franciss@petrobras.com.br
CENPES – Petrobras, RJ, Brazil

ABSTRACT

This paper presents experimental results of vortex-induced oscillation on inclined, rigid and smooth circular cylinders. The relevance of this research project is justified based on the fact that several offshore structures, such as risers, have theirs axis forming an angle in relation to the free stream velocities.

The main purpose of this experimental investigation is to verify the validity of the classical approach of VIV study on inclined structures. This approach consists decomposing the free stream velocity onto the perpendicular direction of the structure axes.

The cylinder used in our experiments had a diameter $D = 32mm$ and an immersed length $L = 672mm$ leading to an aspect ratio $L/D \cong 21$. The models tested, instrumented with load cells, strain gages and extensometer, were mounted on an elastic support based on air bearings and free to oscillate only in cross-flow direction. Measurements of lift and drag global forces and frequency and amplitude of oscillation were carried out.

In order to evaluate the time series of displacement, a mathematic tool was developed based on Hough Transform to detect circles on an image. Fixing a circular target on the model's support and filming each experiment, the time series of displacement were recovered.

The experiments were carried out on a Water Channel Facility at NDF/EP, University of São Paulo. The test section has *7.5m* long, *0.70m* width and *0.70m* height. The Reynolds number range tested was *2000<Re<10000*. Free decays tests allowed to evaluate structural damping of the elastic air base varying in the range *0.006<ζ_s<0.008* and its natural damped frequency in still water $f_n = 0.86Hz$. The total structural oscillating mass was *m = 1.06kg*, leading to a value of mass ratio *m* = 1.96*.

Experiments and Results

The investigation took into account five sets of experiments. The first one (paradigm) consisted in testing a circular cylinder vertically mounted on an elastic support base on air bearings. The amplitude of oscillation was measured by means of a frequency domain analysis on the displacement time series. The peak of non-dimensional amplitude observed was *Ay/D* $\cong$ *0.77*, in agreement with those presented by Khalak and Williamson [1], for similar values of *m** and ζ_s.
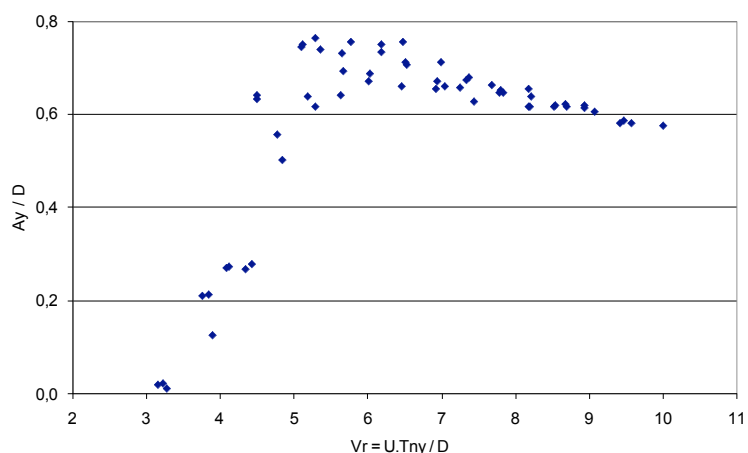

Figure 1 – Non-dimensional response amplitude for the first set of experiments (vertical circular cylinder).

In this first set, the added mass was also measured, following the same procedure described in Fujarra and Pesce [2]. These results of added mass coefficients agree very well with those presented by Vikestad et al. 0, with the same zero-crossing value at $Vr \cong 8$ and an asymptotic value of $C_a. = -1$ for high values of Vr.
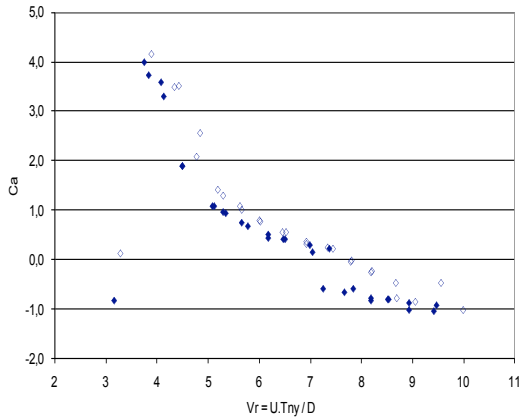

Figure 2 – Added mass coefficient as function of the reduced velocity, Vr (vertical circular cylinder).
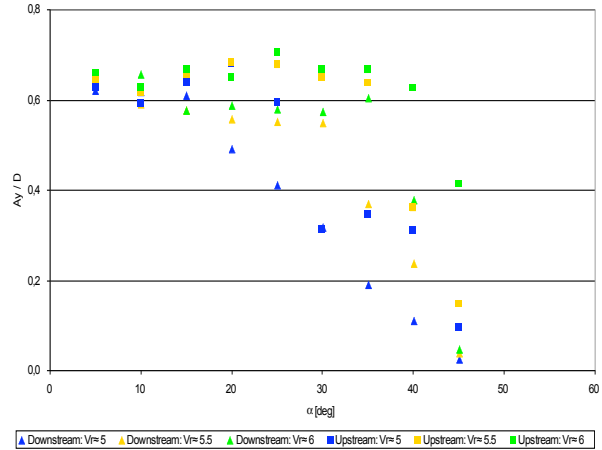

Figure 3 - Non-Dimensional Amplitude for the second set of experiments (circular cylinder inclined downstream and upstream).
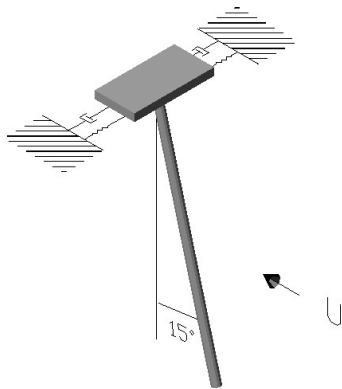

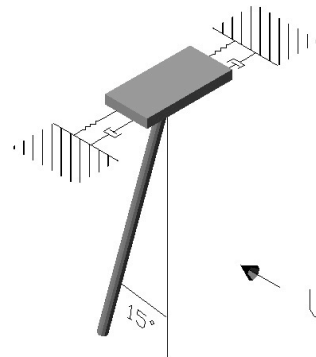Fig 4 - Cylinder Inclined in 15º - Upstream Direction.

Fig 5 - Cylinder Inclined in 15º - Downstream Direction.

In the third set of experiments, all reduced velocity range, *3<Vr<10*, was investigated with the cylinder inclined by an angle α = *20°* and α = *45°*. The peaks of non-dimensional response amplitude were *0.62* and *0.55*, respectively. In terms of synchronization, the behavior for α = *20°* was similar to the paradigm and the one presented for α = *45°*, showing small displacements for higher values of *Vr*.

In the fourth set of experiments, an elliptical cylinder was vertically mounted on the elastic support and subjected to the values of free stream velocities obtained by decomposing onto the cylinder axes. The immersed length of the elliptical cylinder was the same of the one presented on the third set of experiments considering α = *45°*. The peak of response amplitude was *Ay/D $\cong$ 0.50* and occurred in the range *6<Vr<8*.
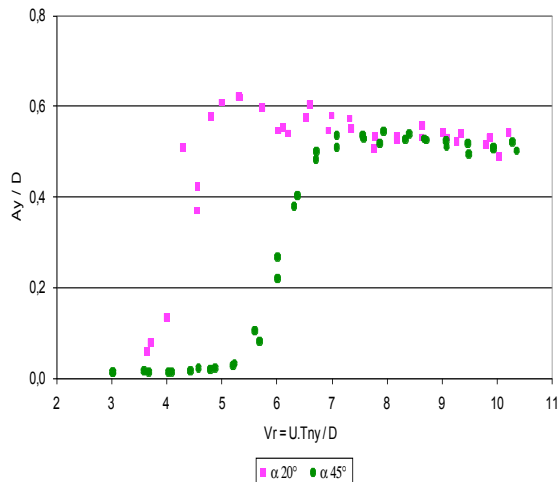
Figure 6 - Non-Dimensional Amplitude for the third set of experiments (circular cylinder inclined $\alpha = 20°$ and $\alpha = 45°$ downstream).
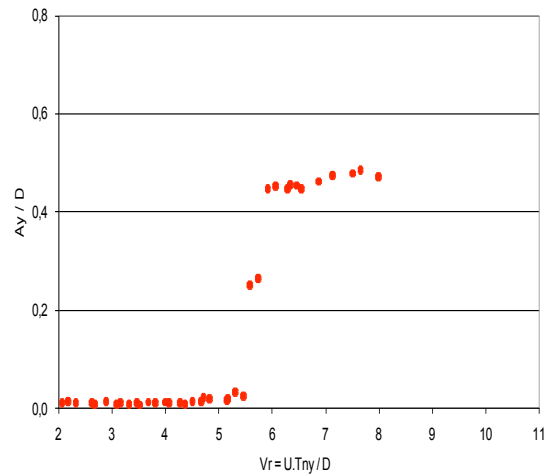
Figure 7 - Non-Dimensional Amplitude for the fourth set of experiments (elliptical and vertical cylinder).

In order to compare the results obtained from the first, third and fourth sets of experiments, the reduced velocities were corrected by the angle: $Vr_{cor} = Vr·cos(\alpha)$, where: $\alpha = 0°$, $\alpha = 20°$ and $\alpha = 45°$.

For the same value of Vr_{cor} the results of non-dimensional response amplitude from the set of experiments 3 and 4 are equivalents, but smaller than the ones from the first set of experiments (see Figure 8).

Intending to verify the influence of the difference of immersed length existent among the set of experiments 1 and 3, a fifth set of experiments was carried out. It consisted in testing the vertical cylinder with the same free stream velocities employed on first set of experiments but with the same immersed length presented in third set of experiments. The peak of non-dimensional response amplitude was *0.50* in all set of experiments (see Figure 9).
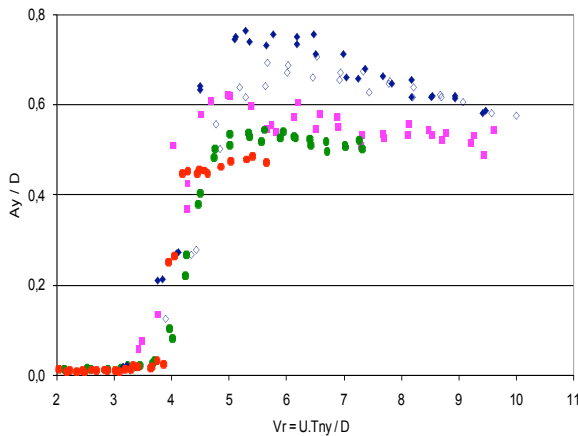

Figure 8 - Non-Dimensional Amplitude for the first, third and fourth set of experiments, correcting the reduced velocity.
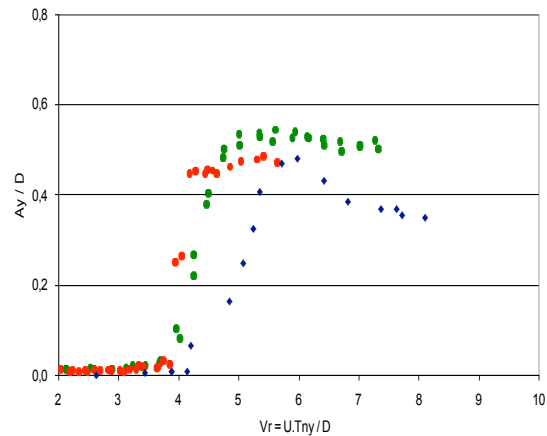
Figure 9 - Non-Dimensional Amplitude for the first, third and fourth set of experiments, correcting the reduced velocity (cylinders with the same immersed length).

Concluding Remarks

The five experimental setups allow to verify that inclined cylinders at angles varying from 0° to 45° have the same dynamic behaviour compared to vertical cylinders, insofar the velocity of the free stream be decomposed on the direction orthogonal to the cylinder axes. The experimental results of A^*, C_D and C_L are consistent with the classical approach of projecting the velocity onto the orthogonal direction to the cylinder axes.

In order to study the vorticity and velocity fields, so to confirm the results herein presented, a PIV (Particle Image Velocimetry) investigation has been planned for 3 sections along the span and values of Vr that produces the higher non-dimensional amplitudes for the fifth set of experiments. The PIV results will be presented in the final version of this paper.

References

[1]   Khalak, A. and Williamson, C.H.K., 1999. "Motions, Forces and Modes Transaction in Vortex-Induced Vibration at Low Mass and Damping". *Journal of Fluids and Structures*: vol. 13, p. 813-851.

[2]   Fujarra, A.L.C. and Pesce, C.P., 2002. "Experiments on VIV added mass with elastically mounted cylinder in water". *Proceeding of the 21st International Offshore Mechanics and Artic Engineering Conference*, Oslo, Norway, 2002.

[3]   Vikestad, K., Vandiver, J.K. and Larsen, C.K., 2000. "Added Mass and Oscillation Frequency for a Circular Cylinder Subject to Vortex-Induced Vibrations and External Disturbance". *Journal of Fluids and Structures*: vol.14, p. 1071-1088.

UPWIND TVD TWO-DIMENSIONAL NUMERICAL SIMULATION OF VORTEX INDUCED VIBRATION OF A CIRCULAR CYLINDER

Juan B. V. Wanderley
LabOceano
COPPE/UFRJ
Rio de Janeiro, RJ, Brazil
juanw@peno.coppe.ufrj.br

Gisele H. B. Souza
Petrobras
Rio de Janeiro, RJ, Brazil
gisele@peno.coppe.ufrj.br

Sergio H. Sphaier
LabOceano
COPPE/UFRJ
Rio de Janeiro, RJ, Brazil
sphaier@peno.coppe.ufrj.br

Carlos Levi
LabOceano
COPPE/UFRJ
Rio de Janeiro, RJ, Brazil
Levi@peno.coppe.ufrj.br

ABSTRACT

Vortex induced Vibration (VIV) plays a very important role in the offshore petroleum exploration. For example, risers used in oil extraction from the sea bed to the offshore platforms are subjected to marine flows that may trigger dangerous VIV oscillations. Many researches have been spending a lot of efforts to understand the complicated flow around bluff bodies to control or even eliminate the VIV occurrence. Numerical simulations have been unsuccessful to predict the VIV amplitudes mainly because of the diffusive nature of the numerical methods. The present two-dimensional numerical investigation is a continuation of previous efforts trying to predict correct amplitudes of the VIV oscillations. The Roe-Sweby scheme is used to solve the slightly compressible RANS equations written in general curvilinear coordinates and the K-ε turbulence model is used to simulate the turbulent flow in the wake of a circular cylinder. The numerical results obtained in the present work agree remarkably well with experimental data obtained from the literature.

INTRODUCTION

Vortex induced vibration is found in many applications in engineering. An important example is the riser in the petroleum exploration. Risers are flexible ducts that are used to carry oil from the sea bed to the offshore platforms. Those flexible ducts are subjected to marine flows that may cause high amplitude oscillations due to vortex shedding that may cause the failure of the structure. Many researchers have been spending time and resources to understand the complicated flow around bluff bodies trying to control or reduce VIV, see Bearman (2000) and Meneghini (1997).

Vortex-induced vibration (VIV) is a direct consequence of lift and drag oscillations due to the vortex shedding. When the frequency of vortex shedding coincides with the structural natural frequency, the VIV can occur with high dangerous amplitudes that may cause failure of the excited structure. For a fixed body, the vortex shedding frequency is a function of the Reynolds number only. For a moving cylinder, the fluid interacts strongly with the cylinder motion and the vortex shedding frequency is captured by the body natural frequency over a wider range of flow speed, Bearman (2000). This is known as lock-in and the extent of this range depends on the structural damping and mass ratio of the cylinder.

Brika and Laneville (1993) reported two modes of oscillation in the lock-in region, say 2S and 2P. In the 2S mode, one vortex is shed in each half cycle of oscillation. In the 2P mode, two vortices are shed in each half cycle. The 2S mode is associated with high amplitudes and is responsible for the high amplitudes found in the upper branch. As the reduced velocity continues to increase, there is a mode change from 2S to 2P mode associated with a sudden decrease in amplitude and a phase shift of 180º between the lift and displacement.
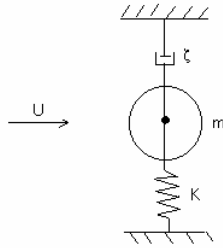
In the present work, the slightly compressible Reynolds averaged Navier – Stokes equations written in general curvilinear coordinates, Wanderley and Levi (2005), is solved numerically for the two-dimensional flow around a circular cylinder using the upwind TVD scheme of Roe (1984) and Sweby (1984) with the flux limiter of van Leer (1979). The Reynolds stresses are obtained through the hypothesis of Boussinesq (1877) and the K-ε turbulence model of Chien (1982).

The correctness of the numerical code implementation has been demonstrated for laminar and turbulent flows around a fixed circular cylinder for three different Reynolds numbers of 40, 100, and 200 for laminar flow, and one Reynolds number of 1000 for turbulent flow. The comparison with other consecrated numerical and experimental data proved the quality of the numerical code and gave confidence for further applications.

To check the code efficiency on VIV investigations, results were obtained duplicating the flow conditions used in the experimental investigation carried out by Khalak and Williamson (1996). They measured the cylinder oscillation amplitude after imposing a progressive increment of the flow speed with Reynolds number varying from 2000 up to 12000. The results obtained in the present investigation agree remarkably well with the experimental data from Khalak and Williamson for the entire range of reduced velocity.

ELASTICALLY MOUNTED CYLINDER: NUMERICAL X EXPERIMENTAL RESULTS

Figure 1 shows the circular cylinder of mass m, supported by spring (k) and damper (ζ), immersed in a uniform flow. The cylinder position and velocity are obtained by the numerical solution of the motion equation (1), where the lift coefficient is obtained by integration of the pressure and frictional stress on the body surface obtained in the numerical solution of the governing equations of the flow field.

$$\ddot{y} + C_\zeta \dot{y} + C_k y = \frac{C_L(R_e)}{2C_\mu} \tag{1}$$

$$C_\mu = \frac{m}{\rho D^2} \quad , \quad C_k = \frac{4\pi^2}{U_r^2} \quad , \quad C_\zeta = \frac{4\pi\zeta}{U_r} \quad , \quad U_r = \frac{U}{f_n d} \tag{2}$$

Figure 1. Set up adopted in the experimental and numerical investigations.

The objective of the present investigation is to duplicate in accurate and reliable way, the benchmarking experimental results obtained by Khalak and Williamson (1996). Therefore, the same experimental setup was considered throughout the numerical simulation and also the same mass ratio of $C\mu$=1.88, damping ratio of ξ=5.42x10^{-3}, and reduced velocity varying from 2 to 12, corresponding to Reynolds number variation from 2000 to 12000.

Figure 2a shows the comparison between the experimental data from Khalak and Williamson (1996) and numerical results obtained in the present work and in Meneguini et al. (1997) for the amplitude of oscillation as a function of reduced velocity. The agreement between the numerical results obtained in the present work and the experimental results obtained in Khalak and Williamson (1996) is remarkable considering the traditional difficulty that numerical simulations have to reproduce experimental results on VIV. In this numerical simulation, all results were obtained by increasing reduced velocity. As reduced velocity increases, the amplitude of oscillation increases and reaches a maximum and then starts decreasing. Figure 2b shows the frequency of oscillation as a function of reduced velocity. The frequency is approximately constant inside the lock-in region, and increases with reduced velocity outside the lock-in region.
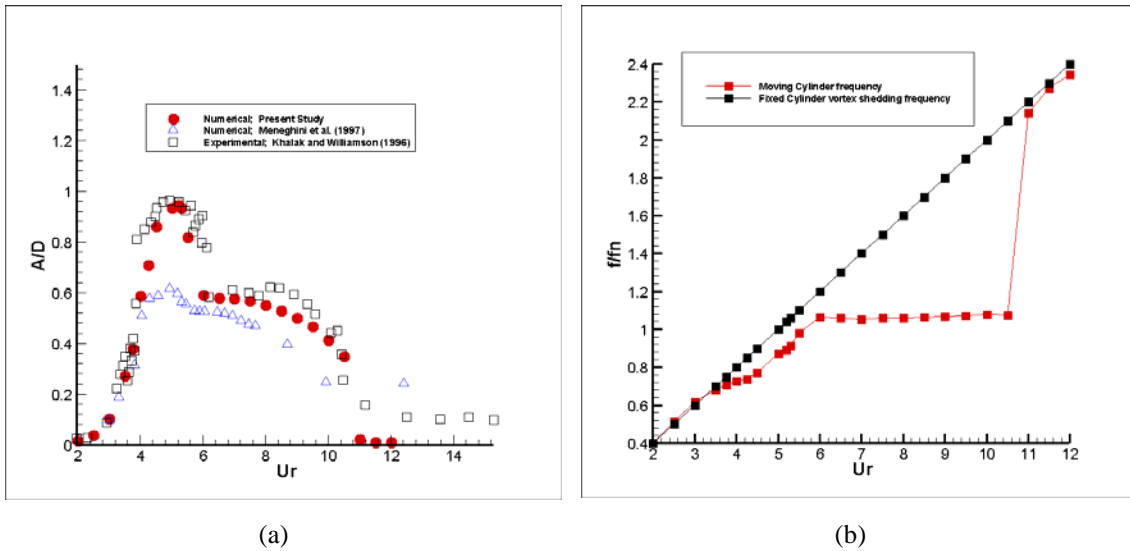

(a)   (b)

Figure 2. Amplitude (a) and frequency (b) of oscillation as a function of reduced velocity

Figure 4 was obtained for reduced velocities Ur=4.0 at the buildup of the upper branch of the amplitude curve of Fig. 2a. Figure 4a shows the time traces of the lift coefficient and displacement of the cylinder and Fig. 4b shows the vorticity field around the cylinder. Figure 4a shows that the lift coefficient and the displacement of the cylinder are in phase and Fig. 4b shows that one vortex is shed in each half cycle of oscillation, which is compatible with the 2S mode of Brika and Laneville (1993) for the initial branch.
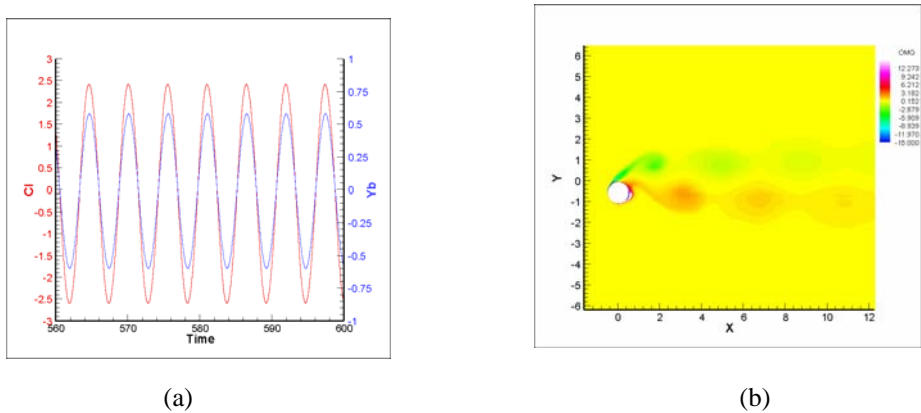

(a)   (b)

Figure 4. Time trace of lift coefficient and displacement (a) and vorticity field around the circular cylinder (b); Ur=4.0

Figure 5 was obtained for reduced velocities Ur=5.2 at the peak of the upper branch of the amplitude curve of Fig. 2a. Figure 5a shows the time traces of the lift coefficient and displacement of the cylinder and Fig. 5b shows the vorticity field around the cylinder. Figure 5a shows that the lift coefficient and the displacement of the cylinder are in phase and Fig. 5b shows that two vortices are shed in each half cycle of oscillation, which is compatible with the 2P mode, but the second vortex of each pair is much weaker than the first one.

(a)   (b)

Figure 5. Time trace of lift coefficient and displacement (a) and vorticity field around the circular cylinder (b); Ur=5.2

Figure 6 was obtained for reduced velocities Ur=6.0 at the lower branch of the amplitude curve of Fig. 2a. Figure 6a shows the time traces of the lift coefficient and displacement of the cylinder and Fig. 6b shows the vorticity field around the cylinder. Figure 6a shows that there is a phase shift of 180° between the lift coefficient and the displacement of the cylinder and Fig. 6b shows that two vortices are shed in each half cycle of oscillation, which is compatible with the 2P mode of Brika and Laneville (1993) for the lower.

| (a) | (b) |

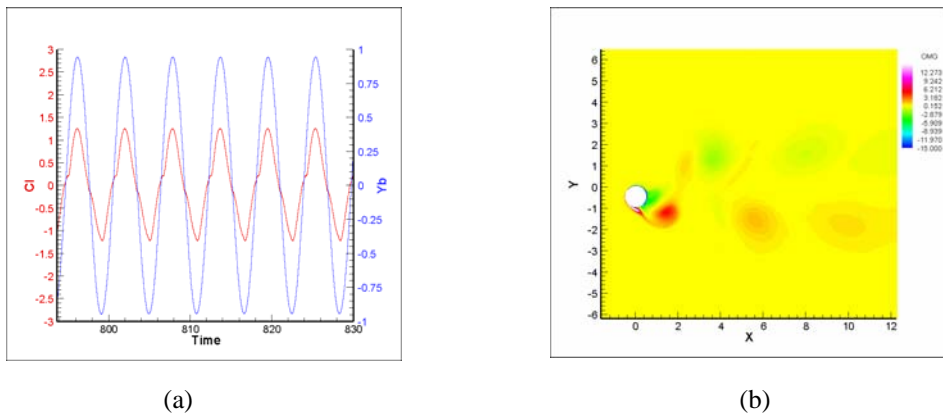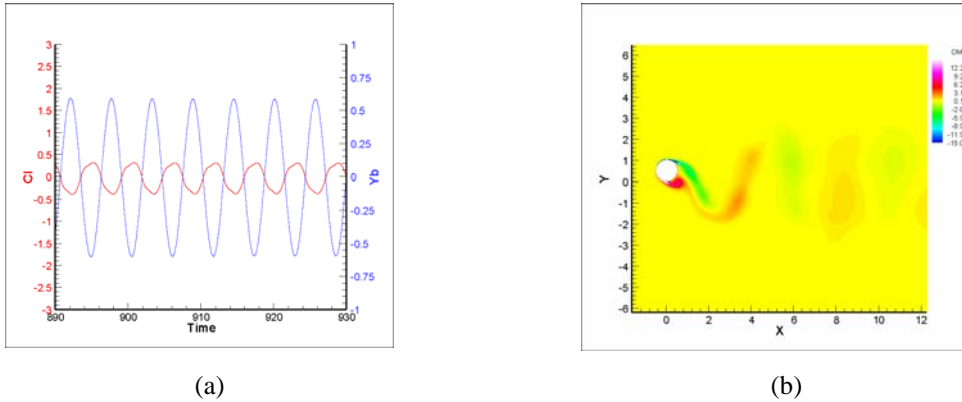Figure 6. Time trace of lift coefficient and displacement (a) and vorticity field around the circular cylinder (b); *Ur*=6.0

CONCLUSIONS

The motivation of the present work was to duplicate through numerical simulation the experimental results obtained by Khalak and Williamson (1996) for the vortex-induced vibrations of a circular elastically mounted cylinder. The slightly compressible formulation was solved using the upwind TVD scheme of Roe (1984) and Sweby (1984) and the turbulent flow in the wake of the cylinder was simulated using the k-ε turbulence model, as proposed by Chien (1982).

The numerical results obtained for the oscillating cylinder agreed very well with those benchmarking experimental data. The mathematical and numerical formulations were able to capture the amplitudes of oscillation, as reported in Khalak and Williamson (1996). At the upper branch, a single vortex is shed in each half cycle of oscillation as in the 2S mode of Brika and Laneville (1993). On the other hand, two vortices are shed in each half cycle of oscillation as in the 2P mode reported by Brika and Laneville (1993) for the lower branch.

The slightly compressible formulation, the Roe – Sweby scheme and the K-ε turbulence model of Chien proved to be a good combination to solve numerically the difficult to simulate VIV problems.

REFERENCES

Anderson, J. D., 1990, Modern Compressible Flow: With Historical Perspective. McGraw-Hill, New York.

Bearman, P. W., 2000, "Developments in Vortex Shedding Research," Workshop on Vortex-Induced Vibrations of Offshore Structures. São Paulo, Brazil.

Boussinesq, J., 1877, "Essai Sur La Théorie Des Eaux Courantes, *Mem. Presentes Acad. Sci.*, vol. 23, Paris, p. 46.

Brika, D. and Laneville, A., 1993, "Vortex Induced Vibrations of a Long Flexible Circular Cylinder", Journal of Fluid Mechanics, 250, pp481-508.

Chien, K. Y. 1982, "Predictions of Channel and Boundary-Layer Flows with a Low-Reynolds-Number Turbulence Model, AIAA J., Vol. 20, pp. 33-38.

Khalak, A., and Williamson, C. H. K., 1996, "Dynamics of a Hydroelastic Cylinder with Very Low Mass and Damping," Journal and Fluids and Structures, **10**, pp. 455-472.

Meneghini, J. R., Saltara, F., and Bearman, P. W., 1997, "Numerical Simulation of Vortex Shedding from an Oscillating Circular Cylinder. Computational Methods and Experimental Measurements," Computational Mechanics Publications. Southampton, UK, editors P. Anangnostopolos, G. M. Carlomagno & C. A. Brebbia, p.409-418.

Roe, P. L., 1984, "Generalized Formulation of TVD Lax-Wendroff Scheme, ICASE Report 84-53.

Sweby, P. K., 1984, "High Resolution Scheme Using Flux Limiter for Hyperbolic Conservation Laws, *SIAM J. Num. Anal.*, vol. 21, pp. 995-1011.

van Leer, B., 1979, "Towards the Ultimate Conservative Difference Scheme, V: A Second-Order Sequel to Godunov's Method, *J. Comput. Phys.*, vol. 32, pp. 101-136.

Wanderley, J. B. V., and Levi, C. A., 2005, "Vortex Induced Loads on Marine Risers", Ocean Engineering, V. 32, pp. 1281-1295.

Effectiveness of the Guided Porosity Concept as VIV Suppressor

FERNANDES, A. C. [(1)], COELHO, F. M. [(1)], FRANCISS, R.[(2)]

[1] COPPE – UFRJ
[2] CENPES – PETROBRAS

email: acfernandes@peno.coppe.ufrj.br

Summary

This works describes the experimental research in water to show the effectiveness of the guided porosity concept as VIV Suppressor. The concept is shortly described and results for three smooth cylinders with and without porosity are presented. The study shows that the concept is essentially a 3D device and depends on parameters such as input and output geometry and position.

Introduction

The guided porosity is an alternative method for the suppression of vortex induced vibrations (VIV) with drag reduction. This contrasts with the strakes which increases considerably the drag forces acting on the cylindrical structure of Risers and Spar Buoy platforms. Guided Porosity is also a type of passive control of VIV with good economical and operational implications if compared with active control methods.

The paper is focused on the application of the concept of guided porosity previously presented by [Fernandes et al, 2000]. This last reference showed the effectiveness of the concept in air. And for the first time the present paper shows the effectiveness of the guided porosity in water. For the verification, experiments were conducted in the Current Channel of the LOC/COPPE/UFRJ (Laboratório de Ondas e Correntes - Waves and Currents Laboratory of COPPE/UFRJ). The cinematic behavior of the cylinder with guided porosity is presented on this paper for three different models.

As previously presented [Fernandes et al, 2000], the basic idea is to allow the flow through the structures (maybe a cap in actual applications) driving by the pressure difference between the stagnation point and the separation point. There is then a natural flow feeding that interferes in the separation itself modifying the original vortex generation. The pressure coefficient, in accordance with potential flow theory is given by (1) (see, for instance, in [White, 1999]) and may be used for estimation. For the stagnation point ($\theta = 0$), $C_P = +1$ and for $\theta = 90^0$, $C_P = -3$. The last point is near the stagnation point which in practice is about 82^0 for laminar flow and about 120^0 for turbulent flow.

$$C_P = 1 - 4\,sen^2\theta \tag{1}$$

where:

$$C_P = \frac{p - p_\infty}{\frac{1}{2}\rho U_\infty^{\,2}} \tag{2}$$

The experimental setup is illustrated in Figure 1-a. The cylinder was free to move on the direction transversal to the current flow. The top was supported by the system presented in Figure 1-. The bottom was free and the distance between the cylinder and the current channel bottom was small enough to assure two-dimensional flow in most of the cylinder. The data acquisition was performed by an image acquisition system [Siqueira et al, 2000] that works with the image contrast between a LED positioned on the top of the system and a dark background provided by a cover during the experiments.

The cylinder design included the porosity provided by an internal flow section (Figure 1-b) that allows the flow to enter at the stagnation point and to leave the cylinder near the external separation point. The area ratio between the entrance and the output must be high enough to assure high volume of flow at the input and high flow velocity at the output.
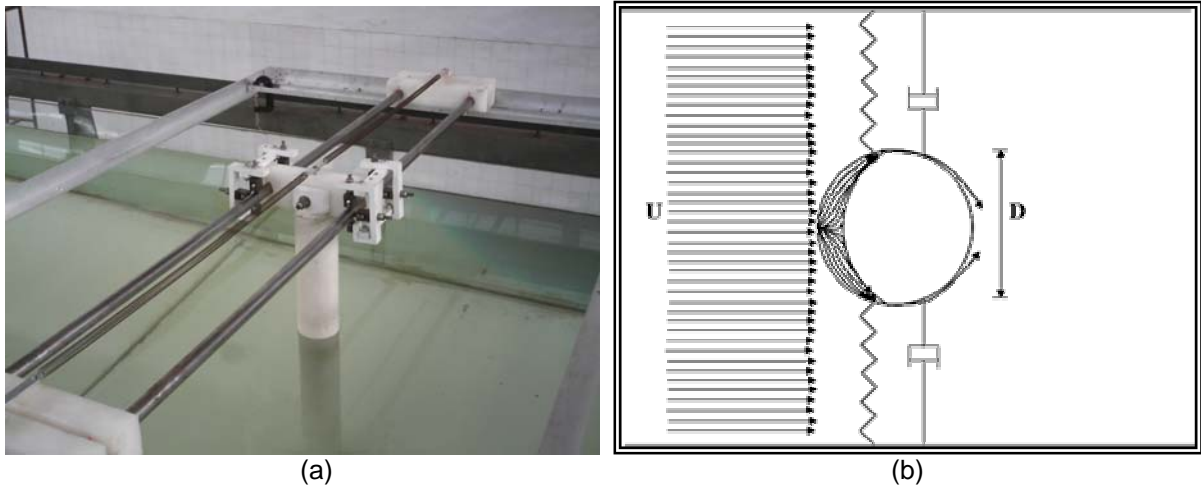
(a)   (b)

Figure 1 – (a) Experimental setup. (b) Schematic representation of guided porosity operation.

Experimental Results

The results are presented in terms of non dimensional amplitude (A/D) for a wide range of reduced velocity ($V_R=U/f_nD$). The Reynolds Number ($Re=UD/\nu$) of the experiments ranges from 1×10^4 to 4×10^4 what indicates that the separation point is at an angle of approximately 82^0 from the stagnation point. Three models with 75 mm of diameter, 800 mm of length and a 460 mm of draft were tested.

Figures 2-a, 2-b and 2-c illustrate the models 1, 2 and 3, respectively. Note the differences in the input and output areas as explained next.

(a)   (b)   (c)
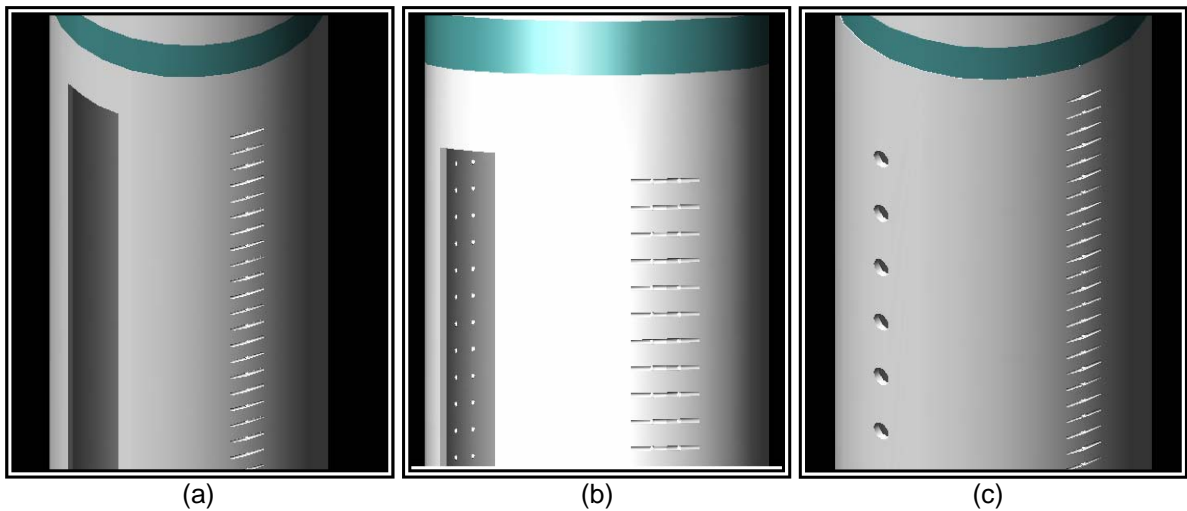
Figure 2 – (a) Model 1. (b) Model 2. (c) Model 3.

The outputs of the three models were designed in a way the flow is tangent to the cylinder at this point. The output holes have 1 mm of diameter. The three models are different in terms of entrance area, number and position of the output holes.

The model 1 has an input as that one illustrated in Figure 2-a, with 10.9 mm of width. The output holes are positioned at an angle of 70^0 from the stagnation point. The distance between these points is 5 mm. The model 2 is similar to model 1, except in the output. The model 2 has two vertical lines of output holes positioned at 70^0 and 80^0 from the stagnation point. The model 3 has an input with holes placed at each 20 mm. The diameter of these holes is 5 mm. The output consists of holes similar to the first two models, but now, placed at 80^0 from the stagnation point.

Figures 3, 4 and 5 present results for models 1, 2 and 3, respectively. These Figures compare cases with and without the action of the guided porosity. As it can be seen in Figure 3, model 1 when working

with guided porosity presents a reduction of *A/D* for a wide range of reduced velocity, except at the lock-in region where the peak amplitude of the model with porosity almost reaches the case without porosity. Note that as previously referred, model 1 has the output placed at 70^0 from the stagnation point.
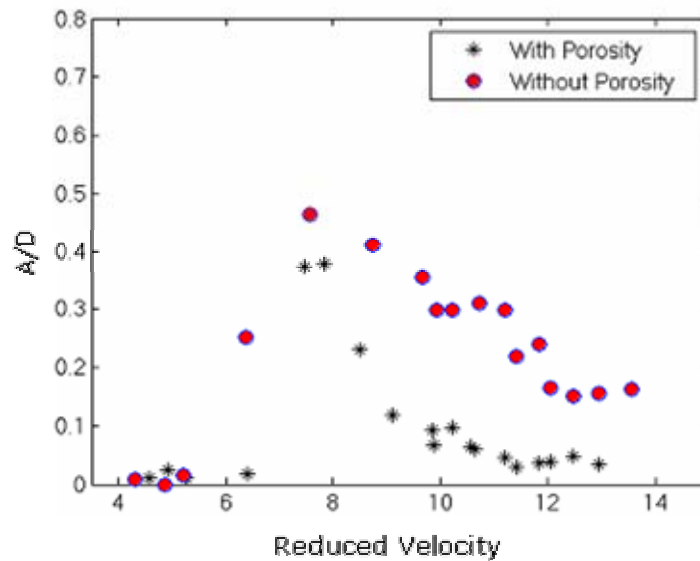

Figure 3: Relation between *A/D* and V_R for the model 1, with and without porosity.

Differently from the results of model 1, Figure 4 presents a significant reduction on the *A/D* for any value of reduced velocity obtained from the experiment. The model 2 has two vertical lines of holes placed at 70^0 and 80^0. The entrance is the same of the model 1 what suggests that the outputs placed near from the separation point makes a significant difference in comparison with the model 1.
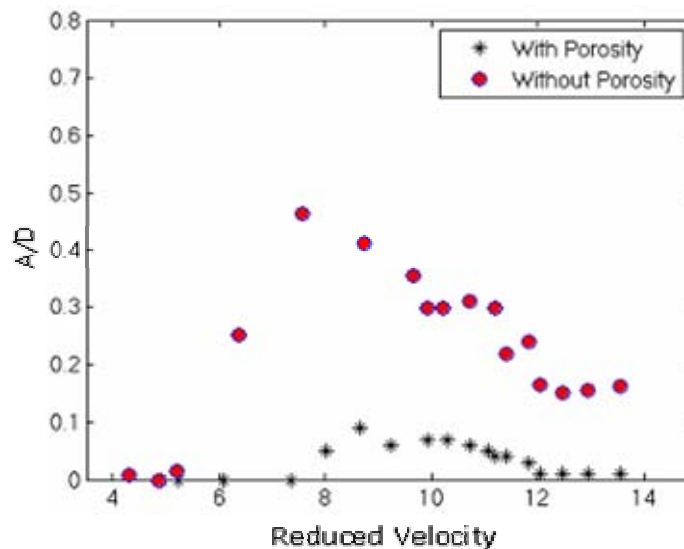

Figure 4: Relation between *A/D* and V_R for the model 2, with and without porosity.

The placement of the outputs near from the separation point seemed to be the key for the correct operation of the concept. However, model 2 presented a higher number of outputs than model 1, and this influence was investigated. The entrance of models 1 and 2 was also unfeasible in operational terms. In order to solve these questions, model 3 was tested with and without porosity.

The model 3 has the same number of holes of model 1. These holes are placed at 80^0 from the stagnation point. The entrance is like that presented in Figure 2-c with dimensions previously mentioned. As it can be observed from Figure 5, the reduction on *A/D* is still very significant for all the values of reduced velocity. It shows clearly that the guided porosity design with outputs placed around 82^0, for laminar flow around cylinders, is strongly effective for VIV reduction.
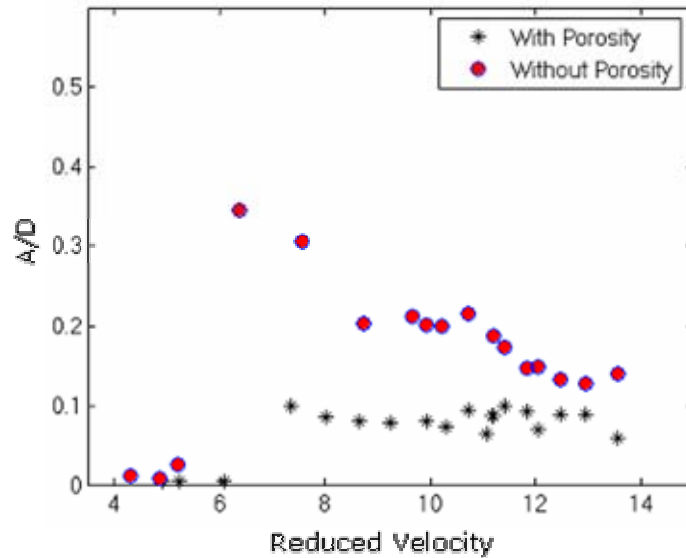
Figure 5: Relation between A/D and V_R for the Model 3, with and without porosity.

Conclusions

The experiments conducted for this work show that applied guided porosity fulfilled all the expectations based on the theory that motivated the application of the guided porosity concept to control VIV.

The guided porosity concept has shown to be highly effective on water as long as the input flow is controlled by the entrance geometry and the output geometry and position. It can be concluded that as close as the output is placed from the theoretical boundary layer separation point, higher is the VIV reduction in terms of amplitude.

Acknowledgments

References

FERNANDES, A.C., ESPERANÇA, P.T.T., SPHAIER, S.H. and SILVA, R.M.C.; **VIV Mitigation: Why not Porosity**; XIX International Symposium on Offshore Mechanics and Arctic Engineering (ETCE/OMAE2000 Joint Conference); New Orleans, Estados Unidos, February 14-17, 2000.

WHITE, F.K.; **Fluid Mechanics**; New York, WCB/McGraw-Hill, 1999.

SIQUEIRA, C. M., VILAÇA, R., NASCIMENTO, F., LEVI, C. and FERNANDES, A.C.; **Medição de Movimento por Imagem**; XVIII Congresso da Sociedade Brasileira de Engenharia Naval, SOBENA 2000, Rio de Janeiro, Brasil; September 18-22, 2000.

Time Domain VIV Analysis of Inclined Towed Pipe Based on Lookup Table of VIV Hydrodynamic Force

Hideyuki Suzuki
University of Tokyo, Department of Environmental and Ocean Engineering
suzukih@naoe.t.u-tokyo.ac.jp

Junichi Minamiura
Mitsubishi Heavy Industries, Ltd, Nagasaki R&D Center

Masahiko Ozaki
Japan Agency for Marine-Earth Science and Technology/CDEX

Yasunori Arima
Dai Nippon Printing, Co.Ltd

Ryota Kimura
University of Tokyo, Department of Environmental and Ocean Engineering

ABSTRACT

Ocean sequestration of CO_2 is considered as a effective measure to reduce Global Warming.   One concept is moving ship concept and a long towed pipe is used to dilute CO_2 into the intermediate water.   Vortex Induced Vibration (VIV) is predicted for the towed inclined pipe.   A time domain VIV simulation method was developed.   The method is a combination of a time domain Finite Element Method (FEM) of underwater line structure and a database of VIV hydrodynamic force obtained from basic experiment on the cylinder subjected to harmonic oscillation.   A filter which estimates vibration parameters, amplitude, frequency and phase of a local response of pipe from the time history of vibration was developed.   Using the estimated parameters of local vibration, instantaneous VIV force is evaluated by consulting the database.   The estimated VIV force is applied to the pipe and repeating the procedure response of towed pipe is calculated.   Basic function of the method was verified.

1. INTRODUCTION

Moving ship concept is proposed for CO_2 dilution into the ocean to reduce Global Warming.   Figure 1 shows the moving ship concept.   A 3000m long pipe is towed and CO_2 is diluted and dissolved into intermediate water around 2500m deep.   Outer diameter of pipe is 0.2m diameter.   To reduce the concentration of CO_2 to harmless level, the towing speed of 2.5m/sec was selected and the pipe experience inclination of 30degrees.   The towed pipe is expected to experience VIV and the response may cause fatigue.   Estimation of VIV response is essentially important to secure the integrity and safety of the system.

This paper presents development of practical time domain analysis method for VIV response of inclined towed pipe. This method is also applicable to production riser, SCR, etc. used in the offshore oil industry.   There are many choices of approaches for the problem.   Analysis methods so far developed is basically categorized into two groups from a viewpoint of VIV hydrodynamic force.   One is a method based on empirical hydrodynamic force model.   The model is formulated based on the basic hydrodynamic force measurement with a pipe section[1-4]. Another group is based on CFD for evaluation of VIV force.   FEM and CFD combined method is desirable but still has some limitation regarding accuracy and associated computational resources.   The proposed method is a practical one.   The analysis method presented in this paper has following characteristics;

1) Time domain FE modeling for structural part.
2) Database of VIV hydrodynamic force obtained from series of basic experiments.
3) High Reynolds number data with a real scale pipe section.
4) A filter to predict parameters of oscillation amplitude, frequency and phase.

In the method, response estimated by the code is the maximum response when the VIV is fully developed and shedding phase along the pipe is assumed to coincide.   Transverse VIV response is considered and In-line VIV is not considered

2. EXPERIMENT TO OBTAIN VIV FORCE

Pipe section of a real scale CO_2 dilution pipe is oscillated and towed.   Force induced on the test section was measured.   The test section is supported by two load cells at both ends of the test section.   The experiment was carried out at Seakeeping and Maneuvering Basin of Mitsubish Heavy Industries, Ltd. at Nagasaki.   Figure 2 shows the oscillation system mounted on towing carriage.   Three pipes with different diameter are used for the experiment.   The length of pipe is 2500mm and force acting on the measurement section with length of 500mm

Fifth Conference on Bluff Body Wakes and Vortex-Induced Vibrations (BBVIV 5)
Costa do Sauipe, Bahia, Brazil, 12 - 15 December 2007

223

was measured and recorded.   The mean position of oscillated pipe is 1.0m from surface and maximum amplitude is 0.3m.

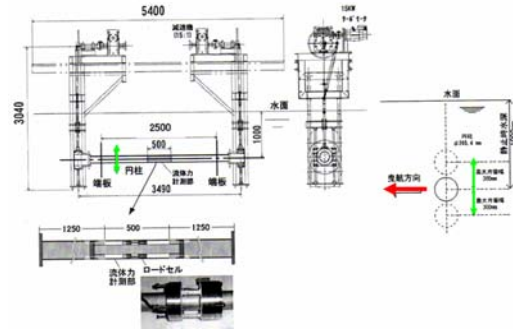Figure 1   Schematic diagram of moving ship concept for CO2 dilution.

Figure 2   Oscillation apparatus.

Reynolds number range realized in the experiment is shown in Table 1.   Dimension and towing condition of pipe for CO2 dilution is shown in Table 2.   The hydrodynamic force obtained from experiment is separated into the two components, one is proportional to acceleration and another is proportional to velocity of pipe.   Added mass coefficient and VIV excitation force coefficient are evaluated based on the following equations.

Added mass coefficient: $\dfrac{F_{acceleration} - MA(2\pi f)^2}{\rho \dfrac{\pi D^2}{4} LA(2\pi f)^2}$ (1)

Damping coefficient: $\dfrac{F_{velocity}}{\dfrac{1}{2}\rho DLUA(2\pi f)}$ (2)

Where $F_{acceleration}$ and $F_{velocity}$ are force components proportional to acceleration and velocity. M is mass of pipe, A is oscillation amplitude, f is oscillation frequency, ρ is density of fluid, D is diameter of pipe and L is length of pipe section.

Table 1   Experiment cases.

Reynolds no. range	Angle to flow		
	0deg.	30deg.	45deg.
$6.6\text{-}9.0\times10^4$	done	done	done
2.8×10^5	done	done	
3.4×10^5	done	done	done
4.0×10^5	done	done	done

Table 2   Dimension and towing condition of pipe for CO2 dilution.

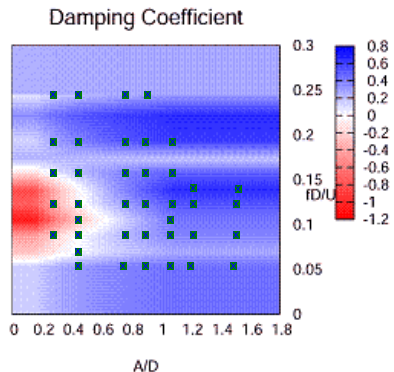|	
Towing speed	2.5m/s
Inner diameter	180mm
Outer diameter	200mm
Material	steel
Water depth of dilution	1500-2500m
Pipe length	Approx. 3000m
Inclination of pipe	Approx. 30deg.
Temperature of sea water	2-16
Kinematic viscosity coefficient	$9.2\text{-}17.2\times10^{-7}$ m^2/s
Reynolds number	$2.9\text{-}5.4\times10^5$

Figure 3   Contour map of damping force coefficient (Re=400000, angle to flow is 0deg.)
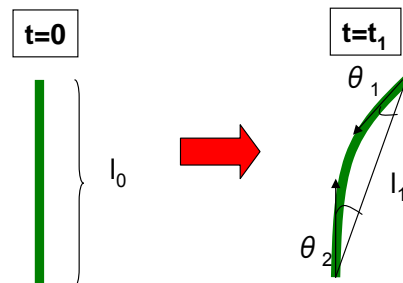

Figure 4   Evaluation of axial force.

3. DATABASE OF VIV FORCE

Database of VIV hydrodynamic force coefficient is constructed from the added mass coefficient and damping force coefficients obtained from the experiments.   The coefficients are formulated as a function of normalized oscillating

amplitude A/D, frequency fD/U, angle to flow θ. Figure 3 shows an example of contour map of the damping force coefficient.

4. VIV ANALYSIS PROGRAM

VIV analysis code was developed based on the time domain FEM code LINE3DLU developed for underwater line structure. Geometrical nonlinearity is considered in the formulation and the code adopts incremental formulation for deformation [6]. The developed code stores time history of displacement of each node and using the developed numerical filter, VIV frequency, amplitude and phase of VIV response of the node is evaluated at each time step. Database of VIV hydrodynamic force is consulted and VIV force amplitude is determined and considering phase, instantaneous force acting on the pipe element is determined and applied to pipe. The length of measurement section is relatively short and VIV force acting on the measurement section is considered uniform without cancellation effect due to phase difference along the length of pipe. The response calculated by this code is considered to correspond to the well developed maximum response.

4.1 Stability Improvement of Analysis Code

Accumulation of error is one of the sources of instability of the incremental time domain analysis and must be avoided. One key point to avoid accumulation of error is evaluation of axial force. Improvement was made by modifying the code to directly calculate elongation of pipe referring to the initial length. For two dimensional case, length of pipe is evaluated by the following equation.

Length of pipe: $l = l_1 \left\{ 1 + \dfrac{1}{8}\left(\theta_1^2 + \theta_2^2\right) \right\}$ (3) \qquad xial force of pipe: $T = EA \dfrac{l - l_0}{l_0}$ (4)

Where l is length of pipe element, l_1 is distance between both ends of pipe element, l_0 is initial length of pipe and θ_1 and θ_2 are angle to the line connecting the both ends of pipe element. T is tension in pipe and E is Young's modulus and A is cross sectional area of pipe. Typical accumulation of error is observed as elongation of vertically suspended long pipe subjected to horizontal oscillation at the top of the pipe. The improved code was tested for 3000m long pipe with fast oscillation cases with period of 4sec and amplitude of 4m.

4.2 Numerical Filter for Detecting Oscillation Parameters

At each time step, VIV amplitude, frequency and phase must be detected from time history of the node displacement. A numerical filter which utilize orthogonality of trigonometric function was developed. Weighting function about time was introduced to put importance to the response close to present time [7]. Changing the frequency of the sinusoidal function, dominant fluctuating component is detected by choosing the frequency which maximize the amplitude Ai given by Eq.(5).

$$A_i = \sqrt{a_i^2 + b_i^2} \qquad (5) \qquad\qquad a_i = k \int_{t-NT}^{t} y(\tau)\sin\left(\frac{2\pi}{T}\tau\right)e^{\alpha\tau}d\tau \qquad (6)$$

$$b_i = k \int_{t-NT}^{t} y(\tau)\cos\left(\frac{2\pi}{T}\tau\right)e^{\alpha\tau}d\tau \qquad (7) \qquad\qquad \phi_i = \arctan\left(\frac{b_i}{a_i}\right) + \frac{\pi}{2}\left(1 - \frac{|a_i|}{a_i}\right) \qquad (8)$$

Where a_i and b_i are sin and cos components of vibration. A_i is oscillating amplitude and ϕ_i is corresponding phase. k is a correction factor given by the equation below to give correct amplitude.

$$k = \frac{2\alpha\left\{\alpha^2 + \left(\dfrac{4\pi}{T}\right)^2\right\}}{\left\{\left(\dfrac{4\pi}{T}\right)^2 - \alpha^2\right\}\left(1 - e^{-\alpha NT}\right)} \qquad (9)$$

Different from fast VIV response, motion of pipe with long period is detected as a drifting component observe in the time history. The component is removed from the time history of nodal displacement.

4.3 Instantaneous VIV Hydrodynamic Force

VIV force amplitude is applied to the pipe considering phase. Damping force given to node i is given by

$$f_i = \begin{cases} -\dfrac{1}{2}\rho D U \dfrac{L_1}{2} A \cdot 2\pi f \cdot \cos\left(2\pi ft + \Phi\right) \\ \qquad\qquad\qquad\qquad (i=1) \\[6pt] -\dfrac{1}{2}\rho D U \dfrac{L_{i-1}-L_{i+1}}{2} A \cdot 2\pi f \cdot \cos\left(2\pi ft + \Phi\right) \\ \qquad\qquad\qquad\qquad (i=2,3,...,n_{max}-1) \\[6pt] -\dfrac{1}{2}\rho D U \dfrac{L_{i-1}}{2} A \cdot 2\pi f \cdot \cos\left(2\pi ft + \Phi\right) \\ \qquad\qquad\qquad\qquad (i=n_{max}) \end{cases} \qquad (10)$$

Where, ρ is density of fluid, D is diameter of pipe, U is relative velocity, L_i is pipe length between node i and i+1, A is VIV amplitude, f is frequency and φ is phase.

5. ANALYSIS RESULTS

Using the developed code, response of real towed pipe is calculated.   Figure 5 shows the in-line deformation of towed pipe.   As predicted by preliminary estimation, pipe inclination of 30degrees was observed.   Figure 6 shows out-of plane deformation of the pipe due to VIV response.   Maximum oscillation amplitude observed in the simulation was 0.5m.
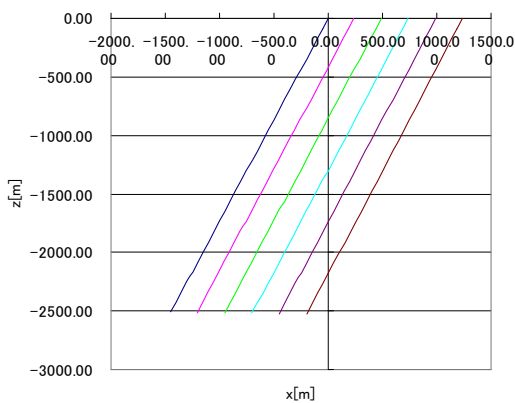

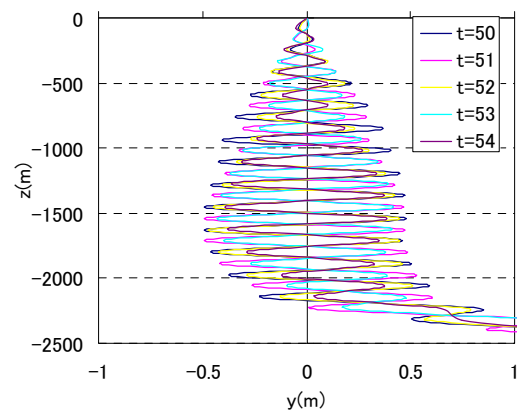Figure 5   In-line deformation of towed pipe.

Figure 6   Out-of-plane response of towed pipe.

6. CONCLUSIONS

Practical VIV simulation code is developed.   The code is a combination of a time domain Finite Element Method (FEM) of underwater line structure and a database of VIV hydrodynamic force obtained from basic experiment on the cylinder subjected to harmonic oscillation.   A filter which estimates vibration parameters, amplitude, frequency and phase of a local response of pipe from the time history of vibration was developed.   Using estimated parameters of local vibration, instantaneous VIV force is evaluated by consulting the database.   The estimated VIV force is applied to the pipe and repeating the procedure response of towed pipe is calculated.   Basic function of the code was verified.   Preliminary investigation was made for VIV response of the towed inclined CO2 dilution pipe.

REFERENCES

1) Roveri and Vandiver, "Slendrex: Using SHEAR7 for Assessment of Fatigue Damage Caused by Current Induced Vibrations", Proceedings of OMAE 2001
2) Vandiver and Jong, "The Relationship between In-Line and Cross-Flow Vortex-Induced Vibration of Cylinders", Journal of Fluids and Structures, 1, 381-399, 1987
3) Lyons et al., "Vortex induced vibrations measured in service in the Foinaven dynamic umbilical, and lessons from prediction", Journal of Fluids and Structures, 17, 1079-1094, 2003
4) Larsen et al., "Empirical Model for Analysis of Vortex Induced Vibrations –Theoretical Background and Case Studies", Proceedings of OMAE 2001
5) Dalheim, "A New Hybrid Numerical Procedure for Prediction of VIV of Risers in Ultra Deep Waters", Proceedings of OMAE 2001
6) Suzuki, H., "Mannual of LINE3DAnalysis Code of   Underwater Line Structure LINE3D ver.4", 1990.
7) Tejima, T., "Research on VIV of Towed Pipe Based on Numerical Analysis of Hydrodynamics and Structural Mechanics", Master's thesis of University of Tokyo, Dept. Of Environmental and Ocean Engineering, 2005.

Hysteresis in VIV at low Re: effect of blockage & m^*

S. Mittal, T.K. Prasanth

Department of Aerospace Engineering
Indian Institute of Technology Kanpur, UP 208 016, India
Email: smittal@iitk.ac.in, Phone: +91 512 2597906, Fax: +91 512 2597561

Abstract

Hysteresis in vortex-induced vibration of a circular cylinder at low Re is investigated in detail. The response of the cylinder is hysteretic at both ends of lock-in/synchronization regime in the laminar regime. This is in contrast to the results for high Re where the hysteresis is known to occur only at the transition from initial to upper branch. The hysteresis in the lower Re end of lock-in is found to depend on blockage and mass ratio (m^*). For a fixed mass ratio, the hysteresis at the lower Re end of lock-in decreases with decrease in blockage. It completely disappears at very low blockage. The hysteresis at the higher Re end of lock-in is unaffected by the blockage. The hysteresis at the lower Re end of lock-in is very large for cylinders with large mass ratios, $m^* \sim O(100)$. For a given blockage, the hysteresis loop width decreases with decrease in m^*, and disappears completely for very low mass ratio. This shows that hysteresis in the lower Re end of lock-in depends on blockage as well as mass ratio. It is also found that beyond a certain m^* hysteresis in the cylinder response occurs even for very low values of blockage. More results for this very interesting phenomenon will be presented at the conference.

1 Introduction

Vortex-induced vibration is associated with various interesting phenomenon like synchronization/lock-in and hysteresis. During lock-in, the vortex shedding frequency of the cylinder becomes equal to the oscillation frequency. Lock-in is also accompanied by large amplitudes of oscillation of the cylinder. Depending on the increasing or decreasing branch of velocity, the cylinder response may exhibit hysteresis at both ends of lock-in (Singh and Mittal (2005)). A comprehensive review on vortex-induced vibration can be found in the review article by Williamson and Govardhan (2004).

In the present work, the hysteresis in the response of the cylinder is studied in detail. The cylinder is free to oscillate in both streamwise and transverse directions. The flow is modeled with incompressible flow equations in primitive variables form and the motion of the cylinder is governed by a simple one degree of freedom spring-mass system in each of the directions along the cartesian axes. A stabilized space-time finite element formulation is utilized to solve the flow equations. To overcome the numerical instabilities arising out of dominant advection terms and equal-order-interpolation for velocity and pressure, the Streamline-Upwind/Petrov-Galerkin (SUPG) and Pressure- Stabilizing/Petrov-Galerkin (PSPG) terms are added to the basic Galerkin formulation. Equal-in-order bilinear basis functions (four noded quadrilateral elements) for velocity and pressure are used. The non-linear equation systems resulting from the finite element discretization of the flow equations are solved using the Generalized Minimal RESidual (GMRES) technique in conjunction with diagonal preconditioners. Details about the mesh moving schemes and finite element formulations can be found in Singh and Mittal (2005).

2 The governing equations

2.1 The incompressible flow equations

Let $\Omega_t \subset \mathbb{R}^{n_{sd}}$ and $(0, T)$ be the spatial and temporal domains respectively, where n_{sd} is the number of space dimensions, and let Γ_t denote the boundary of Ω_t. The spatial and temporal coordinates are denoted by $\mathbf{x}$ and t. The Navier-Stokes equations governing incompressible fluid flow are

$$\rho(\frac{\partial \mathbf{u}}{\partial t} + \mathbf{u} \cdot \boldsymbol{\nabla}\mathbf{u} - \mathbf{f}) - \boldsymbol{\nabla} \cdot \boldsymbol{\sigma} = 0 \qquad \text{on } \Omega_t \times (0, T), \tag{1}$$

$$\boldsymbol{\nabla} \cdot \mathbf{u} = 0 \qquad \text{on } \Omega_t \times (0, T). \tag{2}$$

Here ρ, $\mathbf{u}$, $\mathbf{f}$ and $\boldsymbol{\sigma}$ are the density, velocity, body force and the stress tensor, respectively. The stress tensor is written as the sum of its isotropic and deviatoric parts:

$$\boldsymbol{\sigma} = -p\mathbf{I} + \mathbf{T}, \quad \mathbf{T} = 2\mu\boldsymbol{\varepsilon}(\mathbf{u}), \quad \boldsymbol{\varepsilon}(\mathbf{u}) = \tfrac{1}{2}((\boldsymbol{\nabla}\mathbf{u}) + (\boldsymbol{\nabla}\mathbf{u})^T), \tag{3}$$

where p and μ are the pressure and dynamic viscosity, respectively. Both the Dirichlet and Neumann-type boundary conditions are accounted for, represented as

$$\mathbf{u} = \mathbf{g} \ on \ (\Gamma_t)_g, \quad \mathsf{n} \cdot \boldsymbol{\sigma} = \mathbf{h} \ on \ (\Gamma_t)_h, \tag{4}$$

where $(\Gamma_t)_g$ and $(\Gamma_t)_h$ are complementary subsets of the boundary Γ_t and n is its unit normal vector. The initial condition on the velocity is specified on Ω_t at $t = 0$:

$$\mathbf{u}(\mathbf{x}, 0) = \mathbf{u}_0 \quad on \ \Omega_0, \tag{5}$$

where $\mathbf{u}_0$ is divergence free.

2.2 The equations of motion for a rigid body

A solid body immersed in the fluid experiences unsteady forces and in certain cases may exhibit rigid body motion. The motion of the body, in the two directions along the Cartesian axes, is governed by the following equations:

$$\ddot{X} + 4\pi F_N \zeta \dot{X} + (2\pi F_N)^2 X = \frac{2C_D}{\pi m^*} \qquad for \ (0, T), \tag{6}$$

$$\ddot{Y} + 4\pi F_N \zeta \dot{Y} + (2\pi F_N)^2 Y = \frac{2C_L}{\pi m^*} \qquad for \ (0, T). \tag{7}$$

Here, F_N is the reduced natural frequency of the oscillator, ζ the structural damping ratio, m^* the nondimensional mass of the body while C_L and C_D are the instantaneous lift and drag coefficients for the body, respectively. The free-stream flow is assumed to be along the x-axis. $\ddot{X}$, $\dot{X}$ and X denote the normalized in-line acceleration, velocity and displacement of the body, respectively, while $\ddot{Y}$, $\dot{Y}$ and Y represent the same quantities associated with the cross-flow motion. In the present study, in which the rigid body is a circular cylinder, the displacement and velocity are normalized by the diameter, D, of the cylinder and the free-stream speed, U, respectively. The reduced natural frequency of the system, F_N is defined as $\frac{f_N D}{U}$ where f_N is the natural frequency of the oscillator. Another related parameter is the reduced velocity, U^*. It is defined as $U^* = \frac{U}{f_N D} = 1/F_N$.

The nondimensional mass of the cylinder is defined as $m^* = \frac{4m}{\pi \rho D^2}$ where m is the actual mass of the oscillator per unit length and ρ is the density of the fluid. The force coefficients are computed by carrying an integration, that involves the pressure and viscous stresses, around the circumference of the cylinder.

3 The finite element formulation

To accommodate the motion of the cylinder and the deformation of the mesh, a formulation that can handle moving boundaries and interfaces is employed. In order to construct the finite element function spaces for the space-time method, we partition the time interval $(0, T)$ into subintervals $I_n = (t_n, t_{n+1})$, where t_n and t_{n+1} belong to an ordered series of time levels: $0 = t_0 < t_1 < \cdots < t_N = T$. Let $\Omega_n = \Omega_{t_n}$ and $\Gamma_n = \Gamma_{t_n}$. We define the space-time slab Q_n as the domain enclosed by the surfaces Ω_n, Ω_{n+1}, and P_n, where P_n is the surface described by the boundary Γ_t as t traverses I_n. As is the case with Γ_t, the surface P_n is decomposed into $(P_n)_g$ and $(P_n)_h$ with respect to the type of boundary condition (Dirichlet or Neumann) being imposed. For each space-time slab we define the corresponding finite element function spaces: $(\mathcal{S}_{\mathbf{u}}^h)_n$, $(\mathcal{V}_{\mathbf{u}}^h)_n$, $(\mathcal{S}_p^h)_n$, and $(\mathcal{V}_p^h)_n$. Over the element domain, this space is formed by using first-order polynomials in space and time. Globally, the interpolation functions are continuous in space but discontinuous in time.

The stabilized space-time formulation for deforming domains is then written as follows: given $(\mathbf{u}^h)_{n^-}$, find $\mathbf{u}^h \in (\mathcal{S}_{\mathbf{u}}^h)_n$ and $p^h \in (\mathcal{S}_p^h)_n$ such that $\forall \mathbf{w}^h \in (\mathcal{V}_{\mathbf{u}}^h)_n$, $q^h \in (\mathcal{V}_p^h)_n$,

$$\int_{Q_n} \mathbf{w}^h \cdot \rho \left(\frac{\partial \mathbf{u}^h}{\partial t} + \mathbf{u}^h \cdot \boldsymbol{\nabla} \mathbf{u}^h - \mathbf{f} \right) d\Omega + \int_{Q_n} \boldsymbol{\varepsilon}(\mathbf{w}^h) : \boldsymbol{\sigma}(p^h, \mathbf{u}^h) dQ + \int_{Q_n} q^h \boldsymbol{\nabla} \cdot \mathbf{u}^h dQ$$

$$+ \sum_{e=1}^{n_{el}} \int_{Q_n^e} \frac{1}{\rho} \tau \left[\rho \left(\frac{\partial \mathbf{w}^h}{\partial t} + \mathbf{u}^h \cdot \boldsymbol{\nabla} \mathbf{w}^h \right) - \boldsymbol{\nabla} \cdot \boldsymbol{\sigma}(q^h, \mathbf{w}^h) \right] \cdot$$

$$\left[\rho \left(\frac{\partial \mathbf{u}^h}{\partial t} + \mathbf{u}^h \cdot \boldsymbol{\nabla} \mathbf{u}^h - \mathbf{f} \right) - \boldsymbol{\nabla} \cdot \boldsymbol{\sigma}(p^h, \mathbf{u}^h) \right] dQ$$

$$+ \sum_{e=1}^{n_{el}} \int_{Q_n^e} \delta \boldsymbol{\nabla} \cdot \mathbf{w}^h \rho \boldsymbol{\nabla} \cdot \mathbf{u}^h dQ + \int_{\Omega_n} (\mathbf{w}^h)_n^+ \cdot \rho \left((\mathbf{u}^h)_n^+ - (\mathbf{u}^h)_n^- \right) d\Omega = \int_{(P_n)_h} \mathbf{w}^h \cdot \mathbf{h}^h dP \qquad (8)$$

This process is applied sequentially to all the space-time slabs $Q_0, Q_1, \ldots, Q_{N-1}$. In the variational formulation given by Equation (8), the following notation is being used:

$$(\mathbf{u}^h)_n^\pm = \lim_{\varepsilon \to 0} \mathbf{u}(t_n \pm \varepsilon), \qquad (9)$$

$$\int_{Q_n} (\ldots) dQ = \int_{I_n} \int_{\Omega_n} (\ldots) d\Omega dt, \qquad (10)$$

$$\int_{P_n} (\ldots) dP = \int_{I_n} \int_{\Gamma_n} (\ldots) d\Gamma dt. \qquad (11)$$

The computations start with

$$(\mathbf{u}^h)_0^- = \mathbf{u}_0, \qquad (12)$$

where $\mathbf{u}_0$ is divergence free.

The variational formulation given by Equation (8), includes certain stabilization terms added to the basic Galerkin formulation to enhance its numerical stability. Details on the formulation, including the definitions of the coefficients τ and δ, can be found in the papers by Tezduyar et al. (1992a, 1992b, 1992c). The equations of motion for the oscillator given by Equation (6)-(7) are also cast in the space-time formulation in the same manner as described in the work by Tezduyar et al. (1992c) and Mittal (1992).

4   Results

The cylinder mounted on elastic supports is allowed to oscillate both in streamwise and transverse directions. To encourage high amplitude of oscillations, the structural damping coefficient is set to zero. The springs in both streamwise and transverse directions are assumed to be linear and with same stiffness. To find out the effect of blockage on hysteresis, computations are carried out with a cylinder of non-dimensional mass, $m^* = 10$ at various blockages from 5% to 1% in the laminar regime ($60 < Re < 200$). In order to study the effect of mass ratio on the hysteresis in the lower Re end of lock-in, computations are carried out for various m^* in the range 10 to 100, at 2.5% blockage.

Figure 1 shows the response of the cylinder at the lower as well as the higher Re end of lock-in regime. It is observed that the hysteresis at the lower Re end of lock-in decreases with decrease in blockage and completely disappears at a blockage of 2.5% and less. On the other hand, the hysteresis at the higher Re end of lock-in occurs for all blockages. This shows that the hysteresis at the lower Re end of lock-in depends on blockage.

Figure 2 shows the variation of hysteresis near the lower Re end of lock-in at various mass ratios for a blockage of 2.5%. The cylinder with higher mass ratio is found to have very large hysteresis loops near the lower Re end of lock-in. For example, the cylinder with $m^*=10$ is found to have a hysteresis loop width of 6.5 (in terms of ΔRe). It is observed that as mass ratio is decreased, the hysteresis loop width also reduces, finally disappearing at a lower mass ratio. This indicates that the mass ratio also has a significant role in the hysteresis behavior of the cylinder.

5   Conclusions

The effect of blockage and mass ratio on the vortex-induced vibration of a circular cylinder is investigated using a stabilized finite element method. At a given mass ratio, the hysteresis in the lower Re end of lock-in is found
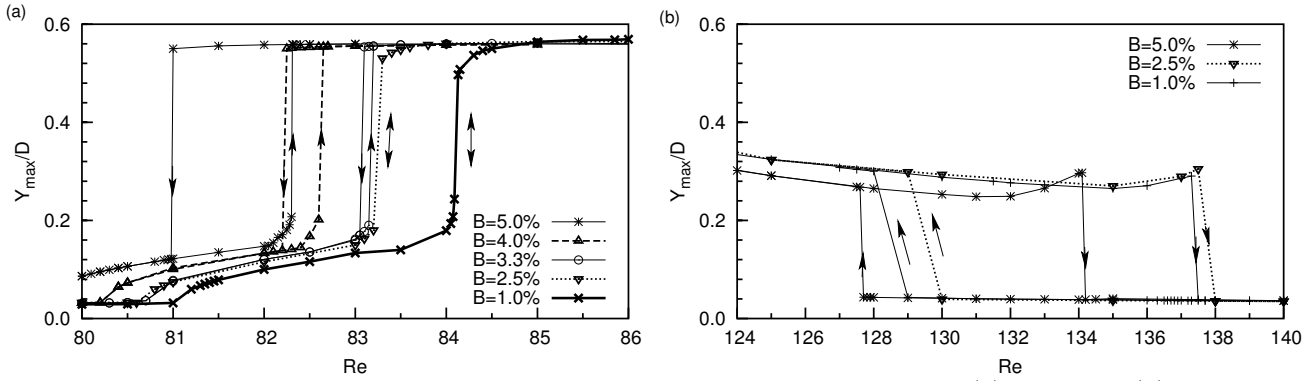
Figure 1: Variation of maximum amplitudes of transverse oscillation with Re near (a) lower and (b) higher Re end of lock-in for a cylinder with $m^* = 10$.
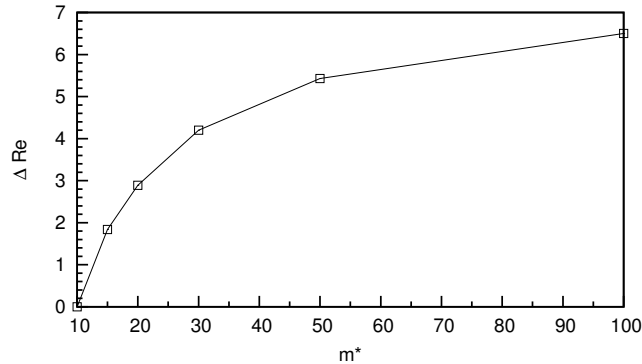

Figure 2: Variation of hysteresis loop width with mass ratio for 2.5% blockage.

to be dependent on blockage. The hysteresis at the higher Re end of lock-in is not affected much by variation in blockage. The hysteresis at the lower Re end of lock-in is very large for cylinders with large mass ratios. At a given blockage, the hysteresis in the lower Re end of lock-in is found to decrease with decrease in mass ratio, before disappearing completely at a very low mass ratio. This shows that both blockage and mass ratio influence the hysteresis behavior near the low Re end of lock-in in the laminar regime. This study shows that the blockage, for VIV experiments at low Re, plays a very important role. In particular, for large m^*, blockage as low as 1% could lead to a hysteretic behavior which may not be observed for an unbounded flow.

References

[1] S.P. Singh, S. Mittal. Vortex-induced oscillations at low Reynolds numbers: hysteresis and vortex shedding modes. *Journal of Fluids and Structures*, 20:1085–1104, 2005.

[2] C.H.K. Williamson, R. Govardhan. Vortex Induced Vibration. *Annual Review of Fluid Mechanics*, 36:413–455, 2004.

[3] T.E. Tezduyar, M. Behr, J. Liou. A new strategy for finite element computations involving moving boundaries and interfaces- the deforming-spatial-domain/space-time procedure, I: the concept and the preliminary tests. *Computer Methods in Applied Mechanics and Engineering*, 94(3):339–351, 1992.

[4] T.E. Tezduyar, M. Behr, S. Mittal, J. Liou. A new strategy for finite element computations involving moving boundaries and interfaces- the deforming-spatial-domain/space-time procedure, II: computations of free-surface flows, two liquid flows and flows with drifting cylinders. *Computer Methods in Applied Mechanics and Engineering*, 94(3):353–371, 1992.

[5] T.E. Tezduyar, S. Mittal, S.E. Ray, R. Shih. Incompressible flow computations with stabilized bilinear and linear equal-order-interpolation velocity pressure elements. *Computer Methods in Applied Mechanics and Engineering*, 95:221–242, 1992.

[6] S. Mittal, T.E. Tezduyar. A finite element study of incompressible flows past a oscillating cylinders and airfoils. *International Journal for Numerical Methods in Fluids*, 15:1073–1118, 1992.

Physics of the temporal and spatial forcing in flows
(wakes, separated flows and boundary layers)

José Eduardo Wesfreid

Physique et Mécanique des Milieux Hétérogènes (PMMH)
Ecole Supériure de Physique et Chimie Industrielles de Paris (ESPCI)
UMR 7636 CNRS - ESPCI – UMPC P6 – PDD P7,
10, rue Vauquelin, 75231 Paris, France
wesfreid@espci.fr

In this talk I will present our results[1] about the stability of flows, under temporal or spatial periodic forcing, underlying the physical mechanisms observed in the different situations I will expose.

Our typical case of study on the temporal forced flows is the wake produced by an oscillating cylinder[2]. We are interested in the new states and patterns of vortex shedding and in the nonlinear mean flow modification in respect to the base state without fluctuations[3], when the bluff body oscillates at different amplitudes and frequencies.

As an extension of previous works,[4] we will relate these modifications with the global properties of the wakes, as it is the case of the drag[5], of the recirculation length, of the frequency and of the deformation of the amplitude of the global mode.[6,7]

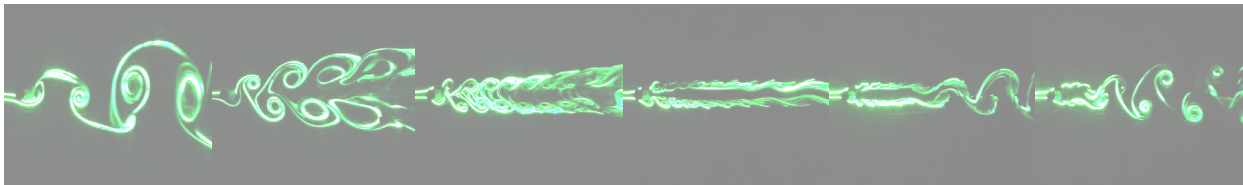*Figure 1: Vortex shedding patterns, in an oscillating bluff body, produced at different temporal forcing parameters (Re=150, forcing frequency = 0.5,1,2,3,4 and 5 times the natural vortex shedding frequency)*

We have studied a spatial periodic forcing or perturbation of the flow using vortex generators and more specifically the influence of vortex generators on the spatial global properties of this flow.

Also as an extension of our previous works on the nonlinear developpement of the Gôrtler instability[8], we will analyze the modifications of the mean flow produced by vortex generators (V.G.) of different wavelengths, study which is important in order to obtain optimal actuators for flow control.[9]
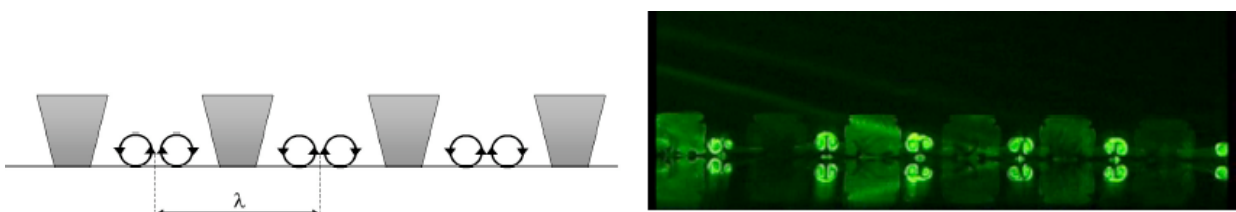

Figure 2: a) Schema of the vortex generators and b) flow cross-section pattern showing the downstream periodic counterrotating streamwise vortex forcing a boundary layer induced by the V.G.

---

[1] *This work has been done in collaboration with Jean-Luc Aider, Jean François Beaudoin, Gilles Bouchet, Olivier Cadot, Thomas Duriez, Ramiro Godoy Diana, Sophie Goujon-Durand, Catherine Marais and Benjamin Thiria*,

[2] Thiria, B.; Goujon-Durand, S.: Wesfreid, J.E., Wake of a cylinder performing rotary oscillations. Journal of Fluid Mechanics 2006, **560**: 123-147

[3] Thiria, B.; Bouchet, G.;Wesfreid, J.E., On the relation between linear stability analysis and mean flow properties in wakes ; preprint 2007

[4] Maurel, A.; Pagneux, V.; Wesfreid, J.E., Mean-Flow Correction As Nonlinear Saturation Mechanism. Europhysics Letters 1995, **32**, (3), 217-222

Zielinska, B. J. A.; Goujon-Durand, S.; Dusek, J.; Wesfreid, J.E., Strongly nonlinear effect in unstable wakes. Physical Review Letters 1997, **79**, (20), 3893-3896.

Wesfreid, J. E.; GoujonDurand, S.; Zielinska, B. J. A., Global mode behavior of the streamwise velocity in wakes. Journal De Physique II 1996, **6**, (10), 1343-1357.

[5] Protas, B.; Wesfreid, J.E., Drag force in the open-loop control of the cylinder wake in the laminar regime. Physics of Fluids 2002, **14**, (2), 810-826

Protas, B.; Wesfreid, J.E., On the relation between the global modes and the spectra of drag and lift in periodic wake flows. Comptes Rendus Mecanique 2003, **331**, (1), 49-54.

[6] Thiria, B.: Wesfreid, J.E., Stability properties of forced wakes. Journal of Fluid Mechanics 2007, **579**: 137-161.

[7] Thiria, B.; Bouchet, G.;Wesfreid, J.E., Critical properties of forced wakes; preprint 2007,

[8] Petitjeans, P.; Wesfreid, J. E., Spatial evolution of Gortler instability in a curved duct of high curvature. Aiaa Journal 1996, **34**, (9), 1793-1800.

[9] Duriez, T.,Aider, J.-L.; Wesfreid, J.E., Base flow modification by streamwise vortices.Application to the control of separated flows Proceedings of FEDSM2006 2006

Dynamics of vortex shedding from cones

S.J.Chetan*, D.S.Luff
Department of Engineering, Queen Mary, University of London,
London E1 4NS
* s.j.chetan@qmul.ac.uk

Introduction

The vortex structure of a slender cone with its axis normal to the flow direction is significantly different to the flow produced around a cylinder. Although the modulated wake of a cone has been well documented (Gaster 1969, 1971, Piccirillo & Van Atta 1993, Williamson 1996) the dynamics of the flow are not well understood. Figure 1 compares the wake of a cylinder and a cone with a taper ratio of 18:1. It can be seen that the wake behind the cone exhibits temporal variations in the vortex structure. The wake has a modulation frequency that is an order of magnitude lower than the vortex shedding frequency (Piccirillo & Van Atta 1993). The taper of a cone influences the dynamics of the already non-linear process of vortex shedding and the present work investigates the differences in the wake flows behind cylinders and cones. The influence of end conditions and the effect of the local Reynolds number along the span of the cone are investigated using both hot-wire anemometry and particle image velocimetry (PIV).
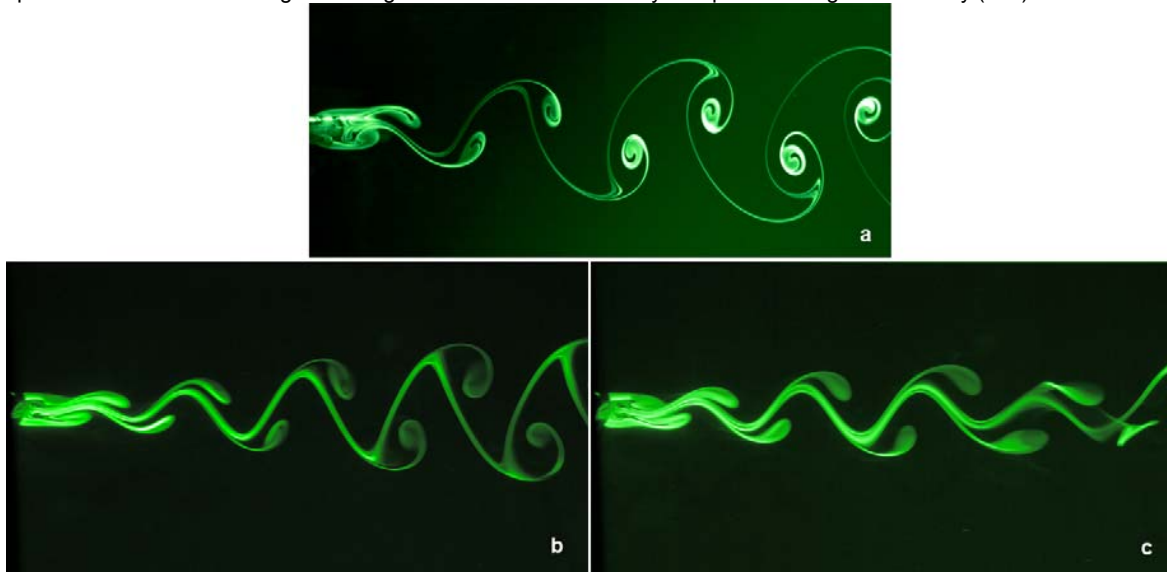

Figure 1. Flow visualisation using fluorescein showing (a) The vortex shedding pattern behind a straight cylinder, (b) and (c) vortex shedding behind a cone with a taper ratio of 18:1 at two instances during the modulation cycle.

Experimental Method

The experiments were conducted in a 300 x 300 mm free surface water channel where the free stream velocity could be varied between 0.02 to 0.035 m/s. For cylinders with Reynolds numbers below 170 the relationship with the Strouhal number is considered to be in the two dimensional regime, (Williamson 1996), and flow velocities were chosen so that local Reynolds numbers were below this value. The blockage ratio of the cone was less than 0.5% and the free stream turbulence level in the working section was 0.3% for the range of velocities used in the present work. A straight cylinder with a diameter of 3 mm and a cone with a taper ratio of 18:1 and a base diameter of 9.5 mm were used. Hot-wire anemometry was used to obtain single point frequency data and PIV was used for velocities and vorticity in both the horizontal and vertical planes. The PIV system consisted of a 190mJ double-pulsed Nd-YAG laser and a CCD camera having a resolution of 2048 X 2048 pixels. Data was obtained at a frame rate of 5Hz and a total of 90 image-pairs were captured per acquisition set. This allowed data to be captured over a complete modulation cycle. The shed vortices were approximately 4 – 5 mm in diameter and an experimental investigation determined that interrogation window sizes of 0.6 mm in the horizontal plane and 1.8mm in the vertical plane were adequate to resolve the vortex structures.

Results

- ### Critical Reynolds Number

Below a critical Reynolds number of 47 (Roshko 1954) the wake from a cylinder is seen to be steady with two attached recirculating zones. At this critical value a Hopf type bifurcation exists and at larger Reynolds numbers vortex shedding occurs (Sreenivasan, 1987). In this case a relationship between the Reynolds number and the square of the velocity amplitude exists and the sudden increase in the square of the velocity amplitude with Reynolds number is well defined at the critical value. Experiments were performed to determine the critical Reynolds number at which the cone started to shed vortices. Data is obtained in regions of the flow relating to equal local diameters of the cone and cylinder, as well as at other locations along the span of the cone. Figure 2 shows the mean square of amplitude of the vortex shedding signal plotted against the local Reynolds number for the straight cylinder and the

cone. The onset condition for vortex shedding for the straight cylinder is clear at a Reynolds number of 47 and the distribution of the amplitude of the vortex shedding signal to be approximately linear up to a Reynolds number of 60. In comparison the cone starts to shed vortices at a Reynolds number of approximately 63, as reported by Gaster (1969) and the onset condition for vortex shedding is not well defined. This was found to be consistent for various local diameters along the span of the cone. Apparently, the mechanism responsible for the onset of vortex shedding is affected with a tapered body. Why the onset conditions and the critical Reynolds numbers are different for a cone is not yet clear and further investigation of the flow field in this Reynolds number regime is required.
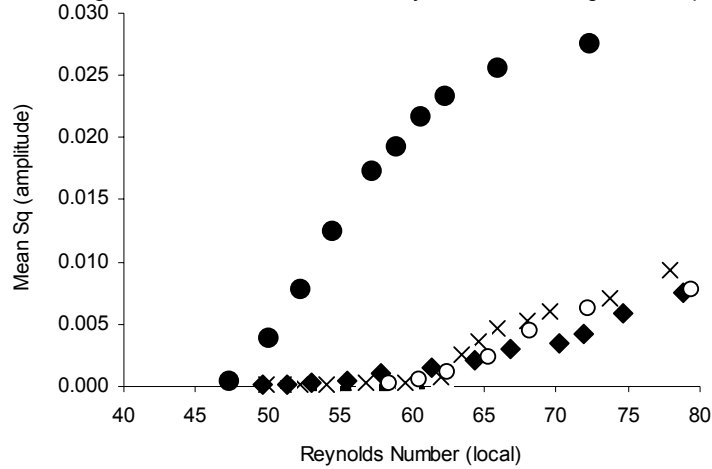

Figure 2. Mean square of hot-wire amplitudes with increases in Reynolds number for a straight cylinder of 3 mm diameter and a cone of taper ratio 18:1 at local diameters (LD) of: ● Straight Cylinder D=3 mm; ▲ Cone LD=2 mm; X Cone LD=3 mm; ◆ Cone LD=3.4 mm; ○ Cone LD=4 mm;

- **Variation of Modulation Frequency**

Hot-wire measurements were made at different locations along the length of the cone and with different free-stream velocities to include the local Reynolds number as a parameter. Figure 3 shows that the modulation frequency is constant at around 0.095Hz along the span of the cone for a constant free-stream velocity of 0.026 m/s. However, vortex shedding frequencies for this flow ranged between 1.1 and 0.7 Hz. At the lower free stream velocity the modulation frequency was again constant, while the vortex shedding frequency changed with local diameter. Therefore, the modulation frequency is not dependent on the local Reynolds number, while the vortex shedding frequency is dependent. This implies a global mechanism is responsible for the modulation.
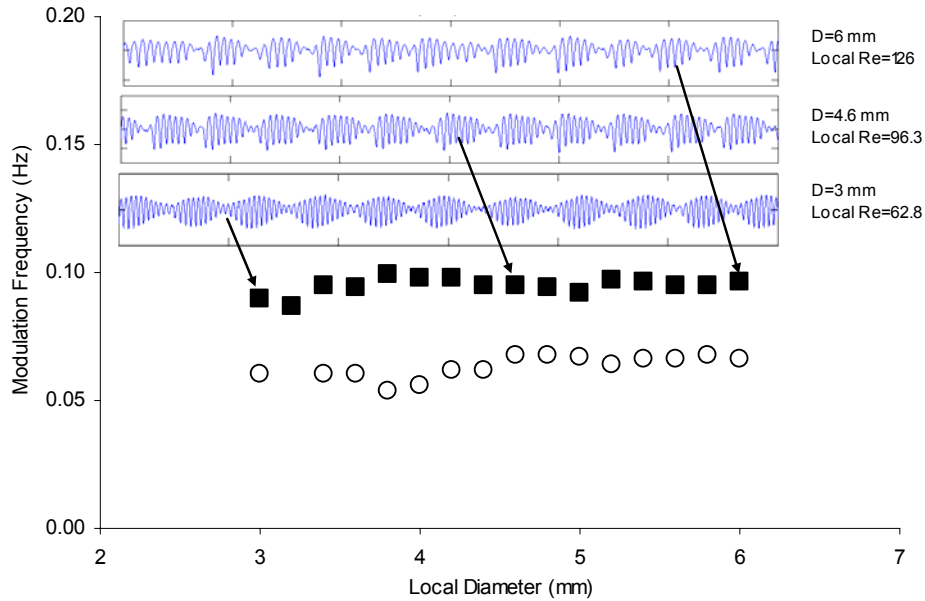

Figure 3. Variation of modulation frequency in the wake of the cone with change in local diameter at two fixed free-stream velocities ○ U=0.022m/s; ■ U=0.026m/s

- **PIV measurements**

Figure 4 shows a plan view of the vorticity field of the wake behind the cone. Velocity fluctuations were measured simultaneously with a hot-wire probe located at X=30, Z=30 mm. The hot-wire measurements provided greater temporal resolution than the PIV measurements and were used to assess at what part of the modulation cycle the PIV images were obtained. Figure 4a shows vortices shed from the cone at a moment that produced high peaks in the modulation cycle. In comparison, Figure 4b shows a moment when the signal is modulated to low peak values and it can be seen that values of vorticity are considerably lower downstream of X=30 mm in this part of the cycle. The vorticity field appeared as in Figure 4b throughout the period of low peak values and appeared similar in nature to flow below the critical Reynolds number in the wake of a cylinder.
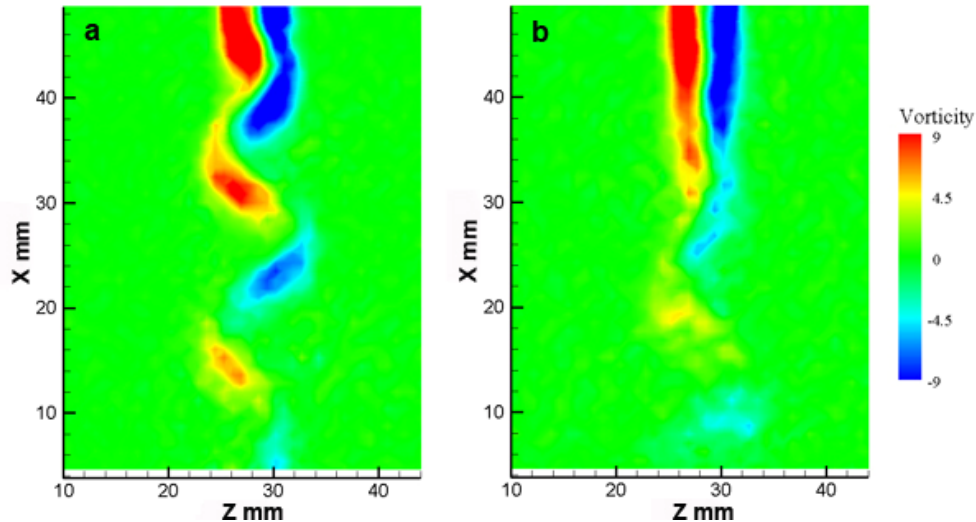

Figure 4. Vorticity contour plots for a free stream velocity of 0.026 m/s and a local diameter of 4 mm. Flow is from top to bottom, with the PIV camera view parallel to the axis of the cone, which is located at (X=50, Z=29). Units of vorticity in 1/s.

In the vertical plane, the values of velocity with respect to time were obtained from the PIV images at specific points along the span of the cone. The velocities were obtained from the location of X = 30 mm and at 1.8 mm intervals along the span of the cone. Thus, effectively a 55 component simultaneous single point measurement array along the span of the cone was realised. The temporal resolution of the PIV was 5 Hz in comparison to the vortex shedding frequency of around 1 Hz and was adequate to resolve the passing of vortices. The passing of one vortex is indicated by a peak and a trough in the velocity signal. The measurement period was around 17 seconds and was greater than the period of one modulation, around 10 seconds. Stream-wise velocity results are presented in the contour plot of Figure 5 with values at 0 seconds indicating the start of the measurement. The base of the cone is located at the top of the figure and the tip beyond the bottom.

The different vortex shedding frequencies produced at different local diameters are clearly evident with fewer vortices produced at the top of the figure than at the bottom. It also appears that there are vortex columns that are not formed along the whole length of the cone with some vortices produced near the tip not reaching the base of the cone. The top of these smaller vortices are circled in the figure. The structure of the flow appears similar to the vortex splitting observed by Piccirillo & Van Atta (1993). These shorter columns appear at regular intervals between vortex columns that span the length of the cone. Also, the length of the vortex columns produced from nearer the tip reduces successively with each column further from the base of the cone. The flow then repeats this cycle starting immediately with a column almost reaching the base of the cone and this repetition has a frequency of approximately 0.1 Hz, the same as for the modulation frequency. The velocity signal is modulated to low peak values in the region located at the top of the shorter vortex column. It, therefore, seems that the mismatch between shedding frequencies at different local diameters causes the modulation of the velocity signal by affecting the structure of the vortex columns. Further investigation is required to determine what flow conditions occur at the termination / splitting of the shorter vortex columns.
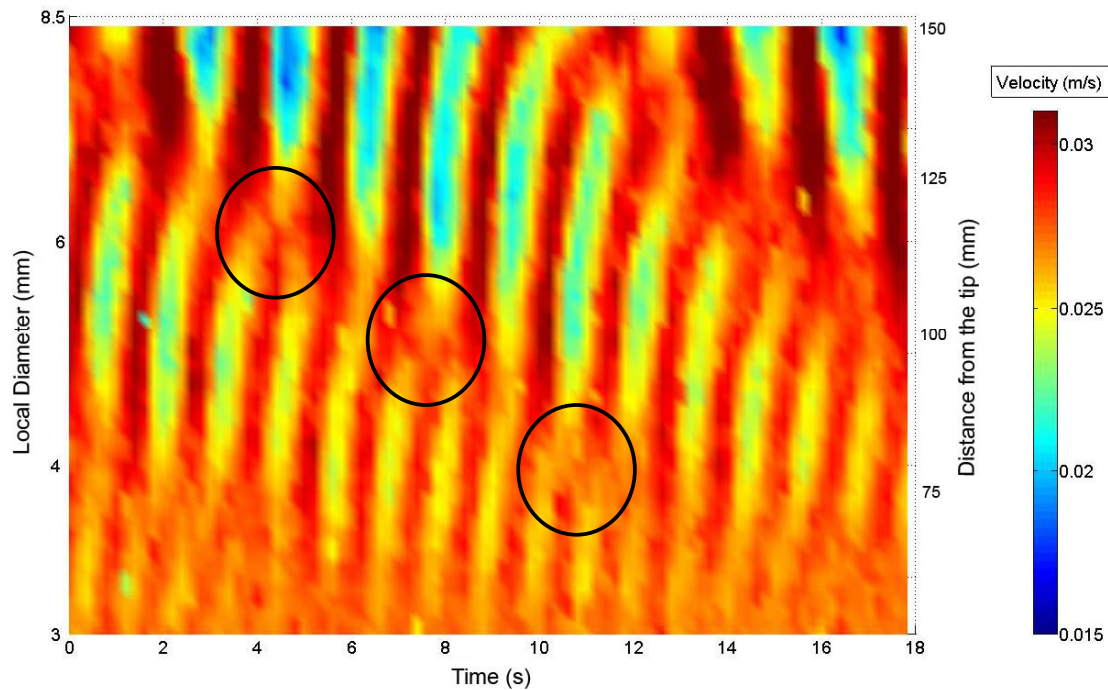
Figure 5. Velocity measurements with time from PIV to yield an effective 55 component array along the span of the cone.

Conclusions

- The mechanism for the onset of vortex shedding from cones is different than from straight cylinders. It appears not to be a Hopf type bifurcation.

- The modulation frequency was found to be constant along the span of the cone indicating a global mechanism is responsible for the modulation of the velocity fluctuations in the wake of a cone.

- Due to the mismatch of vortex shedding frequencies along the span successively shorter vortex columns were produced. The cycle repeated with a period matching the modulation frequency.

- A satisfactory mathematical model which can predict the modulation of the shedding signal from a cone is unavailable.

Acknowledgements

References

Gaster, M. 1969 Vortex shedding from slender cones at low Reynolds numbers. *J.Fluid Mech.* **38**, 565.

Gaster, M. 1971 Vortex shedding from circular cylinders at low Reynolds numbers. *J.Fluid Mech.* **46**, 749.

Picirillo, P. S. & Van Atta, C. W. 1993 An experimental study of vortex shedding behind linearly tapered cylinder at low Reynolds number. *J. Fluid Mech.* **246**, 163.

Roshko, A. 1956 On the development of turbulent wakes from vortex streets. ***NACA Rep.*1191.**

Sreenivasan, K.R., Strykowski, P. J. & Olinger, D.J. 1986 On the Hopf bifurcation, Landau equation and vortex shedding behind circular cylinders. ***Proc. Forum Unsteady Flow Separation,*** ed. K Ghia, p.1. New York: ASME

Williamson, C. H. K. 1996 Vortex dynamics in the cylinder wake. *Ann. Rev. Fluid. Mech.* **28,** 477.

Minimal-energy control feedback for stabilization of bluff-body wakes based on unstable open-loop eigenvalues and left eigenvectors

T. Bewley[1], J. Pralits[2], and P. Luchini[2]
[1]*Flow Control Lab, Dept. of MAE, UC San Diego, USA*
[2]*DIMEC, Università di Salerno, Italy*

An efficient technique is presented to compute minimal-energy stabilizing linear feedback control rules for linear systems. The technique presented extends easily to large-scale convection-dominated nonlinear fluid systems, linearized about unstable equilibria, as it is based solely on the least-stable eigenvalues and the corresponding left eigenvectors of the linearized open-loop system. These eigenvalues and eigenvectors, in turn, may be computed directly from a linearized simulation code via, e.g., Arnoldi or Multigrid strategies for large-scale systems. The linearized simulation code, in turn, may be computed via, e.g., the Complex Step Derivative technique from any trustworthy unsteady flow solver. Application of this procedure to a vortex-induced vibration problem resulting from the flow past a cylinder is discussed.

1 Efficient computation of minimal-energy stabilizing control feedback

It is a classical result in control theory that, if a minimal-energy stabilizing feedback control rule $\mathbf{u} = K\mathbf{x}$ is applied to the linear system $\dot{\mathbf{x}} = A\mathbf{x} + B\mathbf{u}$, the eigenvalues of the closed-loop system $A + BK$ are given by the union of the stable eigenvalues of A and the reflection of the unstable eigenvalues of A into the left-half plane across the imaginary axis. Since we know where the closed-loop eigenvalues of the system are, the requisite feedback gain matrix K in this problem may be computed by the process of *pole assignment*. Applying this process to the equation governing the dynamics of the unstable modes of the system in modal form and then transforming appropriately, this leads to a simple expression for K, as shown below.

1.1 The linear optimal control problem and its solution

Consider first the following optimization problem: for the state $\mathbf{x}$ and the control $\mathbf{u}$ related via the *state equation*

$$\dot{\mathbf{x}} = A\mathbf{x} + B\mathbf{u} \quad \text{on } 0 < t < T \qquad \text{with} \qquad \mathbf{x} = \mathbf{x}_0 \quad \text{at } t = 0, \tag{1}$$

where $\mathbf{x}_0$ is initially unspecified, find the control $\mathbf{u}$ that minimizes the *cost function*

$$J = \frac{1}{2} \int_0^T \left[\mathbf{x}^H Q\mathbf{x} + \mathbf{u}^H R\mathbf{u} \right] dt. \tag{2}$$

Via standard manipulations (see, e.g., Kim & Bewley 2007), it is found that the state and relevant adjoint equations for this optimization problem may be written in the combined matrix form

$$\frac{d\mathbf{z}}{dt} = Z\mathbf{z} \quad \text{where} \quad Z = Z_{2n \times 2n} = \begin{bmatrix} A & -BR^{-1}B^H \\ -Q & -A^H \end{bmatrix}, \quad \mathbf{z} = \begin{bmatrix} \mathbf{x} \\ \mathbf{r} \end{bmatrix}, \quad \text{and} \quad \begin{cases} \mathbf{x} = \mathbf{x}_0 & \text{at } t = 0, \\ \mathbf{r} = 0 & \text{at } t = T, \end{cases} \tag{3}$$

where $\mathbf{r}$ is known as the *adjoint variable*. This ODE, with both initial and terminal conditions, is a *two-point boundary value problem*. It may be solved by assuming there exists a relation between the state vector $\mathbf{x} = \mathbf{x}(t)$ and adjoint vector $\mathbf{r} = \mathbf{r}(t)$ via a matrix $X = X(t)$ such that $\mathbf{r} = X\mathbf{x}$, inserting this assumed form of the solution into the combined matrix form (3) to eliminate $\mathbf{r}$, combining rows to eliminate $d\mathbf{x}/dt$, factoring out $\mathbf{x}$ to the right, and requiring that the result holds for all $\mathbf{x}_0$, from which it follows that X obeys the *differential Riccati equation*

$$-\frac{dX}{dt} = A^H X + XA - XBR^{-1}B^H X + Q \quad \text{where} \quad X(T) = 0. \tag{4}$$

The optimal value of $\mathbf{u}$ may then be written in the form of a *feedback control rule* such that

$$\mathbf{u} = K\mathbf{x} \quad \text{where} \quad K = -R^{-1}B^H X. \tag{5}$$

Finally, if the system is linear time invariant (LTI) and we take the limit that $T \to \infty$, the matrix X in (4) may be marched to steady state. This steady state solution for X satisfies the *continuous-time algebraic Riccati equation*

$$0 = A^H X + X A - X B R^{-1} B^H X + Q, \tag{6}$$

where additionally X is constrained such that $A + BK$ is stable.

Assume now that an eigen decomposition of the composite matrix Z is available such that

$$Z = V \Lambda_c V^{-1} \quad \text{where} \quad V = \begin{bmatrix} V_{11} & * \\ V_{21} & * \end{bmatrix} = \begin{bmatrix} | & | & & | & \\ \mathbf{v}^1 & \mathbf{v}^2 & \dots & \mathbf{v}^n & * \\ | & | & & | & \end{bmatrix} \quad \text{and} \quad \mathbf{v}^i = \begin{bmatrix} \mathbf{x}^i \\ \mathbf{r}^i \end{bmatrix}, \tag{7}$$

where the eigenvalues of Z appearing in diagonal matrix Λ_c are enumerated such that the LHP eigenvalues appear first, followed by the RHP eigenvalues. Defining $\mathbf{y} = V^{-1}\mathbf{z}$, it follows from (3) that $d\mathbf{y}/dt = \Lambda_c \mathbf{y}$. The stable solutions of $\mathbf{y}$ are thus spanned by the first n columns of Λ_c (that is, they are nonzero only in the first n elements of $\mathbf{y}$). Since $\mathbf{z} = V\mathbf{y}$, it follows that the stable solutions of $\mathbf{z}$ are spanned by the first n columns of V. To achieve stability of $\mathbf{z}$ via the additional constraint $\mathbf{r} = X\mathbf{x}$ for each of these directions, denoted $\mathbf{v}^i$ and decomposed as shown above, we must have $\mathbf{r}^i = X\mathbf{x}^i$ for $i = 1 \dots n$. Assembling these equations in matrix form, we have

$$\begin{bmatrix} | & | & & | \\ \mathbf{r}^1 & \mathbf{r}^2 & \dots & \mathbf{r}^n \\ | & | & & | \end{bmatrix} = X \begin{bmatrix} | & | & & | \\ \mathbf{x}^1 & \mathbf{x}^2 & \dots & \mathbf{x}^n \\ | & | & & | \end{bmatrix} \quad \Rightarrow \quad V_{21} = XV_{11} \quad \Rightarrow \quad X = V_{21}V_{11}^{-1}. \tag{8}$$

1.2 The minimal-energy stabilizing feedback control

Selecting $Q > 0$ and $R = R_0/\varepsilon$ with $R_0 > 0$ and $\varepsilon > 0$ in the above derivation, and taking the limit as $\varepsilon \to 0$, we arrive at the what is known as the *minimum-energy stabilizing feedback control*. As Z becomes block triangular in this limit, it is seen immediately that, in this limit, the eigenvalues of Z are given by the union of the eigenvalues of A and the eigenvalues of $-A^H$ for any $Q > 0$ and $R_0 > 0$. Additionally constraining this system to be stable [by the additional constraint $\mathbf{r} = X\mathbf{x}$, with X as constructed in (8)], the eigenvalues of the closed-loop system are selected precisely as the stable eigenvalues of Z; that is, the stable eigenvalues of A together with the stable eigenvalues of $-A^H$.

1.3 The pole assignment problem

Let us focus now on the eigen decomposition of Z in the above derivation:

$$\begin{bmatrix} A & -BR^{-1}B^H \\ -Q & -A^H \end{bmatrix} V_s = V_s \Lambda_{c,s} \quad \text{with} \quad V_s = \begin{bmatrix} V_{11} \\ V_{21} \end{bmatrix}, \tag{9}$$

where the n desired (stable) eigenvalues of the closed-loop system, $\lambda_{c,s}$, appear in the diagonal matrix $\Lambda_{c,s}$, and the corresponding eigenvectors of Z are given by the columns of V_s, which is partitioned as indicated. In the typical pole assignment problem, we prescribe the closed-loop eigenvalues $\lambda_{c,s}$ in advance, then modify the control input $\mathbf{u}$ [equivalently, the upper-right block of the matrix on the LHS of (9)] in order to put these eigenvalues in the desired locations. In the present pole assignment problem, however, we happen to know both the closed-loop eigenvalues $\lambda_{c,s}$ and the upper-right block of the matrix on the LHS of (9); all that remains is for us to compute the corresponding eigenvector matrix V_s. As summarized above, once these eigenvectors are calculated, the desired feedback rule is given by $\mathbf{u} = K\mathbf{x}$ with $K = -R^{-1}B^H X$, where $X = V_{21}V_{11}^{-1}$. Multiplying out (9), it follows immediately that

$$AV_{11} - BR^{-1}B^H V_{21} = V_{11}\Lambda_{c,s}, \tag{10a}$$
$$-QV_{11} - A^H V_{21} = V_{21}\Lambda_{c,s}. \tag{10b}$$

Solving (10b) for V_{11} and substituting the result into (10a) gives

$$AQ^{-1}(A^H V_{21} + V_{21}\Lambda_{c,s}) + BR^{-1}B^H V_{21} = Q^{-1}(A^H V_{21} + V_{21}\Lambda_{c,s})\Lambda_{c,s}, \tag{11a}$$

$$V_{11} = -Q^{-1}(A^H V_{21} + V_{21}\Lambda_{c,s}). \tag{11b}$$

Note that equation (11a) is linear in the unknown matrix V_{21}. Once V_{21} is obtained from this equation, calculation of V_{11} is trivial using (11b) or, equivalently, (10a).

1.4   Simplification of the linear algebra problem in modal form

It is straightforward transform the original linear system to a modal representation of its unstable dynamics. Performing the eigen decomposition $A = S\Lambda S^{-1}$ and multiplying (1) from the left by S^{-1}, it follows that

$$\dot{\boldsymbol{\chi}} = \Lambda\boldsymbol{\chi} + \bar{B}\mathbf{u} \quad \text{where} \quad \boldsymbol{\chi} = S^{-1}\mathbf{x}, \quad \bar{B} = S^{-1}B. \tag{12}$$

Note that Λ is diagonal. Denoting the inverse of the eigenvector matrix as[1] $T^H = S^{-1}$, the portion of (12) governing the unstable dynamics of the system may be written

$$\dot{\boldsymbol{\chi}}^u = \Lambda_u\boldsymbol{\chi}^u + \bar{B}_u\mathbf{u} \quad \text{where} \quad \boldsymbol{\chi}^u = T_u^H\mathbf{x}, \quad \Lambda = \begin{bmatrix} \Lambda_u & 0 \\ 0 & \Lambda_s \end{bmatrix}, \quad T = \begin{bmatrix} T_u & T_s \end{bmatrix}, \quad \bar{B} = \begin{bmatrix} \bar{B}_u \\ \bar{B}_s \end{bmatrix}, \quad \bar{B}_u = T_u^H B. \tag{13}$$

The pole placement process in the minimal-energy stabilizing feedback control problem, as derived in §1.3, can be simplified greatly when applied to the equation for the unstable dynamics of the original system in modal form, as given in (13). Partitioning V_{21} into its respective columns, $V_{21} = \begin{bmatrix} \mathbf{r}^1 & \mathbf{r}^2 & \dots & \mathbf{r}^n \end{bmatrix}$, taking $A = \Lambda_u$, $B = \bar{B}_u$, $Q = I$, $R = I/\varepsilon$, and[2] $\Lambda_{c,s} = -\Lambda_u^H$ in (11a), and applying the above relationships, it follows after some simplifications[3] that (11a) may be written in the simple form

$$[\varepsilon\bar{B}_u\bar{B}_u^H + \text{diag}(d_1^{(k)}, d_2^{(k)}, \dots, d_n^{(k)})]\mathbf{r}^k \triangleq M_k\mathbf{r}^k = 0, \tag{14}$$

where

$$d_i^{(k)} = \begin{cases} (\lambda_i + \lambda_k^H)(\lambda_i^H - \lambda_k^H) & \text{for } i \neq k \\ 0 & \text{for } i = k. \end{cases} \tag{15}$$

Thus, the vectors $\mathbf{r}^k$ lie in the nullspace of M_k, and may be found by the process of Gaussian elimination, manipulating M_k to row-echelon form. In the limit $\varepsilon \to 0$, M_k approaches a diagonal matrix with a zero in the k'th diagonal element, and thus[4] $V_{21} \to I$. In order to avoid taking the difference of two quantities which are almost equal in the computation of V_{11}, we return to (10a), which, in the $\varepsilon \to 0$ limit, may be written in the form

$$\Lambda_u V_{11} + V_{11}\Lambda_u^H = \varepsilon\bar{B}_u\bar{B}_u^H \triangleq \varepsilon C. \tag{16}$$

Defining the $\{i,j\}$'th element of V_{11} as v_{ij}, the $\{i,j\}$'th element of (16) may be written $v_{ij} = \varepsilon c_{ij}/(\lambda_i + \lambda_j^H) \triangleq \varepsilon f_{ij}$. With $V_{11} = \varepsilon F$ and $V_{21} = I$, it follows that $X = F^{-1}/\varepsilon$, and thus the minimal-energy feedback control that stabilizes (13) in the limit that $\varepsilon \to 0$ is given by $\mathbf{u} = \bar{K}\boldsymbol{\chi}^u$ where $\bar{K} = -\bar{B}_u^H F^{-1}$. Writing this feedback in terms of the original state variable $\mathbf{x}$, we have $\mathbf{u} = K\mathbf{x}$ where $K = \bar{K}T_u^H$.

The solution for the minimal-energy stabilizing control feedback problem derived above is now summarized:

Theorem 1. *Consider a stabilizable system $\dot{\mathbf{x}} = A\mathbf{x} + B\mathbf{u}$ with no pure imaginary open-loop eigenvalues. Determine the unstable eigenvalues and corresponding left eigenvectors of A such that $T_u^H A = \Lambda_u T_u^H$ (alternatively, determine the unstable eigenvalues and corresponding right eigenvectors of A^H such that $A^H T_u = T_u\Lambda_u^H$). Define $\bar{B}_u = T_u^H B$ and $C = \bar{B}_u\bar{B}_u^H$, and compute a matrix F with elements $f_{ij} = c_{ij}/(\lambda_i + \lambda_j^H)$. The minimal-energy stabilizing feedback controller is then given by $\mathbf{u} = K\mathbf{x}$, where $K = -\bar{B}_u^H F^{-1}T_u^H$.*

---

[1]Note that the columns of T are referred to as the *left* or *adjoint* eigenvectors of A.

[2]We take $\Lambda_{c,s} = -\Lambda_u^H$ following the discussion in §1.2, noting that all eigenvalues in Λ_u are unstable.

[3]Note that, if Λ is diagonal, the product ΛV corresponds to scaling the i'th *row* of V by λ_i for all i, whereas the product $V\Lambda$ corresponds to scaling the i'th *column* of V by λ_i for all i.

[4]If all unstable eigenvalues of A are distinct, then $d_i^{(k)} \neq 0$ for $i \neq k$; V_{21} necessarily becomes diagonal in this case in the limit that $\varepsilon \to 0$, and its columns may be normalized such that $V_{21} \to I$. If some of the unstable eigenvalues of A are repeated, then there are other solutions as well. However, $V_{21} \to I$ is a valid solution in either case in the limit that $\varepsilon \to 0$.
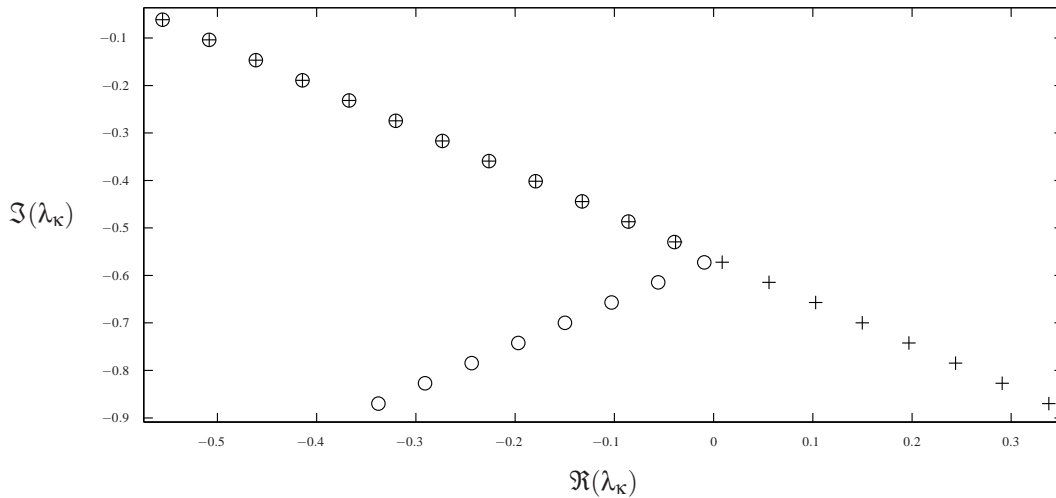
Figure 1: The first twenty eigenvalues of (+) the discretized open-loop system described in §2, and (o) the closed-loop system $A + BK$ after minimal-energy control is applied via the formulae summarized in Theorem 1.

2   Numerical results.

The above algorithm was applied to the following forced convection-diffusion model of weakly nonparallel flows (see Lauga & Bewley 2003, Chomaz *et al.* 1987, 1990)

$$\frac{\partial \psi}{\partial t} + U\frac{\partial \psi}{\partial x} = \mu(x)\psi + \nu\frac{\partial^2 \psi}{\partial x^2} + \delta^\sigma(x - x_f)u \qquad \Leftrightarrow \qquad \frac{\partial \psi}{\partial t} = \mathcal{L}\psi + \delta^\sigma(x - x_f)u, \tag{17}$$

where $U = 6$, $\mu(x) = \mu_0 - [\varepsilon(x - x_t)]^2$, $\nu = 1 - 10i$, $\varepsilon = 0.01$, $x_t = 0.1i$, $x_f = 47$ and $\delta^\sigma(x)$ is a numerical (triangular) approximation of a dirac delta representing pointwise forcing on the system. We have taken the supercriticality $(\mu_0 - \mu_c)/\mu_c = 3$ in the numerical simulation, where $\mu_c \triangleq \mu_a + \varepsilon\Re(\nu^{1/2})$ and $\mu_a \triangleq U^2\Re(\nu)/(4|\nu|^2)$. Results are shown in Figure 1, illustrating that the formulae provided above successfully reflect the unstable eigenvalues of A into the LHP, and leave the stable eigenvalues of A unchanged. Application of this approach to a 2D cylinder wake, using our recently-developed large-scale eigenvalue solver for this class of problems, will be presented at the conference.

References

[1] Chomaz, J.M., Huerre, P., & Redekopp, L.G. 1987 Models of hydrodynamics resonances in separated shear flows *Proceedings of the 6th Symposium on Turbulent Shear Flows*, Toulouse, 321-326.

[2] Chomaz, J.M., Huerre, P., & Redekopp, L.G. 1990 The effect of nonlinearity and forcing on global modes, in *New Trends in Nonlinear Dynamics and Pattern-Forming Phenomena* (ed. P. Coullet & P. Huerre), 259-274, Plenum Press.

[3] Kim, J., & Bewley, T. 2007 A Linear Systems Approach to Flow Control. *Annual Review of Fluid Mechanics* **39**, 383-417.

[4] Lauga, E., & Bewley, T.R. 2003 The decay of stabilizability with Reynolds number in a linear model of spatially developing flows. *Proc. R. Soc. Lond. A* **459**, 2077-2095.

Numerical study of the effect of velocity perturbations on the mechanics of vortex shedding in synchronized bluff-body wakes

S. Balabani[1], E. Konstantinidis[1,2*], C. Liang[3] and G. Papadakis[1]

[1]Department of Mechanical Engineering, King's College London, Strand WC2R 2LS, UK
[2]Department of Engineering and Management of Energy Resources, University of Western Macedonia, Bakola and Sialvera, Kozani 50100, Greece
[3]Department of Mathematics, University of Glasgow, Glasgow G12 8QW, UK

In the present study, we first consider the effect of forced periodic perturbations in the inflow velocity on the mechanics of vortex shedding in the wake of a fixed cylinder by three-dimensional large-eddy simulations. The wake characteristics and the fluctuating forces exerted on the body as well as their phasing are examined as a function of the perturbation/natural wake frequency ratio within the synchronization range. The results agree well with previous experimental findings. We then draw an analogy with different forcing methods such as streamwise and transverse cylinder oscillations. It is shown that some wake response characteristics for these different forcing methods can be unified by considering the perturbations imposed on the relative velocity of the flow vis-à-vis the cylinder as an independent governing parameter instead of the amplitude of cylinder oscillation.

Introduction

The synchronization of vortex shedding from a bluff-body in cross-flow due to periodic external forcing is a well-known phenomenon. Despite similarities noted in numerous studies of synchronized wakes for different forcing methods such as cylinder oscillations in the streamwise or transverse direction, flow or acoustic forcing, etc., there are still some intriguing questions that remain unresolved. For example, the mean drag coefficient increases linearly with amplitude of cylinder oscillation; however, the rate of increase is only 5% for transverse oscillations (Blevins 1990) whereas it can be shown that for streamwise oscillations or equivalent forcing methods it is higher than 30%. Correspondingly, a cylinder oscillating transversely at a non-dimensional amplitude A_y/D = 0.22 (D is the cylinder diameter) results in a decrease of the vortex formation length from 2.6D to 1.2D barely at Re ≈ 1300 (Krisnamoorthy et al 2001) whereas an equivalent streamwise amplitude A_x/D = 0.07 results in a similar decrease from 2.3D to 1.2D at Re = 2150 for flow forcing (Konstantinidis et al. 2003). The above changes occur at a critical excitation frequency that is most efficient in synchronizing the wake fluctuations and appear to be generic features of synchronized wakes associated with modification of the mechanics of vortex shedding. However, why these occur at so different forcing amplitudes for different types of forcing remains unclear. In this paper, we extend the study of synchronized wakes due to periodic fluctuations imposed on the inflow velocity by carrying out large-eddy simulations of the flow about a fixed circular cylinder in order to complement previous experimental work. This approach offers an alternative view of the vortex shedding mechanics that can be used to enhance understanding of synchronized bluff-body wakes.

Computational methodology

For this study, large-eddy simulations of the unsteady flow about a fixed circular cylinder were carried out. The incompressible Navier-Stokes equations were low-pass filtered in space and the resulting equations were solved in a fixed frame of reference. The standard Smagorinsky eddy viscosity model was used for the unresolved scales (C_S = 0.1). A finite-volume method with second order central difference scheme was employed for the spatial discretization on an unstructured collocated grid consisting of 746,688 cells. A second order accurate Crank-Nicholson scheme was employed for time advancement. More details on the numerical scheme and grid independence studies can be found in Liang and Papadakis (2007). The inflow was given a periodic velocity oscillation prescribed by $U(t)=U_m+\Delta u \cdot \sin(2\pi f_e t)$. The computations were carried out for constant mean inflow velocity yielding a Reynolds number of 2580 and for constant amplitude of flow oscillation of 5% of the mean velocity. Two different excitation frequencies were considered within the synchronization range resulting in frequency ratios of f_e/f_o = 1.88 and 2.09 where f_o is the natural frequency of vortex shedding in the unforced wake (computed from simulations). The cylinder length/diameter ratio was $L/D = \pi$ and periodic boundary conditions were employed at the cylinder ends. The extent of the flow domain normal to the cylinder axis was set at 10D with no-slip boundary conditions at the ends in order to emulate the experimental configuration of Konstantinidis et al (2005). At the outflow of the computational domain, a convective boundary condition was employed.

---

[*] Contact e-mail: ekonstantinidis@uowm.gr, efstathios.konstantinidis@kcl.ac.uk

---

Results and discussion

The time traces of the fluctuating forces exerted on the cylinder for both simulations are shown in Fig. 1. The inflow velocity is also shown for reference. Computations start at $t = 0$ from the steady flow solution. After an initial transient of few cycles, the drag $C_D(t)$ and lift $C_L(t)$ coefficients become synchronized with the imposed frequency of inflow perturbation. During the transient, the magnitude of the C_D increases and the fluctuation levels of both C_D and C_L also increase. After the transient, the mean drag coefficient increases by 23% compared to that in steady flow for both cases; this feature will be discussed further below. Most marked is the amplification of the fluctuations in C_D that exhibit a 10-fold increase for both excitation frequencies compared to steady flow levels. Part of this increase can be attributed to the extra inertial forces due to pressure gradients and added mass in accelerating/decelerating flows (Blevins 1990) but this still leaves a substantial increase due to the changes in the fluid force arising from vortex shedding. Correspondingly, C_L fluctuation levels are three times higher than those observed in steady flow for both f_e/f_o values. The very similar response found in both frequency ratios can be understood by the fact that each case lies on either side of a peak response expected in the middle of the synchronization range at $f_e/f_o = 2$ as expected from previous experimental results (Konstantinidis et al 2003) that have shown that the velocity fluctuations in the wake are enhanced and the vortex formation region shrinks in size most markedly in the middle of the synchronization range.

The cycle-to-cycle phase of the fluctuating forces relative to the inflow oscillation was computed from a moving average cross-correlation analysis of the time traces and the results are shown in Fig. 2(a, b). It can be seen that the phases exhibit variations up to 10° about their mean values, i.e., both amplitude and frequency modulations exist in the forces' signature. This finding demonstrates the influence of randomness embedded in the vortex shedding mechanics in turbulent wakes. The importance of the phase of the drag coefficient ϕ_D for the vortex-excited self-sustained streamwise oscillations of flexibly-supported cylinders is that it determines the energy transfer between the fluid and the body (Williamson and Govardhan 2004). It is interesting to note that the variations in the ϕ_D correspond to changes between positive and negative energy transfer for $f_e/f_o = 1.88$. On the other hand, ϕ_D stays below 90° for $f_e/f_o = 2.09$ which implies energy transfer from the cylinder to the fluid.
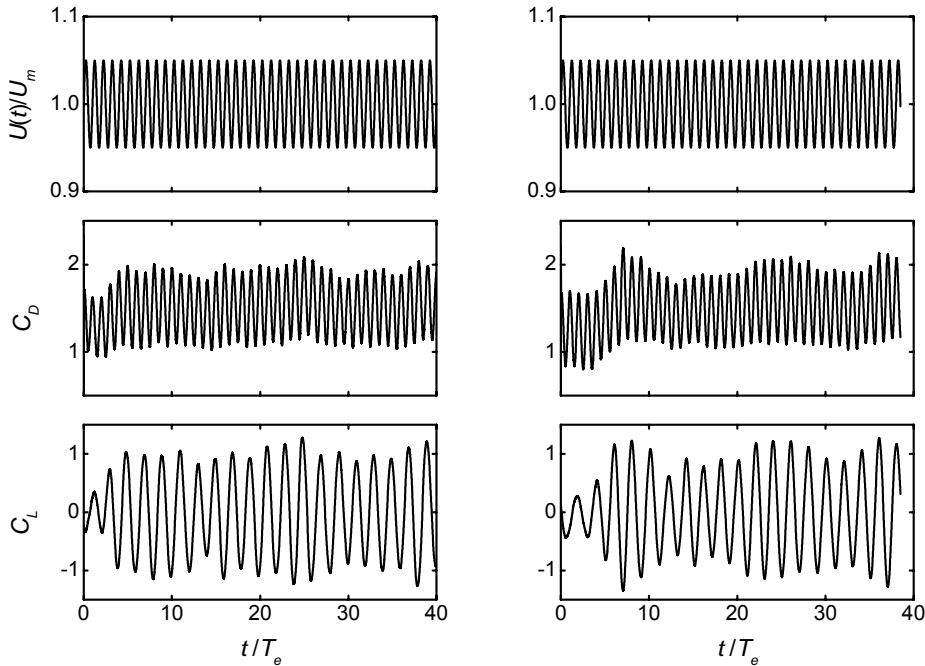

Figure 1. Time traces of the inflow velocity, drag and lift coefficients for $f_e/f_o = 1.88$ (left) and $f_e/f_o = 2.09$ (right).

The phase of the fluctuating forces averaged over the fully-developed part of the simulations (over the final 20 cycles) is shown in Fig. 2(c). Both ϕ_D and ϕ_L show a similar decrease with increasing f_e/f_o. This decrease agrees very well with the previous experimental finding that the phase of vortex shedding is shifted to occur later in the cycle as f_e/f_o increases in the synchronization range (Konstantindis et al 2005). The phasing of vortex shedding inferred from this experimental study is also shown in Fig. 2(c). There is close agreement in the relative change of the phase of the fluctuating forces and that of vortex shedding. Note that ϕ_{lift} is free from inertial effects and therefore can be directly related to changes in the vorticity dynamics in the wake. What is also very interesting is that the difference between ϕ_D and ϕ_L (will be denoted $\Delta\phi$) is very close to that between the phase of the drag and the phase of the vortex lift force $\phi_{Lvortex}$ determined in forced transverse oscillations by Carberry et al (2005); they found that $\Delta\phi$ remains very close to $\approx 40°$ throughout the

synchronization range[1]. Although we have not taken into account the inertial component (apparent mass component in the terminology of Williamson and Govardhan (2004) and Carberry et al (2005)) in order to deduce the phase of the vortex drag force $\phi_{Dvortex}$, it might be noted that this would change the $\Delta\phi$ value by a small amount. In fact, $\phi_D \approx 90°$ for $f_e/f_o = 1.88$ which implies $\phi_{Dvortex} = \phi_D$. Hence, it appears that the phase difference of the vortex lift and drag forces is another generic feature of synchronized bluff-body wakes.
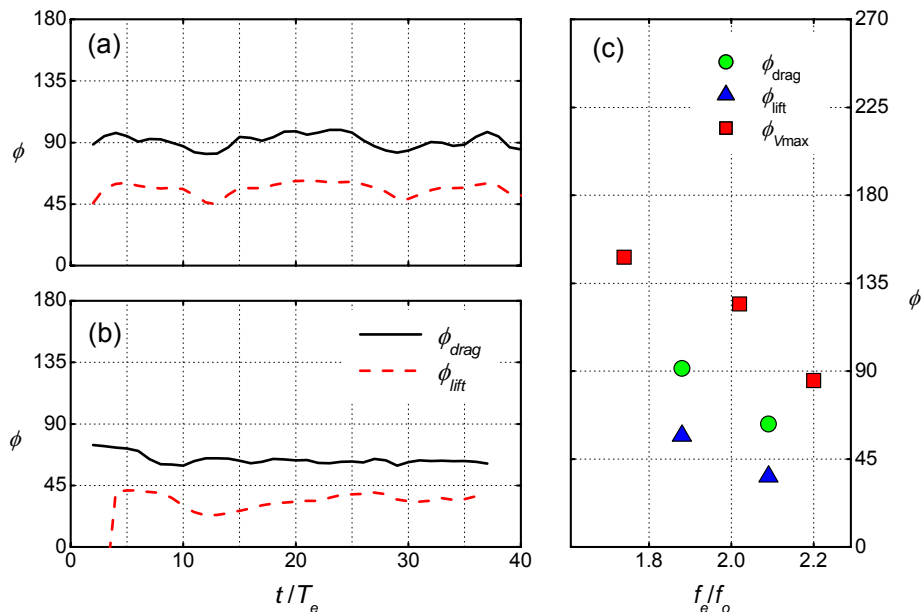

Figure 2 Variation of the phase between the fluctuating forces and the inflow velocity oscillation with non-dimensional time for (a) $f_e/f_o = 1.88$ and (b) $f_e/f_o = 2.09$; (c) the effect of the frequency ratio f_e/f_o on the phase of the fluctuating forces (present results) and the phase of vortex shedding (Konstantinidis et al. 2005).

Figure 3 shows the distribution of the phase-averaged spanwise vorticity at the beginning of the inflow deceleration. Ten instantaneous velocity fields were used to compute each averaged distribution. In order to relate the vortex dynamics in the wake to the forces experienced by the cylinder, the variation of the drag and lift coefficients over an average vortex shedding cycle are also shown in Fig. 3 together with a reference inflow velocity. For $f_e/f_o = 1.88$, a negative clockwise vortex has been shed from the upper side of the cylinder while C_L is minimal and changes to positive from negative values. For $f_e/f_o = 2.09$, the vorticity distribution at the same phase in the forcing cycle corresponds to a phase slightly earlier in the vortex shedding cycle compared to that for $f_e/f_o = 1.88$, i.e. the negative vortex is still loosely connected to its generator. The gradual shift in the phase of vortex shedding agrees well with the corresponding shift in the phase of the forces as shown in Fig. 2(c) and can be inferred from the phase-averaged C_D and C_L variations shown in the lower plots (Fig. 3). Additional simulations are currently carried out at different f_e/f_o values to determine the changes across the entire synchronization range at constant amplitude.

As discussed in the introduction, there is a critical excitation frequency f^* at which the mean drag coefficient exhibits a peak amplification in the synchronization range and Table 1 provides a compilation of recent published data. The ratio f^*/nf_o where $n=2$ for streamwise forcing and $n=1$ for transverse forcing to take into account the fact that the drag fluctuations have a frequency twice that of the lift, appears to be close to unity and the amplification of the mean drag coefficient (C_D) relative to its value without forcing (C_{Do}) is approximately 20-30% for different forcing methods. The ratio f^*/nf_o is less than unity in some cases which requires some clarification but more striking is the difference in the amplitude of forcing - expressed as the ratio of maximum cylinder displacement to its diameter in a steady flow or the equivalent for fixed cylinders – between streamwise and transverse oscillations that produce similar changes; it is an order of magnitude less for streamwise oscillations than for transverse! However, when the same problem is viewed from a different angle, i.e., consider the cylinder to be fixed and the flow to oscillate as in the formulation of the flow configuration in the present study, one finds that the perturbations in the velocity of the flow relative to the fixed cylinder ($\Delta u/U$) are quite close together. This finding demonstrates that the amplitude of velocity perturbations of the flow vis-à-vis the cylinder is a more fundamental parameter to describe the behaviour of synchronized bluff-body wakes than the amplitude of cylinder displacement. The above observation may be a useful step in improving understanding of more complex flow configurations, e.g. combined oscillation of cylinders with two or more degrees of freedom or even vortex-induced vibrations of elastically-supported rigid cylinders.

---

[1] Note that the phase difference $\Delta\phi$ is independent of the reference signal, i.e. cylinder displacement of velocity.

Fifth Conference on Bluff Body Wakes and Vortex-Induced Vibrations (BBVIV 5)
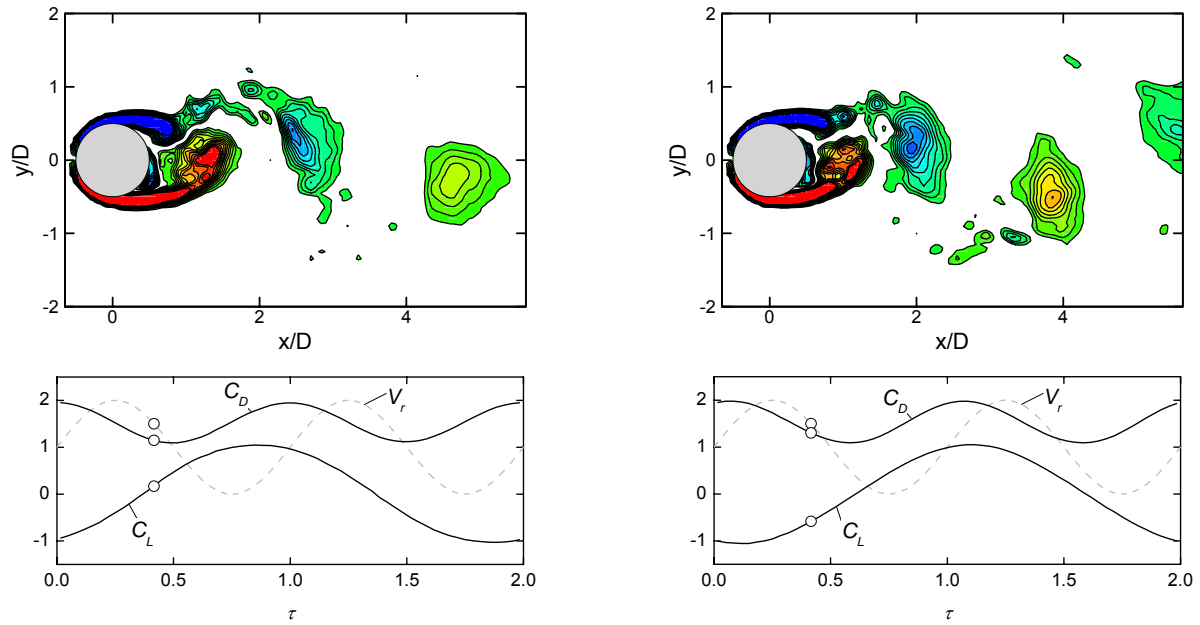Costa do Sauipe, Bahia, Brazil, 12 - 15 December 2007

243

Figure 3 Upper row: phase-averaged patterns of spanwise vorticity distribution at midspan of the cylinder for f_e/f_o = 1.88 (left) and f_e/f_o = 2.09 (right); contour levels: $\omega_z D/U_m$ = ±1.0, ±1.5…±6. The corresponding phase is indicated by circles in the lower row plots that show the variation of the inflow reference velocity $V_r(\tau)$ = 1+sin($2\pi\tau$) and of the phase-averaged forces over two consecutive cycles (= one shedding cycle).

Table 1 Peak mean drag coefficient in the synchronization range.

Study	Perturbation	Re	f^*/nf_o	A/D	$\Delta u/U$	C_D	C_D/C_{Do}
Present	Flow forcing	2580	1.00	0.04	0.05	1.61[a]	1.30
Konstantinidis and Balabani (unpublished data)	Flow forcing	2150	0.99	0.04	0.06	1.34	1.14[b]
Jarza and Podolski (2004)	Flow forcing	3×10^4	0.94	0.03	0.07	1.77	1.27
Nishihara et al (2005)	Streamwise oscillation	1.7×10^4	2.01	0.05	0.12	1.40	1.27
Carberry et al (2005)	Transverse oscillation	2300	0.85	0.40	0.04	1.65	n.a.
Gopalkrishnan (1993)	Transverse oscillation	10^4	0.87	0.30	0.03	1.60	1.35
Dong and Karniadakis (2005)	Transverse oscillation	10^4	1.03	0.30	0.04	1.36	1.22

[a]Estimated from interpolation of LES data to f_e/f_o=2.
[b]Estimated from DPIV wake measurements.

References

Blevins, R.D. (1990) Flow-Induced Vibration, 2nd Edition, Van Nostrand Reinhold, New York.

Carberry, J., Sheridan, J., Rockwell, D. (2005) Controlled oscillations of a cylinder: forces and wake modes. *J. Fluid Mech.* 538, 31–69.

Dong, S., Karniadakis, G. E. (2005) DNS of flow past a stationary and oscillating cylinder at Re = 10,000. *J. Fluids Struct.* 20, 519-531.

Gopalkrishnan, R. (1993) Vortex-induced forces on oscillating bluff cylinders. Ph.D. Thesis, Department of Ocean Engineering, MIT, Cambridge, MA, USA.

Jarza, A., Podolski, M. (2004) Turbulence structure in the vortex formation region behind a circular cylinder in lock-on conditions. Eur. J. Mech. B/Fluids 23, 535–550.

Konstantinidis, E., Balabani, S., Yianneskis, M. (2003) The effect of flow perturbations on the near wake characteristics of a circular cylinder. J. Fluids Struct. 18, 367–386.

Konstantinidis, E., Balabani, S., Yianneskis, M. (2005) The timing of vortex shedding in a cylinder wake imposed by periodic inflow perturbations. J. Fluid Mech. 543, 45–55.

Krishnamoorthy, S., Price, S.J., Païdoussis, M.P. (2001) Cross-flow past an oscillating circular cylinder: synchronization phenomena in the near wake. J. Fluids Struct. 15, 955–980.

Liang, C., Papadakis, G. (2007) Large eddy simulation of pulsating flow over a circular cylinder at subcritical Reynolds number. Comp. Fluids 36, 299–312.

Nishihara, T., Kaneko, S., Watanabe, T. (2005) Characteristics of fluid dynamic forces acting on a circular cylinder oscillated in the streamwise direction and its wake patterns. J. Fluids Struct. 20, 505–518.

Williamson, C.H.K., Govardhan, R. (2004) Vortex-induced vibrations. Ann. Rev. Fluid Mech. 36, 413–455.

Mode switching of a tensioned cable in vortex-induced vibrations using a linear stability approach

R. Violette[a,b], E. de Langre[a], J. Szydlowski[b]

[a] *Département de Mécanique, LadHyX, CNRS – Ecole Polytechnique, 91128 Palaiseau, France*
[b] *Institut Français du Pétrole, 1-4 av de Bois Préau, 92852 Rueil-Malmaison, France*

1. Introduction

Vortex-induced vibration (VIV) is a major concern in regards of fatigue life for offshore structures such as risers. There is a clear need for better understanding of such a phenomena especially in cases of very long slender structures with aspect ratio up to the order 10^3 subjected to depth varying currents. The vortex shedding frequency typically varies linearly with flow velocity assuming constant Strouhal number. In cases of non uniform current this results in different excitation frequencies along the riser which itself has a high modal density. Predicting the modal content of the structure, and thus the riser response with respect to time, in these conditions is quite complex since several vibrations modes can lock-in with the wake (Williamson and Govardhan 2004).

For a tensioned cable subjected to uniform flows, it was experimentally observed that in some cases where the flow velocity is different from the perfect lock-in velocity of a cable vibrations mode, the structure response in time included more than one mode of vibrations (Chaplin et al. 2005). This would suggest that the transition or switch from one locked-on mode to another adjacent is not abrupt, but that there is a velocity range where both modes can exist in the response. We are interested in seeing if this behavior can be reproduced by a linear wake-oscillator model. More precisely, we will use a linear version of the wake-oscillator model developed by Facchinetti et al. (2004b) and Mathelin and de Langre (2005). This non-linear wake-oscillator model was recently validated for long structures in non-uniform flows against DNS computations and experimental results by Violette et al. (2007). Comparisons showed good agreements with both the experimental results and the DNS computations. Figure 1 shows an example of comparison for an infinite tensioned cable subjected to a non-uniform flow. The evolution of displacement with time calculated using a full DNS computation (a) and the one obtained with the non-linear wake-oscillator model (b) are found similar.
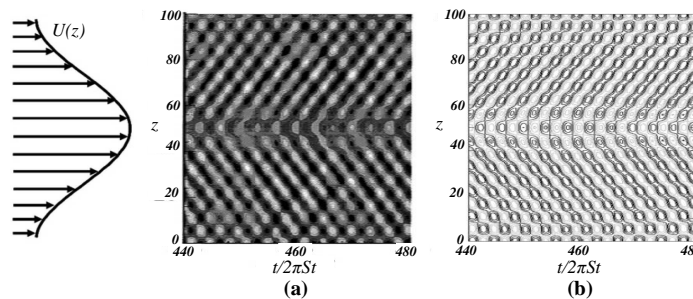

Figure 1 – Infinite tensioned cable under non-uniform flow. Evolution of cable displacement with time and space: (a) DNS prediction (Newman and Karniadakis 1997) and (b) non-linear wake-oscillator model prediction (Violette et al. 2007). In both figures, the displacement level is shown ranging from -0.4 to 0.4 with equally spaced intervals.

2. Linear approach to lock-in

In a recent paper, de Langre (2006) proposed a linear version of the Facchinetti et al. (2004a) VIV prediction model for elastically supported rigid cylinders. Thus, the coupled cylinder/wake dynamic system is formulated in a dimensionless form as

$$\ddot{y} + y = M \left(StUr \right)^2 q$$
$$\ddot{q} + \left(StUr \right)^2 q = A\ddot{y} \quad , \tag{1}$$

where y is the dimensionless cylinder displacement and the wake variable q is the fluctuating lift coefficient $q = 2C_L(t)/C_{L0}$. The term C_{L0} is the fluctuating lift coefficient for a fixed cylinder. The dimensional time and

length are respectively $T = t/\Omega_S$ and $Y = yD$. The parameter Ω_S is the free oscillations pulsation of the cylinder in stagnant water and D is its diameter. In (1) St is the Strouhal number and Ur is the reduced velocity. The coupling parameter M and A are described in details in Facchinetti et al. (2004a). By modal analysis of the coupled linear system (1), one can compute the natural frequency of the system and the growth rate as a function of the reduced velocity Ur. This is showed on Figure 2.

It can be seen that for low Ur, the system possess two natural frequency, one for the solid mode and one for the wake mode. These two frequencies coincide for a certain range of reduced velocities before diverging again at a high Ur. In the range of coinciding frequency, there is a positive growth rate which means that the system is unstable. This instability is referred to as coupled-mode flutter instability. Also plotted on Figure 2 (top) is the frequency prediction of the non linear system. One can observe that the lock-in range and the linear instability range coincide very well. Lock-in can be interpreted as a coupled-mode flutter instability between two coupled linear oscillators (see also Nakamura 1969).

3. Mode switching prediction

We try here to compare the frequency response, or modal response, obtained by the full non-linear wake oscillator model and the linear model in the case of a tensioned cable. The mass ratio used here is taken small ($\mu = 1.785$) in order to get lock-in range overlap. The mass ratio is defined as $(m_{cyl}+m_{fluid})/\rho D^2$ where m_{cyl} and m_{fluid} are the mass per unit length of the cylinder and fluid added mass respectively and ρ is the fluid density. For a tensioned cable, the system (1) is rewritten

Figure 2 – Linear prediction for oscillations frequency (upper figure) and growth rate (lower figure) as a function of the reduced velocity (circle dots). Also shown on the figure is the oscillations frequency predicted by the non-linear model as a function of Ur (solid line).

$$\ddot{y} - \lambda y'' = M\left(StUr\right)^2 q$$
$$\ddot{q} + \left(StUr\right)^2 q = A\ddot{y} \qquad , \qquad (2)$$

where $\lambda = \Lambda/\pi$ and Λ is the aspect ratio of the cable. The reduced velocity is referred here with respect to the first mode frequency. In the linear model, the second derivative with respect to the spanwise direction z in eq. (2) is expended using finite differences method. Thus, for n computation points on the cable, we have $2n$ linear coupled oscillators. The modal analysis is the same as in Section 2. Depending on the reduced velocity Ur studied, we find a number of unstable vibrations modes, i.e. modes with a positive growth rate. We plot the frequency of the two most unstable ones with respect to their growth rate as a function of Ur, Figure 3a. Shown on Figure 3b are the growth rates of the two most unstable vibrations modes of the system as a function of Ur. For the same range of Ur, we performed non-linear computations using the full non-linear wake oscillator model. For each non-linear computation random values of q on each point of order 10^{-3} are used as initial conditions. Oscillations frequency is derived from the evolution of displacement with time using Fourier analysis. Those oscillations frequency predictions are compared on Figure 3a with the linear model results.
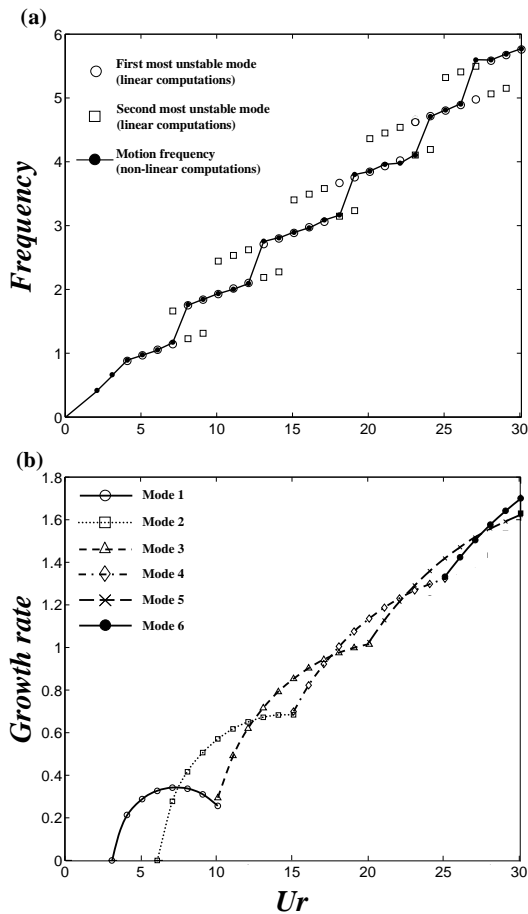
(a)

(b)

Figure 3 – (a) Frequency evolution with reduced velocity for both linear (open signs) and non-linear model solid signs. For the linear model, circles represent the natural frequency of the most unstable and squares are for the second most unstable mode, (b) vibrations modes growth rates obtained by the linear model.
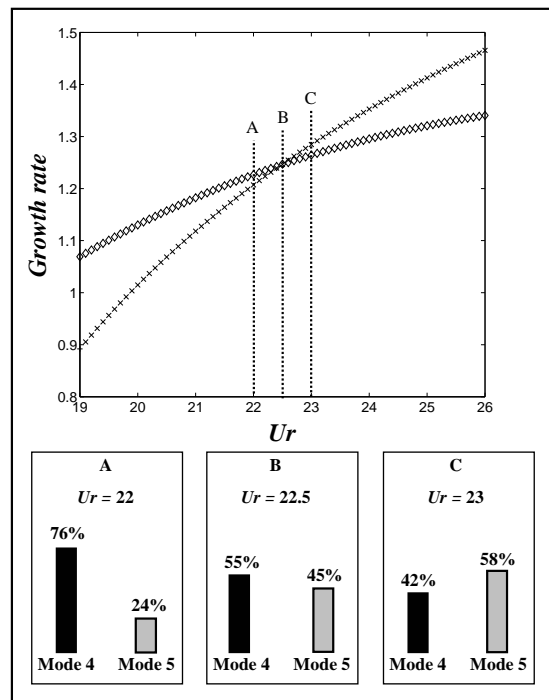

Figure 4 – Transition from Mode four response to Mode five response: (top) growth rate evolution of Mode four (diamond) and Mode five (cross) obtained with the linear model, (Bottom) percentage of occurrence for Mode four and five as dominating modes in the non-linear model statistical study.

Figure 3a shows that there is a good agreement between the predictions of the linear and the non-linear model: the oscillations frequencies predicted by the non-linear model almost always follow the ones of the most unstable mode obtained by the linear model. Thus, the switches or jumps from one mode of vibrations to another predicted by both models are similar. The jumps from one vibrations mode to the other can also be analysed in terms of the growth rates obtained by the linear model, Figure 3b. We can observe that the reduced velocities for which a switch of the mode occurs corresponds to a crossing of growth rate curves. For example, the non-linear model predicts a switch from Mode 2 to Mode 3 at a reduced velocity between 12 and 13. The linear growth rate curves for Mode 2 (open squares) and Mode 3 (open triangles) cross each other around a reduced velocity of 12.5.

We now focus on three cases with slightly different reduced velocities, $Ur = 22$, 22.5 and 23. On Figure 3b, we can see that the growth rate curves of Mode 4 and Mode 5 cross at about $Ur = 22.5$ meaning a mode switch for the cable. For all three studied reduced velocities, we performed 200 independent computations using the full non-linear wake-oscillator model and computed the frequency of the response in the permanent regime. The statistical results appear on Figure 4 (bottom). Also shown on Figure 4 (top) is a zoom on the growth rate curves of Mode 4 and Mode 5. We can observe on Figure 4 that for $Ur = 22.5$, where both growth rates are almost equal, the occurrence of both modes is split in the 200 responses. A slight difference in the growth rates favours significantly the most unstable mode as seen for the case of $Ur = 22$ and 23.

4. Concluding remarks

The numerical results presented here show that for a tensioned cable subjected to uniform cross flow:

(a) the frequency of VIV predicted by a full non-linear wake oscillator model (validated against DNS) can be predicted by a simple linear model computation;

(b) mode switching can be interpreted as a result of crossing of linearly predicted growth rates between modes;

(c) when performing a large number of computations, a small difference in linearly predicted growth rate results in large changes in occurrence of a given vibrations mode in the non-linear wake oscillator predictions.

4. Reference

Chaplin J.R., Bearman P.W, Huera Huarte F.J., Pettenden R.J. 2005. Laboratory measurements of vortex-induced vibrations of a vertical tension riser in a stepped current. Journal of Fluids and Structures; 21: 3-24.

Facchinetti ML, de Langre E, Biolley F. 2004a. Coupling of structure and wake oscillators in vortex-induced vibrations. Journal of Fluids and Structures; 19: 123-140.

Facchinetti ML, de Langre E, Biolley F. 2004b. Vortex-induced travelling waves along a cable. European Journal of Mechanics B/Fluids; 23: 199-208.

de Langre E. 2006. Frequency Lock-in is caused by a coupled-mode flutter. Journal of Fluids and Structures;22:783-791.

Mathelin L, de Langre E. 2005. Vortex-induced vibrations and waves under shear flow with a wake oscillator model. European Journal of Mechanics B/Fluids; 24: 478-490.

Nakamura Y., 1969. Vortex excitation of a circular cylinder treated as a binary flutter. Reports of Research Institute for Applied Mechanics; 17: 217-234. Kyushu University, Fukuoka, Japon

Williamson CHK, Govardhan R. 2004. Vortex-Induced Vibrations. Annual Review of Fluid Mechanics; 413-455.

Violette R, de Langre E, Szydlowski J. 2007. Computation of vortex-induced vibrations of long structures using a wake oscillator model: Comparison with DNS and experiments. Computers and Structures; 85: 1134-1141

Properties of Vortex-induced Vibration of *B/D*=2 Rectangular Cylinder under Slow Change of Wind Speed

F. Nagao*, M. Noda*, A. Iwata**, H. Utsunomiya*

* Department of Civil and Environmental Engineering, The University of Tokushima
** Yokogawa Techno-Information Service Inc.
E-mail fumi@ce.tokushima-u.ac.jp

1. INTRODUCTION

A lot of investigations in concerning to the effects of turbulence of flows on the vortex-induced vibration of bluff bodies have been carried out. However, the effect of the slow change of mean flow speed without any turbulence on the vortex-induced vibrations was not focused on. Properties of the vortex-induced vibration of a box girder bridge deck in sinusoidal wind with very long period were investigated by Utsunomiya, et al [1], in which the effects of slow change of wind speed on the response were observed and quasi-steady forces were not applicable to the vortex-induced vibration in the slowly fluctuating wind even if the change rate of wind speed was extremely slow. Furthermore, the effects of slow change of wind speed on the vortex-induced vibration of basic cross sections, such as circular section and rectangular section with side ratio, *B/D*=2 were also experimentally investigated by authors [2,3].

In the paper, the effects of slow change of wind speed on the vortex-induced vibration of *B/D*=2 rectangular cylinder are experimentally examined under an actively controlled wind tunnel where the fluctuating period of wind speed, *T'*, is one hundred and eighty times longer than the natural period of model, T_o, that is, $T'=180*T_o$. In particular, unsteady aerodynamic forces acting on the section in long period fluctuating wind speed were measured by forced oscillation method.

2. EXPERIMENTAL PROCEDURES

The wind tunnel used here is 1.5m high, 1m wide and 4m long. A fan of the wind tunnel is driven by a D.C. motor. The slow fluctuating wind speed was operated by the control of the driving voltage for a thyristor control unit, where the operating voltage was controlled by a personal computer. For simplicity, the sinusoidal fluctuating wind speed as given in Eq. 1 was used for the long period fluctuation of wind speed.

$$V(t) = U(t)/f_nD = V_c + \Delta V \sin(2\pi t/T') \tag{1}$$

where, V_c is central value of fluctuating reduced wind speed (mean wind speed), ΔV is amplitude of the fluctuating wind speed, D is depth of the rectangular cylinder, f_n is natural frequency of the model, *T'* is period of the fluctuating wind speed. The amplitude of fluctuating wind speed, ΔV, is selected from $0.1*\Delta V/\Delta V_{width}$ to $0.4*\Delta V/\Delta V_{width}$, *where,* ΔV_{width} is the wind speed region of the vortex-induced vibration in uniform flow, as shown in Fig. 1, and ΔV_{width} is 3.25 in this study.

In order to reproduce the complex response properties into the forced oscillation procedure, a new forced oscillation system was made by A.C. servomotor, where the vibration amplitude of model was able to change with the time.

3. RESPONSES IN SLOW FLUCTUATING FLOW

Fig. 2 shows an example of the heaving response of the vortex-induced vibration in the slowly fluctuating flow for V_c=4.5, $\Delta V/V_{width}$=0.3. The time records of the slow fluctuating reduced wind speed, *U/fD*, and the heaving response of model, $2\eta/D$, are shown in Figs. 2 (a) and (b), respectively. These time trajectories form a lissajous curve as given in Fig. 2 (c), where the response curve in the uniform flow was given by solid line. The envelope of the response of the *B/D*=2 rectangular section in the sinusoidal wind speed fluctuation is also synchronized with the same period of the fluctuating wind. However, phase lag between the fluctuating wind and the envelope curve of response exists. That is, the wind speed for the maximum response in the slowly fluctuating wind is usually different from that in the uniform flow as shown in Fig. 2 (c). The maximum response in the fluctuating wind is smaller than that in the uniform flow under the same wind speed region given in the dashed lines in Fig. 2 (c).

Fig. 3 shows the effects of the central speed of the slowly fluctuating wind on the responses of vortex-induced vibrations, where the amplitude of slowly
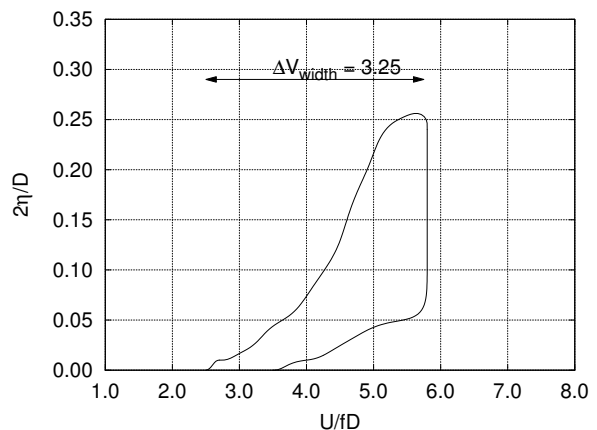

Fig. 1 Response of B/D=2 Rectangular cylinder in Uniform Flow

fluctuating wind is fixed to $\Delta V/\Delta V_{width}$=0.3. The rotary directions of lissajous curves of the responses differ with the change of the central speed. The rotary direction of the lissajous curves is related to the unsteady aerodynamic forces acting on the model, that is, if the excitation forces are acted in the higher wind speed region beyond the central speed, the lissajous curve draws a counter clockwise direction because response is developed in the higher wind speed region. On the contrary, if the excitation forces are given in the region lower than the central speed, the responses increase in lower wind speed region and decrease in higher wind speed region, therefore, the lissajous curve follows clockwise. Moreover, if the damping forces act in the both sides of the central speed, where exciting forces are obtained, the lissajous curve shows the superimposed figure for the preceding patterns, that is, it looked like the shape of infinity, ∞. It should be noted that the vortex-induced oscillations in the slowly fluctuating flow still exist beyond the vortex-induced vibration region for the uniform flow. The large responses in the higher wind speeds are observed where the vortex-induced vibration had disappeared under the uniform flow condition. As well as the higher speed region, the response also appears at lower speed region where the small amplitudes of responses are measured in the uniform flow.

The effects of the amplitude of the slow fluctuating speed at the center wind speed, V_c=4.5 and 5.25 on responses are summarized in Figs. 4 (a) and 4 (b), respectively. For the V_c=4.5, the increase of the amplitude of the fluctuating wind speed induces the increase of amplitudes of the responses. On the contrary, the increase of the amplitude of the fluctuating wind speed at V_c=5.25 decreases the amplitudes of the responses, as given in Fig. 4(b). These relations are also related to the unsteady aerodynamic forces acting on the model.

4. UNSTEADY AERODYNAMIC PROPERTIES

In order to clarify the effect of slow change of wind speed and response amplitude on unsteady aerodynamic properties, three kinds of forced oscillation procedure were developed as shown in Fig. 5,where the central wind speed, Vc is 4.5 and the amplitude of fluctuating wind speed, $\Delta V/\Delta V_{width}$, is 0.4. First pattern is
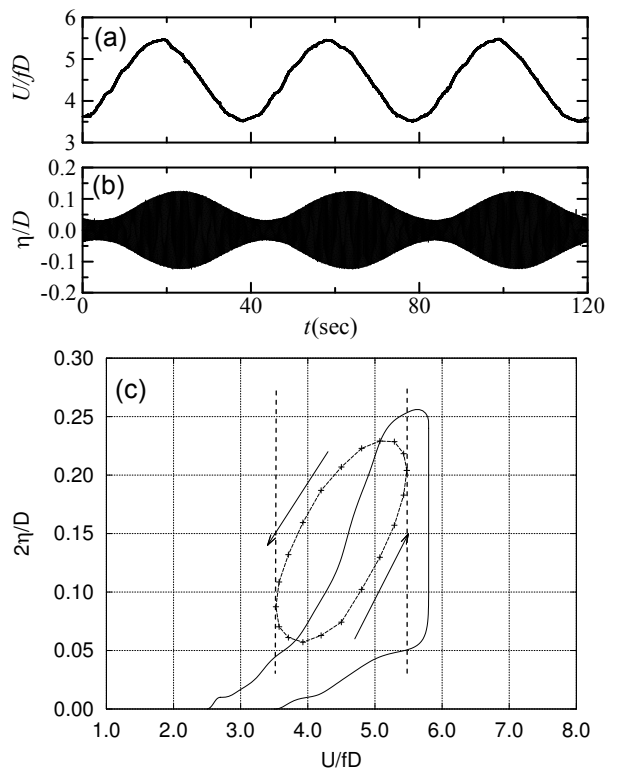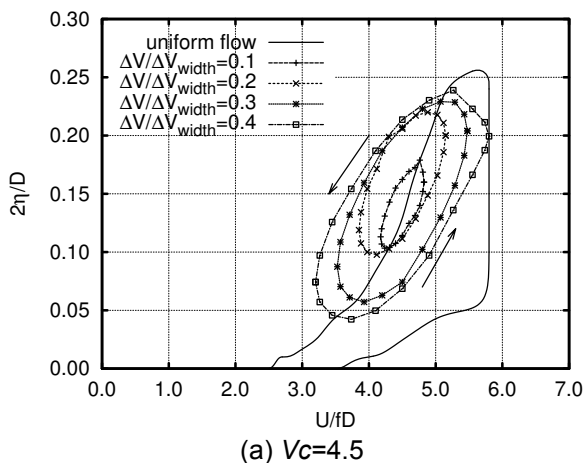

Fig. 2 Records of slow fluctuating wind speed and heaving response and their lissajous curve, $\Delta V/\Delta Vwidth$=0.3, Vm=4.5.
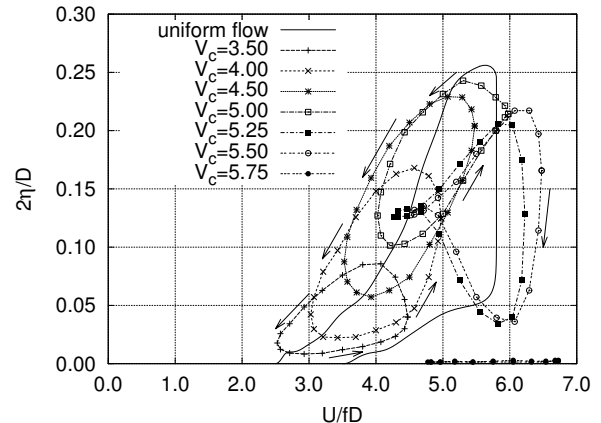

Fig. 3 Effects of central wind speed with $\Delta V/\Delta Vwidth$=0.3,on the responses.
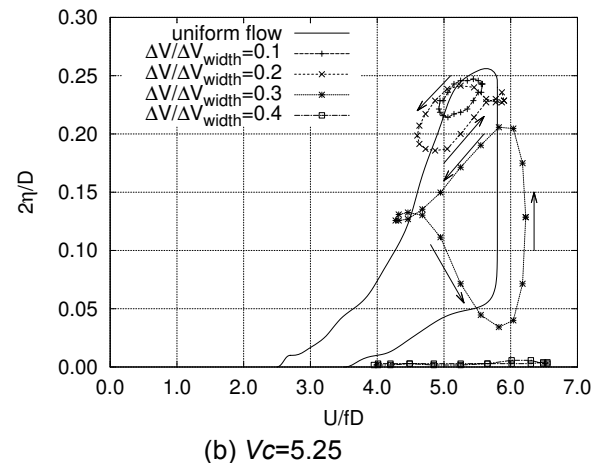

(a) Vc=4.5   (b) Vc=5.25

Fig. 4   Responses of B/D=2 Rectangular cylinder in different amplitudes of slow fluctuating wind speed.

that the wind speed and the heaving amplitude are slowly changed following the lissajous curve of model response in free vibration experiment and this case is called FV-FA. The second one is that the response amplitude is slowly changed however the wind speed is fixed to the central wind speed, (SV-FA). The Third one is that the wind speed is slowly changed and the heaving amplitude is fixed to the average response amplitude, (FV-SA). The unsteady aerodynamic properties were measured at the cross points of FV-FA and SV-FA (Points A and C) and at the cross points of FV-FA and FV-SA (Points B and D). In the conditions for the steady amplitude of response (SA) and the steady wind speed (SV), these points encounter two times in one fluctuation period of the wind speed or the amplitude of response, the data that coincide with the movement direction of FV-FA at these points are used here as given in Table 1.

Fig. 6 shows unsteady pressure properties, (a) Cp; mean pressure coefficients, (b) Cp'; magnitude of fluctuating pressure coefficients, (c) φ; phase lags between displacement and fluctuating pressures and (d) $Wp=Cp'\sin\varphi$; work of unsteady pressures, on the side surface of the model at Points A and C, respectively. From the comparison of Cp at Point A as shown in Fig. 6(a), mean pressures is recovered under the slow decrease of wind speed, $dV/dt<0$. On the other hand, at the Point C, the slow increasing wind speed, $dV/dt>0$, induces larger suction. For larger amplitude, at Point A, separated shear flow would reattach on the side surface near trailing
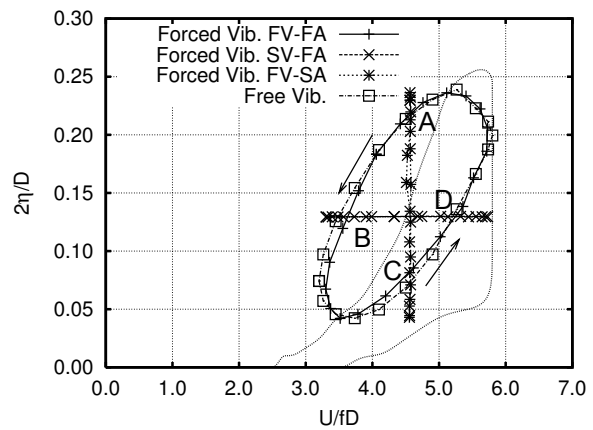

Fig. 5 Forced oscillation patterns and measuring points.

Table 1 Change of wind speed and heaving amplitude at measuring points

Point	dV/dt	$d\eta/dt$
A(FV-FA)	<0	<0
A(SV-FA)	=0	<0
B(FV-FA)	<0	<0
B(FV-SA)	<0	=0
C(FV-FA)	>0	>0
C(SV-FA)	=0	>0
D(FV-FA)	>0	>0
D(FV-SA)	>0	=0

edge, where the recovery of Cp is remarkable. From Fig. 6(b), the distribution of Cp' strongly depended on the heaving amplitude, which mainly controls the reattachment of separated flow. The slow change of wind speed has little effect on Cp', even though the slow decrease of wind speed, $dV/dt<0$, reduces Cp' slightly. As shown in Fig. 6(c), the slow change of wind speed sifts the phase lags toward the same direction of wind speed change, that is, if the wind speed decreases, the phase lags also decrease, in other word, the speed of vortex along side surface is delayed. On the contrary, the increase of wind speed induces the increase of phase lags, therefore the speed of vortex along side surface is accelerated. The distribution of work of unsteady pressures is shown in Fig. 6(d), where the slow decrease of wind speed, $dV/dt<0$, at Point A, reduces the exciting force on leeward half surface and the distribution of work for the slow increasing wind speed, $dV/dt>0$, at Point C, looks like a parallel translation of that for steady state wind speed toward the downstream.

The effects of the change of heaving amplitude of response on pressure properties are summarized in Fig. 7, where the effects of $d\eta/dt<0$ are obtained at Point B and those of $d\eta/dt>0$ are measured at Point D, respectively. From Fig. 7, it is apparent that all pressure properties with and without slow change of heaving amplitude are similar to each other, therefore, the effect of the slow change of heaving amplitude on pressure properties is almost negligible.

5. CONCLUSIONS

The effects of a long-period fluctuation of wind speed on the heaving vortex-induced vibration of B/D=2 rectangular cylinder were experimentally investigated. Following results were obtained.
(1) In the sinusoidal speed fluctuation with very long period, T', where $T'=180*To$, the amplitude of the vortex-induced vibration of model was also periodically varied with the same period of wind speed fluctuation. Beyond the region of vortex-induced vibration for the uniform flow, the response was still existed in the fluctuating flow.
(2) The speed of vortex along side surface, which mainly controls aerodynamic forces, was changed by the slow change of wind speed, dV/dt. However the change of response amplitude, $d\eta/dt$, had little effect on the unsteady aerodynamic forces.

References
1) Utsunomiya, H., Nagao, F., Noda, M. and Tanaka, E.,(2001). "Vortex-induced Oscillation of a Bridge in Slowly Fluctuating Wind", J. Wind Eng. & Ind. Aerodyn, Vol. 89, pp. 1689-1699.
2) Noda, M., Utsunomiya, H., Nagao, F., Arima, E. and Morita, T.,(2004). "Effects of Long-Period Fluctuation on the Response of Vortex-induced Oscillation ", J. Structural Eng., Vol. 50A, pp. 629-636 (in Japanese).
3) Nagao, F., Noda, M., Arima, E. and Utsunomiya, H.,(2005). "Vortex-Induced Vibration of a Circular Pile in Slowly Fluctuating Tidal Current", Proc. 15th Int. Offshore and Polar Eng. Conf., Seoul, Korea, pp.220-225.
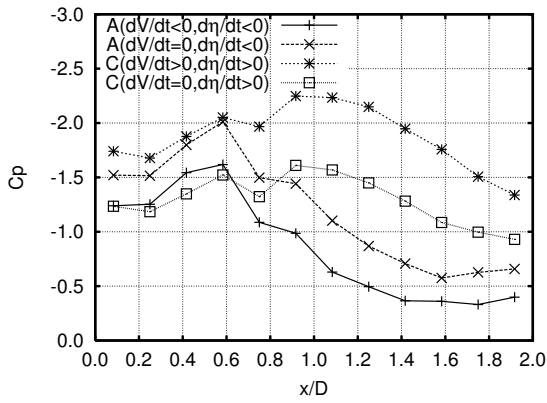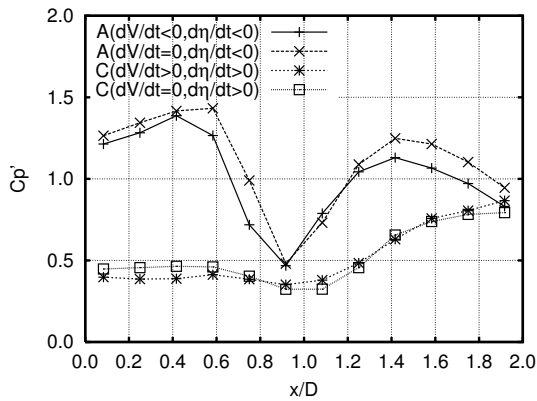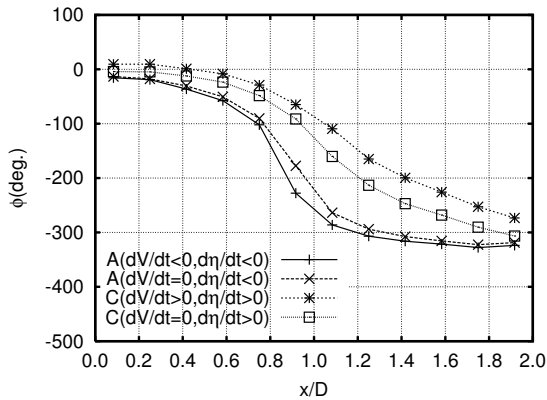
Fifth Conference on Bluff Body Wakes and Vortex-Induced Vibrations (BBVIV 5)
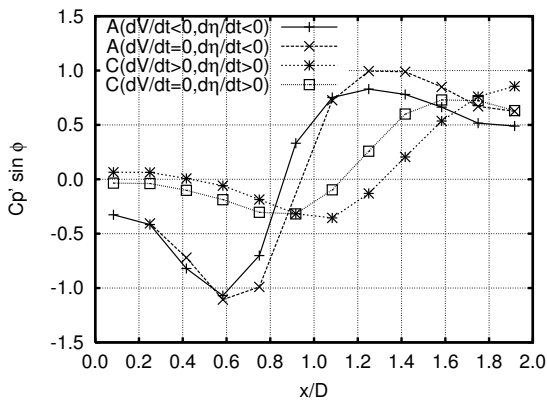Costa do Sauipe, Bahia, Brazil, 12 - 15 December 2007

251

(a) Coefficients of mean pressures

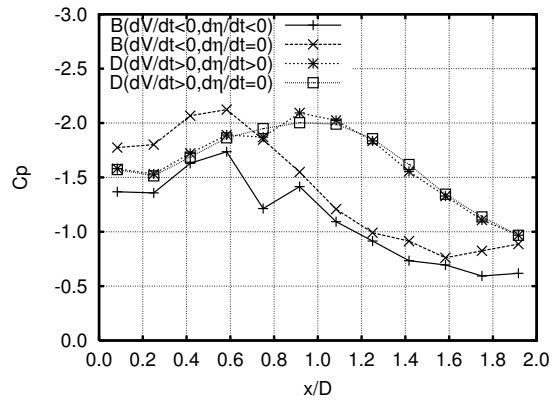(b) Magnitude of fluctuating pressure coefficients

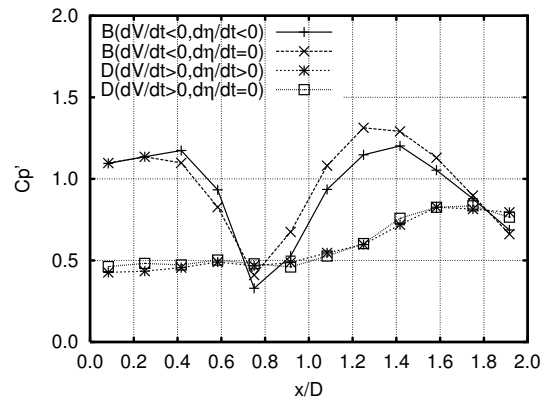(c) Phase lags between fluctuating pressures and displacement of model
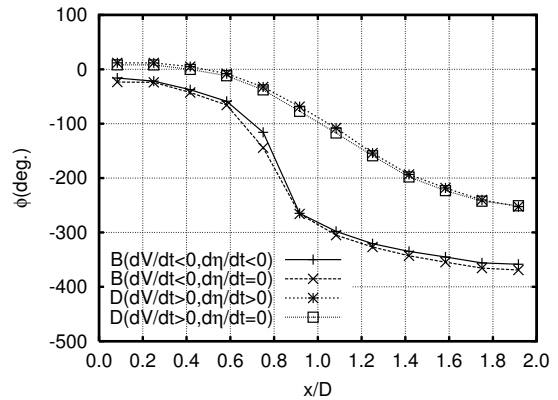
(d) Work of unsteady pressures

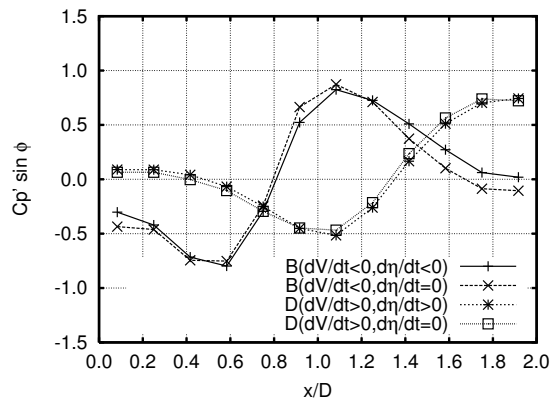Fig. 6　Unsteady pressure properties at Points A and C

(a) Coefficients of mean pressures

(b) Magnitude of fluctuating pressure coefficients

(c) Phase lags between fluctuating pressures and displacement of model

(d) Work of unsteady pressures

Fig. 6　Unsteady pressure properties at Points B and D

Forced wake development caused by fluid, body and free-surface interaction

Serpil Kocabiyik[1], Oleg I. Gubanov[2], Larisa A. Mironova[1]

(serpil@math.mun.ca, oleg@cim.mcgill.ca, larisa@math.mun.ca)

[1] Department of Mathematics and Statistics, Memorial University of Newfoundland,

St. John's, Newfoundland, Canada

[2] Department of Mechanical Engineering, McGill University, Montreal, QC, Canada

The interaction of a free surface wave motion with moving cylindrical bodies has been principally the subject of experimental investigations (see e.g., Sheridan *et al.* (1997), Cetiner and Rockwell (2001), Carberry (2002)). Computations of nonlinear viscous free surface problems including cylindrical bodies are relatively few (see e.g., Reichl *et al.* (2005)). The present study investigates the problem of unsteady flow of a viscous incompressible fluid past a transversely oscillating circular cylinder in the presence of a free surface numerically at a Reynolds number of $R = 200$. The effects of the free surface presence at a submergence depth of $h = 1.25$ are investigated on the near wake structure as well as the fluid forces acting on the cylinder. Calculations are performed at a fixed displacement amplitude of $A = 0.5$ in forcing frequency-to-natural shedding frequency ratio range $0.95 \leq f/f_0 \leq 4$.

Computational flow model and methodology

The upstream uniform flow velocity is U and the cylinder is submerged a distance, h^*, below the position of the undisturbed horizontal free surface. The diameter of the cylinder is d. The characteristic length and velocity scales are taken to be the cylinder diameter, d, and free stream velocity, U, respectively. The dimensionless parameters are the Reynolds number, $R = Ud/\nu$, where ν is the kinematic viscosity of the fluid; the amplitude of the cylinder oscillation, $A = A^*/d$; the frequency ratio, f/f_0, with $f = df^*/U$ and $f_0 = df_0^*/U$ being the dimensionless forcing frequency of the cylinder oscillation and the natural vortex shedding; $Fr = U/\sqrt{dg}$, where g is the acceleration due to gravity. Here, A^* is the dimensional amplitude of the cylinder oscillation, f^* is the dimensional forcing frequency of an oscillating cylinder and f_0^* is the dimensional natural vortex shedding frequency of a stationary cylinder, and h^* is the dimensional submergence depth. The cylinder is initially at rest in a uniform flow with velocity U and then, at time $t = 0$, the cylinder starts to perform transverse oscillations described by $y(t) = -A\cos(2\pi ft)$. Here, $y(t)$ is the dimensionless displacement of cylinder and $t = Ut^*/d$ is the dimensionless time. The dimensionless period of the cylinder oscillation, T, is defined as $T = 1/f$. For transverse oscillations the range near $f/f_0 \approx 1.0$ constitutes the fundamental *lock-on* regime. The fluid flow governed by the full Navier-Stokes equations is only modeled within a two-dimensional computational domain. The motion of the air is neglected and the effect of the ambient pressure exerted on the fluid by the air

is taken into consideration to state the free surface boundary conditions. The governing equations are

$$\frac{d}{dt} \int_{\mathbb{V}} \mathrm{d}V + \int_{\mathbb{A}} \underline{n} \cdot \underline{u} \, \mathrm{d}S = 0,$$

$$\frac{d}{dt} \int_{\mathbb{V}} u \, \mathrm{d}V + \int_{\mathbb{A}} u \left(\underline{n} \cdot \underline{u} \right) \mathrm{d}S = - \int_{\mathbb{A} \cup \mathbb{I}} p \, n_x \, \mathrm{d}S + \frac{1}{R} \int_{\mathbb{A} \cup \mathbb{I}} \underline{n} \cdot \nabla u \, \mathrm{d}S,$$

$$\frac{d}{dt} \int_{\mathbb{V}} v \, \mathrm{d}V + \int_{\mathbb{A}} v \left(\underline{n} \cdot \underline{u} \right) \mathrm{d}S = - \int_{\mathbb{A} \cup \mathbb{I}} p \, n_y \, \mathrm{d}S + \frac{1}{R} \int_{\mathbb{A} \cup \mathbb{I}} \underline{n} \cdot \nabla v \, \mathrm{d}S + \int_{\mathbb{V}} \left(\frac{1}{Fr^2} - 4A\pi^2 f^2 \cos\left(2\pi ft\right) \right) \mathrm{d}V,$$

where $\underline{u} = (u, v, 0)$ is the velocity vector; $\underline{n}$ is the outward normal to the computational cell boundary; $\mathbb{V}$ and $\mathbb{A}$ are the fractional volume and area open to flow, respectively; $\mathbb{I}$ is a part of fluid interface open to flow. Here, special integral form of governing equations can be derived by extending the Reynolds transport theorem and then applying it to control volume containing fluid interface (see Gubanov (2006)). At the solid boundary, the no-slip boundary condition for a viscous fluid, $\underline{u} = \underline{u}_{\text{body}}$, is applied. Free surface boundary conditions are the tangential and normal surface forces, namely

$$\frac{\partial u_n}{\partial \underline{\tau}} + \frac{\partial u_\tau}{\partial \underline{n}} = 0 \quad \text{and} \quad p - p_0 = 0 \quad \text{at the free surface}$$

where p_0 is the atmospheric air pressure, u_τ and u_n denote the tangential and normal velocity components. Surface tension is neglected since a class of flows in which gravitational force plays a more important role than the surface tension is considered. The method of solution is based on a finite volume discretization of the unsteady continuity and the Navier-Stokes equations in their pressure-velocity formulation on a fixed Cartesian grid. The combined volume of fluid and fractional area/volume obstacle representation method due to Hirt and Nichols (1981) and Hirt and Sicilian (1985), and the cut cell method due to Gerrits (2001) are employed to track fluid-air and fluid-body interfaces. Well-posed open boundary conditions due to Gresho and Sani (1998) are applied at the outflow part of the computational domain. A sparse linear system in pressure and velocity components is solved by using the generalized minimal residual method with ILUT preconditioner to advance the simulation of unsteady flow in time.

Validation and results

Several test cases have been calculated using the present approach. The results compare well with other experimental and numerical data. The special case of uniform flow past a stationary horizontal circular cylinder in the presence of a free surface is calculated at the Reynolds number R of 180 in the range of Froude numbers $0 \leq Fr \leq 0.4$ when the depth of cylinder submergence, h/d, is 0.55. Figure 1 shows a comparison between the equi-vorticity plots obtained in the present study and those obtained by Reichl *et al.* (2005). Reichl *et al.* use the commercial CFD software package FLUENT to solve a two-phase fluid flow model. This flow solver is developed using the finite volume method on structured, boundary fitted grid. Bearing in mind that Reichl *et al.* did not use the flow model and methodology as those used in the present work, there is a good qualitative agreement between the results. The numerical simulations are conducted at a Reynolds number of R = 200 for a fixed sub-
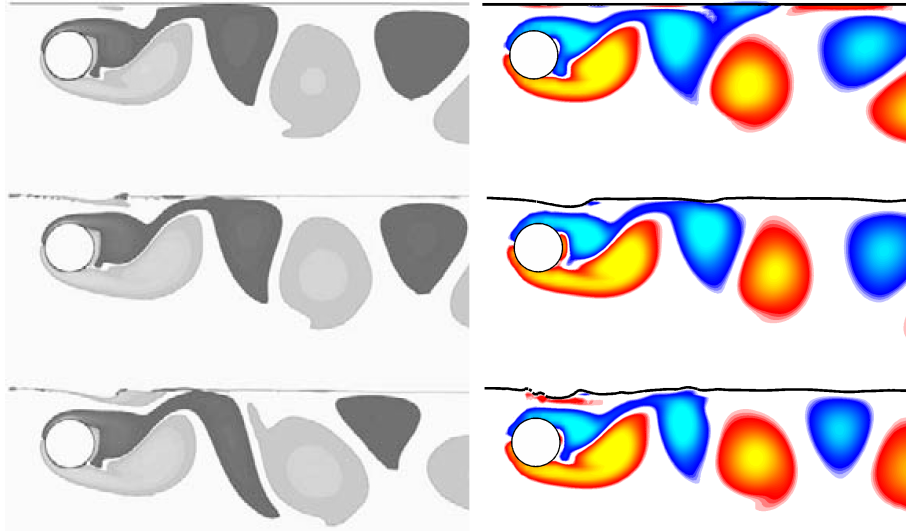
Figure 1: Comparison of the equi-vorticity patterns for the uniform flow past a stationary cylinder in the presence of a free surface at $R = 180$ and $h = 0.55$: $Fr = 0$ (top), $Fr = 0.3$ (middle), $Fr = 0.4$ (bottom): Reichl *et al.* (2005) (left), present (right).

mergence depth, $h = 1.25$, and displacement amplitudes $A = 0.25$ and 0.5 in the frequency ratio range $0.95 \leqslant f/f_0 \leqslant 4.0$. Tables 1 summarize the combined effect of the free surface presence at $h = 1.25$ and f/f_0 on the vortex shedding modes, fluctuating fluid forces, C_L and C_D, and their periods. Table 1 displays the results obtained in the presence of a free surface

f/f_0	Mode	Period of C_L and modes	Period of C_D	C_L and $y(t)$ phase locking	C_D and $y(t)$ phase locking
0.95	**2S**	1T	1T	locked	locked
1.0	**2S**	1T	1T	locked	locked
2.0	**C(4S)**	5T	2T	quasi-locked	quasi-locked
3.0	**C(2S)**	3T	3T	quasi-locked	quasi-locked
4.0	**C(4S)**	4T	3T	quasi-locked	quasi-locked

Table 1: The vortex shedding modes and the phase-locking phenomena between forces and cylinder displacement for R = 200, $A = 0.5$ and $h = 1.25$: $0.95 \leqslant f/f_0 \leqslant 4.0$.

($h = 1.25$) on the shedding modes. The vortex formation modes are categorized using the terminology of Williamson and Roshko (1988). For low frequency ratios, $f/f_0 = 0.95$ and 1.0, the classical Kármán vortex pattern (**2S** mode) occurs per one cycle of cylinder oscillation, T, which confirms experimental findings of Carberry *et al.* (2001). The corresponding power spectrum density of each C_L confirms that the vortex shedding mode period is T at these low frequency ratios when $h = 1.25$. It is interesting to note that the effect of free surface presence at $h = 1.25$ seems to be the period doubling in C_D behaviour for the two frequency ratios $f/f_0 = 0.95$ and 1.0. As a result of increasing f/f_0 from 1.0 to 4.0 the near wake vorticity breaks up to produce different modes of vortex shedding: **2S** per T, **C(4S)**

per $5T$, **C(2S)** per $3T$ and **C(4S)** per $4T$ when $h = 1.25$. In the vortex shedding mode **C(2S)**, per $3T$, the cylinder alternatively sheds a single vortex from each side over $3T$, in which the development of each vortex is a result of coalescence of two weak vortices in the shear layer. Similarly, in the vortex shedding modes **C(4S)**, per $4T$, and **C(4S)**, per $5T$, the cylinder alternatively sheds a single vortex from each side over $4T$ and $5T$, respectively, in which the development of each vortex is a result of coalescence of two weak vortices in the shear layer. Table 1 shows that, at $f/f_0 = 0.95$ and 1.0, C_L and C_D are phase-locked to cylinder displacement, $y(t)$. At $f/f_0 \geqslant 2.0$ and 3.0, C_L and C_D are quasi-phase-locked to $y(t)$ for when $h = 1.25$. A change over from one mode of vortex formation to another one is observed with the increase of f/f_0 beyond $f/f_0 = 1.0$ when $h = 1.25$. In all cases considered C_L shows a periodic behaviour which is consistent with the vortex shedding modes and their periods. This confirms our findings that the vortex lock-on occurs in these cases. However, a change over in the nature of the fluctuations of the drag coefficient is observed with the increase of the frequency ratio.

Acknowledgements

References

[1] J. Sheridan, J.C. Lin and D. Rockwell. Flow past a cylinder close to a free surface. *J. Fluid Mech.*, **330**, 1–30, (1997).

[2] J. Carberry, J. Sheridan and D. Rockwell. *Stationary and oscillating cylinders in the presence of a free-surface*, Proceedings of the 14th Australasian Fluid Mechanics Conference, Adelaide, Australia, 285–788 (2001).

[3] O. Cetiner and D. Rockwell. Streamwise oscillations of a cylinder in a steady current. Part 2: Free-surface effects on vortex formation and loading. *J. Fluid Mech.*, **427**, 29–59, (2001).

[4] J. Carberry. *Wake states of an oscillating cylinder and of a cylinder beneath a free-surface*, PhD Thesis, Monash University, Australia (2002).

[5] P.J. Reichl, K. Hourigan and M.C. Thompson. Flow past a cylinder close to a free surface. *J. Fluid Mech.*, **533**, 269–296, (2005).

[6] O.I. Gubanov *Design of CFD code using high level programming paragdigms: Free surface flows with arbirarily moving bodies*, MSc Thesis, Memorial University of Newfoundland, Canada (2006).

[7] C.W. Hirt and B.D. Nichols. Volume of fluid method for the dynamics of free boundaries. *J. Comput. Phys.*, **39**, 201–225, (1981).

[8] C.W. Hirt and J.M. Sicilian. *A porosity technique for the definition of obstacles in rectangular cell meshes*, Proceedings of the 4th International Conference on Ship Hydrodynamics, Washington, District of Columbia (1985).

[9] J. Gerrits. *Dynamics of liquid-filled spacecraft*, PhD Thesis, Rijksuniversiteit Groningen, Netherlands (2001).

[10] P.M. Gresho and R.L. Sani. *Incompressible Flow and the Finite Element Method*, John Wiley and Sons Ltd., New York (1998).

[11] J. Carberry, J. Sheridan and D. Rockwell. *Stationary and oscillating cylinders in the presence of a free-surface*, Proceedings of the 14th Australasian Fluid Mechanics Conference, Adelaide, Australia, 285–788 (2001).

[12] C. H. K. Williamson and A. Roshko. Vortex formation in the wake of an oscillating cylinder. J. Fluids Struc., **2**, 355-381, (1988)

An Experimental Investigation of the Flow Around Isolated and Tandem Straked Cylinders

Ivan Korkischko[1], Julio R. Meneghini[1], Enrique Casaprima[2], Ricardo Franciss[3]

[1]NDF - *Escola Politécnica*, University of São Paulo, Brazil
[2]E&P - Petrobras, Brazil
[3]CENPES - Petrobras, Brazil

Abstract

This paper presents experimental results concerning the response of circular cylinders with and without strakes. The amplitude response and the wake structures of plain and helically straked circular cylinders are compared. Six different configurantions of straked cylinders with pitches (p) equal to 5D, 10D and 15D and heights (h) equal to 0.1D and 0.2D are investigated. Measurements on the dynamic response oscillations of an isolated plain and straked cylinders, and flow visualization employing fluorescein dye and a PIV system are shown. The models are mounted on an air bearing base. The base is fixed on the test-section of a water channel facility. The air bearing base possess a low-damping and is free to oscillate only in the cross-flow direction. The Reynolds number of the experiments ranges from 1000 to 13000, and reduced velocities, based on natural frequency in still water, vary up to 15. The smaller height strakes (h = 0.1D) do not prevent vortex formation in the region very close to the body, resulting in a decrease of about 50% of the amplitude response compared with the plain cylinder. Lowest amplitude response was found to the p = 10D and h = 0.2D case. The analysis of the vorticity contours shows that the shear layer does not roll close to the body (same result for the other cases with h = 0.2D). It is also presented the amplitude response and the PIV flow visualization for a interference tandem test, in which the upstream cylinder is plain and fixed, and the dowstream is straked and free to oscillate (p = 10D and h = 0.2D case). The center of the cylinders distance is C = 3.4D. It is observed that the downstream straked cylinder oscillates at A/D = 0.57. This result shows that the strakes loose most of its efficiency as a supressor of vortex-induced vibration when the straked cylinder is immersed in a wake formed from an upstream cylinder.

1 Introduction

The damaging oscillations associated with VIV has led to the development of a variety of passive methods to reduce the magnitude of the periodic fluctuating transverse force (lift) resulting from regular vortex shedding with the objective of reducing or even suppressing VIV. These techniques introduce modification in body geometry and involve the introduction of some three-dimensional disturbance into the flow. A wide range of passive VIV suppression methods has been reviewed by Zdravkovich (1981). In most engineering applications the need for simplicity, reliability and low costs has favoured passive control devices over active control techniques.

Helical strakes used in wind engineering are the most successful application of a passive technique and were first studied by Scruton & Walshe (1957). A popular theory about the strakes mechanism is that strakes do not necessarily suppress vortex shedding but they prevent the vortex shedding from becoming correlated along the span. Along with this theory, it is equally possible that the three-dimensionality of the separating flow introduced by the strakes could destroy regular vortex shedding (Brankovic (2004) and Bearman & Branković (2004)). However, the introduction of strakes leads to the need of structure strengthening due the increase in drag force which is very dependent of the strake height.

The Reynolds number of the experiments ranges from 1000 to 13000 and as the separation points are fixed by the strakes, it is expected that the Reynolds number does not affect vortex shedding.

The objective of these experiments is to analyze the efficiency of the strakes and answer some questions regarding the mechanism of VIV attenuation. The four main questions we intend to answer are: Is the desynchronizing of vortex shedding along the span, caused by the helical shape of the strakes, the main cause of VIV attenuation? Is the attenuation caused by the change of the formation length? Is the increase in hydrodynamic damping the main cause of VIV attenuation? Is the efficiency of strakes affected by interference?

2 Experimental Arrangement

The acrylic circular cylinders used in our experiments had a diameter of 32 mm and an immersed length of 690 mm, giving an aspect ratio close to 21.6. The strakes are made of rigid rubber and three sets of pitches are tested: 5D, 10D and 15D. The straked cylinders have a three-start helical pattern configuration and a thin plate geometry. The strakes are attached to the cylinders using a cyanoacrylate adhesive and the cylinders are fitted with end-plugs to ensure complete water-tightness. The height of the strakes were 0.1D and 0.2D. The cylinders are rigidly attached beneath a

Fifth Conference on Bluff Body Wakes and Vortex-Induced Vibrations (BBVIV 5)
Costa do Sauipe, Bahia, Brazil, 12 - 15 December 2007

257

platform on an air bearing system that allowed motion only in a direction transverse to the flow. The end conditions of the cylinders are free surface at the upper end and near wall at the bottom. The gap between the model tip and the bottom of the water channel is about 10 mm. Due to this very small gap, an end plate is not necessary. The current velocity ranges from 0.1 to 0.4 m/s. In such condition, one would expect that the free surface does not affect the overall results. The structure supporting the air bearing base is fixed above a circulating water channel which has a test-section 0.7 m wide, 0.9 m deep and 7.5 m long. The flow velocity can be increased up to 1.0 m/s. The channel presents mean turbulence intensity $TI = 0.022 \pm 0.004$. Further information of the water channel can be found in Ássi (2005). Mean turbulence intensity (TI) is defined by the ratio between the rms of the mean velocity fluctuation and mean velocity, as shown in the Eqn. $TI = \sqrt{\overline{u'^2}}/\bar{u}$.

Typical Reynolds numbers are in the range 1000 to 13000 and reduced velocities, based on natural frequency in still water, vary up to 15 for the air bearing system. Reduced velocity, V_r, is defined as $U/f_w D$, where U is channel flow velocity, D the plain cylinder diameter and f_w the natural frequency in still water. For the air bearing base, the mass ratio m^*, effective mass of the cylinder/displaced mass of water, is 2.10 for all cylinders. Structural damping coefficient in air is $\zeta = 0.015$ for the air bearing system. Damping coefficient in water, ζ_w, varied between 0.052 and 0.17, and is obtained by a still water decay test. The experimental parameters for the experiments are summarized in Tab. 1.

Table 1: Experimental parameter for the air bearing system.

Case	Pitch (p)	Height (h)	f_w (Hz)	ζ_w
5D01D	5D	0.1D	0.781	0.071
5D02D	5D	0.2D	0.781	0.10
10D01D	10D	0.1D	0.781	0.094
10D02D	10D	0.2D	0.781	0.16
15D01D	15D	0.1D	0.781	0.10
15D02D	15D	0.2D	0.781	0.17
Plain	-	-	1.074	0.052

The cylinder motion is measured by an optical system in the air bearings system. Further details of cylinder motion measurements can be found in Ássi (2005). Flow velocity is measured by an electromagnetic flowmeter. The fluorescein dye flow visualization is obtained with a digital video camera.

The PIV system employed in this investigation is composed of a Quantel Brilliant Twins laser, and TSI synchronizer (LaserPulse), camera (PowerView 4 Megapixels) and software (Insight v. 3.53). The images are captured at $5Hz$, the interval between laser pulses is $\Delta t = 1000\mu s$, and the interrogation window 64×64 pixels. The PIV images are taken near the middle of the cylinders immersed height.

3 Experimental Results

3.1 Isolated Circular Cylinders

Figure 1(a) synthetizes the data obtained from experiments of circular cylinders with and without strakes mounted on an air bearings base. The analysis of the results shows clearly the importance of the strake height to the suppression process. Amplitude response for cylinders with $h = 0.2D$ strakes is the lowest. On the other hand, cylinders with $h = 0.1D$ strakes presented significant oscillation, but less than for the plain cylinder. It can be seen in Fig. 1(a) that, comparing the $h = 0.1D$ straked cylinder to the plain cylinder, VIV occurs over a narrower range of reduced velocity. From all the cases studied, the cylinder with $h = 0.2D$ and $p = 10D$ presented the lowest amplitude response. It also can be observed that the pitch apparently affects the range of reduced velocity where it is observed the inferior branch. The bigger the pitch, bigger the range. The transverse amplitude response results of this paper are similar to that found in Bearman & Branković (2004) and Trim *et al.* (2005), where the transverse response is reduced, but it is still significant, for the smaller height strake ($p = 5D$ and $h = 0.14D$ Bearman & Branković (2004), and $p = 5D$ and $h = 0.14D$ Trim *et al.* (2005)), and for the larger height strake ($p = 17.5D$ and $h = 0.25D$ Trim *et al.* (2005)), the transverse response is almost suppressed.

Qualitative flow visualization images are obtained with fluorescein dye (not shown). The Reynolds number is 1800, and the reduced velocity for the plain cylinder is $V_r = 1.6$, and for the straked cylinders, $V_r = 2.2$. The main purpose of this kind of visualization is to serve as a first guide for further quantitative investigation employing more advanced techniques. Even at a low flow velocity, fluorescein dye flow visualization clearly shows the wake structure differences between plain and straked cylinder, and these differences certainly affect the amplitude response of the cylinders (Fig. 1(a)).

Figure 2 presents the vorticity field of plain cylinder for comparison purposes with the straked cylinders. The vorticity field is calculated from the velocity field of the flow with the Laser-PIV technique. The Reynolds number for the PIV flow visualizations is 5000, and the reduced velocity for the plain cylinder is $V_r = 4.7$, and for the straked cylinders, $V_r = 6.4$. Laser-PIV pictures are taken at the maximum amplitude position, and seven different incidence angles (ranging from 0° to 90°) are used. Figure 3 shows seven pictures of the vorticity field of the flow around the straked cylinder with $p = 10D$ and $h = 0.1D$. The analysis of Fig. 3 shows clearly the formation of a clockwise rotation vortex (blue color) and another vortex with anti-clockwise rotation (red color) in the near-wall region of the

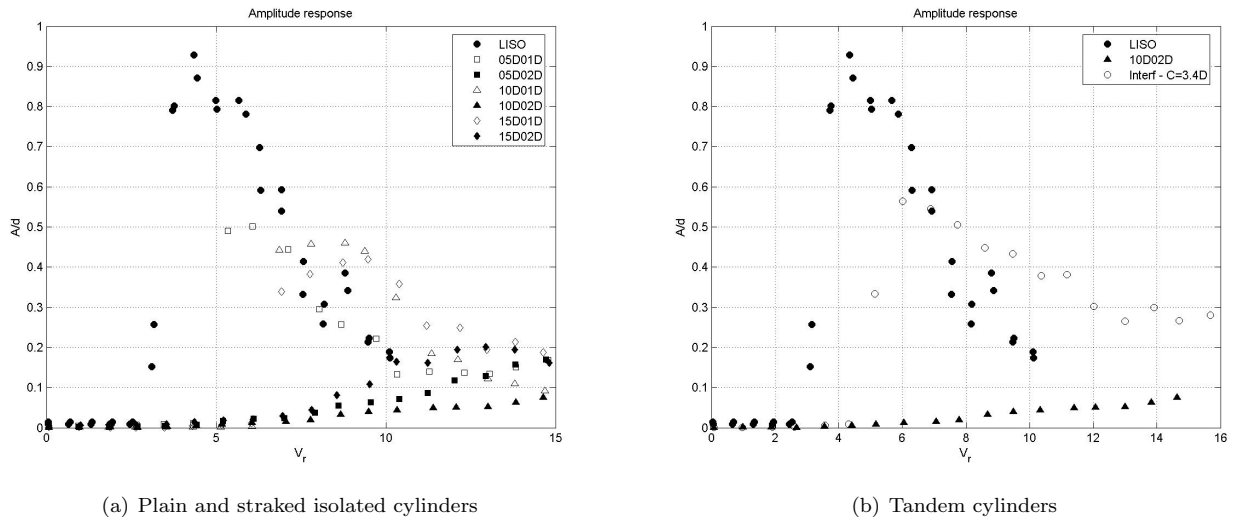(a) Plain and straked isolated cylinders

(b) Tandem cylinders

Figure 1: 1dof amplitude response of cylinders mounted on an air bearing base.

cylinder. It is not observed span-wise correlation of vortex shedding. The small height strake ($h = 0.1D$) have not prevented vortex formation in a near-wall region of the body. Despite the strake helix has caused a non-correlated vortex shedding, this was not sufficient to vanish the oscillation amplitude response. Figure 4 presents the straked cylinder with $p = 10D$ and $h = 0.2D$. This was the case with the lowest oscillation amplitude response. Figure 4 shows clearly that the shear layer does not roll itself in the near-body region. The vortex formation does not occur near the wall of the cylinder and the absence of low-pressure region is clearly noted from the figure. These facts allied with the non-observation of span-wise correlation have resulted in a low amplitude response.

Flow visualization results have shown the main effect of strakes, which changes the vortex shedding mechanism near the wall. A conventional *von Kármán* vortex street is not formed close to the cylinder. Apparently, for the $h = 0.2D$ strakes, the shear layers form themselves and interact in a much greater distance than for a plain or straked cylinders with $h = 0.1D$. To these last, the height of the protrusion was not sufficient to alter the vortex formation dynamics to the point of avoiding its formation close to the cylinders.

(a) Fixed plain cylinder

(b) Oscillating plain cylinder

(c) Tandem arrangement

(d) Tandem arrangement
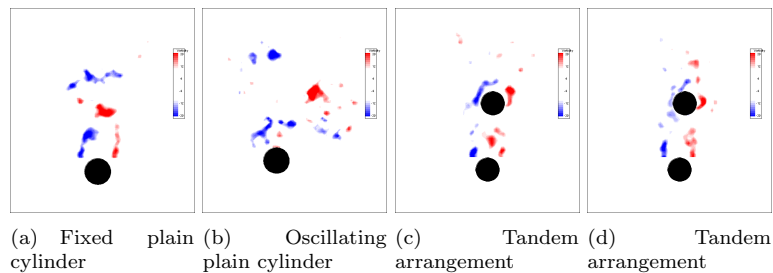
Figure 2: Vorticity field $[s^{-1}]$.

(a) 0° (b) 15° (c) 30° (d) 45° (e) 60° (f) 75° (g) 90°
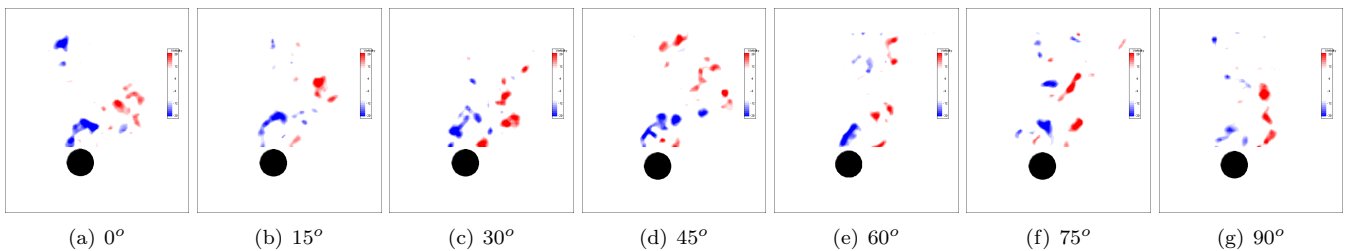
Figure 3: 10D01D straked circular cylinder vorticity field $[s^{-1}]$.

3.2   Tandem Circular Cylinders

The following results are at a preliminary stage and will be followed by a comprehensive research of interference in tandem arrangement of straked circular cylinders. The upstream cylinder is plain and fixed, and the dowstream is straked and free to oscillate ($p = 10D$ and $h = 0.2D$ case). The center of the cylinders distance is $C = 3.4D$. Figure
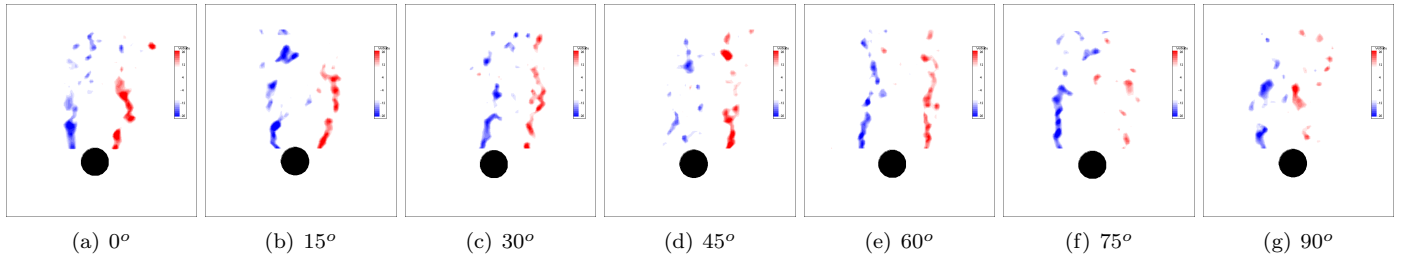
Fifth Conference on Bluff Body Wakes and Vortex-Induced Vibrations (BBVIV 5)
Costa do Sauipe, Bahia, Brazil, 12 - 15 December 2007

259

(a) 0º (b) 15º (c) 30º (d) 45º (e) 60º (f) 75º (g) 90º

Figure 4: 10D02D straked circular cylinder vorticity field $[s^{-1}]$.

1(b) shows that the 10D02D straked cylinder looses effectiveness when it is mounted behind a plain cylinder. It is observed that the downstream straked cylinder oscillates at a maximum amplitude $A/D = 0.57$, which is quite different when compared with the isolated straked cylinder ($A/D = 0.08$).

Figures 2(c) and 2(d) present the vorticity field of the tandem arrangement using the PIV technique. It can be noted the vortex formation in a near-wall region of the downstream straked cylinder, that reduces the straked cylinder effectiveness.

4   Conclusions

Experiments carried out in a water channel with cylinders with and without strakes demonstrate the strong dependency of the oscillation amplitude response with the height of the strake. Flow visualization results have shown that the strakes change the vortex shedding mechanism near the wall. For the $h = 0.2D$ strakes, the shear layers form themselves and interact in a much greater distance than for a plain or straked cylinders with $h = 0.1D$. To these last, the height of the protrusion was not sufficient to alter the vortex formation dynamics to the point of avoiding its formation close to the cylinders. It is not formed a conventional *von Kármán* vortex street for the $h = 0.2D$ straked cylinders. These experiments with low mass and damping cylinders demonstrate the difficulty of suppressing VIV. The principal hydrodynamic mechanisms of VIV attenuation/suppression of strakes could be observed: strakes do not necessarily suppress vortex shedding but they prevent the vortex shedding from becoming correlated along the span and the three-dimensionality of the separating flow introduced by the strakes could destroy regular vortex shedding. This conclusion answers one of the questions raised in the introduction: the change of formation length has great influence in VIV attenuation. Probably, this change in formation length is as important to VIV attenuation as the desynchronisation of vortex shedding along the span. Together with these reasons, the increase in damping has a great influence in VIV attenuation. This probably explains why the strakes with smaller height ($h = 0.1D$) was not so effective. The effect of the increase in damping on VIV should be further investigated. Preliminary results of interference in tandem arrangement shows that that the straked cylinders looses effectiveness in the wake of another cylinder. Further investigation will be conducted varying the cylinders center distance and using a straked upstream cylinder.

References

BEARMAN, P. W. & BRANKOVIĆ, M. 2004 Experimental studies of passive control of vortex-induced vibration. *European Journal of Mechanics B/Fluids* (23), 9–15.

BRANKOVIC, M. 2004 Vortex-induced vibration attenuation of circular cylinders with low mass and damping. PhD Thesis, Imperial College, London, UK.

Ássi, G. R. S. 2005 Estudo Experimental do Efeito de Interferência no Escoamento ao Redor de Cilindros Alinhados. MS Thesis, Escola Politécnica da Universidade de São Paulo, São Paulo, SP, Brasil.

SCRUTON, C. & WALSHE, D. E. J. 1957 Means for avoiding wind-excited oscillations of structures with circular or nearly circular cross section. *Tech. Rep.* 335. Aero Report, Natl. Phys. Lab. (U.K.).

TRIM, A.D., BRAATEN, H., LIE, H. & TOGNARELLI, M.A. 2005 Experimental investigation of vortex-induced vibration of long marine risers. *Journal of Fluids and Structures* (21), 335–361.

ZDRAVKOVICH, M. M. 1981 Review and classification of various aerodynamic and hydrodynamic means for suppressing vortex shedding. *Journal of Wind Engineering and Industrial Aerodynamics* (10), 455–472.

3D flow stability in rotated and inline tube bundles

NICHOLAS KEVLAHAN
DEPARTMENT OF MATHEMATICS & STATISTICS
MCMASTER UNIVERSITY
HAMILTON, CANADA
kevlahan@mcmaster.ca

Vortex shedding in the wake of an isolated circular cylinder begins at $Re \approx 45$. Williamson (1988) found experimentally that the wake starts to become three-dimensional for Reynolds numbers in the range 170 to 180. The transition to three-dimensional shedding is signaled by a discontinuity in the Strouhal frequency versus Reynolds number curve. These results were confirmed and sharpened by Barkley and Henderson (1996), who used numerical Floquet analysis to show that $Re_c = 188.5$.

In this paper we investigate how the tight packing of cylinders in a tube bundle modifies the onset of vortex shedding and three-dimensional flow. In particular, we are interested in the differences between the inline and rotated configurations of tube bundles (i.e. when the mean flow is aligned with, or at 45° to, the axis of the tube bundle). It is well-known that at moderate Reynolds numbers the inline bundles have a jet-like vortex structure, while the rotated bundles have a periodic wake-like structure. Not surprisingly, we find that these distinct vorticity configurations strongly influence the stability properties of flows. The flow in the rotated bundle is very unstable: it becomes three-dimensionally unstable at about $Re = 64$ (just after vortex shedding begins), whereas the inline bundle flow becomes unstable at $Re \approx 132$. The onset of vortex shedding in the inline bundle is delayed until $Re = 119$, and at $Re = 140$ its rms lift is 3.5 times smaller than that of the rotated bundle. The most unstable wavelength is about 1 tube diameter for the rotated bundle, and about 2.6 diameters for the inline bundle (compared to about 4 diameters for an isolated cylinder). The inline bundle has only one unstable mode for moderate Reynolds numbers, and its maximum growth rate increases linearly with Reynolds number. By constrast, the rotated bundle has one instability mode with a maximum growth rate at $Re = 100$, and another (of longer wavelength) that appears for $Re > 166$. These results show that simply changing the orientation of the mean flow dramatically alters the fluid forces and stability properties of the flow. A better understanding of this effect could help improve the design of heat exchangers.

1. METHOD

The two-dimensional flow through inline and rotated square bundles of circular tubes with a pitch to diameter ratio of $P/D = 1.5$ are calculated using the following L^2-penalized equations:

$$(1) \qquad \frac{\partial \boldsymbol{u}}{\partial t} + \boldsymbol{u} \cdot \nabla \boldsymbol{u} + \nabla P = \frac{1}{Re}\Delta \boldsymbol{u} - \frac{1}{\eta}\chi(\boldsymbol{x})\boldsymbol{u},$$

$$(2) \qquad \nabla \cdot \boldsymbol{u} = 0,$$

where the last term on the rhs of (1) approximates the no-slip boundary conditions on the surface of the cylinder as $\eta \to 0$ ($\chi(\boldsymbol{x}) = 1$ or 0 in the solid and fluid regions of the flow, respectively). The external boundary conditions are periodic in both directions, and we consider a unit cell containing one circular cylinder. The Reynolds number $Re = U_\infty D/\nu$, where U_∞ is the mean velocity upstream of the bundle, and D is the tube diameter.

The penalized Navier–Stokes equations (1–2) are solved using a Fourier-transform-based pseudo-spectral method in space [e.g. Vincent and Meneguzzi (1991)] and a Krylov method in time (Edwards et al., 1994). The pseudo-spectral method is computationally efficient and highly accurate for spatial derivatives, while the Krylov method is a stiffly stable explicit method with an adaptive stepsize to maintain a specified error tolerance.

The three-dimensional stability of the flow is determined using the Floquet analysis method described in Barkley and Henderson (1996). In this method a two-dimensional $T-$periodic base flow $\boldsymbol{u}$ is calculated, and then linearly perturbed by modes of the form

$$\boldsymbol{u}'(x, y, z, t) = (\hat{u}(x, y, t)\cos\beta z, \hat{v}(x, y, t)\cos\beta z, \hat{w}(x, y, t)\sin\beta z),$$
$$p'(x, y, z, t) = \hat{p}(x, y, t)\cos\beta z.$$

	Vortex Shedding Re_c	3D flow Re_c	3D flow λ
Isolated	45	188.5 ± 1.0	3.96 ± 0.02
Rotated	55 ± 1	64 ± 0.5	0.9 ± 0.1
Inline	119 ± 1	132 ± 1	2.6 ± 0.3

TABLE 1. Critical Reynolds numbers for transition to vortex shedding and three-dimensional flow, and most unstable spanwise wavelength λ of three-dimensional instability.

This defines a linear operator $\boldsymbol{L}$ and an evolution equation for the perturbations

$$(3) \qquad \frac{\partial \boldsymbol{u}'}{\partial t} = \boldsymbol{L}(\boldsymbol{u}').$$

The solutions of (3) are of the form $\tilde{\boldsymbol{u}}(x,y,z) \exp \sigma t$, where $\tilde{\boldsymbol{u}}$ are $T-$periodic functions, and the complex Floquet multipliers $\mu \equiv \exp \sigma T$ are the eigenvalues of $\boldsymbol{L}$. The flow is three-dimensionally unstable to spanwise perturbations of frequency β if $|\mu| > 1$.

2. RESULTS

In this section we present some preliminary results for flow through inline and rotated tube bundles at moderate Reynolds numbers ($Re < 300$). We will present additional results for fully three-dimensional flows at the conference.

Table 1 shows that the flow through tube bundles is more unstable than the flow past an isolated cylinder. In fact, a two-dimensional vortex shedding regime is essentially impossible for a tightly packed tube bundle. Comparing figures 1(a,b) shows that the rotated tube bundle is much more unstable than the inline bundle. The most unstable three-dimensional wavelength is approximately one tube diameter for the rotated case, and about 2.6 diameters for the inline case. Interestingly, figure 1(a) also shows that the rotated flow is locally most unstable at $Re = 100$, and actually becomes more stable as Reynolds number increases until about $Re = 200$. The discontinuity in the most unstable frequency at $Re \approx 166$ shown in figure 2 strongly suggests the appearance of a new mode of instability. By contrast, figure 1 shows that the maximum growth rate increases linearly for the inline bundle, and the most unstable frequency plateaus at about $\beta = 2.4$.

In figure 3 we compare the maximum growth rates for the rotated and inline tube bundles at $Re = 200$. Note that the rotated bundle retains the $\beta = 2.4$ instability mode of the inline bundle in addition to the dominant higher frequency instability modes.

Taken together, these results demonstrate that rotated and inline tube bundles have very different three-dimensional stability properties. Both configurations are much more unstable than an isolated cylinder: indeed two-dimensional vortex shedding flow is likely impossible in tube bundles. There is only one three-dimensional instability mode in inline flow (which grows linearly with Reynolds number), while rotated flow exhibits a sudden transition to a new lower frequency mode at $Re \approx 166$. These differences are likely due to differences in the wake structure of the two configurations: the rotated bundle has an alternate vortex shedding pattern, while the inline bundle has a jet-like symmetric shedding pattern. These results using linear Floquet stability analysis will be confirmed using full three-dimensional direct numerical simulations (DNS).

REFERENCES

Barkley, D., Henderson, R., 1996. Three-dimensional floquet stability analysis of the wake of a circular cylinder. J. Fluid Mech. 322, 215–241.

Edwards, W. S., Tuckerman, L. S., Friesner, R. A., Sorensen, D. C., 1994. Krylov methods for the incompressible Navier–Stokes equations. J. Comp. Phys. 110, 82–102.

Vincent, A., Meneguzzi, M., 1991. The spatial structure and statistical properties of homogeneous turbulence. J. Fluid Mech. 225, 1–20.

Williamson, C., 1988. Defining a universal and continuous Strouhal-Reynolds number relationship for the laminar vortex shedding of a circular cylinder. Phys. Fluids 31, 2742.
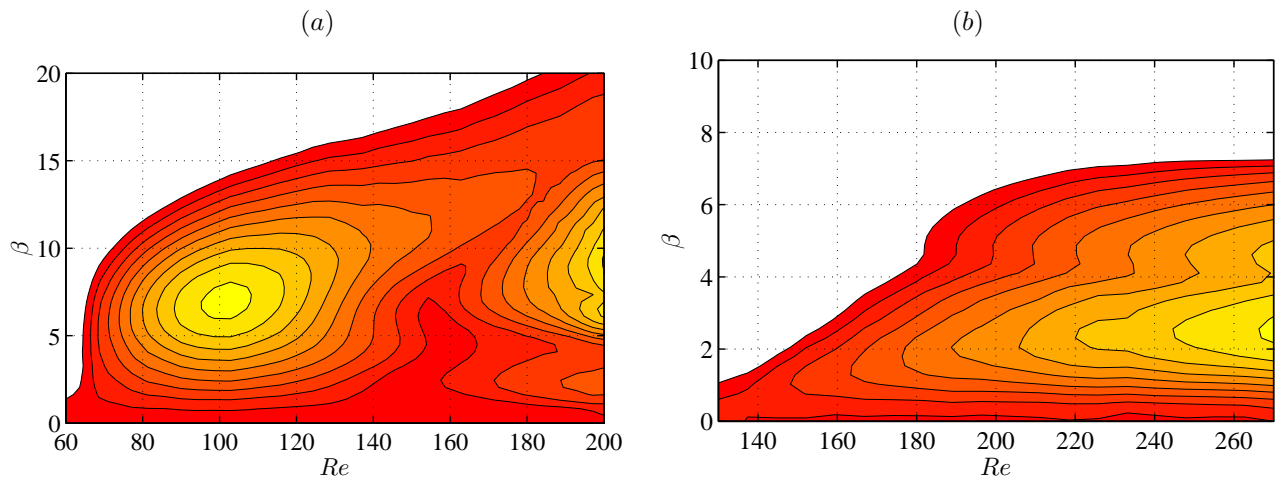
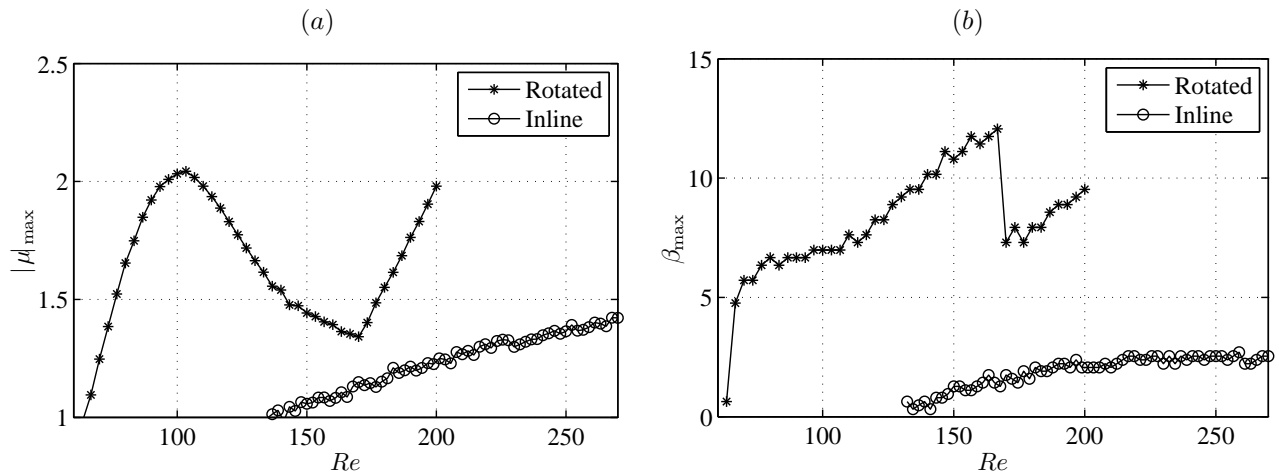FIGURE 1. Contour plots of most unstable Floquet multiplier $|\mu| > 1$. (a) Rotated. (b) Inline.

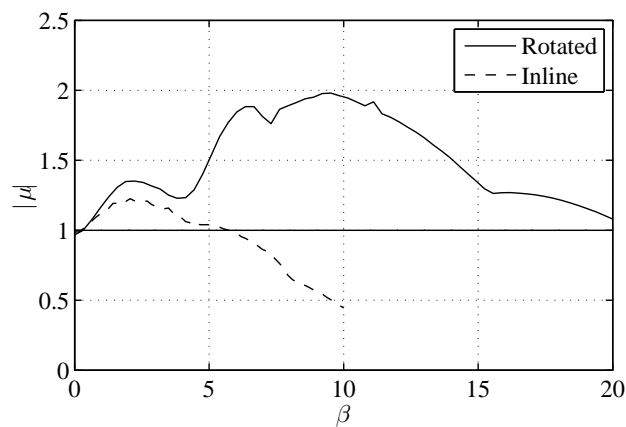FIGURE 2. (a) Maximum growth rate $|\mu|$. (b) Most unstable frequency β.

FIGURE 3. Stability curves at $Re = 200$.

NUMERICAL STUDY OF OSCILLATORY FLOW
PAST FOUR CYLINDERS IN RECTANGULAR ARRANGEMENT

J. Lee
Imperial College of Science, Technology and Medicine
Department of Aeronautics
London SW7 2BY
U.K.

P. Anagnostopoulos and S.A. Seitanis
Aristotle University of Thessaloniki
Department of Civil Engineering
Division of Hydraulics and Environmental Engineering
Thessaloniki 54006
GREECE
email: anagnost@civil.auth.gr

INTRODUCTION

The results of a numerical study of the viscous oscillating flow around four circular cylinders are presented herein, for a constant frequency parameter, β, equal to 50, and Keulegan-Carpenter numbers, KC, ranging between 0.2 and 5. The cylinders were placed on the vertices of a rectangle with two sides normally and two parallel to the oncoming flow, for a pitch ratio in the cross-flow direction, T/D, equal to 2, and a pitch ratio in the streamwise direction, S/D, equal to 1.75. The finite-element method was employed for the solution of the Navier-Stokes equations, in the formulation where the stream function and the vorticity are the field variables. The vorticity contours generated from the solution were used for the flow visualization. At low values of the Keulegan-Carpenter number the flow remains symmetrical with respect to the horizontal axis of symmetry of the solution domain. As the Keulegan-Carpenter number is increased to 4 small asymmetries appear in the flow, which are eventually amplified as KC becomes equal to 5. These asymmetries are associated with an aperiodic flow configuration at consecutive cycles, which becomes almost chaotic as KC grows larger. For characteristic values of the Keulegan-Carpenter numbers considered the vorticity contours and the traces of the hydrodynamic forces are presented, whereas the r.m.s. values of the hydrodynamic forces and the coefficients of the in-line force were evaluated for the entire range of Keulegan-Carpenter numbers examined.

COMPUTATION-RESULTS

Computations were conducted for a constant frequency parameter equal to 50 and various Keulegan-Carpenter numbers ranging between 0.2 and 5. The computational technique is explained in detail by Iliadis and Anagnostopoulos [1] in a study of oscillatory flow past a single cylinder and by Anagnostopoulos *et al.* [2] in a solution of oscillatory flow past a pair of cylinders placed side-by-side to the incident flow, for T/D=1.2. An unstructured mesh of three-node triangular elements was employed for the solution, containing 18,6596 nodes and 36,814 elements.

FLOW FIELD AND FORCE TRACES FOR VARIOUS KC

For various characteristic cases, the flow pattern and the time-dependent hydrodynamic forces will be presented. For relatively low KC values the flow field remains symmetrical with respect to the horizontal axis of symmetry of the computational domain, and periodic at consecutive oscillation cycles. If KC exceeds a critical threshold asymmetries appear in the flow field, which trigger a small aperiodicity at different cycles. As KC grows larger the asymmetries are amplified and lead to an aperiodic flow field at subsequent cycles.

The time-history of the hydrodynamic forces exerted on cylinder 1 (lower left of the cylinders displayed in Figs 2 and 3) for KC=4 are displayed in Fig. 1. The frequency of the in-line force is equal to the oscillation frequency, while the frequency of the transverse force is twice the oscillation frequency. The in-line force on the upper left cylinder is equal to that exerted on the lower left, whereas the transverse force is equal in magnitude but of opposite sign compared to that on the lower left cylinder. The traces of the forces exerted on the lower right cylinder are close to those on the lower left cylinder and those on the upper right cylinder are close to the traces of the upper left cylinder. We also notice that the in-line force is very close to periodic at consecutive cycles, which is not the case for the transverse force. For the
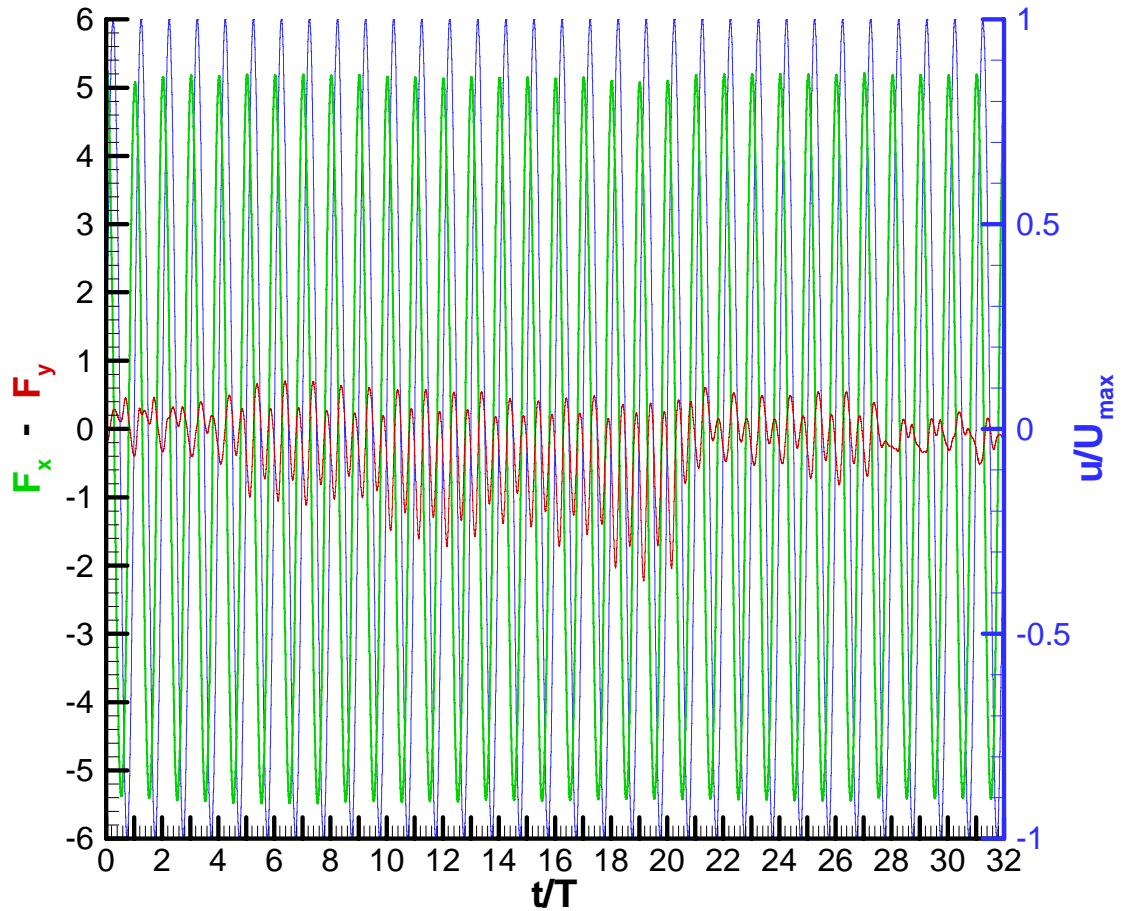
Fifth Conference on Bluff Body Wakes and Vortex-Induced Vibrations (BBVIV 5)
Costa do Sauipe, Bahia, Brazil, 12 - 15 December 2007

265

Figure 1. Traces of the hydrodynamic forces for *KC*=4 and *Re*=200 exerted on lower left cylinder.

cycles between 4 to 20 the mean transverse force is negative, whereas from cycles 28 to 32 is very close to zero.

To investigate possible differences in the flow mode associated with the difference in the transverse force trace, the vorticity contours were generated at various instants in the first half of the ninth and thirty first cycle. The vorticity contours for *KC*=4 in the first half of the ninth cycle are depicted in Fig. 2 and in the first half of the thirty first cycle in Fig. 3. The vortex pattern is almost symmetrical with respect to the horizontal axis of symmetry of the computational domain, but asymmetric with respect to the wake axis of each cylinder. We can observe in Fig. 2 that as *t/T* exceeds 9.25 the vortices generated at the outer edge of each cylinder are stronger than those generated at the inner edge, which is the reason for the negative transverse force on cylinder 1. On the other hand, Fig. 3 reveals that the flow pattern is very close to symmetrical with respect to the centre-line of each cylinder, which provides justification for the almost zero transverse force for *t/T* greater than 27.

R.M.S. HYDRODYNAMIC FORCES AND COEFFICIENTS OF THE IN-LINE FORCE

The values of F_x (r.m.s.) and F_y' (r.m.s.) as functions of *KC* are depicted in Fig. 4. F_y' denotes the difference of F_y from the mean value of F_y in the record. The r.m.s. values of the in-line force decrease as *KC* increases, whereas the values of F_y' (r.m.s.) decrease as *KC* decreases to 2 where it acquires the lowermost value, and then increases slightly as *KC* increases to 5.

The values of the drag and inertia coefficients are depicted in Fig. 5. We can see that the drag coefficient decreases abruptly with *KC* increasing to 2, and then decreases mildly as *KC* increases to 5. On the other hand the inertia coefficient experiences a very mild decrease as *KC* increases to 2, and then a more abrupt decrease as *KC* increases to 5.
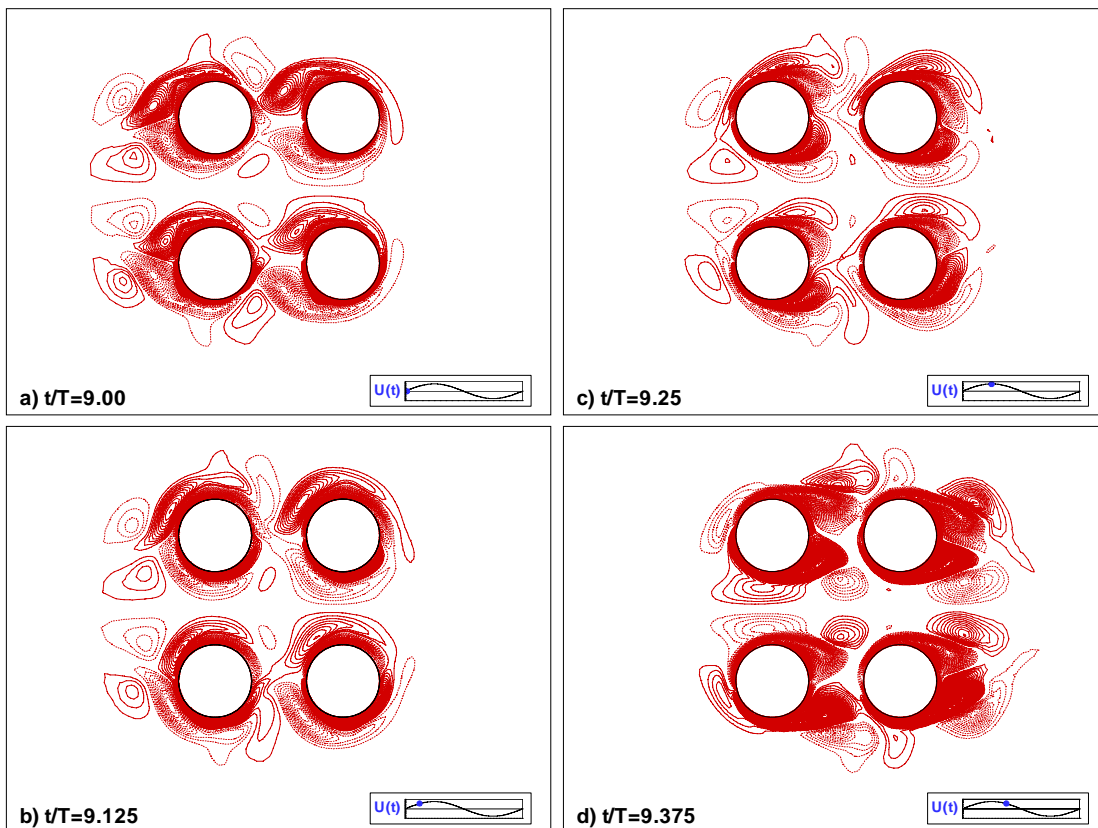
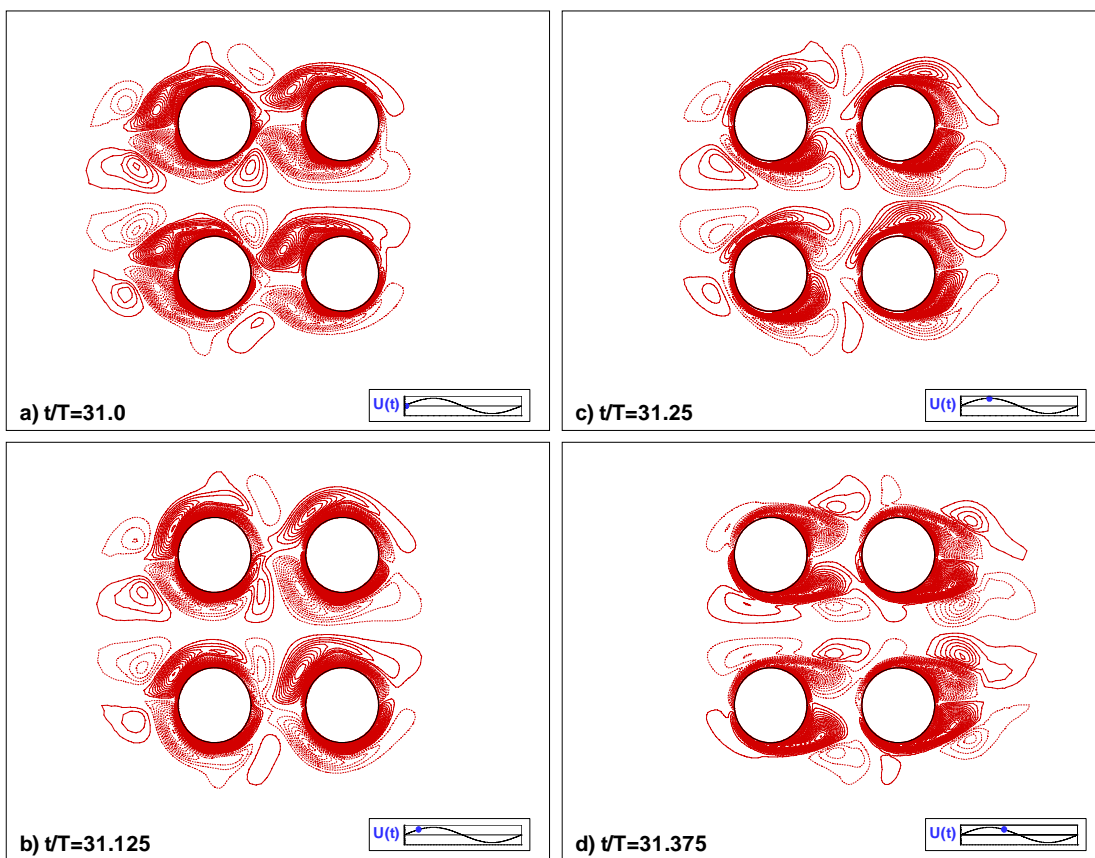**Figure 2. Equivorticity lines for *KC*=4 and *Re*=200 in the first half of the ninth cycle.**

Figure 3. Equivorticity lines for *KC*=4 and *Re*=200 in the first half of the thirty first cycle.
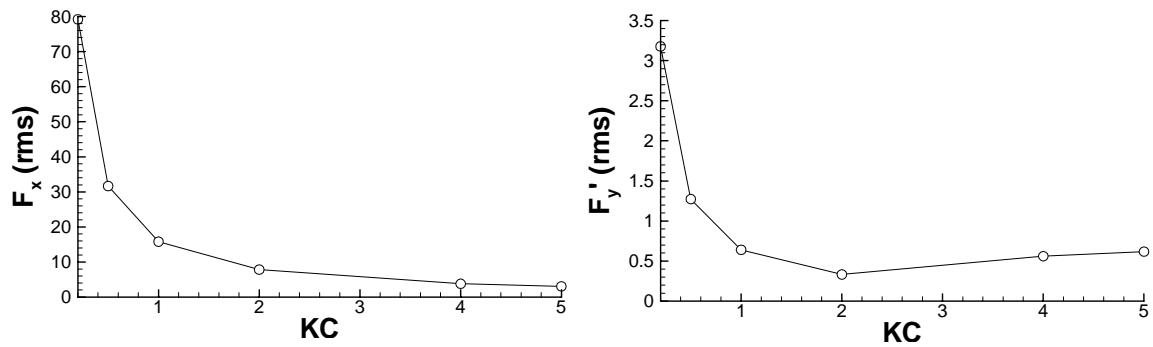
Figure 5. R.m.s. value of the in-line force (left) and of the transverse force (right) vs *KC*.
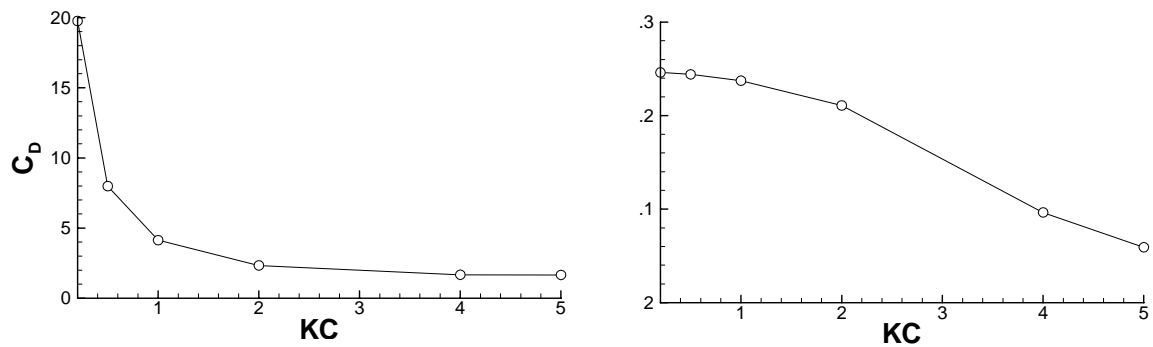

Figure 6. Drag coefficient (left) and inertia coefficient (right) of the in-line force vs *KC*.

CONCLUSIONS

The finite-element study conducted herein revealed the various features of the interactive oscillating flow past four circular cylinders in rectangular arrangement. At values of the Keulegan-Carpenter number lower than 4 the flow near the cylinders remains almost symmetrical with respect to the horizontal axis of symmetry of the solution domain. However, the flow is not symmetrical with respect to the wake axis of each cylinder, due to the interference effects. As the Keulegan-Carpenter number is increased over that value, the asymmetries in the flow are eventually amplified and lead finally to more complex flow patterns. When *KC* becomes equal to 4 or larger the flow pattern becomes aperiodic at consecutive cycles, which reflects on the traces of the hydrodynamic forces exerted on the cylinders, especially on those of the transverse forces. The frequency of the in-line force is equal to the frequency of the oscillating flow, whereas the frequency of the transverse force is twice the oscillation frequency. The amplitude of the in-line force exerted on the cylinders decreases with increasing *KC*, which reflects on the r.m.s. values of this force. The r.m.s. values of the transverse force decrease as *KC* increases to 2 and then experience a mild increase. The drag and inertia coefficients of the in-line force decrease with increasing *KC*, more abruptly the drag coefficient and mildly the inertia coefficient.

REFERENCES

1. Iliadis, G. and Anagnostopoulos, P., 1998, Viscous oscillatory flow around a circular cylinder at low Keulegan-Carpenter numbers and frequency parameters, International Journal for Numerical Methods in Fluids, **26**, 403-442.
2. Anagnostopoulos, P., Koutras, A. and Seitanis, S. A., 2002, Numerical study of oscillatory flow past a pair of cylinders at low Reynolds and Keulegan-Carpenter numbers, In Proceedings of ASME 4th International Conference on Flow-Structure Interactions, Aeroelasticity, Flow-Induced Vibration and Noise, Vol. 3, Paper No 32178 in CD-ROM, New Orleans, U.S.A.

ANISOTROPIC ORGANIZED EDDY SIMULATION APPROACH FOR STRONGLY DETACHED UNSTEADY FLOWS

R. Bourguet[1], M. Braza[1], J.B. Vos[2], R. Perrin[1] and G. Harran[1]

[1]Institut de Mécanique des Fluides de Toulouse, 6 allée du Professeur C. Soula, 31400 Toulouse, France
bourguet@imft.fr, braza@imft.fr
[2]CFS Engineering, PSE-B, 1015 Lausanne, Switzerland

1 The prediction of strongly detached high Reynolds number flows

In the context of high-Reynolds number turbulence modelling, recent advances like Large Eddy Simulation (LES) and hybrid methods (Detached Eddy Simulation, DES) have considerably improved the physical relevance of the numerical simulation. However, the LES approach is still limited to the low-Reynolds number range concerning wall flows and the Unsteady Reynolds Averaged Navier-Stokes (URANS) approach remains a widespread and robust methodology for complex flow computation compared to second-order closure schemes (Differential Reynolds Stress Modelling, DRSM) which involve higher numerical costs and empirical strategies in order to inhibate inherent numerical instabilities. The present study is founded on an advanced URANS approach and follows previous investigations concerning the *Organised Eddy Simulation* (OES) methodology [1] which consists in distinguishing the flow structures to model according to their coherent or chaotic aspect instead of their size as in LES. Classical linear eddy-viscosity models utilize the Boussinesq approximation [2] which establishes a linear relation between the Reynolds stresses and the strain-rate by means of a scalar eddy-viscosity concept, leading to an over-production of turbulent kinetic energy [3] especially in flow regions upstream of the detachment, where the strain-rate is high and the flow is laminar [4]. The Boussinesq law can be written as follows under the incompressibility assumption:

$$-\frac{\overline{u_i u_j}}{k} + \frac{2}{3}\delta_{ij} = -a_{ij} = 2\frac{\nu_t}{k}S_{ij},$$

where $\overline{u_i u_i}$ are the turbulent stresses, k is the turbulent kinetic energy ($k = \frac{1}{2}\overline{u_i u_i}$), δ_{ij} is Kronecker symbol and S the mean strain-rate tensor, defined by $S_{ij} = \frac{1}{2}\left(\frac{\partial U_i}{\partial x_j} + \frac{\partial U_j}{\partial x_i}\right)$. U_i is the mean flow velocity and ν_t is the scalar eddy-viscosity. In the framework of OES methods, an alternative to Non-Linear Eddy-Viscosity Models is suggested to derive a tensorial eddy-viscosity model sensitized for non-equilibrium turbulence [5]. A selective reduction of the eddy-diffusion coefficient, varying according to the non-equilibrium flow regions to reach an improved prediction of the turbulence production, in respect of the flow physics, is expected. The analysis of the stress-strain behaviour is based on a detailed high-Reynolds PIV experiment concerning the incompressible turbulent flow past a circular cylinder.Furthermore, anisotropic misalignment criteria are investigated and a tensorial definition of the eddy-viscosity is put forward, leading to a new Reynolds stress constitutive law. Transport equations for these criteria are derived from SSG second order closure scheme [6]. The predictive capacities of this anisotropy resolving approach are examined by comparison of two-dimensional numerical simulation results issued from NSMB solver with an experimental dataset concerning the incompressible flow around a NACA0012 airfoil at 20° degrees of incidence and Reynolds number 10^5.

2 An anisotropic eddy-viscosity concept based on turbulence structural properties

Investigation of the stress-strain misalignment via 3C-PIV in the cylinder wake

The experiment has been carried out in the wind tunnel S1 of IMFT. The cylinder spans the width of the channel without endplates and has a diameter D of 140mm, giving an aspect ratio $L/D = 4.8$ and a blockage coefficient $D/H = 0.208$. the Reynolds number based on the upstream velocity and the cylinder diameter is 1.4×10^5. Three-component measurements have been performed by means of stereoscopic PIV. The procedure used is reported in [7]. In the present study, the median plan has been considered at half distance spanwise and located in the near-wake region. The near periodic nature of the flow, due to the von Kármán vortices, allows the definition of a phase. In the following, all quantities are phase-averaged. Angles between the principal directions of the strain-rate and turbulence anisotropy tensors are quantified.

The main coherent vortex regions are delimited by the Q criterion. The first principal directions of each tensor are represented in Fig. 1(a). In specific flow regions their misalignment becomes predominant. The largest misalignment is observed near the vortex center ($x_1/D = 1$, $x_2/D = 0.03$). The best alignment is reached in free shear flow regions (Fig. 1(b)).
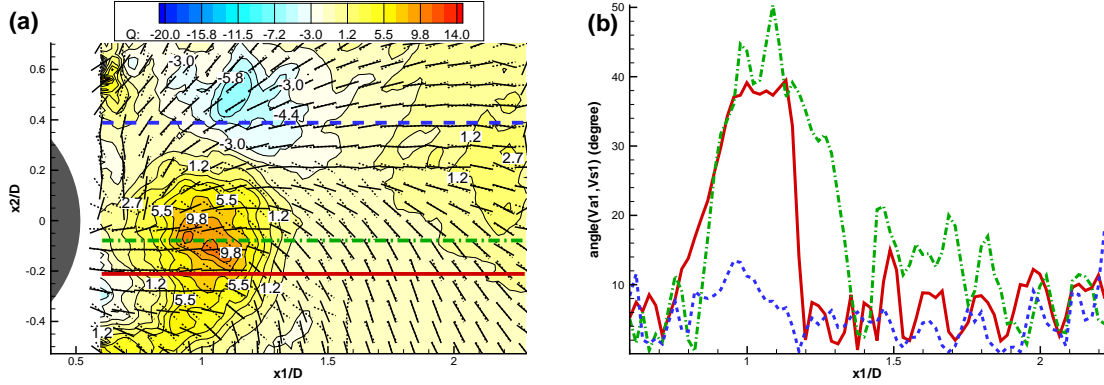

Figure 1: (a) $-a$ (dashed) and S (solid) first principal directions and Q criterion iso-contours at phases $\varphi = 50^o$. (b) Angle variation between $-a$ and S first principal directions along the three lines in bold in (a).

The tensorial eddy-viscosity concept

The previous analysis concerning the specific decorrelations between Reynolds stress and mean strain-rate tensors in each space direction demonstrates the relevance of a constitutive law taking account of the individual contribution of each element of a spectral decomposition which is applied to the strain-rate tensor. The following definition of an anisotropic eddy-diffusion coefficient can be suggested by an extension of the scalar C_μ definition, for $i = 1, 2, 3$:

$$C_{\mu_i} = \frac{\left| a_{jk} \left(v_i^S\right)_k \left(v_i^S\right)_j \right|}{\eta_i} = |C_{Vi}| \frac{\varepsilon}{k} \quad \text{where} \quad C_{Vi} = -\frac{a_{jk} \left(v_i^S\right)_k \left(v_i^S\right)_j}{\left|\lambda_i^S\right|}.$$

$\eta_i = \frac{k|\lambda_i^S|}{\varepsilon}$ is a vectorial version of $\eta = \frac{k\|S\|}{\varepsilon}$ mean flow/turbulent time scale rate which emphasises the non-equilibrium turbulence regions [8].

Therefore a consistent definition of the eddy-viscosity as a symmetric tensor ν_{tt} is suggested on the basis of a positive directional eddy-viscosity ν_{td} :

$$(\nu_{tt})_{ij} = (\nu_{td})_k \left(v_k^S\right)_i \left(v_k^S\right)_j \quad \text{with} \quad (\nu_{td})_i = |C_{Vi}| \, k. \tag{1}$$

Expression (1) leads to a weighted summation of S spectral decomposition:

$$S_{ik} (\nu_{tt})_{kj} = (\nu_{td})_l \lambda_l^S \left(v_l^S\right)_i \left(v_l^S\right)_j = (\nu_{td})_l (S_l)_{ij}, \tag{2}$$

and thus, the linear EVM behaviour law can be generalised as:

$$-\overline{u_i u_j} + \frac{2}{3} k \delta_{ij} = 2 S_{ik} (\nu_{tt})_{kj} - \frac{2}{3} R \delta_{ij}, \tag{3}$$

where $R = (\nu_{td})_i \lambda_i^S$ is the trace of $S_{ik} (\nu_{tt})_{kj}$. From expression (2), the symmetry property of the turbulence anisotropy tensor is ensured. The tensorial definition enables a selective reduction of the effect of one (or more) elements of the strain-rate tensor spectral decomposition with respect to the corresponding physical alignment (or misalignment) between the associated principal directions. Moreover, if a perfect alignment is observed in an equilibrium and isotropic strain region the tensorial expression degenerates into a classical Boussinesq-like scalar model. A comparison between normal and shear Reynolds stress fields evaluated from the PIV experiment and from modelling via (3) and measured stress tensor is presented in Fig. 2 and can be regarded as an "experimental" validation. The modelled quantities present a good match with the experiment for both normal and shear Reynolds stresses.
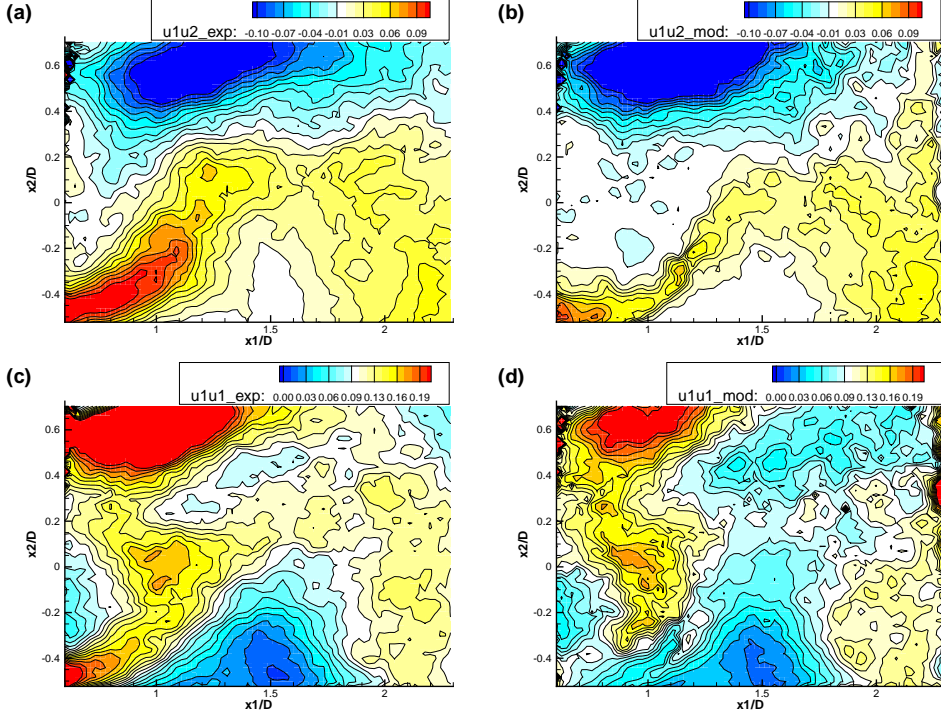
Figure 2: *Comparison between phase-averaged Reynolds stresses $\overline{u_i u_j}$ obtained directly from the PIV experiment (a) shear and (c) normal, and those evaluated via equation (3) and experimental strain-rate tensor (b) shear and (d) normal at phase $\varphi = 50^o$.*

First order anisotropic eddy-viscosity model

From a degeneration of the Speziale, Sarkar and Gatski second order closure scheme [6], three advection equations are derived to transport the C_{Vi} coefficients as state variables of the physical system, in a similar way as [9] for a non-directional criterion.

For $q = 1, 2, 3$:

$$
\begin{aligned}
\frac{DC_{Vq}}{Dt} &= \left(\frac{4}{3} + c_3^* II_a^{\frac{1}{2}} - c_3 \right) \frac{(V_q)_{ij} S_{ij}}{|\lambda_q^S|} + (2 - 2c_4) \frac{(V_q)_{ij} a_{ik} S_{jk}}{|\lambda_q^S|} - \frac{c_2}{\eta_q} (V_q)_{ij} a_{ik} a_{kj} \\
&+ (2 - 2c_5) \frac{(V_q)_{ij} a_{ik} \Omega_{jk}}{|\lambda_q^S|} + (1 - c_1) \frac{\varepsilon}{k} C_{Vq} + (1 + c_1^*) C_{Vq} a_{ij} S_{ij} + \frac{c_2 II_a}{3\eta_q} \\
&+ \frac{2(c_4 - 1)}{3} \frac{a_{ij} S_{ij}}{|\lambda_q^S|} - \frac{1}{|\lambda_q^S|} \left(a_{ij} \frac{D(V_q)_{ij}}{Dt} + C_{Vq} \frac{D|\lambda_q^S|}{Dt} \right) + D^{C_{Vq}}
\end{aligned}
$$

where $D^{C_{Vq}}$, the diffusion term can be approximated by $D^{C_{Vq}} = \frac{\partial}{\partial x_i} \left(\left(\nu + \frac{(\nu_{tt})_{ij}}{\sigma_{C_{Vq}}} \right) \frac{\partial C_{Vq}}{\partial x_j} \right)$.

$II_a = a_{ij} a_{ij}$, $(V_q)_{ij} = \left(v_q^S\right)_i \left(v_q^S\right)_j$ and the seven constants c_i and c_i^* are those of the SSG DRSM.

3 Numerical implementation and validation test-case: unsteady sperated flow past a NACA0012 airfoil

On the basis of the OES $k - \varepsilon$ turbulence model, the previous transport equations were implemented in the finite volume Navier-Stokes Multi-Block (NSMB) code [10]. The isotropic OES version of the $k - \varepsilon$ two-equation closure scheme is founded on Chien's low Reynolds number model [11] where eddy-diffusivity coefficient and damping function were reconsidered to take into account of the turbulent kinetic energy spectrum modification induced by the extraction of phase-avared quantities in non-equilibrium turbulent configurations.The predictive capacities of the present anisotropic turbulence model are analysed on a well-documented two-dimensional test-case [12], at first. The incompressible unsteady flow past au NACA0012 airfoil at 20° degrees of incidence and Reynolds number 10^5 is simulated by means of the present model.

As presented in Fig. 3, the C_{V_i} criteria transported by the additional equations allow a local modulation of the eddy-diffusion coefficient, leading to specific reductions in highly sheared region and in the near-wake coherent structures. In the far-wake where a certain equilibrium is reached, a uniformisation of the criterion is observed. Comparison between the experimental and computed aerodynamic efforts emphasizes the quality of the anisotropic model. AOES model values are slightly higher than experimental ones and present a significant accuracy compared to Chien's k-ε [11] and OES k-ε [1] models. The relative errors are

Figure 3: *First misalignment criterion C_{V1} and iso-lines of the vorticity $\omega_y = \pm 0.25$ (bold lines), NACA0012 airfoil at 20° degrees of incidence, $R_e = 10^5$ and $M = 0.18$ (NSMB simulation).*

$< 2.5\%$ for the lift coefficient and $< 2\%$ for the drag coefficient, which demonstrates the capacity of the present approach to predict with a high physical reliability this strongly detached turbulent flow.

	$\overline{C_x}$	$\overline{C_z}$
Experiment [12]	0.32	0.75
Chien's k-ε [11]	0.33	0.80
OES k-ε [1]	0.36	0.86
AOES k-ε	0.325	0.77
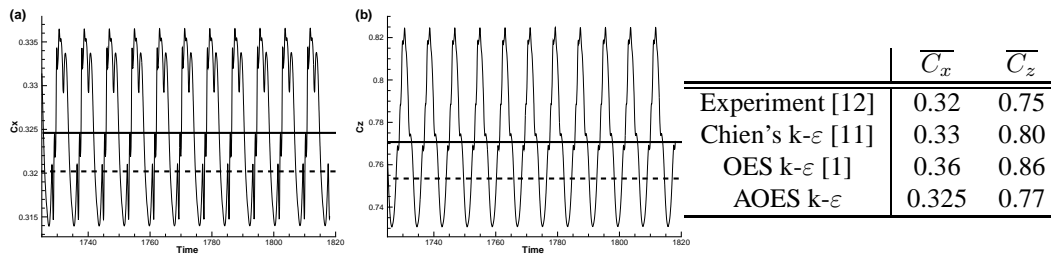
Figure 4: *(a) drag and (b) lift coefficients computed by means of the present anisotropic model (solid curve), time-averaged simulation values (bold solid line) and experimental results (dahsed line). Table comparing the time-averaged aerodynamic coefficients issued from experiment and modelling.*

4 Conclusion and prospects

On the basis of an experimental quantification of the misalignment between the phase-averaged turbulent stresses and the strain-rate tensor in the regions of the coherent vortices, an anisotropic first order eddy-viscosity model was elaborated by means of a tensorial eddy-viscosity concept. The two-dimensional version of this tensorial first order model was validated on a relevant test-case and the comparison of the simulated global aerodynamic coefficients to experimental datas emphasizes the promising predictive capacity of this turbulence modelling approach. The fully three-dimensional version of the present model is being implemented in NSMB solver and the physical relevance of this approach will be examined in strongly detached 3D configurations as the high-Reynolds number cylinder wake flow.

References

[1] M. BRAZA, R. PERRIN and Y. HOARAU. *Turbulence Properties in the cylinder wake at high Reynolds number*. J. Fluids and Structures, 22:755-771, 2006.

[2] J. BOUSSINESQ. *Théorie de l'écoulement tourbillant*. Mém. prés. par div. Sav. à l'Acad. Sci., Paris, 23:46-50, 1877.

[3] P.S. KLEBANOFF. *Characteristics of Turbulence in a Boundary Layer with Zero Pressure Gradient*. NACA Technical Note, 3178, 1954.

[4] G. JIN and M. BRAZA. *A two-equation turbulence model for unsteady separated flows around airfoils*. AIAA J. , 32(11):2316-2320, 1994.

[5] R. BOURGUET, M. BRAZA, R. PERRIN and G. HARRAN. *Anisotropic eddy-viscosity concept for strongly detached unsteady flows*. AIAA J., 45(5):1145-1149, 2007.

[6] C.G. SPEZIALE, S. SARKAR and T.B. GATSKI. *Modeling the pressure strain correlation of turbulence: an invariant dynamical systems approach*. J. Fluid Mech., 227:245-272, 1991.

[7] R. PERRIN, M. BRAZA, E. CID, S. CAZIN, F. MORADEI, A. BARTHET, A. SEVRAIN and Y. HOARAU. *Near-wake turbulence properties in the high Reynolds incompressible flow around a circular cylinder by 2C and 3C PIV*. 6th ERCOFTAC International Symposium on Engineering Turbulence Modelling and Measurements - ETMM6, proceedings, 2005, J. Flow Turb. and Combust, in print.

[8] C.G. SPEZIALE and X.H. XU. *Towards the development of second-order closure models for non-equilibrium turbulent flows*. Int. J. Heat and Fluid Flow, 17:238-244, 1996.

[9] A.J. REVELL, S. BENHAMADOUCHE, T. CRAFT, D. LAURENCE and K. YAQOBI. *A stress-strain lag eddy viscosity model for unsteady mean flow*. Eng. Turb. Model. and Exp., 6:117-126, 2005.

[10] J.B. VOS, A. RIZZI, D. DARRACQ and E.H. HIRSCHEL. *Navier-Stokes solvers in European aircraft design*. Prog. Aero. Sci., 38:601-697, 2002.

[11] K.Y. CHIEN. *Predictions of Channel and Boundary-Layer Flows with a Low-Reynolds-Number Turbulence Model*. AIAA J., 20(1):33-38, 1982.

[12] E. BERTON, D. FAVIER and C. MARESCA. *Progress in Computational Flow-Structure Interaction*. Notes on Numerical Fluid Mechanics, 81, Springer, 2002.

Numerical simulation of the flow in the wake of Ahmed body using Detached Eddy simulation and URANS modeling

G. Martinat[*], Y. Hoarau[**], F. Dehaeze[*], M. Braza[*]

[*] : Institut de mécanique des fluides de Toulouse
[**] : Institut de mécanique des fluides et solides de Strasbourg
martinat@imft.fr

1 Introduction

Because of the complexity of cars aerodynamics and in order to simplify studies, Ahmed car body has become a reference geometry (Ahmed et al, 1984). Past experimental studies have shown that the topology of this complex fully three dimensionnal flow is dependant from the slant angle of the geometry considered.

The Ahmed car body is a nearly rectangular geometry with round bounded front and a slant on the back. When the slant angle is under 30 degrees, the flow has an unsteady topology. Two vortices are created on the side edges of the slant. Over the slant, the flow separates and reattaches later on the slant. Two counter-rotating vortices are created on the rear face of the body. When the slant angle is above 30 degrees, the vortex over the slant doesn't reattach and is then more intense as the sides vortices. For this case, the flow remains steady. Figure 1 shows the evolution of average drag coefficient with the slant angle, we can notice the discontinuity in drag variation ofr slant angle above 30°.

In this study, we will concentrate on the 25° slant angle geometry which is a well documented DESider (EC program in the 6th Framework Programme, under Contract No. AST3-CT-2003-502842) and Ercoftac test case (Experiment from Lienhart et al, 2000). A preliminary study has shown that if classical URANS approaches are able to provide good results for a steady flow (for example in the case of the Ahmed body with a slant angle above 30°), the results are not accurate enough for an unsteady three dimensional flow as examined in this study. In this study, DES and DDES methods will be compared to advanced URANS methods like OES and Menter's SST-SAS models.
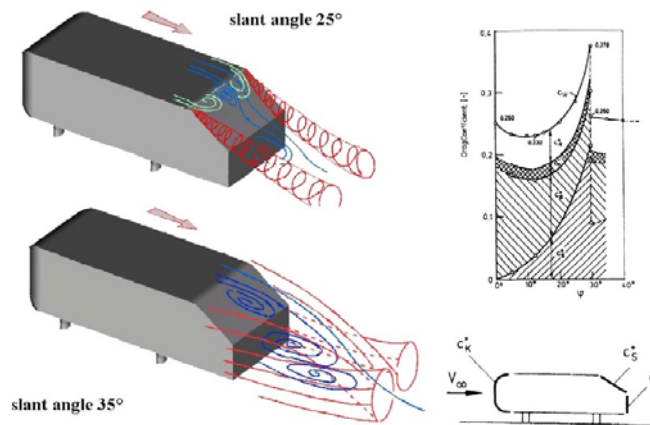
Figure 1: Flow in the wake of the Ahmed car body (left, courtesy of S. Becker and H. Lienhart, LSTM Erlangen), and the drag coefficient of the body, fonction of the slant angle φ (right; from Ahmed and al., 1984)

2 Turbulence modelling

DES modelling

As said in Travin and al, 2000, "*A Detached-Eddy Simulation is a three-dimensionna numerical simulation using a single turbulence model, which functions as a sub-grid scale model in regions where the grid density is fine enough for a Large-Eddy Simulation, and as a Reynolds-Averagemodel in regions where it is not*".

The DES length scale is chosen according to : $l_{DES} = \min(l_{RANS}, C_{DES} \times \Delta)$, where C_{DES} is the DES constant calibrated by means of homogeneous, isotropic turbulence spectrum, and Δ is the largest dimension of the elementary control volume cell, $\Delta = \max(\Delta x, \Delta y, \Delta z)$.

For the one equation Spalart-Allmaras model (Spalart and Allmaras, 1993), it gives :

$$l_{DES} = \min(d_\omega, C_{DES} \times \Delta)$$

where d_ω is the distance from the wall.

DDES modelling

In order to avoid a transition from URANS to LES in the shear layer that could produce non physical artefacts, Spalart et al, (2006) introduced a modification of the *r* parameter of the spalart-allmaras model (Spalart and Allmaras, 1993) in :

$$r_d \equiv \frac{v_t + v}{\sqrt{U_{i,j}U_{j,i}}\,\kappa^2 d^2}$$

By adding v on the numerator they ensure that r_d remains away from 0 in the near wall regions. Then we can write $f_d = 1 - \tanh\left(\left[8r_d\right]^3\right)$ which is 1 away from the wall an 0 in the near wall regions where $r_d \ll 1$. Finally we have : $l_{DES} = d_\omega - f_d \max(0, d_\omega - C_{DES}\Delta)$. If $f_d = 0$, we obtain $l_{DES} = d_\omega$ which yields to RANS modelling and if $f_d = 1$, $l_{DES} = \min\left(d_\omega, C_{DES} \times \Delta\right)$ which yields to the classical DES modelling (Spalart et al, 1997).

OES modelling

The periodic nature of the flow past an oscillating airfoil allows us the definition of phase averaged quantities. The flow is classically decomposed into a mean component, a periodic fluctuation and a random fluctuation (Reynolds, 1971) : $U_i = \overline{U_i} + \widetilde{U_i} + \widetilde{u_i}$. The phase averaged quantities are then : $\langle U_i \rangle = \overline{U_i} + \widetilde{U_i}$ (Cantwell and Coles, 1984).

Due to a non linear interaction of the chaotic structures with the organised structures, the slope of the fluctuation spectrum in the inertial part is different than the one of equilibrium turbulence. As a consequence, the production is not equal to the dissipation like in the RANS equilibrium turbulence modelling, but instead we need to reconsider the turbulence time and length scales.

In this context of advanced URANS methods, EMT2/IMFT has developed the Organised Eddy Simulation (O.E.S) approach (Braza and al,2006). It consists in distinguishing the structures to be resolved from the one to be modelled on the basis of their physical nature, organised or chaotic and not on their size (as this is the case in the LES approach).

From the second order moment closure DRSM of (Launder and al, 1975), a modified two equation model has been derived where the turbulence length scales have been modified in the sense of evaluation of the C_μ eddy diffusion coefficient and of the damping turbulence law towards the wall (Braza and al, 2006 and Jin and Braza, 1994). A schematic representation of OES compared to LES modelling is given in figure 2.

In this context, the isotropic OES modelling is derived from the *k-ε* Chien model (Chien, 1982). The modification for O.E.S are given by the following equations :

$$f_\mu = 1 - \exp(-0.0002\,y^+ - 0.000065\,y^{+2})$$

$$C_\mu = 0.02$$

This model was compared to experimental study provided by LABM laboratory on a NACA0012 at 20° of incidence for a Reynolds number of 10^5
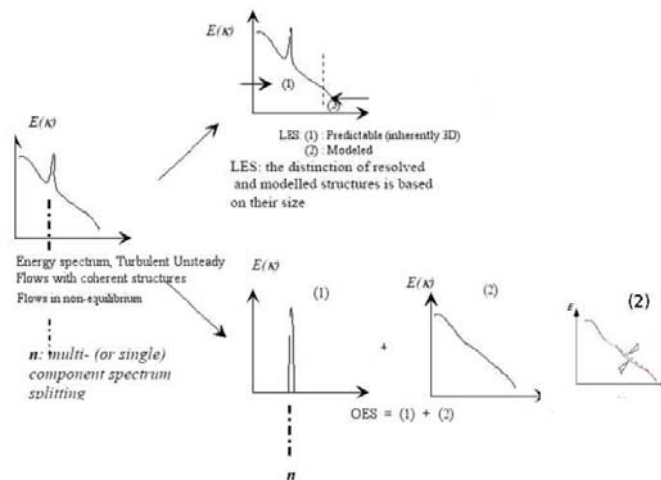

Figure 2 Schematic representation of OES modelling versus URANS and LES approaches

SST-SAS modelling

The following definition is given for Scale Adaptative Simulation in (Menter and Egorov, 2006) :
SAS allow the simulation of unsteady flows with both RANS and LES content in a single model environment. As SAS formulations use the Von Karman length scale as a second external scale, they can automatically adjust to resolved features in the flow. As a result, SAS develops LES-like solution in unsteady regions, without a resort to the local grid spacing. A description of the model and results on some test cases are given in (Menter and Egorov, 2006).

3   Numerical configuration

For all computations, the NSMB (Navier Stokes Multi Blocks, Vos and al, 1998) solver, which is structured compressible solver, is used. Central fourth order space scheme and dual time stepping with second order implicit backwards time-scheme are used. The three million nodes meshgrid was provided by Chalmers thanks to DESider project is shown on figure 3.
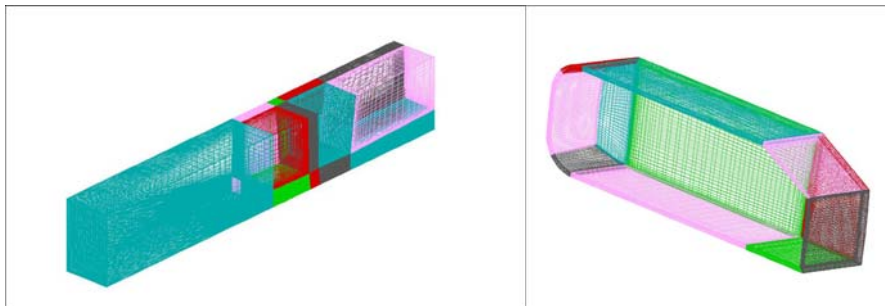
Figure 3 : Slice and close view of the mesh used for computations

4   Results on the 25° slant angle Ahmed car body

e. Figure 5 shows the velocity profiles obtained using DES modelling. The flow separation is overestimated on the slant of the body on U and W velocities. This overestimation could be explained by the fact that the mesh used was originally designed for LES and for that reason is well refined near wall.That near wall refinement could be the reason of a transition from URANS to LES in the boundary layer and then induce a non physical separation. This is confirmed by figure 6 which shows Q criterion surfaces : the DDES computations shows finer structure than the DES computation which shows a flow topology that is close to the steady case.
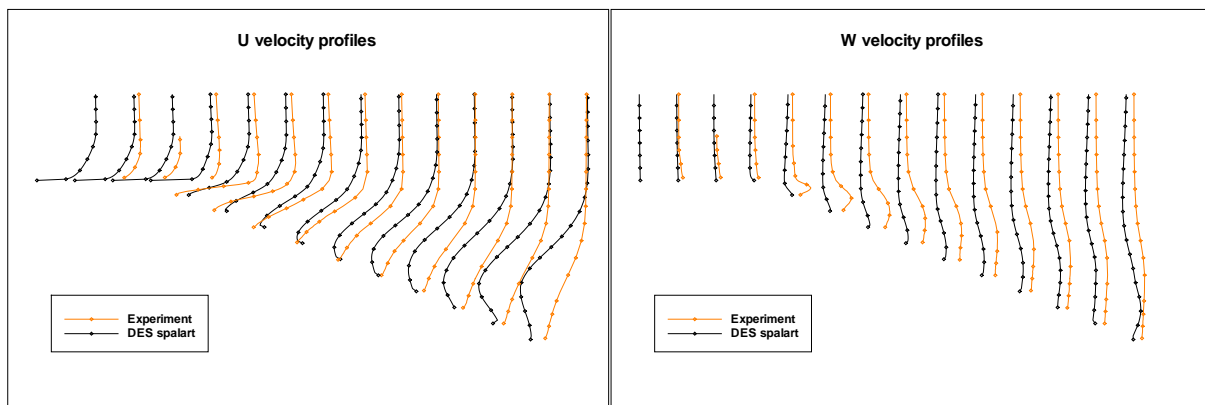
Figure 5 : U and W velocity profiles using DES modelling on 25° Ahmed body.

As average quantities are not completely converged on DDES, OES ans SAS computations, they will not be shown on this paper but are still in progress.

5   Conclusion

In this study, computations using DES, DDES and advanced URANS modelling (Organised Eddy Simulation and SAS modelling) are compared. DES results are promising but the separated region is overestimated probably due to a transition from URANS to LES into the boundary layer. For this reason, DDES should give more accurate results avoiding that transition into the boundary layer and delaying it into a non-separated

region. SAS and OES averaged results are not converge yet to be compared to the experiment but computations are in progress and are expected to give accurate results.
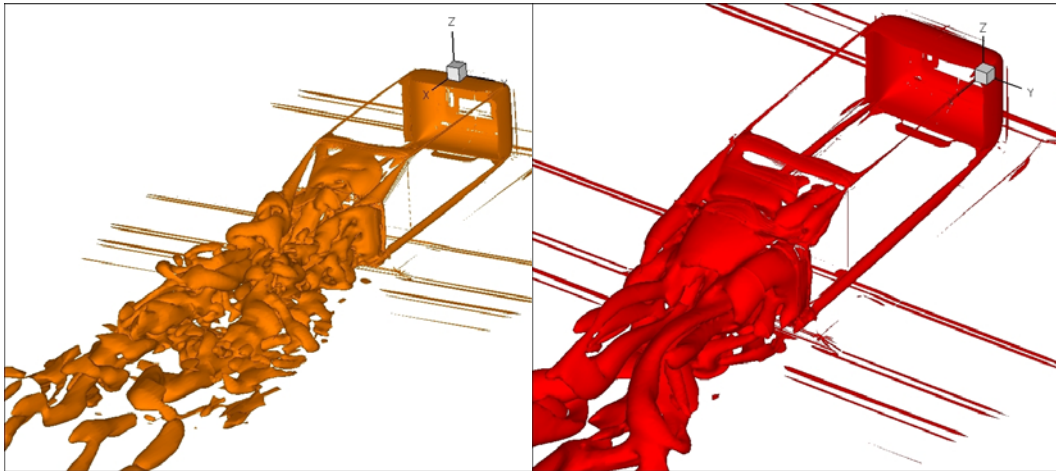

Figure 6 : Q criterion on DDES modelling (left) and DDES modelling (right)

References

Ahmed, S.L. and Ramm, G. (1984) : Some salient features of the averaged ground vehicle wake. SAE technical paper 840300.

Lienhardt, H. and Stoots, C. and Becker, S. (2000) : Flow and turbulence structure in the Wake of a simplified Car model (Ahmed model). DGLR Fach symposium. der AG STAB, Stuttgart university, 15-17nov 2000.

Travin, A. and Shur, M., and Strelets, M. and Spalart P.R. (2000) : Detached eddy simulation past a circular cylinder. Flow, turbulence and combusiton, 63.

Spalart, P.R. and Allmaras, S.R. (1993) : A one equation turbulence modelm for aerodynamics flows. AIAA Paper, 92-0439

Spalart, P.R. and Deck, S. and Shur, M.L. and Squires, K.D. and Srelets, M.Kh and Travin, A. (2006) : A new version of detached eddy simulation, resistant to ambiguous grid densities.

Spalart, P.R. and Jou, W.-H. and Strelets, M. and Allamras, S.R. (1997) : Comments on feasibility of LES for wings, and on a hybrid RANS/LES approach. Proceedings of first AFOSR international conference on DNS/LES, Runston Louisiana. Greyden press.

Reynolds, W.C. and Hussain, A.K.M.F (1971) : The mechanics of an organized wave in turbulent shear flow. Part 3. Theoretical models and comparison with experiments. Journal of fluid mechanics, 54.

Cantwell, B. and Coles, D. (1984): An experimental study of entrainment an transport in the turbulent wake of a circular cylinder. Journal of fluid mechanics, 136.

Braza, M. and Perrin, R. and Hoarau, Y. (2006) : Turbulence properties in the cylinder wake at high Reynolds number. Journal of fluids and structures, 22.

Launder, B.E. and Reece, G.J. and Rodi, W. (1975) : Progress in the development of a Reynolds-stress turbulence closure. Journal of fluid mechanics, 68.

Jin, G. and Braza, M. (1994) : A two equation turbulence modelfor unsteady separated floxs around airfoils. AIAA Journal, 32

Chien, K. (1982) : Prediction of channel and boundary-layer flows with a low Reynolds number turbulence model. AIAA Jounal, 20.

Hoarau, Y. and Braza, M. and Tzabiras, G. and Allain, C. and Berton, E. and Favier, D. and Maresca, C. (2002) : Prediction of turbulent unsteady aerodynamic flows with a pronouced periodic character. Proceedings of IUTAM symposium on unsteady separated flows, Toulouse, France.

Menter, F.R. and Egorov, Y. (2006) : SAS turbulence modelling of technical flows. Direct and Large-Eddy simulation, Springer.

Vos, J. and Chaput, E. and Arlinger, B. and Rizzi, A. and Corjon, A. : Recent advances in aerodynamics inside the nsmb (Navier Stokes Multi Blocks) consortium. AIAA Paper, 1998-0802

Author Index